

REPORT DOCUMENTATION PAGE

AFRL-SR-BL-TR-00-

Public reporting burden for this collection of information is estimated to average 1 hour per response, including the time for reviewing instructions, searching existing data sources, gathering the data, reviewing the collection of information, Send comments regarding this burden estimate or any other aspect of this collection of information, in Operations and Reports, 1215 Jefferson Davis Highway, Suite 1204, Arlington, VA 22202-4302, and to the Office of Management and Budget, Paperwork Project, Washington, DC 20503.

plating and reviewing
rate for Information

0729

1. AGENCY USE ONLY (Leave blank)		2. REPORT DATE December, 1996		3.	
4. TITLE AND SUBTITLE 1996 Summer Research Program (SRP), Summer Faculty Research Program (SFRP), Final Reports, Volume 3A, Phillips Laboratory				5. FUNDING NUMBERS F49620-93-C-0063	
6. AUTHOR(S) Gary Moore					
7. PERFORMING ORGANIZATION NAME(S) AND ADDRESS(ES) Research & Development Laboratories (RDL) 5800 Uplander Way Culver City, CA 90230-6608				8. PERFORMING ORGANIZATION REPORT NUMBER	
9. SPONSORING/MONITORING AGENCY NAME(S) AND ADDRESS(ES) Air Force Office of Scientific Research (AFOSR) 801 N. Randolph St. Arlington, VA 22203-1977				10. SPONSORING/MONITORING AGENCY REPORT NUMBER	
11. SUPPLEMENTARY NOTES					
12a. DISTRIBUTION AVAILABILITY STATEMENT Approved for Public Release				12b. DISTRIBUTION CODE	
13. ABSTRACT (Maximum 200 words) The United States Air Force Summer Research Program (USAF-SRP) is designed to introduce university, college, and technical institute faculty members, graduate students, and high school students to Air Force research. This is accomplished by the faculty members (Summer Faculty Research Program, (SFRP)), graduate students (Graduate Student Research Program (GSRP)), and high school students (High School Apprenticeship Program (HSAP)) being selected on a nationally advertised competitive basis during the summer intersession period to perform research at Air Force Research Laboratory (AFRL) Technical Directorates, Air Force Air Logistics Centers (ALC), and other AF Laboratories. This volume consists of a program overview, program management statistics, and the final technical reports from the SFRP participants at the Phillips Laboratory.					
14. SUBJECT TERMS Air Force Research, Air Force, Engineering, Laboratories, Reports, Summer, Universities, Faculty, Graduate Student, High School Student				15. NUMBER OF PAGES	
				16. PRICE CODE	
17. SECURITY CLASSIFICATION OF REPORT Unclassified	18. SECURITY CLASSIFICATION OF THIS PAGE Unclassified	19. SECURITY CLASSIFICATION OF ABSTRACT Unclassified	20. LIMITATION OF ABSTRACT UL		

UNITED STATES AIR FORCE
SUMMER RESEARCH PROGRAM -- 1996
SUMMER FACULTY RESEARCH PROGRAM FINAL REPORTS

VOLUME 3A

PHILLIPS LABORATORY

RESEARCH & DEVELOPMENT LABORATORIES

5800 Uplander Way
Culver City, CA 90230-6608

Program Director, RDL
Gary Moore

Program Manager, AFOSR
Major Linda Steel-Goodwin

Program Manager, RDL
Scott Licoscas

Program Administrator, RDL
Johnetta Thompson

Program Administrator
Rebecca Kelly

Submitted to:

AIR FORCE OFFICE OF SCIENTIFIC RESEARCH

Bolling Air Force Base

Washington, D.C.

December 1996

20010321 047

AAM 01-06-1293

PREFACE

Reports in this volume are numbered consecutively beginning with number 1. Each report is paginated with the report number followed by consecutive page numbers, e.g., 1-1, 1-2, 1-3; 2-1, 2-2, 2-3.

Due to its length, Volume 3 is bound in two parts, 3A and 3B. Volume 3A contains #1-22. Volume 3B contains reports #23-37. The Table of Contents for Volume 3 is included in both parts.

This document is one of a set of 16 volumes describing the 1996 AFOSR Summer Research Program. The following volumes comprise the set:

VOLUME

TITLE

1	Program Management Report
	<i>Summer Faculty Research Program (SFRP) Reports</i>
2A & 2B	Armstrong Laboratory
3A & 3B	Phillips Laboratory
4	Rome Laboratory
5A, 5B & 5C	Wright Laboratory
6	Arnold Engineering Development Center, Wilford Hall Medical Center and Air Logistics Centers
	<i>Graduate Student Research Program (GSRP) Reports</i>
7A & 7B	Armstrong Laboratory
8	Phillips Laboratory
9	Rome Laboratory
10A & 10B	Wright Laboratory
11	Arnold Engineering Development Center, United States Air Force Academy, Wilford Hall Medical Center, and Wright Patterson Medical Center
	<i>High School Apprenticeship Program (HSAP) Reports</i>
12A & 12B	Armstrong Laboratory
13	Phillips Laboratory
14	Rome Laboratory
15A&15B	Wright Laboratory
16	Arnold Engineering Development Center

SFRP FINAL REPORT TABLE OF CONTENTS

i-xviii

1. INTRODUCTION	1
2. PARTICIPATION IN THE SUMMER RESEARCH PROGRAM	2
3. RECRUITING AND SELECTION	3
4. SITE VISITS	4
5. HBCU/MI PARTICIPATION	4
6. SRP FUNDING SOURCES	5
7. COMPENSATION FOR PARTICIPATIONS	5
8. CONTENTS OF THE 1996 REPORT	6

APPENDICIES:

A. PROGRAM STATISTICAL SUMMARY	A-1
B. SRP EVALUATION RESPONSES	B-1

SFRP FINAL REPORTS

SRP Final Report Table of Contents

Author	University/Institution Report Title	Armstrong Laboratory Directorate	Vol-Page
DR Richelle M Allen-King	Washington State University , Pullman , WA Reduction Kinetics in a Batch Metallic Iron/Water System:Effect of Iron/Water Exposure	AL/EQC _____	2- 1
DR Anthony R Andrews	Ohio University , Athens , OH Investigation of the Electrochemiluminescent Properties of Several Natural & Synthetic Compounds	AL/EQC _____	2- 2
DR Deborah L Armstrong	Univ of Texas at San Antonio , San Antonio , TX Development of A primary Cell Culture Preparation for Studying Mechanisms Governi ng Circadian Rhyth	AL/CFTO _____	2- 3
DR Robert L Armstrong	New Mexico State University , Las Cruces , NM Microparticle Bioluminescence	AL/CFD _____	2- 4
DR Maureen E Bronson	Wilkes Univ School of Pharmacy , Wilkes-Barre , PA Lack of Effect of UltraWideband Radiation on Pentylenetetrazol-Induced Convulsions in Rats	AL/OER _____	2- 5
DR Marc L Carter, PhD, PA	University of South Florida , Tampa , FL Assessment of the Reliability of Ground-Based Observers for the Detection of Aircraft	AL/OEO _____	2- 6
DR Jer-Sen Chen	Wright State University , Dayton , OH A Study of Data Compression Based on Human Visual Perception	AL/CFHV _____	2- 7
DR Cheng Cheng	Johns Hopkins University , Baltimore , MD Sequential Optimization Algorithm for Personnel Assignmt Based on Cut-Off Profiles & Rev of Brogden	AL/HRM _____	2- 8
DR Elizabeth T Davis	Georgia Institute of Tech , Atlanta , GA Perceptual Issues in Virtual Environments & Other Simulated Displays	AL/CFHP _____	2- 9
DR Keith F Eckerman	Univ of Tennessee , Knoxville , TN	AL/OEB _____	2- 10
DR Paul A Edwards	Edinboro Univ of Pennsylvania , Edinboro , PA A Viartion Fuel Identification- Neural Network Analysis of the Concentration of Benzene and Naphtha	AL/EQC _____	2- 11

Author	University/Institution Report Title	Armstrong Laboratory Directorate	Vol-Page
DR Randolph D Glickman	Univ of Texas Health Science Center , San Antonio , TX A Study of Oxidative Reactions Mediated by Laser-Excited Ocular Melanin	AL/OEO	2- 12
DR Ellen L Glickman-Weiss	Kent State University , Kent , OH The Effect of Short Duration Respiratory Musculature Training on Tactical Air Combat	AL/CFTF	2- 13
DR Irwin S Goldberg	St. Mary's Univ of San Antonio , San Antonio , TX Development of a Physiologically-Based Pharmacokinetic Model for the Uptake of Volatile Chemicals	AL/OES	2- 14
DR Robert J Hirko	University of Florida , Gainesville , FL Investigation of The Suitability of Tactile and Auditory Stimuli for use in Brain Actuated Control	AL/CFHP	2- 15
ISU VPP Acct4212313(Dooley)	Iowa State University , Ames , IA Determination of the Influence of Ultrawideband Exposure of Rts During Early Pregnancy on Pregnancy	AL/OER	2- 16
DR Andrew E Jackson	Arizona State University , Tempe , AZ A Description of Integrated Joint Use Initiatives to Satisfy Customer Reqmts Across Govt Academia	AL/HRA	2- 17
DR John E Kalns	Ohio State University , Columbus , OH	AL/AOHR	2- 18
DR Nandini Kannan	Univ of Texas at San Antonio , San Antonio , TX Modeling Decompression Sickness Using Survival Analysis Techniques	AL/CFTS	2- 19
DR Antti J Koivo	Purdue Research Foundation , West Lafayette , IN Skill Evaluation of Human Operators	AL/CFBA	2- 20
DR Suk B Kong	Incarnate Word College , San Antonio , TX Aromatic Hydrocarbon Components in Diesel, Jet-A And JP-8 Fuels	AL/OEA	2- 21
DR Xuan Kong	Northern Illinois University , De Kalb , IL Mental Workload Classification via Physiological Signal Processing: EOG & EEG Analyses	AL/CFHP	2- 22

SRP Final Report Table of Contents

Author	University/Institution Report Title	Armstrong Laboratory Directorate	Vol-Page
DR Charles S Lessard	Texas A & M Univ-College Station , College Station , TX Preliminary Studies of Human Electroencephalogram (EEG) Correlates of GzAcceleration Tolerance	AL/CFTO	2- 23
DR Audrey D Levine	Utah State University , Logan , UT Biogeochemical Assessment of Natural Attenuation of JP-4 Contaminated Ground Water	AL/EQC	2- 24
DR David A Ludwig	Univ of N.C. at Greensboro , Greensboro , NC The Illusion of Control & Precision Associated w/Baseline Comparisons	AL/AOCY	2- 25
DR Robert G Main	Cal State Univ, Chico , Chico , CA Designing Instruction For Distance Learning	AL/HRT	2- 26
DR Phillip H Marshall	Texas Tech University , Lubbock , TX Time to Contact Judgments in The Presence of Static and Dynamic Objects: A Preliminary Report	AL/HRM	2- 27
MS Sandra L McAlister	Stonehill College , North Easton , MA	AL/AO	2- 28
MR Bruce V Mutter	Bluefield State College , Bluefield , WV Environmental Cost Analysis:Calculating Return on Investment for Emerging Technologies	AL/EQP	2- 29
DR Sundaram Narayanan	Wright State University , Dayton , OH Java-Based Application of the Model-View-Controller Framwork in Developing Interfaces to interactive	AL/HRT	2- 30
DR Karl A Perusich	Purdue University , South Bend , IN Examining Alternate Entry Points in a Problem Using Fuzzy Cognitive Maps	AL/CFHI	2- 31
DR Judy L Ratliff	Murray State Univ , Murray , KY A Study of The Ability of Tunicates to be used as Global Bioindicators	AL/EQC	2- 32
DR Paul D Retzlaff	Univ of Northern Colorado , Greeley , CO Computerized Neuropsychological Assessment of USAF Pilots	AL/AOCN	2- 33

SRP Final Report Table of Contents

Author	University/Institution Report Title	Armstrong Laboratory Directorate	Vol-Page
DR William G Rixey	University of Houston , Houston , TX The use of Solid-Phase Microextraction (SPME) for the low level Detection of BTEX and PAHs In Aqueou	AL/EQC	2- 34
DR Ali M Sadegh	CUNY-City College , New York , NY Investigation of Neck Models for Predicting Human Tolerance to Accelerations	AL/CFBE	2- 35
DR Kandasamy Selvavel	Claflin College , Orangeburg , SC Truncated Bivariate Exponential Models	AL/AOEP	2- 36
DR Barth F Smets	University of Connecticut , Storrs , CT Biodegradation of 2-4-DNTand 2,6-DNT in Mixed Culture Aerobic Fluidized Bed Reactor and Chemostat	AL/EQC	2- 37
DR Mary Alice Smith	University of Georgia , Athens , GA A Study of Apoptosis During Limb Development	AL/OET	2- 38
DR Daniel P Smith	Utah State University , Logan , UT Bioremediation & its Effect on Toxicity	AL/EQW	2- 39
MR. Joseph M Stauffer	Indiana State University , Terre Haute , IN Joint Corrections for Correlation Coefficients	AL/HRMA	2- 40
DR William B Stavino	Univ of Texas Health Science Center , San Antonio , TX Studies to Identify Characterisctic Changes in the Urine Following Ingestion of Poppy seed	AL/AOT	2- 41
DR William A Stock	Arizona State University , Tempe , AZ Application of Meta-Analysis to Research on Pilot Training	AL/HRA	2- 42
DR Nancy J Stone	Creighton University , Omaha , NE Engagement, Involvement, and Self-Regualted Learnign Construct and Measurement Development to Asses	AL/HRT	2- 43
DR Brenda M Sugrue	Univ of Northern Colorado , Greeley , CO Aptitude-Attribute Interactions in Test Performance	AL/HRTI	2- 44

SRP Final Report Table of Contents

Author	University/Institution Report Title	Armstrong Laboratory Directorate	Vol-Page
DR Stephen A Truhon	Winston-Salem State University, Winston-Salem, NC Mechanical Specialties in the U.S. Air Force: Accession Quality & Selection Test Validity	AL/HRM	2 - 45
DR Mariusz Ziejewski	North Dakota State University, Fargo, ND Validation of the Deformable Neck Model for A +Gz Acceleration	AL/CFBV	2 - 46

SRP Final Report Table of Contents

Author	University/Institution Report Title	Phillips Laboratory Directorate	Vol-Page
DR Graham R Allan	New Mexico Highlands University, Las Vegas, NM Temporal and Spatial Characterization of a Synchronously-Pumped Periodically-Poled Lithium Niobate Optical	PL/LIDN	3 - 1
DR Brian P Beecken	Bethel College, St. Paul, MN Testing of a Dual-Band Infrared Focal Plane Array & An Infrared Camera Sys	PL/VTRP	3 - 2
DR Mikhail S Belen'kii	Georgia Inst of Technology, Atlanta, GA Tilt Sensing Technique w/Small Aperture Beam & Related Physical Phenomena	PL/LIG	3 - 3
DR Asoke K Bhattacharyya	Lincoln University, Jefferson City, MO Part A: Effect of Earth's Surface & Loss on the Resonant Frequencies of Buried Objects	PL/WSQ	3 - 4
DR Joseph M Calo	Brown University, Providence, RI Transient Studies of the Effects of Fire Suppressants in a Well-Stirred Combustor	PL/GPID	3 - 5
DR James J Carroll	Youngstown State University, Youngstown, OH Examination of Critical Issues in the use of (178) hf For High Energy Density Applications	PL/WSQ	3 - 6
DR Soyoung S Cha	Univ of Illinois at Chicago, Chicago, IL A Study on Hartmann Sensor Application to Flow Aero-Optics Investigation Through Tomographic Recons	PL/LIMS	3 - 7
DR Tsuchin Chu	Southern Illinois Univ-Carbondale, Carbondale, IL	PL/RKS	3 - 8
DR Kenneth Davies	Univ of Colorado at Boulder, Boulder, CO Studies of Ionospheric Electron contents and High-Frequency Radio Propagation	PL/GPIM	3 - 9
DR Judith E Dayhoff	Univ of Maryland, College Park, MD Dynamic Neural Networks: Prediction of an Air Jet Flowfield	PL/LIMS	3 - 10
DR Ronald R DeLyser	University of Denver, Denver, CO Analysis of Complex Cavities Using the Finite Difference Time Domain Method	PL/WSTS	3 - 11
DR Andrew G Detwiler	S Dakota School of Mines/Tech, Rapid City, SD Evaluation of Engine-Related Factors Influencing Contrail Prediction	PL/GPAB	3 - 12
DR Itzhak Dotan	The Open University of Israel, Tel-Aviv Israel Studies of Ion-Molecule Reaction Rates at Very High Temperatures	PL/GPID	3 - 13

SRP Final Report Table of Contents

Author	University/Institution Report Title	Phillips Laboratory Directorate	Vol-Page
DR Omar S Es-Said	Loyola Marymount University, Los Angeles, CA On the Matis Selection of Durable Coatings for Cryogenic Engineer Technology	PL/RKE	3 - 14
DR Jeffrey F Friedman	University of Puerto Rico, Mayaguez, PR Testing the Frozen Screen Model of Atmospheric Turbulence	PL/LIMI	3 - 15
DR John A Guthrie	University of Central Oklahoma, Edmond, OK Ultrawide-Band Microwave Effects Testing on an Electronic System	PL/WSMA	3 - 16
DR George W Hanson	Univ of Wisconsin - Milwaukee, WI A Volumetric Eigenmode Expansion Method for Dielectric Bodies	PL/WSQ	3 - 17
DR Mayer Humi	Worcester Polytechnic Inst., Worcester, MA Wavelets and Their Applications to the Analysis of Meteorological Data	PL/GPAA	3 - 18
DR Christopher H Jenkins	S Dakota School of Mines/Tec, Rapid City, SD Shape Control of An Inflated Thin Circular Disk	PL/VT	3 - 19
DR Dikshitulu K Kalluri	University of Lowell, Lowell, MA Electromagnetic Wave Transformation in a Two-Dimensional-Space-Varying and Time-Varying Magnetoplasma	PL/GPIA	3 - 20
DR Aravinda Kar	University of Central Florida, Orlando, FL Thick Section Cutting w/Chemical Oxygen-Iodine Laser & Scaling Laws	PL/LIDB	3 - 21
DR Spencer P Kuo	Polytechnic University, Farmingdale, NY Theory of Electron Acceleration by HF-Excited Langmuir Waves	PL/GPI	3 - 23
DR Andre Y Lee	Michigan State University, East Lansing, MI Characterization Methods for Adhesion Strength Between Polymers & Ceramics	PL/RKS	3 - 24
DR Bruce W Liby	Manhattan College, Riverdale, NY Acousto-Optic Retro-Modulator	PL/VTRA	3 - 25
DR Feng-Bao Lin	Polytechnic Inst of New York, Brooklyn, NY Structural Ballistic Risk Assessment-Fracture Modeling	PL/RKEM	3 - 26
DR M Arfin K Lodhi	Texas Tech University, Lubbock, TX Theory, Modeling & Analysis of AMTEC	PL/VTP	3 - 27

SRP Final Report Table of Contents

Author	University/Institution Report Title	Phillips Laboratory Directorate	Vol-Page
DR Ronald A Madler	Embry-Riddle Aeronautical University, Prescott, AZ Estimating the Area of Artificial Space Debris	PL/WSAT	3 - 28
DR Carlos A Ordonez	University of North Texas, Denton, TX Boundary Conditions at A Plasma-Facing Surface	PL/WSQA	3 - 29
DR Michael J Pangia	Georgia Southwestern Coll, Americus, GA Further Analysis of Kilohertz Order Waves Associated with Electron Beam Operations on STS46	PL/GPSG	3 - 30
DR Ronald M Pickett	University of Lowell, Lowell, MA Temporal-Displacement Stereograms of the Ionosphere: An Exploration of Their Utility in the Analysis of Equatorial Emission Depletion Bands	PL/GPIA	3 - 31
DR Edgar Sanchez-Sinencio	Texas A&M Univ-College Station, College Station, TX Low Voltage Analog Circuit Design for Radiation Tolerance	PL/VTER	3 - 32
DR Joseph C Slater	Wright State University, Dayton, OH Smart Structure/Actuator Modeling 7 Design for the Integrated Ground Demonstration Lab	PL/VTI	3 - 33
DR Ashok Srivastava	Louisiana State University, Baton Rouge, LA Modeling of Total Dose Response of SOI N-MOSFETS for Low Power CMOS Circuits	PL/VTER	3 - 34
DR James M Stiles	University of Kansas, Lawrence, KS The Potential Applications of Super-Resolution & Array Processing to Space-Based Radars	PL/VTRA	3 - 35
DR Charles M Swenson	Utah State University, Logan, UT Balloon Launch Retromodulator Experiment	PL/VTRA	3 - 36
DR Miguel Velez-Reyes	University of Puerto Rico, Mayaguez, PR Regularization Methods for Linear and Nonlinear Retrieval Problems	PL/GPAS	3 - 37

SRP Final Report Table of Contents

Author	University/Institution Report Title	Rome Laboratory Directorate	Vol-Page
DR A F Anwar	University of Connecticut, Storrs, CT A Study of Quantum Wells Formed in Al _x Ga _{1-x} As _y Sb _{1-y} /In _z Ga _{1-z} As/Al _x Ga _{1-x} As _y Sb _{1-y} Heterostructures	RL/ER	4 - 1
DR Ercument Arvas	Syracuse University, Syracuse, NY An Assessment of the Current State of the Art of Stap from an Electromagnetics Point of View	RL/OCSS	4 - 2
DR Ahmed E Barbour	Georgia Southern University, Statesboro, GA Formal Verification Using ORA Larch/VHDL Theorem Prover	RL/ERDD	4 - 3
DR Milica Barjaktarovic	Wilkes University, Wilkes Barre, PA Formal Specification and Verification of Missi Architecture Using Spin	RL/C3AB	4 - 4
DR Daniel C Bukofzer	Cal State Univ, Fresno, Fresno, CA Performance Analysis & Simulation Results of Delay & Spread Spectrum Modulated Flip Wave-Signal Gene	RL/C3BA	4 - 5
DR Xuesheng Chen	Wheaton College, Norton, MA Optical and Non-Destructive Methods to Determine the Composition and Thickness of an IN _x GA _{1-x} AS/INP	RL/ERX	4 - 6
DR Jun Chen	Rochester Inst of Technology, Rochester, NY A Study of Optoelectronic Feedback-Sustained Pulsation of Laser Diodes at 1300 nm & 780 nm	RL/OCPA	4 - 7
DR Everett E Crisman	Brown University, Providence, RI Evaluation of Semiconductor Configurations as Sources for Optically Induced Microwave Pulses	RL/ERAC	4 - 8
DR Digendra K Das	SUNYIT, Utica, NY Techniques for Determining of the Precision of Reliability Predictions and Assessments.	RL/ERSR	4 - 9
DR Matthew E Edwards	Spelman College, Atlanta, Ga The Analysis of PROFILER for Modeling the Diffusion of Aluminum-Copper on a Silicon Substrate	RL/ERDR	4 - 10
DR Kaliappan Gopalan	Purdue University - Calumet, Hammond, IN Speaker Identification & Analysis of Stressed Speech	RL/IRAA	4 - 11
DR Joseph W Haus	Rensselaer Polytechnic Institute, Troy, NY Mode-Locked Laser Models and Simulations	RL/OCPA	4 - 12

SRP Final Report Table of Contents

Author	University/Institution Report Title	Rome Laboratory Directorate	Vol-Page
DR James P LeBlanc	New Mexico State University, Las Cruces, NM Multichannel Autoregressive Modeling & Spectral Estimation Methods for Airborne Radar Environment	RL/OCSS	4 - 13
DR David J McLaughlin	Northeastern University, Boston, MA A Review of Microwave Terrain Clutter Measurements at Bistatic	RL/ERCS	4 - 14
DR Hrushikesh N Mhaskar	Cal State Univ, Los Angeles, Los Angeles, Ca Neural Beam Steering & Direction Finding	RL/ERAA	4 - 15
DR Ronald W Noel	Rensselaer Polytechnic Institute, Troy, NY A Low Dimensional Categorization Technique for C Source Code	RL/C3CA	4 - 16
DR Jeffrey B Norman	Vassar College, Poughkeepsie, NY Frequency Response of Semiconductor Photorefractive Matls: ZnTe:Mn:V, GaAs:Cr, & CdMnTe:V	RL/OCPA	4 - 17
DR Glenn E Prescott	University of Kansas Center for Research, Lawrence, KS Rapid Prototyping of Software Radio Sys Using Field Programmable Gate Arrays & DSP Microprocessors	RL/C3BB	4 - 18
DR Mark R Purtill	Texas A&M Univ-Kingsville, Kingsville, TX A Network Flow Heuristic for Graph Mapping	RL/C3CB	4 - 19
DR Mysore R Rao	Rochester Inst. Of Technology, Rochester, NY Detection of Concealed Objects in Images: Investigation into Wavelet Transform Based Object Isolation Techniques	RL/OCSM	4 - 20
DR Scott E Spetka	SUNY of Tech Utica, Utica, NY Integrating a Multimedia Database & WWW Indexing Tools	RL/IRD	4 - 21
DR Gang Sun	University of Massachusetts-Boston, Boston, MA Confined Optical Phonon Modes in Si/ZnS Superlattices	RL/EROC	4 - 22

SRP Final Report Table of Contents

Author	University/Institution Report Title	Wright Laboratory Directorate	Vol-Page
DR Mohammad S Alam	Purdue University, Fort Wayne, IN Fast Infrared Image Registration and High Resolution Reconstruction for Real Time Applications	WL/AAJT	5 - 1
DR Dominick Andrisani II	Purdue University, West Lafayette, IN A Fast Fourier Transform Analysis of Pilot Induced Oscillations	WL/FIGC	5 - 2
DR Pnina Ari-Gur	Western Michigan University, Kalamazoo, MI Texture and Microstructure of Hot Rolled Ti-6Al-4V	WL/MLLN	5 - 3
DR James D Baldwin	University of Oklahoma, Norman, OK Statistical Analysis of Fatigue Crack Growth Rate Data for 7075-T6 Aluminum Damaged by Prior Corrosion	WL/FIB	5 - 4
DR Armando R Barreto	Florida International Univ, Miami, FL Deconvolution of The Space-Time Radar Spectrum	WL/AAMR	5 - 5
MR Larry A Beardsley	Univ of Texas at Austin, Austin, TX The Use of Wavelets and Neural Networks in Data Compression, Data Fusion and Their Effects on Target Identification	WL/MNGA	5 - 6
DR Raj K Bhatnagar	University of Cincinnati, Cincinnati, OH Variable Width Template Construction for ATR with HRR Data	WL/AACR	5 - 7
DR Alley C Butler	University of Cincinnati, Cincinnati, OH Importance of Current Crowding and Self-Heating in a CdS/LaS Cold Cathode	WL/MLIM	5 - 9
DR Reaz A Chaudhuri	University of Utah, Salt Lake City, UT A Novel Compatibility/Equilibrium Based Iterative Post-Processing Approach for Axisymmetric Brittle	WL/MLBM	5 - 11
DR Julian Cheung	New York Inst. Of Technology, New York, NY New Techniques for Non-Cooperative Target Identification	WL/AACT	5 - 12
DR Milton Cone	Embry-Riddle Aeronautical University, Prescott, AZ Of Match Maker and Metrics	WL/AACF	5 - 13
DR Robert R Criss	Randolph-Macon Woman's College, Lynchburg, VA Optical Studies of Two Novel Electro-Explosive Devices	WL/MNMF	5 - 14

SRP Final Report Table of Contents

Author	University/Institution Report Title	Wright Laboratory Directorate	Vol-Page
DR Robert J DeAngelis	Univ of Nebraska - Lincoln, Lincoln, NE Granin Size Effects in the Determination of X-Ray Pole figures and Orientation Distribution Function	WL/MNM	5 - 15
DR Yujie J Ding	Bowling Green State University, Bowling Green, OH Investigation of Photoluminescence Intensity Saturation and Decay, and Nonlinear Optical Devices in Semiconductor Structures	WL/AADP	5 - 16
DR Gregory S Elliott	Rutgers State Univ of New Jersey, Piscataway, NJ Laser Based Diagnostic Techniques for Combustion and Compressible Flows	WL/POPT	5 - 17
DR Altan M Ferendeci	University of Cincinnati, Cincinnati, OH Vertical 3-D Interconnects for Multichip Modules	WL/AADI	5 - 18
DR Dennis R Flentge	Cedarville College, Cedarville, OH Kinetic Studies of the Thermal Decomposition of Demnum and X-1P Using the System for Thermal Diagnostic Studies (STDS)	WL/POSL	5 - 19
DR Himansu M Gajiwala	Tuskegee University, Tuskegee, AL Novel Approach for the Compressive Strength Improvement of Rigid Rod Polymers	WL/MLBP	5 - 20
DR Allen G Greenwood	Mississippi State University, Mississippi State, MS A Framework for Manufacturing-Oriented, Design-Directed Cost Estimation	WL/MTI	5 - 21
DR Rita A Gregory	Georgia Inst of Technology, Atlanta, GA Affects of Int'l Quality Standards on Bare Base Waste Disposal Alternatives	WL/FIVC	5 - 22
DR Michael A Grinfeld	Rutgers University, Piscataway, Piscataway, NJ Mismatch Stresses, Lamellar Microstructure & Mech	WL/MLLM	5 - 23
DR Awatef A Hamed	University of Cincinnati, Cincinnati, OH Inlet Distortion Test Considerations for High Cycle Fatigue in Gas Turbine Engines	WL/FIM	5 - 24
DR Stewart M Harris	SUNY Stony Brook, Stony Brook, NY Compositional Modulation During Epitaxial Growth of Some III-V Heterostructures	WL/MLPO	5 - 25
DR Larry S Helmick	Cedarville College, Cedarville, OH Effect of Humidity on Wear of M-50 Steel with a Krytox Lubricant	WL/MLBT	5 - 26
DR Kenneth L Hensley	University of Oklahoma, Norman, OK Hyperbaric Oxygen Effects on the Postischemic Brain	MED/SGP	5 - 27

SRP Final Report Table of Contents

Author	University/Institution Report Title	Wright Laboratory Directorate	Vol-Page
DR Iqbal Husain	University of Akron, Akron, OH Fault Analysis & Excitation Requirements for Switched Reluctance Starter-Generators	WL/POOC	5 - 28
DR David W Johnson	University of Dayton, Dayton, OH In Situ Formation of Standards for the Determination of Wear Metals in Perfluoropolyalkylether Lubricating Oils	WL/MLBT	5 - 29
DR Marian K Kazimierczuk	Wright State University, Dayton, OH Aircraft Super Capacitor Back-Up System	WL/POOC	5 - 30
DR Edward T Knobbe	Oklahoma State University, Stillwater, OK Corrosion Resistant Sol-Gel Coatings for Aircraft Aluminum Alloys	WL/MLBT	5 - 31
DR Michael C Larson	Tulane University, New Orleans, LA Cracks at Interfaces in Brittle Matrix Composites	WL/MLLM	5 - 32
DR Douglas A Lawrence	Ohio University, Athens, OH Analysis & Design of Gain Scheduled Missile Autopilots	WL/MNAG	5 - 33
DR Junghsen Lieh	Wright State University, Dayton, OH Determination of 3D Deformations, Forces and Moments of Aircraft Tires with a Synchronized Optical and Analog System	WL/FIVM	5 - 34
DR Chun-Shin Lin	Univ of Missouri - Columbia, Columbia, MO Neural Network Technology for Pilot-Vehicle Interface & Decision Aids	WL/FIGP	5 - 35
DR Zongli Lin	SUNY Stony Brook, Stony Brook, NY Control of Linear Sys with Saturating Actuators with Applications to Flight Control Systems	WL/FI	5 - 36
DR Kuo-Chi Lin	University of Central Florida, Orlando, FL Study on Dead Reckoning Translation in High Level Architecture	WL/AASE	5 - 37
DR James S Marsh	University of West Florida, Pensacola, FL A Conceptual Model for Holographic Reconstruction & Minimizing Aberrations During Reconstruction	WL/MNSI	5 - 38
DR Paul Marshall	University of North Texas, Denton, TX Computational Studies of the Reactions of CH3I With H and OH	WL/MLBT	5 - 39

SRP Final Report Table of Contents

Author	University/Institution Report Title	Wright Laboratory Directorate	Vol-Page
DR Hui Meng	Kansas State University, Manhattan, KS Investigation of Holographic PIV and Holographic Visualization techniques for Fluid Flows and Flames	WL/POSC	5 - 40
DR Douglas J Miller	Cedarville College, Cedarville, OH Band Gap Calculations on Oligomers with an All-Carbon Backbone	WL/MLBP	5 - 41
DR Ravi K Nadella	Wilberforce University, Wilberforce, OH Hydrogen & Helium Ion Implantations for Obtaining High-Resistance Layers in N-Type 4H Silicon Carbide	WL/MLPO	5 - 42
DR Krishna Naishadham	Wright State University, Dayton, OH Hydrogen & Helium Ion Implantations for Obtaining High-Resistance Layers in N-Type 4H Silicon	WL/MLPO	5 - 43
DR Timothy S Newman	Univ of Alabama at Huntsville, Huntsville, All A Summer Faculty Project for Anatomical Feature Extraction for Registration of Multiple Modalities of Brain MR	WL/AACR	5 - 44
DR Mohammed Y Niamat	University of Toledo, Toledo, OH FPGA Implementation of the Xpatch Ray Tracer	WL/AAST	5 - 45
DR James L Noyes	Wittenberg University, Springfield, OH The Development of New Learning Algorithms	WL/AACF	5 - 46
DR Anthony C Okafor	University of Missouri - Rolla, Rolla, MO Assessment of Developments in Machine Tool Technology	WL/MTI	5 - 47
DR Paul D Orkwis	University of Cincinnati, Cincinnati, OH Assessing the Suitability of the CFD++ Algorithm for Advanced Propulsion Concept simulations	WL/POPS	5 - 48
Dr Robert P Penno	University of Dayton, Dayton, OH Grating Lobes in Antenna Arrays	WL/AAMP	5 - 49
DR George A Petersson	Wesleyan University, Middletown, CT Absolute Rates for Chemical Reactions	WL/MLBT	5 - 50
DR Mohamed N Rahaman	University of Missouri - Rolla, Rolla, MO Effect of Solid Solution Additives on the Densification & Creep of Granular Ceramics	WL/MLLN	5 - 51

SRP Final Report Table of Contents

Author	University/Institution Report Title	Wright Laboratory Directorate	Vol-Page
DR Martin Schwartz	University of North Texas, Denton, TX AB Initio Modeling of the Enthalpies of Formation of Fluorocarbons	WL/MLBT	5 - 52
DR Thomas E Skinner	Wright State University, Dayton, OH A Method for Studying Changes in Tissue Energetics Resulting from Hyperbaric Oxygen Therapy	MED/SGP	5 - 53
DR Marek Skowronski	Carnegie Melon University, Pittsburgh, PA Investigation of Structural Defects in 4H-SiC Wafers	WL/MLPO	5 - 54
DR Grant D Smith	Univ of Missouri - Columbia, Columbia, MO Theoretical Investigation of Phthalocyanin Dimers	WL/MLPJ	5 - 55
DR James A Snide	University of Dayton, Dayton, OH Aging Aircraft: Preliminary Investigation of Various Materials and Process Issues	WL/MLLP	5 - 56
DR Yong D Song	North Carolina A & T State University, Greensboro, NC Memory-Base Control Methodology with Application to EMRAAT Missile	WL/MNAG	5 - 57
DR Raghavan Srinivasan	Wright State University, Dayton, OH Microstructural Development During Hot Deformation	WL/MLIM	5 - 58
DR Janusz A Starzyk	Ohio University, Athens, OH Feature Selection for ATR Neural Network Approach	WL/AACA	5 - 59
DR Alfred G Striz	University of Oklahoma, Norman, OK On Multiobjective Function Optimization in Engineering Design	WL/FIB	5 - 60
DR Barney E Taylor	Miami Univ - Hamilton, Hamilton, OH Optical and Electro-Optical Studies of Polymers	WL/MLBP	5 - 61
DR Joseph W Tedesco	Auburn University, Auburn, AL Effects of Airblast Characteristics on Structural Response	WL/MNSA	5 - 62
DR Scott K Thomas	Wright State University, Dayton, OH The Effects of Curvature on the Performance of a Spirally-Grooved Copper-Ethanol Heat Pipe	WL/POOS	5 - 63
DR James P Thomas	University of Notre Dame, Notre Dame, IN Subcritical Crack Growth of Ti-6Al-4V Under Ripple Loading Conditions	WL/MLLN	5 - 64
DR Karen A Tomko	Wright State University, Dayton, OH Grid Level Parallelization of an Implicit Solution of the 3D Navier-Stokes Equations	WL/FIM	5 - 65

SRP Final Report Table of Contents

Author	University/Institution	Arnold Engineering Development Center	Vol-Page
Report Title	Directorate		
DR Saad A Ahmed		AEDC	6 - 1
	King Fahd Univ of Petroleum & Minerals, Saudi, Arabia		
	Turbulence Statistics & Energy Budget of a Turbulent Shear Layer		
DR Csaba A Biegl		AEDC	6 - 2
	Vanderbilt University, Nashville, TN		
	Turbine Engine Blade Vibration Analysis System		
DR Frank G Collins		AEDC	6 - 3
	Tennessee Univ Space Institute, Tullahoma, TN		
	Laser Vapor Screen Flow Visualization Technique		
DR Randolph S Peterson		AEDC	6 - 4
	The University of the South, Sewanee, TN		
DR Robert L Roach		AEDC	6 - 5
	Tennessee Univ Space Institute, Tullahoma, TN		
	A Process for Setting Up Computation of Swirling Flows in the AEDC H-3 Heater		

SRP Final Report Table of Contents

Author	University/Institution Report Title	U.S. Air Force Academy Directorate	Vol-Page
DR Ryoichi Kawai	Univ of Alabama at Birmingham, Birmingham, AL A Massively Parallel Ab Initio Molecular Dynamics Simulation of Polymers & Molten Salts	USAFA	6 - 6

SRP Final Report Table of Contents

Author	University/Institution	Air Logistic Centers	Vol-Page
Report Title	Directorate		
DR Sandra A Ashford		OCALC	6 - 7
	University of Detroit Mercy, Detroit, MI		
	Evaluation of Current Jet Engine Performance Parameters Archive, Retrieval and Diagnostic System		
MR Jeffrey M Bigelow		OCALC	6 - 8
	Oklahoma Christian Univ of Science & Art, Oklahoma City, OK		
	Enhancing Tinker's Raster-to-Vector Capabilities		
DR K M George		OCALC	6 - 9
	Oklahoma State University, Stillwater, OK		
	A Computer Model for Sustainability Ranking		
DR Jagath J Kaluarachichi		OCALC	6 - 10
	Utah State University, Logan, UT		
	Optimal Groundwater Management Using Genetic Algorithm		

INTRODUCTION

The Summer Research Program (SRP), sponsored by the Air Force Office of Scientific Research (AFOSR), offers paid opportunities for university faculty, graduate students, and high school students to conduct research in U.S. Air Force research laboratories nationwide during the summer.

Introduced by AFOSR in 1978, this innovative program is based on the concept of teaming academic researchers with Air Force scientists in the same disciplines using laboratory facilities and equipment not often available at associates' institutions.

The Summer Faculty Research Program (SFRP) is open annually to approximately 150 faculty members with at least two years of teaching and/or research experience in accredited U.S. colleges, universities, or technical institutions. SFRP associates must be either U.S. citizens or permanent residents.

The Graduate Student Research Program (GSRP) is open annually to approximately 100 graduate students holding a bachelor's or a master's degree; GSRP associates must be U.S. citizens enrolled full time at an accredited institution.

The High School Apprentice Program (HSAP) annually selects about 125 high school students located within a twenty mile commuting distance of participating Air Force laboratories.

AFOSR also offers its research associates an opportunity, under the Summer Research Extension Program (SREP), to continue their AFOSR-sponsored research at their home institutions through the award of research grants. In 1994 the maximum amount of each grant was increased from \$20,000 to \$25,000, and the number of AFOSR-sponsored grants decreased from 75 to 60. A separate annual report is compiled on the SREP.

The numbers of projected summer research participants in each of the three categories and SREP "grants" are usually increased through direct sponsorship by participating laboratories.

AFOSR's SRP has well served its objectives of building critical links between Air Force research laboratories and the academic community, opening avenues of communications and forging new research relationships between Air Force and academic technical experts in areas of national interest, and strengthening the nation's efforts to sustain careers in science and engineering. The success of the SRP can be gauged from its growth from inception (see Table 1) and from the favorable responses the 1996 participants expressed in end-of-tour SRP evaluations (Appendix B).

AFOSR contracts for administration of the SRP by civilian contractors. The contract was first awarded to Research & Development Laboratories (RDL) in September 1990. After

completion of the 1990 contract, RDL (in 1993) won the recompetition for the basic year and four 1-year options.

2. PARTICIPATION IN THE SUMMER RESEARCH PROGRAM

The SRP began with faculty associates in 1979; graduate students were added in 1982 and high school students in 1986. The following table shows the number of associates in the program each year.

YEAR	SRP Participation, by Year			TOTAL
	SFRP	GSRP	HSAP	
1979	70			70
1980	87			87
1981	87			87
1982	91	17		108
1983	101	53		154
1984	152	84		236
1985	154	92		246
1986	158	100	42	300
1987	159	101	73	333
1988	153	107	101	361
1989	168	102	103	373
1990	165	121	132	418
1991	170	142	132	444
1992	185	121	159	464
1993	187	117	136	440
1994	192	117	133	442
1995	190	115	137	442
1996	188	109	138	435

Beginning in 1993, due to budget cuts, some of the laboratories weren't able to afford to fund as many associates as in previous years. Since then, the number of funded positions has remained fairly constant at a slightly lower level.

3. RECRUITING AND SELECTION

The SRP is conducted on a nationally advertised and competitive-selection basis. The advertising for faculty and graduate students consisted primarily of the mailing of 8,000 52-page SRP brochures to chairpersons of departments relevant to AFOSR research and to administrators of grants in accredited universities, colleges, and technical institutions. Historically Black Colleges and Universities (HBCUs) and Minority Institutions (MIs) were included. Brochures also went to all participating USAF laboratories, the previous year's participants, and numerous individual requesters (over 1000 annually).

RDL placed advertisements in the following publications: *Black Issues in Higher Education*, *Winds of Change*, and *IEEE Spectrum*. Because no participants list either *Physics Today* or *Chemical & Engineering News* as being their source of learning about the program for the past several years, advertisements in these magazines were dropped, and the funds were used to cover increases in brochure printing costs.

High school applicants can participate only in laboratories located no more than 20 miles from their residence. Tailored brochures on the HSAP were sent to the head counselors of 180 high schools in the vicinity of participating laboratories, with instructions for publicizing the program in their schools. High school students selected to serve at Wright Laboratory's Armament Directorate (Eglin Air Force Base, Florida) serve eleven weeks as opposed to the eight weeks normally worked by high school students at all other participating laboratories.

Each SFRP or GSRP applicant is given a first, second, and third choice of laboratory. High school students who have more than one laboratory or directorate near their homes are also given first, second, and third choices.

Laboratories make their selections and prioritize their nominees. AFOSR then determines the number to be funded at each laboratory and approves laboratories' selections.

Subsequently, laboratories use their own funds to sponsor additional candidates. Some selectees do not accept the appointment, so alternate candidates are chosen. This multi-step selection procedure results in some candidates being notified of their acceptance after scheduled deadlines. The total applicants and participants for 1996 are shown in this table.

1996 Applicants and Participants			
PARTICIPANT CATEGORY	TOTAL APPLICANTS	SELECTEES	DECLINING SELECTEES
SFRP	572	188	39
(HBCU/MI)	(119)	(27)	(5)
GSRP	235	109	7
(HBCU/MI)	(18)	(7)	(1)
HSAP	474	138	8
TOTAL	1281	435	54

4. SITE VISITS

During June and July of 1996, representatives of both AFOSR/NI and RDL visited each participating laboratory to provide briefings, answer questions, and resolve problems for both laboratory personnel and participants. The objective was to ensure that the SRP would be as constructive as possible for all participants. Both SRP participants and RDL representatives found these visits beneficial. At many of the laboratories, this was the only opportunity for all participants to meet at one time to share their experiences and exchange ideas.

5. HISTORICALLY BLACK COLLEGES AND UNIVERSITIES AND MINORITY INSTITUTIONS (HBCU/MIs)

Before 1993, an RDL program representative visited from seven to ten different HBCU/MIs annually to promote interest in the SRP among the faculty and graduate students. These efforts were marginally effective, yielding a doubling of HBCU/MI applicants. In an effort to achieve AFOSR's goal of 10% of all applicants and selectees being HBCU/MI qualified, the RDL team decided to try other avenues of approach to increase the number of qualified applicants. Through the combined efforts of the AFOSR Program Office at Bolling AFB and RDL, two very active minority groups were found, HACU (Hispanic American Colleges and Universities) and AISES (American Indian Science and Engineering Society). RDL is in communication with representatives of each of these organizations on a monthly basis to keep up with their activities and special events. Both organizations have widely-distributed magazines/quarterlies in which RDL placed ads.

Since 1994 the number of both SFRP and GSRP HBCU/MI applicants and participants has increased ten-fold, from about two dozen SFRP applicants and a half dozen selectees to over 100 applicants and two dozen selectees, and a half-dozen GSRP applicants and two or three selectees to 18 applicants and 7 or 8 selectees. Since 1993, the SFRP had a two-fold applicant

increase and a two-fold selectee increase. Since 1993, the GSRP had a three-fold applicant increase and a three to four-fold increase in selectees.

In addition to RDL's special recruiting efforts, AFOSR attempts each year to obtain additional funding or use leftover funding from cancellations the past year to fund HBCU/MI associates. This year, 5 HBCU/MI SFRPs declined after they were selected (and there was no one qualified to replace them with). The following table records HBCU/MI participation in this program.

SRP HBCU/MI Participation, By Year				
YEAR	SFRP		GSRP	
	Applicants	Participants	Applicants	Participants
1985	76	23	15	11
1986	70	18	20	10
1987	82	32	32	10
1988	53	17	23	14
1989	39	15	13	4
1990	43	14	17	3
1991	42	13	8	5
1992	70	13	9	5
1993	60	13	6	2
1994	90	16	11	6
1995	90	21	20	8
1996	119	27	18	7

6. SRP FUNDING SOURCES

Funding sources for the 1996 SRP were the AFOSR-provided slots for the basic contract and laboratory funds. Funding sources by category for the 1996 SRP selected participants are shown here.

1996 SRP FUNDING CATEGORY	SFRP	GSRP	HSAP
AFOSR Basic Allocation Funds	141	85	123
USAF Laboratory Funds	37	19	15
HBCU/MI By AFOSR (Using Procured Addn'l Funds)	10	5	0
TOTAL	188	109	138

SFRP - 150 were selected, but nine canceled too late to be replaced.

GSRP - 90 were selected, but five canceled too late to be replaced (10 allocations for the ALCs were withheld by AFOSR.)

HSAP - 125 were selected, but two canceled too late to be replaced.

7. COMPENSATION FOR PARTICIPANTS

Compensation for SRP participants, per five-day work week, is shown in this table.

1996 SRP Associate Compensation

PARTICIPANT CATEGORY	1991	1992	1993	1994	1995	1996
Faculty Members	\$690	\$718	\$740	\$740	\$740	\$770
Graduate Student (Master's Degree)	\$425	\$442	\$455	\$455	\$455	\$470
Graduate Student (Bachelor's Degree)	\$365	\$380	\$391	\$391	\$391	\$400
High School Student (First Year)	\$200	\$200	\$200	\$200	\$200	\$200
High School Student (Subsequent Years)	\$240	\$240	\$240	\$240	\$240	\$240

The program also offered associates whose homes were more than 50 miles from the laboratory an expense allowance (seven days per week) of \$50/day for faculty and \$40/day for graduate students. Transportation to the laboratory at the beginning of their tour and back to their home destinations at the end was also reimbursed for these participants. Of the combined SFRP and

GSRP associates, 65 % (194 out of 297) claimed travel reimbursements at an average round-trip cost of \$780.

Faculty members were encouraged to visit their laboratories before their summer tour began. All costs of these orientation visits were reimbursed. Forty-five percent (85 out of 188) of faculty associates took orientation trips at an average cost of \$444. By contrast, in 1993, 58 % of SFRP associates took orientation visits at an average cost of \$685; that was the highest percentage of associates opting to take an orientation trip since RDL has administered the SRP, and the highest average cost of an orientation trip. These 1993 numbers are included to show the fluctuation which can occur in these numbers for planning purposes.

Program participants submitted biweekly vouchers countersigned by their laboratory research focal point, and RDL issued paychecks so as to arrive in associates' hands two weeks later.

In 1996, RDL implemented direct deposit as a payment option for SFRP and GSRP associates. There were some growing pains. Of the 128 associates who opted for direct deposit, 17 did not check to ensure that their financial institutions could support direct deposit (and they couldn't), and eight associates never did provide RDL with their banks' ABA number (direct deposit bank routing number), so only 103 associates actually participated in the direct deposit program. The remaining associates received their stipend and expense payments via checks sent in the US mail.

HSAP program participants were considered actual RDL employees, and their respective state and federal income tax and Social Security were withheld from their paychecks. By the nature of their independent research, SFRP and GSRP program participants were considered to be consultants or independent contractors. As such, SFRP and GSRP associates were responsible for their own income taxes, Social Security, and insurance.

8. CONTENTS OF THE 1996 REPORT

The complete set of reports for the 1996 SRP includes this program management report (Volume 1) augmented by fifteen volumes of final research reports by the 1996 associates, as indicated below:

1996 SRP Final Report Volume Assignments

LABORATORY	SFRP	GSRP	HSAP
Armstrong	2	7	12
Phillips	3	8	13
Rome	4	9	14
Wright	5A, 5B	10	15
AEDC, ALCs, WHMC	6	11	16

APPENDIX A – PROGRAM STATISTICAL SUMMARY

A. Colleges/Universities Represented

Selected SFRP associates represented 169 different colleges, universities, and institutions, GSRP associates represented 95 different colleges, universities, and institutions.

B. States Represented

SFRP -Applicants came from 47 states plus Washington D.C. and Puerto Rico. Selectees represent 44 states plus Puerto Rico.

GSRP - Applicants came from 44 states and Puerto Rico. Selectees represent 32 states.

HSAP - Applicants came from thirteen states. Selectees represent nine states.

Total Number of Participants	
SFRP	188
GSRP	109
HSAP	138
TOTAL	435

Degrees Represented			
	SFRP	GSRP	TOTAL
Doctoral	184	1	185
Master's	4	48	52
Bachelor's	0	60	60
TOTAL	188	109	297

SFRP Academic Titles	
Assistant Professor	79
Associate Professor	59
Professor	42
Instructor	3
Chairman	0
Visiting Professor	1
Visiting Assoc. Prof.	0
Research Associate	4
TOTAL	188

Source of Learning About the SRP		
Category	Applicants	Selectees
Applied/participated in prior years	28%	34%
Colleague familiar with SRP	19%	16%
Brochure mailed to institution	23%	17%
Contact with Air Force laboratory	17%	23%
<i>IEEE Spectrum</i>	2%	1%
<i>BIIHE</i>	1%	1%
Other source	10%	8%
TOTAL	100%	100%

APPENDIX B – SRP EVALUATION RESPONSES

1. OVERVIEW

Evaluations were completed and returned to RDL by four groups at the completion of the SRP. The number of respondents in each group is shown below.

Table B-1. Total SRP Evaluations Received

Evaluation Group	Responses
SFRP & GSRPs	275
HSAPs	113
USAF Laboratory Focal Points	84
USAF Laboratory HSAP Mentors	6

All groups indicate unanimous enthusiasm for the SRP experience.

The summarized recommendations for program improvement from both associates and laboratory personnel are listed below:

- A. Better preparation on the labs' part prior to associates' arrival (i.e., office space, computer assets, clearly defined scope of work).
- B. Faculty Associates suggest higher stipends for SFRP associates.
- C. Both HSAP Air Force laboratory mentors and associates would like the summer tour extended from the current 8 weeks to either 10 or 11 weeks; the groups state it takes 4-6 weeks just to get high school students up-to-speed on what's going on at laboratory. (Note: this same argument was used to raise the faculty and graduate student participation time a few years ago.)

2. 1996 USAF LABORATORY FOCAL POINT (LFP) EVALUATION RESPONSES

The summarized results listed below are from the 84 LFP evaluations received.

1. LFP evaluations received and associate preferences:

Table B-2. Air Force LFP Evaluation Responses (By Type)

Lab	Evals Recv'd	How Many Associates Would You Prefer To Get ? (% Response)											
		SFRP				GSRP (w/Univ Professor)				GSRP (w/o Univ Professor)			
		0	1	2	3+	0	1	2	3+	0	1	2	3+
AEDC	0	-	-	-	-	-	-	-	-	-	-	-	-
WHMC	0	-	-	-	-	-	-	-	-	-	-	-	-
AL	7	28	28	28	14	54	14	28	0	86	0	14	0
FJSRL	1	0	100	0	0	100	0	0	0	0	100	0	0
PL	25	40	40	16	4	88	12	0	0	84	12	4	0
RL	5	60	40	0	0	80	10	0	0	100	0	0	0
WL	46	30	43	20	6	78	17	4	0	93	4	2	0
Total	84	32%	50%	13%	5%	80%	11%	6%	0%	73%	23%	4%	0%

LFP Evaluation Summary. The summarized responses, by laboratory, are listed on the following page. LFPs were asked to rate the following questions on a scale from 1 (below average) to 5 (above average).

2. LFPs involved in SRP associate application evaluation process:
 - a. Time available for evaluation of applications:
 - b. Adequacy of applications for selection process:
3. Value of orientation trips:
4. Length of research tour:
5.
 - a. Benefits of associate's work to laboratory:
 - b. Benefits of associate's work to Air Force:
6.
 - a. Enhancement of research qualifications for LFP and staff:
 - b. Enhancement of research qualifications for SFRP associate:
 - c. Enhancement of research qualifications for GSRP associate:
7.
 - a. Enhancement of knowledge for LFP and staff:
 - b. Enhancement of knowledge for SFRP associate:
 - c. Enhancement of knowledge for GSRP associate:
8. Value of Air Force and university links:
9. Potential for future collaboration:
10.
 - a. Your working relationship with SFRP:
 - b. Your working relationship with GSRP:
11. Expenditure of your time worthwhile:

(Continued on next page)

12. Quality of program literature for associate:
13. a. Quality of RDL's communications with you:
 b. Quality of RDL's communications with associates:
14. Overall assessment of SRP:

Table B-3. Laboratory Focal Point Responses to above questions

	<i>AEDC</i>	<i>AL</i>	<i>FJSRL</i>	<i>PL</i>	<i>RL</i>	<i>WHMC</i>	<i>WL</i>
<i># Evals Recv'd</i>	0	7	1	14	5	0	46
<i>Question #</i>							
2	-	86 %	0 %	88 %	80 %	-	85 %
2a	-	4.3	n/a	3.8	4.0	-	3.6
2b	-	4.0	n/a	3.9	4.5	-	4.1
3	-	4.5	n/a	4.3	4.3	-	3.7
4	-	4.1	4.0	4.1	4.2	-	3.9
5a	-	4.3	5.0	4.3	4.6	-	4.4
5b	-	4.5	n/a	4.2	4.6	-	4.3
6a	-	4.5	5.0	4.0	4.4	-	4.3
6b	-	4.3	n/a	4.1	5.0	-	4.4
6c	-	3.7	5.0	3.5	5.0	-	4.3
7a	-	4.7	5.0	4.0	4.4	-	4.3
7b	-	4.3	n/a	4.2	5.0	-	4.4
7c	-	4.0	5.0	3.9	5.0	-	4.3
8	-	4.6	4.0	4.5	4.6	-	4.3
9	-	4.9	5.0	4.4	4.8	-	4.2
10a	-	5.0	n/a	4.6	4.6	-	4.6
10b	-	4.7	5.0	3.9	5.0	-	4.4
11	-	4.6	5.0	4.4	4.8	-	4.4
12	-	4.0	4.0	4.0	4.2	-	3.8
13a	-	3.2	4.0	3.5	3.8	-	3.4
13b	-	3.4	4.0	3.6	4.5	-	3.6
14	-	4.4	5.0	4.4	4.8	-	4.4

3. 1996 SFRP & GSRP EVALUATION RESPONSES

The summarized results listed below are from the 257 SFRP/GSRP evaluations received.

Associates were asked to rate the following questions on a scale from 1 (below average) to 5 (above average) - by Air Force base results and over-all results of the 1996 evaluations are listed after the questions.

1. The match between the laboratories research and your field:
2. Your working relationship with your LFP:
3. Enhancement of your academic qualifications:
4. Enhancement of your research qualifications:
5. Lab readiness for you: LFP, task, plan:
6. Lab readiness for you: equipment, supplies, facilities:
7. Lab resources:
8. Lab research and administrative support:
9. Adequacy of brochure and associate handbook:
10. RDL communications with you:
11. Overall payment procedures:
12. Overall assessment of the SRP:
13.
 - a. Would you apply again?
 - b. Will you continue this or related research?
14. Was length of your tour satisfactory?
15. Percentage of associates who experienced difficulties in finding housing:
16. Where did you stay during your SRP tour?
 - a. At Home:
 - b. With Friend:
 - c. On Local Economy:
 - d. Base Quarters:
17. Value of orientation visit:
 - a. Essential:
 - b. Convenient:
 - c. Not Worth Cost:
 - d. Not Used:

SFRP and GSRP associate's responses are listed in tabular format on the following page.

Table B-4. 1996 SFRP & GSRP Associate Responses to SRP Evaluation

	Arnold	Brooks	Edwards	Eglin	Griffis	Hanacom	Kelly	Kirtland	Lackland	Robins	Tyndall	WPAFB	average
# res	6	48	6	14	31	19	3	32	1	2	10	85	257
1	4.8	4.4	4.6	4.7	4.4	4.9	4.6	4.6	5.0	5.0	4.0	4.7	4.6
2	5.0	4.6	4.1	4.9	4.7	4.7	5.0	4.7	5.0	5.0	4.6	4.8	4.7
3	4.5	4.4	4.0	4.6	4.3	4.2	4.3	4.4	5.0	5.0	4.5	4.3	4.4
4	4.3	4.5	3.8	4.6	4.4	4.4	4.3	4.6	5.0	4.0	4.4	4.5	4.5
5	4.5	4.3	3.3	4.8	4.4	4.5	4.3	4.2	5.0	5.0	3.9	4.4	4.4
6	4.3	4.3	3.7	4.7	4.4	4.5	4.0	3.8	5.0	5.0	3.8	4.2	4.2
7	4.5	4.4	4.2	4.8	4.5	4.3	4.3	4.1	5.0	5.0	4.3	4.3	4.4
8	4.5	4.6	3.0	4.9	4.4	4.3	4.3	4.5	5.0	5.0	4.7	4.5	4.5
9	4.7	4.5	4.7	4.5	4.3	4.5	4.7	4.3	5.0	5.0	4.1	4.5	4.5
10	4.2	4.4	4.7	4.4	4.1	4.1	4.0	4.2	5.0	4.5	3.6	4.4	4.3
11	3.8	4.1	4.5	4.0	3.9	4.1	4.0	4.0	3.0	4.0	3.7	4.0	4.0
12	5.7	4.7	4.3	4.9	4.5	4.9	4.7	4.6	5.0	4.5	4.6	4.5	4.6
Numbers below are percentages													
13a	83	90	83	93	87	75	100	81	100	100	100	86	87
13b	100	89	83	100	94	98	100	94	100	100	100	94	93
14	83	96	100	90	87	80	100	92	100	100	70	84	88
15	17	6	0	33	20	76	33	25	0	100	20	8	39
16a	-	26	17	9	38	23	33	4	-	-	-	30	
16b	100	33	-	40	-	8	-	-	-	-	36	2	
16c	-	41	83	40	62	69	67	96	100	100	64	68	
16d	-	-	-	-	-	-	-	-	-	-	-	0	
17a	-	33	100	17	50	14	67	39	-	50	40	31	35
17b	-	21	-	17	10	14	-	24	-	50	20	16	16
17c	-	-	-	-	10	7	-	-	-	-	-	2	3
17d	100	46	-	66	30	69	33	37	100	-	40	51	46

4. 1996 USAF LABORATORY HSAP MENTOR EVALUATION RESPONSES

Not enough evaluations received (5 total) from Mentors to do useful summary.

5. 1996 HSAP EVALUATION RESPONSES

The summarized results listed below are from the 113 HSAP evaluations received.

HSAP apprentices were asked to rate the following questions on a scale from
1 (below average) to 5 (above average)

1. Your influence on selection of topic/type of work.
2. Working relationship with mentor, other lab scientists.
3. Enhancement of your academic qualifications.
4. Technically challenging work.
5. Lab readiness for you: mentor, task, work plan, equipment.
6. Influence on your career.
7. Increased interest in math/science.
8. Lab research & administrative support.
9. Adequacy of RDL's Apprentice Handbook and administrative materials.
10. Responsiveness of RDL communications.
11. Overall payment procedures.
12. Overall assessment of SRP value to you.
13. Would you apply again next year? Yes (92 %)
14. Will you pursue future studies related to this research? Yes (68 %)
15. Was Tour length satisfactory? Yes (82 %)

	Arnold	Brooks	Edwards	Eglin	Griffiss	Hanscom	Kirtland	Tyndall	WPAFB	Totals
# resp	5	19	7	15	13	2	7	5	40	113
1	2.8	3.3	3.4	3.5	3.4	4.0	3.2	3.6	3.6	3.4
2	4.4	4.6	4.5	4.8	4.6	4.0	4.4	4.0	4.6	4.6
3	4.0	4.2	4.1	4.3	4.5	5.0	4.3	4.6	4.4	4.4
4	3.6	3.9	4.0	4.5	4.2	5.0	4.6	3.8	4.3	4.2
5	4.4	4.1	3.7	4.5	4.1	3.0	3.9	3.6	3.9	4.0
6	3.2	3.6	3.6	4.1	3.8	5.0	3.3	3.8	3.6	3.7
7	2.8	4.1	4.0	3.9	3.9	5.0	3.6	4.0	4.0	3.9
8	3.8	4.1	4.0	4.3	4.0	4.0	4.3	3.8	4.3	4.2
9	4.4	3.6	4.1	4.1	3.5	4.0	3.9	4.0	3.7	3.8
10	4.0	3.8	4.1	3.7	4.1	4.0	3.9	2.4	3.8	3.8
11	4.2	4.2	3.7	3.9	3.8	3.0	3.7	2.6	3.7	3.8
12	4.0	4.5	4.9	4.6	4.6	5.0	4.6	4.2	4.3	4.5
Numbers below are percentages										
13	60%	95%	100%	100%	85%	100%	100%	100%	90%	92%
14	20%	80%	71%	80%	54%	100%	71%	80%	65%	68%
15	100%	70%	71%	100%	100%	50%	86%	60%	80%	82%

TEMPORAL AND SPATIAL CHARACTERISATION OF A SYNCHRONOUSLY-PUMPED
PERIODICALLY-POLED LITHIUM NIOBATE OPTICAL PARAMETRIC OSCILLATOR

Dr. Graham R. Allan
Assistant Professor
Department of Physics

New Mexico Highlands University
National Avenue
Las Vegas NM 87701

Final Report for:
Summer Faculty Research Program
Phillips Laboratory

Sponsored By:
Air Force Office of Scientific Research
Bolling Air Force Base
Washington DC

&

Phillips Laboratory

August 96

TEMPORAL AND SPATIAL CHARACTERISATION OF A SYNCHRONOUSLY-PUMPED PERIODICALLY-POLED LITHIUM NIOBATE OPTICAL PARAMETRIC OSCILLATOR

Dr. Graham R. Allan
Assistant Professor
Department of Physics
New Mexico Highlands University

Abstract

To fully characterise the dynamics of a synchronously-pumped, periodically-poled, Lithium Niobate, optical parametric oscillator requires fast detection with high spatial-resolution. The introduction of a fiber-coupled fast detector, in parallel with standard techniques, has enabled clean experimental access to dynamics that are lost in the temporal and spatially averaging of large area, "slow" detectors. A fast rise-time ($\tau_{\text{rise}} \leq 25$ ps cf. $\tau_{\text{pulse}} \sim 100$ ps) fiber-coupled via a 25 μm diameter fiber to the experiment has enabled more detailed measurements of the on-axis pump depletion at the temporal center of the pulse, which was found to be typically 84% and appears to be limited by back conversion.

Maximum percentage pump-depletion occurs at the temporal and spatial center of the $\sim 1\text{MW}/\text{cm}^2$, 100 ps (FWHM) pump pulse. At higher irradiances the percentage pump depletion diminishes. A series of spatial profiles, that recorded the near-field irradiance of the transmitted pump at the rear of the nonlinear optical crystal, during the temporal center of the pulse shows the evolution of the transmitted pump as a function of incident power. The plots clearly show pump depletion and the onset of back-conversion of the signal to pump.

TEMPORAL AND SPATIAL CHARACTERISATION OF A SYNCHRONOUSLY-PUMPED PERIODICALLY-POLED LITHIUM NIOBATE OPTICAL PARAMETRIC OSCILLATOR

Graham R. Allan

Introduction

Optical parametric oscillators, OPO's, are now well established as a means of generating widely tunable coherent radiation in regions of the electro-magnetic spectrum which are normally difficult to access via conventional coherent sources. However, the utility of OPO's as a tool in nonlinear optics research is still limited by their low output intensities. A material which shows significant promise as a nonlinear optical medium in which to efficiently generate widely tunable, coherent, near-infrared radiation with useful intensities is Periodically-Poled Lithium Niobate, PPLN. In recent work a cw-pumped PPLN OPO was reported with a pump conversion efficiency of 93%,¹ and, using similar measuring techniques in a synchronously pumped PPLN OPO, pump conversion efficiency of 75 %² was measured with moderate output powers and wide tunability. However, due to the dynamical nature of a synchronously pumped OPO, full characterisation also requires fast detection and high spatial resolution. In this report the optical characterization of PPLN OPO is extended to temporally and spatially resolve the dynamical nature of the synchronously pumped PPLN OPO.

An OPO is a nonlinear optical device for generating tunable coherent radiation that is down-converted from the pump frequency, ω_p , such that the sum of the generated signal frequency, ω_s , and idler frequency, ω_i , satisfy $(\omega_s + \omega_i) = \omega_p$. As in the above referenced works this research is performed in the singly-resonant configuration, where the cavity Q is high for the signal frequency but low for the pump and idler. Feedback is achieved by circulating the signal within the OPO cavity and aligning for temporal and spatial overlap of the signal and pump within the PPLN crystal. This results in a gain in the signal strength for each pass through the crystal. The gain mechanism is a $\chi^{(2)}$ nonlinear effect; maximum pump conversion takes place at the spatial and temporal center of the pump pulse, where the photon's E-field is largest. To fully measure the OPO's output dynamics the detection system must be fast and sample a small area compared to the temporal pulse-width and beam diameter. If not, then one automatically measures an averaged output, integrated over space and time, and a fund of information on the dynamics of the OPO may be lost.

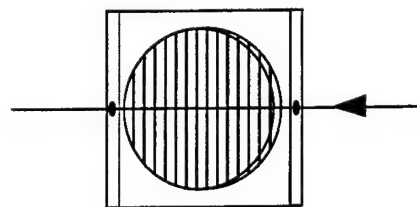
The ever-continuing push for more usable power has resulted in synchronously pumped cavity designs. In such a configuration (and at pump pulse fluence easily achievable with a picosecond, mode-locked Nd:Yag laser), sufficient energy may be deposited in the signal-field that back

conversion may take place. In this regime the signal becomes sufficiently large so as to act as a source, resulting in the signal and idler back-converting to the pump frequency. This results in sub-optimal performance of the OPO. This effect is expected to be observed after the system has reached steady-state, during strong pumping, and at the spatial and temporal center of the pump pulse. To be able to observe this phenomenon directly requires fast detection techniques and high spatial resolution. In this report the optical characterization of PPLN OPO is extended to temporally and spatially resolving such dynamical effects.

Methodology

The employed methodology is to characterise the performance of the singly-resonant PPLN OPO using standard measurements; pump depletion, conversion efficiency, signal strength recorded as a function of cavity length and incident power, and to introduce fast detection with high spatial resolution.

A schematic of the general experimental layout is shown in figure 1. A Coherent Antares ND:YAG operating at $1.064\ \mu\text{m}$ in quasi-cw mode produced an $\sim 80\ \text{MHz}$ train of pulses, nominally $100\ \text{ps}$ FWHM at $20\ \text{W}$ average power. The pump power injected into the OPO cavity through mirror C1 is controlled by the halfwave plate and analyzer and measured by a large area power meter at M1. The pump is mechanically chopped at $40\ \text{Hz}$ with a 100:1 duty cycle minimize bulk heating of the crystal. This reduces the pump train to $250\ \mu\text{s}$ bursts every $25\ \text{ms}$. The buildup to steady state in this resonator occurs in $\sim 50\ \mu\text{s}$, and the chopper window is sufficiently wide to establish steady-state oscillation, where in the single pass gain is balanced by the round-trip cavity losses. The OPO cavity is a "bow-tie" ring resonator. The crystal is positioned centrally between mirrors C1 and C2, each of radius $75\ \text{cm}$, separated by $86\ \text{cm}$. The cavity is folded via flat reflectors C3 and C4. The optical path of the OPO is matched to the temporal-mode spacing of the pump using C4. The pump is spatially mode matched to the OPO cavity with an external telescope producing a symmetrical Gaussian beam of $150\ \mu\text{m}$ half-width ($1/e$). The crystal is mounted on an externally-controlled oven to enable temperature tuning of the signal and idler frequencies. The crystal of LiNbO_3 is $15\ \text{mm} \times 15\ \text{mm} \times 500\ \mu\text{m}$ thick, with a poling period of $29.75\ \mu\text{m}$ through a central area of $13\ \text{mm}$ diameter. The depleted pump, having passed through the crystal is partially reflected by mirror C2 and leaves the resonator through C3.



Schematic of the PPLN, showing poled region and orientation to beam.

A large area power meter placed after a high reflectance splitter at $1.51\ \mu\text{m}$, M6, monitors the transmitted pump power. The cavity and crystal are optimised for operation at the signal

wavelength of $1.51\mu\text{m}$. The signal frequency is coupled from the cavity at mirrors C2 and C3. The fast temporal and spatially-resolving detection system follow in the diagnostic arm of the experiment. Depending on the measurement, a $1.51\mu\text{m}$ or $1.064\mu\text{m}$ transmission filter was inserted downstream of M6.

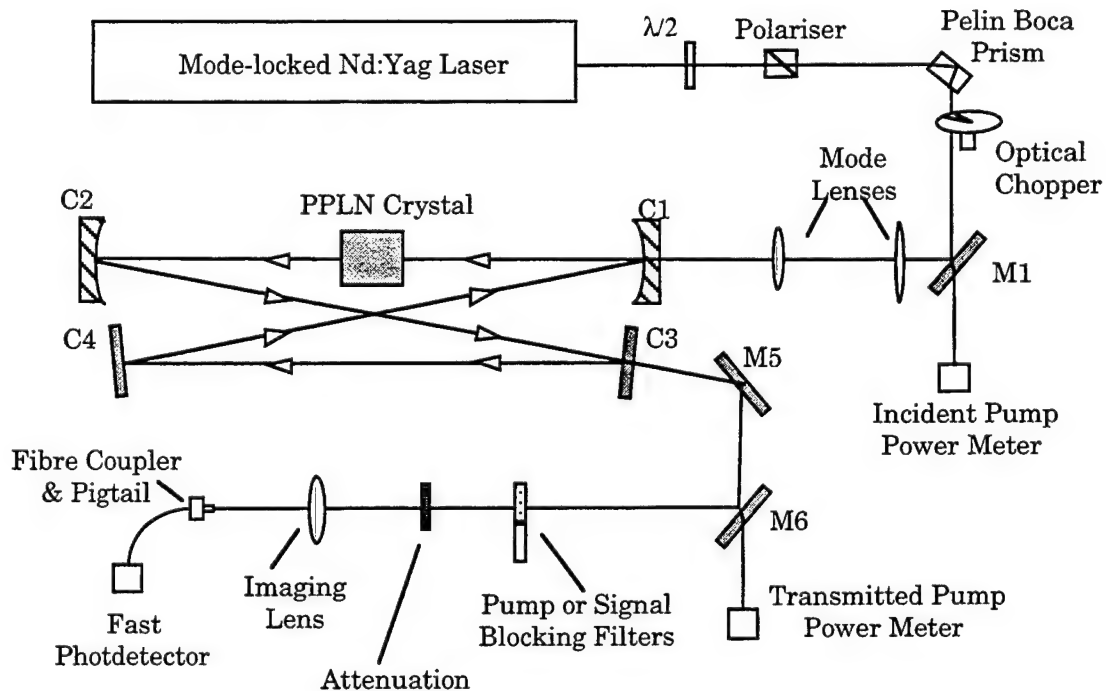


Figure 1. Schematic of the experimental layout showing the cavity geometry.

The second harmonic of $1.51\mu\text{m}$ was removed and attenuation, when needed, introduced. The fast photodetector is a New Focus 10-410 with a rise time of $\leq 25\text{ ps}$, connected to an S-4 Tektronics sampling head. The detector was fiber coupled to the experiment through a $25\mu\text{m}$ diameter fiber mounted in a three-axis, computer-controlled positioning stage with sub-micron accuracy and repeatability. The fiber input is placed in the image plane of the output face of the crystal, which is formed by the imaging lens in the diagnostic arm of the experiment.

Operational Characterisation

Synchronising pump and signal using cavity length tuning.

The efficiency of the pumping scheme is measured as a function of OPO cavity length. This technique establishes temporal and spatial overlap between pump and signal. By altering the cavity length, a temporal delay is introduced between the circulating signal and the pump. Unlike conventional gain media there is no gain storage, hence signal amplification can only take place during temporal and spatial overlap of pulses. Optimum cavity length was found for the system

alignment from the peak in output signal. Figure 2 is a typical result, the input pump irradiance, the transmitted pump irradiance the signal irradiance were recorded as a function of cavity length.

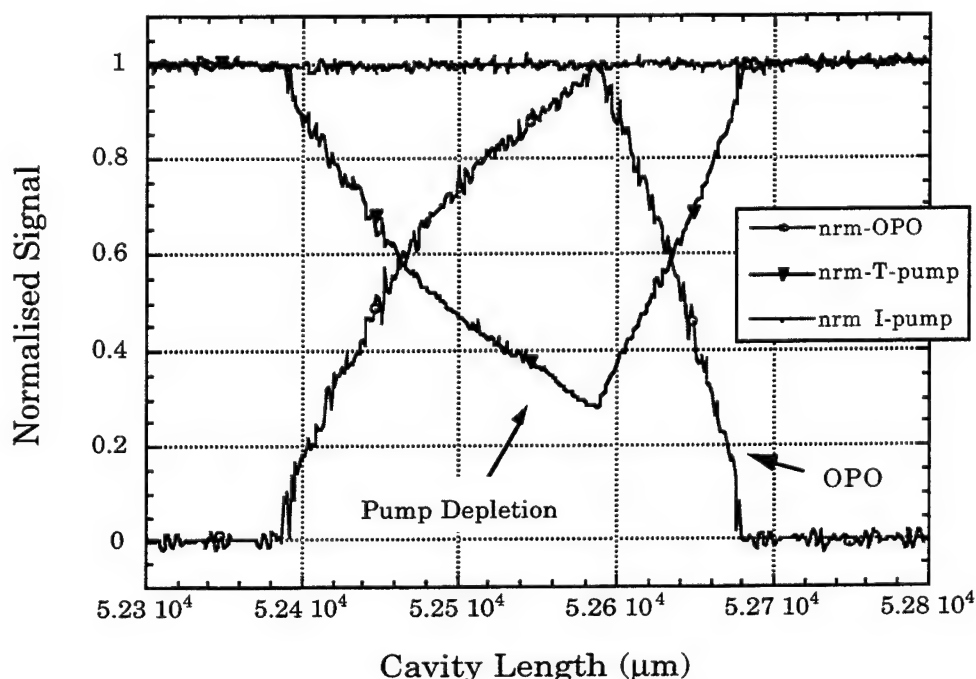


Figure 2. Plot of the normalised incident pump, transmitted pump and signal irradiance as a function of cavity length. The depletion in the transmitted pump is clearly seen as the OPO signal increases. Synchronicity is at the local maximum in the OPO signal

This is essentially a differential transmission measurement that accounts for cavity losses, $(T_{p \text{ off}} - T_{p \text{ sync}}) / T_{p \text{ off}}$, where $T_{p \text{ off}}$ is the pump transmission of the cavity and crystal off synchronicity, $T_{p \text{ sync}}$ is the transmission on synchronicity and gives the spatial and temporal averaged pump depletion. A typical value for depleted pump during optimum performance of the PPLN OPO is 75 %. This figure agrees with other work.

Threshold of Oscillation

To ensure optimum spatial overlap the cavity was positioned for synchronicity and the cavity alignment adjusted for lowest threshold for signal oscillation. The transmitted pump and OPO signals were then recorded as a function of incident power. Figure 3 is a typical plot of the transmitted pump and signal as the incident power is increased. The transmission of the pump is essentially linear until threshold, where the pump down-converts to ω_s and ω_i , depleting the transmitted pump. This depletion increases until approximately two times threshold where, (see

figure 4), the depletion appears to saturate. Above twice threshold the slope of the OPO signal decreases. This is indicative of back conversion from signal to pump. Figure 4 clearly shows the change in pump depletion with increasing incident power.

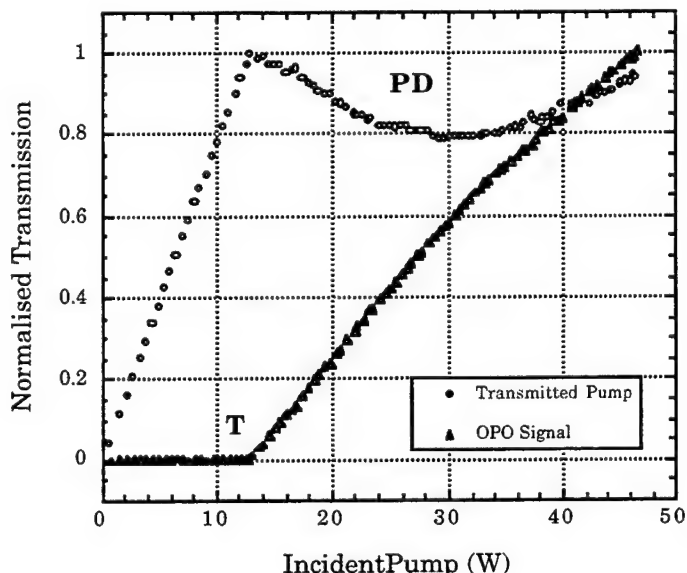


Figure 3. Plot of the OPO signal and transmitted pump as a function of incident pump power, showing threshold 'T' and pump depletion, 'PD'.

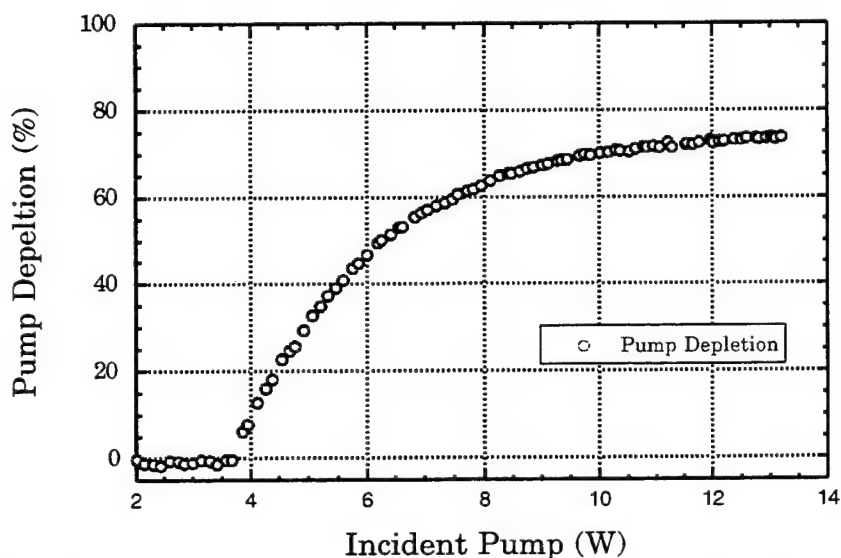


Figure 4. Plot of the pump depletion measured with a large area detector. The pump depletion approaches 75%.

Temporal and Spatially Resolved Dynamics of the PPLN OPO.

The results plotted in figures 2 through 4 were all taken with the large area detectors and are the spatial and temporal integral of the pulse. Since this is a dynamic system using a synchronous

pumping scheme it is important to monitor the system with temporal and spatial-resolving diagnostics. Again, the above characterisation methods were employed, in addition to which a fast detector fiber-coupled to the experiment was introduced. The fiber was positioned in the crystal's image plane, formed by a lens external to the cavity, so as to record the near field irradiance of the transmitted pump. Great care was taken to ensure alignment of the fiber input to the image plane. A technique was developed which ensured finding the image plane: A mask was introduced close to the output surface of the crystal, impinging on half of a very weak pump beam; The spatial profile was then recorded as a function of both axial distance from the imaging lens, with and without the mask; A comparison of the profiles indicates the image plane when the peak heights are similar. The results are plotted in appendix A. The image plane was found to be stable over time and was unaffected by scanning of the cavity length using reflector C4.

Synchronising pump and signal using cavity length tuning.

The cavity scans were repeated monitoring the spatial and temporal center of the pulse. The spatial center was obtained from an x-y scan of the transmitted pump profile (OPO blocked) and positioning the fibre on the peak of the pulse. A narrow, variable, electronically-delayed sampling window of ~ 20 ps width was set to record the peak voltage from the fast detector.

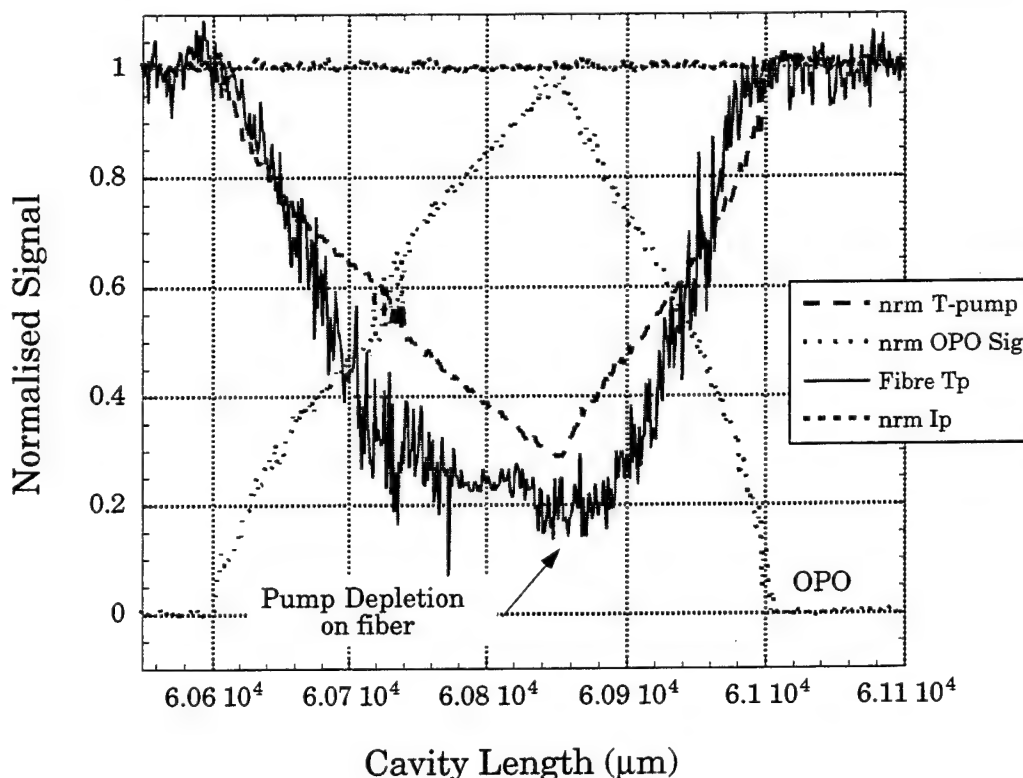


Figure 5. Cavity length scan recorded using the fast detector gated for the temporal center of the pump pulse and positioned on the spatial center of the pump profile in the back image plane. See text.

Figure 5 is a plot of the normalised pump transmission showing the time and space-resolved signal; for comparison the large area detector measurements are included. The transmitted pump depletion measured by the fast system is greater; occurs over a larger cavity length and is skewed to shorter cavity lengths.

Threshold of Oscillation

Again the cavity length was adjusted to synchronize pump and signal. The fiber was positioned in the image plane at the peak of the pulse and the fast detector sampling window set for the center of the pulse. Figure 6 is a plot of the normalised transmitted pump, recorded on the fast detector at the spatial and temporal center of the pulse as a function of increasing power, plotted as inverted closed triangles, also shown for comparison are the standard measurements-- open squares and circles.

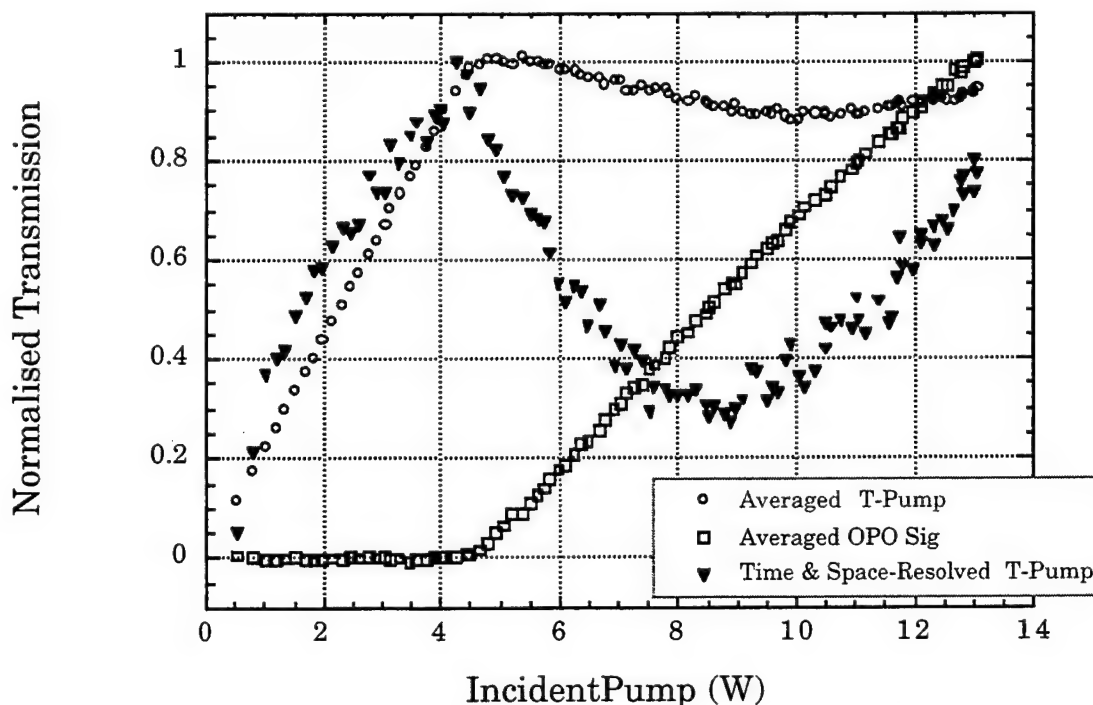


Figure 6. Plot of the normalised, transmitted pump recorded on the fast detector at the spatial and temporal center of the pulse. The OPO signal and transmitted pump recorded by the large area detectors are shown for comparison.

It is evident from this result that the on-axis temporal center of the pulse undergoes greater pump depletion. The pump experiences a "reversed-saturable-absorption" like effect, increasing absorption with increasing power, where $(\Delta I_{\text{transmitted } p} / \Delta I_{\text{incident } p})$ is negative. Increasing power results in more efficient conversion of the pump photons to signal and idler photons. The

pump continues to be depleted with increasing pump power until approximately twice threshold, where the on axis transmission increases. At approximately twice threshold the signal generation efficiency decreases, $(\Delta I_{\text{signal}}/\Delta I_{\text{incident p}})$, again suggesting back conversion from signal to pump.

To see more clearly the behavior of the on-axis pump depletion, the percentage pump depletion for both the fast and slow detectors is plotted as a function of incident power in figure 7. From this figure it is evident that the on-axis pump depletion at the temporal center of the pump pulses is larger than the averaged measurement. The most significant difference is that the pump depletion reduces after approximately twice threshold, a fact completely obscured in the lower trace of figure 7. The on-axis pump depletion at temporal center is 84 %. Above twice threshold the percentage pump depletion diminishes, possibly due to back conversion of the signal to the pumping frequency.

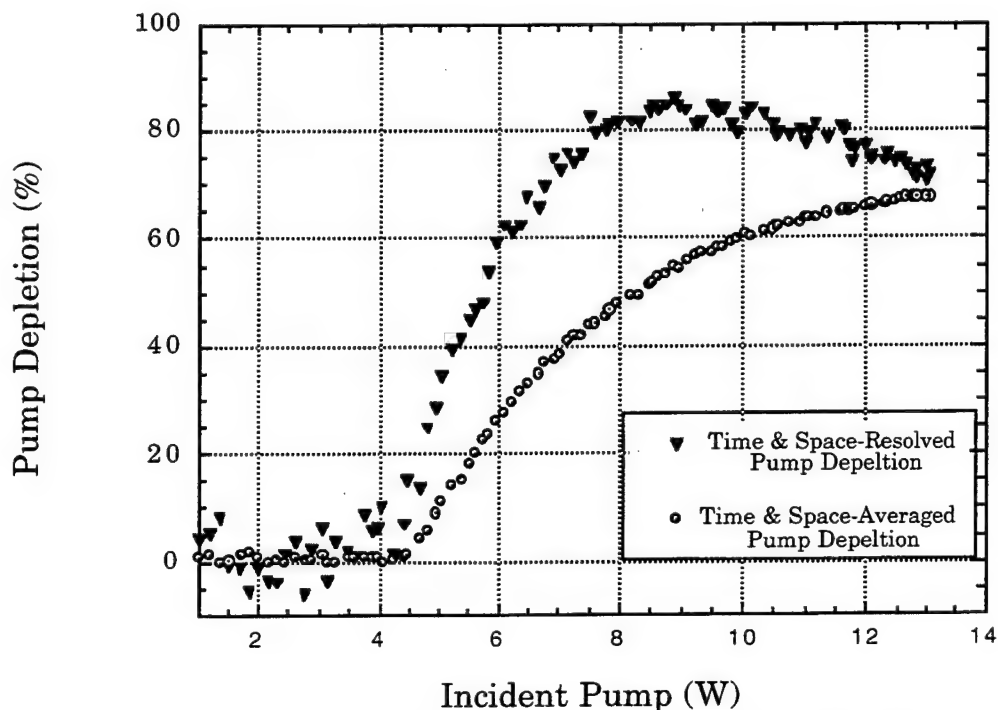
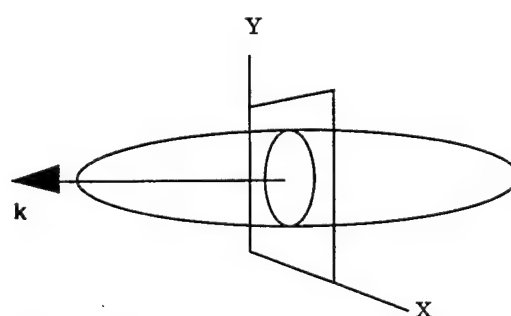


Figure 7. Plot of the percentage transmitted pump's depletion as a function of incident power. The time and space resolved measurements, solid inverted triangles, clearly show a greater percentage pump depletion which then reduces with increasing pump power.

Temporally Resolved Spatial Profile of the Transmitted Pump

The incident pump is a symmetrical Gaussian beam of 150 μm halfwidth (1/e). The imaged profile of the transmitted pump is recorded in Figure 8A, (pump below OPO threshold). The spatial

profile of the signal is physically smaller than the pump which is a result of two mechanisms, losses in the OPO resonator and the down-conversion process. The effect of back conversion should be manifest as an increase in transmitted pump. Since back conversion is also a $\chi^{(2)}$ effect the back conversion would be narrower in profile than the pump. Preliminary research data, recorded in figure 8, would tend to confirm this. In this experiment the cavity was carefully aligned for temporal and spatial overlap. Again the temporal window was set at the peak of the pump pulse, and the signal on the fiber recorded as a function of x and y. The profiles recorded were in the image plane of the rear face of the OPO PPLN crystal. A series of profiles was recorded starting below threshold and increasing to maximum incident power. The three dimensional figures plot the irradiance through a vertical profile at the temporal center of the transmitted pump pulse, (see inset).



Inset Showing the spatial profile recorded through the center of the pulse

The vertical scale indicates the absolute magnitude of the transmitted pump. All plots are normalised to fit the plotting space and show increased detail on the mid-range profiles, where pump depletion greatly reduces the signal. The threshold for OPO oscillation was 0.22 I, where I corresponds to maximum power, and this profile is recorded in figure 8B. Figure 8A is the incident pump profile just below threshold. Above threshold the overall profile decreases, with maximum depletion taking place at the center of the beam --Figures 8, C & D. Continuing past twice threshold, the overall profile starts to grow a narrow cone in the region where the pump has been depleted. This also corresponds to spatial overlap between pump and signal. This central cone is tentatively ascribed to back conversion. The cone continues to grow with increasing incident power, Figures 8E-H. Figure 8H clearly shows that an annulus is formed by the remainder of the incident pump that has not been down converted with a narrow central cone. The central cone is formed by the back conversion of signal and idler into the pump wavelength. Since the signal is proportional to the square of the pump irradiance and the back converted frequency is proportional to the square of the signal, the cone appears much narrower than the pump.

Conclusions.

In this report it has been shown that to fully characterise the dynamics of the PPLN OPO requires time and space-resolving techniques in parallel with averaged measurements. This characterization allows clean experimental access to the dynamics and has enabled more detailed measurements of the on-axis pump depletion at the temporal center of the pulse, which was found to

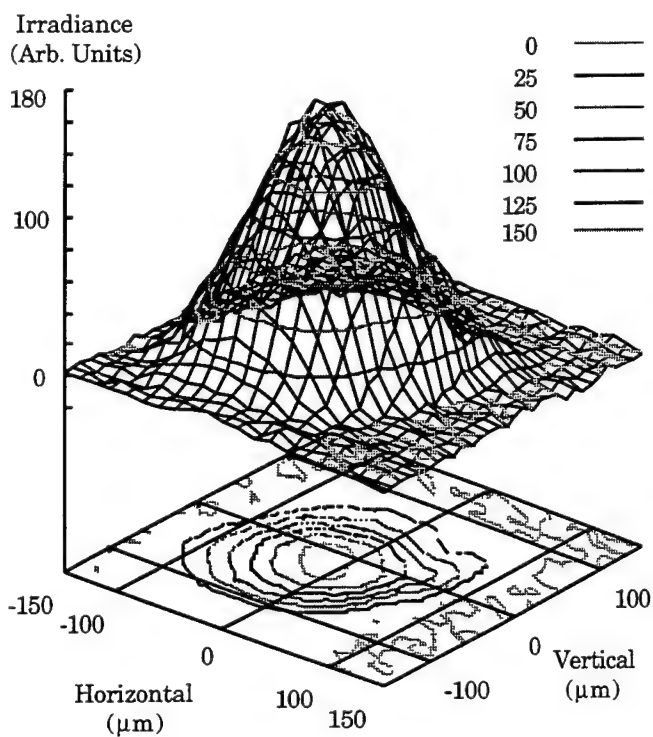


Figure A. Transmitted Pump Profile
Below OPO Threshold ($I=0.2$)

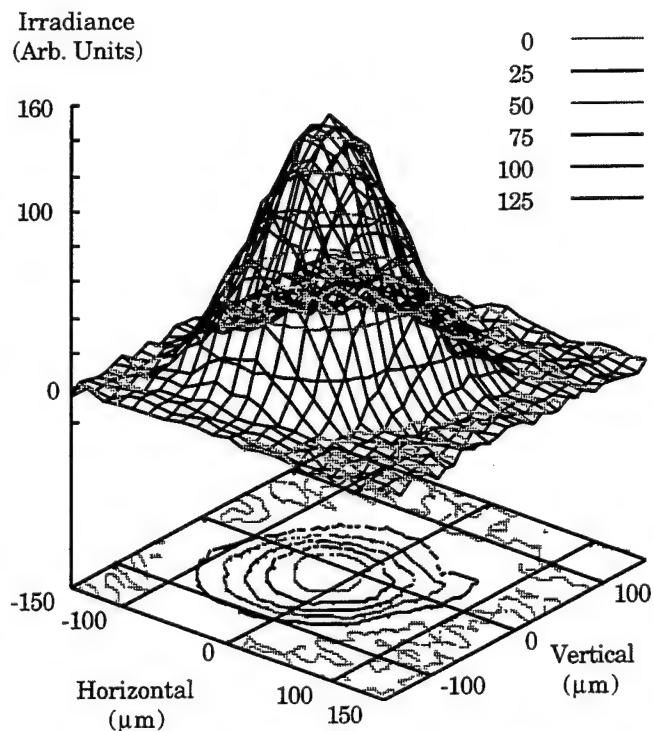


Figure B. Transmitted Pump Profile
at OPO Threshold ($I=0.22$)

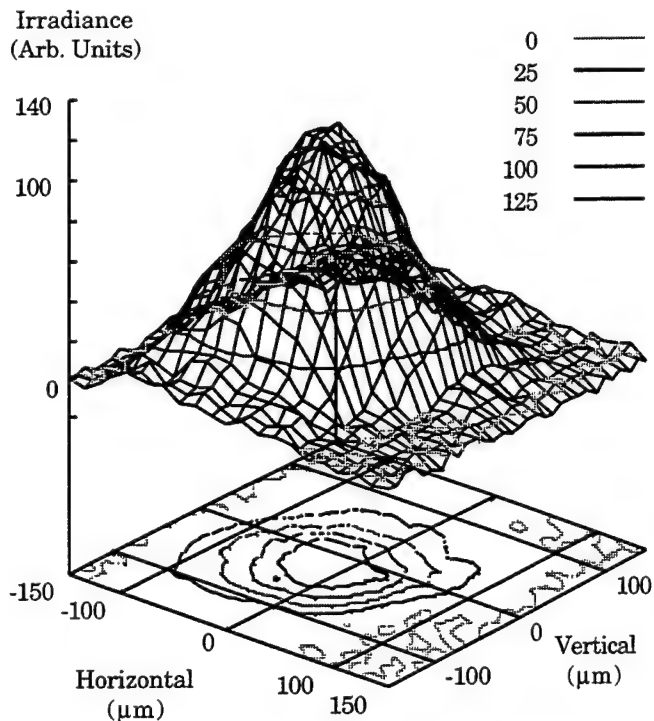


Figure C. Transmitted Pump Profile OPO
Just Above Threshold ($I=0.25$)

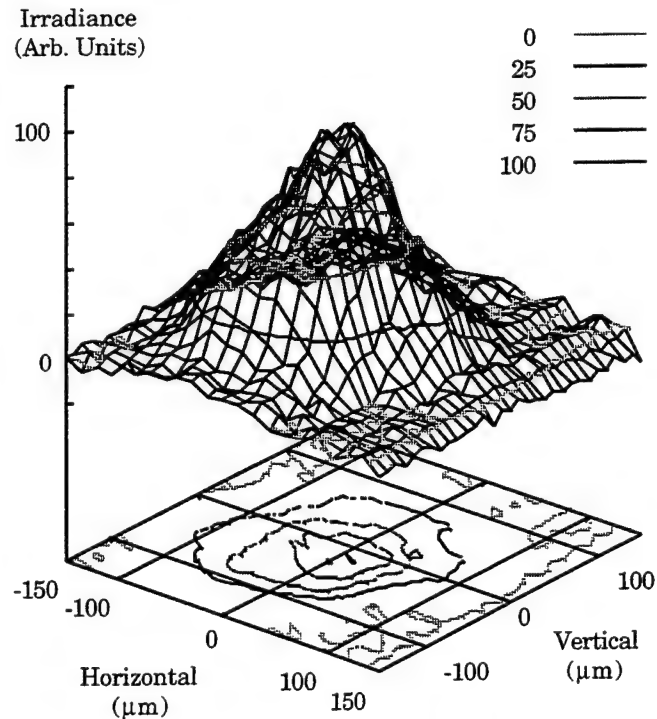


Figure D. Transmitted Pump Profile
($I=0.42$)

Figure 8. Transmitted Pump Profiles at the Temporal Center of the Pulse for increasing Incident Pump Powers (I). Sequence shows the growth of a narrow central spike at irradiances greater than twice threshold

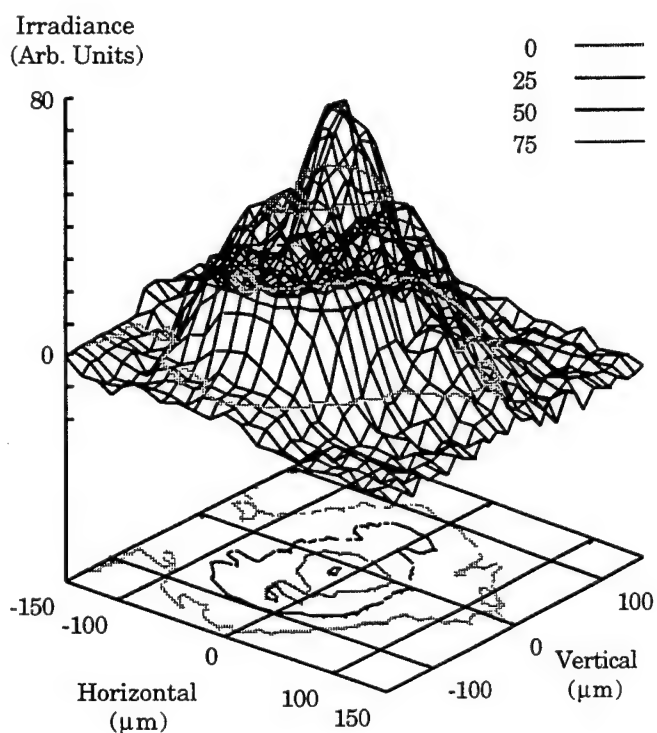


Figure E. Transmitted Pump Profile Back-conversion Spike forms ($I=0.52$)

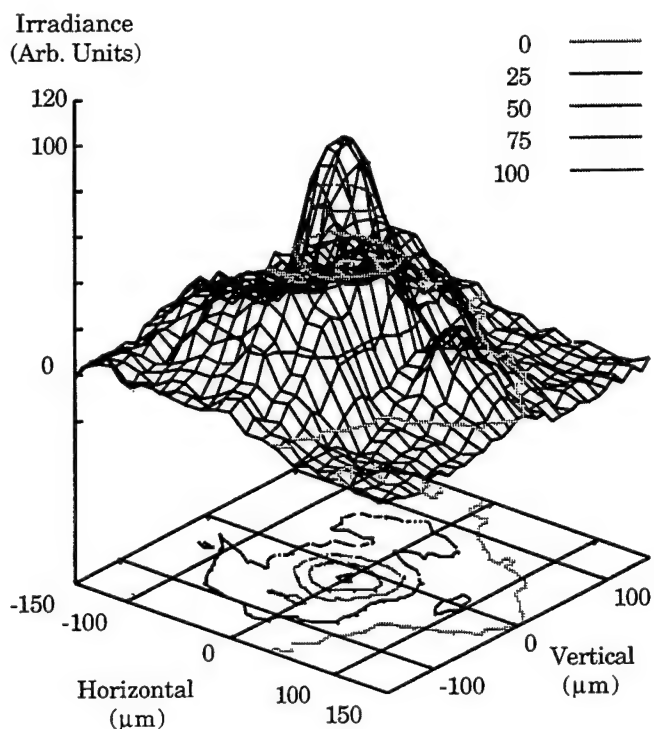


Figure F. Transmitted Pump Profile Back-conversion Spike ($I=0.62$)

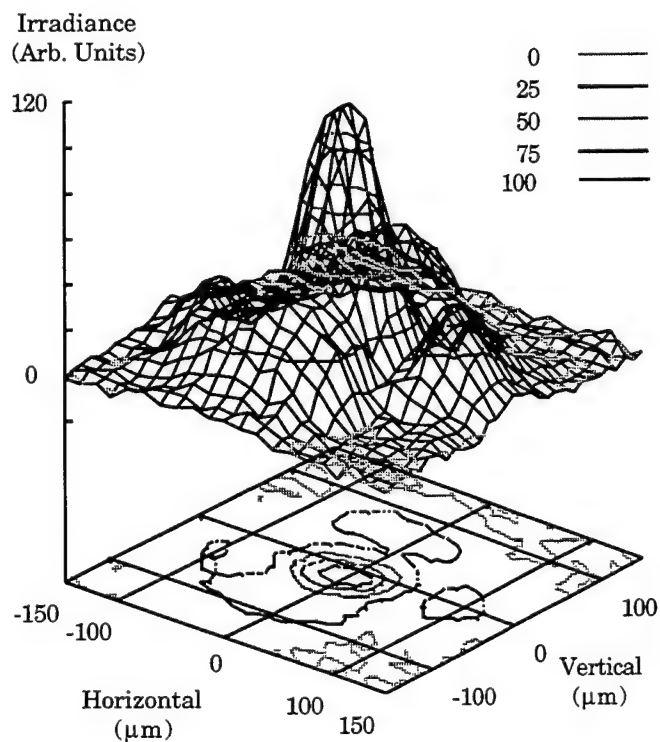


Figure G. Transmitted Pump Profile Back-conversion Spike Grows ($I=0.72$)

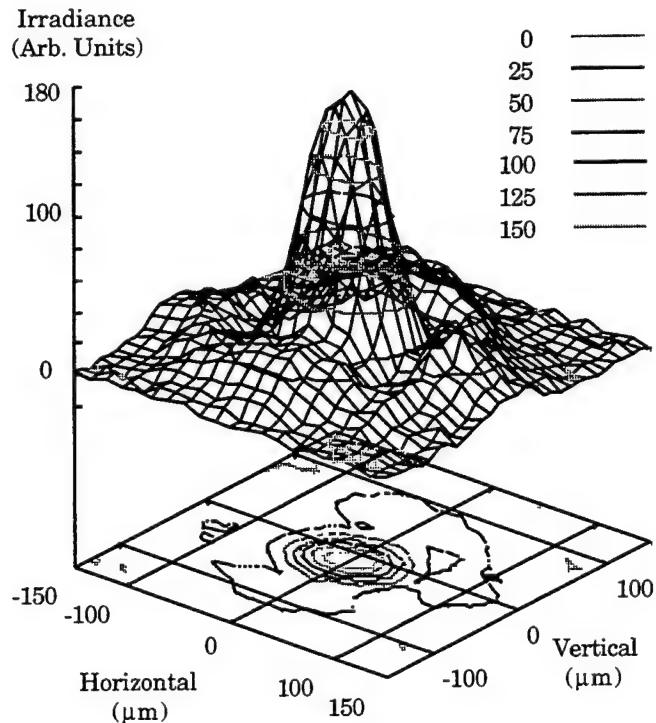


Figure H. Transmitted Pump Profile Spike & Anulus ($I=1.0$)

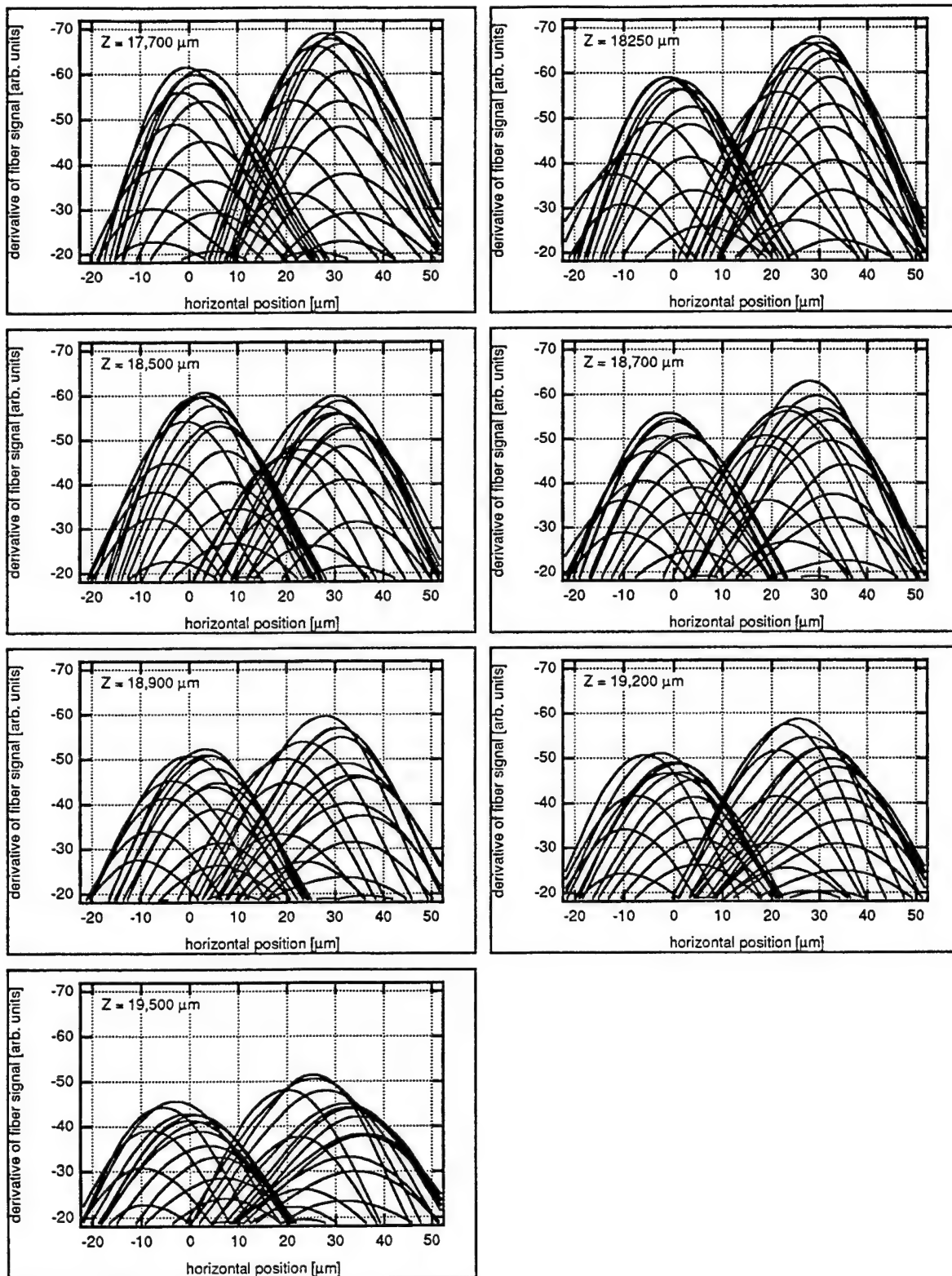
Figure 8. Transmitted Pump Profiles at the Temporal Center of the Pulse for increasing Incident Pump Powers (I). Sequence shows the growth of a narrow central spike at irradiances greater than twice threshold

be typically 84% and appears to be limited by back conversion. Other data, not reported here, on the PPLN OPO concentrates on the temporal and spatially-resolved evolution of the signal and pump during switch-on and build-up to steady-state operation. This extensive data will be analysed in the coming months.

Further optimization of the system requires studying the pump depletion as a function of crystal length, incident pump spatial profile and temporal pulse length. It may be possible to extract more signal power using a Gaussian reflector, in this case optimized for greater transmission of the signal, on-axis thereby reducing the intracavity, on-axis signal intensity and consequently back conversion.

References

1. Walter R. Bosenberg, Alexander Dobshoff, and Jason I. Alexander, "93% pump depletion, 3.5-W continuous-wave, singly-resonant optical parametric oscillator." Opt. Lett. 21, 1336 (1996)
2. S. D. Butterworth, V. Pruneri and D. C. Hanna, "Optical parametric oscillations in periodically poled lithium niobate based on continuous-wave synchronous pumping at 1.047 μm ." Opt. Lett. 21, 1345 (1996)



Appendix A. Plots of the spatial derivative of the pump irradiance, with and without mask, as a function of (Z) distance along the optical axis from the imaging lens. Focus is $\sim 18,500 \mu\text{m}$. In this plane $18,500 \mu\text{m}$ from the imaging lens, the near-field irradiance at the object can be measured.

**TESTING OF A DUAL-BAND INFRARED FOCAL PLANE ARRAY
AND AN INFRARED CAMERA SYSTEM**

Brian P. Beecken
Associate Professor
Department of Physics

Bethel College
3900 Bethel Drive
St. Paul, MN 55112

Final Report for:
Summer Faculty Research Program
Phillips Laboratory

Sponsored by:
Air Force Office of Scientific Research
Bolling Air Force Base, DC

and

Phillips Laboratory

August 1996

TESTING OF A DUAL-BAND INFRARED FOCAL PLANE ARRAY AND AN INFRARED CAMERA SYSTEM

Brian P. Beecken
Associate Professor
Department of Physics
Bethel College

ABSTRACT

Progress was made on the development of a portable test station for Lockheed Martin's dual-band IR FPA. The appropriate method for running the required clocks was determined to be an Altera EPM5064 programmable logic device combined with a test station being built by Wallace Instruments. The timing patterns required for operation of the dual-band FPA were determined. A second project was the evaluation of an Infrared Camera system. The greatest limitations apparent in this initial evaluation appeared to be software related. The primary problem is the inability to obtain raw data from the FPA and the lack of documentation explaining how the raw data was processed by the software. This situation resulted in skewed histograms of pixel values obtained while viewing a uniform scene. Such histograms should have been normally distributed, but instead appeared to have secondary peaks. Subtraction of one frame of data from another was successful in eliminating the effects which skewed the histograms.

TESTING OF A DUAL-BAND INFRARED FOCAL PLANE ARRAY AND AN INFRARED CAMERA SYSTEM

Brian P. Beecken

Introduction

The Passive Sensors Branch (PL/VTRP) in the Space Sensors Division of Phillips Laboratory is engaged in virtually every aspect of the development of optical sensors. Consequently, I was able to choose from a wide variety of possible projects. Unfortunately, none of these experimental research topics had all the necessary pieces in place for a fast start. The decision was made to begin work on several tasks in the expectation that the equipment would eventually arrive and then one project would become the focus of my attention. Four different projects were begun.

The first project involved the use of a new Fourier Transform Infrared Spectroscopy system to study materials for possible use as ultraviolet detectors. I conducted a literature search on this subject and assisted in floating the lab's optical table. Unfortunately, the spectroscopy system, although it arrived as scheduled, did not initially have the required resolution and was lacking a dewar. Thus the system was rendered essentially useless during my time at Phillips lab.

A second project was the testing of IR hot-electron transistors (IHET). Before tests could be made, the devices had to be inspected under a microscope and a proper pinout diagram made. After this was accomplished, a test dewar needed to be prepared and wired. The IHET's are driven by two bias voltages, and the output signal consists of a very small current. The appropriate bias supplies and electrometer were located and connected via an IEEE-488 bus to a personal computer. Under my supervision, a Lab View program was then written by an undergraduate student. The Lab View program was designed to step the bias voltages through an appropriate range at a chosen rate

while recording the resulting current values. Initial checks of the instrumentation and software were made on simple resistors. At this point, however, the equipment required to proceed on another project became available, and actual testing of the IHET was never performed. However, all the appropriate preparations have been made, so hopefully someone else can get off to a quick start.

Considerably more headway was made in two other projects, although neither of these came together in time to be completely finished during my tenure at Phillips lab. The main sections of this paper serve as reports on the progress made on each of the projects: the development of a portable test station for a dual-band focal plane array, and the testing of a "first-of-its-kind" IR camera system.

1 Development of a Portable Test Station for Dual-Band IR Focal Plane Arrays

Lockheed Martin IR Imaging Systems has recently developed a dual-band FPA which simultaneously images with perfect registration in both MWIR and LWIR. Although the primary responsibility for testing and characterization of this device will be handled by a Phillips Lab contractor, Ball Aerospace, a need was seen for a portable test station that would allow the device to be tested in the field. This somewhat parallel effort required the adaptation of the general purpose portable test station currently being developed for PL/VTRP by Wallace Instruments. The Wallace Instruments test station is designed to run only 18 clocks, whereas the dual-band FPA requires 25 clocks. The number of clocks required by the dual-band FPA is unusually high and would present a difficulty for most testers. Lockheed Martin itself faced this problem during its internal testing and circumvented it by using a standard Pulse Instruments test station to drive some of the clocks and a programmable logic device (PLD) to drive the remainder. In addition to the unusual method of obtaining the large number of clocks, Lockheed Martin had failed to provide an adequate, clear, and complete description of the timing patterns

required for the FPA's various modes of operation. The primary goal of this project quickly became the determination of the appropriate solution to the timing problem.

1.1 Programmable Logic Devices

First, an investigation was made into Programmable Logic Devices (PLD's)—their capabilities and their use. Lockheed Martin had put together a test box which housed their PLD, and our hope was to duplicate it. A PLD is an IC with many gates whose interconnections can be programmed. They come in two basic types: combinational (logic gates only), which provide an output based on a combination of inputs, and sequential (logic gates plus on-chip D-type registers), which provide an output based both on the inputs *and* on previous states. The timing task clearly requires the latter.

PLD's are a natural choice for designing arbitrary synchronous state machines. They are flexible in that if the timing pattern does not work or needs to be modified, another PLD can be programmed and substituted without requiring the circuit to be re-wired. This feature also allows multiple versions of the same test setup simply by exchanging PLD's.

PLD's are programmed with a programmer, a piece of hardware that encodes the PLD, often by burning fuses. Programmers connect via a serial port to a personal computer which must run some form of programming software. The software varies widely in complexity and sophistication. The simplest merely allows you to select which connections to be made at the gate level. Some allow you to specify the Boolean expressions or truth tables and the software does the rest, including optimization of the program and a simulation. A complex design may require making a few hundred connections out of thousands of possibilities. This situation makes it exceedingly unlikely that someone would succeed in correctly specifying them all manually. Consequently, the choice of an appropriate programmer and its software is an important decision.

For the sake of expediency, it seemed reasonable to attempt to replicate the Lockheed Martin test box as closely as possible. Lockheed uses the Altera EPM5064 which Arrow

Electronics stocks and sells for \$30.99. The EPM5064 is an IC with a quartz window, which facilitates the erasure of the logic with a UV light source.

Programmers are made by a variety of manufacturers and can be used to program a wide variety of devices. PL/VTRP has already used and had good success with similar products made by BP Microsystems. Unfortunately, their programmer for this PLD costs \$3,495. At the other extreme, Modular Circuit Technology manufactures a programmer that JDR Microdevices sells for only \$499. A logical approach seemed to be the Altera programmer, the PL-ASAP2, which runs the Altera programmer software, MAX+PLUS II. Since Lockheed used Altera software to program its PLD, this approach had the potential for using Lockheed's source code for the PLD timing. Thus, using the Altera programmer and software should provide both the timing control that PL/VTRP would like and an easy method of accessing Lockheed's baseline configuration.

The Altera programmer and software are sold by Arrow for \$1995 and require a \$250 adapter for the particular PLD to be programmed. Before making such an investment I went to a demonstration of the product conducted by Altera's local representative, Nelco Electronix. After the demonstration, I learned that the Ball Aerospace people who work at PL/VTRP use the Altera programmer and software to do *all* the timing required for any FPA they are testing. This discovery saved the necessity of purchasing another programmer and provided us with in-house expertise in the programming of PLD's. The only purchase required was the particular PLD, the EPM5064, and the adapter for it.

1.2 Clocks and Biases for the Dual-Band FPA

After the appropriate method of generating timing patterns was determined, the next logical step was to determine precisely what those patterns were and how they might be altered for particular types of testing. It would seem that this would be a relatively simple task with the appropriate documentation provided by Lockheed Martin. Unfortunately, the documentation was difficult to understand, had numerous typographical

errors, and as it turned out, was substantially incomplete. Part of the problem undoubtedly arose because many terms and diagrams in the documentation were initially made for internal communication among those who already had familiarity with the device. The remainder of this subsection is devoted to a summary of the pertinent information about the Dual-Band FPA timing that has been gleaned after much study of the Lockheed Martin documents and a long conversation with the designer of the readout processor, Allen Hairston of Lockheed-Martin.

An early hurdle was deciphering Lockheed's use of multiple labels for the same bias or clock. The labels tend to vary depending on whether they are used on a master list, a timing diagram, a timing program, or on the device pinout. The following table lists both labels used in the documentation to describe the same bias or clock.

Identical Labels

VSS	=	VSSD
VDD	=	VDDD
VDSUB	=	VDDSUB
OUTM	=	LWOUT
OUTL	=	MWOUT
PCLK	=	PCK
PSNC	=	PLD SYNC

In addition to these duplicate names, all of which have been confirmed by Hairston, I initially thought that MRAL and MRAM were the same as RADL and RADM, respectively. Hairston pointed out that these are *not* the same.

Apparently, at Lockheed the PCLK, or "pixel clock," is generated by the Pulse Instruments system and is then fed into the PLD to clock it. At this point, PCLK is also passed on to the FPA. Another PI clock, PSNC, is also required by the PLD. Altogether, the Pulse Instruments system provides 12 clocks that go directly to the FPA and 2 clocks that are used to clock the PLD. The PLD generates 12 clocks and passes along the pixel clock to the FPA. There are a total of 25 clocks required by the FPA.

A hand drawn timing diagram was provided by Allen Hairston. Although it is numbered only to 110 states, it actually shows 156 states. After 110 there are no changes in what the clocks are doing. The output that correlates with this diagram is 18 dead states + 66 data out states + 6 dead + 66 data out, for a total of 156 states or one subframe. This diagram represents what Hairston calls "33-33" timing, which means 33 subframes of midwavelength and 33 subframes of long-wavelength. The subframes are averaged, but *not* read out simultaneously. The cycle through 156 states must be repeated 33 times for a total of 5,148 states in the timing pattern for one frame.

Hairston says "11-33" timing is Lockheed's standard condition: 11 mid-wavelength subframes and 33 long-wavelength subframes constituting one frame. Unfortunately, the hand drawn timing diagram does not illustrate this condition. If it did, it would have to be three times longer than it is. There would be two repetitions of 156 states (2 subframes) in which the mid-wavelengths are not being read out but the long-wavelength subframes are, and then a third series of 156 states (1 subframe) during which both bands are being read out. Thus, the total number of states in this timing pattern for one frame are $156 \times 3 \times 11 = 5,148$.

Correlating the Pulse Instruments coded timing with the hand drawn diagram was not an easy task, partly because the code provided initially was not complete. Recently, Mark Grammer of Ball Aerospace obtained from Lockheed timing coded in the Pulse Instruments style for all 25 clocks for both 11-33 timing and 33-33 timing. He determined that there are four Pulse Instruments clock states for each clock state on Hairston's hand drawn diagram. This fact has been confirmed by Kent Kuhler of Lockheed. It is also true that Lockheed has a 6 clock offset between their Pulse Instruments clocks and their PLD clocks. A memo from Kuhler to Grammer explains this in somewhat more detail and suggests eliminating the offset if all clocks were to be run from the same system. Note that the offset does not show up in Hairston's hand drawn diagram. One other noteworthy aspect of Kuhler's memo is that it lists the six clocks that must be altered when changing from 11-33 timing to 33-33 timing. They are LMM, RSM, AVM, MRAM,

RADM, and RADL. It is also true that clock VRFC becomes irrelevant in 33-33 timing and is therefore labeled as NUSE in some of the documentation.

1.3 Summary

Lockheed Martin did deliver some dual-band FPA's as promised. An Altera PLD and adapter were also obtained late in the summer. Unfortunately, Wallace Instruments never did deliver any part of the test station, so the adaptation of the test station for the dual-band FPA could not occur. Hopefully, however, significant progress was made in determining what will be required in order to use the Wallace test station to test the dual-band FPA's. At least a few more of the pieces are in place. In addition, significant progress was made in deciphering the documentation provided by Lockheed Martin. Near the end of the summer I worked closely on the timing issues with Mark Grammer. As of this writing, it appears that Mark has the functional timing patterns that are required for testing, and Ball Aerospace is planning to begin testing in the very near future.

2 Performance Evaluation of the LSTAT Infrared Camera System

As part of the LSTAT program, Rockwell International and Maxwell Laboratories have recently delivered a portable mid-wavelength infrared camera system to Phillips Laboratory. This "first-of-a-kind" camera is almost state-of-the-art. It was designed for the express purpose of demonstrating a wide range of infrared capabilities, with a particular focus on the observation of rocket launches during the 1997 Rome Laboratory scaled rocket tests.

The LSTAT camera is a portable camera system with a 640×480 FPA that is designed to work in the MWIR. Accordingly, the lens is $3\text{--}5\text{ }\mu\text{m}$. The system is controlled and operated with a 486DX2/66MHz personal computer, which also serves to drive the

monitor which displays the output. The FPA and the dewar are cooled with a closed cycle cryo-cooler which has its own power supply.

Unfortunately, there is virtually no documentation with the camera system. Dr. James Duffey of Maxwell demonstrated the operation of the camera to me, and he has written a one and a half page set of instructions for turning the camera on and getting it running. However, there is no information, besides limited software help menus, on how to operate the fairly complex and sophisticated software that runs the camera.

Overall, the camera works well and gives very vivid imagery of common objects close to room temperature, such as human bodies. The software does an excellent job performing gain and offset corrections that make the scene look quite uniform to the eye. The camera can also be run without the gain and offset corrections, and the result is dramatically different. The picture is very grainy with many dark spots and one large dark streak across the array. In addition to gain and offset corrections, the software allows for bad pixel replacement. This feature appears to fill in every offending pixel with an average value from those pixels around it. There is one cluster of bad pixels on the array which are roughly circular and show up on the monitor as a dark spot with a diameter on the order of $3/8$ of an inch. After bad pixel replacement is done this spot shrinks to approximately $1/8$ of an inch in diameter.

2.1 Software Shortcomings

Clearly the software is very complex and handles some very sophisticated chores as it processes the data stream that flows from the FPA. Regrettably, the user interface gives many indications that it was put together quite quickly. Here is an incomplete list:

- Most of the menu options do not indicate whether choosing the option will bring up a dialog box or whether it will immediately execute the option.
- The help windows are littered with typographical errors.

- Several help windows are only a line or two long and do little more than restate the options that motivated the user to request help.
- Several help windows state that “this procedure is not yet complete,” or that “this section is in the process of being updated.”
- Not all of the image is viewable on the monitor. It appears that several rows and columns are missing, but not in equal quantities on opposite sides.
- When the *DSP test* is run, the resulting message appears positive, but then the software locks up and must be rebooted.
- Under *Display Setup*, clicking to change the units to Celsius will yield an error message that states you cannot take the square root of a negative number. Then the software crashes.
- According to the help menu on *Save Image*, the only way that consecutive frames can be captured and saved is by checking the option *use DSP for capture* in the save window. (Incidentally, the maximum number of frames that can be saved in this manner is listed as 6.) When an image is averaged over up to 6 frames and stored with this box checked, it can no longer be viewed. If the box is left unchecked, then a file that contains an average of several frames can easily be viewed. This is a potentially serious issue because it calls into question what the DSP boards are doing. It also negates the possibility of recording successive frames.
- When saving an image there are two file formats possible: *.mat* which according to the help window is a Matlab readable file, and *.img* which is a raw image with the individual pixel values recorded in binary and preceded by a header. (Details about the header are available in the help windows.) If an image is saved and then viewed and then saved again, it appears that the file is corrupted—primarily the edge pixels, but the header may change also. This seems to be the case even if the viewed image is saved in the same format as the original.

- The bad pixel replacement options are located in a very unexpected place: under the *Setup* menu, in the *Image Orientation* window.

Most of the problems listed above are merely of the nuisance variety. There are, however, three problems with the software that impede progress toward quantitative measurements. First, under the *Image* menu is the window labeled *Image Statistics*. It contains a histogram of the pixels with each bin being the digital value a pixel can have and the height indicating the number of pixels with that value. Unfortunately, the horizontal axis is usually nonlinear, with gaps forming and closing depending on the scale chosen. The part of the array that is being histogrammed, is adjustable by sliding bars on the display. A boxed area appears on the monitor indicating which pixels are in the histogram. Numbers are displayed which are supposed to indicate the position and size of the box, but they are unreliable. Apparently, the user is supposed to be able to click on these numbers and enter values by hand. Unfortunately, attempting to do this results in very erratic behavior and has caused the software to crash. Another problem is the inability to print out the histogram or even to store it in a file.

The difficulties in the image statistics feature of the software are unfortunate. Attempts to make quantifiable estimates of the cameras performance would be greatly facilitated by the capabilities that are purportedly here. To be fair, the help window for these features does state that they are not yet fully implemented. So there is hope that these tools may soon be available.

A second problem involves the replacement of bad pixels. There are two important aspects of this process. First, what scheme is used to replace the bad pixels, and second, how the bad pixels are determined. As mentioned above, the replacement scheme is chosen in the *Image Orientation* window. Unfortunately, this window does not describe the various options. Instead, the user must pick from a list of file names ending in .prs.

The determination of which pixels are bad is a bit of a mystery. Statements in the help windows seem to indicate that during the offset and gain correction those pixels outside of some correction range are considered bad. These statements are confirmed

by a display which appears after offset and gain correction is performed and indicates the number of bad pixels. The number varies from one correction to another, but it is usually around 4 %. Presumably addresses for the bad pixels are then placed in a file like "last.bad." However, in the *Uniformity Correction* window there is a *choose bad pixel file* option. Here there are four listed options, but no matter which the user checks, the top one, *permanent file*, is always the one checked after the calibration is done. Despite this observation, I believe that a new bad pixel file is created during each calibration and the bad pixels listed in it are the ones replaced. This purely subjective opinion is based on the significant improvement that occurs each time bad pixels are replaced.

The third problem is a very difficult obstacle to overcome in any quantitative evaluation of the camera's performance. It is the almost complete lack of information regarding what the software is doing to the data coming off the FPA. It would be extremely helpful if there was an explanation of how the software does its offset and gain corrections. The results look good, but how were they obtained? The next subsection discusses this and related issues.

2.2 Pixel Values

Before data of any quantitative significance can be obtained, it is necessary to have a thorough understanding of the numerical values obtainable for individual pixels. Under the *Image* menu, there is an option called *pixel intensity*. Choosing this option allows the user to select individual pixels with the mouse. A pointer, x-y coordinates, and an intensity value are displayed on the monitor. The intensity value can range from 0 to 4095, clearly the base 10 equivalent of a 12 bit binary number. Under *Image Statistics*, the histogram displays bins over the same range and calls this axis *A/D Counts*. It seems very clear that these are the same numbers.

As mentioned before, when a file is saved, the user has two options. It can be saved as raw image file with a .img extension, or it can be saved as a Matlab file with a .mat extension. Despite the efforts of someone familiar with Matlab, Anjali Singh, she was

unable to pull these files up into Matlab running on a Sun workstation. The .img files were more useful. I was able to enlist the help of a programmer who wrote a short C program which converted the 16 bit integers representing individual pixel values into base 10 format. The files were then readable in a standard spreadsheet program. Direct comparison of individual values on the spreadsheet with those selected by the cursor on the saved, displayed image showed perfect correlation.

As would be expected, the offset and gain correction, as well as the bad pixel replacement, will affect the values of the pixels. However, it is vitally important to understand that even if these options are turned off, the pixel values are *not* representative of the digital values coming from the camera. Under the *Setup* menu there is a *video setup* window that allows the user to change *video gain* and *video offset*. The video gain can take values of 0, 1, 2, or 3. The video offset has thousands of different settings. Both of these parameters have a major impact on the value of each pixel.

Raising the video gain parameter stretches the pixel values out so that two different intensities in the actual scene will have values that are farther apart in the 12 bit range. The effect is much like increasing the contrast on a monitor. An increase in the video offset of about 10 causes a decrease of roughly 100 in the pixel values. (The inverse relationship and factor of ten is surprising.) This additive effect is analogous to changing the brightness control on a monitor.

Apparently the digital signal coming off the array is processed in several different ways. For the pixels, the video offset is an additive shift and the video gain represents some multiplicative factor. Likewise, individual pixels can undergo an offset and gain correction, and some pixels deemed as bad might be replaced. Offset and gain correction can be turned off, or replaced with a global offset and gain correction of the users choice (an option under the *calibration* menu). Of course, bad pixel replacement can also be turned off, but the video gain and video offset parameters will always be affecting the pixel values. Unfortunately, all of these parameters affect the data in undetermined ways. This circumstance severely restricts the collection of quantitative data.

2.3 Data

An estimate of the camera's field of view was made using a meter stick. The camera was focused nearly at infinity, and marks were made on a wall at the edges of the image displayed on the camera's monitor. Simple trigonometry yielded a vertical field of view of 7° and a horizontal field of view of 9° . The angle given is the one subtended by the viewed area as measured from the center of the lens system. As reported earlier, not all of the detector image is visible on the particular monitor supplied. If the monitor is replaced with a standard VGA unit, it is possible that then every line and row put out by the FPA may be viewable. Hence, the field of view numbers given here are only estimates.

Offset and gain correction is necessary to obtain anything close to a quality image. During the offset and gain correction procedure, the software requests both a uniform warm and a cool source to completely cover the lens and provide two points as a basis for the correction. Typically the lens cap is put on for a "cool" source and a human hand is used to cover the lens for a "warm" source. Dr. Duffey and others at Maxwell apparently spent considerable time and effort attempting to find the best warm source for the higher temperature. According to the lab book that accompanied the camera, they were only able to achieve marginal improvement over the warm hand. The lens cap and hand sources were used for most of the offset and gain corrections done during the week I tested the camera system.

On one occasion, after offset and gain correction using room temperature and skin temperature, a match was lit in view of the camera. The image showed considerable blooming from this very bright IR object. In these excessively bright areas, the image had a stationary background graininess and nonuniformity, appearing much like that of the uncorrected image. On another occasion, I used a piece of foam soaked in liquid nitrogen as the cool correction source and the lens cap as the warm source. After this offset and gain correction, human skin had a mottled and grainy stationary background much—like what occurred earlier when the match was lit—although there was no noticeable

blooming. Most likely, both the hot flame for the cap/hand calibration and the skin for the LN_2 /cap calibration are far enough outside of the correction range that the inherent nonuniformity of the FPA is observed in the camera's image.

After using offset and gain correction with the lens cap and hand, the lens cap was reinstalled on the lens. Then images of the lens cap were saved in .img files and analysed. Some files consisted merely of one frame, while others utilized the camera software option of saving the average of multiple frames. The files were then converted to into standard spreadsheet files and histograms were made. Each data point on the histogram corresponds to one bin—the width of which is equal to the smallest increment available in a 12 bit system. If the data had not been manipulated by the software, one would expect that the resulting histogram would be a Poisson distribution. The actual result, however, cannot be Poisson because the mean value is altered by the video offset. Of course, the mean value of a Poisson distribution is its variance. Thus, the variance as determined by the mean value would be arbitrary even though it is clear that the shape of the distribution must be determined by the response of detector elements to incident photons. All of these histograms showed a definite asymmetry, with the steep side being on the lower count side and a long tail extending to the higher count bins. The histograms of single frames were not smooth. As the number of frames in the average was increased, a definite secondary peak appeared on the higher count side of the mean (cf., Figure 1).

The double peak was interesting. Realizing that the FPA readout is divided into four quadrants, I decided to make separate histograms of the left side of the image and the right side of the image. The right half showed virtually no sign of the secondary peak, whereas the histogram of the left side showed two peaks of almost equal height (cf., Figure 2). This observation would appear to indicate that the two quadrants on the left side had slightly different offsets, even after offset and gain correction had been performed. This hypothesis may have been confirmed by breaking down the data into four separate quadrant histograms, but there was not enough time available for such

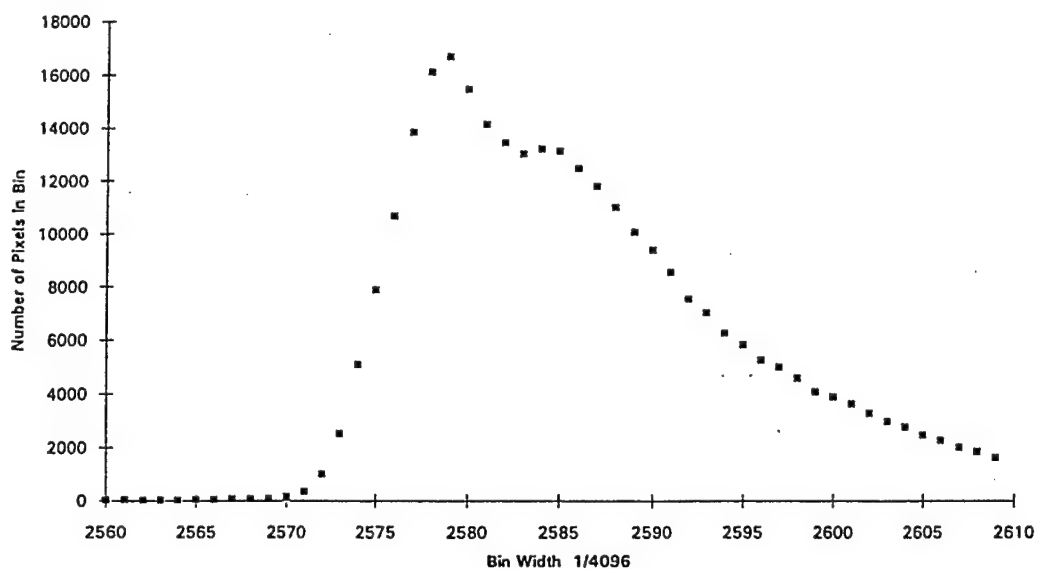


Figure 1: Histogram of 100 frame averages taken at room temperature have a secondary peak.

analysis.

Data files were also subtracted from one another on a pixel by pixel basis. The results were then put in a histogram. The mean values of these histograms were within about one bin width of zero for both single frames and for the difference of 16 averaged frames subtracted from another 16 averaged frames. When 100 averaged frames were subtracted from another 100 averaged frames, the resulting histogram had a mean that was 2.7 bins removed from zero. This shift is interpreted as a drift in lens cap temperature resulting from the long period of time (over 3 minutes) required to take 100 frames of data. The histograms appeared to be quite Gaussian in shape, being quite narrow. The single frame difference had a standard deviation of 3.7 bins, whereas both the 16 and 100 frame average difference had a standard deviation of 1.8 bins. Apparently, further averaging no longer reduces the inherent photon noise.

The very Gaussian appearance of the difference histograms was expected. All gain and offset corrections, in addition to nonlinearities, optical effects, and bad pixels, should be removed during the pixel-by-pixel subtraction. Thus, in effect, the distribution that

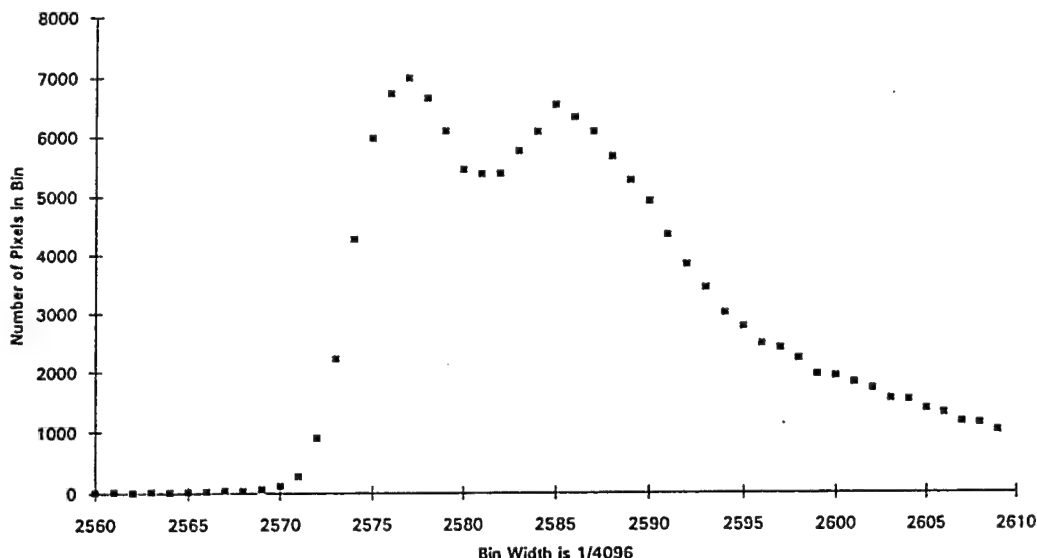


Figure 2: The histogram of only the left half of the FPA for 100 frame averages.

results from the subtraction should really be the subtraction of one Poisson distribution from another. With this camera system and its software, this is the closest one can come to getting "raw" data. An unexpected observation was made when it became apparent by looking at the spreadsheet that those numbers that represented the differences near the edges of the array were generally somewhat smaller than those near the center. Earlier, I had noticed that more radiation falls in the center of the array, apparently due to vignetting caused by the lens system. The lower light levels would imply lower incident photon rates and thus lower photon noise. The lower noise shows up as smaller differences between frames.

One day a double piece of aluminium foil was inserted into the camera's dewar and attached to the cold stem so as to completely cover the FPA's field of view. The dewar was then pumped out and cooled in the standard manner. No offset and gain correction was possible because the camera could not view two different temperatures. Interestingly, whereas before there were both bright and dark speckles in the image, under these conditions only bright specks appeared and no longer could the bad cluster of pixels be observed. The image had four distinct quadrants, with the two on the right

being significantly darker than the two on the left. The histograms of one frame, 16 frame averages, and 100 frame averages all showed very distinct and separate peaks. The peaks were of comparable height and were separated by values similar to the individual value differences between the left and right sides that could be picked off the monitor using the *pixel intensity* option. It seems certain that the double peak is caused by different dark current levels in the different quadrants of the uncorrected data.

Difference histograms were made in the same manner as before and they again were very Gaussian in appearance with extremely narrow peaks. The means were all close to zero with the one frame difference being the farthest from zero at a 0.24 bin offset. Presumably the LN₂ block did not drift as much in temperature during 100 frame averaging as the lens cap did. The standard deviations of the histograms were all more than their room temperature counterparts: 5.0 bins for the one frame, 2.9 for the 16 frame, and 2.7 for the 100 frame. As before, the standard deviation did not shrink significantly when going from 16 frames to 100 frames.

Surprisingly, under the *Setup* menu, in the *Video Setup* window, the integration time and the frame rate of the FPA itself can be adjusted. While the camera had the LN₂ block, the mean value of all pixels was recorded for different integration times. The results were quite linear as is evident from Figure 3. Data were taken at video gains of both 1 and 2. As expected, the data for the larger gain has a greater slope. For each integration time the mean value was found for several different frame averages. Whether there was only one frame taken or there were 100 frames averaged together, the average pixel value was essentially unchanged. The averages of the pixel values were obtained from the *Image Statistics* window. The only time that the integration time was not set at 2.03 msec was when these data were obtained.

2.4 Summary

Substantial progress was made in evaluating the IR camera system. Unfortunately, most of the limitations discovered were caused by the software, rather than the performance

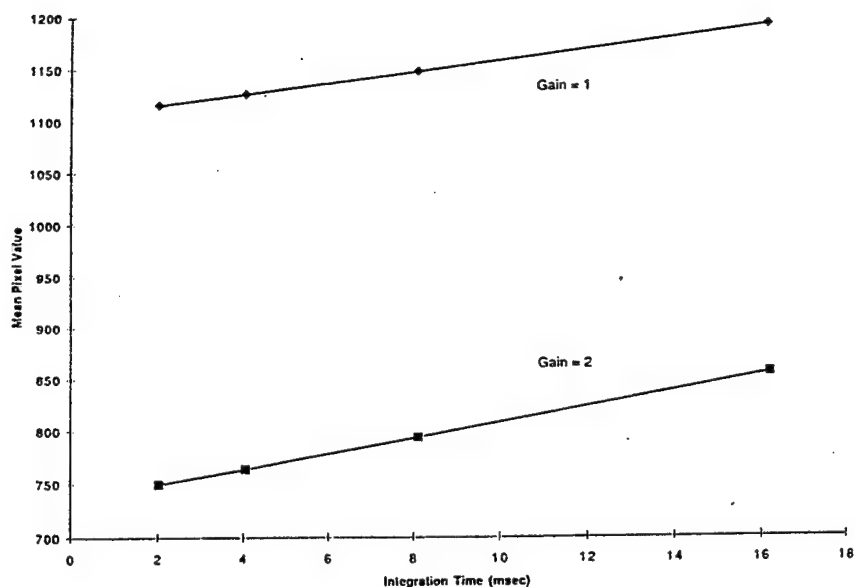


Figure 3: Mean value of all pixels plotted as a function of integration time. The dewar is blocked off at the cold stem. Note that the data for the greater gain setting has a slightly greater slope.

of the hardware itself. Originally, we had hoped to determine whether the system performance was background limited, and if so, at what temperature background it would no longer be operating at BLIP. Instead, much time was spent trying to learn the nuances and intricacies of the software. A number of problems were identified and are reported here. Progress was made on determining what the software does to the raw data and how it goes about doing it, but our knowledge of this important aspect of the camera system is still inadequate. Concrete data was taken on things like the camera's field of view, and histograms were made of the individual pixel values on the array. These histograms showed significant asymmetry, probably caused by the software processing, but histograms resulting from subtraction of frames had the expected Gaussian shape. One puzzling aspect of the data was an apparent difference in the offset values for one quadrant. This last result has not been confirmed and should be examined further.

TILT SENSING TECHNIQUE WITH A SMALL APERTURE BEAM AND RELATED
PHYSICAL PHENOMENA

Mikhail S. Belen'kii
Principle Research Scientist
Electro-optics, Environment, and Materials Laboratory

Georgia Tech Research Institute
Georgia Institute of Technology
925 Dalney Street
Atlanta, Georgia 30332-0834

Final Report for:
Summer Faculty Research Program
Phillips Laboratory

Sponsored by:
Air Force Office of Scientific Research
Bolling Air Force Base, DC

and

Phillips Laboratory

September 1996

TILT SENSING TECHNIQUE WITH A SMALL APERTURE BEAM AND RELATED PHYSICAL PHENOMENA

Mikhail S. Belen'kii
Principle Research Scientist
Electro-optics, Environment, and Materials Laboratory
Georgia Tech Research Institute
Atlanta, Georgia 30332-0834

Abstract

A tilt sensing technique which does not require transmitting laser irradiance through the main optical train is described. The method exploits a small aperture beam transmitted from behind a portion of the primary mirror of the main telescope. The main and auxiliary telescopes are used simultaneously to measure the LGS image motion. A one-axis component of the full aperture tilt is determined by subtracting the tilt measured with the main telescope, from that measured with an auxiliary one. The two effects, namely a tilt angular anisoplanatism and tilt focus anisoplanatism, which determine the required parameters of the tilt measurement scheme and the tilt sensing error, are studied by taking into account a finite outer scale of turbulence and vertical distribution of the strength of turbulence. A tilt angular correlation scale and tilt averaging function are quantitatively estimated. Parameters of the tilt measurement scheme are determined. The two experiments, namely Polaris jitter and Moon-edge jitter experiments are designed and carried out. The goal of the first experiment is to determine the effect of non-Kolmogorov stratospheric turbulence on the star image motion. A second experiment was designed to study a tilt angular correlation and to obtain the data which are required to design a tilt sensing experiment with a LGS. The two additional experiments are designed as a part of the Summer Research Program. A technical objective of one of these experiments is to study a LGS image motion for a monostatic laser beacon method and to test the technique for remote sensing of the vertical profile of $C_n^2(h)$ by using a modified LGS scheme. The technical objective of another experiment is to demonstrate and test a technique for sensing full aperture tilt with a laser guide star.

TILT SENSING TECHNIQUE WITH A SMALL APERTURE BEAM AND RELATED PHYSICAL PHENOMENA

Mikhail S. Belen'kii

Introduction

By sensing and compensating for the atmospheric wavefront aberrations in real time, adaptive optics systems {1-3} can potentially provide us with a diffraction limited resolution for the large aperture telescopes. However, a conventional laser guide star (LGS) adaptive optics method does not permits us to sense full aperture tilt. That inability to sense full aperture tilt greatly limits the area of the sky accessible for adaptive optics correction. This area is limited to about 0.1 %. To achieve full sky coverage, a tilt sensing techniques with a LGS should be developed.

The technique that permits us to sense full aperture tilt with a laser beacon has been recently proposed {4,5}. This technique exploits a full aperture beam transmitted through the main optical train and two auxiliary telescopes separated in transverse directions. A tilt decorrelation due to angular anisoplanatism is used in this method to eliminate the contribution of the down propagation path to the tilt measured with an auxiliary telescope. This contribution is eliminated by averaging a LGS image motion over a laser beacon angular extent. The proposed technique, however, cannot be used for the mesospheric sodium layer. That is because of the fluorescence of the optical train.

A tilt sensing technique which does not require transmitting laser irradiance through the main optical train was developed as a part of the Summer Research Program. This technique exploits a small aperture beam transmitted from behind a portion of the primary mirror of the main telescope. The main and auxiliary telescopes are used simultaneously to measure the LGS image motion. A one-axis component of the full aperture tilt is equal to the difference between the measurements of LGS motion taken with the main and auxiliary telescopes. This technique does not require transmitting laser irradiance through the main optical train. Due to this fact it might be used for the mesospheric sodium layer.

A tilt angular anisoplanatism and tilt focus anisoplanatism are studied by taking into account a finite outer scale of turbulence and vertical distribution of the strength of turbulence. A tilt angular correlation scale and tilt averaging function are quantitatively estimated. The required parameters of a tilt measurement scheme and a tilt sensing error are determined.

The Polaris and Moon-edge jitter experiments were designed and carried out. The first experiment was designed to determine the effect of non-Kolmogorov stratospheric turbulence on the star image motion. The goal of a second experiment was to measure a tilt angular correlation and to obtain the data which are required to design a tilt sensing

experiment with a LGS. Two additional experiments were also designed. One of these experiments is devoted to a study of a LGS image motion for a monostatic laser beacon scheme. Even though such a scheme does not permit us to sense full aperture tilt, it can be used to sense vertical profile of $C_n^2(h)$ remotely. The technical objective of the other experiment is to demonstrate and test a technique for sensing full aperture tilt with a laser guide star.

Tilt sensing technique with a small aperture beam

Let us assume that a small aperture beam with the radius, a_0 , which is much smaller than the radius of the primary mirror of the main telescope, $a_0 \ll a_L$, is transmitted from behind a portion of the primary mirror, for example, behind a secondary mirror. Due to turbulence this beam is displaced at an angle φ_{LB} (see Fig. 1). This angle might be presented as a sum

$$\varphi_{LB} = \varphi_{FA} + \varphi_{LT}(\rho). \quad (1)$$

Here φ_{FA} is the full aperture tilt for the primary mirror, and $\varphi_{LT}(\rho)$ is the local tilt depending on the beam director position. The overall beam tilt, φ_{LB} , does not depend on the size of the primary mirror, but both tilt components, φ_{FA} , and, $\varphi_{LT}(\rho)$, depend on this size.

As one of the term in the sum presented by Eq. (1) is the full aperture tilt, φ_{FA} , the correlation of the angular motion of the small aperture beam with the image motion of a natural star observed with the main telescope, φ_{NS} , coincides with the star jitter variance $\langle \varphi_{LB} \varphi_{NS} \rangle = \langle \varphi_{FA}^2 \rangle = \langle \varphi_{NS}^2 \rangle$. This result is consistent with Eq. (6) in [4]. The last equation has the form $\langle \varphi_{LB} \varphi_{NS} \rangle = 4.05 \cdot 2^{1/6} \int_0^H C_n^2(\xi) (1 - \xi/H) (a_r^2(\xi) + a_L^2)^{-1/6} d\xi$, where $a_r(\xi)$ is the average size of the beam. By neglecting the average size of the beam, as compared with the telescope radius, $a_r \ll a_L$, and neglecting the path weighting function for the sodium beacon, from the above expression one can also determine that the correlation $\langle \varphi_{LB} \varphi_{NS} \rangle$ coincides with the jitter variance for a natural star $\langle \varphi_{LB} \varphi_{NS} \rangle \cong \langle \varphi_{NS}^2 \rangle$.

Let us assume that the laser beacon, formed by a small aperture beam, is observed with an auxiliary telescope. The tilt measured with an auxiliary telescope tilt, φ_A , contains an additional tilt component, φ_{SS} ,

$$\varphi_A = \varphi_{LB} + \varphi_{SS}, \quad (2)$$

which is due to the contribution of the down propagation path. Because of the tilt anisoplanatism, the tilt component corresponding to the down propagation path, φ_{SS} , depends on FOV of the receiver, θ_R . If FOV of the receiver is much larger than the tilt angular correlation scale, $\theta_R \gg \theta_l$, similar to that for the scheme with a full aperture beam [4,5], the contribution of a down propagation path might be eliminated by averaging a LGS image motion over a laser beacon angular extent. Therefore, the overall beam tilt, φ_{LB} , corresponding exclusively to the upward propagation might be measured with an auxiliary telescope. However, besides the full aperture tilt, φ_{FA} , this

tilt contains the local tilt $\varphi_{LT}(\rho)$. The local tilt should be eliminated. It can be done by using both the main and auxiliary telescope simultaneously to measure a laser beacon image motion.

In {4} it was shown that, due to the reciprocity of propagation paths, the full aperture tilt, φ_{FA} , in the strictly backward direction is perfectly compensated. However, it is not compensated in the lateral direction. Therefore, with the main telescope only the local tilt, $\varphi_{LT}(\rho)$, can be measured: $\varphi_M = \varphi_{LB} - \varphi_{FA} = \varphi_{LT}(\rho)$. At the same time, with an auxiliary telescope one can measure the sum $\varphi_A = \varphi_{LB} + \varphi_{SS}$. The implication is that the full aperture tilt, φ_{FA} , might be determined by subtracting the tilt measured with the main telescope, φ_M , from that measured with an auxiliary one, φ_A ,

$$\varphi_{FA} = \varphi_A - \varphi_M. \quad (3)$$

With a single auxiliary telescope only a one-axis tilt component might be sensed. To sense the two tilt components, the two receiving telescopes are required.

In the scheme with a full aperture beam {4,5} an uncontrolled motion of the main telescope does not affect the tilt sensing accuracy. That is because both the transmitting beam and the starlight pass through the same optical train. However, this is not true for a small aperture beam. In this case, an uncontrolled telescope motion should be eliminated. It can be done by measuring the differential motion of the two beams at the output of the telescope, or at the distance where the atmospheric turbulence effect is negligibly small. One of the beams is a high power laser beam transmitted from behind a portion of a primary mirror, and another beam is a low power beam transmitted through the main optical train. A description of a tilt sensing technique with a small aperture beam is presented in {6}.

Tilt angular anisoplanatism

The angular correlation of the tilts for two plane waves arriving at the telescope of diameter D_a at the angle 0 and θ is considered by using the Zernike polynomials expansion for the atmospheric wave-front distortions {7-10}. For the von Karman power spectrum of the refractive-index fluctuations $\phi_n(K) = 0.033C_n^2(K^2 + K_{0K}^2)^{-11/6}$, where $K_{0K} = 3.08/L_0$, a tilt correlation coefficient has the form

$$b_{x,y}(\theta) = \frac{\int_0^H dh C_n^2(h) \cdot \int_0^\infty dK (K^2 + K_{0K}^2)^{-11/6} J_2^2(K) \left[J_0\left(\frac{2\theta h}{D_a} K\right) \mp J_2\left(\frac{2\theta h}{D_a} K\right) \right] / K}{\int_0^H dh C_n^2(h) \cdot \int_0^\infty dK (K^2 + K_{0K}^2)^{-11/6} J_2^2(K) / K}, \quad (4)$$

where J_0 and J_2 are the Bessel functions. The negative sign in Eq. (4) corresponds to the longitudinal, or parallel to the separation θ , tilt, X, whereas the positive sign corresponds to the lateral tilt, Y. The tilt correlation coefficients calculated by using Eq. (4) for the vertical profile $C_n^2(h)$ given by the model $C_n^2(h) = C_{n0}^2 \exp(-h/\bar{h})$ are shown in Fig. 2. Here \bar{h} is the effective altitude, or characteristic scale, of the turbulent atmosphere determined by the ratio

$\bar{h} = \mu_1 / \mu_0$ of the first two moments for the vertical profile $C_n^2(h)$: $\mu_0 = \int_0^\infty C_n^2(h) dh$ and $\mu_1 = \int_0^\infty C_n^2(h) h dh$. If the parameters C_{n0}^2 and \bar{h} are equal to $C_{n0}^2 = 2.37 \times 10^{-15} m^{-2/3}$ and $\bar{h} = 934 m$, respectively, the two moments μ_0 and μ_1 for the above $C_n^2(h)$ model coincide with that for the Hufnagel-Valley (HV₅₇) model [11,12]. For the HV-54 model these parameters equal $C_{n0}^2 = 8.55 \times 10^{-16} m^{-2/3}$ and $\bar{h} = 3,466 m$.

The tilt structure function, or tilt anisoplanatism, $D_y(\theta)$, is related to the tilt angular correlation coefficient $b_y(\theta)$ through the equation

$$D_y(\theta) = \langle [a_y(0) - a_y(\theta)]^2 \rangle = 2\sigma_y^2(L_0/D)[1 - b_y(\theta/\theta_t)], \quad (5)$$

where σ_y^2 is a one-axis tilt variance depending on the ratio L_0/D . Therefore, one can calculate the tilt structure function by knowing the correlation coefficient $b_y(\theta)$ and the variance σ_y^2 .

From Fig. 2 it is shown that the tilt angular correlation coefficients gradually decrease with increasing the angular distance θ . For small separation ($\theta \ll \theta_t$) they have the asymptote $b_{x,y}(\theta) \sim 1 - (\theta/\theta_t)^2$. For the large angular separation $\theta \gg \theta_t$ and for the Kolmogorov model with $L_0 = \infty$ the asymptote has the form $(\theta/\theta_t)^{-1/3}$. For a finite outer scale L_0 and large angular separation θ , the correlation coefficients for the lateral and longitudinal tilt have the asymptotes $(\theta/\theta_t)^{-1}$ and $(\theta/\theta_t)^{-2}$, respectively. Therefore, the asymptotes and the tilt angular correlation coefficients behavior for the finite and infinite outer scale are different. The implication is that the Kolmogorov model with infinite outer scale ($L_0 = \infty$) does not permit us to describe the tilt angular correlation.

One can introduce the tilt angular correlation scale, θ_t , as the distance between the propagation paths over which the correlation coefficient b_y decreases to the level e^{-1} ($b_y(\theta_t) = e^{-1}$). From the numerical estimates for $b_y(\theta)$ presented in Fig. 2, it is easy to find that the tilt correlation scale θ_t is equal to

$$\theta_t = \alpha(L_0/D)D/\bar{h}, \quad (6)$$

where α is the coefficient of proportionality. This coefficient describes the effect of the outer scale of turbulence L_0 on the tilt correlation scale. When $\alpha = \text{constant}$, the tilt correlation scale θ_t is proportional to D , however, due to the dependence $\alpha(L_0/D)$, the tilt correlation scale θ_t varies with the telescope diameter D non-linearly. The latter is seen in Table 1, where the estimates for the tilt correlation scale θ_t for different models $C_n^2(h)$ and outer scale L_0 are presented.

The tilt correlation scale θ_t increases with increasing both the telescope diameter D and the outer scale L_0 . The correlation scale θ_t is smaller for the model HV-54 than that for the model HV₅₇. The latter is due to the fact that the HV-54 model contains stronger turbulence at high altitudes than the model HV₅₇. The high altitude turbulence more

severely degrades the tilt angular correlation than that near the ground. The implication is that one can expect the tilt correlation scale to be smaller at the sites with good seeing conditions than that at the sites with bad seeing.

Table 1. Tilt angular correlation scale, θ_i , arcsec							
Telescope diameter, D_a m		0.1	0.2	0.3	0.5	1.5	3.5
HV-54, h = 3,466 m	$L_0=3$ m	13	21	26	33	69	139
	$L_0=6$ m	17	27	35	46	87	172
HV ₅₇ , h = 934 m	$L_0=3$ m	48	78	96	122	255	516
	$L_0=6$ m	63	100	130	170	323	638

A tilt anisoplanatism was recently measured with a 2.4 m telescope in [13]. A tilt angular correlation with a variable aperture was measured in [14]. According to [14], for a 0.35 m aperture a tilt angular correlation drops down to 0.2 at an angular distance of 90 arcsec. This is consistent with the estimates for the HV-54 model and $L_0 > 6$ m.

In Fig. 3 the tilt correlation coefficient $b_y(\theta)$ is plotted versus θ/θ_i . In this scale the curves corresponding to different outer scale of turbulence, L_0 , coincide with each other, and represent a universal tilt correlation curve. According to [5], the image jitter variance of an incoherent secondary source, $\langle \bar{\varphi}_{ss,y}^2 \rangle$, is related to the tilt angular correlation coefficient, $b_y(\theta)$, by the equation

$$\langle \bar{\varphi}_{ss,y}^2 \rangle = \frac{2\langle \varphi_{ps}^2 \rangle}{\theta_r} \int_0^{\theta_r} b_y(\theta/\theta_i)(1 - \theta/\theta_r) d\theta, \quad (7)$$

where $\langle \varphi_{ps}^2 \rangle$ is the image jitter variance of a point source for an auxiliary telescope. The dependence of the ratio $\langle \bar{\varphi}_{ss,y}^2 \rangle / \langle \varphi_{ps}^2 \rangle$ on FOV of the receiver, or the tilt averaging function, calculated by using the universal curve for $b_y(\theta)$, is shown in Fig. 4. It is seen that the ratio $\langle \bar{\varphi}_{ss,y}^2 \rangle / \langle \varphi_{ps}^2 \rangle$ diminishes to the level 10^{-1} if $\theta_r \approx 25 \cdot \theta_i$, and it diminishes to the level $5 \cdot 10^{-2}$ if $\theta_r \approx 75 \cdot \theta_i$. The above curve permits us to estimate the parameters of a tilt measurement scheme. The three parameters, namely, an auxiliary telescope diameter, D_a , FOV of this telescope, θ_r , and the separation, Δ , should be estimated. As the tilt correlation scale θ_i is proportional to an auxiliary telescope diameter, $\theta_i \approx \alpha \cdot D_a$, this diameter should be small. However, the fact that the variance $\langle \varphi_{ps}^2 \rangle$ increases with decreasing an auxiliary telescope diameter, $\langle \varphi_{ps}^2 \rangle \approx D_a^{-1/3}$, should be also taken into account.

The estimated parameters of the tilt measurement scheme for the sodium LGSs and for $L_0 = 3$ m are presented in Table 2. For the estimated parameters a tilt sensing error due to contribution of a down propagation path is of the order of 15% for a 1.5 m telescope.

According to Table 2, the distance, Δ , between the main and auxiliary telescope for the sodium beacons is of the order of several kilometers. By using the linearity property of the integral expression in Eq. (7) this distance might be reduced. Indeed, if an array of the two auxiliary telescopes is used to sense a one-axis tilt component, an integral in Eq. (7) might be divided into two parts: $\int_0^{\theta_r} f(\theta) d\theta = \int_0^{\theta_{r_1}} f(\theta) d\theta + \int_{\theta_{r_1}}^{\theta_r} f(\theta) d\theta$. Here θ_{r_1} is FOV of one of the receivers, which senses the Rayleigh portion of the scattering column, or Rayleigh LGS, and $\theta_r - \theta_{r_1}$ is FOV of another receiver, which senses the sodium LGS. Due to the fact that the angular size of the sodium LGS is reduced, a smaller distance between the main and auxiliary telescope, Δ , is required. The results of analysis of a tilt angular anisoplanatism are presented in (15). A tilt sensing error is another important characteristic of the tilt measurement technique.

Table 2. Parameters of the tilt measurement scheme for the sodium beacons				
LGS altitude, H, Km	LGS range, $2a_{v11}, Km$	Auxiliary telescope diameter, D, m	FOV of the receiver, $\theta_r, arc\ min$	Separation between the telescopes, Δ, km
HV-54 model				
90	20	0.2	13.3	1.6
HV _{5/7} model				
90	20	0.2	39	4.7

Tilt sensing error and tilt focal anisoplanatism

The accuracy of sensing tilt is characterized by the normalized mean square difference between the instantaneous tilt for a scientific object, or natural star, φ_{NS} , and that for the laser beacon at the same zenith angle,

$$\delta = \left(\langle (\varphi_{LGS} - \varphi_{NS})^2 \rangle \right)^{1/2} / \langle \varphi_{NS}^2 \rangle^{1/2} = \delta_z / \langle \varphi_{NS}^2 \rangle^{1/2}. \quad (8)$$

Here $\langle \varphi_{NS}^2 \rangle^{1/2}$ is the natural star jitter rms. By taking into account that the LGS tilt, φ_{LGS} , contains four statistically independent components, $\varphi_{LGS} = \varphi_{LB} + \bar{\varphi}_{SS} + \varphi_{TM} + \varphi_{PSLB}$, which might contribute to the tilt sensing error, one can present the δ_z^2 in the form $\delta_z^2 = \delta_{FA}^2 + \langle \bar{\varphi}_{SS}^2 \rangle + \langle \varphi_{TM}^2 \rangle + \langle \varphi_{PSLB}^2 \rangle$. Here φ_{TM} is the tilt component corresponding to an uncontrolled telescope motion; φ_{PSLB} represents a pointing stability of the transmitting beam, and $\delta_{FA}^2 = \langle (\varphi_{NS} - \varphi_{LB})^2 \rangle$.

Due to the fact that for the tilt sensing technique with a full aperture beam the main telescope motion contributes simultaneously to the image motion of a natural star and motion of the transmitting beam, an uncontrolled motion

of the main telescope φ_{TM} does not affect the accuracy of sensing tilt. Therefore, one can exclude this component from the analysis. The component $\langle \varphi_{PSLB}^2 \rangle$ representing the pointing stability of a laser beam might be eliminated by selecting an appropriate laser and/or expanding the laser beam to the size of the main telescope. The implication is that the two components: $\langle \overline{\varphi}_{SS}^2 \rangle$ and δ_{FA}^2 contribute to the tilt sensing error δ_{Σ}^2 . The component, $\langle \overline{\varphi}_{SS}^2 \rangle$, is due to the contribution of a down propagation path to the LGS image motion, or due to tilt anisoplanatism. The component, δ_{FA}^2 , is caused by the deviation of the ray trajectories for the transmitting beam from that for a star wave.

To estimate the tilt focus anisoplanatism, $\delta_{FA}^2 = \langle \varphi_{NS}^2 \rangle + \langle \varphi_{LB}^2 \rangle - 2\langle \varphi_{LB}\varphi_{NS} \rangle$, the three moments $\langle \varphi_{NS}^2 \rangle$, $\langle \varphi_{LB}^2 \rangle$, and $\langle \varphi_{NS}\varphi_{LB} \rangle$ should be evaluated. These moments were calculated in {4} for the Kolmogorov spectrum with infinite outer scale ($L_0 = \infty$). Here we take into account a finite outer scale L_0 . Similar to {4} both the tilt for the transmitting beam, $\varphi_{LB} = \rho_{LB}/H$, and for the star, $\varphi_{NS} = \rho_{NS}/F$, are characterized through the corresponding energy centroids ρ_{LB} and ρ_{NS} , respectively. The radius-vector of the energy centroid of the laser beam at altitude H is determined by the formula $\vec{\rho}_{LB} = \int I(H, R) \vec{R} d^2 R / P_0$, where $I(H, R)$ is the intensity distribution in the cross section of the beam, and $P_0 = \int I(H, R) d^2 R$ is the total beam energy. A star image energy centroid is equal to $\vec{\rho}_{NS} = \int I_f(R) \vec{R} d^2 R / P_0$, where $I_f(R)$ is the intensity distribution in the focal plane, and $P_0 = \int I_f(R) d^2 R$ is the total flux of a star light passing through the telescope.

The expression for $\vec{\rho}_{LB}$ has the form

$$\vec{\rho}_{LB} = \frac{1}{2P_0} \int d\xi \int d^2 R I(H, R) \nabla_R \varepsilon(\xi, R). \quad (9)$$

Here, $\nabla_R \varepsilon$ is the transverse gradient of the dielectric permittivity. By using a geometric-optics representation for the phase fluctuations in a plane wave, the expression for the star image energy centroid might be presented in the form

$$\vec{\rho}_{NS} = \frac{1}{2P_0} \int d\xi \int d^2 R T(R) \nabla_R \varepsilon(\xi, R). \quad (10)$$

By using Eqs. (9) and (10), one can calculate the moments that are needed to estimate the tilt sensing error δ_{FA}^2 . The calculations might be performed by using the Furutsu-Novikov formula, {16} which permits us to "split" the correlations of the integral $I(\xi, R)$ and local $\varepsilon(\xi, R)$ quantities, and an approximation of a Markovian random process for the process ε . The process ε is assumed to be a Gaussian and homogeneous. That permits us to present the correlation $B_\varepsilon(x, \vec{\rho}, x^1, \vec{\rho}^1)$ in the form {16}

$$B_\varepsilon(x, \vec{\rho}, x^1, \vec{\rho}^1) = \delta(x - x^1) \times 2\pi \int d^2 K \exp(-i\vec{K}(\vec{\rho} - \vec{\rho}^1)) \phi_\varepsilon(\vec{K}), \quad (11)$$

where $\phi_\varepsilon(\vec{K})$ is the power spectrum of the dielectric permittivity fluctuations, $\phi_\varepsilon(K) = 4\phi_n(K)$.

By using Eqs. (9)-(11), the above assumptions and Gaussian approximation for the telescope transmitting function, $T(\rho)$, one can obtain

$$\langle \varphi_{LB} \varphi_{NS} \rangle = 2^{1/6} \bar{s} \int_0^H C_n^2(\xi) (1 - \xi/H) \{ [a_e^2(\xi) + a_L^2]^{-1/6} - [(a_e^2(\xi) + a_L^2 + (2L_0^*)^2)^{-1/6}] \} d\xi, \quad (12)$$

$$\langle \varphi_{LB}^2 \rangle = \bar{s} \int_0^H C_n^2(\xi) (1 - \xi/H)^2 \{ [a_e^2(\xi)]^{-1/6} - [a_e^2(\xi) + 2(L_0^*)^2]^{-1/6} \} d\xi, \quad (13)$$

$$\langle \varphi_{NS}^2 \rangle = \bar{s} \int_0^H C_n^2(\xi) \{ a_L^{-1/3} - (a_L^2 + 2(L_0^*)^2)^{-1/6} \} d\xi, \quad (14)$$

where $\bar{s} = 4.05$, $L_0^* = L_0 / 2\pi$, $a_e(\xi)$ is the average size of the beam, and a_L is the transmitting telescope radius. This radius coincides with the initial radius of the beam, $a_L = a_0$. For $H/\bar{h} \gg 1$ Eqs. (12)-(14) might be simplified by replacing $a_e(\xi)$ with the expression $a_e(\xi) = a_0(1 - \xi/H)$.

From Eqs. (12)-(14), it follows that similar to that for the higher order wave-front distortions {17,18}, the error caused by tilt focus anisoplanatism, δ_{FA}^2 , decreases with increasing the LGS altitude H . The absolute value of the tilt focus anisoplanatism error δ_{FA}^2 also decreases with increasing the telescope radius, as $\delta_{FA}^2 \approx (a_L)^{-1/3}$, but the normalized value of the tilt focus anisoplanatism, $\delta_{FA}^2 / \langle \varphi_{NS}^2 \rangle$, does not depend on the aperture size a_L . This is due to the fact that both variance for the natural star, $\langle \varphi_{NS}^2 \rangle$, and for the beam, $\langle \varphi_{LB}^2 \rangle$, as well as the correlation term, $\langle \varphi_{NS} \varphi_{LB} \rangle$, are proportional to $(a_L)^{-1/3}$.

Let us consider the transmitting telescope having a 1.5 m diameter, and the receiving telescope having a 0.2 m diameter. The numerical estimates show that for $H = 10$ km, $L_0 = 3$ m and for the HV-54 model, the total tilt sensing error is $\delta_z = 0.34 \langle \varphi_{NS}^2 \rangle^{1/2}$. For the HV₅₇ model this error equals to $\delta_z = 0.46 \langle \varphi_{NS}^2 \rangle^{1/2}$. It should be noted that the tilt sensing error δ_z decreases with increasing the LGS altitude and FOV of the receiver.

Experimental study of the polaris image motion

In order to reduce a tilt sensing error caused by focus anisoplanatism, a LGS altitude should exceeds the altitude of the tropopause ($H = 10$ km). In this case a non-Kolmogorov stratospheric turbulence (at the altitudes $H > 10$ km) might contribute to the LGS image motion, as well as, to the image motion of a scientific object. The stratospheric turbulence effect on the star image motion was quantitatively estimated in {19}. To verify the theoretical predictions, a Polaris jitter experiment was designed and carried out at the Starfrier Optical Range (SOR) at the Phillips Laboratory. The experiment was designed and conducted jointly with the SOR personnel.

The goal of the experiment was to obtain high resolution spatial and temporal statistics for the image motion of a star. Polaris was selected for this experiment due to the following reason. A non-Kolmogorov stratospheric turbulence produces an effect on the star image motion, which is similar to that for uncontrolled motion of the

telescope. The effect of uncontrolled telescope motion is eliminated if the telescope is motionless. Due to slow angular motion, Polaris permits us to make measurements with both bolted, or motionless, and unbolted telescope. In a bolted case the mechanical telescope motion is eliminated.

The experiment was performed at the 1.5 m telescope by using a 64 x 64 CCD (Lincoln Laboratory) camera. Data was collected by using five different aperture masks ($D = 0.1, 0.2, 0.5, 0.75$ and 1.5 m) in conduction with the appropriate ND filters to keep incident flux constant and to achieve maximum flux without saturating the camera. Each data run consists of 20000 frames recorded at 200 Hz and 400 Hz over 100s and 50 s, respectively.

The telescope viewed Polaris with a symmetrical 38×38 arcsec FOV, yielding resolution of 06 arcsec/pixel. The telescope was first pointed toward Polaris and bolted in position such that the earth's rotation causes the image of Polaris to track horizontally across FOV (at approximately $1\text{ }\mu\text{ rad/sec}$). The K-mirror was used to ensure the stellar image tracks along one CCD channel without crossing into an adjacent channel. Next, the telescope was unbolted and followed (pointed at) Polaris, keeping the image centered as data collected. Comparison of the two data sets permits us to isolate of atmospheric and mechanical jitter.

The data was collected during four nights. Meteorological data was recorded for each experimental session including wind speed and direction, coherent diameter (r_0) and isoplanatic angle (θ_0). The data were processed, and the following dependencies were determined:

- a dependence of the Polaris jitter variance on the telescope diameter and seeing conditions;
- a dependence of the temporal power spectra of the Polaris motion on the telescope diameter;
- a dependence of the temporal correlation coefficient of the image jitter on the aperture size.

As an example, in Fig. 5 a dependencies of one-axis jitter variances on the telescope diameter are presented. According to the theoretical predictions based on the Kolmogorov model [20], a star jitter variance, σ^2 , should gradually decrease with increasing the telescope diameter as $\sigma^2 \approx D^{-1/3}$. However, the experimental curves in Fig. 5 do not follow this prediction. For a telescope diameter larger than $D \geq 0.75\text{ m}$ these curves are saturated and do not depend on D . The implication is that the Kolmogorov model for the turbulent power spectrum does not permit us to explain the measured data. To interpret the data, one should assume an additional source of turbulence with the spectrum which is different from the Kolmogorov model and with the scale that is larger than the telescope diameter.

A special test has been performed to estimate influence of the internal turbulence within an optical path on the measured data. The image motion of an internal source was measured with the same experimental set up. The estimates show that the jitter variance of an internal source is more than one order magnitude smaller than that for a natural star.

The temporal power spectra for telescope diameter $D = 0.1$ and 1.5 m for the Polaris are shown in Fig. 6. For comparison, at the same plot the power spectra for the internal source are also shown. It is seen, that power spectra for the Polaris greatly exceeds that for the internal source. In the high frequency range the Polaris power spectra follow to the dependence $f^{-8/3}$, whereas in the low frequency range they obey to the $f^{-2/3}$ law. The knee frequency relates to the telescope diameter through the equation $f_k = D^{-1}$. The power spectra slope in the high frequency range is not consistent with the theoretical predictions. An additional analysis of the collected data is required, and a more sophisticated theoretical model is needed for interpretation of the measured data.

Experimental study of the tilt angular anisoplanatism

In a tilt sensing technique with a LGS a tilt decorrelation due to angular anisoplanatism is used to isolate the tilt component corresponding to the upward propagation path. Therefore, to design a tilt sensing experiment with a LGS, the tilt angular correlation scale for the site should be known. The tilt correlation scale might be estimated by using the theoretical model if data for the vertical profile $C_n^2(h)$ and outer scale of turbulence L_0 are available. However, there is no reliable information about the atmospheric characteristics. To overcome this difficulty a Moon-edge jitter experiment has been designed and conducted at the SOR.

The experimental set up for this experiment was similar to that for the Polaris jitter experiment. The K-mirror was used to ensure the Moon edge be parallel to one CCD channel without crossing into an adjacent channel. Five different aperture masks ($D = 0.1, 0.2, 0.5, 0.75$ and 1.5 m) were used when the Moon-edge image motion was measured.

The edge of the Moon might be considered as an extended incoherent source. Therefore, by measuring an angular motion of a small segment of the Moon image a lateral, or transverse to the image, tilt might be measured. By measuring angular motion the two small segments at different angular separations a tilt angular correlation might be estimated. To avoid the influence of the mechanical motion telescope, a tilt structure function was calculated from the measured data.

A preliminary analysis shows that the tilt correlation scale strongly depends on the aperture size, and it increases with increasing a telescope diameter. As an example, the tilt structure functions for different aperture masks versus angular separation between the observation points are shown in Fig. 7. In the future collected data will be processed, and detailed analysis of the results obtained will be performed.

Additional experiments design

The two additional experiments have been designed as a part of the Summer 96' Research Program. The technical objective of the first experiment is to study a LGS image motion for a monostatic laser beacon scheme. Even though a laser beacon image in the conventional monostatic LGS scheme is motionless, according to the theoretical analysis, a LGS image motion might be measured if the transmitter and receiver have different diameters. This

theoretical prediction will be verified in the planned experiment. In addition, this experiment will permit us to test a remote sensing method for measuring vertical profile of $C_n^2(h)$ by using a modified monostatic LGS technique. For this purpose a LGS image motion and motion of a natural star will be measured simultaneously.

The second experiment is designed to demonstrate and test a technique for sensing full aperture tilt with a LGS. In this experiment a one-axis tilt component will be sensed by using an auxiliary 8-inch telescope and 1-D CCD array. A full aperture Nd:YAG laser beam will be focused at 10 km by using a 1.5 m telescope. This telescope will be pointed at Polaris. The two measurements will be performed simultaneously. A Polaris image motion will be measured with the main (1.5 m) telescope, while an image motion of a laser beacon will be measured with an auxiliary telescope. A comparison of these two measurements will permit us to estimate the accuracy of sensing tilt with a laser beacon. Both above experiments are currently in preparation.

Summary

The following results have been obtained as a part of the Summer Research Program:

- 1) A tilt sensing technique with a small aperture beam transmitted from behind a portion of the primary mirror of the main telescope is developed. This technique does not require transmitting laser irradiance through the main optical train. Due to this fact it can be used for the mesospheric sodium layer;
- 2) A tilt angular anisoplanatism and tilt focus anisoplanatism, the two effects which determine the required parameters of the tilt measurement scheme and a tilt sensing error, are studied by taking into account a finite outer scale of turbulence and vertical distribution of the strength of turbulence. A tilt angular correlation scale and tilt averaging function are estimated. The required parameters of a tilt measurement scheme and a tilt sensing error are determined;
- 3) The Moon-edge and Polaris jitter experiments are designed and carried out. The first experiment is devoted to measurements of a tilt angular correlation, while the goal of the second experiment is to study the effect of non-Kolmogorov stratospheric turbulence on a star image motion. The data have been collected and processed, and a preliminary analysis of the results obtained was performed;
- 4) Two additional experiments have been designed. One experiment is designed to measure a LGS image motion for a monostatic scheme, the objective of the other experiment is to demonstrate and test a technique for sensing full aperture tilt with a LGS.

Acknowledgments

The author expresses his appreciation to the AFOSR RDL Summer Research Program personnel for the administrative support and to the SOR researches lead by R. Q. Fugate for fruitful collaboration.

References

1. R. Q. Fugate, D. L. Fried, G. A. Ameer, B. R. Boeke, S. L. Browne, P. H. Roberts, R. E. Ruane, and L. M. Wopat, "Measurements of atmospheric wavefront distortion using scattering light from a laser guide-star," *Nature (London)* 353, 144-146 (1991).
2. C. A. Primmerman, D. V. Murphy, D. A. Page, B. G. Zollars, and H. T. Barclay, "Compensation of atmospheric optical distortion using a synthetic beacon," *Nature (London)* 353, 141-143 (1991).
3. R. Q. Fugate, B. L. Ellerbroek, C. H. Higgins, M. P. Jelonek, W. J. Lange, A. C. Slavin, W. J. Wild, D. M. Winker, J. M. Wynia, J. M. Spinhirne, B. R. Boeke, R. E. Ruane, J. F. Moroney, M. D. Oliker, D. W. Swindle, and R. A. Cleis, "Two generation of laser-guide-star adaptive-optics experiments at the Starfire Optical Range," *J. Opt. Soc. Am., A* 11, 310-324 (1994).
4. M. S. Belen'kii, "Full aperture tilt measurement technique with a laser guide star," in Atmospheric Propagation and Remote Sensing IV, J. Christopher Dainty, Editor. Proc. SPIE 2471, 289-300 (1995).
5. M. S. Belen'kii, "Tilt angular anisoplanatism and full aperture tilt measurement technique with a laser guide star," submitted to *Appl. Opt.*
6. M. S. Belen'kii, "Tilt angular correlation and full aperture tilt measurement techniques with a laser guide star," The European Symposium on Satellite Remote Sensing, Taormina, Italy, 24-26 September 96, Invited Paper.
7. R. J. Noll, "Zernike polynomials and atmospheric turbulence," *J. Opt. Soc. Am.*, 63, 207-211 (1976).
8. G. C. Valley and S. M. Wandzura, "Spatial correlation of phase-expansion coefficients for propagation through atmospheric turbulence," *J. Opt. Soc. Am.*, 69, 712-717 (1979).
9. P. H. Hu, J. Stone, and T. Stanley, "Application of Zernike polynomials to atmospheric propagation problems," *J. Opt. Soc. Am. A* 6, 1595-1608 (1989).
10. R. J. Sasiela and J. D. Shelton, "Transverse spectral filtering and Mellin transform techniques applied to the effect of outer scale on tilt and tilt anisoplanatism," *J. Opt. Soc. Am. A* 10, 646-660 (1993).
11. The HV_{57} turbulence model was developed by modifying a conventional Hufnagel-Valley turbulence model¹⁵ so that at zenith the coherence diameter equals 0.05 m and isoplanatic angle is 7 urad for $\lambda = 0.5 \mu\text{m}$. This model corresponds to the conditions in the region of Albuquerque, New Mexico.
12. G. C. Valley, "Isoplanatic degradation of tilt correction and short-term imaging systems," *Appl. Opt.*, 19, 574-577 (1980).
13. A. Sivaramakrishnan, R. J. Weymann, and J. W. Beletic, "Measurements of the angular correlation of stellar centroid motion," *Astron. J.* 110, 430-438(1995).
14. T. Berkelfeld and A. Glindenmann, "Measurements of the isoplanatic angle of the wavefront tilt," Summaries of the papers presented at the topical meeting, Adaptive Optics, Maui, Hawaii, 8-12 July 96, pp. 206-208.

15. M. S. Belen'kii, "Principle of equivalency of the phase difference and off-axis tilt sensing technique with a laser guide star," SPIE Annual Meeting, Denver, Colorado, 4-9 August 96, Paper Number 2828-31.
16. S. M. Rytov, Yu. A. Kravtsov, and V. I. Tatarskii, Principles of Statistical Radiophysics, Vol. 4, Wave Propagation Through Random Media, Berlin; Springer-Verlag (1989).
17. D. L. Fried and J. Bulsher, "Analysis of fundamental limits to artificial-guided-star adaptive-optics-system performance for astronomical imaging," J. Opt. Soc. Am. A 11, 277-287(1994).
18. G. A. Tyler, "Bandwidth considerations for tracking through turbulence," J. Opt. Soc. Am. A 11, 358-367 (1994).
19. M. S. Belen'kii, "Effect of the stratosphere on star image motion," Optics Letters, Vol. 20, 1359-1361 (1995).
20. I. Tatarskii, Wave Propagation in a Turbulent Medium, McGraw-Hill Book Company, New York (1961).

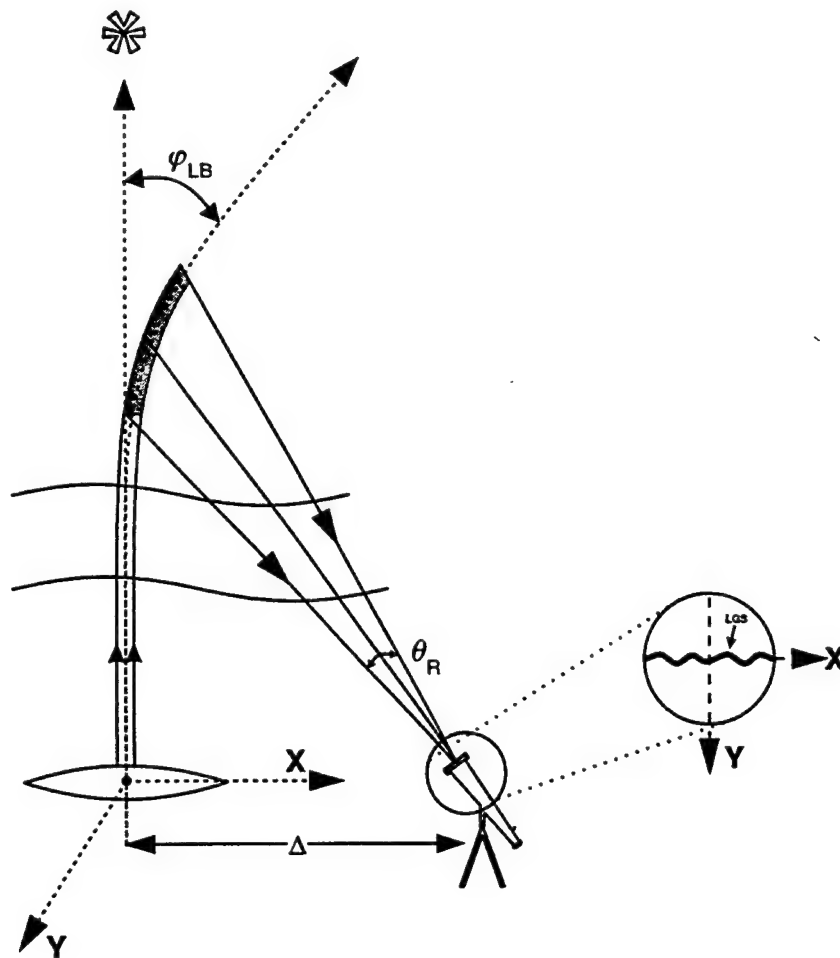


Fig. 1. Configuration of the tilt measurement scheme with a small aperture beam.

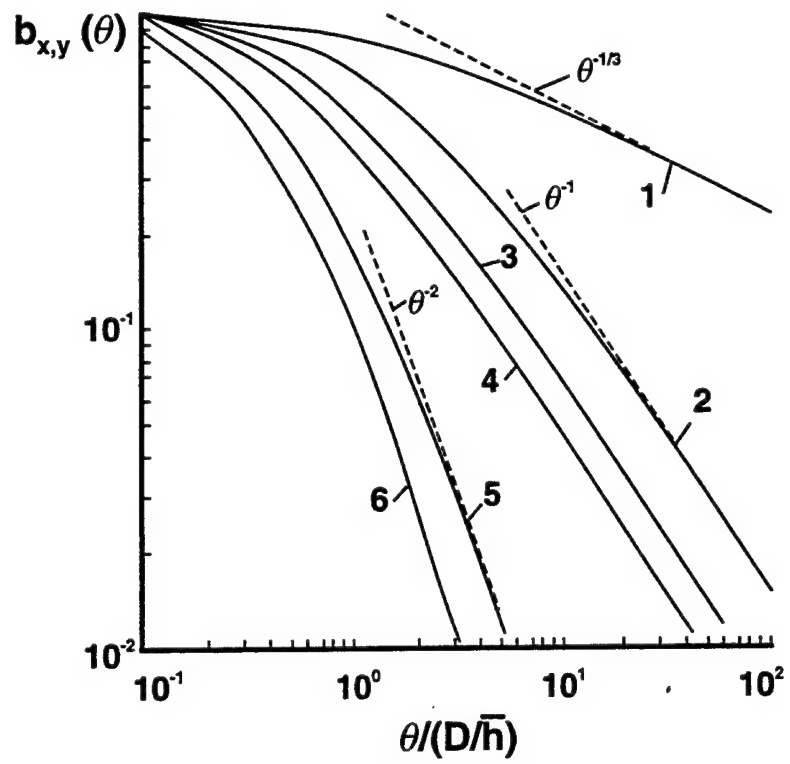


Fig. 2. Angular correlation coefficient for the lateral and longitudinal tilts on the vertical propagation path. Curves 1 - 4 correspond to the lateral tilt, and curves 5 and 6 correspond to the longitudinal one. Ratio L_0/D is equal to infinity for curve 1, $L_0/D = 50$ for curve 2, $L_0/D = 10$ for curves 3 and 5, and $L_0/D = 3$ for curves 4 and 6.

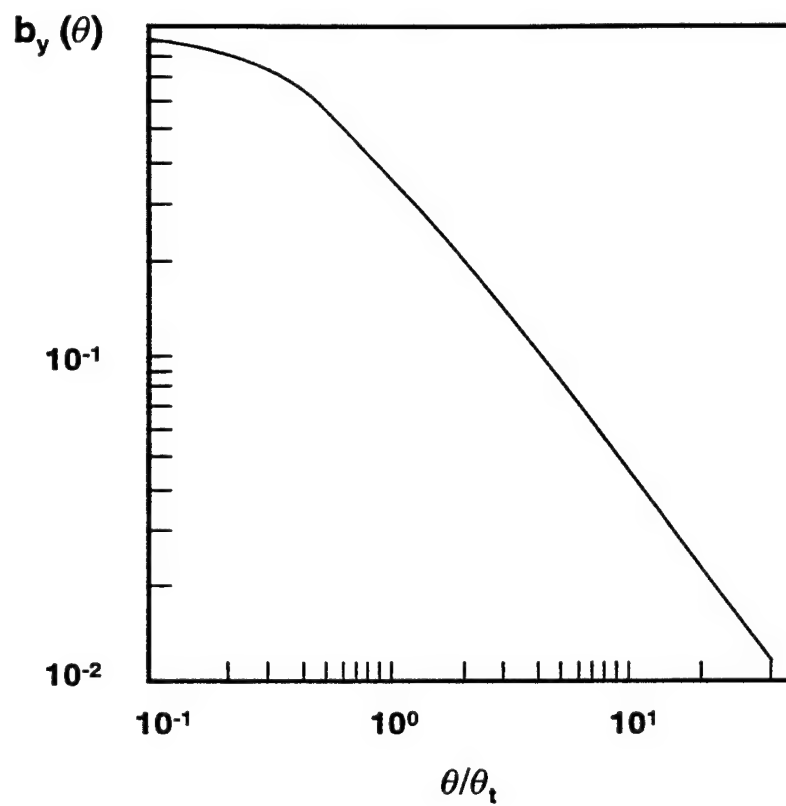


Fig. 3. Universal dependence of the tilt correlation coefficient on the angular separation.

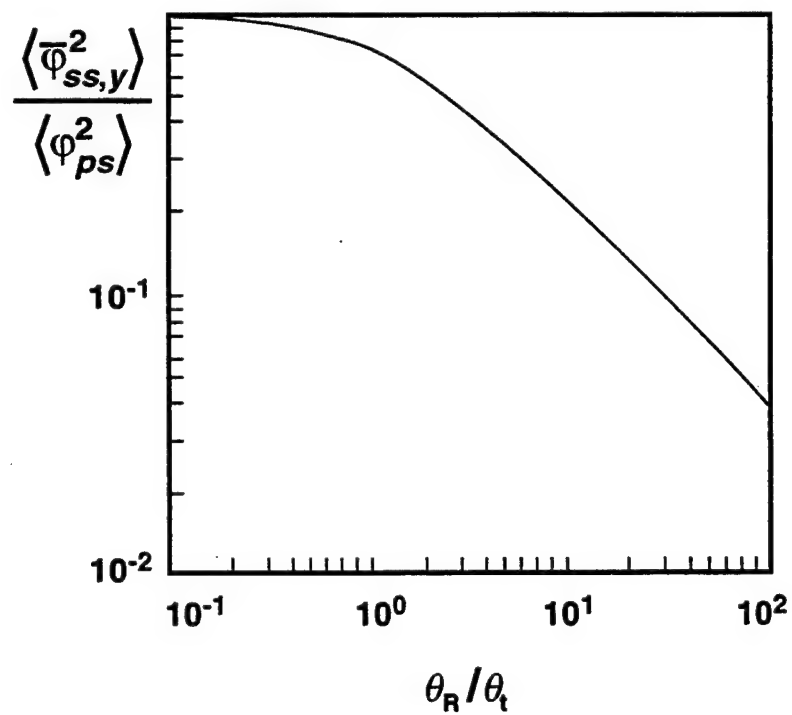


Fig. 4. Tilt averaging function.

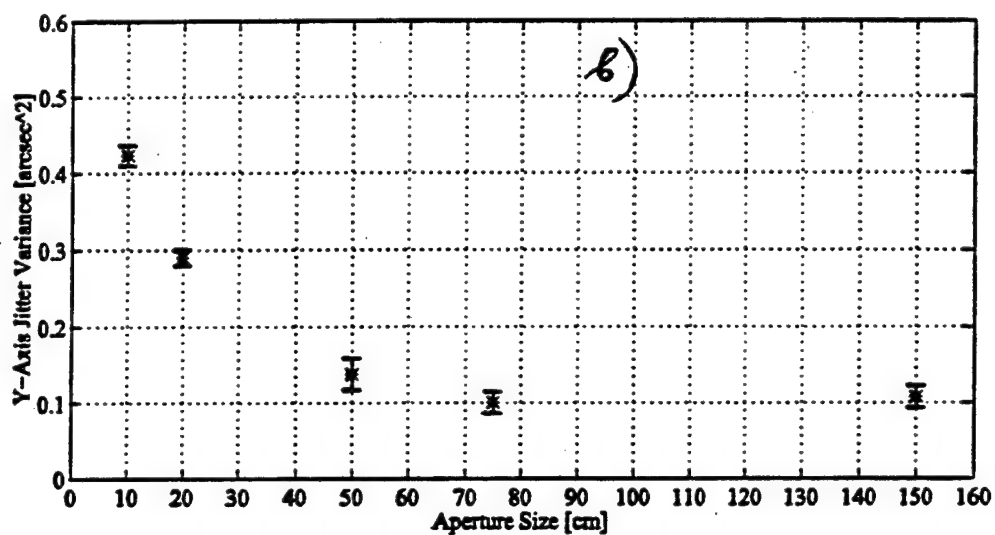
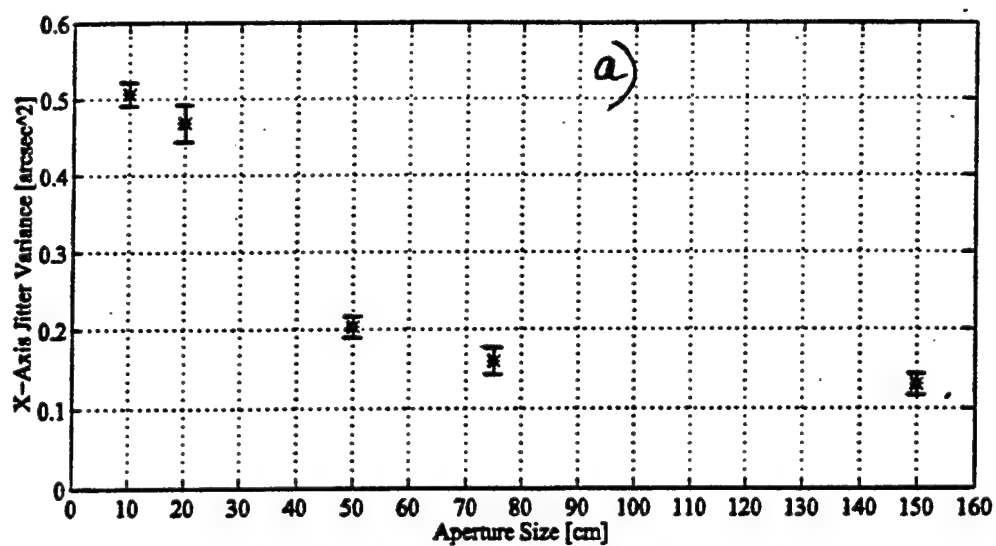


Fig. 5 a & b. Dependencies of the one-axis Polaris image jitter variances on the telescope diameter.

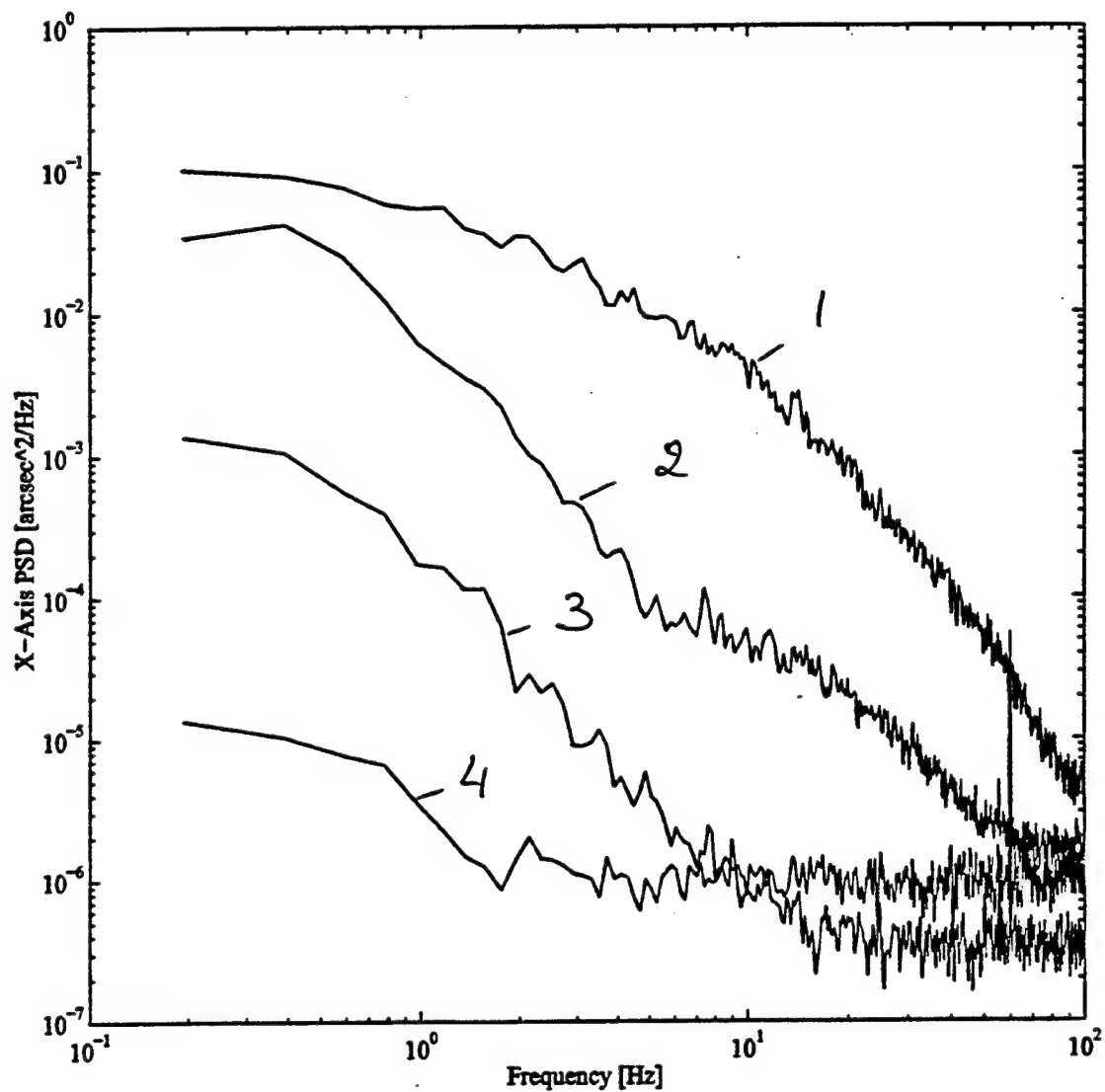


Fig. 6. Temporal power spectra of the Polaris image motion. Curves 1 and 2 correspond to the Polaris for $D = 0.1$ m and $D = 1.5$ m, respectively. Curves 3 and 4 correspond to the internal source for $D = 0.1$ and 1.5 m, respectively.

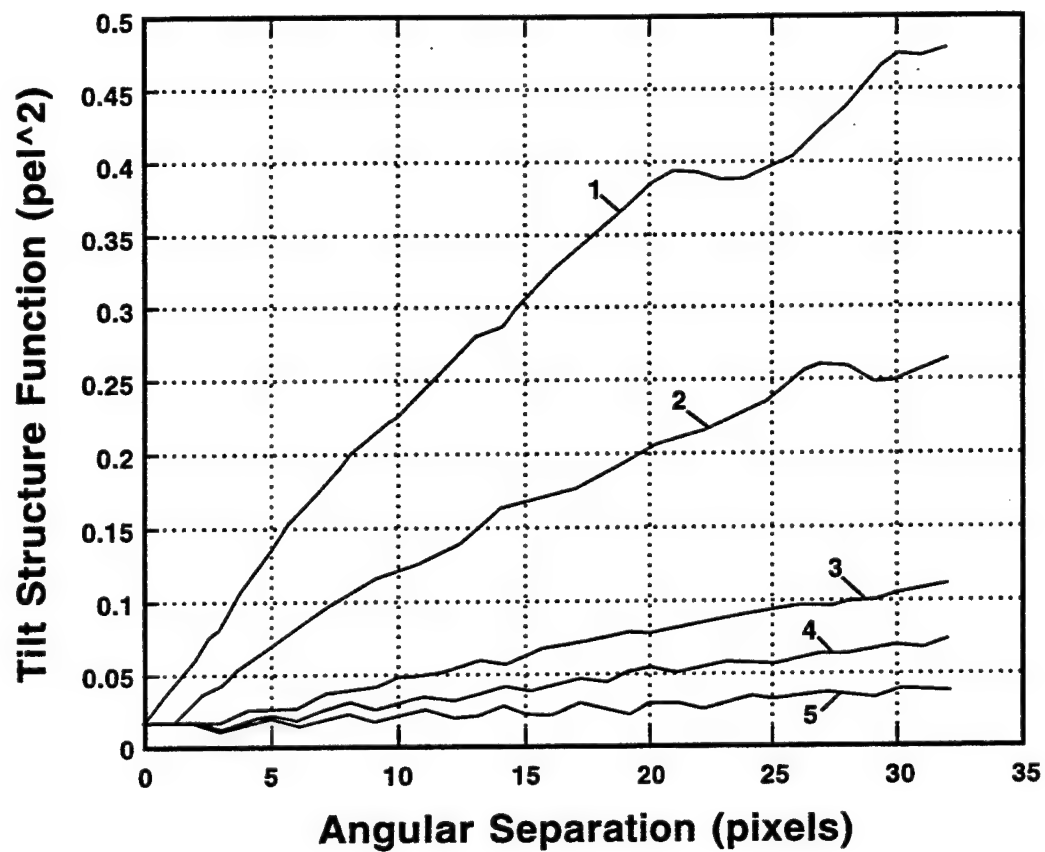


Fig. 7. Dependence of the tilt structure function on the angular separation between the observation points. The telescope diameter $D = 0.1$ m for curve 1, $D = 0.2$ m for curve 2, $D = 0.5$ m for curve 3, $D = 0.75$ m for curve 4, and $D = 1.5$ m for curve 5.

AFOSR SUMMER RESEARCH REPORT

ON

THE STUDY OF

**PART A: EFFECT OF EARTH'S SURFACE AND LOSS ON THE
RESONANT FREQUENCIES OF BURIED OBJECTS**

**PART B: ADAPTIVE PROCESSING FOR OBJECT
IDENTIFICATION**

By

Asoke K. Bhattacharyya

Department of Computer Science and Technology

Lincoln University

Damel 312

Jefferson City, MO 65109

Sponsored by

**Air Force Office of Scientific Research
Calver City, CA**

and

**Phillips Laboratory
Kirtland AFB
Albuquerque, NM 87117
November 1996**

PART A

EFFECT OF EARTH'S INTERFACE AND LOSS ON THE RESONANT FREQUENCIES OF A BURIED OBJECT

Introduction:

There is a renewed interest for identification of buried objects with the availability of Ground Penetrating Radar (GPR) [1-6] in both civilian and military applications. Transient radar techniques have been used in view of the current developments in short-pulse antennas [7,8], detection and identification of buried objects [6-8]. An important tool for identification is the well-known singularity expansion method [9-13]. This exploits the fact that the late-time response of a target can be expressed in terms of a sum of damped exponentials, each one characterized by a set of complex resonant frequencies. The resonant frequencies are aspect independent but the intensities are aspect dependent. For objects buried in earth, the target resonant frequencies change with the depth and the material of the earth. Hence, it is necessary to do a systematic study on how much change of resonant frequencies will occur with the presence of interface and the loss inside the ground. This information about resonant frequency changes are needed to upgrade the capability of the already existing complex resonant frequency signature library. This will enable one to identify 'known' objects under adverse environments. Complex resonant frequencies of a mirror object was calculated in [14,15]. Recently [16,17], Method of Moments has been utilized to calculate the complex resonant frequencies of buried wires and bodies of revolution in lossy soil. The half space Green's function was computed in [16] using complex image technique.

In a previous work [14,15] as well as in [16,17], it was shown that the resonant frequencies spiral around the free space resonant frequencies. In [14,15], only conducting half-plane was considered. In the present work, we use a general interface between air and ground and also a general lossy half space ground. As in [14,15], an image coefficient has been defined. The image coefficient is zero and there is no change in resonant frequencies when the target is in free space. The set of complex resonant frequencies to the left of the complex plane are the reference resonant frequency set for the particular target in free space. This report studies the change in resonant frequencies of a buried thin wire as a function of different parameters, such as, the wire depth, loss in the medium, and excitation modes of the wires.

FORMULATION:

The geometry and coordinate system of the detection and identification of a buried object (a thin wire) are shown in Figure 1. The ground is assumed to be a nonmagnetic lossy half space and can assume arbitrary values of electrical permittivity ϵ and conductivity σ .

Referring to a previous work[14], the change in resonant frequency due to the presence of air-ground interface and the lossy half space is given by-

$$\Delta S_{sy/as}, \alpha' \cong \frac{\sqrt{\epsilon_r} - \sqrt{\epsilon_r}}{\sqrt{\epsilon_r} - \sqrt{\epsilon_r}} S_{\alpha'} \mu_0 \frac{\text{Exp}(-2 \pi D)}{8 \pi D}$$

$$\text{where, } v = \frac{\langle j(r); \text{Exp}(-\gamma(z+z'))L \rangle; j(r)}{j(r); Z(r, r', S); j(r)}$$

$$S_{sy/as} \equiv S + \Delta S_{sy/as}$$

with,

R_r = The normal incidence reflection coefficient at the interface incident from medium 2

μ_0 = Permeability of free space

$S = \Omega + j\omega$

$L = 2D$, where D is the depth of the object

S' = Complex unperturbed resonant frequency

j = Mode current density

r, r' = The two position vectors on the surface of the object

$Z(r, r', s)$ = Derivative of $Z(r, r', s)$ at the unperturbed complex pole

$Z(r, r', s) = s^{-1}(r) \cdot G(r, r', s) \cdot 1(r)$, where $G(r, r', s)$ is the Green's function of the scenario.

The denominator becomes equal to-

$$\langle j(r); (\mu s \cdot G(r, r'; s) \cdot s' + S \mu S \cdot \partial G(r, r'; s) \cdot s) \cdot S' \rangle j(r) \rangle$$

with [18],

$$E = \frac{1}{\omega \epsilon} \left(-\frac{d^2}{dz^2} + k^2 \right) \int \int J(\theta', z') \text{Exp}(-jkR)/4 R a dz' d\theta'$$

$$R = \sqrt{(z - z')^2 + 4 a^2 \sin^2(\theta - \theta')}$$

With thin wire approximation, $R = \sqrt{(z - z')^2 + a^2}$, where a is the radius of the wire and $J(\theta', z') = I(z')/2\pi a$, where $I(z')$ is the current flowing through the wire and is given by: $I = I_0 \sin m k (l/2 - z')$. Having obtained the Green's function, we can determine the denominator of the image coefficient. Evaluation of the numerator is straightforward.

Results and Discussions

A computer program in Fortran 77 was prepared and tested using the analytical steps outlined above. The input parameters are: dimensions of the object, depth of the object, the ground parameters. The test object in this study is a thin wire arbitrarily oriented. The resonant frequencies of thin wires with the interface as the ground plane has been computed elsewhere[14]. The output quantity is the change in resonant frequency of the thin wire with different parameters. Fig. 2 shows the change in resonant frequency versus $2D/L$ of a buried wire with the x-direction cosine equal to unity at a depth of 0.2 meter. The relative dielectric constant and conductivity are 10.0 and 0.02 respectively. The discontinuity at the air-ground interface is characterized by the complex reflection coefficient of the air-ground interface. Fig. 3 shows the same plot with a relative dielectric constant of 100. The variation of resonant frequency when the wire is at a depth of 10 meters is shown in Fig. 4. Fig. 5 shows the change in resonant frequency when the interface is replaced by a perfectly electrically conducting ground plane. Table 1 gives a comparison of the typical change of resonant frequency of a thin wire of given length under different parameters compared.

TABLE 1

Typical Changes in Resonant Frequency With parameters

$L = 0.5$ meter; $\sigma_2 = 0.02$ mhos/meter; $D/2L = 4.0$

Unperturbed Resonant frequency = $0.675E08$

$D = 0.2$ m $\epsilon_r = 10$	$D = 0.2$ m $\epsilon_r = 100$	$D = 10$ m $\epsilon_r = 100$	$D = 0.2$ m $\epsilon_r = 10$ (PEC Interface)
0.665 E03	0.105 E05	0.188E04	0.128 E04

References:

1. D.L. Moffatt and R.J. Puskar-'A subsurface electromagnetic pulse radar', Geophysics, Vol. 41, June 1976, pp. 506-518
2. N. Osumi and K. Ueno,'Microwave holographic imaging of underground objects', IEEE Trans. Antennas and Propagat., Vol. AP-33, No. 2, Feb 1985, pp. 152-159
3. L. Peters Jr. and J.D. Young-' Applications of subsurface transient radars', in E.K. Miller (Ed.)-'Time-Domain Measurements in Electromagnetics', Vam Nostrand Reinhold, New York, 1986
4. G.S. Smith and W.R. Scott, Jr.-'A scale model for studying ground penetrating radar', IEEE Trans. Antennas and Propagat., Symp. Digest, Vol. 3, July 1993, pp. 1250-1253
5. C. Liu and C. Shen,'Numerical simulation of subsurface radar for detecting buried objects', ibid, Vol. 29, Sept. 1991, pp. 795-798
6. J. Young, M. Pourier and L. Peters Jr., 'A review of current ground penetrating radar', IEEE Trans. Antennas and Propagat., Symp. Digest, Vol. 3, July 1992, pp. 1250-1253
7. H.L. Bertoni, L. Carin and I.B. Felsen (Ed.s)-'Ultra-wideband Short-Pulse Electromagnetics I', Plenum Press, NY, 1994
8. L. Carin and L.B. Felsen(Eds.)-'Ultra-Wideband Short-Pulse Electromagnetic II', Plenum Press, 1995
9. C.E. Baum,'On the singularity expansion method for the solution of electromagnetic interaction problems', Air Force Weapons Laboratory Intercation Notes, Note 88, 1971

10. L. Marin, 'Natural mode representation of transient scattered fields', IEEE Trans. Antennas and Propagat., Vol. AP-21, Nov 1973, pp. 809-818
11. F.M. Fische, 'On the analysis of scattering and antenna problems using singularity expansion technique', ibid, Vol. AP-21, Jan 1973, pp. 53-62
12. M.L. Van Blaricum and R. Mittra, 'A technique for extracting the poles and residues of a system directly from its transient response', ibid, Vol. AP-23, Nov 1975, pp. 777-781
13. D.G. Dudley, 'Parametric modeling of transient electromagnetic systems', radio Science, Vol. 14, 1979, pp. 387-396
14. C.E. Baum, T.H. Shumpert and L.S. Biggs, 'Perturbation of the SEM poles of an object by a mirror object', Sensor and Simulation Note, Note 309, Sept. 1987
16. S. Vitebskiy and L. Carin, 'Resonances of perfectly conducting wires and bodies of revolution buried in a lossy, dispersive half space', IEEE Trans. Antennas and Propagat., to appear

Legends to the Illustrations:

Figure 1: Geometry and Coordinate System of the Buried Object Problem

Figure 2: Change in Resonant Frequency Versus $2D/L$: Air-Ground Interface
 $D=0.2, \epsilon_r = 10, \Omega = -0.7069E08; f = 0.675 E08$

Figure 3: Change in Resonant Frequency Versus $2D/L$: Air-Ground Interface
 $D = 0.2, \epsilon_r = 100, \Omega = -0.7069 E08, f = 0.675 E08$

Figure 4: Change in Resonant Frequency Versus $2D/L$: Air-Ground Interface
 $D = 10 \text{ meters}, \epsilon_r = 10, \Omega = -0.7069 E08, f = 0.675 E08$

Figure 5: Change in Resonant frequency Versus $2D/L$: Perfectly Conducting Interface
 $D = 0.2, \epsilon_r = 10, \Omega = -0.7069 E08, f = 0.675 E08$

PART B

ADAPTIVE FILTERING FOR OBJECT IDENTIFICATION

Abstract: This scheme incorporates an adaptive filter of Wiener type to do a correct signal estimate when a signal is received in presence of noise. A computer simulation of an adaptive filter using Least Mean Square(LMS) algorithm is attempted with input as signal plus noise. a noise estimate is made and a filter is designed to give a close estimate of the signal. Most signal processors are suited for its implementation.

Technical Approach:

Two signals, x_k and y_k , are simultaneously applied to the adaptive filter(Fig. 1). y_k is the contaminated signal containing both the desired signal, s_k and the noise n_k , assumed uncorrelated with each other. The signal x_k is a measure of the contaminating signal which is correlated in some way with n_k . x_k is processed by the digital filter producing an estimate, \hat{n}_k , of n_k . The digital filter output, \hat{n}_k is subtracted from the contaminated signal y_k

$$\hat{s}_k = y_k - \hat{n}_k = s_k + n_k - \hat{n}_k \quad \dots \quad \dots \quad \dots \quad (1)$$

The Wiener filter produces an optimum estimate of the part of y_k that is correlated with x_k which is then subtracted from y_k to yield e_k , the output. Assuming a finite impulse response(FIR) filter structure with N weights., the error, e_k , between the Wiener filter output and the primary signal, y_k , is given by-

$$e_k = y_k - \hat{n}_k = y_k - W^k X_k = y_k - \sum_{i=0}^{N-1} w(i) x_{k-i} \quad \dots \quad \dots \quad \dots \quad (2)$$

where, X and W , the input signal vector and weight vector, respectively, are given by-

$$X = \begin{bmatrix} x_k \\ x_{k-1} \\ \vdots \\ x_{k-(N-1)} \end{bmatrix} ; W = \begin{bmatrix} w(0) \\ w(1) \\ \vdots \\ w(N-1) \end{bmatrix} \quad (3)$$

The square of the error is-

$$e_k^2 = y_k^2 - 2 y_k X_k^T W + W^T X_k X_k^T W \quad \dots \quad \dots \quad \dots \quad (4)$$

The implementation of the LMS algorithm can be done along the following steps:

(1) Each weight $w(i)$, $i = 0, 1, 2, \dots, N-1$, is initially set to a fixed value, such as 0.

For each subsequent sampling instants, $k = 1, 2, \dots$, carry out steps (2) to (4) below:

(2) The filter output is computed using:

$$\hat{n}_k = \sum_{i=0}^{N-1} w_k(i) x_{k-i} \quad \dots \quad \dots \quad (5)$$

where $w_k(i)$'s are the prediction coefficients

(3) The error estimate is computed:

$$e_k = y_k - \hat{n}_k \quad \dots \quad \dots \quad (6)$$

(4) The next filter weight is updated using:

$$w_{k+1}(i) = w_k(i) + 2 \mu e_k x_{k-i} \quad \dots \quad \dots \quad (7)$$

Testing:

A FORTRAN program was prepared to do adaptive filtering using the above algorithm. The program has been tested using a test example. In this example, the signal $s_k = A_s \sin(2\pi f t) + A_n \cos(2\pi f t)$ where A_s and A_n are the desired signal and undesired noise amplitude. The noise estimate was done using (5) and the signal was estimated. Fig. 2 shows the plots of signal plus noise, only signal, noise and signal estimates for different values of A_n . The signal amplitude was equated to unity. The length(N) of the filter is assumed to be 30, the delay equal to 1, initial value for adaptive filter coefficients equal to zero, Fig. 2 shows the plot for $A_n = 1.00$ and Fig. 3 for $A_n = 0.2$. The signal estimation comes out lot better in Fig. 3 than in Fig. 2. The key is to be able to make a proper noise estimate in a given scenario to get an adequate signal estimate. The discrepancy between the actual signal and the estimated signal in a noisy environment is much smaller for $A_n = 0.2$.

References:

1. E.C. Ifeachor and B.W. Jervis-'Digital Signal Processing', Addison-Wesley, 1993, Chapter 9

Legends to the Illustrations:

Fig. 1: Block Diagram of Adaptive Filter as a Noise Canceller

Fig. 2: Plot of $S+N$, only S , Noise and Signal Estimates Versus Time in Milliseconds
with $N=30$, $M = 1$, $W_0=0$, $\mu = 0.04$ and $A_n = 1.00$

Fig. 3: Plot of $S+N$, Only S , Noise and Signal Estimates Versus Time in Milliseconds
with $N=30$, $M=1$, $W_0=0$, $\mu = 0.04$ and $A_n = 0.2$

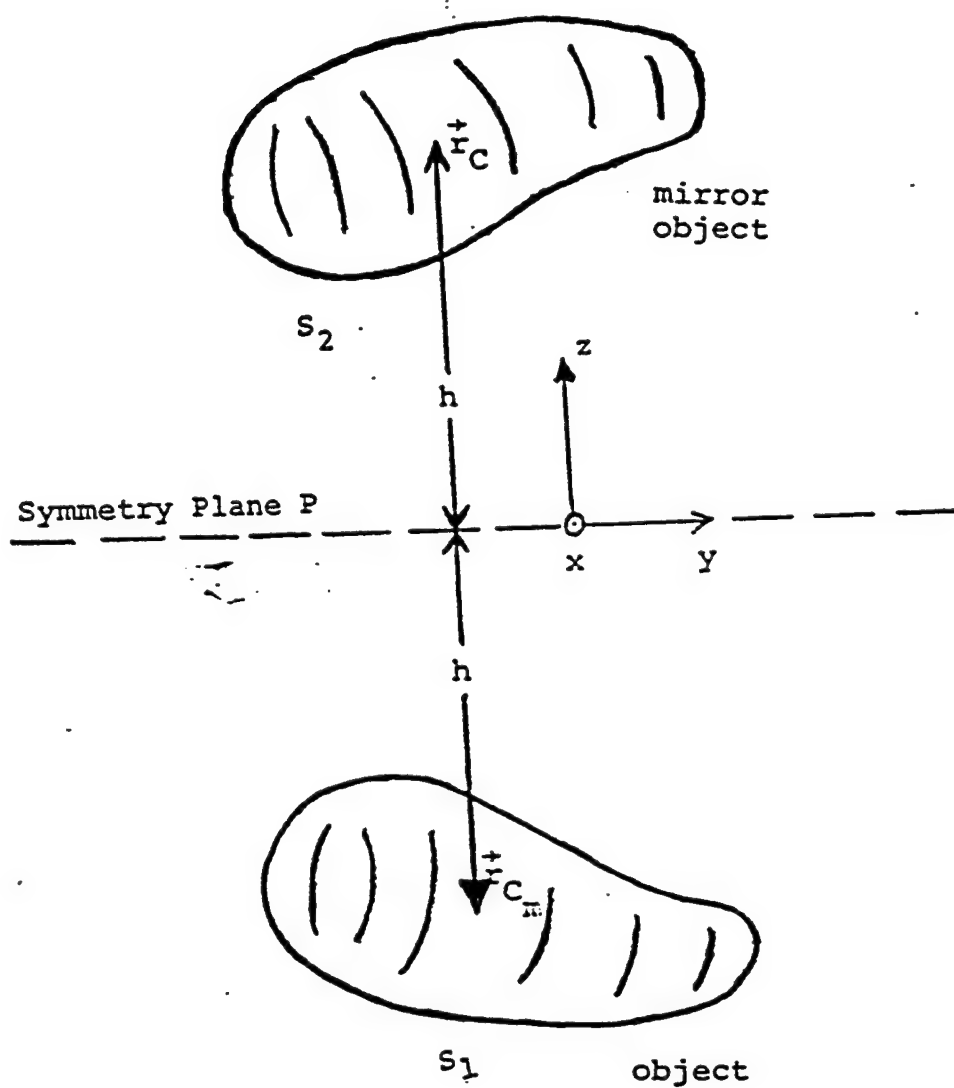
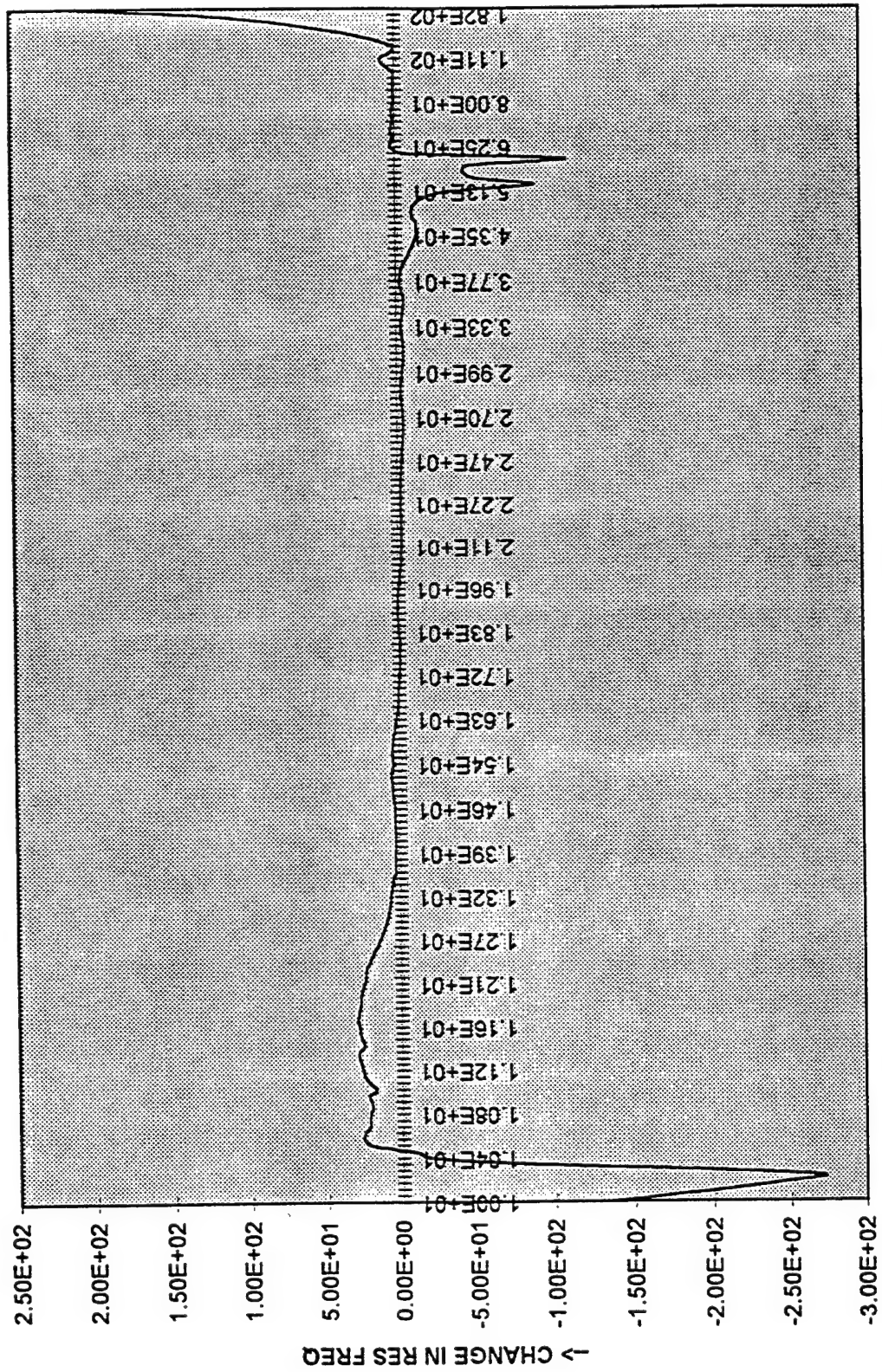


Figure 1: Geometry and Coordinate System of the Buried Object Problem

CHANGE IN RES FREQUENCY::THIN WIRE::AIR-GROUND

D=10M;EPSR=100;SIGMA=0.02



-> 2D/L

Figure 2: Change in Resonant Frequency Versus 2D/L : Air-Ground Interface
D=0.2, $\epsilon_r = 10$, $\Omega = -0.7069E08$; $f = 0.675 E08$

CHANGE IN RES FREQUENCY::THIN WIRE::PEC GROUND

D=0.2M;EPSR=10;SIGMA=0.02

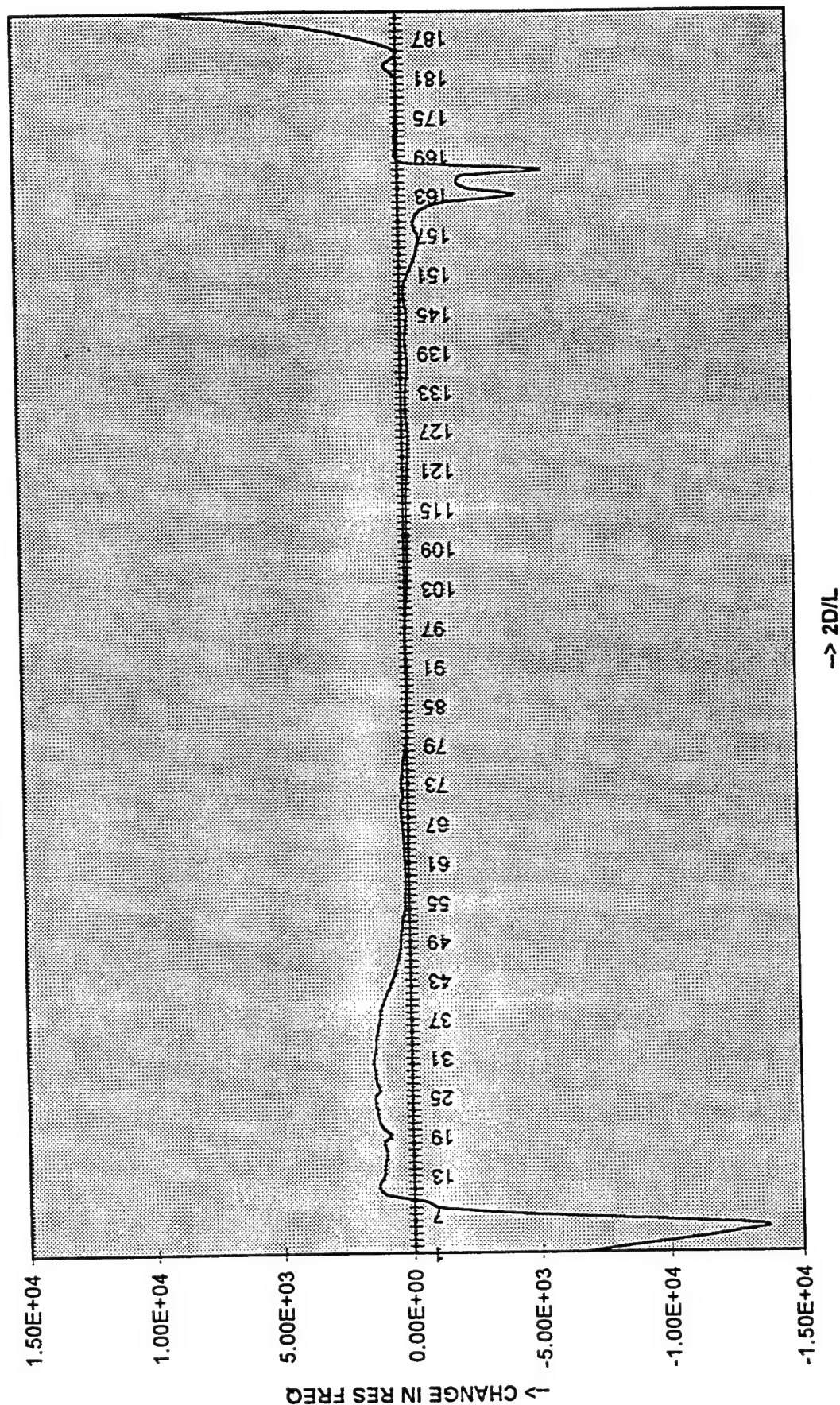


Figure 3: Change in Resonant Frequency Versus 2D/L : Air-Ground Interface
D = 0.2, $\epsilon_r = 100$, $\Omega = -0.7069 \text{ E08}$, $f = 0.675 \text{ E08}$

CHANGE IN RES FREQUENCY::THIN WIRE::AIR-GROUND

D=0.2;EPSR=10;SIGMA=0.02

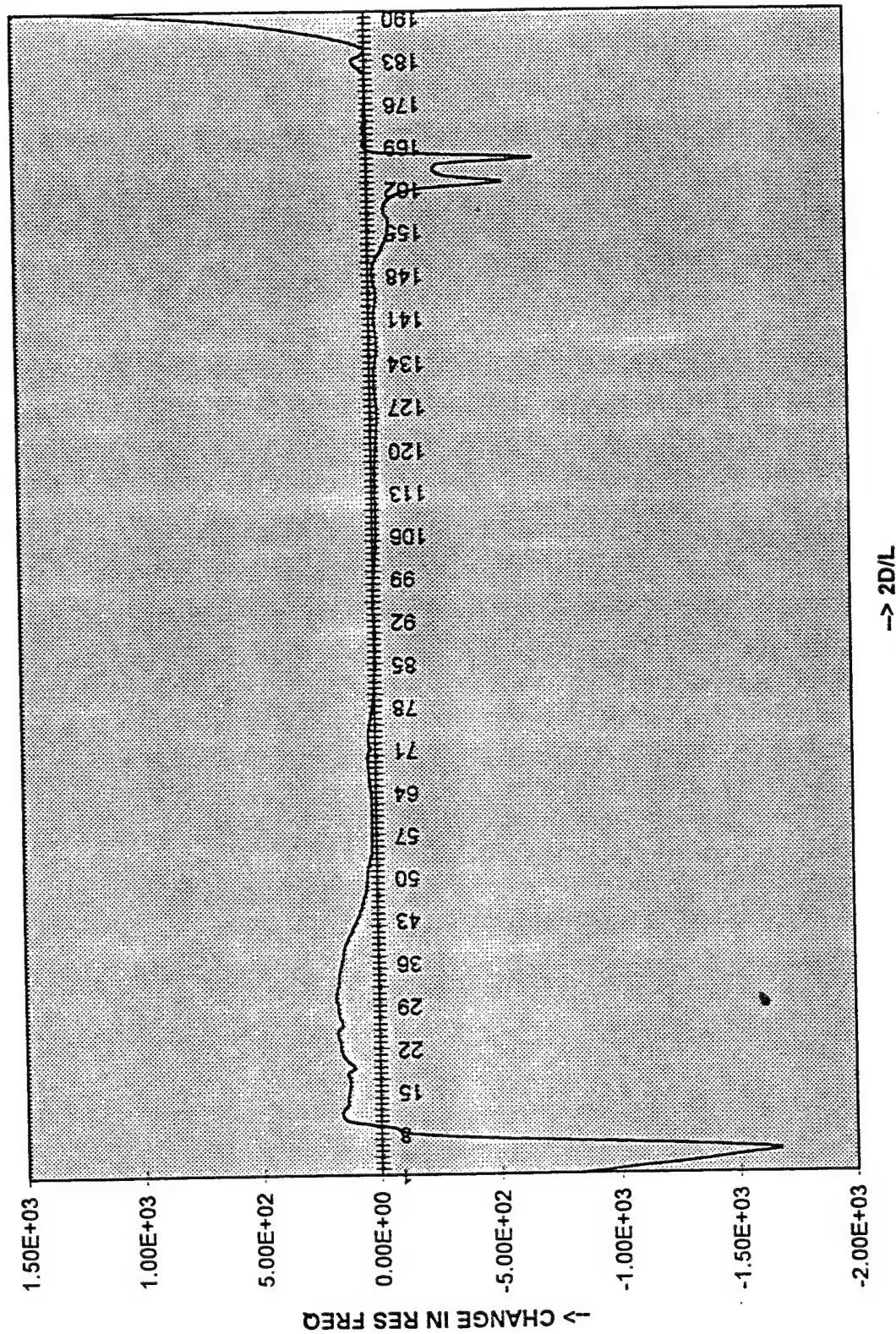


Figure 4: Change in Resonant Frequency Versus 2D/L: Air-Ground Interface
D = 10 meters, $\epsilon_r = 10$, $\Omega = -0.7069$ E08, $f = 0.675$ E08

CHANGE IN RES FREQUENCY::THIN WIRE::PEC GROUND

D=0.2M;EPSR=10;SIGMA=.02

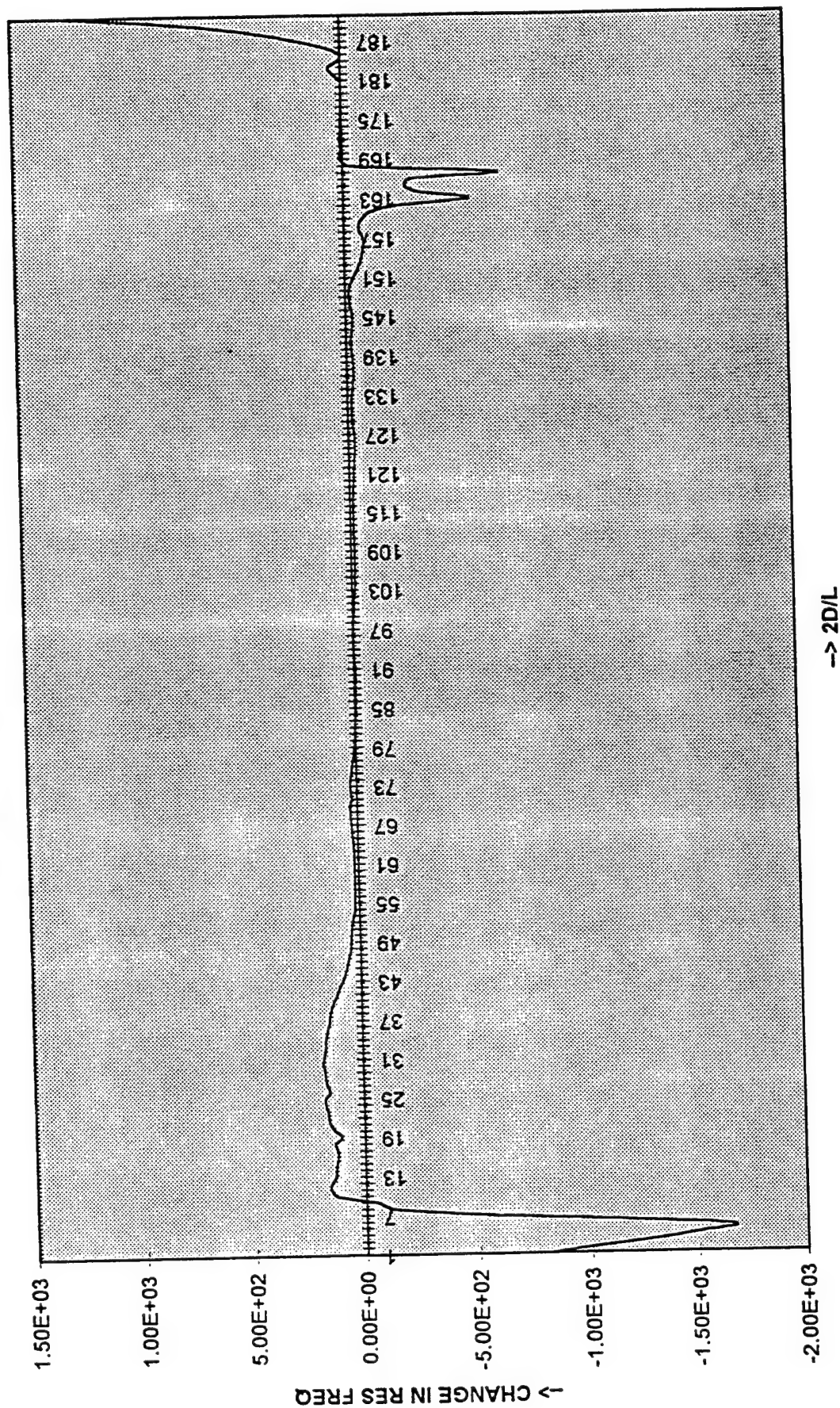


Figure 5: Change in Resonant frequency Versus 2D/L: Perfectly Conducting Interface
D = 0.2, $\epsilon_r = 10$, $\Omega = -0.7069$ E08, $f = 0.675$ E08

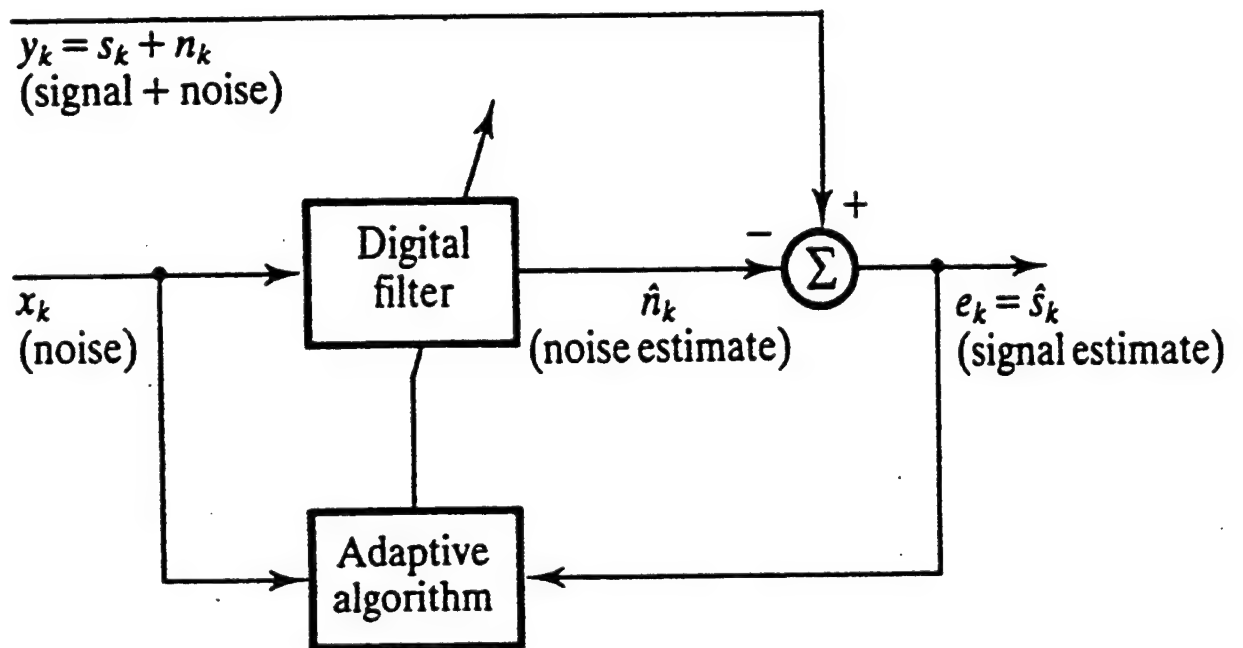


Fig. 1: Block Diagram of Adaptive Filter as a Noise Canceller

ADAPTIVE FILTERING OF NOISY SIGNALS

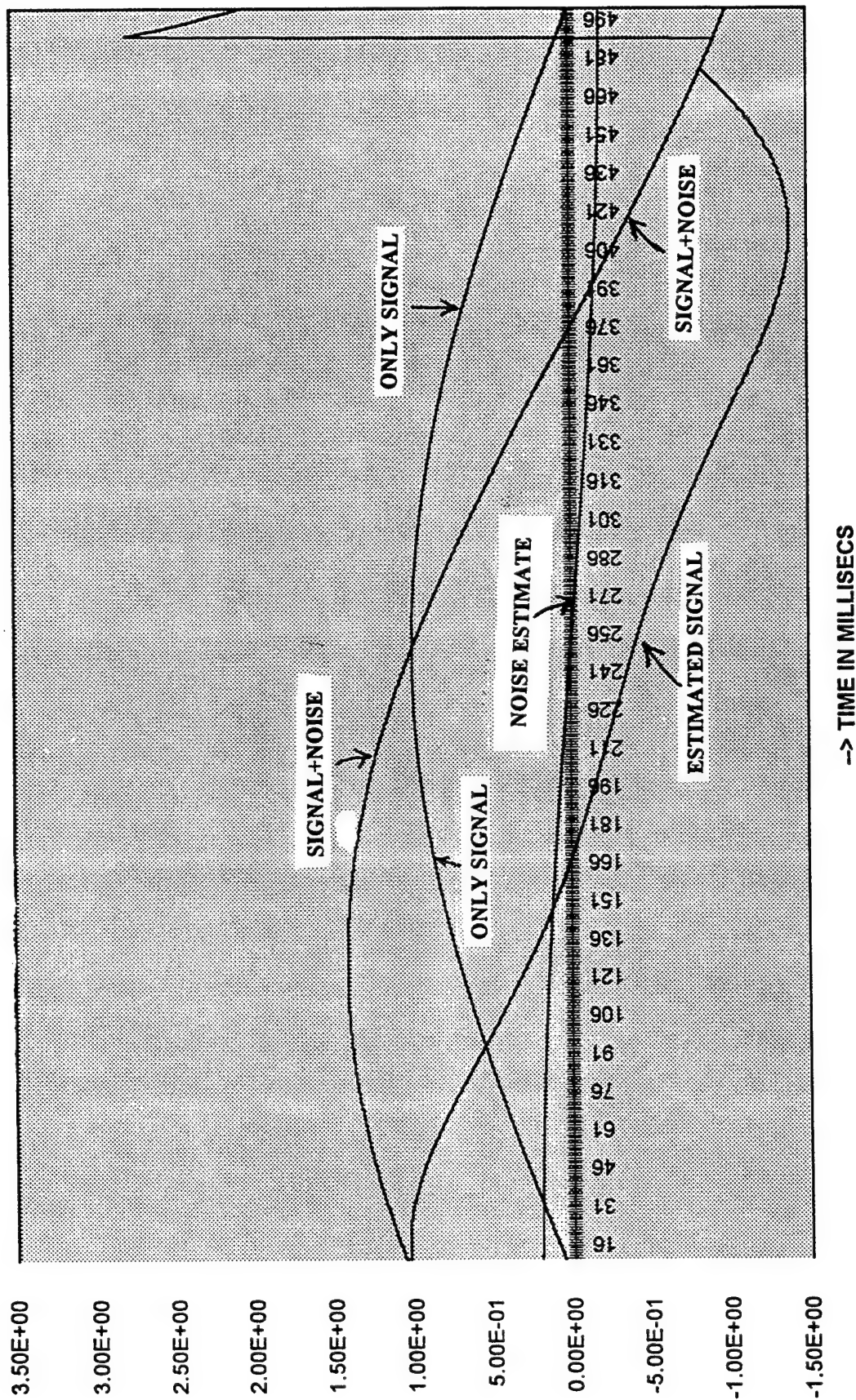


Fig. 2: Plot of S+N, only S, Noise and Signal Estimates Versus Time in Milliseconds
with $N=30$, $M=1$, $W_0=0$, $\mu=0.04$ and $\Lambda_n=1.00$

ADAPTIVE FILTERING

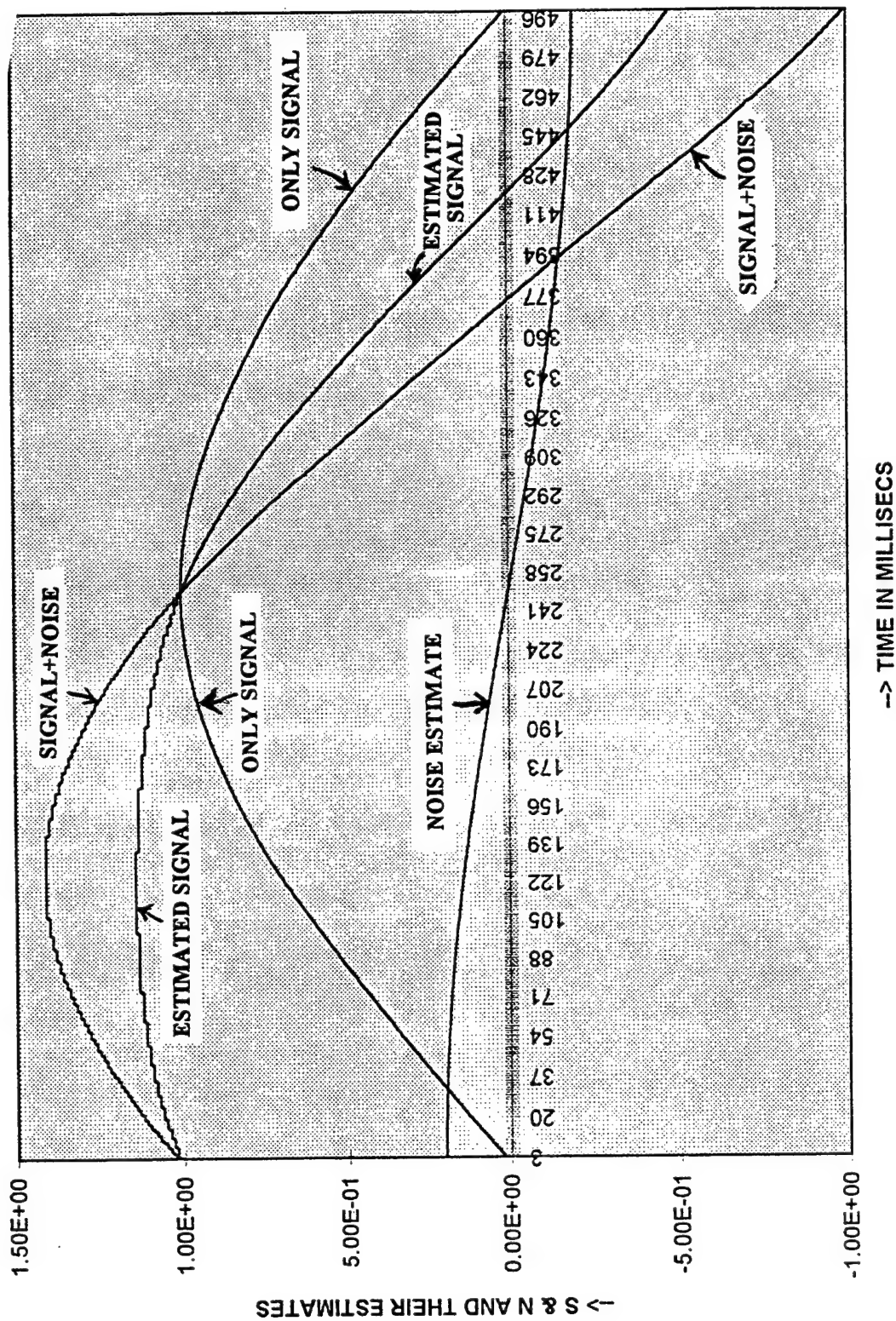


Fig. 3: Plot of S+N, Only S, Noise and Signal Estimates Versus Time in Milliseconds
with $N=30, M=1, W_0=0, \mu=0.04$ and $\Lambda_n=0.2$

TRANSIENT STUDIES OF THE EFFECTS OF FIRE SUPPRESSANTS
IN A WELL-STIRRED COMBUSTOR

J.M. Calo
Professor
Division of Engineering

BROWN UNIVERSITY
Providence, RI 02912

Final Report for
Summer Faculty Research Program

Phillips Laboratory
Geophysics Directorate
Ionospheric Effects Division (GPID)
Hanscom AFB, MA 01731

Sponsored by:
Air Force Office of Scientific Research
Bolling Air Force Base, DC

and

Phillips Laboratory

September 1996

TRANSIENT STUDIES OF THE EFFECTS OF FIRE SUPPRESSANTS IN A WELL-STIRRED COMBUSTOR

J.M. Calo
Professor
Division of Engineering
BROWN UNIVERSITY
Providence, RI 02912

Abstract

The effects of three different fire suppressants on the transient behavior of the composition of the effluent gas from a combustor were investigated in an experimental program conducted at the Well Stirred Reactor (WSR) facility at Wright-Patterson Air Force Base during the months of July and August 1996. A quadrupole mass spectrometer, that was originally designed and constructed to sample rocket exhaust gases, was used to sample the effluent gas composition from the WSR. These experiments employed premixed propane/air and methane/air gas mixtures at near-atmospheric pressure in the WSR. Transient measurements were performed on the effects of injecting the fire suppressants Halon 1301 (CF_3Br), pentafluoroethane (C_2HF_5 , HFC-125), and trifluoroiodomethane (CF_3I) into air/fuel mixtures at various concentration levels using a fast, pulsed valve system. Selected results from the experimental program are presented and discussed. It was concluded that the three fire suppressants exhibit some similarities in their behavior in combustion environments, as well as some distinct differences.

In order to interpret the resultant transient responses of product species, it is essential to know the time response of the entire reactor system. Consequently, a fluid mechanical model of the jet ring distributor was developed. Results from this model were then used to simulate the transient response of the jet ring to tracer pulses. It was concluded that the jet ring effectively introduces a significant amount of dispersion into the system response. This is not due to fluid mechanical "mixing," but rather to the variable time delay imposed by the jet tubes at different locations along the jet ring; i.e., those near the inlet feed tube have a faster response than those further along the ring. This also means that the characteristic decay times observed for inert tracer pulses will differ from the intrinsic residence time of the WSR, and they will also be more similar; i.e., the tracer response is "integrated" somewhat by the jet ring.

A considerable amount of data were obtained during the experimental program. The detailed analysis of these data will be performed with the aid of the preceding model of the reactor system, coupled with the CHEMKIN II package of codes developed to model complex multispecies, multireaction systems, such as the combustion environment in the WSR. It is anticipated that the project will be continued in some manner so that this work can be completed and brought to a successful conclusion.

TRANSIENT STUDIES OF THE EFFECTS OF FIRE SUPPRESSANTS IN A WELL-STIRRED COMBUSTOR

J.M. Calo

Background

The ban on the use of Halon 1301 in fire suppression systems for Air Force gas turbine engines, requires the identification of effective replacements. However, thus far the search for more environmentally benign replacement agents has identified only less effective substitutes. The interactions of chemical agents, such as Halon 1301, in combustion environments is a complex thermo- and physicochemical process which is still not completely understood [1,2,3]. In fact, it has been shown that even Halon 1301 can actually *enhance* combustion under certain conditions [3]. Consequently, the search for safe, effective substitute fire suppressant agents would benefit considerably from advancing the fundamental understanding of the interaction of fire suppressants with the complex combustion gas milieu. This is the primary objective of the work reported here.

The effects of three different fire suppressant agents on the transient behavior and composition of the effluent gas from a combustor were investigated in an experimental program conducted at the Well Stirred Reactor (WSR) facility at Wright-Patterson Air Force Base during the months of July and August 1996. A quadrupole mass spectrometer, that was originally designed and constructed to sample rocket exhaust gases, was used to sample the effluent gas composition from the WSR. These experiments employed premixed propane/air and methane/air gas mixtures at near-atmospheric pressure in the WSR. Transient measurements were performed on the effects of injecting the fire suppressants Halon 1301 (CF_3Br), pentafluoroethane (C_2HF_5 , HFC-125), and trifluoriodomethane (CF_3I) into air/fuel mixtures at various concentration levels using a fast, pulsed valve system.

Analysis of the resultant transient data requires knowledge of the time response of the entire reactor system. Consequently, an analysis of the residence time distribution (RTD) of the jet ring (distributor)/reactor combination was also performed.

Experimental

The Well Stirred Reactor (WSR) facility, located in the Fuels and Lubricants Group of Wright Laboratories at Wright-Patterson Air Force Base, Ohio, has been well described elsewhere [4,5]. The reactor is cast from alumina insulating cement in two halves which together form a toroidal shape, 250 ml in volume. Gas is admitted into the WSR via 32, 1.0 mm I.D. jets, made from alumina tubes, located 20° off radius and held in place in the jet ring assembly which serves as the gas distributor for the reactor. The jets intensely mix the reactor contents and are responsible

for its well-mixed behavior. The gas outlet is located in the center of the top half of the reactor, 90° to the feed gas flow, and exhausts into a large diameter plug flow reactor (PFR) section. Nominal reactor operating parameters include residence times on the order of 6 - 18 ms, operation up to 5 atm pressure and 2300K due to the use of zirconia-coated refractory materials.

The three different fire suppressants were introduced into the WSR *via* a fast, pulsed solenoid valve manufactured by the General Valve Corporation. These valves were originally developed for molecular beam laser spectroscopy experiments. The valves are set for 2 ms at rated voltage, but can achieve even shorter pulse widths by overdriving with a 300V pulse for 165 μ s. The valve on and off times were controlled with the mass spectrometer microcomputer. The minimum "open" time used in the current experiments was 5 ms, which was the same as the resolution of the mass spectrometer data collection system.

The effluent gas from the reactor was sampled into the mass spectrometer *via* an air-cooled quartz probe, which was connected to the bottom of the WSR through a drilled-out stainless steel Swagelok™ fitting with a graphite ferrule. The opening of the probe was positioned 1-2 mm away from the toroidal combustion volume. The flow rate through the probe was controlled by a pump which was throttled to approximately 8-10 slm. The probe was about 35.5 cm in length, with an I.D. of 0.28 cm. Under typical sampling conditions, the probe was operated at temperatures greater than 100°C in order to prevent water vapor condensation.

The quadrupole mass spectrometer was designed and constructed by the GPID Branch of the Ionospheric Effects Division, Geophysics Directorate of the Phillips Laboratory. The gas from the sampling probe flowed through a stainless steel cap which was maintained at temperatures greater than 100°C. Part of the gas was sampled through a 100 μ m orifice into a two-stage, differential vacuum system, pumped by three turbomolecular pumps. The volume between the inlet orifice and the skimmer element was maintained at about 10^{-4} torr. The flow sampled through the skimmer was admitted to the mass spectrometer stage which typically operated at about 10^{-6} - 10^{-7} torr.

The mass spectrometer was controlled *via* a digital interface with a laptop computer. Other than for diagnostic scans over a selected mass range, the mass spectrometer was run in a "mass programming" mode. That is, while the fast solenoid valve was pulsing a particular fire suppressant into the WSR, certain selected mass peaks were monitored for a preset sampling time in a sequential fashion. The signal intensities of these selected mass peaks were recorded as a function of time. The final transient response is actually the averaged sum of the responses for a large number of fire suppressant pulses.

Krypton gas was used as an inert tracer to determine the time response of the reactor system. Figure 1 presents some typical data obtained for the ignited reactor operating with methane as the fuel. As shown, the krypton pulses reflect the varying duration of the valve "open" time. Also, as indicated in the figure caption, the apparent characteristic time constant for the pulse rise is on the order of 45 ms and that for the pulse decay is 22 ms. These are both significantly longer than the WSR residence time which was about 12 ms. Analysis of the transient response of the entire

reactor system indicates that the longer time constants observed are caused by a combination of dispersion of the tracer upstream of the jet ring where the pulsed gas mixes with the feed flow, as well as dispersion caused by the time delay of the gas feed to all the jets in the jet ring distributor (see below).

Results and Discussion

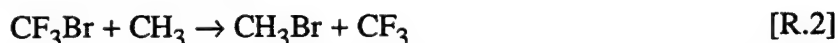
Halon 1301

The principal ion fragments which have been reported for electron impact ionization of CF_3Br are: 69 - CF_3^+ (100%); 148 and 150 - CF_3Br^+ (11.2%); 129 and 131 - CF_2Br^+ (8.9%); 50 - CF_2^+ (5.8%); 79 and 81 - Br^+ (5.8%); 41 - CF^+ (4.3%); and 12 - C^+ (1.8%) [6]. Since this pattern is never observed in the current work, it is concluded that, in general, little Halon 1301 survives the WSR under the current experimental conditions; i.e., it is primarily converted to other species. This is entirely consistent with the anticipated behavior of CF_3Br in combustion environments. Since the C-F bond energy is much greater than that of C-Br (~500 kJ/mol vs. 295.4 kJ/mol, respectively) [7], Halon 1301 readily decomposes *via*:

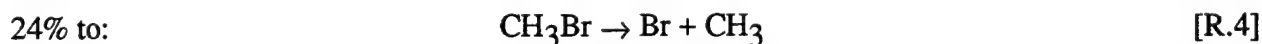
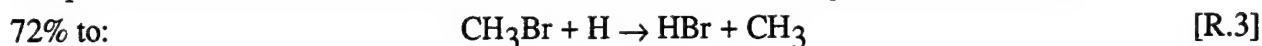


Indeed, the fire retardant properties of Halon 1301 have been attributed to the reaction of the Br and CF_3 radicals liberated in this manner with other species in the flame such as to remove chain carriers from the reaction mechanism [1,3].

Recent work suggests that at short residence times (~0.1 s) under steady-state conditions only a small fraction (~8%) of Halon 1301 decomposes *via* [R.1], with the majority (92%) reacting with methyl radicals to form CH_3Br *via* [3]:



The product of this reaction, methyl bromide, is an important species in the decomposition mechanism of Halon 1301 in combustion environments. Indeed, this species has been detected by GC-MS [3]. However, the parent peaks for this species (masses 94 and 96) were generally not observed in the current work. This is undoubtedly because of the weak C-Br bond (292.9 kJ/mol) [7] and the fact that methyl bromide is rapidly consumed to produce HBr. Battin-Leclerc *et al.* [3] computed that at a residence time of 0.5 s the consumption of CH_3Br is primarily *via*:



In addition to [R.3], HBr is generally produced by abstraction of H by Br radicals from fuel-related hydrocarbons, as well as by direct abstraction of Br by H from CF_3Br :



Due to all the various sources, HBr is the major stable species produced by the decomposition of

CF_3Br in combustion environments. Indeed, this is the prevalent species that was observed in the spectra whenever Halon 1301 was introduced in the WSR.

It was previously established that the major stable products from the addition of Halon 1301 to the combustor were HF and HBr [8]. Figure 2 presents the transient response of HF^+ ($m/e = 20$) and masses, $m/e = 79$ ($^{79}\text{Br}^+$), 80 (H^{79}Br^+), 81 ($^{81}\text{Br}^+$), and 82 (H^{81}Br^+). As shown, The 79/81 ratio was typically close to unity, consistent with the natural bromine isotopic abundance of 0.507/0.493 [7]. As shown, however, the 82 signal was significantly less than that for 80, so there are probably additional contributions to 80 than from H^{79}Br^+ . Electron impact fragmentation of HBr is known to produce Br^+ at a little less than half the the intensity of the HBr^+ signal. Battin-Leclerc *et al.* [3] noted that the Br radical concentration should closely follow that of HBr in the reactor, except at very long residence times, although it is less by almost two orders of magnitude. With the sampling configuration that was used in the current experiments, Br radicals probably do not survive the gas sampling system as such, and, therefore, there must also be some contribution to the Br^+ signal as ion fragments from more stable brominated species in addition to HBr, such as CH_3Br , and Br_2 . The parent ion peaks for Br_2^+ , 158 and 162, were not observed. However, due to the weak Br-Br bond (192.8 kJ/mol) [7], it is expected that Br^+ would be the predominant ion produced from Br_2 .

As shown in Figure 2, although the rise of mass 20 is quite similar to that of the inert krypton tracer, its decay is much longer. This is interpreted as being indicative of the flame chemistry which produces HF as a terminal stable product *via* a number of different reactions. The HBr^+/Br^+ signals also seem to follow the HF^+ rise and decay as well, consistent with the hypothesis that these mass peaks too are indicative of stable product species.

The other series of major ion peaks associated with the CF_3Br pulses are masses 47, 66, and 85, as discussed above, which are attributed to the ions CFO^+ , CF_2O^+ , and CF_3O^+ , respectively. As shown in Figure 3, unlike the behavior of mass 20 (HF^+), which exhibits a longer characteristic decay time, the response of masses 47 and 66 are significantly shorter, following the inert krypton tracer response quite closely. This is the type of response that would be expected as being indicative of intermediate product species in the flame chemistry, that react further to form more stable terminal product species. As shown in Figure 4, the responses of masses 47 and 66 are approximately proportional to the concentration level of the Halon 1301 pulses. Their responses also exhibit a distinct "double-peaked" behavior under these conditions.

As shown in Figure 5, the behavior of mass 85 is decidedly different than that of masses 47 and 66 (as shown in Figure 4). Although it also varies monotonically with the concentration level of the Halon 1301 pulses, it does not exhibit the same "double-peaked" behavior, and definitely lags the responses for the other two masses.

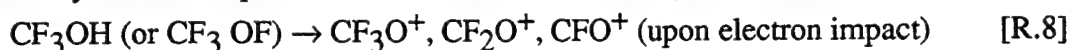
Figure 6 presents an example of the behavior of these three mass peaks with WSR residence time. It is quite evident that both the relative and absolute magnitudes of the three peaks are

sensitive to the WSR residence time on the time-scales involved. For example, while mass 85 is the smallest signal by far for a residence time of 19 ms, it becomes the largest signal for residence times of 12 ms and 6 ms. Thus mass 85 reflects characteristics of a species which forms early in the interactions of Halon 1301 with the combustion environment, and is then consumed in subsequent reactions.

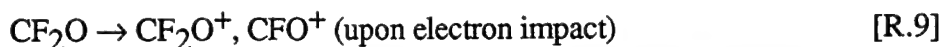
Reaction mechanisms that have been developed to describe the behavior of CF_3Br in combustion environments, all include FCO (mass 47) and CF_2O (mass 66), carbonyl fluoride [1,2,3]. The latter is a stable, colorless, pungent, toxic gas [9] which can certainly survive the gas sampling system. CF_2O is produced in the WSR primarily by the reactions:



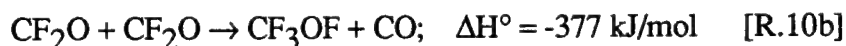
Since these two reactions are both much faster than the bond scission reaction for the decomposition of CF_3Br , [R.1], it is logical that the mass 66 (CF_2O^+) signal would parallel the behavior of the Br^+/HBr^+ mass numbers, at least early in the reaction mechanism, and that it would increase with increasing levels of CF_3Br (i.e., CF_3). This is consistent with the data presented in Figures 2 and 3. FCO, on the other hand, is a radical species which cannot survive the gas sampling tube to the inlet of the mass spectrometer. However, FCO^+ can be produced as an ion fragment of stable species such as CF_2O , or CF_3OF (see below). In Figure 4, it is noted that mass 47 signal is consistently less than that of mass 66, which is consistent with mass 47 being a fragment ion. It is also noted that the "double-peaked" responses of masses 47 and 66 become notable only when the mass 85 signal is high (e.g., at lower residence times), and that the mass 85 response coincides quite well with the second peak of the "double-peaked" responses. This is consistent with some contribution to masses 47 and 66 due to fragmentation of the parent species of mass 85 caused by electron impact in the ion source of the mass spectrometer; i.e.:



as well as:



Mass 85 must arise from a parent species of at least molecular weight 85 or higher. It is noted that the species CF_3OF has been reported in the literature [10], although it is not currently included in the Halon 1301 combustion codes [1,2,3]. However, from the various Halon-associated radicals that are present in the combustion system, it is certainly plausible that CF_3OF can be produced from a number of radical termination reactions, such as:



which are all exothermic, as calculated from enthalpy of formation data [7]. Ionization of CF_3OF

would almost certainly result primarily in the production of the fragment ion CF_3O^+ , since the O-F bond is the weakest in the molecule by far at 182 kJ/mol [7]. Moreover, the parent ion peak would be mass 104. It is noted that a very small, but measurable amount of mass 104 was typically detected whenever mass 85 was most intense.

CF₃I

Due to its chemical similarity to Halon 1301, the behavior of CF_3I in the combustor was expected to be quite similar as well. The products of the interaction of CF_3I with the combustion environment were primarily HF and HI, which were observed as mass peaks 127 (which includes contributions from all iodine-containing species) and 128. In addition, molecular iodine, I_2 , was evident as a purplish gas in the effluent from the combustor. Mass peaks 47, 66, and 85 are also present, as shown in Figure 7, at intensities that are quite similar to those in Figure 6 (although mass 85 is somewhat larger for CF_3I , under similar conditions). The major difference that is apparent in Figure 7 is that mass 85 has a longer characteristic decay time than for masses 47 and 66, unlike for Halon 1301. Also, the "double-peaked" behavior of masses 47 and 66 is not apparent, and the three signals seem to superimpose more than was noted for Halon 1301. These are all indicators that there may be some differences in the combustion reaction mechanism for these two species. It was also noted that for similar concentration levels, CF_3I seemed to be slightly more effective insofar as bring the reactor to "near-blowout" conditions.

HFC-125

HFC-125 (C_2HF_5) exhibited somewhat different behavior than the other two fire suppressants used in the current investigation. Its fire suppressant action is generally believed to be more physical than chemical. This was substantiated by the observation that it took about an order of magnitude more HFC-125 than the other two agents to bring the reactor to "near-blowout" conditions. In addition, HFC-125 behaved as fuel in that the reactor temperature pulsed by as much as 50K in synchronization with the HFC-125 pulses. Neither CF_3Br or CF_3I exhibited this behavior; i.e., the reactor temperature always remained constant during pulsing.

Figure 8 presents the behavior of masses 20, 47, 66, and 85. As shown, the latter three exhibit behavior similar to that observed for CF_3I . In this figure mass 85 is the smallest of the three, but this is primarily due to the longer residence time of the WSR, as is evident in the data in Figure 6. In addition, the decay of the mass 85 response appears to be longer than that for mass 47 and 66, just as was observed in Figure 7 for CF_3I .

In Figure 8, the mass 20 (HF) response is plotted on a linear scale to accentuate the fact that the pulse peak exhibits a minimum. This behavior is preceded by a large increase in the mass 19 (F^+) signal, accompanied by a similar increase in the mass 37 ($\text{H}_2\text{O}\cdot\text{H}_3\text{O}^+$) water cluster signal,

which was used to monitor water indirectly due to the very large mass 18 parent water peak which saturated the mass spectrometer. This appears to be related to the apparent behavior of HFC-125 as a fuel. That is, initially it decomposes and combusts to form water and various fluorine-containing species, and then it begins to participate in the reaction chemistry in a fashion more similar to that of CF_3Br and CF_3I . If this is indeed the case, transient data such as these for HFC-125 and similar species, may eventually provide improved insight concerning fire suppression mechanisms in general.

Transient Response of the System (RTD of the Jet Ring)

In order to properly analyze the transient data, it is necessary to know the time response of the entire system consisting of the pulsed valve/jet ring/reactor combination. The residence time distribution (RTD) of the WSR is known to be exponential, characterized by a time constant equal to the reactor residence time.

The WSR jet ring is annular with an O.D. of 11.8 cm and I.D. of 10.8 cm. The annular ring has a rectangular cross section, 1 cm wide x 0.635 cm in height. The jet ring holds the 32 jet tubes of the WSR in place at its I.D., and serves as a manifold/distributor for the air/fuel mixture through the jet tubes into the reactor volume. The RTD of the jet ring is not known, and, therefore, an analysis was conducted to characterize its behavior. The results of this analysis are presented in detail in a report on this topic [11]. Due to the current lack of space, only a brief summary of the resultant model is presented here. The calculation procedure is as follows.

(1) From the specified gas flowrate in the (5/16" I.D.) inlet feed tube, the value of the inlet velocity in each half of the jet ring, w_{in} , is determined from continuity:

$$A_o v_o = 2 A_{ring} w_{in} \quad [1]$$

where A_o and A_{ring} are the cross sectional areas of the inlet feed tube and jet ring, respectively, and v_o is the gas velocity in the inlet feed tube. The pressure at the entrance to this half of the jet ring is given by application of the Bernoulli equation along a streamline from the feed tube to the inlet of one half of the jet ring:

$$P_{in} = P_o + \rho (v_o^2 - w_{in}^2)/2, \quad [2]$$

where P_o is the pressure in the feed tube.

(2) The calculation then proceeds around the ring in both ($\pm\theta$) directions, with the pressure drop in the control volumes between jets tubes given by:

$$dP/d\theta = -(\rho f w^2/8) \phi \quad [3]$$

(3) The flow rate through each jet tube, $(dm/dt)_j$, is determined in the following manner. It is assumed that the flow in the jet tubes is adiabatic and compressible since they are well insulated from their surroundings and the reactor, and the thermal conductivity of alumina is quite low. In order to calculate the mass flowrate through each tube, it was first assumed that choked (sonic) flow was attained at the tube exit ($M_e = 1$). In this case, the Mach number at the tube inlet, M , is

given by the expression [12]:

$$(1 - M^2)/kM^2 + [(k+1)/2k] \ln[(k+1)M^2/(2 + (k-1)M^2)] + (1 - kM^2)/(kM^2) = fL/d, \quad [4]$$

where k is the heat capacity ratio of the gas, L is the jet tube length, and d is its diameter. This expression is solved using Newton's method updating the average friction factor in the jet tube, f , at each iteration. The ratio of the pressure at this point in the tube, P , to the exit pressure, P_e , is then determined from [12]:

$$P/P_e = (1/M) [(k+1)/(2 + (k-1)M^2)]^{1/2} \quad [5]$$

This ratio is then compared to the ratio P/P_0 , where P_0 is the reactor pressure, which was approximately atmospheric. Choked flow at the jet tube exit is confirmed if $P_e \geq P_0$.

If $P_e < P_0$, then the flow at the jet tube exit is subsonic. In this case, the correct Mach numbers at the tube inlet and exit must be found. This is done in an iterative fashion by first assuming sonic flow at the jet tube exit ($M_e = 1$) and the Mach number, M , at the inlet determined from the original choked flow calculation. These values are used to determine the Mach number at the jet tube exit by solving the following transcendental expression using Newton's method [12]:

$$P/P_e = (M_e/M) [(2 + (k-1)M_e^2)/(2 + (k-1)M^2)]^{1/2} \quad [6]$$

The resultant value of M_e is then used in the following expression for isentropic, compressible flow in a duct of constant cross section to yield an updated value for the Mach number at the jet tube inlet, M [12]:

$$1/(2M^2) - [(k+1)/2] \ln(M) + [(k+1)/4] \ln[1 + (k-1)M^2/2] = kfx/d + C, \quad [7]$$

where C is a constant of integration evaluated at the jet tube exit ($M = M_e$, $x = L$). The resultant value of M (@ $x = 0$) is then compared to the initially assumed value, and the entire process involving Eqns. [6] and [7] is iterated until the assumed and calculated values of the Mach number at the jet tube inlet, M , agree within a specified tolerance. This calculation procedure also yields the corresponding value of the exit Mach number which is updated during the calculation, as well as the average friction factor, f , which is also updated during the course of the iterative calculation.

The resultant Mach number at the jet tube inlet is then used to determine the gas density at this point from the isentropic flow relations. The jet tube mass flowrate is then given by:

$$(dm/dt)_j = \rho M (k R T_{in})^{1/2} (\pi/4) d^2, \quad [8]$$

(4) The pressure change due to removal of gas from the jet ring *via* the jet tubes is determined from the integrated energy balance:

$$P_2 = P_1 + \rho (w_1^3 - w_2^3)/(2w_2) \quad [9]$$

where, P_2 and w_2 are the pressure and jet ring velocity downstream of the jet tube, and P_1 and w_1 are the corresponding values upstream of the jet tube.

(5) The sum of the flow rates through all the jet tubes is compared to the total specified flow rate, and the pressure in the feed inlet tube is adjusted (i.e., iterated) until they agree. The calculation is symmetric in the $\pm\theta$ directions. Therefore, the velocity must tend to zero in the control volume between jets 16 and 17 (i.e., at $\theta = \pi$), and the pressure must achieve a maximum

at the same location.

The preceding calculation procedure was implemented on an EXCELTM spreadsheet using a separate MACRO that was written to calculate the flow in the jet tubes.

Jet Ring Distribution Results

Figure 9 presents the resultant pressure and velocity distributions for the case of 390 slm of air and 28.7 slm of methane (equivalence ratio, $\phi = 0.7$), characteristic of the 6 ms residence time combustion runs that were conducted in the WSR. For these conditions, the flow in all the jet tubes was sonic (i.e., choked flow at the jet tube exits; $M_e = 1$, and $P_e \geq P_o$). As shown, the gas velocity in the jet ring decreases discretely at each jet tube, corresponding to the amount of gas which flows into the reactor at that point, as determined by continuity. The pressure in the jet ring decreases due to wall friction, and increases due to the momentum loss at each jet tube. The overall effect is to progressively increase the jet ring pressure until one-half of the way around the ring, whereupon it then begins to decrease to match the inlet pressure at the end of the ring. As shown in Figure 9, the pressure distribution is perfectly symmetric with respect to the two halves of the jet ring. This is also reflected in the gas distribution through the jet tubes. Although the flowrate through the jet tubes increases progressively to the midpoint of the jet ring, the flow *maldistribution* is practically negligible, with the flowrate differing by less than 1% from the minimum to the maximum. The results for all the various flowrates used were all qualitatively similar, with the exception that subsonic flow occurred in the jet tubes for all conditions except those in Figure 9.

Contrary to the results of the preceding calculations, tracer tests conducted on a room temperature jet ring that had been removed from the reactor, revealed significant fluid maldistribution. An example of these data are presented in Figure 10, which is a compilation of tracer responses from selected individual jets. For perfect distribution, the response of "mirror image" jet pairs from each half of the jet ring should be exactly the same. As shown, however, although the responses of the jet pairs superimpose quite well near the feed tube inlet (e.g., #1-32), they progressively separate as the flow proceeds through the ring, such that the response for #20 is much slower than for #12, and it is even slower than for #16. This indicates that the flow is quite asymmetric, with the zero velocity point occurring beyond π radians, and with more gas flowing through the jets located from π to 2π , than for those between 0 and π . However, this jet ring differed from the one that was used in the combustor for all the current experiments. It was an older one fitted with all stainless steel jet tubes, that had already experienced significant service in the combustor. Some of the tubes were obviously worn, and some were noncircular and partially "crimped" at the exit. Nine of the jet tubes (#1, 4, 8, 12, 16, 20, 24, 28, and 32) were replaced with alumina tubes of the same type used in the reactor for the combustion runs, but the remaining 23 were the original stainless steel tubes. Consequently, it is hypothesized that the fluid maldistribution resulted from jet tubes which had much lower conductances than the others.

In order to demonstrate the effect of variations in jet tube conductance, four of the jet tube flowrates (for #7, 8, 9, and 10) were arbitrarily set to zero for the case of 390 slm air/28.7 slm methane. The results of this calculation are presented in Figures 11. As clearly shown, the pressure maximum in the jet ring shifted from π radians between jets #16 and #17 to between jets #18 and #19. The pressure in the feed tube also increased from 225 kPa to 260 kPa in order to maintain the specified flowrate.

Response to an Inert Tracer

The velocity distributions in the jet ring, determined in the manner described above, can then be used to predict the response of the jet ring/reactor combination to a pulse of inert tracer. A mass balance on a tracer injected into the inlet tube of the jet ring for the control volumes between jets, where the gas velocity, w , is constant *via* continuity, is given by:

$$\partial C / \partial t = -(1/R_2) w \partial(C) / \partial \theta, \quad [10]$$

where C is the tracer concentration (e.g., kg/m^3 , or any other convenient units). The total concentration of tracer in the effluent from the WSR is given by:

$$V_{\text{WSR}} \partial C / \partial t = \Sigma \{ (dm/dt)_j C_j / \rho \} - C Q \quad [11]$$

where the summation is over all (32) jets, C_j is the tracer concentration as a function of time at the source point in the jet ring for each jet tube, and Q is the total effluent volumetric flowrate from the WSR, and V_{WSR} is its volume (250 cm^3).

The results of a simulation in comparison to krypton tracer data are presented in Figure 12. As shown, there is good agreement between the calculation and the data, even though the model has not yet been optimized. The principal conclusion of this result is that the jet ring effectively introduces a significant amount of dispersion into the system response. This is not due to fluid mechanical "mixing" in the jet ring, but rather to the variable time delays imposed by the jet tubes at different locations along the jet ring; i.e., those near the inlet feed tube have a faster response than those further along the ring. This also means that the characteristic decay times observed for inert tracer pulses will differ from the intrinsic residence time of the WSR, and will also be more similar; i.e., the tracer response is "integrated" somewhat by the jet ring.

Summary and Conclusions

The WSR/REMS apparatus has been demonstrated to be capable of monitoring both the steady-state and dynamic behavior of the WSR combustor.

It was concluded that the three fire suppressants exhibit certain similarities in their behavior in combustion environments, as well as some distinct differences. The major product species produced by their injection into the WSR combustor are HF (for all three), HBr (for CF_3Br), and HI (for CF_3I). All three fire suppressant agents also produced significant mass peaks at 47, 66,

and 85, which are attributed to the ion series CFO^+ , CF_2O^+ , and CF_3O^+ , respectively. CF_2O^+ is most probably the parent ion peak of the stable species, carbonyl fluoride. High levels of this very toxic gas were produced at short reactor residence times. Masses 47 and 85, CFO^+ and CF_3O^+ , are most probably fragment ions from stable neutral species such as CF_3OF and CF_3OH . These latter species should be included in fire suppressant reaction mechanisms.

In order to interpret the resultant transient responses of product species, it is essential to know the time response of the entire jet ring distributor/reactor system. Consequently, a fluid mechanical model of the jet ring distributor was developed. Results from this model were then used to simulate the transient response of the jet ring to tracer pulses. It was concluded that the jet ring effectively introduces a significant amount of dispersion into the system response. This is not due to fluid mechanical "mixing," but rather to the variable time delay imposed by the jet tubes at different locations along the jet ring; i.e., those near the inlet feed tube have a faster response than those further along the ring. This also means that the characteristic decay times observed for inert tracer pulses will differ from the intrinsic residence time of the WSR, and they will also be more similar; i.e., the tracer response is "integrated" somewhat by the jet ring.

A considerable amount of data were obtained during the experimental program. The detailed analysis of these data will be performed with the aid of the preceding model of the reactor system, coupled with the CHEMKIN II [13] package of codes developed to model complex multispecies, multireaction systems, such as the combustion environment in the WSR. In particular, the PSR (perfectly stirred reactor) modules from this code [14] are being used to model the behavior of the WSR. The sampling line is being modeled using the constant pressure version of the CHEMKIN II code, by adapting an approach that has been previously used at the Phillips Laboratory to model the variation in stratospheric gas composition due to sampling through a tube in laminar flow [15]. The latter will be used to assess the survivability of reactive species in the sampling system.

It is anticipated that the transient data coupled with the model analysis will aid in the identification of the key reactions in the mechanisms responsible for the behavior of fire suppressants in combustion systems. (It is noted that the "built-in" sensitivity analysis options in the CHEMKIN II codes will be especially helpful in such mechanistic investigations.) This approach could also be used to determine kinetic rates for the reactions involved. The unique capabilities of the REMS/WSR apparatus could be used to identify and measure in a definitive, quantitative manner the efficacy of candidate fire suppressants using only minimal pulsed amounts, as well as aid in the assessment of the important environmental effects of using fire suppressants in combustion systems relevant to Air Force operations.

References

- [1] P.R. Westmoreland, D.R.F. Burgess, Jr., W. Tsang, and M.R. Zachariah, paper presented at Eastern States Section, The Combustion Institute, October, 1993.
- [2] C.K. Westbrook, *Comb. Sci. Tech.* **34**, 201 (1983).
- [3] F. Battin-Leclerc, G.M. Côme, and F. Baronnet, *Comb. Flame* **99**, 644 (1994).
- [4] J. Zelina and D.R. Ballal, "Combustion Studies in a Well Stirred Reactor," AIAA 94-0114, presented at the 32nd Aerospace Sciences Meeting, January, 1994, Reno, NV.
- [5] J. Zelina and D.R. Ballal, "Combustion and Emission Studies Using a Well Stirred Reactor," AIAA 94-2903, presented at the 30th AIAA/ASME/SAE/ASEE Joint Propulsion Conference, June, 1994, Indianapolis, IN.
- [6] V.H. Diebler, R.M. Reese, and F.L. Mohler, *J. Res. N.B.S.* **57**, 113 (1956).
- [7] Handbook of Chemistry and Physics, 75th, D.R. Lide, ed., CRC Press, Boca Raton, 1994.
- [8] J.M. Calo, Final Report for AFOSR Summer Faculty Research Program, September 1995.
- [9] W. Braker and A.L. Mossman, Matheson Gas Data Book, 6th ed., Matheson Co., Lyndhurst NJ, 1980, p. 144.
- [10] J. Czarnarski, E. Castellano, and H.J. Schumacher, *Chem. Comm.* 1255 (1968).
- [11] J.M. Calo, T. Miller, J.O. Ballenthin, R. Striebich, J. Blust, and M. Getz, *The Residence Time Distribution (RTD) of the Well-Stirred Reactor (WSR)*, Phillips Laboratory, Geophysics Directorate, Ionospheric Effects Division (GPID), Hanscom AFB, MA, in preparation.
- [12] J.A. Roberson and C.T. Crowe, *Engineering Fluid Mechanics*, Houghton Mifflin Co., Boston, 1990, p. 424.
- [13] R.J. Kee, F.M. Rupley, and J.A. Miller, "CHEMKIN II: A FORTRAN Chemical Kinetics Package for the Analysis of Gas-Phase Chemical Kinetics," SAND89-8009B, November, 1991, Sandia National Laboratories, Livermore, CA.
- [14] P. Glarborg, R.J. Kee, J.F. Grcar, and J.A. Miller, "PSR: A FORTRAN Program for Modeling Well-Stirred Reactors," SAND86-8209, February, 1986, Sandia National Laboratories, Livermore, CA.
- [15] J.M. Calo, "Composition Alteration of Stratospheric Air Due to Sampling Through a Flow Tube," AFGL-TR-84-0045, Ionospheric Physics Division, Air Force Geophysics Laboratory, Hanscom AFB, MA, 1984.

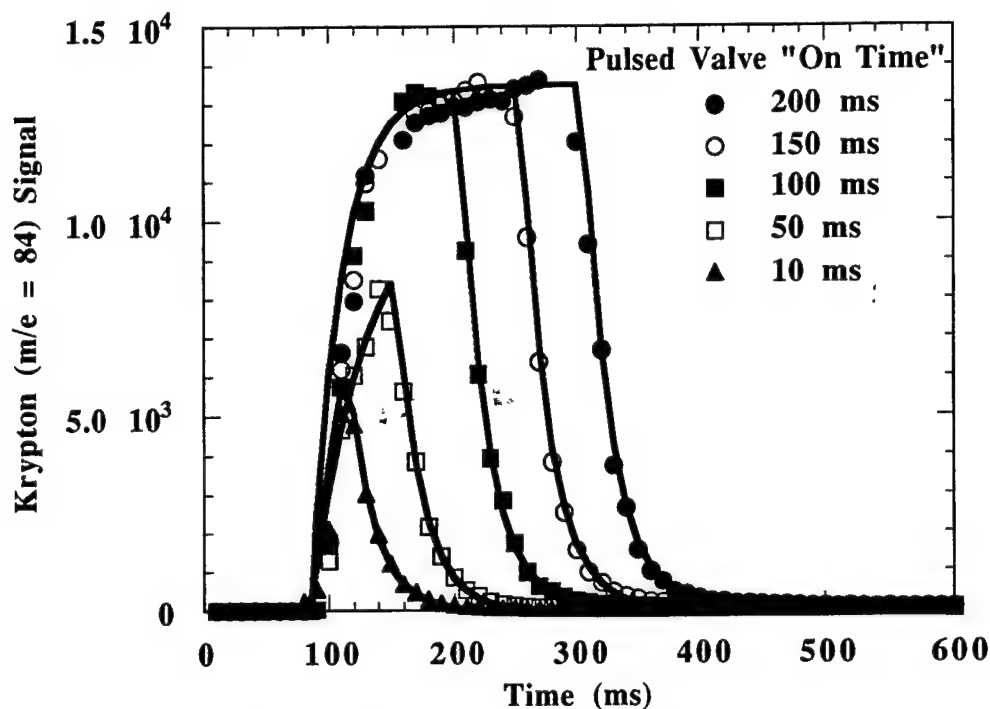


Figure 1. Krypton signal responses for variable duration pulses and the corresponding fits to the data for the ignited WSR operating with 200 slm air and 14.7 slm methane ($\tau \approx 12$ ms). The characteristic time constant for the pulse rise is ~ 45 ms, and 22 ms for the pulse decay, which differs significantly from τ .

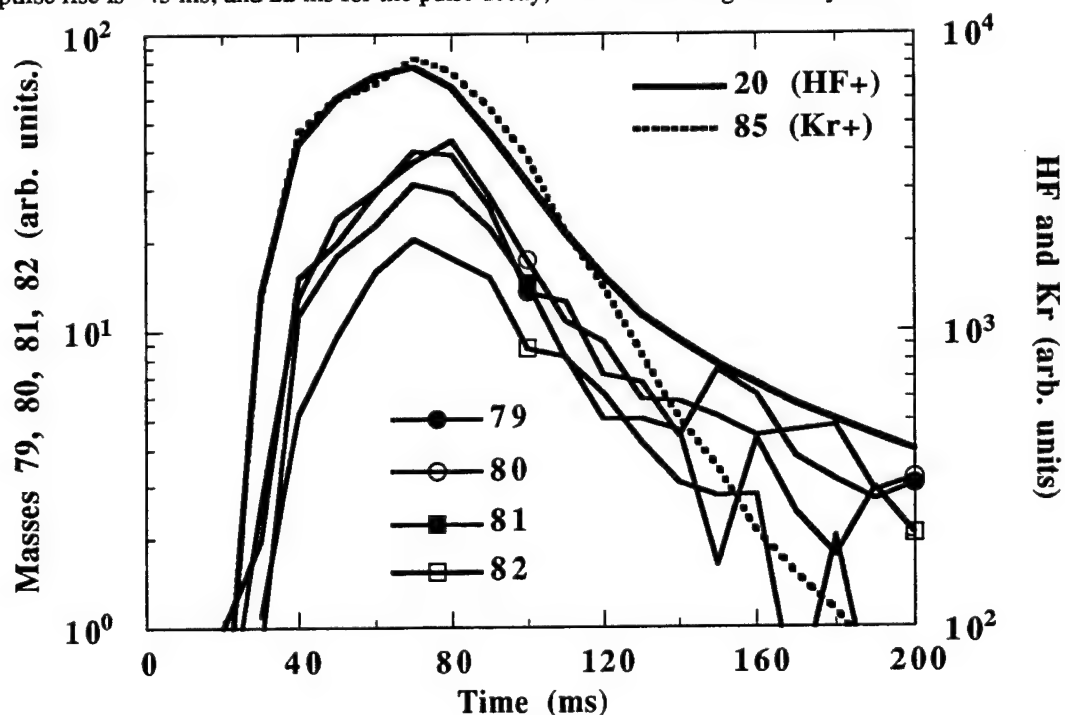


Figure 2. HBr^+/Br^+ and HF^+ signal responses to 1% Halon 1301 pulses of 50 ms duration into the ignited WSR operating with 200 slm air and 5.9 slm propane ($\tau \approx 12$ ms). The Kr^+ response is plotted as a reference.

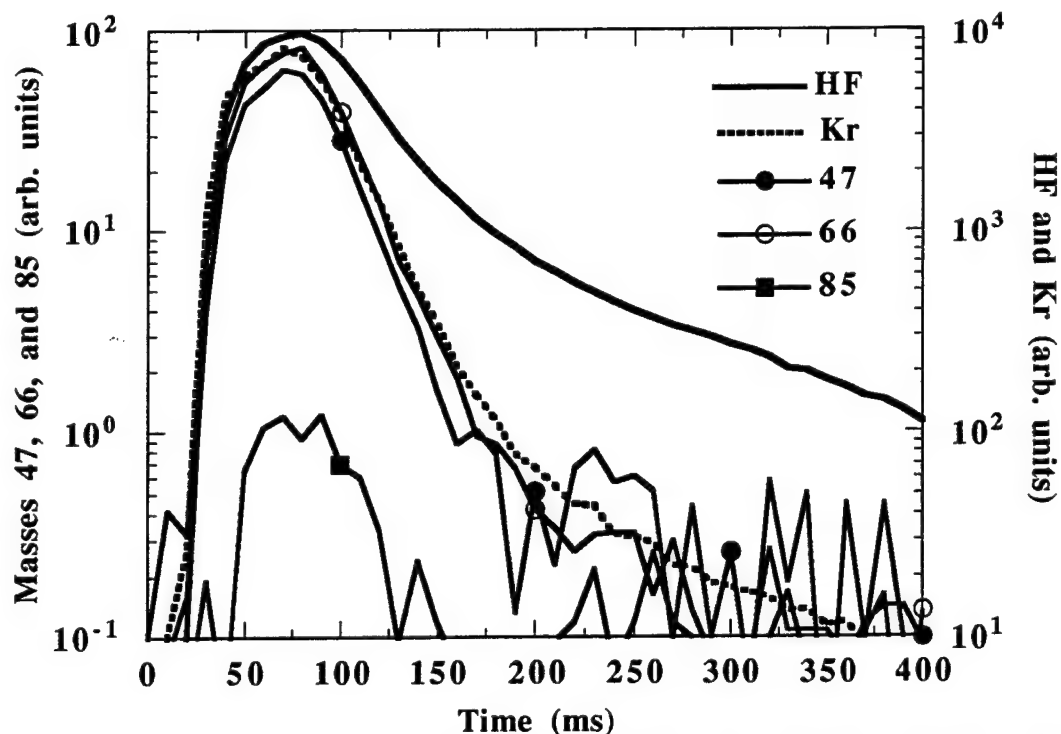


Figure 3. Mass 47, 66 and 85 signal responses for 0.75% Halon 1301 pulses of 50 ms duration into the ignited WSR operating with 150 slm air and 3.5 slm propane ($\tau \approx 19$ ms). The Kr^+ inert tracer response is plotted as a reference.

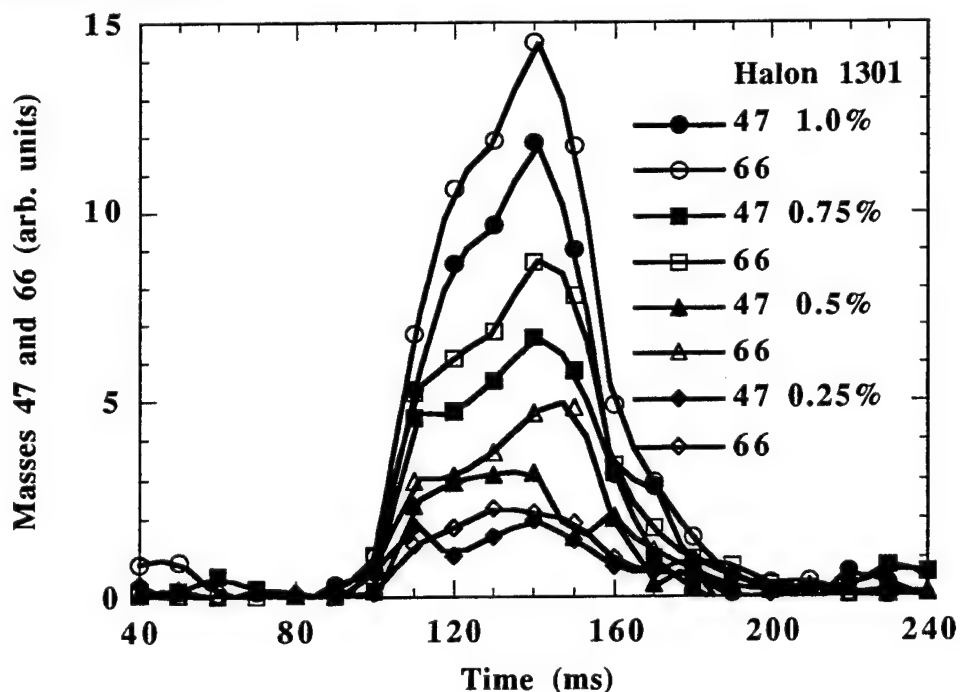


Figure 4. Mass 47 and 66 signal responses as a function of Halon 1301 concentration level of 50 ms pulses into the ignited WSR operating with 200 slm air and 5.9 slm propane ($\tau \approx 12$ ms).

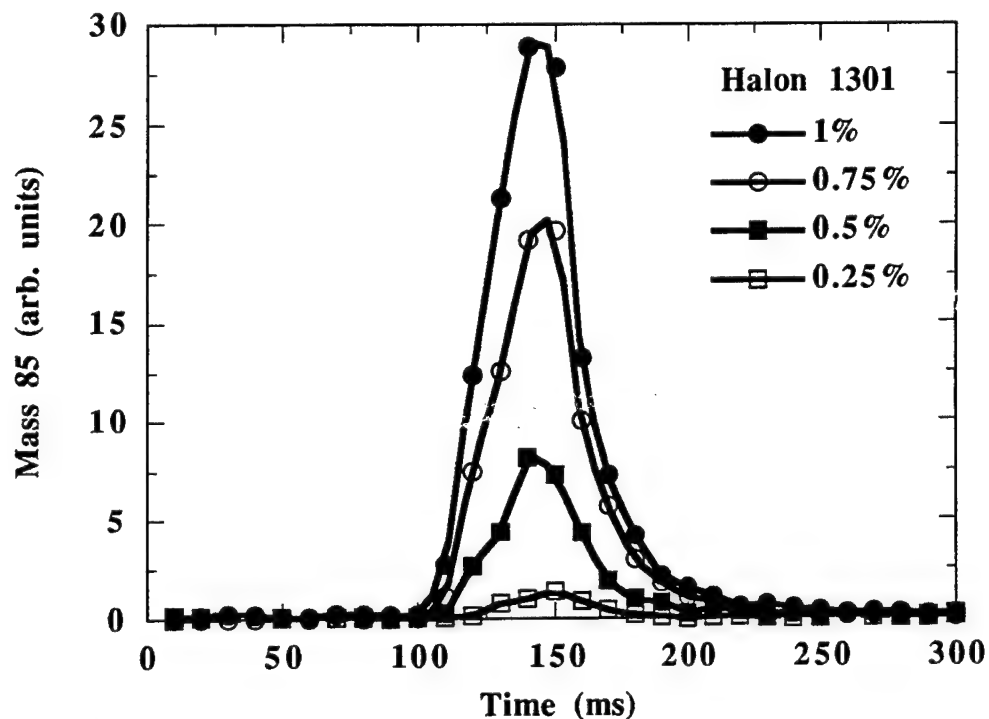


Figure 5. Mass 85 signal response as a function of Halon 1301 concentration level of 50 ms pulses into the ignited WSR operating with 200 slm air and 5.9 slm propane ($\tau \approx 12$ ms).

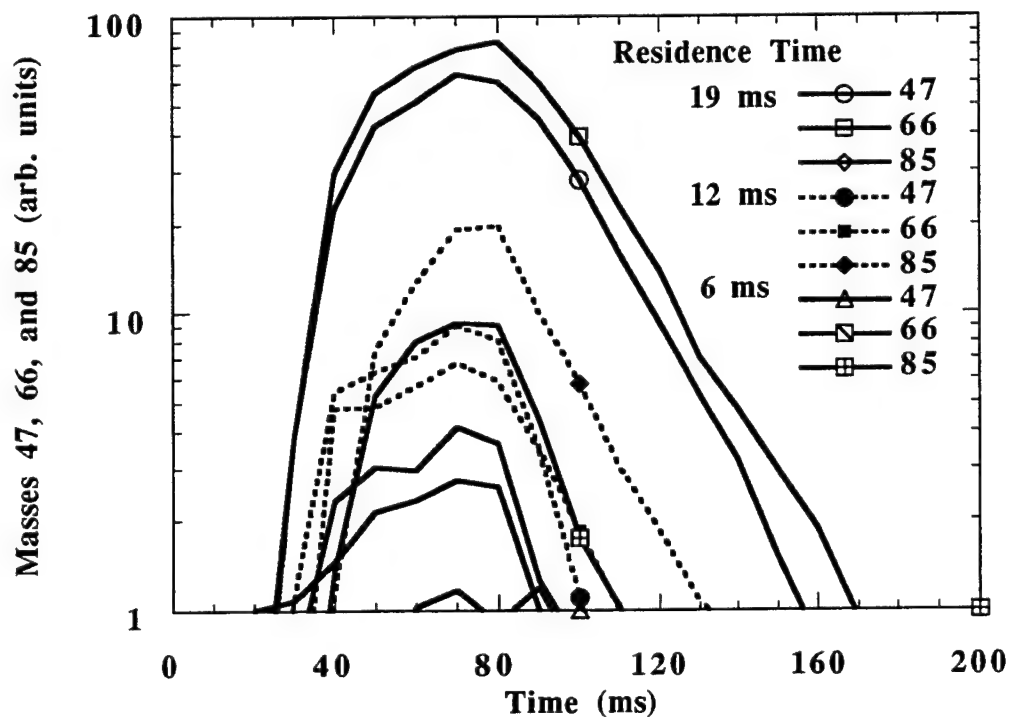


Figure 6. Mass 47, 66, and 85 signal responses for 0.75% Halon 1301 50 ms pulses as a function of WSR residence time.

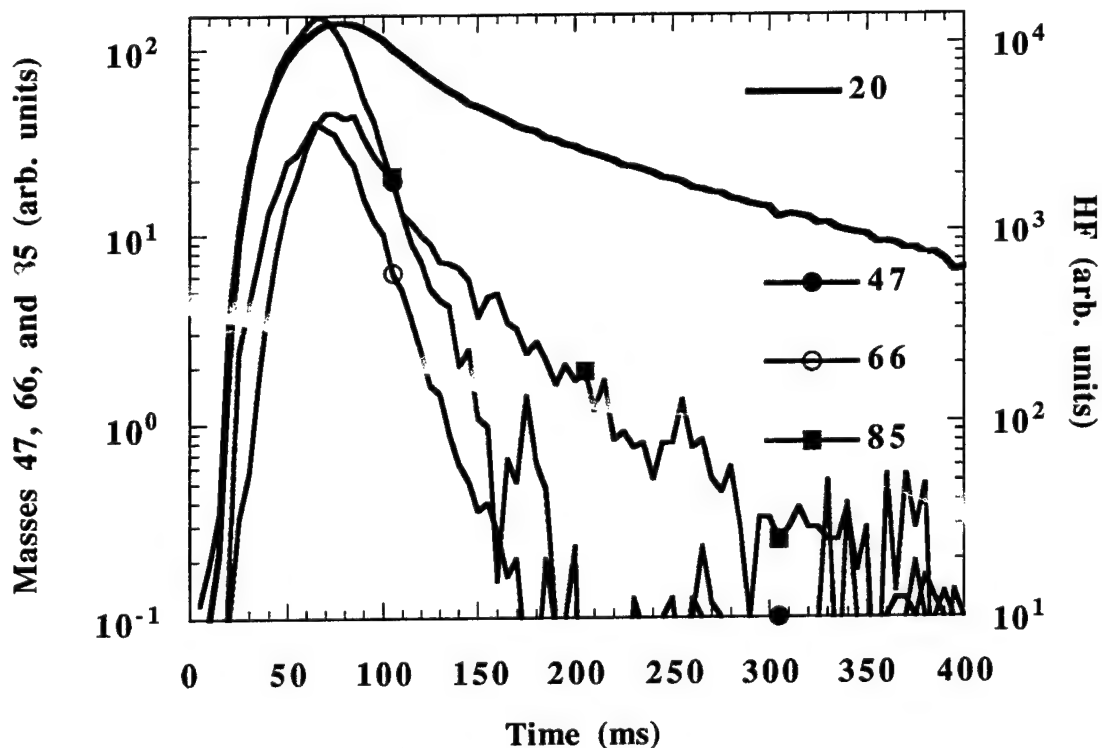


Figure 7. Mass 47, 66 and 85 signal responses for 0.75% CF_3I pulses of 50 ms duration into the ignited WSR operating with 200 slm air and 14.8 slm methane ($\tau \approx 12$ ms).

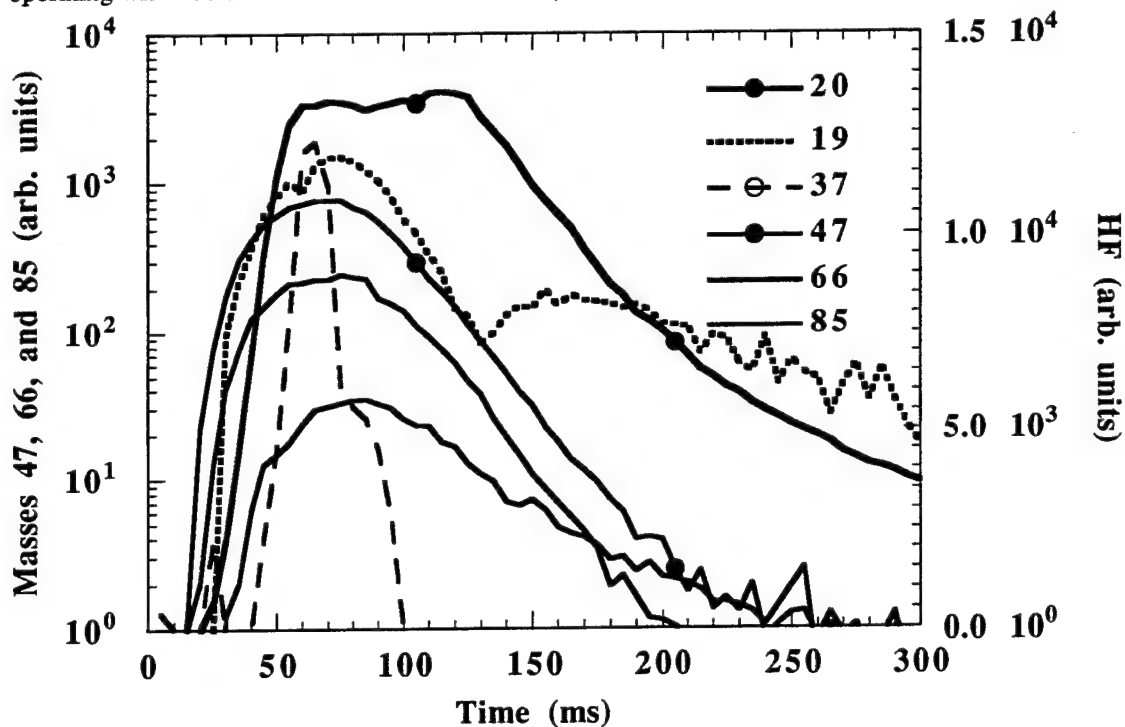


Figure 8. Mass 19, 20, 37, 47, 66 and 85 signal responses for 0.75% HFC-125 pulses of 50 ms duration into the ignited WSR operating with 150 slm air and 5.25 slm methane ($\tau \approx 19$ ms).

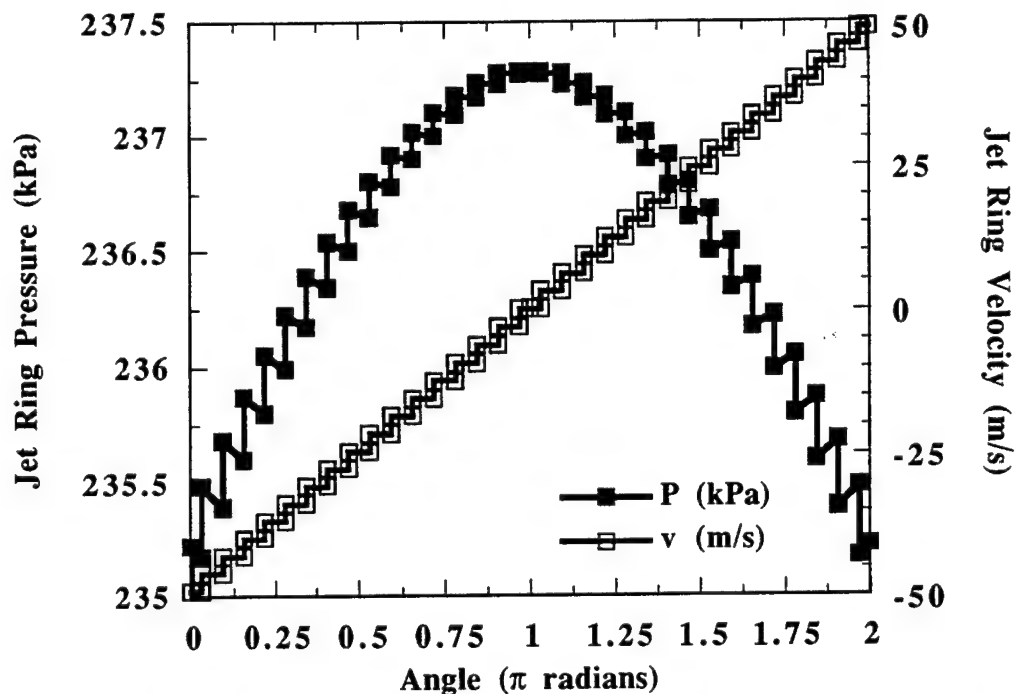


Figure 9. Pressure and velocity distributions in the jet ring for a flowrate of 390 slm air and 28.7 slm methane ($\phi = 0.7$). For this calculation, there was good agreement between the resultant inlet feed tube pressure of 225 kPa, and the experimental value of about 224 kPa. The jet ring temperature was assumed constant at 300°C. Sonic flow conditions occurred in all the jet tubes.

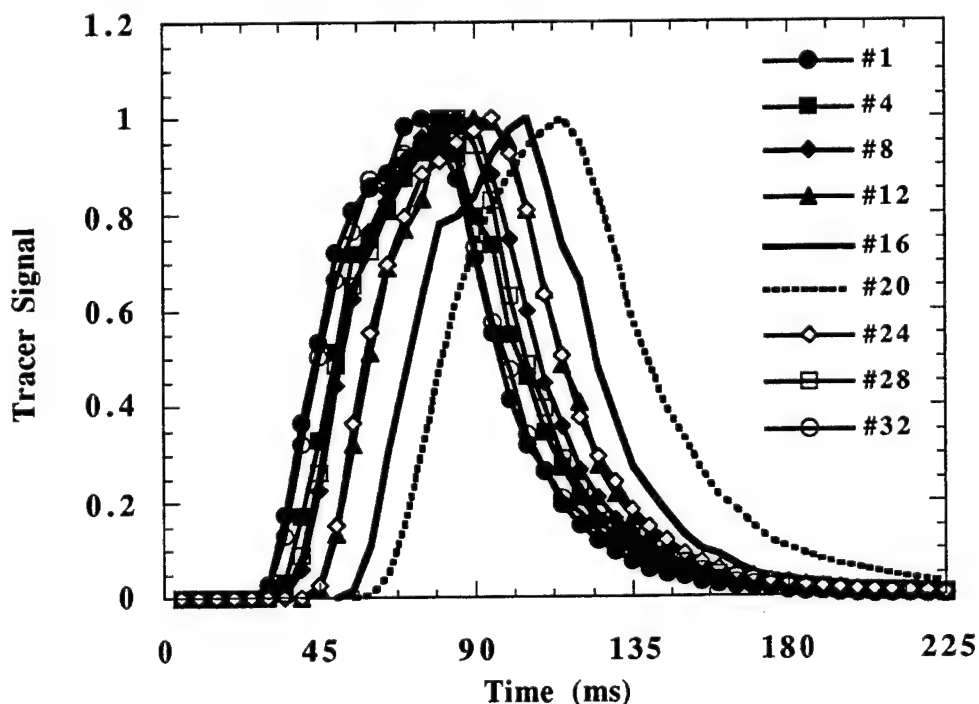


Figure 10. Tracer (50 ms CF_3Br pulses at room temperature) response of selected jets in the jet ring at a flowrate of 200 slm of air. The jets are counted counterclockwise from the inlet feed tube. "Mirror-image" jet pairs: 1-32, 4-28, 8-24, 12-20; 16 is located at $\theta = 31\pi/32$.

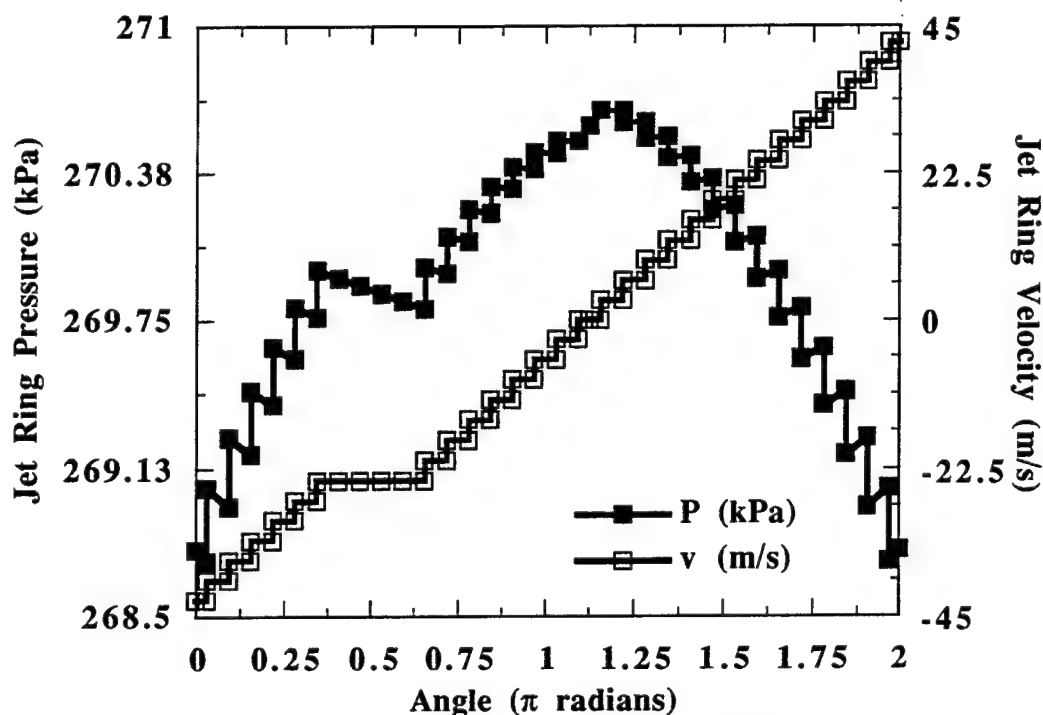


Figure 11. Pressure and velocity distributions in the jet ring for a flowrate of 390 slm air and 28.7 slm methane ($\phi = 0.7$), with jets 7,8,9, and 10 plugged. The resultant inlet feed tube pressure is 260 kPa. The jet ring temperature was assumed constant at 280°C. Sonic flow conditions occurred in all the jet tubes.

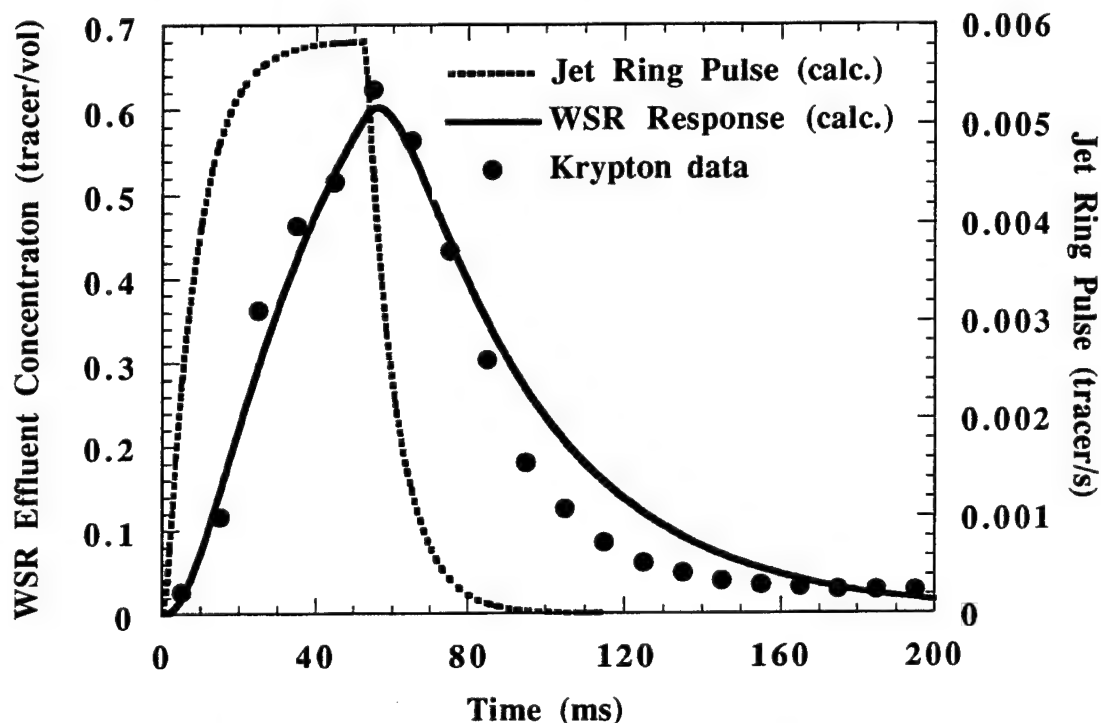


Figure 12. Comparison of WSR response calculated from the jet ring/WSR model to krypton tracer data obtained from the ignited WSR operating with 200 slm air and 14.7 slm methane ($\tau \approx 12$ ms).

**EXAMINATION OF CRITICAL ISSUES IN THE USE OF ^{178}Hf
FOR HIGH ENERGY DENSITY APPLICATIONS**

**James J. Carroll
Assistant Professor
Department of Physics and Astronomy**

**Youngstown State University
One University Plaza
Youngstown, OH 44555-3616**

**Final Report for:
Summer Faculty Research Program
Phillips Laboratory
Kirtland, AFB**

**Sponsored by:
Air Force Office of Scientific Research
Bolling Air Force Base, DC**

and

Phillips Laboratory

September, 1996

EXAMINATION OF CRITICAL ISSUES IN THE USE OF ^{178}Hf FOR HIGH ENERGY DENSITY APPLICATIONS

**James J. Carroll
Assistant Professor
Department of Physics and Astronomy
Youngstown State University**

Abstract

The second nuclear isomer of ^{178}Hf stores 2.445 MeV per nucleus for a half-life of 31 years. Therefore, samples containing this isomer provide an attractive high energy density material, on the order of a gigaJoule per gram. This stored energy is normally released as gamma rays during the spontaneous decay of the isomer. However, experimental studies have indicated that it may be possible to trigger this release without resorting to fission or fusion reactions (with their negative aspects). In this event, ^{178}Hf may prove to be important for a number of applications related to the mission of the US Air Force, including rocket propulsion, agent defeat and advanced light source or laser development. This report examines a number of critical issues which must be resolved prior to a complete evaluation of the potential for the 31-year isomer of ^{178}Hf . The status of experimental and theoretical efforts along these lines will be discussed.

EXAMINATION OF CRITICAL ISSUES IN THE USE OF ^{178}Hf FOR HIGH ENERGY DENSITY APPLICATIONS

James J. Carroll

INTRODUCTION

Considerable attention has recently become focused on the potential for nuclear isomers in applications related to the mission of the United States Air Force. These include rocket propulsion, agent defeat and advanced light source or laser development. The performance of innovative concepts along these lines would be greatly enhanced by reductions in weight and the ability to produce high-energy photons (gamma rays) without the negative consequences of fission or fusion reactions. This enhancement may be possible with the natural advantages of nuclear isomers.

A nucleus can exist in a number of excited states, each storing energy and lasting for some time before returning to its lowest-energy, or ground state. This decay is usually accompanied by the emission of gamma rays which carry away the excess energy. Most excited-state lifetimes are shorter than nanoseconds, but many nuclides possess a few excited states which are characterized by lifetimes as long as 10^{15} years. These "metastable" states are called *nuclear isomers* and provide the ultimate in high-energy density materials. Energy storage can reach the level of a few MeV per nucleus, on the order of a gigaJoule per gram at solid densities. The long lifetimes arise from weak coupling between the metastable states and the radiation field, and so isomeric decays are characterized by high-multipolarity transitions. At the same time this poor coupling would appear to inhibit any attempt to trigger the release of the stored energy upon demand, without resorting to fission or fusion reactions. However, experimental studies conducted in academia

over the past decade indicate that triggering may indeed be possible using photons (x rays) of relatively low energy. This opens attractive possibilities for a number of applications, depending upon the particular properties of the isomer and the trigger parameters. This report examines a number of critical issues related to the potential use of the 31-year isomer of ^{178}Hf for these applications.

FUNDAMENTALS

The attractive features of ^{178}Hf as a high-energy density material follow from its rich manifold of excited states which includes several isomers. Figure 1 shows a subset of those states as a schematic energy-level diagram where the arrangement of the levels into columns emphasizes the band structure. This isotope falls into the class of nuclei (common in the rare-earths) which are well-deformed from a spherical shape, being in this case prolate. Within this shape individual nucleons undergo motion which can be described by an independent-particle model with a deformed (Nilsson) potential [1]. Single-particle excitations provide the *intrinsic* states of the nucleus, which are shown in Fig. 1 as the levels lying at the bottom of each column. Each intrinsic state has an angular momentum with quantum number I and the projection of this angular momentum upon the deformation axis is quantized by Ω . Due to the presence of definite symmetry, the nucleus behaves as a quantum rotor and additional excited states arise from its collective motion. The resulting rotational levels provide a band structure built upon each intrinsic state. The total angular momentum, with quantum J , arises from the addition of rotational quanta and the angular momentum of the intrinsic state. The projection of the total angular momentum upon the deformation axis is quantized by K and thus the value of K for each member within a band is determined by that of the intrinsic state which serves as the

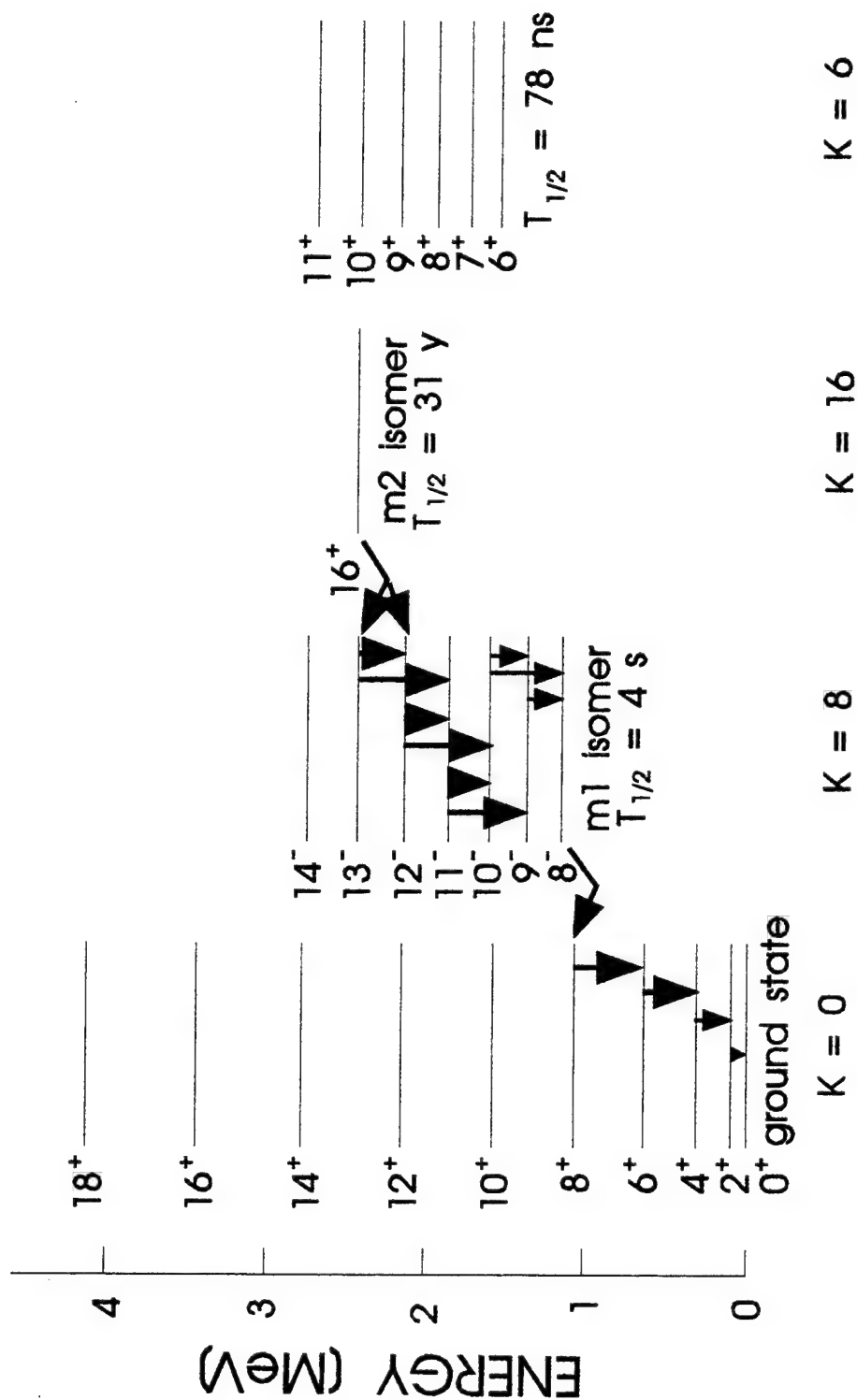


Figure 1: Partial schematic energy-level diagram [5] for ^{178}Hf . The arrows indicate the transitions which provide the spontaneous emission cascade from the 31-year isomer at 2.445 MeV. The levels in the ground-state rotational band are yrast to $J = 10$.

bandhead. Only if axial symmetry is maintained does K remain a good quantum number: K is therefore an approximate or asymptotic quantum number. The angular momenta of band members follow the rule $J = K, K + 1, K + 2, \dots$, with the exception that only even J occur for rotational states build upon a 0^+ intrinsic state. High angular momentum can therefore occur for large- J intrinsic states that are *deformation-aligned*, or as rotational levels with large J , but small K (*rotation-aligned*).

The radiative decay of any excited state is governed by the standard selection rules for electromagnetic transitions: $\Delta J \leq l$, where l , is the multipolarity of the radiation field, and $\Delta\pi = (-1)^l, (-1)^{l+1}$ for electric and magnetic transitions, respectively. A value of $\Delta\pi = -1$ indicates a change in parity in the transition. The probability of an electromagnetic decay from an excited state having angular momentum and parity, $(J^\pi)_i$ to a state having $(J^\pi)_f$ may be estimated by considering that of a transition due to a single particle, i. e. by employing Weisskopf units. For example, the transition rate for electric dipole ($l = 1$) radiation is given by the [2]

$$w = (1.03 \times 10^{14} \text{ s}^{-1}) A^{2/3} E_\gamma^3, \quad (1)$$

where E_γ is the transition energy in MeV, A is the mass number of the nucleus and w is in s^{-1} . The radiative lifetime of the upper state, τ is given by the inverse of the transition rate.

An additional complication arises for well-deformed nuclei such as ^{178}Hf . Another selection rule must be satisfied *provided K remains a good quantum number*: $\Delta K \leq l$. A transition characterized by a given l based upon the needed ΔJ may prove to be strongly inhibited if the ΔK of the transition is greater than the multipolarity (a *K forbidden* transition). This is quantified by the *degree of K forbiddenness*, $\nu = |\Delta K - l|$ and the transition rate is reduced by the

factor f' where the *hindrance* per degree of forbiddenness is f . Extremely long lifetimes against spontaneous gamma emission can arise when deformation-aligned intrinsic states of high angular momentum are located at relatively low energy. Such states occur with some regularity in the rare-earth region due to the existence of many single-particle orbitals with large Ω near the Fermi surface. Levels of comparable J to which modest-multipolarity transitions would otherwise be likely are rotational states with much smaller values of K . These are often the *yrast states* which have the highest total angular momenta for a given energy and are usually members of the ground-state band. Metastability resulting from this structure is referred to as being caused by an *yrast trap*. As can be seen from Eq. (1), a small transition energy can also inhibit gamma emission, leading to isomers which are *spin trapped*.

Figure 1 shows that the $J^\pi = K^\pi = 16^+$ level of ^{178}Hf is an example of an isomer which is both yrast and spin trapped. This isomer stores 2.445 MeV for a half-life of 31 years and is designated as $^{178}\text{Hf}^{m2}$ in deference to the "first" metastable having a 4-s half-life lying at lower energy ($^{178}\text{Hf}^{m1}$). The initial step of the spontaneous decay of the 31-year isomer occurs primarily by a 12.7-keV transition to the 13^+ member of the $K = 8$ band, requiring an electric octupole transition (E3, where $\ell = 3$). Since $K = 16$ for $^{178}\text{Hf}^{m2}$, the transition is characterized by a 5-fold degree of K forbiddenness and $f \approx 100$ [3]. Therefore, a further increase of $(100)^5$ is expected in the Weisskopf estimate for the isomer lifetime [4] of approximately 0.1 s. The predicted lifetime is therefore on the order of 10^9 years, compared with the measured half-life of 31 years [5].

The 31-year isomer of ^{178}Hf provides a nearly ideal high-energy density material that can be produced in the metastable level using cyclotrons or nuclear reactors. However, in order to be useful for applications the triggered release of this energy upon demand must be viable. The most

attractive scenario for triggering would provide a relatively small amount of additional energy by inelastically scattering particles or photons (x rays) [6]. This would serve to *pump* the ^{178}Hf nucleus from the isomer into a higher-lying level. That level could simply be a rotational state built upon the isomer that would decay back to the metastable state. This process would not serve to release the stored energy. Pumping that provides many MeV of excitation energy could release the stored energy by reaching levels at very high energy which might lie among states having values of K intermediate between that of the isomer and ground-state bands. The resulting decay cascade would employ a number of transitions between bands, each providing only a modest ΔK . This would be interesting from a physical standpoint, but not for applications due to the excessive requirements on pump fluence. The preferred mechanism would employ the smallest trigger (pump) energy possible. However, for this to be successful it is necessary that the trigger excite the nucleus from the 31-year isomer to a state which allows transitions having large ΔK without large hindrances.

Experimental studies performed over the past decade indicate that states having this property do occur with some regularity in the region of masses near ^{178}Hf . Full details of these studies may be found elsewhere [6,7]. Systematics were developed from more than 1,200 measurements in which the production of isomers of eighteen nuclides from the corresponding ground states was accomplished by the excitation of intermediate states using x rays. For isotopes having mass numbers near $A = 178$, a particular class of "giant" intermediate states (elsewhere called *giant pumping resonances*) were identified to lie at 2.5 to 2.8 MeV above the ground state. The probability of isomer production through these levels was measured by the *integrated cross section* for the reaction in which a photon was inelastically scattered to excite the

intermediate state. This type of reaction is designated as (γ, γ') where γ represents the incident photon and γ' represents the outgoing (scattered) photon. The appellation "giant" is due to the magnitude of the integrated cross sections measured for the production of isomers, more than 10^4 larger than typical (γ, γ') reactions. Even more important was the demonstration of triggering for the one isomer which was readily available for testing. This was $^{180}\text{Ta}^m$, the only naturally occurring isomer and nature's rarest stable isotope ($^{180}\text{Ta}^m$ has a lifetime in excess of 10^{15} years, while the ^{180}Ta ground state has a half-life of only 8.1 h) [5]. The results obtained for $^{180}\text{Ta}^m$ showed that the release of the 75 keV stored in the $J = 9$ isomer was triggered by x rays having an energy of 2.8 ± 0.1 MeV. Again the integrated cross section was found to belong to the class of giant intermediate states.

The triggering of energy release from one isomer has been experimentally demonstrated and systematics developed for the intermediate states responsible for this and the excitation of isomers for eighteen other isotopes. These systematics indicate that giant intermediate states which permit the production or triggering of high-K isomers in the $A = 178$ region should lie between 2.5 - 2.8 MeV [6,7], although the exact placement may depend somewhat on differences in single-particle structure. Integrated cross sections for such states are on the order of 100 eV-b. The focus for applications on the 31-year isomer of ^{178}Hf reflects these systematics:

- 1) $^{178}\text{Hf}^{m2}$ stores an attractive 2.445 MeV per nucleus, or 1.3 GJ per gram (at solid densities and 100% inversion)
- 2) $^{178}\text{Hf}^{m2}$ has a half-life of 31 years unless triggered.
- 3) $^{178}\text{Hf}^{m2}$ lies falls the mass range wherein giant intermediate states have been found:

- a) $^{178}\text{Hf}^{\text{m}2}$ should lie no more than about 300 keV below the likely position of a giant intermediate state.
- b) $^{178}\text{Hf}^{\text{m}2}$ should be triggered with an integrated cross section that is comparable to that observed for the triggering of ^{180}Ta .

CRITICAL ISSUES

General

A number of questions remain to be answered prior to a complete evaluation of the potential of $^{178}\text{Hf}^{\text{m}2}$ for applications. These include:

- 1) Demonstration of triggering
 - a) Measurement of energy needed to trigger with photons or particles.
 - b) Measurement of integrated cross section for trigger process.
- 2) Determination of output gamma cascades and matching of these with applications.
- 3) Development of a theoretical understanding of the mechanism which permits triggering (and production) of isomers despite large ΔK .

The answers to questions 1a) and 1b) rely entirely upon experiments and these are currently underway as part of a collaboration between the University of Texas at Dallas, Youngstown State University, the Joint Institute for Nuclear Research, Dubna, Russia, and the Center for Nuclear and Mass Spectroscopy, University of Orsay, France. A preliminary experiment was conducted in March, 1996 using alpha particles from the tandem accelerator at Orsay incident upon a sample containing $^{178}\text{Hf}^{\text{m}2}$ produced in Dubna. Data analysis is ongoing, but real-time spectra are consistent with successful triggering. A further round of experiments to employ inelastic proton scattering is planned for December, 1996.

Output Spectrum

A determination of the output spectrum of gamma rays produced by triggering also depends on the results of experiments. A choice of output may be possible if more than one intermediate state is found which permits triggering with different energies. A full evaluation is not possible at this time, but the adopted nuclear data allows consideration of the various known gamma cascades which would likely result from an excitation of $^{178}\text{Hf}^{\text{m}2}$ to an intermediate state lying about 300 keV higher in energy. A selection of these decay cascades are listed in Table I along with that resulting from the spontaneous decay of the 31-year isomer. Although it is unknown which cascades may be populated by triggering of $^{178}\text{Hf}^{\text{m}2}$, several are quite attractive. Many of the component transitions shown are very short lived (< 1 ns). However, the output spectrum which begins with production of the $J^\pi, K^\pi = 14^-, ?$ level at 2.573 MeV ($T_{1/2} = 68 \mu\text{s}$) would be well matched to the temporal characteristics of typical pulsed-power machines which might be used for triggering. Likewise, production of the $J^\pi, K^\pi = 11^+, 6^+$ state at 2.700 MeV would initially lead through a fast cascade to the $K^\pi = 6^+$ bandhead at 1.553 MeV which has a half-life of 77.5 ns. These cascades might well prove useful for applications in which a short-duration flash of gamma rays was desired. In addition to the temporal features this output spectrum contains penetrating 1-MeV gamma rays with high intensity.

Other applications might benefit from gamma rays of lower energy (100's of keV) emitted over a period of several seconds. This occurs in any triggered cascade which leads to the production of the 4-s isomer at 1.147 MeV. Cascades include those beginning with the 68- μs level at 2.573 MeV, the level at 2.700 MeV, the level at 2.485 MeV, and the level at 2.749 MeV.

Table I. Listing of output transitions accessible by a trigger of about 300 keV or less [5]. Unplaced levels and transitions are not included here. Intensities are per decay of the initial state in the cascade. The $2^+ \gamma$ refers to the $K = 2$ gamma vibrational band.

Level energy [keV]	Half-life	Transition ($J^\pi, K^\pi \rightarrow J^\pi, K^\pi$)	Gamma energy [keV]	Gamma intensity [%]		Level energy [keV]	Half-life	Transition ($J^\pi, K^\pi \rightarrow J^\pi, K^\pi$)	Gamma energy [keV]	Gamma intensity [%]
--------------------	-----------	--	--------------------	---------------------	--	--------------------	-----------	--	--------------------	---------------------

Spontaneous decay				
2,445	31 y	$16^+, 16^+ \rightarrow 13^-, 8^-$	12.7	0 (conv.)
2443		$13^-, 8^- \rightarrow 12^-, 8^-$	296.8	9.9
		$13^-, 8^- \rightarrow 11^-, 8^-$	574.2	90.1
		$12^-, 8^- \rightarrow 11^-, 8^-$	277.4	1.3
2136		$12^-, 8^- \rightarrow 10^-, 8^-$	535.0	8.6
		$11^-, 8^- \rightarrow 10^-, 8^-$	257.6	17.4
		$11^-, 8^- \rightarrow 9^-, 8^-$	495.0	74.0
1601		$10^-, 8^- \rightarrow 9^-, 8^-$	237.4	9.3
		$10^-, 8^- \rightarrow 8^-, 8^-$	454.1	16.7
		$9^-, 8^- \rightarrow 8^-, 8^-$	216.7	83.3
1147	4 s	$8^-, 8^- \rightarrow 8^+, 0^+$	88.9	66.7
1058	2.8 ps	$8^+, 0^+ \rightarrow 6^+, 0^+$	426.4	97.1
631	11.2 ps	$6^+, 0^+ \rightarrow 4^+, 0^+$	325.6	64.3
306		$4^+, 0^+ \rightarrow 2^+, 0^+$	213.4	81.3
93	1.5 ns	$2^+, 0^+ \rightarrow 0^+, 0^+$	93.2	17.4

2700		$11^+, 6^+ \rightarrow 10^+, 6^+$	266.6	42.5
		$11^+, 6^+ \rightarrow 9^+, 6^+$	517.1	57.5
		$10^+, 6^+ \rightarrow 9^+, 6^+$	250.6	20.3
2434		$10^+, 6^+ \rightarrow 8^+, 6^+$	481.6	22.3
		$9^+, 6^+ \rightarrow 8^+, 6^+$	231.4	46.6
		$9^+, 6^+ \rightarrow 7^+, 6^+$	441.8	31.2
1952		$8^+, 6^+ \rightarrow 7^+, 6^+$	210.3	68.8
1741		$7^+, 6^+ \rightarrow 6^+, 6^+$	187.7	100
1553	77.5 ns	$6^+, 6^+ \rightarrow 4^+, 2^+ \gamma$	169.5	4.4
		$6^+, 6^+ \rightarrow 8^-, 8^-$	406.6	2.4
		$6^+, 6^+ \rightarrow 6^+, 0^+$	921.8	61.5
		$6^+, 6^+ \rightarrow 4^+, 0^+$	1247.4	31.7
		$4^+, 2^+ \gamma \rightarrow 4^+, 0^+$	1077.8	3.0
1384		$4^+, 2^+ \gamma \rightarrow 2^+, 0^+$	1291.3	1.4
1147	See spontaneous decay cascade			
632	See spontaneous decay cascade			
307	See spontaneous decay cascade			
94	See spontaneous decay cascade			

2778	33 ps	$14^+, 0^+ \rightarrow 12^+, 0^+$	626.9	100
2151	0.6 ps	$12^+, 0^+ \rightarrow 10^+, 0^+$	579.7	100
1572	1.0 ps	$10^+, 0^+ \rightarrow 8^+, 0^+$	512.4	100
1059	See spontaneous decay cascade			

2573	68 μ s	$14^-, ? \rightarrow 16^-, 16^+$	126.1	0.7
		$14^-, ? \rightarrow ?$	140.3	20.8
		$14^-, ? \rightarrow ?$	437.0	35.6
		$14^-, ? \rightarrow ?$		
2445	See spontaneous decay cascade			

Table I. (Continued).

2485	$12^-, 8^-_2 \rightarrow$	348.5	27.0
	$12^-, 8^-$		
	$12^-, 8^-_2 \rightarrow$ $11^-, 8^-$	626.2	73.0
2137	See spontaneous decay cascade		
1859	See spontaneous decay cascade		

2749	$14^-, 8^- \rightarrow$ $12^-, 8^-$	612.6	100	
2136	See spontaneous decay cascade			

Triggering Mechanism

One of the lingering concerns regarding $^{178}\text{Hf}^{\text{m}2}$ has been the need for low-energy triggering to provide a large ΔK in order to reach the output cascades listed in Table I. For example, in order to initiate the attractive cascade which begins with the 2.700 MeV, $J^\pi, K^\pi = 11^+, 6^+$ state, a change of 10 units of angular momentum projection must occur. A successful low-energy trigger would require excitation to an intermediate state less than about 300 keV above the isomer through a strongly-allowed transition. The structure of the intermediate state then must permit a similarly strong transition to a low-K band and thus such intermediate levels have been referred to as *K-mixing states*. If K remains a good quantum number for the intermediate state, or levels into which it might decay, then the critical transitions (isomer to intermediate, intermediate to output) would be expected to be severely hindered. However, this is in conflict with experiments already discussed [6,7] which demonstrated the triggering of $^{180}\text{Ta}^{\text{m}}$ ($\Delta K = 8$ from isomer to ground-state band) with large integrated cross section, as well as complimentary results for the production of isomers in neighboring nuclides.

A number of experimental studies have been performed which point to the existence of K mixing in the spontaneous decay of rare-earth isomers. These are listed in Table II. The initial transitions from the isomers vary considerably in terms of intensity and provide ΔK ranging from

Table II. Isomers experimentally shown to spontaneously decay through large ΔK transitions with measurable intensity. Intensities are per isomer decay.

Nuclide	Isomer			Decay target			Comments	References
	Energy [MeV]	$J^\pi (K^\pi)$	$T_{1/2}$	Energy [MeV]	$J^\pi (K^\pi)$	Intensity [%]		
^{172}Hf	3.319	$12^-(12^-)$		2.064	$12^+(0^+)$	24	Only one decay branch from the isomer observed	9,10
^{174}Hf	3.312	$14^+(14^+)$	$3.7 \mu\text{s}$	2.685	$12^+(?)$	0.7	Other transitions known - 1.1% directly to ground-state band	11,12,13
^{175}Hf	3.016	$35/2^- (35/2^-)$	$1 \mu\text{s}$	2.941	$33/2^- (5/2^-)$	0.05	Other transitions known - 28.4% to states with $\Delta K = 5$	13
^{176}W	3.746	$14^+(14^+)$	35 ns	2.801	$14^+(0^+)$	10	Other transitions known - over 50% to ground-state band	3,14,15
^{179}W	3.349	$35/2^- (35/2^-)$	750 ns	2.738	$31/2^- (23/2^-)$	82	Other transitions known - 95% to states with $\Delta K = 6 - 12$	8,16

6 to 15. Two of the most striking results are the decays of the isomers of ^{172}Hf (3.319 MeV, $K^\pi = 12^-$) and ^{179}W (3.349 MeV, $K^\pi = 35/2^-$), which occur with intensities of 24% and 82% through $\Delta K = 12$ and 6, respectively. These intensities should be unmeasurable in the conventional model which would characterize these transitions as being strongly K forbidden. Yet the transitions provide large ΔK with high probability and populate levels (labeled as "target" in Table II) at 2.064 MeV and 2.738 MeV, respectively. It is instructive to compare these level energies with that which triggers $^{180}\text{Ta}^m$ at $2.8 \pm 0.1 \text{ MeV}$ and those which populate isomers at

2.5 - 2.8 MeV. The spontaneous decay of the other short-lived isomers listed in Table II also exhibit initial transitions providing large ΔK , but with much smaller, albeit measurable intensities. The target-state energies for these transitions are 2.685 MeV, 2.941 MeV and 2.801 MeV.

The experimental results of Table II support the suggestion [7] that the relatively short lifetimes seen there are due to the fact that K-mixing intermediate states occur at energies between 2.5 - 2.8 MeV, lower than the isomers. In the case of ^{180}Ta the isomer lies well below the K-mixing intermediate level and therefore additional energy is required to trigger a non-spontaneous decay cascade. Likewise, it can be expected that $^{178}\text{Hf}^{\text{m}2}$ lies below a K-mixing level, although much closer due to the isomer's 2.445 MeV energy.

Two models have been proposed in order to explain the magnitude of K mixing required for the spontaneous decays of Table II. The first model [8] mixes high- and low-K components into the wavefunction of target states via Coriolis forces (the wavefunctions of isomers are relatively pure). This occurs in the vicinity of band crossings, typically near $J = 12$. The model has been used with considerable success to explain the anomalous $\Delta K = 6$ decay of the 750-ns isomer of ^{179}W . Coriolis mixing with a fixed nuclear shape was calculated using the cranking model by "tilting" the cranking axis. A new *t band* of states was generated which included the 2.738-MeV target level. That intermediate state was shown to be of mixed-K composition, being approximately 50% $K^\pi = 23/2^-$ and 50% $K^\pi = 7/2^-$. The spontaneous decay of the isomer to the high-K component of the target wavefunction can therefore be considered as obeying the usual K selection rule, but with a greatly reduced *effective* degree of K forbiddenness.

The second model [3] considers K mixing as being the result of collective, large-amplitude fluctuations of nuclear shape which destroy its axial symmetry. Axial symmetry is lost when a

triaxial shape occurs, quantified by the *triaxiality parameter* γ . A value of $\gamma = 0^\circ$ corresponds to a prolate shape with axial symmetry, giving deformation-aligned states like K isomers. An identical shape is arrived at by an irrotational change to $\gamma = -120^\circ$, but then $K = 0$ (rotation-aligned). At $\gamma = -60^\circ$ the nucleus is oblate and intermediate values of γ reflect a triaxial shape. In this model K-mixing transitions from an isomer to yrast states is interpreted as being caused by tunneling through a potential barrier parametrized by the γ degree of freedom. The γ -tunneling model has shown initial success in understanding spontaneous isomer decays in ^{174}Hf and ^{176}W . Coriolis mixing is also important in the former case, but does not contribute significantly for ^{176}W . A final resolution of the mechanism responsible for K-mixing transitions is not presently available, but detailed studies for individual nuclides as well as examinations of systematics are underway [13,17,18]. It is worth noting that the subject of high-K isomers and K mixing has already reached sufficient maturity to have gained the attention of non-specialists [19].

SUMMARY

A number of important questions remain to be answered before the potential of $^{178}\text{Hf}^{m2}$ can be fully examined. Direct investigations are underway or planned which will determine the existence and properties of a K-mixing trigger level which releases the energy stored in the isomer. Theoretical models are being developed which show promise in understanding the mechanisms through which K mixing transitions can occur with large probabilities. Systematics indicate that $^{178}\text{Hf}^{m2}$ can be triggered with relatively low-energy photons and with significant probability. Still, even if "giant" integrated cross sections for K-mixing states are found, further enhancements in triggering efficiency may be needed. A study along these lines is currently being planned [20]. At present, $^{178}\text{Hf}^{m2}$ remains high risk due to the absence of definitive answers to the

critical issues. However, the high payoff inherent in this high-energy density material as a non-fission or fusion radiation source, along with the interesting physics, continue to motivate examination.

REFERENCES

1. *Nuclear Models*, W. Greiner and J. A. Maruhn (Springer, New York, 1995).
2. *Theoretical Nuclear Physics, Volume 1: Nuclear Structure*, A. deShalit and H. Feshback (Wiley, New York, 1990) p. 702.
3. B. Crowell, P. Chowdhury, D. J. Blumenthal, S. J. Freeman, C. J. Lister, M. P. Carpenter, R. G. Henry, R. V. F. Janssens, T. L. Khoo, T. Lauritsen, Y. Liang, F. Soramel and I. G. Bearden, *Phys. Rev. C* **53**, 1173 (1996).
4. R. G. Helmer and C. W. Reich, *Nucl. Phys.* **A211**, 1 (1973).
5. *National Nuclear Data Center Online Evaluated Nuclear Structure Data File (ENSDF)*, Brookhaven National Laboratory, 1996.
6. C. B. Collins and J. J. Carroll, *Laser Phys.* **5**, 209 (1995) and references cited therein.
7. C. B. Collins, J. J. Carroll, Yu. Ts. Oganessian and S. A. Karamian, *Laser Phys.* **5**, 280 (1995) and references cited therein.
8. P. M. Walker, G. D. Dracoulis, A. P. Byrne, B. Fabricius, T. Kibédi, A. E. Stuchbery and N. Rowley, *Nucl. Phys.* **A568**, 397 (1994).
9. P. M. Walker, G. D. Dracoulis, A. P. Byrne, T. Kibédi and A. E. Stuchbery, *Phys. Rev. C* **49**, 1718 (1994).
10. D. M. Cullen, C. Baktash, M. J. Fitch, I. Frosch, R. W. Gray, N. R. Johnson, I. Y. Lee, A. O. Macchiavelli, W. Reviol, X.-H. Wang and C.-H. Yu, *Phys. Rev. C* **52**, 2415 (1995).

11. P. M. Walker, G. Sletten, N. L. Gjørup, M. A. Bentley, J. Borggreen, B. Fabricius, A. Holm, D. Howe, J. Pedersen, J. W. Roberts and J. F. Sharpey-Schafer, *Phys. Rev. Lett.* **65**, 416 (1990).
12. G. Sletten, N. L. Gjørup, S. Juutinen, A. Maj, J. Nyberg, P. M. Walker, D. M. Cullen, P. Fallon, A. N. James, J. F. Sharpey-Schafer, M. A. Bentley, A. M. Bruce and B. J. Varley, *Nucl. Phys.* **A520**, 325 (1990).
13. N. L. Gjørup, P. M. Walker, G. Sletten, M. A. Bentley, B. Fabricius and J. F. Sharpey-Schafer, *Nucl. Phys.* **A582**, 369 (1995).
14. B. Crowell, P. Chowdhury, S. J. Freeman, C. J. Lister, M. P. Carpenter, R. G. Henry, R. V. F. Janssens, T. L. Khoo, T. Lauritsen, Y. Liang, F. Soramel and I. G. Bearden, *Phys. Rev. Lett.* **72**, 1164 (1994).
15. P. M. Walker and G. D. Dracoulis, *Phys. Rev. Lett.* **72**, 3736 (1994).
16. F. Bernthal, B. B. Back, O. Bakander, J. Borggreen, J. Pedersen, G. Sletten, H. Beuscher, D. Haenni and R. Lieder, *Phys. Lett.* **74B**, 211 (1978).
17. P. M. Walker, *J. Phys. G: Nucl. Part. Phys.* **16**, 233 (1990).
18. G. D. Dracoulis, F. G. Kondev, A. P. Byrne, T. Kibédi, S. Bayer, P. M. Davidson, P. M. Walker, C. Purry and C. J. Pearson, *Phys. Rev. C* **53**, 1205 (1996).
19. P. M. Walker and G. D. Dracoulis, *Phys. World*, February, 1994.
20. J. J. Carroll, Summer Extension Research Program (SERP) proposal (in preparation).

**A STUDY ON HARTMANN SENSOR APPLICATION
TO
FLOW AERO-OPTICS INVESTIGATION THROUGH TOMOGRAPHIC
RECONSTRUCTION**

**Soyoung Stephen Cha
Associate Professor
Department of Mechanical Engineering**

**University of Illinois at Chicago
2039 ERF, 842 West Taylor Street
Chicago, IL 60607-7022**

**Final Report for:
Summer Research Faculty Program
Phillips Laboratory**

**Sponsored by:
Air Force of Scientific Research
Bolling Air Force Base, DC**

and

Phillips Laboratory

August 1996

A STUDY ON HARTMANN SENSOR APPLICATION
TO
FLOW AERO-OPTICS INVESTIGATION THROUGH TOMOGRAPHIC
RECONSTRUCTION

Soyoung Stephen Cha
Associate Professor
Department of Mechanical Engineering
University of Illinois at Chicago

Abstract

The aero-optics research group of the Lasers and Imaging Directorate at Phillips Laboratory conducts tomographic reconstruction for imaging three-dimensional flow fields by employing the Hartmann sensor. The system based on Hartmann sensors can provide rapid sampling of two-dimensional projections of a field, that is, real-time capability in data acquisition. However, it provides integrated gradient-data along the optical paths of probing rays. The current practice of reconstruction has depended on an existing computational tomographic technique that utilizes integrated optical pathlength data. During this summer research, the investigator analyzed the currently employed software for reconstruction, formulated a new tomographic reconstruction algorithm, and provide a strategy for assimilating these two techniques into a single package. He also investigated a strategy and conducted concurrent analysis for achieving a long-term goal of utilizing a currently-available wind-tunnel facility, that is, Turbulent Boundary Layer Generator, for aero-optics research. This can be accomplished by tomographically reconstructing flow fields with the Hartmann sensor.

A STUDY ON HARTMANN SENSOR APPLICATION TO FLOW AERO-OPTICS INVESTIGATION THROUGH TOMOGRAPHIC RECONSTRUCTION

Soyoung Stephen Cha

1. Introduction

Optical tomography can be of great value, especially in flow field imaging in aero-dynamics or aero-optics. It provides merits in its noninvasiveness, instantaneous capture of gross-fields, measurement accuracy, and spatial resolution as compared with conventional techniques. However, practical application of the technique to the flow testing facilities at various Air Force laboratories requires that pertinent application problems be thoroughly examined.

Currently, the aero-optics research group of the Lasers and Imaging Directorate at Phillips Laboratory conducts tomographic reconstruction for imaging three-dimensional (3-D) flow fields by employing the Hartmann sensor. The Hartmann system allows rapid sampling of two-dimensional projections of a field to be measured and thus continuous real-time data acquisition of fast transient phenomena. The Hartmann sensor, however, provides integrated gradient-data of refractive-index along an optical ray unlike integrated optical pathlength data in interferometric tomography.

The optical tomographic system, which is currently utilized at Phillips Laboratory, consists of two parts: that is, the Hartmann-sensor hardware for obtaining gradient projection data of flow fields and computational software for reconstructing the fields from projections. During the short summer research program, the principal investigator (PI) (Professor S. S. Cha) has carefully examined the structure of this tomographic system to accomplish the following objectives. Firstly, he devised a new approach that allows flow-field reconstruction with the gradient projection data that can be directly obtained from the Hartmann sensor. It is thus unlike the present practice that resorts to an additional data

processing of integration for obtaining optical pathlength data. He then formulated a strategy for assimilating the newly developed algorithm into the existing software with minimal modification to form a convenient versatile single package. Secondly, Phillips laboratory has an available facility named Turbulent Boundary Layer Generator (TBLG) [1]. This wind tunnel was designed to investigate the aero-optical effects of turbulent boundary layers. One of the objectives of the summer research was to investigate the feasibility of using the facility for a long-term goal: that is, tomographic image reconstruction of the boundary layer flows generated by the wind tunnel with the Hartmann sensor for aero-optics research of image aberration. To achieve this long-term goal, the PI formulated a strategy in developing both hardware and software, proposed a preliminary hardware concept and design to accommodate the peculiar facility configuration, and conducted pertinent theoretical analyses to approximately extract design parameters and thus to draw important conclusions for reasonably assessing confidence in the effort.

The brief summary of the investigation results by the PI, including approaches, methodology, and analyses are summarized hereafter: that is, Section 2 for the first objective of computational reconstruction from gradient projection data; and Section 3 for the second objective of utilization of the TBLG wind tunnel.

2. Tomographic Reconstruction from Gradient Data

One approach of computational tomographic reconstruction from projection data is to approximate the field $f(x,y)$ to be reconstructed with a finite series.

$$f(x,y) = \sum_i^M \sum_j^N C_{ij} b_{ij}(x,y) \quad (1)$$

where b_{ij} and C_{ij} are an expansion term (basis function) and the corresponding coefficient, respectively. The tomographic projection (line-integral transform or two-dimensional (2-D) Radon transform) is then

$$p(\rho, \theta) = \sum_i^M \sum_j^N C_{ij} a_{ij}(\rho, \theta) \quad (2)$$

where a_{ij} , θ , and ρ are the Radon transform of b_{ij} , projection angle, and distance of a data point from the optical axis, respectively. In a series expansion method, the coefficients C_{ij} can be determined by setting up linear algebraic equations with measurement data $p(\rho, \theta)$ once the series pairs of b_{ij} and a_{ij} are determined. Many techniques are available for solving linear algebraic equations, including algebraic reconstruction technique (ART), maximum likelihood estimation, maximum entropy method, least square method, conjugate gradient method, etc.

In series expansion, the basis functions can be either local or nonlocal. The individual terms of nonlocal basis functions differ from each other while sharing the same entire domain of definition. They thus limit the number of terms to be employed and are inconvenient to use. Unless a special means as in a curvilinear method [2] is provided, they are defined in a common circle enclosing the flow region. That is, it is difficult to conform to the boundary shape and inefficiency arises for expanding the non-flow region into a series if the flow is non-circular. On the contrary, the approach of local basis functions (LBFs) employs locally-defined functions of the same functional representation except for displacements of individual terms for repetition throughout the field to be reconstructed. It is thus very adaptable to boundary shapes and easy to use, consisting of repeating LBFs that occupy a small region. The fixed grid method (FGM) that is currently employed at Phillips Laboratory is an example of LBF methods. However, since it approximates a field with discontinuous LBFs of constant value, it cannot provide gradient values for direct application to the data from the Hartmann sensor. Thus the methods based on continuous LBFs are recommended.

The continuous LBFs formulated for gradient-data reconstruction during the summer research can be represented by Eq. (3).

$$b_{ij}(x, y) = b(r_{ij}) = \begin{cases} 1 - 2\left(\frac{r_{ij}}{R}\right)^2 + \left(\frac{r_{ij}}{R}\right)^4 & \text{for } r_{ij} \leq R \\ 0 & \text{for } r_{ij} > R \end{cases} \quad (3)$$

$$\text{where } r_{ij} = \left\{ [x - (i-1)\Delta l]^2 + [y - (j-1)\Delta l]^2 \right\}^{1/2}.$$

r_{ij} is the distance from the local coordinate origin at the center of a LBF as demonstrated in Fig. 1.

Since it is circularly symmetric, it lends itself easily to analytical expressions for projections of both optical pathlength and gradient data as explained below. Without respect to the projection angle, the gradients of all LBFs normal to any projection become

$$b_{ij}^g(x, y) = b^g(r_{ij}) = -\frac{4}{R}\left(\frac{r_{ij}}{R}\right) + \frac{4}{R}\left(\frac{r_{ij}}{R}\right)^3 \quad (4)$$

If we find the projections (Radon transform) of Eq. (3),

$$a_{ij}(\rho, \theta) = a(\rho_{ij}) = \begin{cases} \frac{16}{15} \sqrt{R^2 - (\rho_{ij})^2} \left[1 - 2\left(\frac{\rho_{ij}}{R}\right) + \left(\frac{\rho_{ij}}{R}\right)^4 \right] & \text{for } \rho_{ij} \leq R \\ 0 & \text{for } \rho_{ij} > R \end{cases} \quad (5)$$

$$\text{where } \rho_{ij} = \rho + \left[(i-1)^2 \Delta l^2 + (j-1)^2 \Delta l^2 \right]^{1/2} \sin(\theta - \alpha) \text{ and}$$

$$\alpha = \tan^{-1}[(j-1)/(i-1)].$$

ρ_{ij} is the distance of a probing ray from the local coordinate origin and α is the angle to the local coordinate origin, as shown in Fig. 1. Similarly to Eq. (5), the projection of the gradient of a LBF, Eq. (4), becomes

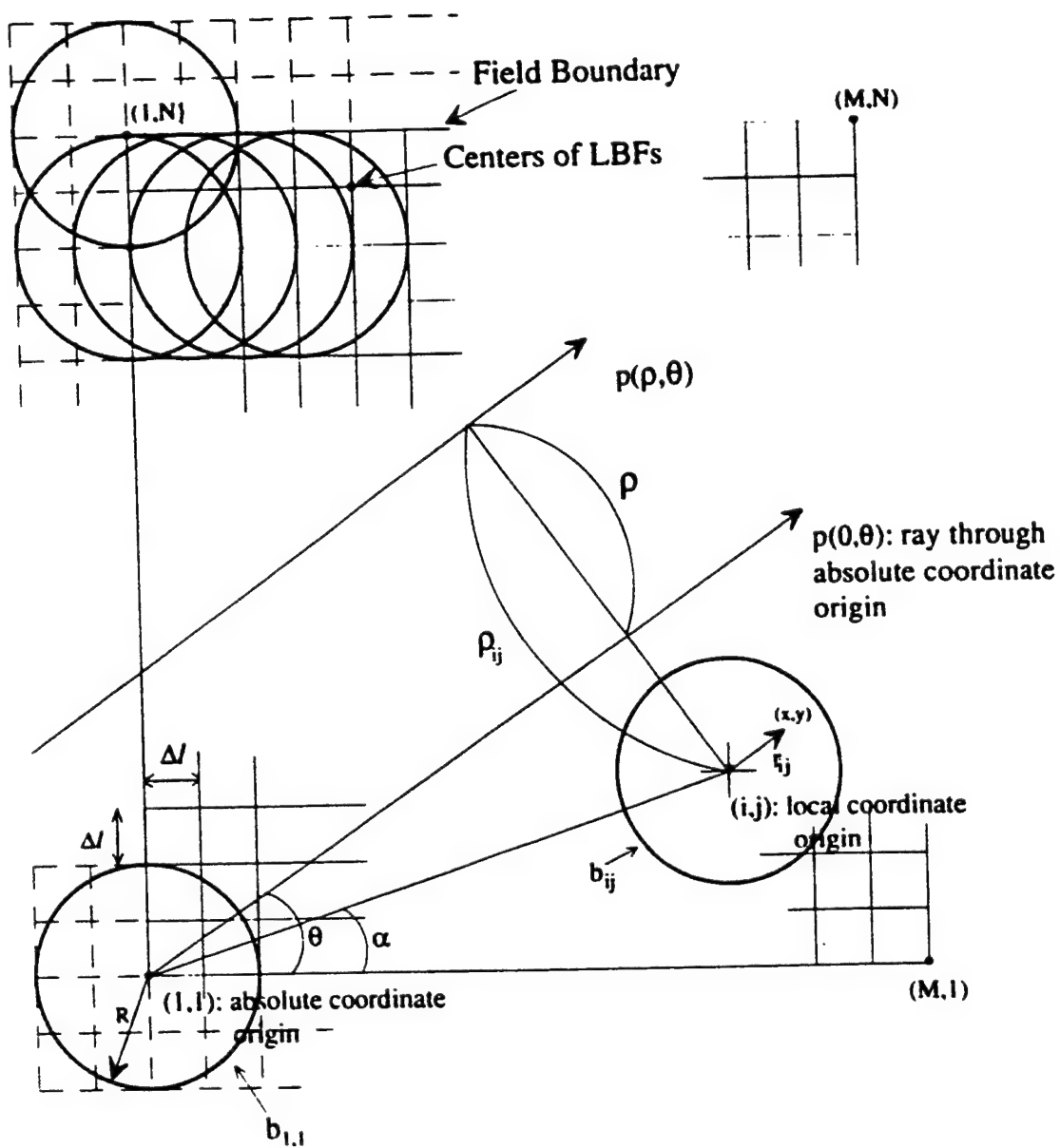


Figure 1. Coordinate systems and nomenclature for the LBF series expansion.

$$a_{ij}^{\varepsilon}(\rho, \theta) = a^{\varepsilon}(\rho_{ij}) = \begin{cases} -\frac{16}{3} \frac{\rho_{ij}}{R} \left[1 - \left(\frac{\rho_{ij}}{R} \right)^2 \right]^{3/2} & \text{for } \rho_{ij} \leq R \\ 0 & \text{for } \rho_{ij} > R \end{cases} \quad (6)$$

The counterpart of Eq.(2) then becomes

$$p^{\varepsilon}(\rho, \theta) = \sum_i^M \sum_j^N C_{ij} a_{ij}^{\varepsilon}(\rho, \theta) \quad (7)$$

where $p^{\varepsilon}(\rho, \theta)$ is the integrated gradient data from the Hartmann sensor. As usual, we can determine c_{ij} by setting up linear algebraic equations (7) with measurement data and solving them. The field can then be reconstructed by Eq. (1) with Eq. (3).

In addition to the LBF of Eq.(3), it is also possible to employ other polynomial functional forms of different order. An example can be

$$b_{ij}(x, y) = b(r_{ij}) = \begin{cases} 1 - 3 \left(\frac{r_{ij}}{R} \right)^2 + 2 \left(\frac{r_{ij}}{R} \right)^3 & \text{for } r_{ij} \leq R \\ 0 & \text{for } r_{ij} > R \end{cases} \quad (8)$$

Detailed discussions of local and nonlocal basis functions and corresponding transform pairs can also be found in References 3 and 4.

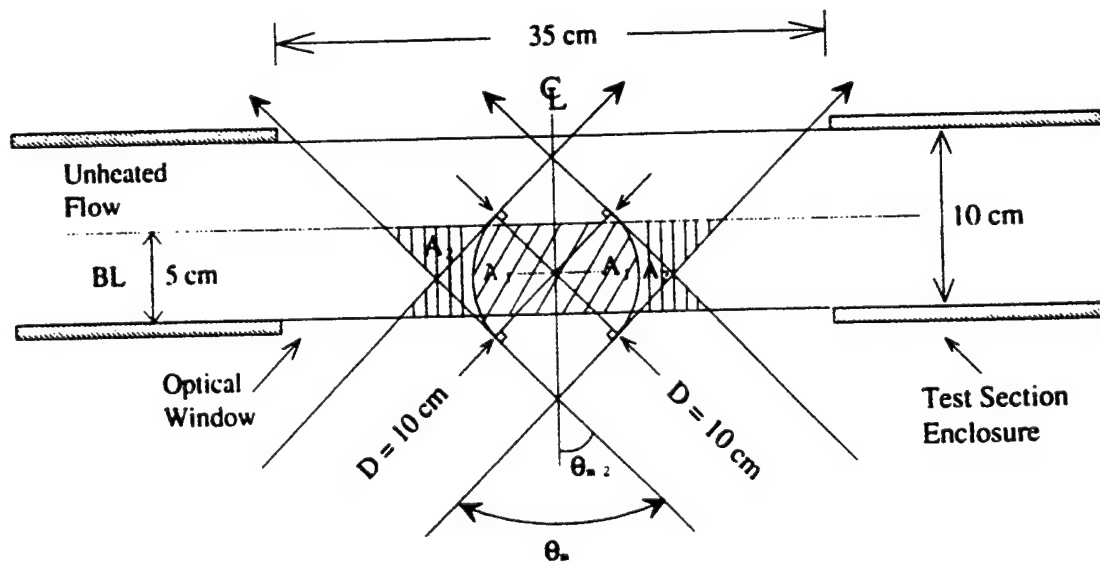
The LBF approach has the merits over those based on nonlocal basis functions as previously mentioned. In addition, as seen, it can also provide analytical expressions of transform pairs in series expansion of gradient fields. This is not possible with nonlocal basis functions. Hence, the formulated method presented here is advantageous in using both optical pathlength data as from multidirectional interferometry and integrated gradient data as from Hartmann sensor. Since all series expansion methods differ only in setting up Eq. (2) with measurement data, the formulated LBF method can be easily incorporated into the

tomographic reconstruction software at Phillips Laboratory. The detailed schemes of software modification for the LBF incorporation are discussed in References 5-9.

3. Tomographic Flow Reconstruction of Turbulent Boundary Layer Generator (TBLG)

Tomographic reconstruction of turbulent flow boundary layers (BLs) generated by the TBLG with the Hartmann sensor poses some challenges due to the peculiar testing configurations and operating environments that produce ill-posed projection data and reconstruction fields.

Figure 2 shows the test section dimensions of the TBLG where the BL of 5 cm thickness and field scanning aperture of 10 cm diameter are assumed for a typical operation for the analyses in this section. As easily noticed in Fig. 2, the issues to be raised and answered in reconstruction can be as follows. First, the flow field is much larger than a typical Hartmann sensor of 2.8 cm in diameter. That is, we need to expand the field scanning aperture as larger as possible from the direct scanning that results in the size of the Hartmann sensor. The aperture diameter of 10 cm as assumed can practically be an approximate limit. If so, an appropriate means for expansion needs to be devised. Second, the finite window and the enclosure prohibit complete angular scanning and additionally, the BL continually extends beyond both ends of the test section. Only part of the long flow strip can thus be scanned as indicated by areas A_1 and A_2 in Fig. 2. This raises a reconstruction problem from a limited-aperture limited-data set. The question is then how much reconstruction accuracy is expected and what computational reconstructor can be employed. Third, since the BL is generated with a heated wall, the optical window at the test section is heated and expected to contribute to the refractive-index change outside the flow field. It also generates a hot plume of natural convection along the optical window. The degree of these disturbances needs to be estimated to assess their effects on the flow field reconstruction and a special means may thus be required for minimizing these effects. The summary for addressing the aforementioned issues is presented hereafter.



Symbols: A_1 = area with maximum scanning θ_m D = aperture diameter in field scanning
 A_2 = area with angular scanning $< \theta_m$ θ_m = maximum scanning angle
 BL = boundary layer

Figure 2. Schematic of the TGLB test section and BL area scanned by the Hartmann sensor.

3.1 Proposed Optical System for Capturing Large-Field Projections with Small Hartmann Sensors

The current tomographic field-projection system uses collimated beams for obtaining projections with Hartmann sensors. If so, many large-diameter beam collimators and collectors are required for obtaining large-field projections. This approach is impractical, resulting in an expensive and bulky setup. Figure 3 shows a schematic of a proposed system. The holographic element can produce many converging cone-beams, which can be filtered and collimated for imaging on Hartmann sensors. The collectors (collimators), being small, are inexpensive and the system can be compact. Even though it is a fan-beam arrangement, the collected data can be equivalent to those shown in Fig. 2 if they are sorted for parallel rays.

3.2 Effects of Limited Aperture and Limited Data on Reconstruction and Computational Reconstruction Scheme

3.2.1 Estimation of error Propagation

Reconstruction errors in optical tomography depend on various factors; that is, noise in data, scanning angle, number of projections and number of data points per projection, computational reconstructor employed, field shape, etc. It is thus difficult to assess reconstruction errors unless a realistic simulation is conducted for actual experimental hardware and computational software. Here, crude estimation results of reconstruction errors due to the long-strip flow, or equivalently due to the limited aperture, are presented by adopting a rather terse approach based on hand calculation. Details of calculation can be found in Reference 10.

The reconstruction operation is near-linear and hence the flow reconstruction can be considered to be equivalent to the combination of two reconstructions of areas A_1 and A_2 . Previous investigations [11-12] indicate that angular scanning up to 60° can produce

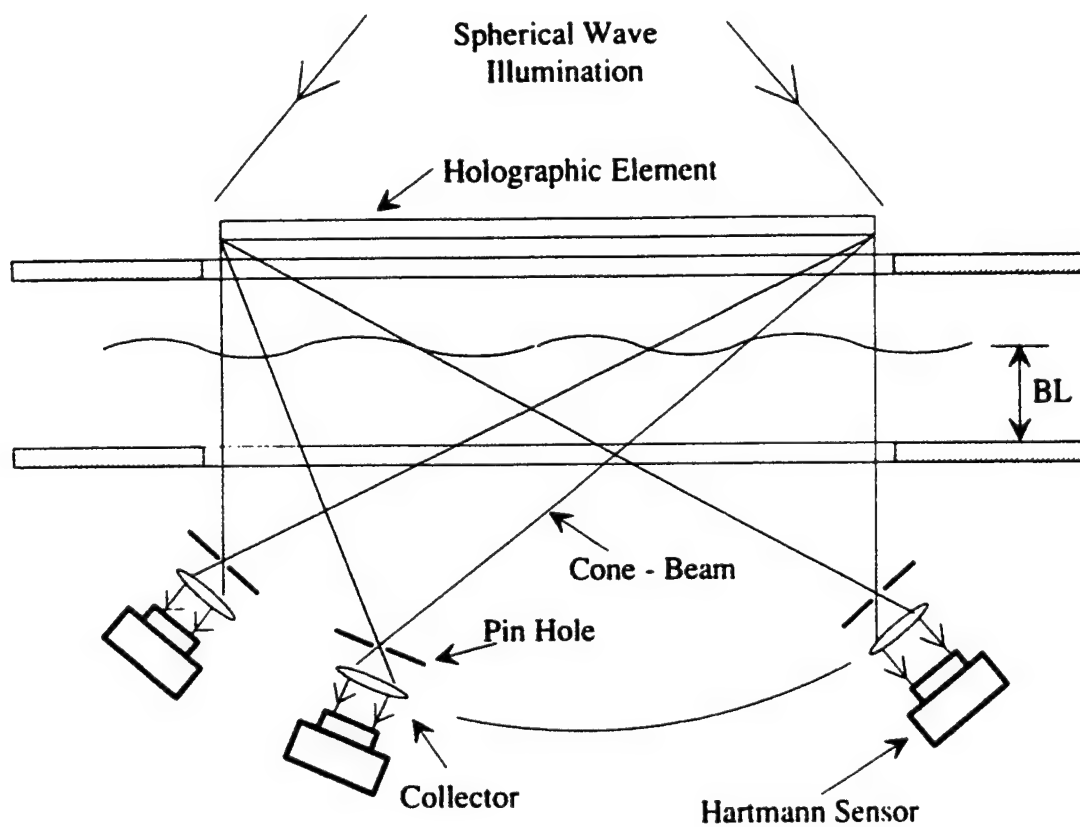


Figure 3. Proposed tomographic field-projection system with Hartmann sensors.

reasonable reconstruction accuracy when the entire field is contained in the scanning aperture and an appropriate computational reconstructor is chosen. Area A_1 in Fig. 2 can be scanned with $\theta_m=100^\circ$ and can thus be reconstructed with good accuracy by using a proper reconstructor.

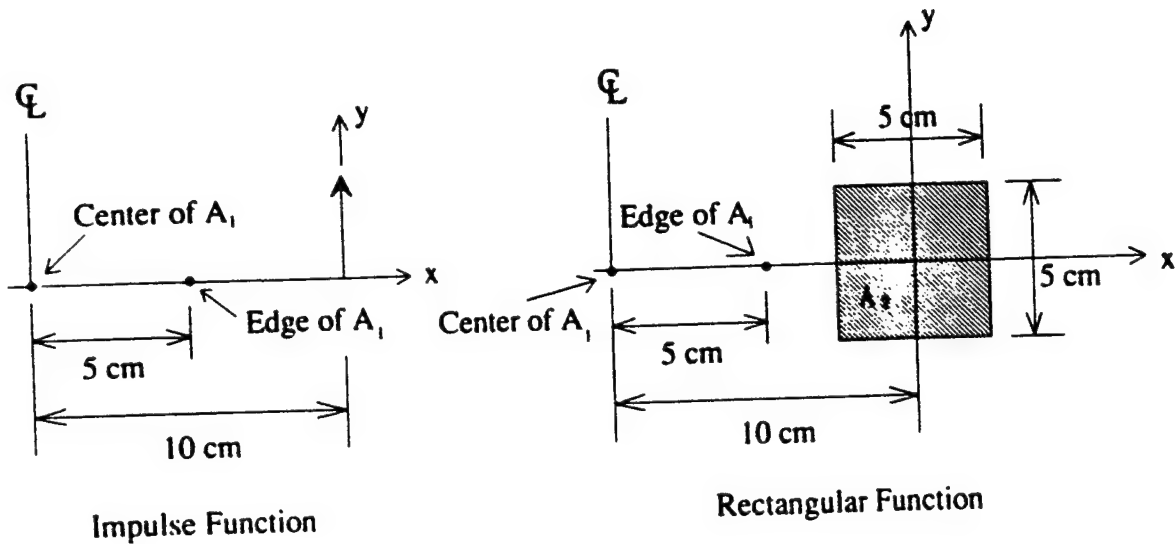
The long-strip field mandates a limited aperture and thus a limited scanning angle. The scanning angle of area A_2 varies from zero to the maximum θ_m with average $\theta_a=\theta_m/2$. We expect that the reconstruction of this area becomes inaccurate and its effect propagates into the center region of area A_1 of our interest. It is difficult to analytically assess the error propagation of a specific reconstructor except for the Fourier Transform method (FTM) [13,14]. The FTM requires complete data with the full scanning angle of 180° . For analyses, we choose the FTM; however, the following assumptions are made for simple assessment.

(1) Area A_2 is scanned with a half of the scanning angle θ_m of Area A_1 for which proper selection of a reconstructor yields good accuracy. The reconstruction error propagation of area A_2 can be approximated by that of FTM with the area scanned by a half of the scanning angle of 180° for which FTM yields good accuracy.

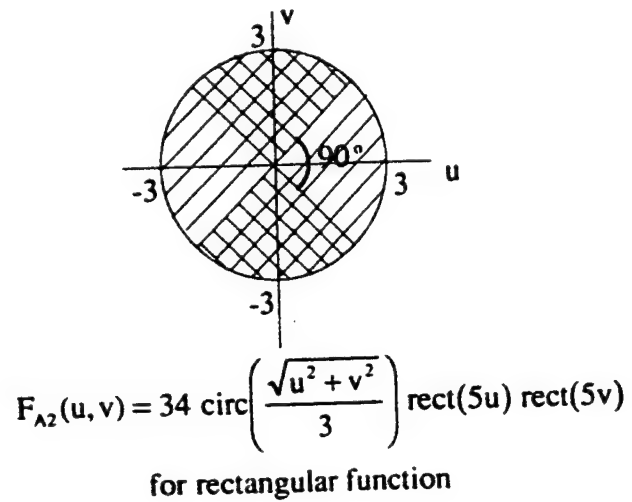
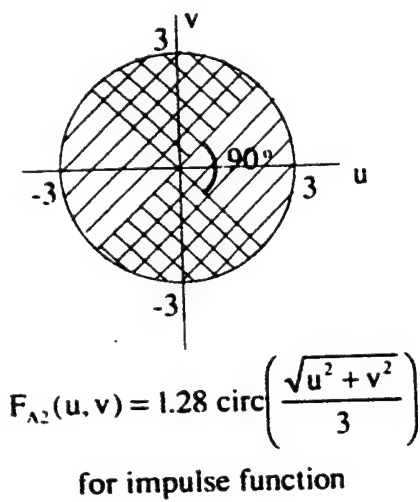
(2) 60 lenslets of the Hartmann sensor cover the field-scanning aperture of 10cm in diameter. Hence, its detectable or cutoff spatial frequency M is approximately 3.

(3) Test field f_{A_1} and f_{A_2} to be reconstructed for areas A_1 and A_2 are of uniform unit value.

The energy of f_{A_2} is thus 46.5, which is equal to its area. The local region of A_2 near A_1 has more projection energy and geographical affinity to influence A_1 in error propagation; however, it produces less errors, having a scanning angle close to the maximum value. The region of A_2 far from A_1 has an opposite trend. For this reason, f_{A_2} is further approximated by an impulse function or a rectangular function whose centers are approximately at the centroid of area A_2 as shown in Fig. 4(a). This makes the analysis simple. The composite of one-dimensional Fourier transforms of projections becomes the two-dimensional Fourier transform of the field under full angle scanning [13,14]. The Fourier transforms



(a) approximation of unit field f_{A2} in area A_2



- (b) Fourier transforms of projection data of f_{A2} with the cutoff detection frequency: non-zero in all shaded areas for full angular scanning and non-zero only in double-shaded areas for half angular scanning

Figure 4. Representation of test field f_{A2} and its Fourier transform F_{A2} under the investigating scenarios.

F_{A_2} obtained from measured projection data of these approximating fields are also shown in Fig. 4(b). The Fourier transform energy under full angular scanning is maintained at the same value of 46.5 for both of the fields after cutting off the detection frequency.

(4) Noise has a multiplying effect on the reconstruction as the degree of data ill-posedness increases. However, its effect is not considered here.

Based on the above assumptions, Field f_{A_2} scanned with a limited aperture, which results in restricted angular scanning, can be represented by $F_{A_2}^h(u, v)$ defined only in the shaded area of the Fourier transform domain in Fig. 4(b). If so, the reconstructed field $f_r^h(x, y)$ can be found by inverse Fourier transform.

$$f_r^h(x, y) = F^{-1}\{F_{A_2}^h(u, v)\} \quad (10)$$

The numerical inversion was carried out for both an impulse and rectangular function with the following results at the edge and center of area A_1 .

(1) Impulse Function:

$$(i) \text{ At the edge of area } A_1, f_r^h(-5, 0) = 0.012 \quad (11)$$

The effect of A_2 at the other side is negligible. Hence, the total effect is 1.2% in reconstruction error propagation.

$$(ii) \text{ At the center of Area } A_1, f_r^h(-10, 0) = 0.0023 \quad (12)$$

The effect of A_2 at the other side is the same. Hence, the total effect is 0.46% in reconstruction error propagation.

(2) Rectangular Function

$$(i) \text{ At the edge of area } A_1, f_r^h(-5, 0) = 0.24 \quad (13)$$

The effect of A_2 at the other side is negligible. Hence, the total effect is 24% in reconstruction error propagation.

$$(ii) \text{ At the center of area } A_1, f_r^b(-10,0) = 0.042 \quad (14)$$

The effect of A_2 at the other side is the same. Hence, the total effect is 8.4% in reconstruction error propagation.

Two values of error effects at the edge of A_1 show some difference between the impulse function and rectangular function. Further precise assessment may thus be needed. The values at the center of A_1 are very low. The flow reconstruction near the center can thus be reliable. The FTM employed here for error analysis is not a good reconstructor to be applied under the ill-posed data conditions. The error propagation can be substantially minimized through adoption of other proper reconstructors as indicated in Section 3.2.2.

3.2.2 Proposed Computational Reconstruction Scheme

As seen in Fig. 2, the TBLG flow poses a peculiar reconstruction problem. First, the field boundary to be reconstructed is substantially different from the conventional circular or rectangular shape. Second, the reconstruction error of the outer region A_2 , being scanned with a severely-limited angle, may substantially affect the central region of A_1 of our interest. Reconstruction accuracy heavily depends on computational tomographic techniques. We may select 3–4 good candidates; however, each of them still has different merits. For TBLG tomography, a hybrid approach that simultaneously deploys three typical techniques in reconstruction of a single flow is thus proposed as described below. In this manner, the strengths of these techniques can be combined together to alleviate the effect of the ill-posed nature in reconstruction.

- (1) Curvilinear Nonlocal-Basis-Function Method (NBFM): Being defined in a common circular domain, ordinary NBFMs are inflexible to adapt to a different boundary shape. In ill-posed reconstruction, defining the exact boundary as close as possible is very important for minimizing errors. They also have difficulty in providing good local resolution with many series terms, being defined in the same entire domain; however, they can offer an advantage in finding a smoothed global shape with a small number of

series terms. The proposed curvilinear NBFM [2] can conform to peculiar boundary shapes while maintaining the aforementioned merit of NBFMs.

(2) Continuous Local-Basis-Function (LBF) Method: LBFs are good in easily adapting to unconventional boundary shapes and providing local resolution. Current practices of LBFs use optical pathlength data, that is, integrated values. The Hartmann sensor provides gradient data. Unlike a field confined in the aperture and with diminishing zero values at the boundary, TBLG flows cannot provide reference values in integration of the gradient data for generation of pathlength data, that is, integral constants. The continuous LBF method presented in Section 2 can thus be a good candidate. For the method, we can reconstruct the refractive-index field directly from Eq. (1) as before. Further improvement can also be made by incorporating the following concept of the variable grid method (VGM) [12]. For limited-aperture restricted-angular scanning, some local areas are more heavily scanned than others. This intrinsic spatial resolution information in data needs to be reflected in reconstruction if possible. That is, the heavily scanned area can provide better spatial resolution and vice-versa. If we attempt the same good resolution for both of the heavily and sparsely scanned areas, it produces ill-conditioned algebraic equations and thus increases reconstruction errors. VGM is a LBF method that can reflect the intrinsic spatial resolution information by generating different basis (domain of definition) sizes according to the degree of scanning. It can thus provide good reconstruction resolution and accuracy for the area of interest.

(3) Complementary Field Method (CFM): In ill-posed reconstruction, the utilization of *a priori* information is very important. This narrows down the search space of reconstruction and thus the reconstruction accuracy. Typical *a priori* information can be previous field reconstruction, positiveness or negativeness of field values, known local values, etc. CFM [15] is a reconstruction approach for efficient utilization of *a priori* information. Being iterative, it can also be employed as a main driver in alternately adopting various reconstructors in reconstructing a flow.

3.3 Effect of Optical Window Heating and Compensation Scheme

The investigation of the optical window effects is important for accurately determining TBLG BL flows. Based on the preliminary results [16], limited presentation is made here. Further complete analysis and investigation for alleviating the effects will be continued in the future.

The refractive-index of the window changes before and after generating the inside flow. The change is substantial as compared with that by the TBLG flow. The contribution by the natural-convection plume outside the window is relatively small but still needs to be considered. Fortunately, these changes are fairly uniform over the surface. They also do not fluctuate: that is, they are in a steady state during operation. These changes can thus be accurately predictable for compensation. Some possible means are indicated below as examples.

- (1) Temperature can be measured with thermocouple probes at some locations including inside window wall, outside window wall, and middle of the thermal plume. From the thermocouple measurements, the effects can be calculated and these external contributions can be subtracted out.
- (2) By a separate means, the refractive-indices of the optical windows and the thermal plume can be measured. An example is to coat the inside surface of the window for partial reflection and measure the refractive-indices from the side of the Hartmann sensors shown in Fig. 2.

4. References

1. B. Abel, L. Sharma, J. Craddock, T. T. Kang, J. Martin, and E. Rinehart, All Optical Imaging Brassboard Program: Optical Distortion Properties of Turbulent Boundary Layer Along a Heated Wall, Technical Report, Rocketdyne Division, Rockwell, International, Canoga Park, CA, August, 1992.

2. E. Yu, S. S. Cha, and A. W. Burner, Interferometric Tomographic Measurement of an Instantaneous Flow Field under Adverse Environments, SPIE Proceedings Vol. 2546, p. 33, 1995.
3. S. S. Cha, Interferometric Tomography for Three-Dimensional Flow Fields via Envelope Function and Orthogonal Series Decomposition, Opt. Eng., Vol. 27, p.557, 1988.
4. H. Sun and S. S. Cha, Computational Tomographic Reconstruction for Limited Ill-Posed Interferometric Data, Opt. and Lasers in Engng., Vol. 17, p.167, 1992.
5. S. S. Cha, Notes on Local Basis Functions, Informal Report for Summer Work at Phillips Laboratory, July 31, 1996.
6. S. S. Cha, Notes on ART, Informal Report for Summer Work at Phillips Laboratory, July 31, 1996.
7. S. S. Cha, Modification of Subroutine prjcm for LBF Method, Informal Report for Summer Work at Phillips Laboratory, August 5, 1996.
8. S. S. Cha, Subroutines and Their Variables, Informal Report for Summer Work at Phillips Laboratory, July 31, 1996.
9. S. S. Cha, Flow Chart of Subroutines and I/O Variables, Informal Report for Summer Work at Phillips Laboratory, July 31, 1996.
10. S. S. Cha, Estimation of Reconstruction Error due to Limited Size Aperture in Tomographically Capturing the Extended Region of TBLG, Informal Report for Summer Work at Phillips Laboratory, August 20, 1996.
11. D. W. Sweeney and C. M. Vest, Measurement of Three-Dimensional Temperature Fields above Heated Surfaces by Holographic Interferometry, Int. J. Heat Mass Transfer, Vol. 17, p. 1443, 1974.
12. D. J. Cha and S. S. Cha, Holographic Interferometric Tomographic for Limited Data Reconstruction, AIAA J., Vol. 34, p.1019, 1996.
13. R. A. Crowther, D. J. DeRosier and A. King, The Reconstruction of a Three-Dimension Structure from Projections and Its Application to Electron Microscopy, Proc. R. Soc. London. Sec.A: 317, p.319,1970.

14. R. N. Bracewell and S. J. Wernecke, Image Reconstruction over a Finite Field of View, J. Opt. Soc. Am., p.1342, 1975.
15. S. S. Cha and H. Sun, Tomography for Reconstructing Continuous Fields from Ill-Posed Multidirectional Data, Appl. Opt., Vol. 29, p. 251, 1990.
16. S. S. Cha, Problems to Be Considered for Tomographic Reconstruction of TBLG, Informal Notes for Summer Work at Phillips Laboratory, August 20, 1996.

Tschin Chu's report was not available at the time of publication.

STUDIES OF IONOSPHERIC ELECTRON CONTENTS AND HIGH-FREQUENCY
RADIO PROPAGATION

Kenneth Davies
Ajunct Professor
Department of Electrical and Computer Engineering

University of Colorado
Boulder, CO 80309-0425

Final Report for:
Summer Faculty Research Program
Phillips Laboratory

Sponsored by:
Air Force Office of Scientific Research
Bolling Air Force Base, DC

and

Phillips Laboratory

September 1996

STUDIES OF IONOSPHERIC ELECTRON CONTENTS AND HIGH-FREQUENCY
RADIO PROPAGATION

Kenneth Davies

Ajunct Professor

Department of Electrical and Computer Engineering

University of Colorado

Boulder, CO 80309-0425

Abstract

The research involves temporal and spatial variations of the ionosphere and the overlying protonosphere and their effects on radio systems. Total electron content affects the time delays of transionospheric radio signals and, therefore, is important in navigation and positioning satellite systems. Several topics have been started that will be continued by future co-operation. Single frequency Global Positioning System (GPS) receivers require corrections for time delays in the ionosphere and the protonosphere. Ionospheric models, such as the USAF's Parameterized Ionospheric Model (PIM), allow predictions of ionospheric delays but the effect of the protonosphere is usually ignored. The main source of information on the protonospheric content is the ATS-6 Radio Beacon Experiment and these results are surveyed and compared with outputs of a current protonospheric model based on physical principles. In another project the ionospheric electron contents from PIM are compared with Faraday contents measured at Hamilton MA over the years 1967 to 1995.

The GPS provides an important new tool for the investigation of ionosphere structure and some uses of GPS in measurements of : total electron contents, electron density profiles, and ionospheric restraints on the measurement of tropospheric water vapor are discussed. The construction of TEC regional maps over Central Europe illustrates the potential of GPS in ionospheric applications.

The ionosphere profoundly affects the propagation of high frequency (3-30 Mz) radio signals. Propagation models are available that give information on optimum operating frequencies and signal strengths provided by a given transmitting system (including given output power, antenna characteristics, modulation, etc.) It is planned to use the USAF PRISM model as part of a real-time upgrade for short-term forecasting of HF propagation conditions. Discussions have been held on possible display formats for use by radio operators with the user friendly HF Propagation Resource Manager (PROPMAN) developed by Rockwell.

STUDIES OF IONOSPHERIC ELECTRON CONTENTS AND HIGH-FREQUENCY RADIO PROPAGATION

Kenneth Davies

Introduction

While at Phillips Lab. several projects were started that will be concluded, in collaboration with Phillips Lab. staff, on my return to Colorado. The following are the main projects started during my stay: (1) Protonospheric electron contents from the ATS-6 Radio Beacon Experiment, (2) Ionospheric electron content measurements from Faraday rotation measurements at Hamilton MA, (3) Comparisons of these measurements with electron contents from current models of the protonosphere and the ionosphere, (4) Short-term (24 h) forecasting of high-frequency radio propagation conditions using the recently developed Parameterized Real-Time Ionospheric Specification Model (PRISM) and ways in which the outputs of PRISM can be displayed for operational purposes, (5) Studies of the ionosphere using the Global Positioning System, and (6) Ionospheric contamination of tropospheric water vapor measured with GPS. These topics will be discussed briefly in this report and the final results will be published in the scientific literature.

I express my sincere thanks to Dr. David N. Anderson and staff for their help, kindness, and co-operation during my stay at Phillips Laboratory.

Review of protonospheric electron content

The protonosphere is that part of the outer atmosphere, above about 1000 km, in which the dominant ion is H^+ . The electron content is important to users of systems such as GPS because it introduces signal delays which result in errors of position. Continuous measurements of the protonosphere columnar content, N_p , were obtained from group delay content (N_T) and the Faraday content (N_F) of radio signals transmitted from the ATS-6 geostationary satellite between July 1974 and December 1978 (see Davies 1980). Today these data form the major source of knowledge of the geographical and temporal variations of the protonospheric electron content.

Data on protonospheric content ($N_p = N_T - N_F$) are summarized in Table 1. These data have been gleaned from various sources including published papers and reports and unpublished reports. The percent ratio N_p/N_T is given and, where possible, ranges of values of N_p and N_T , separately. Table 1 shows that N_p varies between about one TEC unit ($1 \text{ TEC unit} = 1 \times 10^{16} \text{ el.m}^{-2}$) and about four TEC units. Note that the ratio

N_p/N_T varies from about 10% during the day over the U.S.A., to as much as 80% at night at Kiruna, Sweden which is at a high latitude. However some of these data cover only a few days whereas other data sets cover a number of months and, therefore, may not be representative of the average state. To within the accuracy of measurement, there is no marked dependence of N_p on latitude except possibly in low magnetic latitudes. In low magnetic latitudes N_p is uncertain because the radio ray path is nearly perpendicular to the geomagnetic field and, therefore, the Faraday rotation is small. Thus, to a first approximation, the protonospheric content is about 3 TEC units and, essentially, is independent of time and geographical location. Thus the variations of the ratio N_p/N_T arises mainly from the variations of N_T . Most of the ATS-6 measurements were made for low sunspot numbers, however, data for Palehua, Hawaii show that, between December 1977 (SSN = 57) and December 1978 (SSN = 118), N_p was essentially the same so that there is no experimental evidence for a sunspot cycle dependence of N_p . When N_p values are calculated using a first principles model, which includes ionosphere-protonosphere coupling and coupling of plasma to the magnetically conjugate region, they will be compared with the observed data (Davies et al. 1996). However, we can construct a simple climatological model of the protonosphere in middle latitudes in which the electron content is 3 TEC units and which is independent of geographical location, local time, and sunspot number.

Observed and modeled total electron contents and slab thicknesses

The Faraday electron content has been measured at Hamilton MA from 1967 through 1990, and similar measurements are available for other locations, e.g. Boulder 1987 to 1995. Further, the US Air Force has developed a climatological model, a parameterized ionospheric model, called PIM, which is composed of diurnally reproducible runs of several physical ionospheric models (Daniell et al. 1995). While the model has been checked against measured critical frequencies, no corresponding calibrations against total electron contents have been made. Such a calibration is of value when the model is used to calculate transionospheric effects. PIM outputs include: critical frequency (i.e. maximum electron density), total electron content, and the equivalent slab thickness ($= \text{TEC}/N_{\text{max}}$). Figure 1 contains global maps of TEC for 00 UT (top) in March 1988, a time of low solar noise flux, and in March 1990 (bottom) when the solar flux was high. Both the absolute values and the contour shapes are different. For high solar fluxes the TEC gradients are considerably larger than those for low solar fluxes. The global structure is dominated by the equatorial anomaly which consists of two areas of high TEC with peak contents located near $\pm 15^\circ$ magnetic latitude. Figure 2 shows monthly PIM slab thicknesses and the observed data. In 1981, high flux, there is relatively good agreement of the levels of TECs, especially around the time of diurnal maximum. In 1983, moderate F10.7, and in 1986, low F10.7, PIM underestimates the TEC. This is particularly evident at night when the maximum electron density decays faster than the total content.

TABLE 1
Some data on ionospheric and protonospheric contents :

PLACE	YEAR	MON	LAT	LON	N _p /N _T %		NT	NP	REF
					DA Y	NIGH T			
Ootacamund	75	11	11	77				7	1
Sao Paulo	75	5	-24	314				0.5_2	2
Huancayo	77		-12	285	21	40	5_40	3_10	
Palehua	77_78		21	202	12	50	5_90	2_6	
Ahmedabad	76	8	23	74		6	64	5_50	3
Dallas	74	8,12	33	263	9	44	7_24	2_3	4
Tokyo			36	140				3_3	5
Boulder	74_75		40	255	10	40	5_25	1_4	6
Danvers	74_75	8,10	40	272	8	50	5_34	2_3	7
Ft Mon	74_75		40	286	15	40	5_14	1_3	2
Hamilton	74_75		43	289	12	40		2_3	12
Bozeman	74	8,12	46	249	10	40	4_22	1_3	4
Graz	75	11	47	15	27	38	7_17	2_3	8
Lannion	75_76		49	356	18	65			9
Aberystwyth	75_76		52	356	19	40	18_32	3-5	10
Lindau	75	11	52	10	23	36	5_18	2_3	8
Lancaster	75_76		54	359	16	46	31_34	3_6	11
Kiruna	75	11	62	20	19	80		1_2.2	2

AVG

15 45

Sources

1. Sethia et al. 1978
2. Soicher 1976
3. Deshpande et al. 1977
4. Davies et al. 1977
5. Davies 1980
6. Fritz 1976
7. Poletti-Liuzzi et al. 1976
8. Davies et al. 1979
9. Fleury 1979
10. Hajeb-Hosseinih et al. 1979
11. Poulter and Hargreaves 1980
12. Kersley and Klobuchar 1978

Radio propagation updating

In spite of some 50 years of denigration, the high frequency spectrum (3 Mhz to 30 Mhz) continues to be an invaluable asset both as a primary means of communication and as a backup in times of conflict. HF radio is cost effective in natural and civil disaster situations and, frequently, has been the only means of communications available. The efficiency and reliability of HF radio has been enhanced by the development of such systems as the Automatic Link Establishment (ALE). With a scanning receiver and assigned frequencies, ALE provides information on the optimum frequency, it establishes the link, and notifies the operator. HF systems operate within nominal 3 kHz bands resulting in high spectrum efficiency at low cost. However, for those operators who do not have access to systems such as ALE ionospheric propagation advice is useful as, for example, warnings of impending: sudden ionospheric disturbances, ionospheric storms, and polar cap disturbances.

Because of the high spatial and temporal variability of the ionosphere, forecasts of high-frequency propagation conditions some 24 h ahead are made by the USAF 50th Weather Squadron and distributed to the civilian community via NOAA's Space Environment Service Center in Boulder, CO. These qualitative forecasts, which are updated every 6 h, are based on ionospheric soundings and on observations of prevailing circuit behavior (e.g. see Davies 1990, Section 9.8) e.g. circuits from Europe to the United States. The usable high-frequency band is limited on the upper frequency end by signal penetration (insufficient electron density) while the lower frequency limit is set by ionospheric absorption, insufficient signal/noise. These limits vary from day to day, with local time, and especially during ionospheric storms.

Recent development of the Parameterized Real-Time Ionospheric Specification Model (PRISM) (see Anderson 1993) has introduced a new means of updating the forecasts. This model specifies ion (NO^+ , O_2^+ , O^+) and electron densities, globally from 90 km to 1600 km, and is designed to incorporate all near real-time ground-based and satellite-borne ionospheric sensor data. PRISM has the capability of adjusting PIM to any and all real-time ionospheric data that are available. These data include both bottom-side profiles from digital sounders and in-situ sensors on the Defence Meteorological Satellite Program (DMSP) satellites that are in 840 km orbits. PRISM not only produces ion and electron density profiles from 90 to 1600 km every 2° latitude from 90°N to 90°S and every 5° longitude over 24 h UT, but also specifies the auroral oval boundary and the location and depth of the high latitude ionospheric trough. Together with D.N. Anderson, K. Walker and J. Lapriore we have examined some possible ways for displaying the model output for operational purposes. We started with the user friendly PROPMAN (short for Propagation Resource Manager) obtained from D. Roesler of Rockwell, Cedar Rapids IA. The basic data base for PROPMAN is IONCAP (e.g. Davies 1990, Chapter 12). The program calculates the optimum frequency band (2 MHz wide) for communication between a given transmitter and receiver locations with specified

transmitter power, antennas, etc. PROPMAN gives signal/noise on the optimum channel and on adjacent channels. PROPMAN is a display program and provides a basis for more sophisticated displays using outputs from PRISM. Additional outputs from PROPMAN include advisories on: x-ray flares, polar cap absorptions, and ionospheric storms. Numerous options are available such as a plot of the usable frequency band for the coming 24 h, a comprehensive world-wide station list, a table of maximum usable frequencies and lowest usable frequencies, circuit data, etc. A useful presentation of PRISM output, for a given transmitter installation, would be contours of signal strength and signal/noise over the surrounding region. PROPMAN gives time dispersion of the received signal for estimating the maximum usable information transmission rate.

Ionospheric studies using the Global Positioning System

The era of Faraday content measurements using very high frequency radio signals from geostationary satellites is essentially over owing to an international agreement to allocate this frequency band for aircraft-to-ground communication. Now, however, a new era has commenced in which dual frequency transmissions from the 24 GPS satellites can be used to measure the time delay and, hence, the total electron content between satellite and ground (see Hofmann-Wellenhof et al. 1993). The 20200 km height of the GPS satellites corresponds to a magnetic L-shell of approximately 3.2, which is slightly less than the nominal value of $L = 4$ for the plasmapause above which the plasma density drops by about two orders of magnitude. Thus GPS signals measure the total electron content (ionosphere + protonosphere). GPS -tecs are available as by-products of geodetic measurements from networks such as the International GPS Geodynamics Service (IGS) and/or other (e.g. meteorological) networks. This extensive coverage enables construction of global and/or regional maps of TEC which are of value in near-real-time assessment of ionospheric weather. Contour maps of GPS-TEC over Central Europe have been constructed using IGS stations there and a sample set of hourly maps are shown in Figure 3. These data were obtained by fitting suitable mathematical functions of latitude, longitude, time, and solar flux, to the total electron contents (Jakowski and Jungstand 1994). The maps show changes in the structure of the TEC that can occur during a single day. In particular notice, at 17 UT and 18 UT, there are large intrusions of plasma from regions of high total content into regions of low electron content.

Comparison of Faraday electron contents for GOES2 to Boulder with GPS-TECs show good agreement over several days and noon values are in good agreement with 5-day smoothing. Nighttime values do not show particularly good agreement partly because the night values, particularly in winter, are comparable with the accuracy of measurement (Davies and Hartmann 1996).

Future work in this area includes comparisons of GPS-TECs with total electron contents obtained from low polar orbiting Navy Navigation Satellite System (NNSS) at approximately 1000 km and 90 min. orbits.

These satellites provide meridional profiles at approximately fixed time and these will be compared with GPS-TECs. NNSS-TECs measured at Gibilmania, Italy; Aquila, Italy; Graz, Austria; and Lindau, Germany are shown in Figure 4 as functions of geographic latitude. On this occasion there is excellent agreement between the overlapping data so this will be compared with similar TECs obtained from GPS.

GPS and tropospheric water vapor

Rocken et al. (1993) have shown that the integrated tropospheric water vapor content can be calculated using time delay data from a network of ground-based GPS stations, provided that additional accurate surface meteorological measurements are available at the IGS sites. The precipitable water vapor (PWV) is defined as the depth of water that would result when all the tropospheric water vapor in a vertical column of the troposphere is condensed to liquid. Table 2 gives an idea of the relative magnitudes of the delays in: the ionosphere (30 m), the dry troposphere (300 cm), and the wet troposphere (0 to 30 cm). Thus, a 10% accuracy in the water vapor content requires the removal of 99.9% of the ionospheric time delay, which is only possible by including high-order ray-path corrections (Brunner and Gu, 1991).

TABLE 2.

Relative delays in ionosphere, dry troposphere, and wet troposphere

Ionosphere	30 m
Dry troposphere	300 cm
Wet troposphere	0 to 30 cm
For 10% accuracy of the wet part	3 cm

Because of the possibility that there is a residual ionospheric contamination that can affect the water vapor content, a small project has been started in which daily water vapor contents at Denver CO will be compared with maximum electron densities over Boulder, at a distance of about 50 km. It will be particularly interesting to see whether there are noticeable apparent water vapor changes on days of major ionospheric TEC changes such as those that occur during ionospheric storms. Noon water vapor contents at Denver in 1995, obtained from the University Navigation Consortium, UNAVCO, in Boulder are plotted in Figure 5. This plot will be continued in the next few years when ionospheric contributions to the total delay will increase as the sunspot numbers increase starting in 1997.

Future Work

The following projects will be completed and the results published in the open literature:

- (1) Protonospheric and ionospheric electron contents, observed and modeled.
- (2) Maps of GPS and NNSS total electron contents over Central Europe.
- (3) Effects of the ionosphere on tropospheric water vapor measured with GPS.

Acknowledgments

I wish to extend my thanks to the following for cooperation and help during my Associateship:

D.N. Anderson, R Daniell, D. Decker, P. Doherty, P. Fougere, and J.A. Klobuchar.

References

- Anderson, D.N., The development of global, semi-empirical ionospheric specification models, in Ionospheric Effects Symposium, IES-93, ed. J.M. Goodman, Document PB94-181930, National Technical Information Service, 5285 Port Royal Road, Springfield VA 22161 353-363 (1993)
- Brunner, F.K., and M. Gu, An improved model for the dual frequency ionospheric correction of Gps observations, *Manusc. Geod.*, 16, 205-214 (1991)
- Daniell, R.E., L.D. Brown, D.N. Anderson, M.W. Fox, P.H. Doherty, D.T. Decker, J.J. Sojka, and R.W. Schunk, Parameterized ionospheric model: A global ionospheric parameterization based on first principles models, *Radio Sci.*, 30, 1499-1510 (1995)
- Davies, K., Recent progress in satellite radio beacon studies with particular emphasis on the ATS-6 Radio Beacon Experiment, *Space Sci. Rev.*, 25, 357-430 (1980)
- Davies, K., *Ionospheric Radio*, P. Peregrinus, London (1990)
- Davies, K., W. Degenhardt, G.K. Hartmann, and R. Leitingner, Electron content measurements over the U.S.: Joint Radio Beacon Program, NOAA/MPAE/GRAZ, Station Report ATS-6 94°W, Max-Planck-Institute for Aeronomy, Katlenburg-Lindau, Germany (1977)
- Davies, K., W. Degenhardt, G.K. Hartmann, and R. Leitingner, Some measurements of total electron content made with the ATS-6 radio beacon, in *Symp. Beacon Sat. Meas., Plasmaspheric and Ionospheric Properties*, ed. P.F. Checcacci, IROE, Florence, Italy, 20.2-20.7 (1979)
- Davies, K., J.A. Klobuchar, T. Roelofs, P.H. Doherty, H-L Lee, R.E. Daniell, and R.G. Rastogi, A review of current knowledge of the total electron content of the earth's protonosphere obtained from ATS-6 Radio Beacon Experiment and comparisons with model results, in preparation (1996)
- Davies, K., and G.K. Hartmann, Ionospheric studies using the Global Positioning System, *Kleinheubacher Berichte*, 39 (1996)

Deshpande, M.R., R.G. Rastogi, H.O. Vats, G. Sethia, H. Chandra, R.V. Bhonsle, and H.S. Sawant, Scientific Report on ATA-6 Radio Beacon Studies, Phys. Res. Lab., Ahmedabad (1977)

Hofmann-Wellenhof, B., H. Lichtenegger, and J. Collins, Global Positioning System, Theory and Practice, 2nd. ed, Springer-Verlag, Wien, New York (1993)

Fleury, R., Plasmaspheric-ionospheric contents deduced from ATS-6 measurements over Lannion, in Symp. Beacon Sat. Meas., Plasmaspheric and Ionospheric Properties, ed. P.F. Checcacci, IROE, Florence, Italy, 16.1-16.5 (1979)

Fritz, R.B., ATS-6 radio beacon electron content measurements at Boulder, July 1974-May 1975, Report UAG-58, World Data Center A, NOAA, Boulder CO (1976)

Hajeb-Hosseineh, H., L. Kersley, and K.J. Edwards, Ionospheric/protonospheric electron content studies using ATS-6, in Symp. Beacon Sat. Meas., Plasmaspheric and Ionospheric Properties, ed. P.F. Checcacci, IROE, Florence, Italy, 19.1-19.5 (1979)

Jakowski, N., and A. Jungstand, Modelling the regional ionosphere by using GPS observations, in Proc. Intl. Beacon Symp., ed L. Kersley, Aberystwyth, U.K., 366-369 (1994)

Kersley, L., and J.A. Klobuchar, Comparison of protonospheric electron measurements from the American and European sectors, Geophys. Res. Letters, 5, 123(1978)

Poletti-Liuzzi, D.A., K.C. Yeh, and C.H. Liu, Simulation and measurement of the plasmaspheric electron content, in The Geophysical Use of Satellite Beacon Observations, ed M. Mendillo, Boston Univ., 197-218 (1976)

Poulter, E.M., and Hargreaves, J.K., Electron content measurements at Lancaster: Harmonic analysis of ATS-6 measurements, in Propagation Effects in Space/Earth Paths, AGARD Conf. Proc. CP284, ed. H.J. Albrecht, 27.1-27.14 (1980)

Rocken, C., R. Ware, T. van Hove, F. Solheim, C. Alber, J. Johnson, M. Bevis, and S. Businger, Sensing atmospheric water vapor with the Global Positioning System, Geophys. Re. Lett., 20, 2631-2634 (1993)

Sethia, G., M.R. Deshpande, and R.G. Rastogi, The solar wind influences plasmaspheric content, *Nature*, 276, 482 (1978)

Soicher, H., Comparative ionospheric and plasmaspheric electron contents from three world regions, *Nature*, 264, 46-48 (1976)

Figure Titles

Figure 1 Global distribution of the total electron content of the ionosphere at 00 UT at the Vernal Equinox at low (top), and at high (bottom) sunspot numbers, from the parameterized ionospheric model (PIM).

Figure 2 Monthly mean vertical slab thicknesses at Hamilton, MA in winter, equinox, and summer, for low, medium, and high sunspot numbers: (1) observed, (2) from PIM.

Figure 3 Hourly maps of GPS total electron contents over Central Europe. TECs are in units of 10^{15}el.m^{-2}

Figure 4 Variation with geographical latitude of the ionospheric total electron content measured at: Gibilmania, Italy; Aquila, Italy; Graz, Austria; and Lindau, Germany, on February 21, 1995.

Figure 5 Scatter plot of the daily noon precipitable water vapor contents at Denver, CO obtained from GPS radio delays.

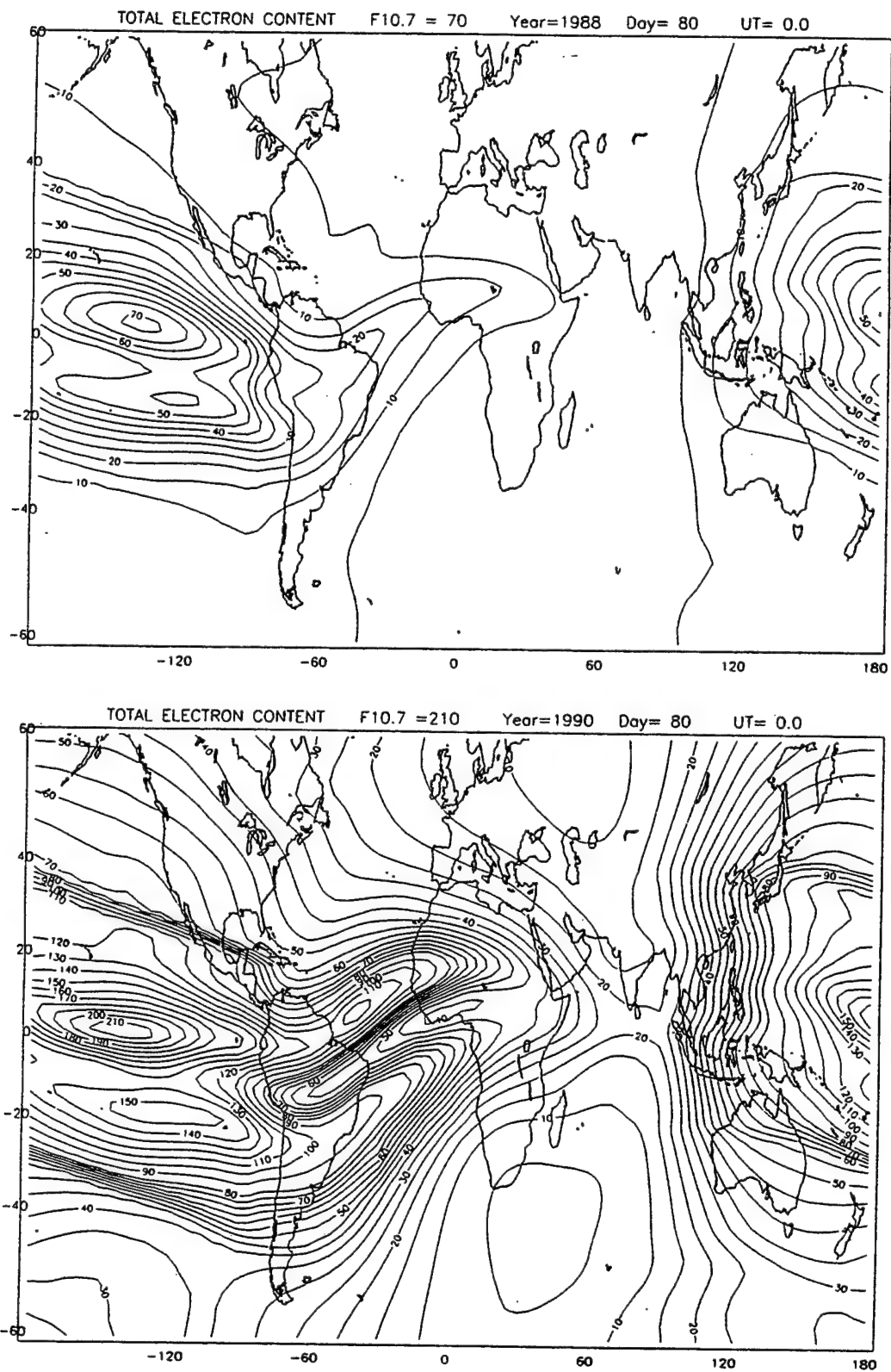


Figure 1 Global distribution of the total electron content of the ionosphere at 00 UT at the Vernal Equinox at low (top), and at high (bottom) sunspot numbers, from the parameterized ionospheric model (PIM).

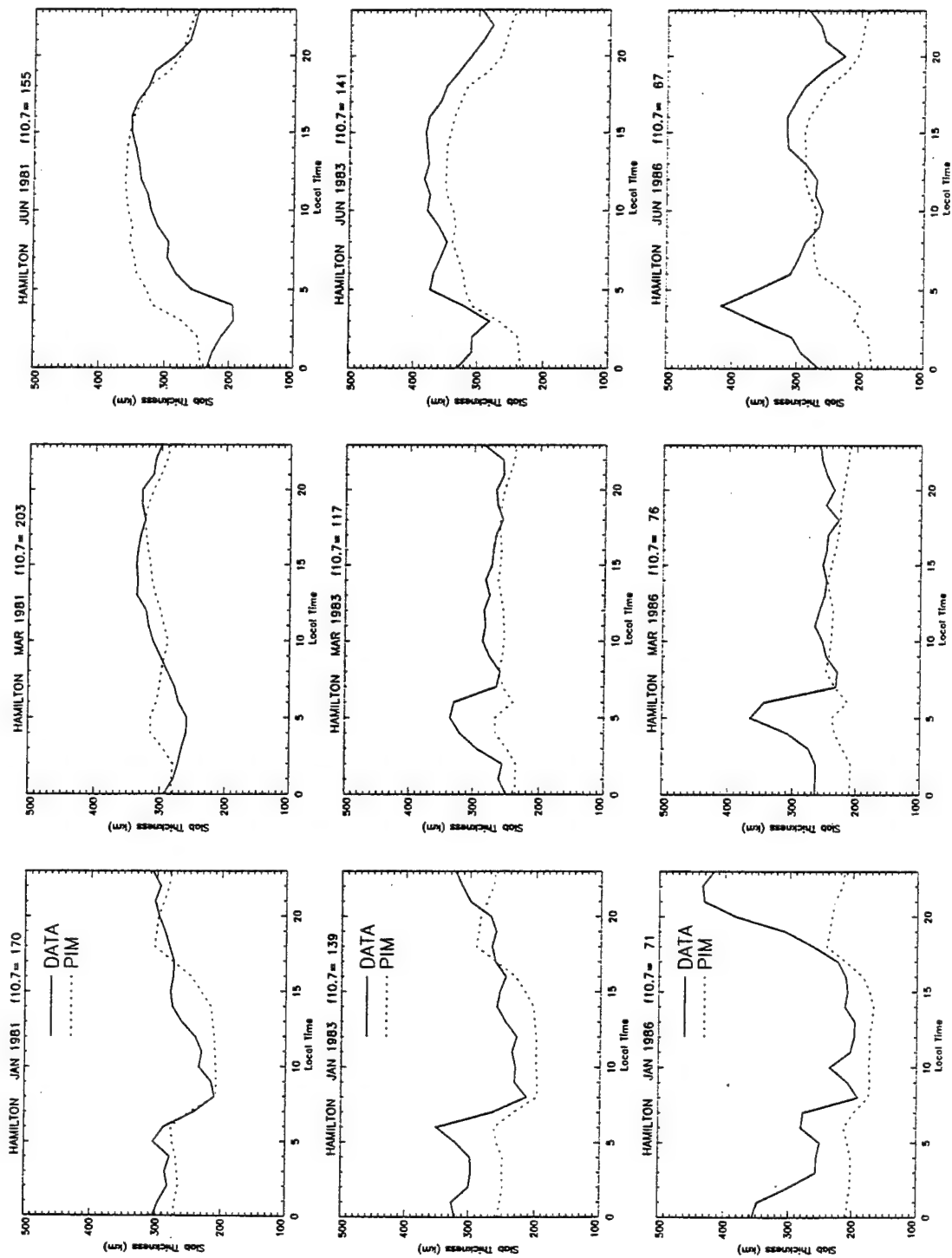


Figure 2 Monthly mean vertical slab thicknesses at Hamilton, MA in winter, equinox, and summer, for low, medium, and high sunspot numbers: (1) observed, (2) from PIM.

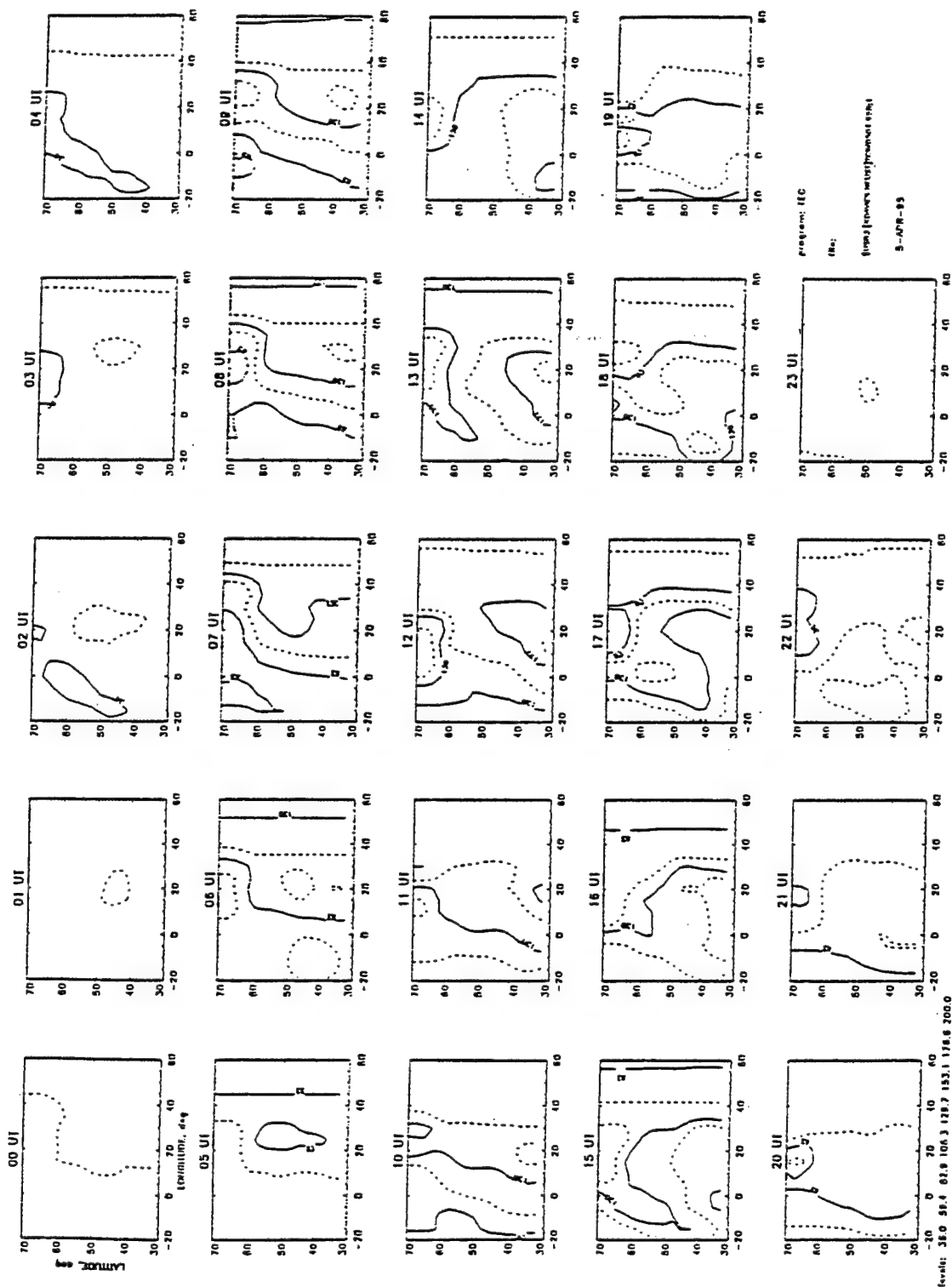


Figure 3 Hourly maps of GPS total electron contents over Central Europe. TECs are in units of $10^{15} \text{ el.m}^{-2}$

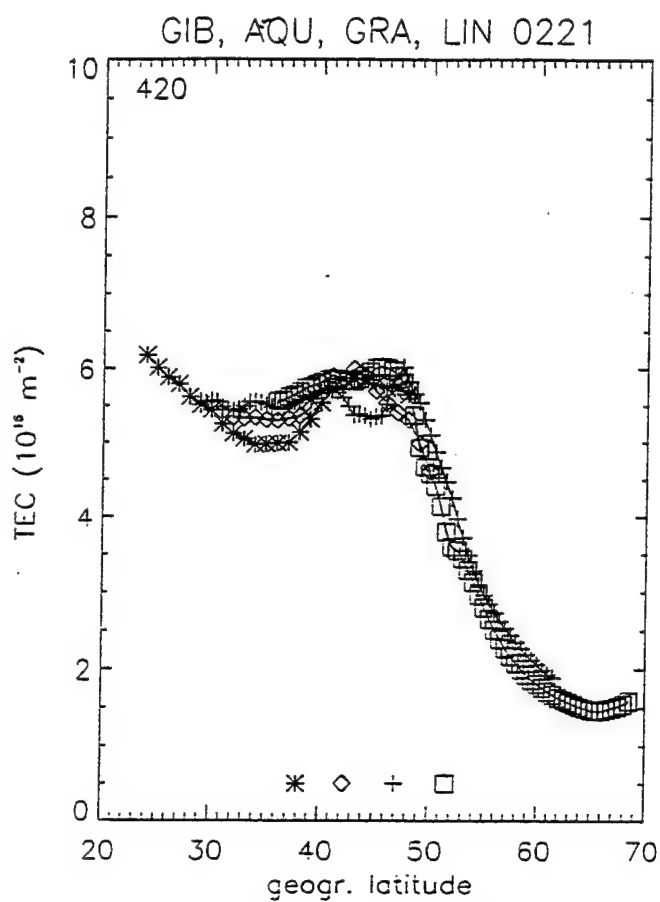


Figure 4 Variation with geographical latitude of the ionospheric total electron content measured at: Gibilmania, Italy; Aquila, Italy; Graz, Austria; and Lindau, Germany, on February 21, 1995.

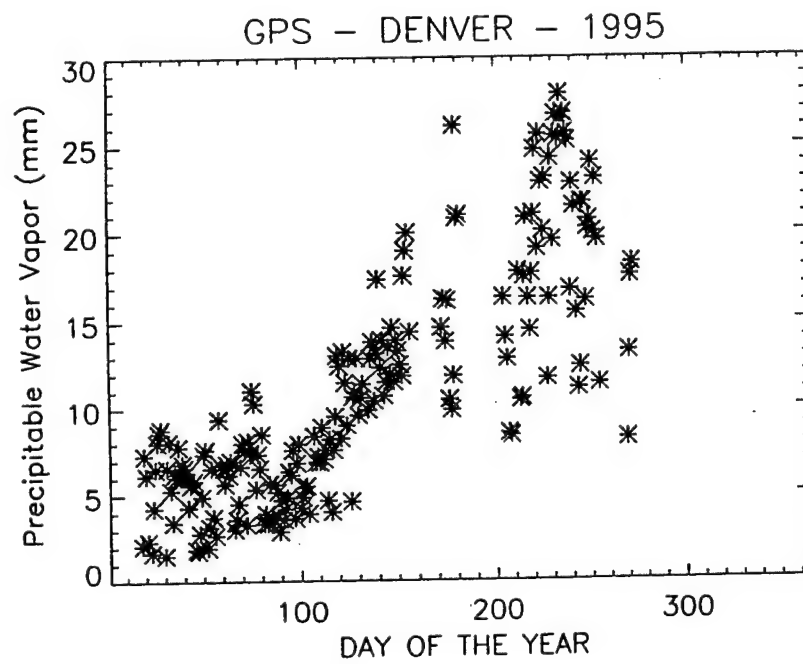


Figure 5 Scatter plot of the daily noon precipitable water vapor contents at Denver, CO obtained from GPS radio delays.

Dynamic Neural Networks: Prediction of an Air Jet Flowfield

Judith E. Dayhoff
Assistant Research Scientist
Institute for Systems Research

University of Maryland
College Park, MD 20742

Final Report for:
Summer Faculty Research Program
Phillips Laboratory
3550 Aberdeen Ave., S.E.
Kirtland Air Force Base
Albuquerque, NM 87117-5776

Laboratory Focal Point:
Dr. Lenore McMackin

Sponsored by:
Air Force Office of Scientific Research
Bolling Air Force Base, Washington, D. C.
and
Phillips Laboratory

October 15, 1996

Dynamic Neural Networks: Prediction of an Air Jet Flowfield
Abstract

A neural network with time-delay elements has been used to analyze and predict the dynamic structure of an air jet flow. A jet flow of hot air was produced in the laboratory, and measured at multiple downstream positions to determine the amount of optical refraction produced at the interface between the hot air flow and the surrounding cooler air ([MVF95] [MMC⁺95]). A series of measurements were taken over time, at varying distances from the jet flow. Using this data, we have trained neural networks to perform time-series analysis prediction on each data signal. The neural networks contained time-delay elements on their input signal as well as time-delay elements on multiple interconnections between each pair of neurons in the network. The networks had a feed-forward architecture, and were capable of training their weights and time-delays through a gradient descent approach. These networks, called time-delay neural networks (TDNNs) and adaptive time-delay neural networks (ATNNs), have been previously shown to be able to predict limit cycle oscillations and chaotic oscillations ([LDL94], [LDL95]). A network was trained successfully on each data signal recorded. The average performance of the neural networks was high, as they usually predicted 80 % to 93 % of the variation in the signals. The data appeared irregular, with no discernable pattern by eye. Predictions were performed on a one-step-ahead basis, and future studies are planned to expand this work to a prediction of two to five steps ahead, and to the analysis of longer data signals. Further research is underway to more fully develop and exploit the computational abilities of dynamic neural networks.

1 Introduction

Dynamic neural networks include architectures that imbue the network with properties that are dynamic over time, such as the ability to model and predict time series that are complex or chaotic, the ability to evoke oscillations in the network, and the capability of training the network on oscillations, including complicated oscillations that do not appear to repeat exactly over any observed length of time. Networks that are promising for time series predictions include feed-forward architectures with time-delay elements, such as the time-delay neural network (TDNN) and the adaptive time-delay neural network (ATNN). These networks adapt weights and sometimes time-delays, and have proven highly effective in being trained to produce limit cycle oscillations and chaotic time series ([LDL94], [LDL95]).

We have researched the possibility that neural networks can be used to predict optical wave front distortions in a flow field, where dynamically changing air flows can distort optical signals. The refraction of an optical signal changes dynamically over time because of the continuous motion and turbulence in a warm air flow. Whereas individual points of laser light are refracted by the air flow, which has been experimentally measured, entire images would also be distorted. Our long-term goal is to be able to restore an optical image at a high resolution, by compensating for the distortion in a timely fashion, utilizing the neural network's prediction. In this study, we are predicting refraction of an individual laser light signal with a neural network, so that the neural network prediction can later be used to compensate for the refraction and to stabilize and clarify the reception of the light signal.

An experiment was previously devised and implemented at the Phillips Laboratory to measure the optical refraction of the boundary between a hot air flow and the surrounding cooler air ([MMC⁺95]). Sensors were configured to detect the change in position of a laser light after it passes through a warm jet air flow. The sensor consisted of a lateral effects detector (LED), which is a dual-axis photodiode that can measure the centroid location of an incident laser beam. The LED works similar to typical photodiodes in that it induces a current proportional to the intensity of the beam. The current is divided among four strip terminals, where current is measured, and the position of the beam is then calculated.

With the LED sensors, data measurements were taken at varied distances and from different orientations. Each data channel reports refraction over a series of time steps. Measurements included data taken at different distances from the origin of the jet flow, in x and y directions, and under varying conditions of forced flow, non-forced flow, and background.

A neural network approach was applied to the air flow data. A time history of measurements was used to train the neural network to predict the next measurement in the sequence. A series of preliminary training runs were performed in which networks were trained on the first 500 data points and tested on the next 1000 data points. A high performance was attained, with the neural network predictions explaining about 90 % of the variation. These results are highly promising and motivate further studies on neural network prediction of air flow data.

The neural networks used for air flow prediction were feed-forward configurations with three layers. Time-delay elements were included on both layers of weights, causing inputs to the network to include a time history of data. In addition, time-delays on the

hidden-to-output layer allowed the output layer to receive a time history of hidden unit activations. Adaptive training was performed on the weights, and, in some cases, on the time-delays as well. A new training run was done on each data signal. For each data signal, the network configuration was left the same but a different set of initial starting weights was used. Training converged successfully in almost all cases where the data was collected with forced or non-forced air. For background measurements, the neural network often did not converge, as the measurements were extremely small. In a few cases, background recordings were predicted by the neural network, presumably because of ambient perturbations present in the air flow.

This report covers our methodology next in Section 2, describing the neural networks, their architectures and training, as well as the experimental setup for collecting the data that was analyzed. Results on the analysis and prediction of wave front distortions are covered in Section 3, and conclusions are discussed in Section 4. Appendix A discusses a related dynamic neural network architecture that was also studied.

2 Methodology

2.1 Wave Front Sensing

Figure 1 shows the heated air-jet flow generation system. A blower pumps air across a heater and into a plenum chamber, which becomes a source for heated air to flow upwards into a nozzle to form a jet of heated air from a 2.5-cm opening. The air-jet flow then rises vertically, and a laser beam is passed through the heated air as it moves upwards. The

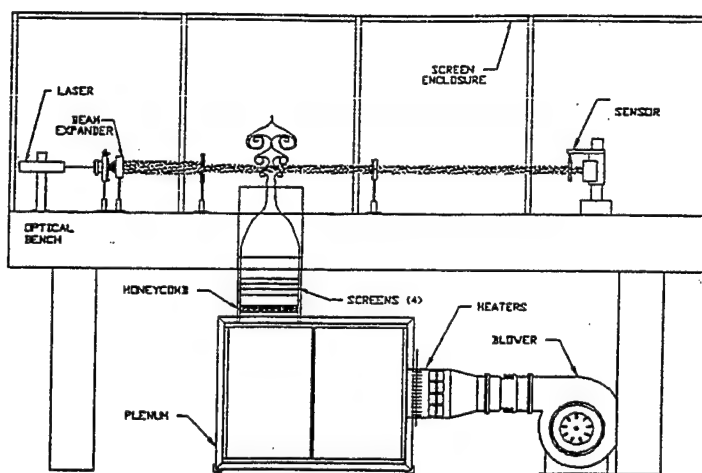


Figure 1: Air jet flow apparatus. Reprinted with permission.

sensor receives the laser light and measures the focal spot intensity on a plane, placed perpendicular to the laser light beam. The velocity of the flow center is 4.5 m/s on average, and the average temperature of the air in the jet is approximately 10 degrees C above ambient.

The distance of the sensor above the nozzle can be varied, and a spectrum of data was taken at different distances. Measurements were taken above the nozzle and perpendicular to the air flow. These measurements were taken in the x and y directions in the plane perpendicular to the air flow. The experimental conditions included (1) forced air flow, (2) non-forced air flow, and (3) background. Thus, for each height above the nozzle, 6 data streams were taken, consisting of two different directions under each of the three air flow conditions.

The sensor was a lateral effects detector (LED), which is comprised of a dual-axis photodiode. The LED induces a current from which the centroid location of an incident laser beam can be calculated. The current is proportional to the intensity of the beam, and is divided among four strip terminals, where current is measured, so that the position

of the beam can be calculated [Lun96].

2.2 Neural Networks with Embedded Time-Delays

The time-delay neural network (TDNN) originally proposed by Waibel ([Wai89], [WHH⁺89], [HW92]) employs time-delays on connections and has been successfully applied to phoneme recognition, classification of spatiotemporal patterns ([LDL92c]), and missile discrimination ([LDR95]). In the TDNN architecture, each neuron takes into account not only the current information from its input neurons of the previous layer, but also a certain amount of past information from those neurons due to delays on interconnections. Typically the time delays are evenly spaced over a time interval called the frame window, although arbitrary time delays may be used. Training is done with spatiotemporal patterns, one or more signal channels over time, and the classification of those patterns is reported at each time step by the output layer. After training, the weights are strengthened along those interconnections whose time delays are important to recognition.

The adaptive time-delay neural network (ATNN), which adapts time delays as well as weights during training, is a more advanced version of the TDNN. The result is a dynamic learning technique for spatiotemporal classification and for time series prediction ([LDL92a]). The ATNN model employs multiple interconnections between each pair of neurons in a feed-forward configuration, with each interconnection having its own weight and time-delay. Both time delays and weights are adjusted according to system dynamics in an attempt to achieve the desired optimization. The adaptation of the delays and weights are derived based on the gradient descent method to minimize the error during

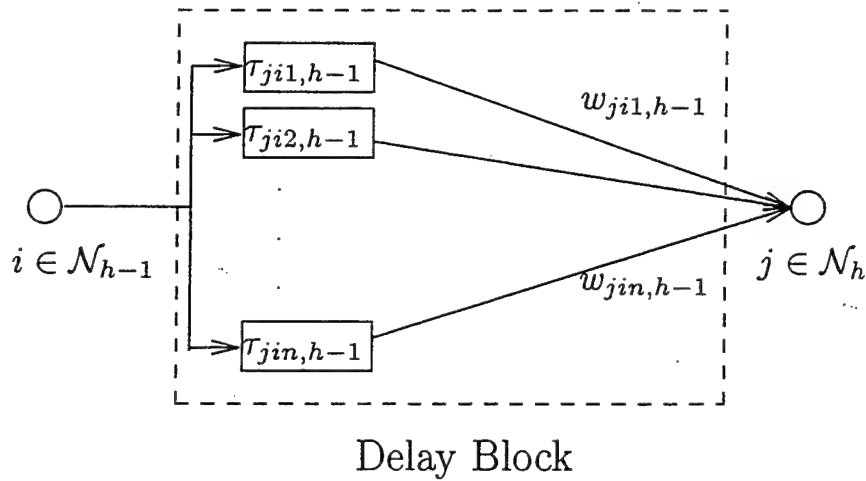


Figure 2: Delay block in a time-delay neural network.

training. Processing units do not receive data through a fixed time window, but gather important information from various time delays which are adapted via the learning procedure.

The schematic architecture of the connections from one processing unit to another processing unit of the ATNN is depicted in Figure 2. The configuration of multiple interconnections between a single pair of units, each with its own delay, is called a delay block. Node i of layer $h-1$ is connected to node j of the next layer h , with the connection line k having an independent time delay $\tau_{jik,h-1}$ and synaptic weight $w_{jik,h-1}$.

The entire network is constructed by the delay blocks that connect neurons layer by layer, as illustrated in Figure 3. It is not necessary to have the same number of delays for different units in the same layer or the same delay values from different units, because the computation is local for each interconnection. Each connection can have an arbitrary delay value and each pair of neurons can have any number of delayed interconnections.

In the TDNN, the adaptation variables are the weights, and in the ATNN, the adaptation variables are time-delays and weights. Each node sums up the net inputs from the

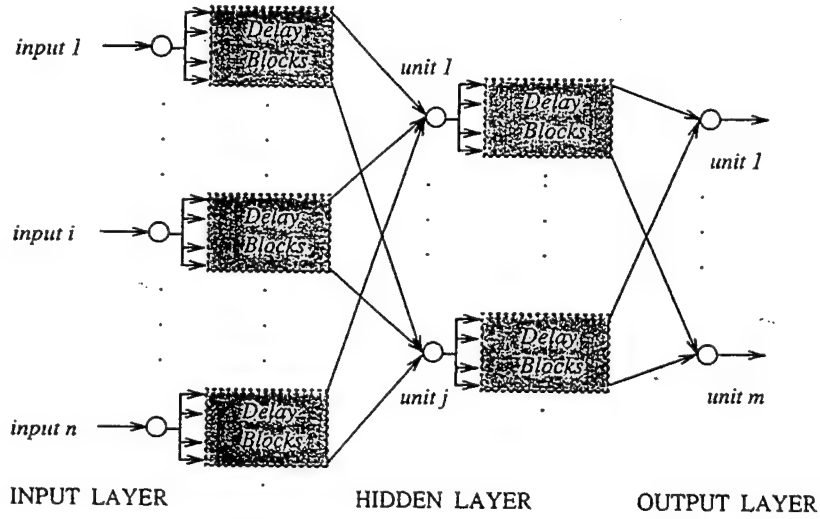


Figure 3: Time-delay neural network depicted as built from delay blocks.

activation values of the previous neurons, through the corresponding time delays on each connection line, that is, at time t_n (e.g., time step n) unit j on layer h receives a weighted sum

$$S_{j,n} = \sum_i \sum_k w_{jik,h-1} a_{i,h-1}(t_n - \tau_{jik,h-1}) \quad (1)$$

where $a_{i,h-1}(t)$ is the activation of unit i in layer $h-1$ at time t . Then the output of node j is governed by a nondecreasing sigmoid function as follows

$$f(S) = 2/(1 - e^{-S}) - 1 \quad (2)$$

where S is the incoming sum, as in (1).

The adaptation of the delays and weights are derived based on the gradient descent method to minimize the error function E during training, where

$$E(t_n) = 1/2[\sum_j (d_j(t_n) - a_{j,h}(t_n))^2] \quad (3)$$

where $d_j(t_n)$ is the target value for output unit j at time t_n .

The weights and time delays are updated step by step proportional to the opposite

direction of the error gradient, repectively,

$$\Delta w_{jik,h} = -\eta_1 \delta E(t_n) / \delta w_{jik,h} \quad (4)$$

$$\Delta \tau_{jik,h} = -\eta_2 \delta E(t_n) / \delta \tau_{jik,h} \quad (5)$$

where η_1 and η_2 are the learning rates.

The derivation of this algorithm has been previously addressed ([DD91], [DD93], [LDL92b], [LDL92a]). The learning rules may be summarized as follows

$$\Delta w_{jik,h-1} = \eta_1 \delta_{j,h}(t_n) a_{i,h-1}(t_n - \tau_{jik,h-1}) \quad (6)$$

$$\Delta \tau_{jik,h-1} = -\eta_2 \delta_{j,h}(t_n) w_{jik,h-1} a'_{i,h-1}(t_n - \tau_{jik,h-1}) \quad (7)$$

where

$\delta_{j,h}(t_n) = (d_j(t_n) - a_{j,h}(t_n))f'(S_{j,h}(t_n))$ if j is an output unit, and

$\sum_p \sum_q \delta_{p,h+1}(t_n) w_{pq,h}(t_n) f'(S_{j,h}(t_n))$ if j is a hidden unit.

Characterization and application of the ATNN network has been addressed previously ([LDL95]).

2.3 Dynamic Neural Networks

Neural networks with time-delay elements can learn dynamic behavior by training to produce complex oscillations or limit cycles. Previous research has demonstrated training of TDNN and ATNN networks on a chaotic sequence ([LDL94]) and on limit cycle attractors ([LDL95]). The type of air flow data analyzed in this report has previously been shown to contain similar dynamic fluctuations ([MVF95]). Thus the TDNN and ATNN approach is

highly promising. We have also examined an extension to this approach through researching a single-layer recurrent network with random weights which can be altered to evoke chaotic behavior spontaneously without training. Appendix A gives a brief summary of this research.

3 Results

TDNN neural networks were trained on a series of recorded air jet flows. The configuration used was 1 input unit, 3 hidden units, and one output unit. There were two interconnections connecting each pair of neurons in a feed-forward direction. For each pair, one interconnection had no time-delay (e.g., a time-delay of zero), and the other interconnection had a time-delay of one time step. In our initial set of training runs, reported here, the weights were trained and the time-delays were held fixed. The learning rate parameter, η , was started at 0.2, its highest value, and then relaxed linearly to take on lower and lower values over 20,000 iterations of training. The final learning rate value was 0.08. Training was terminated automatically after 20,000 iterations.

The data sets were prepared from more than fifty recordings of air jet flows, taken at varying distances from the flow nozzle. Distances varied from 0.5 diameters to 8.0 nozzle diameters. Conditions of air jet flow included forced air and non-forced air flow, and background noise recordings. Angles at which optical distortion were taken included an x-direction and a y-direction, both perpendicular to the flow of the air.

Each data recording constituted one time series to be learned and predicted by one neural network. The neural network was initialized, by generating small random weights,

before training began on each time series. The first 500 data measurements were used as the training set, and the next 1000 measurements were a testing performance set. A verification set was not needed to provide a stopping criterion for the neural network, because the network training was terminated after 20,000 iterations automatically. Future experiments are planned in which a verification set will be used for a stopping criterion, to possibly boost performance. Training was quite successful nevertheless because the relaxation of the η parameter effectively stopped training at relatively favorable times.

Table 1 summarizes the performance attained by the trained neural networks. The performance reported is a computation that reflects the percent variation in the data that is explained by network predictions. First a ratio is computed. The numerator of the ratio is the root-mean-square of the network's error compared to its target values, as follows.

$$R = \sqrt{(1/n) \sum_k (d(t_k) - a(t_k))^2} \quad (8)$$

where $d(t_k)$ is the target value at time t_k , and $a(t_k)$ is the output value at time t_k . The denominator of the ratio is the standard deviation of the target values (e.g., the data measurements).

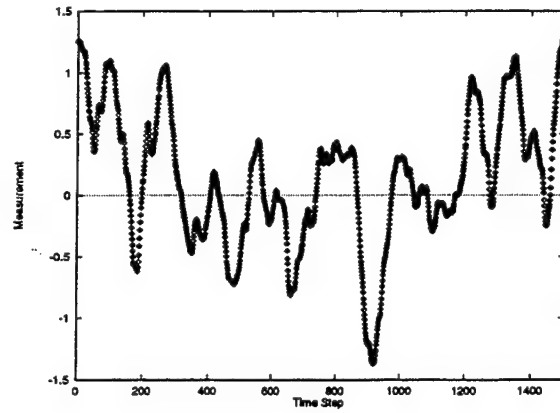
$$S = \sqrt{(1/n) \sum_k (d(t_k) - d_{mean})^2} \quad (9)$$

where d_{mean} is the average target (measurement) value. The ratio is then R/S , and the value $F = 1 - R/S$ reflects the fraction of variation in the data that the network explained through its predictions.

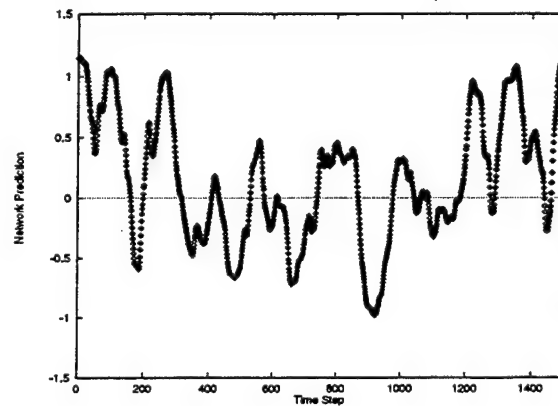
Performance varied between 72% and 93% for forced and non-forced air experiments. The background measurements were typically of much smaller magnitude compared with the air flow experimental data. For most of the background trials, the neural network did

Dist	x/y	1st 500	2nd 500	3rd 500
----	---	---	---	---
Forced:				
05	x	75	76	72
05	y	88	88	88
20	x	92	93	92
20	y	87	86	85
30	x	90	88	92
30	y	89	88	89
35	x	92	78	81
35	y	90	91	86
40	x	93	89	90
40	y	89	89	90
50	x	92	88	60
50	y	99	81	82
60	x	92	86	93
60	y	89	88	87
70	x	91	90	92
70	y	0	0	0
80	x	93	79	91
80	y	92	87	87
Non-forced:				
35	x	91	84	75
35	y	88	81	86
40	x	93	88	90
40	y	91	84	87
50	x	90	82	80
50	y	87	84	78
60	x	93	66	85
60	y	85	85	86
70	x	0	0	0
70	y	11	0	0
80	x	94	79	86
80	y	92	83	76
Background:				
35	x	0	0	0
35	y	0	0	0
40	x	0	0	0
40	y	40	43	46
50	x	93	94	92
50	y	0	0	0
60	x	95	94	94
60	y	48	41	30
70	x	0	0	0
70	y	30	14	41
80	x	79	81	82
80	y	19	15	98

Table 1: Performances of trained neural networks.



(a)

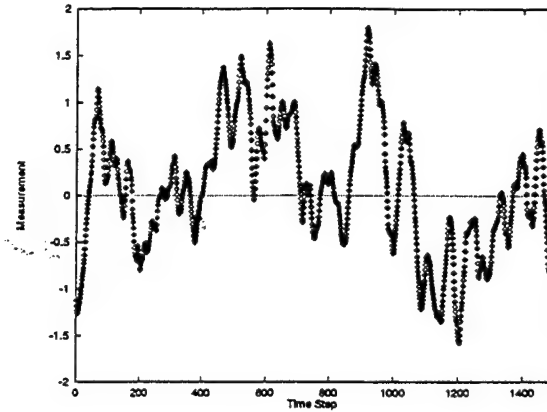


(b)

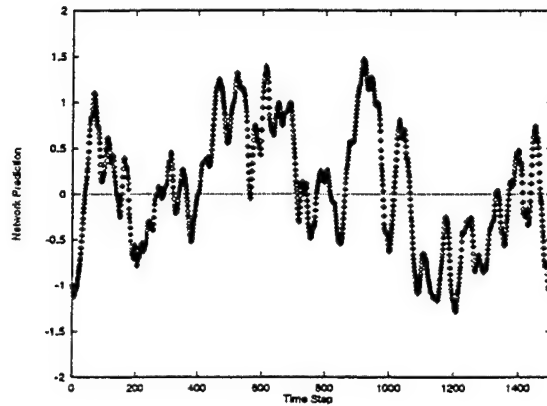
Figure 4: Optical distortion due to hot air flow, forced air measured at 8.0 diameters from nozzle. (a) Measurements. (b) Prediction by trained neural network. 1500 data points in each graph. Orientation: x direction.

not converge to be able to predict the noise. However, the background tends to oscillate irregularly, and in some cases the neural network converged to a prediction of a substantial portion of the measurement variations.

Figure 4 shows results for forced air flow measurements taken at 8.0 diameters from the flow nozzle. Figure 4 (a) shows the first 1500 measurements taken, from the x direction orientation, and Figure 4(b) shows the predictions for those measurements provided by the trained neural network. The first 500 of the time steps shown were the training set,



(a)

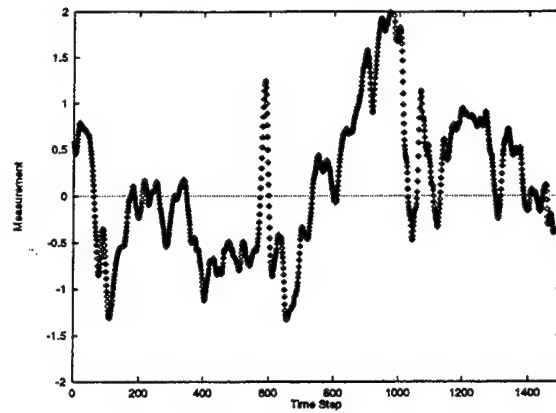


(b)

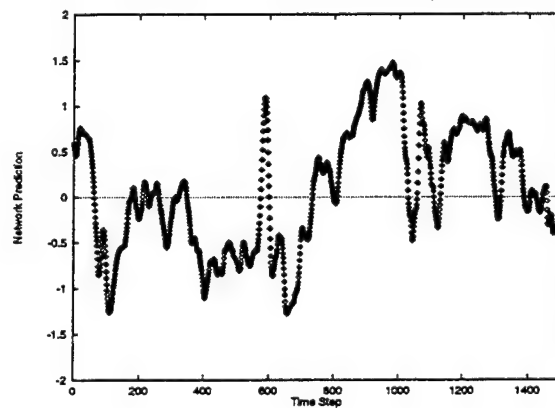
Figure 5: Optical distortion due to hot air flow, forced air measured at 8.0 diameters from nozzle. (a) Measurements. (b) Prediction by trained neural network. 1500 data points in each graph. Orientation: y direction.

and the remainder were the performance testing set. The prediction follows the data extremely well, with the exception that at some of the peaks the prediction does not reach the magnitude of the data. Figure 5 is analogous but for the y direction orientation.

Figure 6 shows results for non-forced air flow measurements taken at 8.0 diameters from the flow nozzle. Figure 6 (a) shows the first 1500 measurements taken, from the x direction orientation, and Figure 6(b) shows the predictions for those measurements provided by the trained neural network. The first 500 of the time steps shown were the



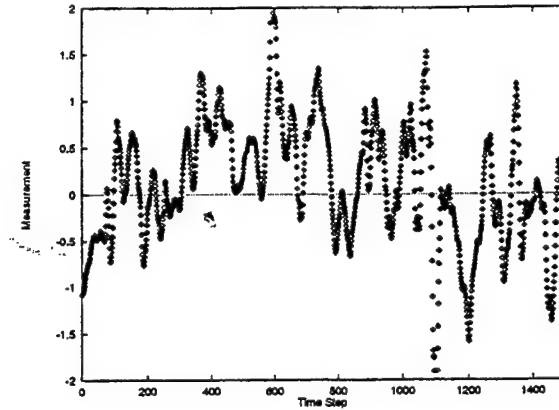
(a)



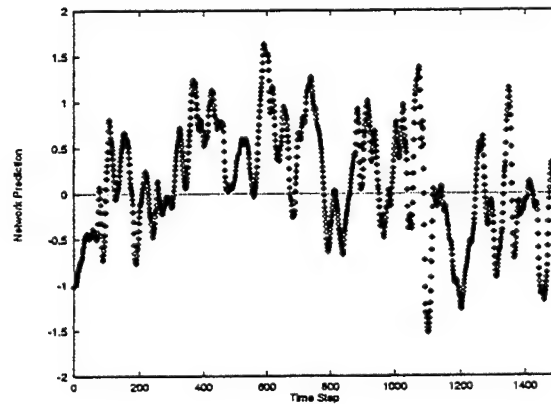
(b)

Figure 6: Optical distortion due to hot air flow, non-forced air measured at 8.0 diameters from nozzle. (a) Measurements. (b) Prediction by trained neural network. 1500 data points in each graph. Orientation: x direction.

training set, and the remainder were the performance testing set. The prediction follows the data extremely well, with the exception that at some of the peaks the prediction does not reach the magnitude of the data. Figure 7 is analogous but for the y direction orientation.



(a)



(b)

Figure 7: Optical distortion due to hot air flow, non-forced air measured at 8.0 diameters from nozzle. (a) Measurements. (b) Prediction by trained neural network. 1500 data points in each graph. Orientation: y direction.

4 Conclusions

A set of preliminary runs were performed on neural network modeling of turbulent air flow phenomena. Neural networks with time-delay elements were successfully trained to predict the amount of optical distortion caused by the flow of warm air out of a nozzle, in an environment where the air is cooler. The optical distortion was caused by the changing optical refraction of the boundary between the warm and cooler air.

Future research could address remaining computational issues following the results

shown here. Further training experiments on neural networks are motivated, to extend this work. Extensions include the following considerations: (1) prediction of longer periods of time of air flow distortions, (2) prediction of more than one time-step ahead (3) benchmarking of data with simpler, non-neural network prediction methods, (4) sparse sampling of data for predictions of more than one step ahead, (5) testing of performance for alternative stopping criteria on training the networks, (6) alternative error-training methods, and (7) specific timing considerations for building a correction device based on the neural network predictions. These are important steps towards the final goal of using neural network predictions to correct optical distortions due to dynamically changing air flow patterns.

5 Appendix A: A Dynamic Neural Network

We have researched the problem of how to utilize the attractors in a dynamic neural network to perform pattern recognition and classification ([PD95]). A random network is constructed with sparse interconnections in a single layer of neurons. A multiplier g can be applied to all of the weights at the same time and, when g is increased, chaotic behavior occurs. An external pattern is then applied to the network as a fixed bias, and a pattern-to-oscillation map can be constructed.

The neural units are simple biologically-inspired nodes, performing a weighted sum followed by a nonlinear squashing function f .

$$a_j(t+1) = f(\sum_{i=1}^N g w_{ji} a_i(t)) + \alpha e_i \quad (10)$$

where g in (10) is the multiplier for all weights in the network, and the weights are randomly assigned with variation $1/k$ where k is the number of randomly selected inputs to each node. E is the fixed external pattern applied as a bias to the network, and α_i is the strength with which the external pattern is applied. This network has previously been studied and theoretically considered ([DCQS93], [DCQS95], [QDS95], [CDQS94], [SCS88]).

The P.I. has developed a method for evoking a pattern-to-oscillation map for this network, where the oscillations are constricted to be either a finite-state (n -state) oscillation or a limit cycle. First, a network with no external pattern ($E=0$) is applied, and g is

increased to produce chaotic behavior. Then an external pattern E is applied. Transients are passed by iterating the network through (8) and (9) above. If the evoked attractor satisfies the oscillation criterion, then the evoked oscillation is the result of the pattern-to-oscillation map for pattern E . If the evoked attractor is too chaotic, then the strength α must be increased for pattern E . If the evoked attractor is a fixed point, then the strength α must be decreased to produce more complex dynamics. Through an algorithm for making successive adjustments to α , the pattern-to-oscillation map can be constructed uniquely for all patterns, given the initial chaotic network. This algorithm has been proposed by the P.I. and constitutes an advance in the development of new dynamic neural networks.

References

- [CDQS94] B. Cessac, B. Doyon, M. Quoy, and M. Samuelides. Mean-field equations, bifurcation map and chaos in discrete time neural networks. *Physica D*, 74:24–44, 1994.
- [DCQS93] B. Doyon, B. Cessac, M. Quoy, and M. Samuelides. Control of the transition of chaos in neural networks with random connectivity. *International Journal Bifurcation and Chaos*, 3(2):279–291, 1993.
- [DCQS95] B. Doyon, B. Cessac, M. Quoy, and M. Samuelides. Mean-field equations, bifurcation map and chaos in discrete time, continuous state, random neural networks. *Acta Biotheoretica*, 43:169–175, 1995.
- [DD91] S. P. Day and M. Davenport. Continuous-time temporal back-propagation with adaptive time delays. Neuroprose archive, Ohio State University. Accessible on Internet via anonymous ftp on archive.cis.ohio-state.edu, in pub/neuroprose/day.tempora.ps August, 1991., 1991.
- [DD93] S. P. Day and M. R. Davenport. Continuous-time temporal back-propagation with adaptive time delays. *IEEE Trans. on Neural Networks*, 4(2):348–354, March 1993.
- [HW92] P. Haffner and A. Waibel. Multi-state time delay neural networks for continuous speech recognition. In S. J. Hanson J. E. Moody and R. P. Lippmann, editors, *Advances in Neural Information Processing Systems*, volume 4, pages 135–142, Denver 1992, 1992. Morgan Kaufmann, San Mateo.
- [LDL92a] D.-T. Lin, J. E. Dayhoff, and P. A. Ligomenides. Adaptive time-delay neural network for temporal correlation and prediction. In *Intelligent Robots and Computer Vision XI: Biological, Neural Net, and 3-D Methods, Proc. SPIE*, volume 1826, pages 170–181, Boston, November, 1992.
- [LDL92b] D.-T. Lin, J. E. Dayhoff, and P. A. Ligomenides. A learning algorithm for adaptive time-delays in a temporal neural network. Technical Report SRC-

TR-92-59, Systems Research Center, University of Maryland, College Park, Md 20742, May 15 1992.

- [LDL92c] D.-T. Lin, J. E. Dayhoff, and P. A. Ligomenides. Trajectory recognition with a time-delay neural network. In *International Joint Conference on Neural Networks*, volume 3, pages 197–202, Baltimore, 1992. IEEE, New York.
- [LDL94] D.-T. Lin, J. E. Dayhoff, and Panos A. Ligomenides. Prediction of chaotic time series and resolution of embedding dynamics with the ATNN. In *World Congress on Neural Networks*, volume 2, pages 231–236, San Diego, CA, 1994. INNS Press, New York.
- [LDL95] D.-T. Lin, J. E. Dayhoff, and Panos A. Ligomenides. Trajectory production with the adaptive time-delay neural network. *nn*, 8(3):447–461, 1995.
- [LDR95] D.-T. Lin, J. E. Dayhoff, and C. L. Resch. Target discrimination with neural networks. Technical Report ISR-TR-95-54, Institute for Systems Research, University of Maryland, College Park, MD 20742, 1995.
- [Lun96] T. G. Luna. Linear stochastic estimation of optical beam deflection through a heated round turbulent jet. Master's thesis, University of New Mexico, Department of Mechanical Engineering, Albuquerque, NM, 1996.
- [MMC⁺95] L. McMackin, B. Masson, N. Clark, K. Bishop, R. Pierson, and E. Chen. Hartmann wave front sensor studies of dynamic organized structure in flow-fields. *AIAA Journal (American Institute of Aeronautics and Astronautics)*, 33(11):2158–2164, 1995.
- [MVF95] L. McMackin, D. G. Voetz, and J. S. Fender. Chaotic attractors in the transition region of an air-jet flow. ., 1995.
- [PD95] P. J. Palmadesso and J. E. Dayhoff. Attractor locking in a chaotic network: stimulus patterns evoke limit cycles. *Proceedings of World Congress on Neural Networks (WCNN)*, 1:254–257, 1995.
- [QDS95] M. Quoy, B. Doyon, and M. Samuelides. Dimension reduction by learning in a discrete time chaotic neural network. *Proceedings of World Congress on Neural Networks (WCNN)*, 1:300–303, 1995.
- [SCS88] H. Sompolinsky, A. Crisanti, and H. J. Sommers. Chaos in random neural networks. *Phys. Rev. Let.*, 61(3):259–262, 1988.
- [Wai89] A. Waibel. Modular construction of time-delay neural networks for speech recognition. *Neural Computation*, 1:39–46, 1989.
- [WHH⁺89] A. Waibel, T. Hanazawa, G. Hinton, K. Shikano, and K. Lang. Phoneme recognition using time-delay neural networks. *IEEE Trans. on Acoust., Speech, Signal Processing*, 37(3):328–339, 1989.

**Analysis of Complex Cavities Using
The Finite Difference Time Domain Method**

**Ronald R. DeLyser
Assistant Professor of Electrical Engineering
Department of Engineering**

**University of Denver
2390 S. York Street
Denver, CO 80208-0177**

1

**Final Report for:
Summer Faculty Research Program
Phillips Laboratory**

**Sponsored by:
Air Force Office of Scientific Research
Bolling Air Force Base, Washington, D.C.
And
Phillips Laboratory, WSA
Kirtland AFB, N.M.**

September, 1996

Analysis of Complex Cavities Using
The Finite Difference Time Domain Method

Ronald R. DeLyser
Assistant Professor of Electrical Engineering
Department of Engineering
University of Denver

Abstract

The Finite Difference Time Domain method has been used to analyze a Celestron 8 telescope and a satellite sensor. The specific program used, TEMAC3D (Temporal ElectroMagnetic Analysis Code), was written by John H. Beggs of Mississippi State University. TEMAC3D along with its graphical user interface, XTEAR (X-window Temporal Electromagnetic Analysis and Response), was ported to an IBM RS6000 at the University of Denver. Other supporting software, TSAR (Temporal Scattering And Response) from Lawrence Livermore National Laboratory and BRL-CAD, a computer aided design package from Ballistic Research Laboratory resided on SUN Workstations at the Satellite Assessment Center at Phillips Laboratory, Kirtland AFB, NM. BRL-CAD and TSAR are currently in the process of being ported to the IBM RS6000.

The Celestron-8 telescope was modeled as an antenna and as a scatterer. TEMAC3D results for the antenna model (aperture field and radiation plots) compare favorably to previous studies ([2] and [3]) using the Finite Element Method. Another sensor was modeled and time domain response at specific locations within the sensor were determined. The time domain information was Fast Fourier Transformed to the frequency domain to determine frequency response of the sensor. Due to a problem with possible instability of TEMAC3D for this model, future studies will investigate using a larger number of pad cells and adding a realistic finite conductivity to the Germanium lens and filters. The inverse problem (the radiation problem) will then be done to determine sensitive angles of incidence.

Introduction

The analysis of the Celestron-8 Telescope began on February 1, 1995, and was funded by AFOSR contract F49620-C-0063. The objective of this contract was to perform numerical analysis on this telescope (Figure 1). Analysis continued using the Method of Moments (MoM) and the Finite Element Method (FEM) for rest of 1995 and the first quarter of 1996. The programs used for these analyses were CARLOS-3D [1] (MoM) and the High Frequency Structure Simulator (HFSS), a commercially available FEM program from Hewlett Packard. Results of these analyses are reported in [2], [3] and [4].

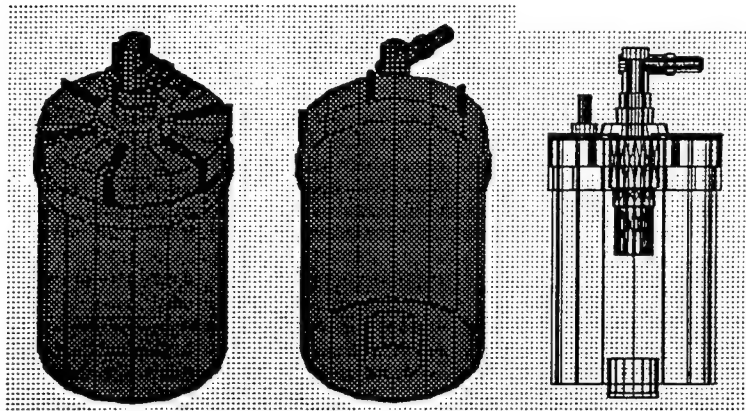


Figure 1. Celestron-8 telescope.

The fundamental quantity that was to be calculated using CARLOS-3D was quality factor of the cavity. The equation that was used was the classic one given by [5][6]

$$Q = \omega \frac{U}{P} \quad (1)$$

where ω is the angular frequency, U is the total energy in the cavity and P is the power exiting the cavity. Problems with near field calculations in CARLOS-3D which were needed for calculation of U and P were discovered and reported in [2] and [4]. HFSS was then explored as a possible alternative. Since scattering problems could not be done with HFSS, the problem solved with this software was the inverse of the scattering problem, the radiation (antenna) problem. The cavity was excited from an internal port and the port scattering parameter and antenna radiation properties were studied. Problems with HFSS included memory and disk space requirements, and asymmetrical mesh generation which produced asymmetric radiation patterns in planes where they should be symmetrical. These problems are reported in [2] and [3]. The inherent problems with CARLOS-3D and the computational expense of HFSS suggested that yet another method may be more suited to our studies. We decided to explore the Finite Difference Time Domain (FDTD) method.

Temporal ElectroMagnetic Analysis Code (TEMAC3D) and Supporting Codes¹

TEMAC3D [7] is a FDTD code developed by John H. Beggs of Mississippi State University for use in modeling High Power Microwave antennas, ultra-wideband antennas and for electromagnetic coupling calculations. It is a FORTRAN code which is based on the three dimensional implementation of the FDTD method [8] and has the following capabilities: (1) treatment of perfectly conducting, lossy dielectric, and lossy magnetic materials; (2) second order Liao outer radiation boundary condition; (3) transient near to far field transformation capability to obtain scattered far fields at multiple scattering angles; (4) band limited, Gaussian, hyperbolic secant, unit step, hyperbolic cosine unit step and ramped sinusoid incident pulses with arbitrary incidence directions and polarization. (5) Custom pulse or raw time-domain data excitation. (6) Plane wave or point source incident excitation; (7) near field sampling capability anywhere within the computational domain; (8) diagnostic output files; (9) standardized input deck for reading simulation variables; (10) field sampling is specified by character strings; (11) benchmark problems; (12) C-preprocessor capability; and (13) steady state antenna calculations, including a steady state near to far field transformation.

A suite of peripheral software is needed to generate solid models, generate the Finite Difference (FD) mesh, view the mesh for consistency, generate the problem name list and header files, and view the results of the analysis. The solid model geometry file is generated by BRL-CAD version 4.4 which is available from Ballistics Research Laboratory, Aberdeen proving Ground, MD. This file is then used as input to ANASTASIA, a component of TSAR, Temporal Scattering And Response, from Lawrence Livermore National Laboratory, CA. ANASTASIA generates a mesh given the number of "pad" cells² and the size of the cell. IMAGE (another component of TSAR) is used to view the mesh (a few examples will be given below) to be sure that you really get what you intended. This mesh file is then an input for XTEAR (X-window Temporal Electromagnetic Analysis and Response) [7] which is a graphical user interface designed for input of all relevant parameters for the FDTD simulations using TEMAC3D. (Again, specific examples are given below.) Since XTEAR was written using the scripting language TCL/TK, these software packages (version 7.3 of TCL and version 3.6 of TK) also have to be installed on the computer used to run XTEAR. Finally, software is needed to view output fields as a function of time, frequency and/or position, generate far-field scattering and/or radiation plots, and do Fast Fourier Transforms (FFT). FORTRAN programs were provided by John Beggs for far zone processing and radiation plots. I used Mathcad 6.0 [9] for doing the FFTs, and spatial, temporal and frequency dependent field visualization, and DeltaGraph Pro 3.5 [10] for radiation plots.

¹ I will not go into details of the FDTD method or choices made for meshes, excitation or post processing. For a detailed discussion of these issues, see [8].

² Pad cells occupy the space between the outermost model cells and the outermost cells of the problem space which implement the absorbing boundary conditions.

The computer where we installed and ran TCL/TK, TEMAC3D and XTEAR³ is at the University of Denver (DU) and is an IBM RS6000 model 570 Powerstation with 512 MBytes of RAM and a 6.5 GBytes of disk space. This was also the machine that was used for the HFSS and CARLOS-3D analyses so that comparisons of the FDTD method with the FEM method can be readily made⁴. I was unable to install BRL-CAD at DU (contrary to the BRL literature, the IBM is not supported) and therefore, could not install TSAR (BRL-CAD is necessary for TSAR.) I therefore used BRL-CAD, ANASTASIA and IMAGE on a SUN Workstation at the Satellite Assessment Center at Phillips Lab. Mesh files generated at Phillips Lab were then sent to DU for processing by XTEAR and numerical analysis by TEMAC3D. BRL personnel are currently working on porting BRL-CAD to an IBM RS6000 at Phillips Lab.

The Model for the Celestron 8 Telescope

Figure 2 shows an FDTD mesh for the Celestron-8 modeled as an antenna and a detail showing the change for the Celestron-8 modeled as a scatterer. (See [2] for further details on this telescope and our earlier study.) The mesh shown is only for the material that is not free space and includes a probe at center height that simulates one of the

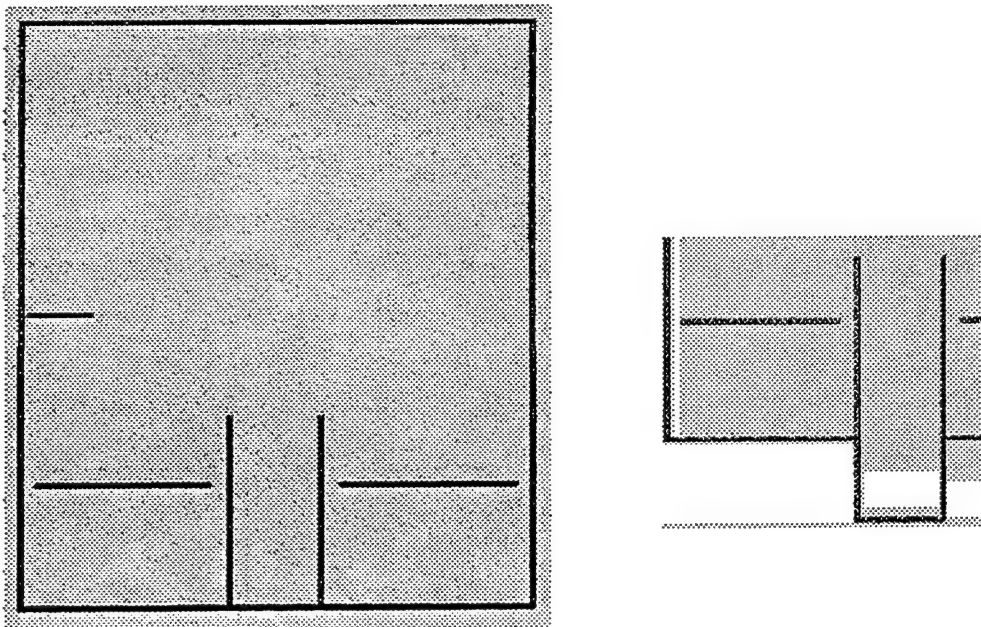


Figure 2. The FDTD mesh for the Celestron 8 telescope modeled as an antenna.

³ These installations were not straight forward. Information on porting this software to the IBM RS6000 is available from the author or from Capt. Tim Fromm, PL/WSTS, Kirtland AFB, NM 87117-5776.

⁴ Comparisons with CARLOS-3D are not made because time spent investigating problems with the code [2] limited our use to frequencies only up to 2 GHz.

tests reported in [2] and [3]. The other mesh does not have a probe and simulates tests for the scattering problem. The extent of the problem space is a rectangular parallelepiped completely enclosing the model plus at 5 pad cells in each direction. The radii of curvature for the primary (lower) and secondary (center in the upper plane) mirrors are not simulated since the resulting mesh will not resolve this. This particular model has cubic cells measuring 2 mm on a side. The problem space is $130 \times 130 \times 178$ cells. An estimate of the RAM needed to accommodate this problem is 30 times the number of cells plus 10 % overhead. This comes to approximately 99 MBytes of RAM. The cells should be no larger than 1/10 of a wavelength so that in the dielectric (dielectric constant of 3.4) window (upper plane) which corresponds to a frequency of ~ 8.1 GHz. Another model was generated with cell sides of 1.15 mm and is expected to take ~ 500 MBytes of RAM. That model will be good for frequencies up to ~ 25 GHz. The HFSS model, which used all of the computational resources, had a high frequency limit of 5 GHz.

The Model for the Sensor

I was also tasked to analyze a sensor from a satellite of which a drawing of the cross-section is shown in Figure 3. A solid model from measurements of this drawing was made. Various views and dimensions are shown in Figures 4 - 6. The detail of these drawings cannot be captured with a reasonably sized mesh⁵ so some further simplifications were made: (1) Rounded corners have been squared. This makes drawing the model with BRLCAD a reasonable task. The meshing process will do this in the long run anyway. (2) The short, narrow gap between the central cavity region and the lower cavity regions remains. This is because some energy may propagate through this gap due to its shortness. (3) The long narrow gap between the lower cavity regions has been closed. I view this gap as a waveguide below cutoff and little if no energy will propagate through it due to its length. (4) Short, narrow gaps in the cavity areas are filled with metal. These areas add little volume to the cavity and are so narrow as to prevent energy propagation.

The layered area in the center of the drawing has been modified to show details of the filter area (the top most layer) which is composed of a metal frame and accompanying filters and detectors (Figures 7 - 9). Below the filters is an air gap. Below that is a layer of Mylar upon which the detectors (bismuth/tellurium thermopiles - Figure 8) are mounted. Since the resolution of the mesh will be 1 mm and the filter, air gap and Mylar lie in slanted regions, I decided to make the Mylar and air regions 1.5 mm thick, and the filter region 2 mm thick. This will prevent the regions from touching each other during the meshing process. The center cross-section of the mesh is shown in Figure 10. A close-up of the sensor area is shown in Figure 11. Note that the large metal areas below the sensor are hollowed out. This ultimately results in a much smaller mesh file since the background is free space

⁵ The lens and filters are made of Germanium with a dielectric constant of 14. A 1 mm mesh size then will be good for frequencies up to ~ 8 GHz and require ~ 180 MBytes of RAM. A model with a .7 mm mesh size will be good to ~ 11.5 GHz and take ~ 500 MBytes of RAM.

and that does not get specified in the file. The model that I ran with TEMAC3D had this area filled in which may be computationally more efficient since the program sets the total fields to 0 in a perfect conductor.

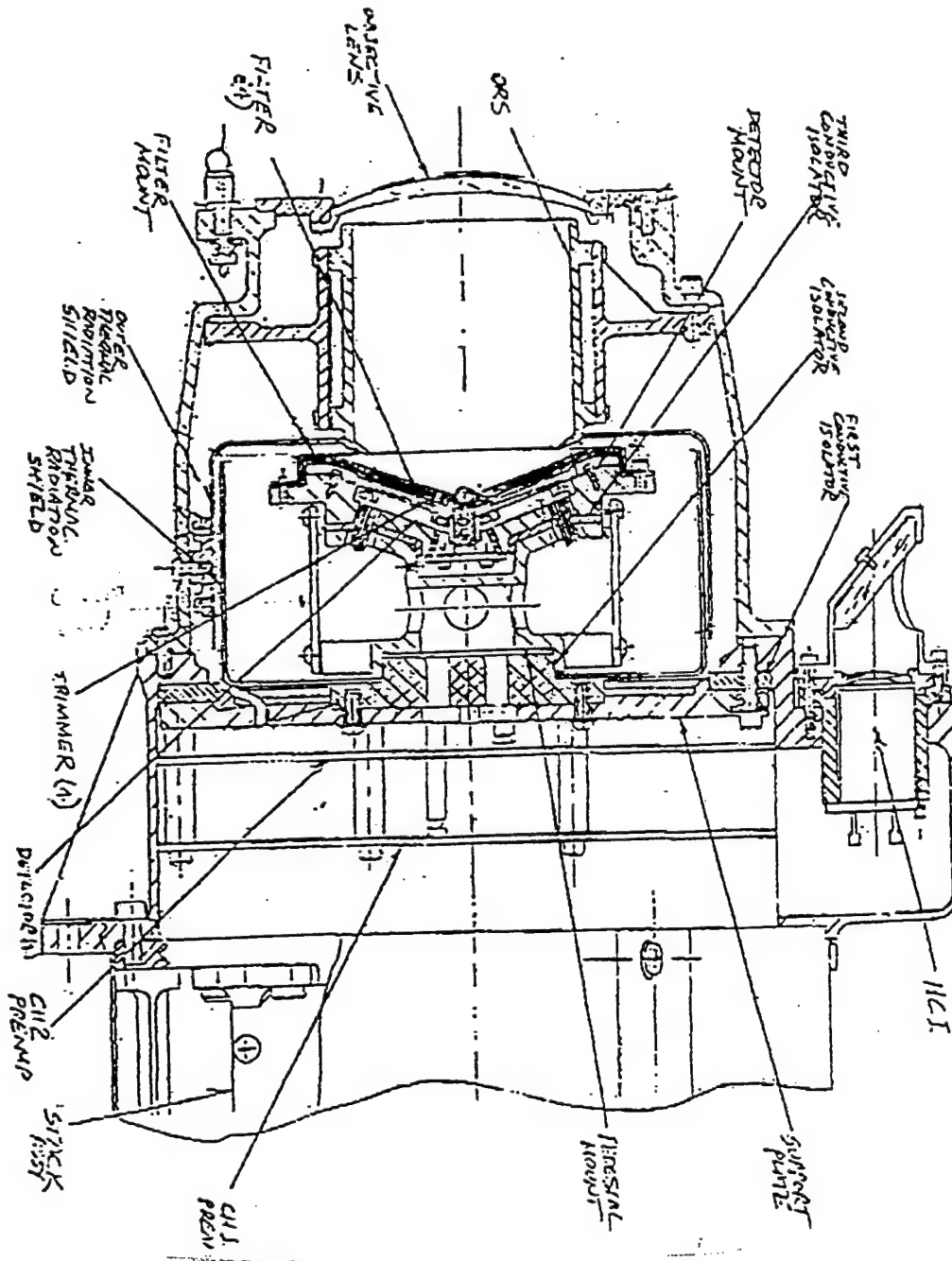


Figure 3. The cross-section drawing of the sensor.

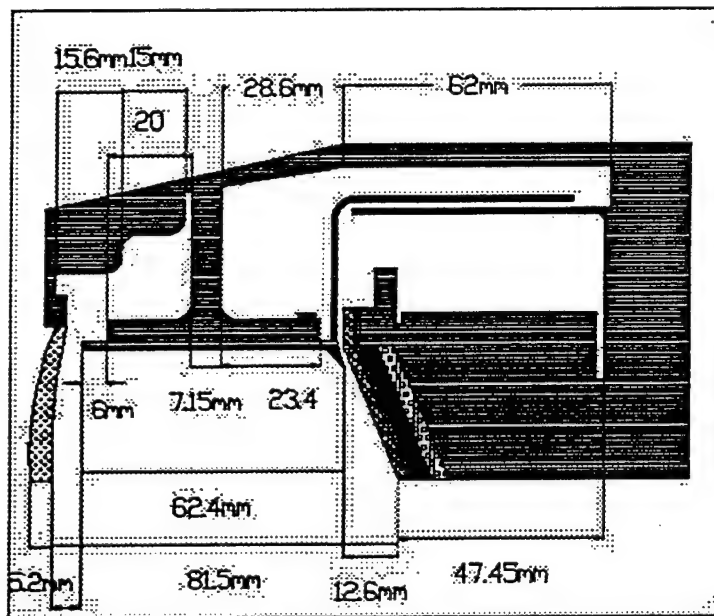


Figure 4. Dimensioned drawing of the sensor.

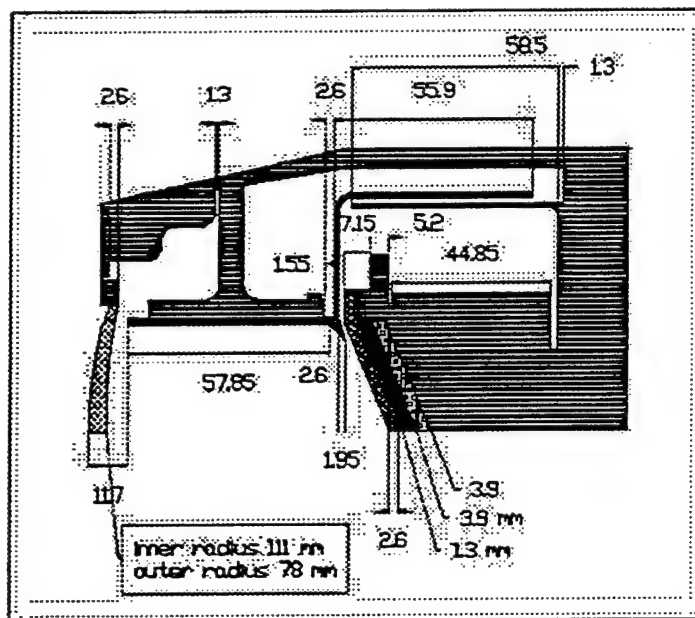


Figure 5. Dimensioned drawing of the sensor. (The lens radii were later determined to be 163 mm and 96 mm.)

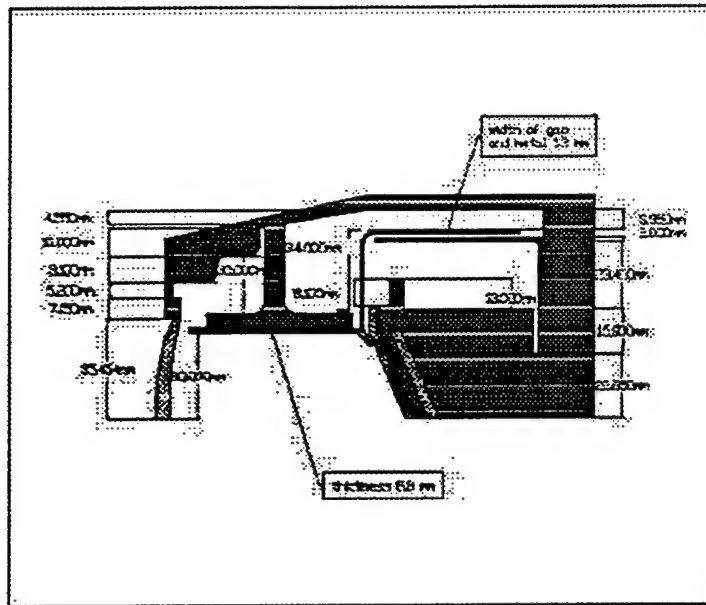


Figure 6. Dimensioned drawing of the sensor.

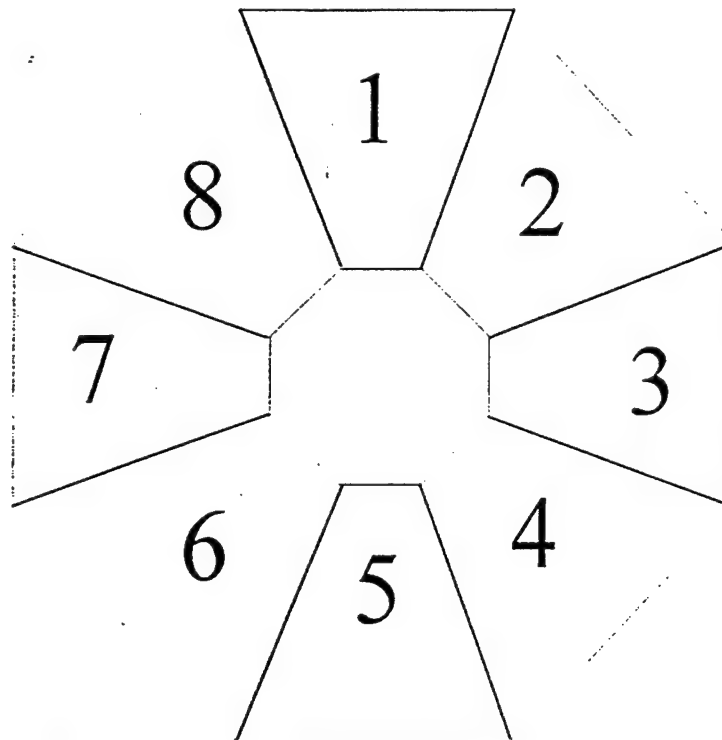


Figure 7. Octagonal filter frame.

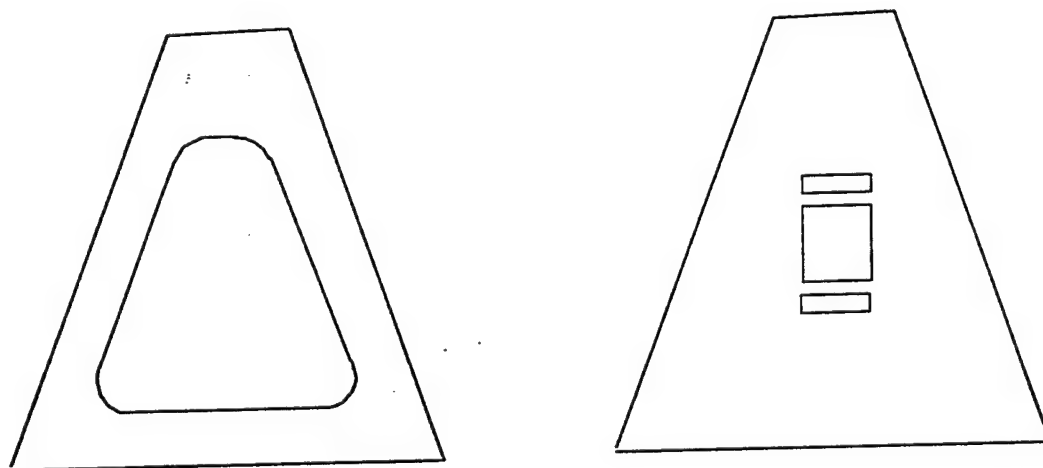


Figure 8. Filter and thermopile detectors (8 total.)

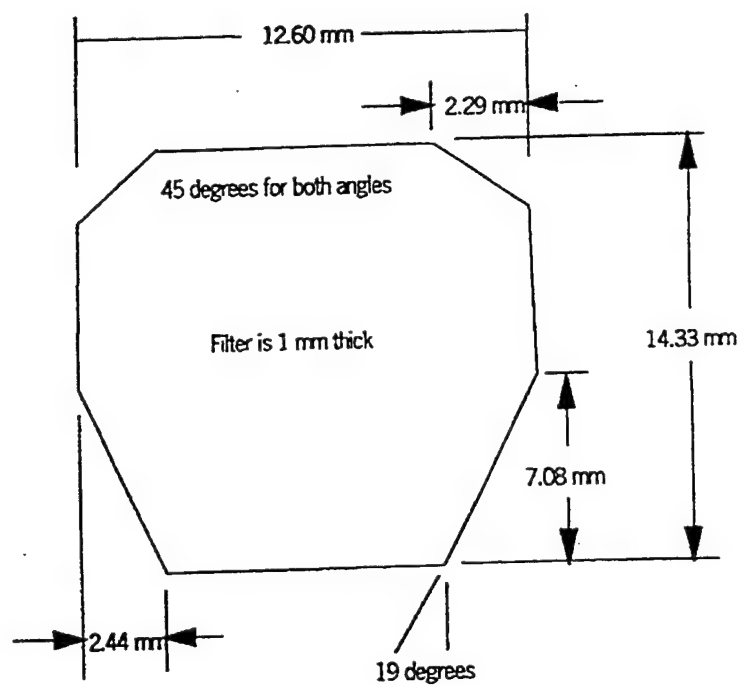


Figure 9. Filter dimensions.

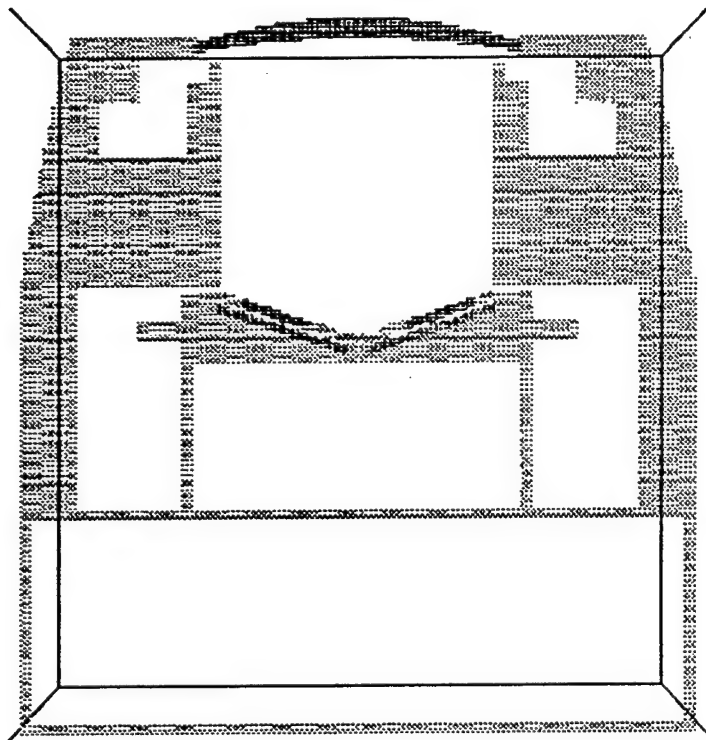


Figure 10. Cross-section of the sensor mesh.

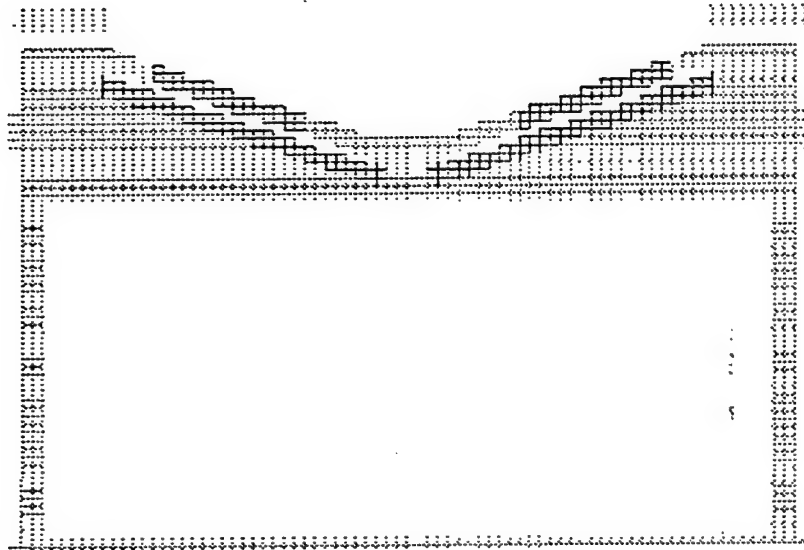


Figure 11. Close-up of the sensor mesh.

Results for the Celestron-8

A ramped sine wave of appropriate frequency was used for the probe excited Celestron-8 model. It was ramped to steady state over a time period of 5 cycles. The simulations were run for 2048 time steps at 3.85 psec time intervals. I used a "slice sensor" in the aperture to output the total electric fields in that plane. The aperture fields for the 1.395 GHz and 1.82 GHz resonances (these frequencies were chosen based on measured data reported in [3]) are shown in Figures 12 and 13. Qualitatively, the plots compare well with the FEM analysis on a comparably sized open cylinder using HFSS [3]. However, for this analysis, the fields are much stronger on the side of the aperture where the probe is located. The excitation of the probe in the FDTD analysis is different from that for the FEM analysis using HFSS. In the FDTD analysis, an electric field excitation along the x-axis in the cell between the probe and the side of the cylinder is specified. In the FEM model, the excitation is modeled as the center conductor of a coaxial cable. As such, the direction of the electric field is in the plane of the cylinder. Another FDTD model without the probe but with the same excitation yielded similar field patterns with lower magnitudes.

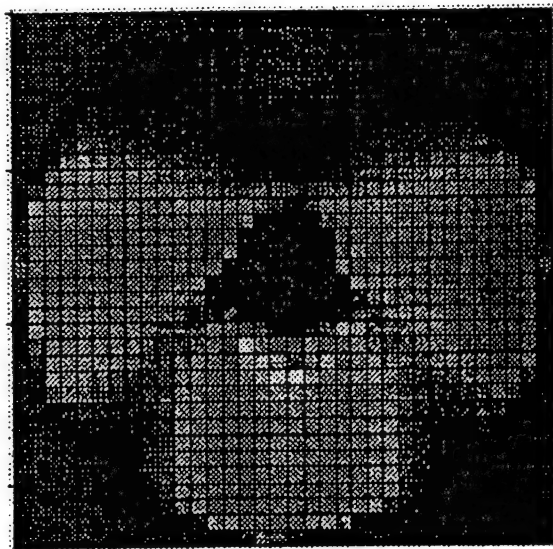


Figure 12. Celestron-8 aperture fields at 1.395 GHz.

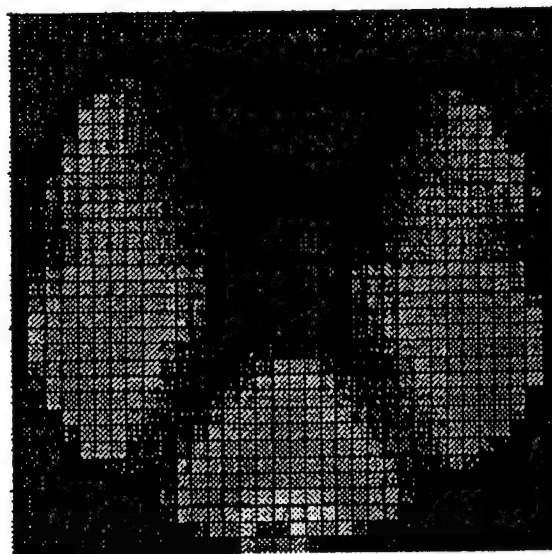


Figure 13. Celestron-8 aperture fields at 1.82 GHz.

Radiation plots for these two frequencies are shown in Figures 14 and 15. Care must be taken when comparing these results with those in [3]. The radiation plots in [3], in addition to being for an open cylinder are for the magnitude of the electric fields versus angle, while these results are for antenna gain versus angle for the two different polarization. The radiation plots for the HFSS results are also not to be trusted because of the fact that they are not symmetric in the $\phi=90^\circ, 270^\circ$ plane (the plane perpendicular to the probe plane). This problem is due to the non-uniform adaptive meshing scheme used in HFSS. Notice that we do have symmetry in this plane (the yz plane) for the FDTD analysis. Obviously, we have a symmetrical mesh in the FDTD model.

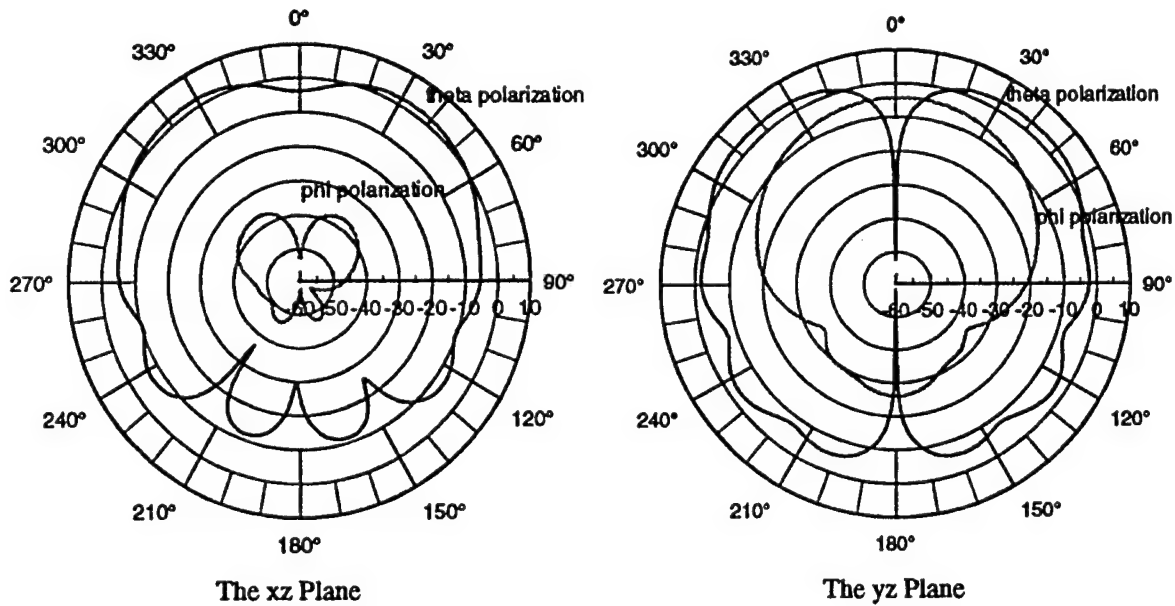


Figure 14. Celestron-8 radiation plots at 1.395 GHz.

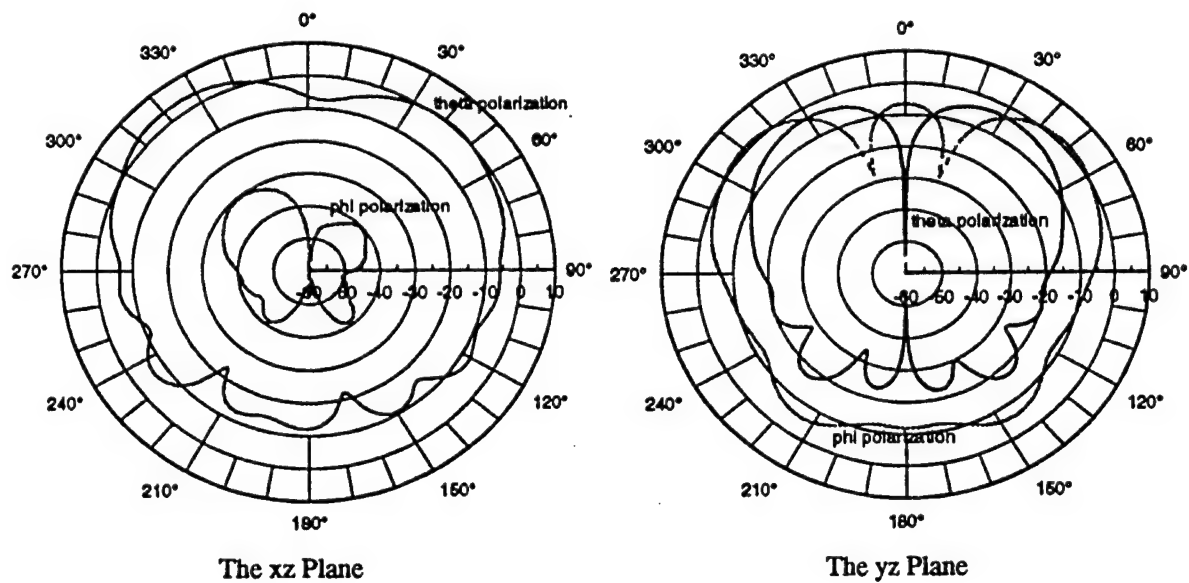


Figure 15. Celestron-8 radiation plots at 1.82 GHz.

The excitation for the scattering problem was an x-polarized plane wave incident on the top (see Figure 2) of the telescope. The time domain excitation is a Gaussian pulse with a rise time of 85.88 psec, a half-power pulse width of 84.78 psec, a truncation pulse width of 582.0 psec and a time step of 3.849 psec. This gives an 100 dB frequency limit of 15 GHz. The frequency response for this pulse is shown in Figure 16.

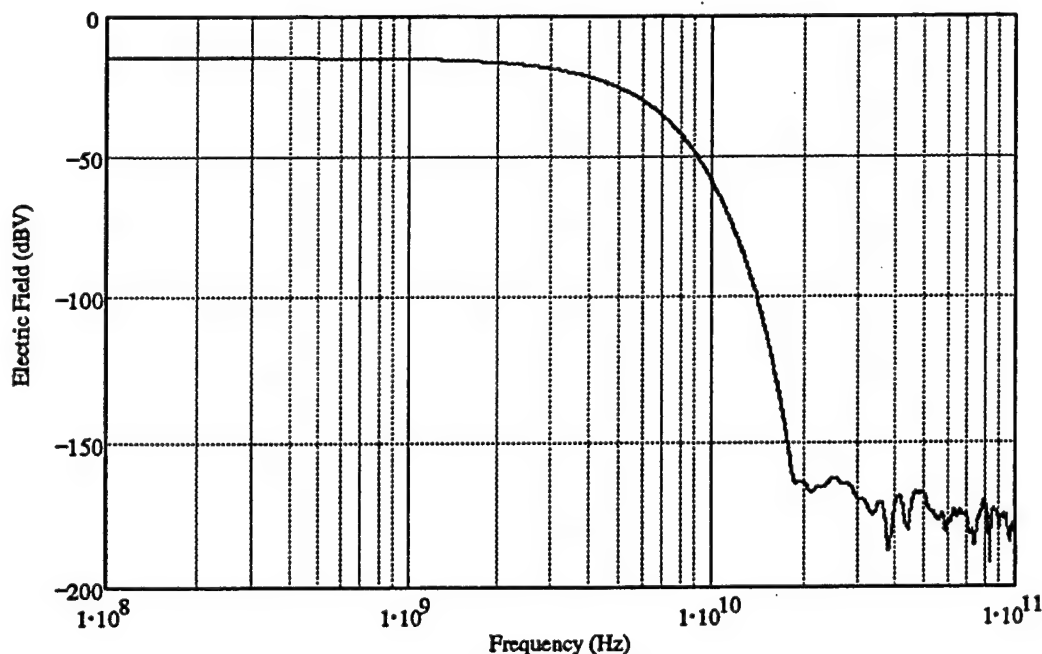


Figure 16. Frequency domain plot of the plane wave excitation for the Celestron-8.

Field point sensors were placed in the lower extension to the small cylinder 25 mm from the lower, closed end. These "field sensors" allow for the output of a number of quantities of interest. Sensors were also placed at the location where the probe excited modes had its point source excitation. Figures 17, 18 and 19 show time and frequency domain plots of the x component of the electric fields at these two locations. The time domain plots show the characteristic exponential decay of the fields in a resonant cavity. Figure 17 clearly shows the high frequency content of the signal in the eye piece location versus the lower frequency content (Figure 18) of the probe location in the large cylinder region of the telescope. Of course this also shows up in the frequency response plot of Figure 20 where smaller cylinder cutoff frequency is indicated by the sharp rise in gain at ~ 4.3 GHz. It is clear that the large cylindrical region of the telescope behaves like a large circular waveguide (cutoff is at ~ 750 MHz) which has a lower cutoff frequency than the smaller diameter waveguide region leading to the eye piece.

Figure 20 shows the results of tests [5] where the telescope was excited by a transmitting antenna placed 40.0 inches in front of the aperture. A small horn antenna was mounted at the bottom of the smaller inner cylinder where the eyepiece is normally attached. Unfortunately, the location of the transmitting antenna was too close for true plane wave excitation, but the general trend of an increasing gain which levels out above ~ 7 GHz for the testing is compared with the same trend leveling out at ~ 9 GHz for the numerical analysis. Also recall that the grid for this model is only strictly accurate to ~ 8.1 GHz. Results for frequencies above 10 GHz should not be trusted. Investigations are planned for a higher frequency model.

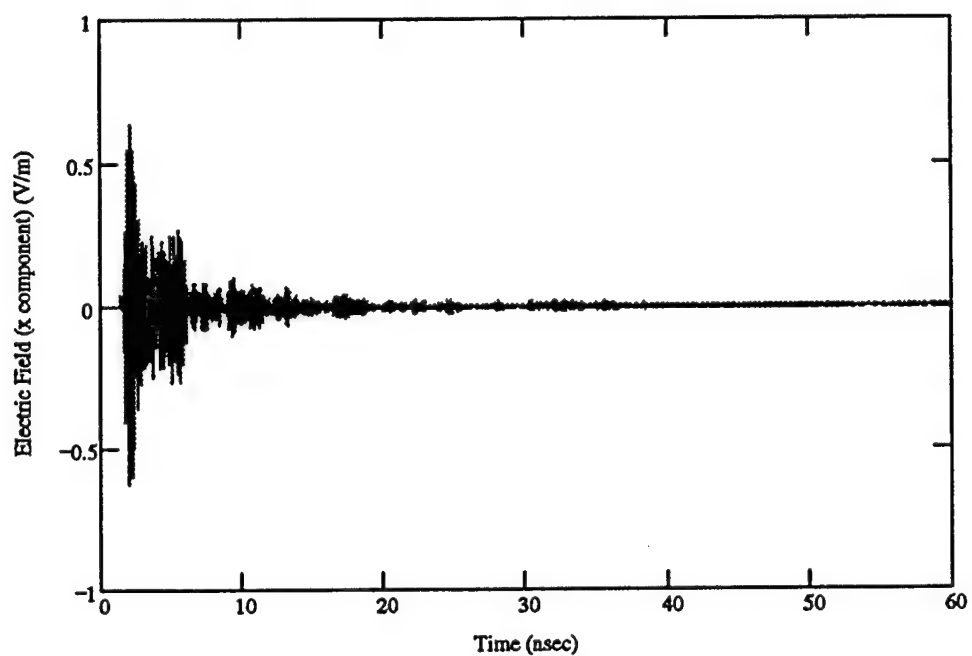


Figure 17. Electric field (x component) at the eye piece location of the Celstron-8.

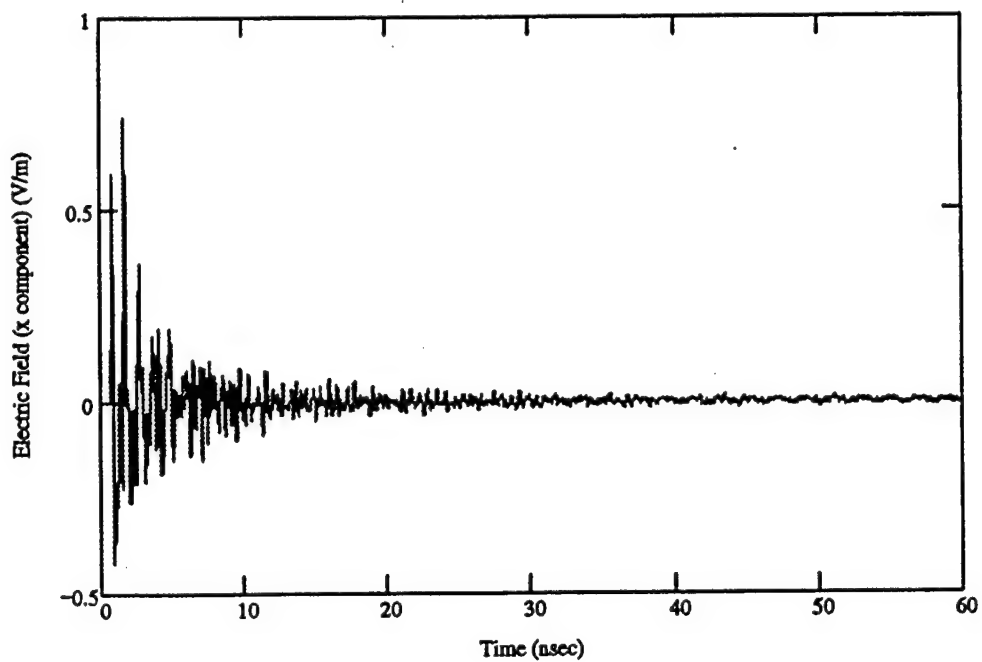


Figure 18. Electric field (x component) at the probe location of the Celstron-8.

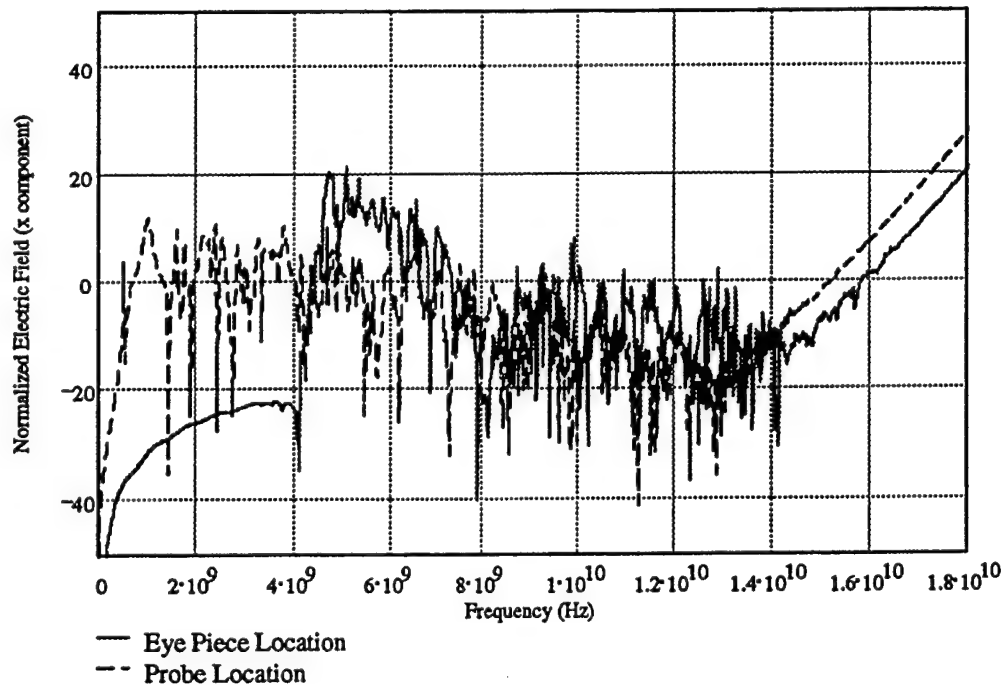


Figure 19. Frequency response of the plane wave excitation of the Celestron-8 model.

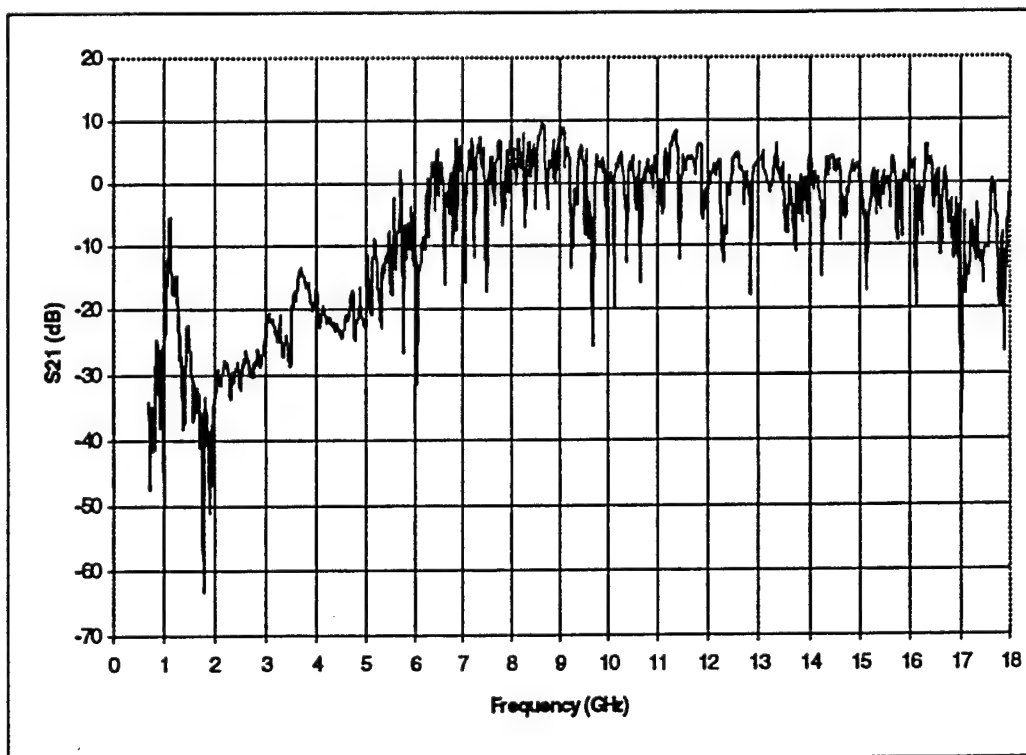


Figure 20. Test results as reported in [5].

Results for the Sensor

The sensor model was illuminated from the top (see Figure 10) with a y-polarized plane wave. The time domain excitation is a Gaussian pulse with rise time of 70.3 psec, half-power pulse width of 69.4 psec, truncation pulse width of 476.5 psec and a time step of 1.924 psec. This gives an 80 dB frequency limit of 16.4 GHz. The frequency response for this pulse is shown in Figure 21. Field point sensors were put in the air region between one of the filters and the Mylar substrate. For these sensors, I elected to output the total electric fields in the x, y and z directions. From this information, I calculated the field tangential to the Mylar layer.

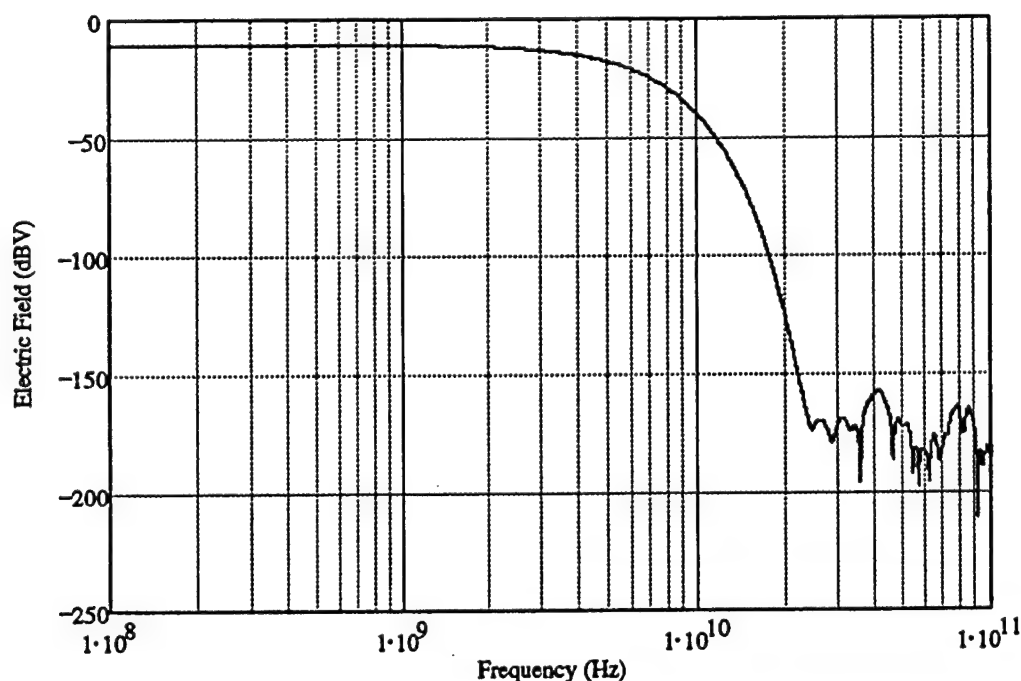


Figure 21. Frequency domain plot of the plane wave excitation for the sensor model.

An initial run with 1024 time steps took ~ 5 hours and showed substantial ringing of the fields. This is to be expected. Because of the high dielectric constant of the lens (14), the cavity will not have as low a Q as that of the Celestron-8. A longer run of 32,768 time steps (~ 155 hours) yielded a time history for the tangential field shown in Figure 22. The FFT was taken of the entire history and is shown in Figure 23. The fact the time domain signal indicates that the energy is still building up in the cavity was a source of concern. The magnitude of the time domain response of the order of 10^7 V/m indicates that there is a problem with this simulation. It is clear that, from an energy standpoint, this is not physically realizable. Discussions with colleagues lead to some possible causes that will have to be investigated in follow-on studies: (1) There may not be enough pad cells; I have used 5 in this simulation. Increasing the amount to 10 may fix the problem. (2) The conductivity of the Germanium

material has been ignored. A resistivity of 40 ohm-cm will be used in an improved model. Again, this loss may improve stability. (3) We feel that this problem is strictly with this model because of the similar simulation which was done on the Celstron-8 reported above. The dielectric window in this telescope is Plexiglass with a dielectric constant of 3.4. This resulted in a reduced Q of the cavity, which contributed to the stability of the simulation.

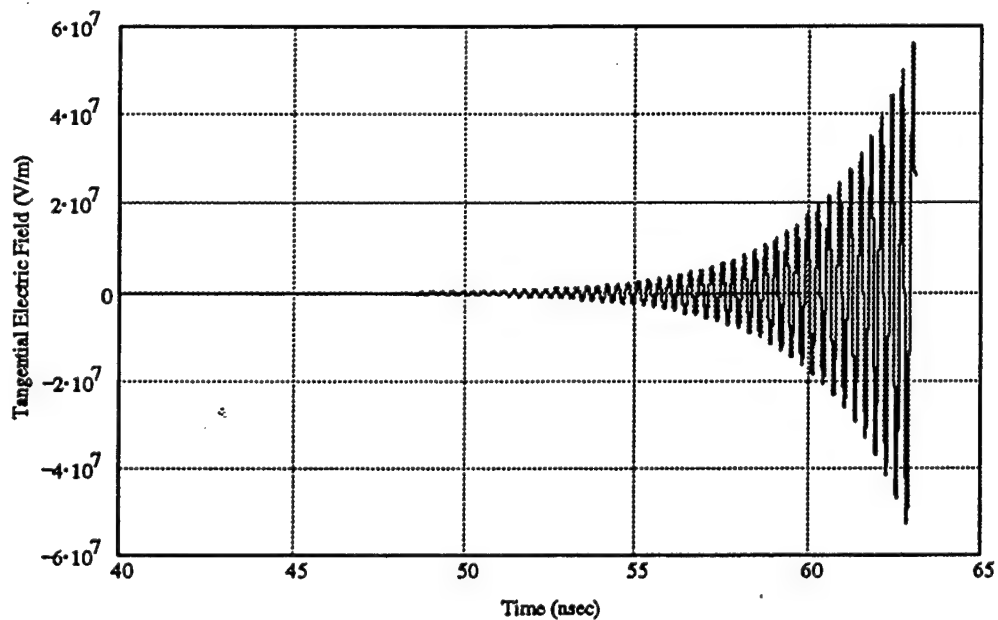


Figure 22. Time domain response for the short pulse - 32,768 time steps.

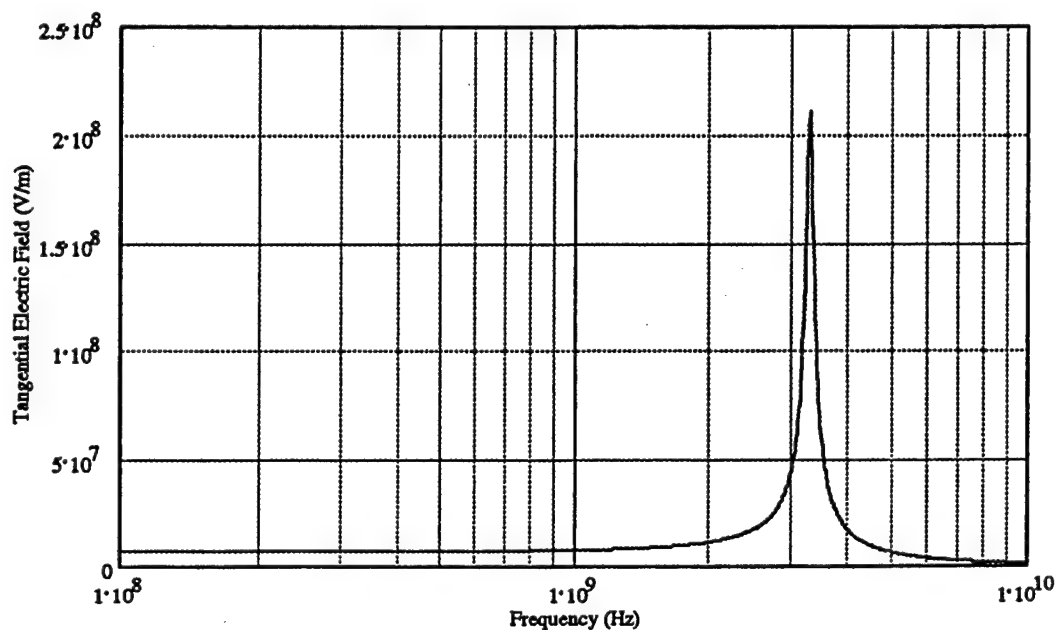


Figure 23. Frequency domain response for the short pulse - 32,768 time steps.

Conclusions and further areas for study

CARLOS-3D is an efficient code for radar cross-section, however it cannot be used to calculate fields inside a cavity [2, 4]. HFSS is an efficient code for calculating fields inside a cavity but has problems with mesh generation which produces suspicious far-field radiation results. It also cannot be used for scattering problems. In general, other MoM and FEM codes suffer from the same limitations. The preliminary results reported here show that TEMAC3D (assuming that the instability problem can be fixed) is an effective tool for analysis of complex cavities. It can be used to treat a cavity as a scatterer in order to find frequency response of a particular field location inside the cavity. Once frequencies of interest are identified, TEMAC3D can be used to analyze the cavity as a radiator (antenna with a specified point source internal to the cavity) in order to find angles of incidence that are particularly sensitive. Once these are found, the frequency response can be repeated at these angles.

Future work should continue on the Celestron-8 telescope and the sensor using TEMAC3D with plane wave excitation using a narrower pulse, producing a wider frequency response, and using meshes with smaller cells and possibly more pad cells. Models that will require ~500 MBytes of RAM have been generated which will be good to ~25 GHz for the Celestron-8 and ~ 11.5 GHz for the sensor. The process of generating a frequency response at a point of interest inside the cavities, followed by radiation models at the most sensitive frequencies, followed by frequency response models at the sensitive angles should be pursued. Where possible, this information should be used to define test parameters for future experiments on the sensor and in the case of the Celestron-8 to compare to test data already generated.

Some improvements to TEMAC3D could be made: (1) Implementation of perfect magnetic and perfect electric boundaries would allow the user to specify ground planes or apply symmetry to problems, thus reducing computational requirements. (2) The capability of saving all information periodically would allow the user to restart the problem from the last saved time step. This would be valuable in the case of cavity problems where the problem has not been run long enough for the fields to "ring down" or for the case of a power outage or machine lock-up. (3) Adapting the program for parallel processing would speed up the simulation significantly.

REFERENCES

- [1] J.M. Putnam, L.N. Madgyesi-Mitschang and M.B Gedera, CARLOS-3D™ Three Dimensional Method Of Moments Code, McDonnell Douglas Aerospace-East, December 1992.
- [2] R. R. DeLyser and P. Ensaf, "Analysis To Determine The Quality Factor Of A Celestron-8 Telescope", Final Report for the Summer Faculty Research Program, Sponsored by the Air Force Office of Scientific Research and Phillips Laboratory, September, 1995.
- [3] R. R. DeLyser and H. Pohle, "Finite Element Method Analysis of the Celestron-8 Telescope," *The Twelfth Annual Review of Progress in Applied Computational Electromagnetics*, Naval Postgraduate School, Monterey, CA, 18-22 March, 1996.
- [4] R. R. DeLyser, P. Ensaf and P. McDaniel, "Method of Moments Analysis of the Celestron-8 Telescope," *The Twelfth Annual Review of Progress in Applied Computational Electromagnetics*, Naval Postgraduate School, Monterey, CA, 18-22 March, 1996.
- [5] R. R. DeLyser and P. Ensaf, "Analysis to Determine the Quality Factor of a Complex Cavity," Final Report for the Summer Faculty Research Program, Sponsored by the Air Force Office of Scientific Research and Phillips Laboratory, September, 1994.
- [6] R. R. DeLyser, "An Analysis Approach to Determine Quality Factors of Large , Complex Cavities," Final Report for the Summer Faculty Research Program at the Phillips Laboratory, Sponsored by the Air Force Office of Scientific Research, September, 1993.
- [7] John H. Beggs, James D. Letterio and Sydney A. Blocher, Jr., *User Manual for XTEAR and TEMAC3D Computational Electromagnetic Time-Domain Codes*, available from Sydney A. Blocher, Jr., Phillips Laboratory/WSM, 3550 Aberdeen Ave. SE, Kirtland AFB, NM 87117.
- [8] K. S. Kuntz and R. J. Luebbers, *The Finite Difference Time Domain Method for Electromagnetics*, CRC Press, Boca Raton, FL, 1993.
- [9] Mathcad Plus 6.0, MathSoft, Inc., 101 Main St., Cambridge, MA 02142, 1995.
- [10] DeltaGraph Pro 3.5, DeltaPoint, Inc., 2 Harris Court Suite B-1, Monterey, CA 93940, 1995.

EVALUATION OF ENGINE-RELATED FACTORS
INFLUENCING CONTRAIL PREDICTION

Andy Detwiler
Research Professor
Institute of Atmospheric Sciences

South Dakota School of Mines and Technology
501 East Saint Joseph Street
Rapid City, SD 57701-3995

Final Report for:
Summer Faculty Research Program
Phillips Laboratory

Sponsored by:
Air Force Office of Scientific Research
Bolling Air Force Base, DC

August, 1996

EVALUATION OF ENGINE-RELATED FACTORS INFLUENCING CONTRAIL PREDICTION

Andy Detwiler
Research Professor
Institute of Atmospheric Sciences
South Dakota School of Mines and Technology

Abstract

Forecasting the probability of contrail formation has been a long-standing problem for the United States Air Force. The theory applicable to contrail formation continues to develop as more observations become available. A critical factor in contrail formation is the ratio of water to heat in the exhaust from aircraft engines. In the 1950's, as the first formal theoretical descriptions of contrail formation by gas turbine-powered aircraft were developed by Air Force meteorologists, this ratio was taken to be determined solely by the properties of the fuel. Reasonable results were obtained when applying this theory to forecast where contrail formation would be expected. In recent years, as more efficient medium- and high-bypass engines have been added to the Air Force inventory, it is apparent that the ratio of water to heat in the engine exhaust plume, at the point in the plume where contrails initially condense depends on other factors. These include non-steady state engine settings, variations in fuel properties, extraction of accessory bleed air, bypass ratio, and propulsion efficiency. Variations in contrail factor of up to ~50% from a standard fuel-derived value are possible, leading to changes in contrail onset temperature of up to 5°C for a given environment in which onset temperatures are near -50°C.

1. Contrail Formation

Condensation trails form behind aircraft when they fly in sufficiently cold and humid air. This is an example of a cloud formed by isobaric mixing of warmer air that, while not saturated, contains a relatively high mixing ratio of water vapor, with colder air that also is not saturated and contains a relatively low mixing ratio of water vapor. Under suitable conditions it is possible for saturation to be reached in some mixtures of these two types of air. The process of cloud formation by mixing has been understood at least since the beginning of modern meteorology in this century and is described in detail in many of the classic modern texts (e.g. Geddes, 1921; Petterssen, 1956; Haltiner and Martin, 1957; Iribarne and Godson, 1981).

Here the process of contrail formation is illustrated with a standard mixing diagram as shown in Figure 1. Isobaric mixing at 300 mb ambient total pressure between air characterized by mixing ratio and temperature represented on the diagram by Point A, with air represented by Point B, will produce mixtures whose mixing ratio and temperature lie along a straight line connecting the two points. This line will be called the mixing line. Mixtures that are mostly A will lie near A on the diagram. Mixtures that are mostly B will lie near B. If the axes' scales on the diagram are linear, then the distance from the end points is inversely proportional to the proportion of that type of air in the mixture.

Taking this diagram to represent mixing between the exhaust plume trailing behind an aircraft engine and its environment, the core of the plume will initially be pure A, the environment will be pure B, and the fringe of the plume will contain a range of mixtures representing by all points in between. As time goes on, mixing will continue. Eventually the plume will be infinitely diluted by mixing with ambient air, and all parcels will have properties depicted by A..

The saturation mixing ratio relative to a plane surface of liquid water is indicated by the curved solid line. If the mixing line crosses above the saturation line for some mixtures, and suitable condensation nuclei are present (there is an ample supply of them in aircraft engine exhaust), then liquid water droplets will nucleate in these mixtures and they will become cloudy. This is illustrated in Figure 2, showing the same mixing process diagrammed in Figure 1, but looking in detail at the range of temperatures over which saturation occurs.

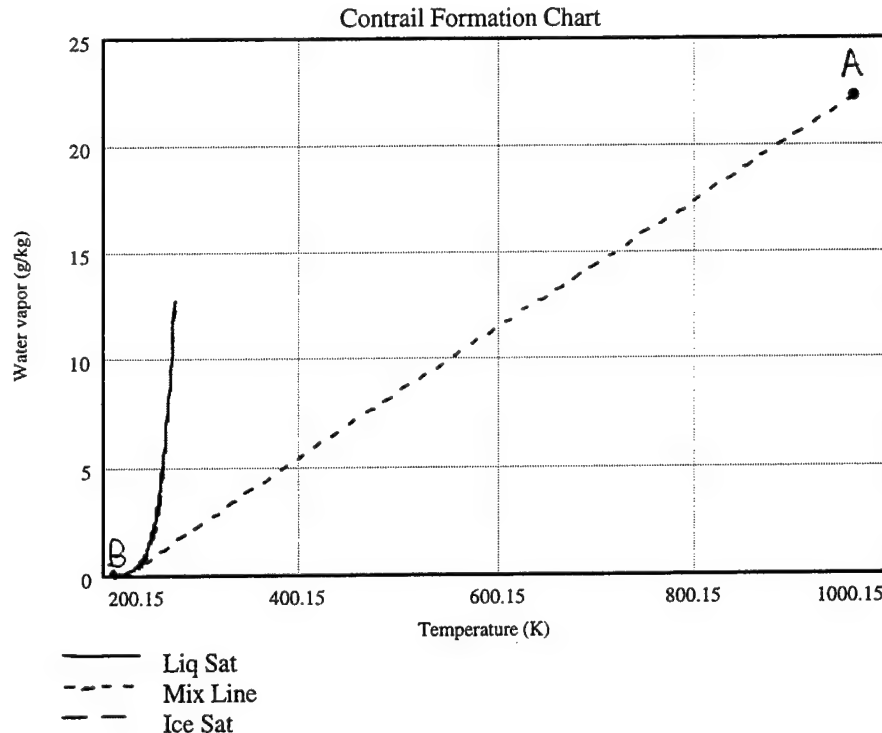


Figure 1: Short-dashed line represents the properties of mixtures of air between source A (temperature = 222 K, water vapor mixing ratio = 0.04 g/kg) and source B (temperature = 973.15 K, water vapor mixing ratio = 22.6 g/kg). Solid line represents saturation mixing ratio with respect to liquid water, and long-dashed line represents saturation mixing ratio with respect to ice, with the saturation curves plotted only for temperature less than 273.15 K.

The slope of the mixing line for contrail formation is determined by the ratio of water vapor to heat produced by fuel combustion in the engine. This water and heat are mixed into the air flowing through the engine. In some installations some of the heat may not exit into the exhaust plume with the water. This will increase the slope. In many installations virtually all of the heat and water produced by combustion exit together and the slope of the mixing line is completely determined by the fuel used. Once the slope is known, a line with this slope can be drawn just tangent to the saturation line on a mixing diagram. This line then represents the dividing line between conditions in which contrails will form (ambient conditions represented by a water vapor mixing ratio and temperature to the left of the line) and those in which they will not (to the right of the line). The slope of the saturation line increases monotonically with temperature. The greater the ratio of water to heat in the exhaust, the greater will be the slope of the mixing line, the further to the right

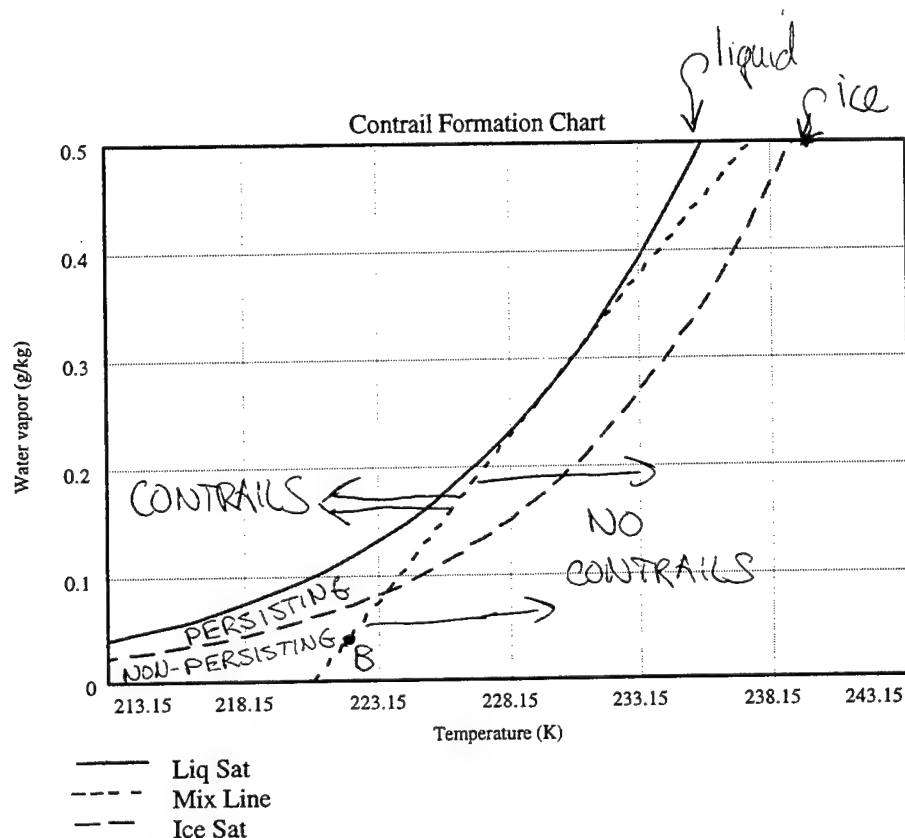


Figure 2: Same as Figure 1, but showing in detail the lower left portion of the mixing line.

it will fall on the diagram when it is just tangent to the saturation line, and the higher will be the maximum temperatures at which contrails will form at a given pressure and relative humidity.

An empirical observation is that initial condensation at the fringes of the mixing plume does not occur unless saturation with respect to liquid water occurs, but the initially nucleated liquid droplets quickly freeze if the ambient temperature is near -40°C or below. It is not uncommon for air in the upper troposphere to be clear but in a state of supersaturation with respect to ice. If a contrail forms in such air, the frozen droplets will persist and grow as ice particles, making a persistent contrail.

Considering a simple turbojet engine, and its contrail formation, the mixing line characterizing a given engine/fuel combination should have the same slope for all ambient pressures when the engine is in a steady-state. Combustion, no matter how efficient, generates CO_2 and H_2O and adds it in constant proportions to the air flowing through the engine. In a steady state there can be no storage of heat or the engine would heat up and burn up! Similarly, water is being generated in a typical engine at the rate of 100's of grams per second, and all water generated

has to leave the engine. In this ideal case, a mixing line for a given engine will vary in slope depending only on the ratio of water to heat generated during combustion, which is directly determined by the mole ratio of hydrogen to carbon in the fuel, and its heat of combustion. At greater ambient pressures the saturation lines will fall further to the right on the diagram, as the same saturation vapor pressure (a function only of temperature) represents a smaller mixing ratio at higher ambient pressures. Comparing mixing at two different pressures, the mixing line is just tangent to the saturation curve when it is further to the right on the diagram representing mixing at a higher pressure. This means that the threshold temperature for contrail formation is higher, for a given engine, fuel, and ambient humidity, at lower altitude (higher pressure).

2. Contrail Factor

The slope of the mixing line in Figures 1 and 2, in the context of mixing to produce contrails, has come to be called the "contrail factor". (Appleman, 1953) Assuming that all of the water and heat are thoroughly mixed in the exhaust plume issuing from the engine (a reasonable assumption for the turbojet engines in use in the 1950's when Appleman finalized his work), the ratio of water to heat in the exhaust is entirely determined by the properties of the fuel. Assuming further that this heat is used to raise the temperature of ambient air with a specific heat characteristic of air at common meteorological temperatures, Appleman computed a contrail factor of $0.0336 \text{ (g/kg)/}^{\circ}\text{C}$.

Appleman derived his estimate of this ratio from a report of the Great Britain Naval Meteorological Branch from 1943. However, fuel used in the jet aircraft of the West in the 1950's and later is uniformly characterized by a composition and heat of combustion that yields a contrail factor in this scenario of near $0.0295 \text{ (g/kg)/}^{\circ}\text{C}$ (e.g. Pilie and Jiusto, 1958).

The contrail factor is computed from fuel properties as follows. The typical military jet fuel category JP-4 has a specified minimum heat of combustion of $\sim 18400 \text{ BTU/lb}$ ($4.28 \times 10^7 \text{ J/kg}$). The common civilian jet fuel in current use is Jet-A, which has a somewhat looser specification but a minimum heat of combustion the same as JP-4. The water produced during combustion can be estimated from a generic chemical equation describing combustion of hydrocarbon fuels like the kerosenes used in modern engines is:



In this equation, kerosene fuels are treated as a mixture of chains of various lengths of H-C-H groups, represented by the generic formula CH_2 . The symbol δH represents heat released during combustion, and the other components have their common chemical meanings. The molecular weight of CH_2 is 14 g/mole while that of H_2O is 18 g/mole. Thus for every unit weight of fuel burned, an estimated 18/14 or 1.29 unit weights of water are produced. Using a specific heat at constant pressure for air of 1005 J/(kg°C), and assuming that all heat of combustion goes into raising the temperature of air, the ratio of water added to heating produced in air passing through the engine is computed to be

$$1290 \text{ (g/kg H}_2\text{O)} / [(4.28 \cdot 10^7 \text{ J/kg}) / (1005 \text{ J/(kg°C)})] = 0.0303 \text{ (g/kg H}_2\text{O)} \text{ } ^\circ\text{C}^{-1} \quad (2)$$

Common jet kerosene fuels from the 1950's onward have a composition closer to $\text{CH}_{1.94}$, yielding the contrail factor of 0.0295 (g/kg) $^\circ\text{C}^{-1}$ computed by Pilie and Jiusto (1958).

The fuel discussed in the British report used by Appleman apparently had a higher ratio of H to C, yielding the ratio of water produced to fuel consumed of 1.4 reported by Appleman. It apparently also had a lower heat of combustion, compared to JP-4, of only 10000 cal/g ($4.18 \cdot 10^7 \text{ J/kg}$) as reported by Appleman, roughly 2.4% lower than the current JP-4 specification. Thus the ratio of water to temperature rise used in the analysis by Appleman is ~12% higher than is appropriate to common jet fuels actually in use at that time and today.

Contrail factors can also be computed from measured fuel flow m_f , engine air flow m_a , ambient static temperature T_a , and exhaust exit total (stagnation) temperature T_{E0} . One form of the estimate is presented in Saatzer (1995b)

$$\text{CF} = [1.3 \ m_f] / [(m_a)(T_{E0} - T_a)] \quad (3)$$

where "1.3" represents the ratio of water mass generated per unit mass of fuel combusted (One water molecule is produced for each CH_2 group oxidized. The ratio of molecular weights is 18/14 which is ~1.3.). The fuel flow m_f multiplied by 1.3 is used to estimate the water added to the exhaust by combustion. Fuel flow can be neglected with respect to the air flow m_a , in the denominator for all practical calculations, as the air flow is usually not known to better than ~2%, and typical fuel/air ratios are 3-4%. The engine exit total temperature T_{E0} is a measure of the total energy, thermal plus directed kinetic energy of motion, created by combustion and added to the engine exhaust. The difference $(T_{E0} - T_a)$ is proportional to the energy added by combustion.

A several-month flight test program involving turbojet-powered T-33's is described in Saatzer (1995b). Contrail factors were computed from engine measurements using equation (3) during climb, descent, and steady level flight. Contrail factors inferred for the T-33 ranged from 0.025 to 0.039 (g/kg)/°C. Factors as low as 0.025 were obtained during engine decelerations/descents, values near 0.032 in steady flight, and factors as high as 0.039 during accelerations/climbs. Reasons for this variation are discussed below. The median value of 0.032 (g/kg)/°C⁻¹ for steady flight is slightly higher than the value estimated from fuel properties. Good agreement was obtained between contrail factors inferred from the observed contrail onset temperature, and those computed from aircraft operating parameters.

Less adequate agreement has been obtained in other sets of observations. Knollenberg (1972), Konrad and Howard (1974), Busen and Schumann (1995), Schumann (1996) and Schumann et al (1996) describe observations of contrails forming at temperature several degrees warmer than predicted from a mixing analysis using a contrail factor based on fuel properties. A set of observations obtained from a field program sponsored by Phillips Laboratory in the fall of 1995 also yielded a group of contrail observations in conditions too warm to be explained by a contrail factor based on fuel properties. Significantly, most of these observations involve contrail formation from aircraft powered by medium- to high-bypass ratio fanjets.

3. Refining the Estimate of Contrail Factor

3a. Non-steady engine operation

It has been noted above that non-steady engine settings in the study of Saatzer (1995b) resulted in a deviation in contrail factor of ~25%, as computed from fuel flow and exhaust gas temperature. An accelerating engine heats the air to a temperature higher than the previous hardware temperature, warming it to a new higher temperature and robbing the exhaust of some of its thermal energy during this heating process. The opposite occurs during deceleration. As the engine slows and fuel flow diminishes, the engine hardware dumps excess heat into the cooler exhaust until it cools to the new exhaust temperature. The observed variation in contrail factor of ~30% could result in variations in contrail onset temperature of ~3°C around that predicted using a contrail factor near 0.030 (g/kg) °C, with higher contrail factors leading to higher onset temperatures.

3b. Variations in fuel properties

Another possible source of variability is variability of fuel characteristics. The computation of contrail factor from a chemical description of fuel combustion appeared above. Jet kerosene, if it were exactly represented by the chemical formula C_nH_{2n} used in that discussion, would have a percentage of hydrogen by weight of $2/14$, or 14.3%. In fact, jet kerosene is not composed exclusively of long chains of CH_2 groups, but in addition has significant fractions of aromatic and other hydrocarbon species having a lower ratio of H to C. On the average, then, there are slightly less than 2 H's for each C.

Looking at the minimum specification for the military fuels JP-4, JP-5, and JP-8 (P. Heberling, GE Aircraft Engine Business Group, personal communication), minimum specifications are 13.4% hydrogen. This would correspond to an approximate average composition of $CH_{1.94}$. Individual batch samples in one collection of analyses made available to the author ranged in H content up to 13.9%. A 13.4% hydrogen-content would decrease the ratio of the mass of water generated per unit mass of fuel consumed to 1.25. There would be a reduction in contrail factor, compared to that estimated using an assumption of a perfect CH_2 fuel, by 5%. The highest value for hydrogen-content in the US literature is the one used by Appleman (1953). His estimate of 1.4 kg of water for every kg of fuel burnt would require an H-content of 15.4% and an average composition of $C_nH_{2.15n}$.

The heat of combustion is the other fuel parameter involved in estimating the contrail factor following the approach of Appleman. Fuel types JP-4, JP-6, JP-8, Jet-A and Jet-B have a minimum specification of 18,400 BTU/lb (4.28×10^7 J/kg), while the JP-5 specification is 18,300 BTU/lb (4.26×10^7 J/kg). A few results from analysis of actual samples (Heberling, personal communication, and Schumann et al, 1996) yield values no more than 1.5% higher than this. In this collection of analyses higher hydrogen content correlates with higher heat of combustion, opposite in trend to the fuel properties specified in Appleman (1953) which had a higher hydrogen-content and lower heat of combustion than for modern jet kerosenes. If hydrogen-content and heat of combustion covary positively, this will yield a proportionally smaller effect on the computation of contrail factor than if H-content and heat of combustion varied independently.

It is reasonable to conclude that variations in fuel properties might produce a variation in contrail factor, compared to the " CH_2 " value $0.0303 \text{ g/kg } ^\circ\text{C}^{-1}$, of not more than 6%. Contrail factor values would be more likely to be less than this and less likely to be greater. A variation of 6%

corresponds to a variation in critical temperature of $\sim 0.6^{\circ}\text{C}$ at 300 mb ambient pressure, a typical cruise flight level.

Some of the disagreements between observed onset temperatures and those calculated assuming steady flight cannot be explained by non-steady engine condition or variation in fuel properties. There are additional modifications to the computation of contrail factor that may explain the discrepancies.

3c. Compressor bleed air

After combustion, the hot expanded gases in a jet engine expand through the turbine section. Some energy is extracted by the turbine which is attached to a shaft that drives the compressor ahead of the combustor, while the rest of the energy leaves the engine through the exhaust nozzle. The energy extracted by the turbine, in an ideal engine, is exactly equal to the energy put into the air ahead of the combustor. Therefore, in an ideal engine, no net power is lost. In a real engine, a combined power loss on the order of 10% occurs in the extraction of energy by the turbine and addition of energy by the compressor. This energy is not "lost" from the exhaust plume. This "loss" is represented by heat energy that can't do work, and the heat is still present in the air passing through the engine and out the exhaust nozzle.

In most aircraft installations, air is drawn from the compressor section of a gas turbine engine for several purposes. Work has been done on this air to compress it, so if it leaves the engine it represents a loss of energy originally generated by combustion. Some air is passed over the combustors to cool the metal containers, and some passes around the combustors and is forced through channels in the turbine blades to cool them. Since this air is dumped back into the core engine air flow, this bleed air does not represent a net energy loss.

Other air may be extracted to pass through channels along the leading edges of wings and nacelles for de-icing, or to run heating, air conditioning and other auxiliary equipment in the aircraft. The enthalpy in this air is lost to the engine. As much as 10% or more of the total airflow through the engine may be extracted and not returned to the engine, to be used elsewhere for auxiliary purposes, depending on system demands and throttle settings. This results in a loss of thrust, of course. Total inlet airflow would have to be increased (requiring a higher turbine rotation rate) to maintain thrust and fuel flow possibly adjusted to maintain the design fuel-air ratio in the

combustion section. It typically is not the case that the same amount of water will be generated with or without extracting this bleed air, for a given thrust level. Thus the water content of the exhaust usually would not be the same with or without the auxiliary bleed and the change in contrail factor as accessory bleed air percentage is increased is a complicated quantity to estimate.

The percentage drop in exhaust energy content due to bleed air extraction will vary with engine cycle, and will be higher for higher cycle pressure ratios. Preliminary estimates using the default turbojet engine cycle in the "ONX" and "OFFX" software packages (Mattingly, 1990) suggest that percentage energy losses, on the order of half of the percentage bleed air mass losses, may represent a rough upper limit. Such losses would raise the contrail onset temperature by $\sim 0.5^{\circ}\text{C}$.

3d. Separation of heat between core and fan streams

In fan/bypass engines, all of the water vapor generated by combustion ends up in the core airstream, but some of the combustion energy is transferred by the fan or prop to air outside this core. Thus the core will have a higher contrail factor than would be computed based on fuel properties. It is possible for wisps of this core air to be turbulently mixed through the sheath of fan air or propwash aft of the engine without completely mixing with the sheath air, thus eventually mixing with the environmental air with a contrail factor somewhere in-between that of the core stream, and that produced by complete mixing with the fan stream/propwash i.e., the theoretical contrail factor estimated from fuel properties.

Peters (1993) obtained engine manufacturer's data on several engines from which to calculate contrail factors. These engine types included the turbojet, low- and high-bypass engines. The data included tailpipe moisture and temperature, for a wide range of power settings, flight Mach numbers, and flight levels. He does not say so explicitly, but for the fan/bypass engines it appears that he used numbers characteristic of the engine core exhaust. He gives the following characteristic contrail factors for each type of engine:

non-bypass - $0.0360 \text{ g/kg } ^{\circ}\text{C}^{-1}$

low-bypass - $0.0400 \text{ g/kg } ^{\circ}\text{C}^{-1}$

high-bypass - $0.0490 \text{ g/kg } ^{\circ}\text{C}^{-1}$

Schumann et al (1997) simulated the mixing of the fan and core streams for the 3:1 bypass ratio engines on the aircraft whose contrails were described in Busen and Schumann (1995). Their

conclusions were that incomplete mixing was important only in the first 0.1 s (~16 m aft of exit plane) of plume evolution and that the increase in contrail factor would produce an increase in critical temperature of 0.1 to 0.5 °C. Saatzer (1995a) estimated from observations of contrail onset temperatures by high-bypass ratio, engines that the core stream was only diluted by ~12% mixing with the fan stream at the point where condensation first occurred, yielding a contrail factor ~25% higher than that computed from fuel properties. The increase in critical temperature at 300 mb would be ~2.5°C over that computed using a contrail factor based on fuel properties. However, Saatzer did not include the correction for propulsion efficiency (discussed next) in his inversion from observed critical temperature to revised contrail factor. If he had, he would have estimated much higher mixing fraction and a much smaller change in contrail factor due to mixing.

Saatzer (1995a) suggests contrail factors for the same 3 categories used by Peters (1993)

non-bypass - 0.0300 g/kg °C⁻¹

low-bypass - 0.0340 g/kg °C⁻¹

high-bypass - 0.0390 g/kg °C⁻¹

3e. Efficiency of propulsion

Knollenburg (1972) was perhaps the first US worker to remark that the energy generated in a gas turbine engine and used to do work pushing an aircraft through the air is not present in the exhaust plume, thus increasing the contrail factor over the value estimated from combustion of fuel. He did not provide a quantitative development of this correction. Schumann (1996) refers to earlier German developments by Schmidt in which this same correction is advanced and a quantitative evaluation is made, although the work is not available in the United States. Busen and Schumann (1995) and Schumann et al (1996) used the work correction in their analysis of contrail observations. Saatzer (1995a) describes this correction, but does not utilize it in his analysis.

In order to consider this process, it is necessary to define thrust, propulsive work, and two forms of propulsion efficiency. For simplicity, these ideas will be discussed within the framework of steady constant-speed constant-level flight.

Thrust can be defined as

$$F_T = m_T (u_e - u_o) \text{ kg m s}^{-2} \quad (4)$$

where F_T is thrust in N, m_T is the mass flow rate of air plus fuel through the engine (kg s^{-1}), u_e is the exhaust speed of the air relative to the exit nozzle (m s^{-1}), and u_o is the forward airspeed of the aircraft (m s^{-1}). The quantity $(u_e - u_o)$ represents the net increase in speed delivered by the engine to the air it processes, where u_o would be the speed with which air enters the engine and u_e the speed with which it leaves.

Work done in moving the aircraft through the air can be described as force times distance, and the rate of work accomplished (or power dissipated in propulsive work), P_w , as force times distance divided by time

$$P_w = F_T u_o \text{ kg m}^2 \text{ s}^{-3} \quad (5)$$

Thus nothing needs to be known about the details of the drag on the airframe in order to calculate the energy being dissipated by this drag, if drag is balanced by thrust and airspeed, engine mass flow, and engine exhaust speed are known.

The rate of total energy added by the engine to the exhaust plume, P_T , can be described as the sum of the thermal and kinetic energy in the gases emitted from the exhaust nozzle per unit time, with the thermal and kinetic energy at the inlet subtracted.

$$P_T = m_T [c_p(T_{se} - T_{so}) + 1/2 (u_e^2 - u_o^2)] \text{ kg m}^2 \text{ s}^{-3} \quad (6)$$

where c_p is the specific heat of air at constant pressure, T_{se} is the static temperature at the exit plane where gas leaves the engine, and T_{so} is the ambient (static) temperature. The thermal part of this energy represents energy that does not do any propulsive work. The kinetic part of this energy, P_{KE} , can do some work

$$P_{KE} = 1/2 m_T (u_e^2 - u_o^2) \text{ kg m}^2 \text{ s}^{-3} \quad (7)$$

In the context of an exhaust plume mixing with its environment, as mixing occurs and the plume decelerates the directed kinetic energy will be converted to random molecular motion, i.e. thermal energy. Thus the sum of kinetic plus thermal energy eventually becomes completely thermal energy as mixing progresses.

Finally, the rate of energy production by combustion, P_c , is

$$P_c = \dot{m}_f Q \quad \text{kg m}^2 \text{s}^{-3} \quad (8)$$

where \dot{m}_f is the fuel flow (kg s^{-1}) and Q is the heat of combustion (J kg^{-1}). In an ideal engine, where all of the energy generated by combustion is in the exhaust stream, $P_T = P_c$.

The efficiency with which the kinetic energy added to the air passing through the engine is converted to propulsive work is

$$\eta_{KE} = P_w/P_{KE} = [(u_e - u_0) u_0] / [1/2(u_e^2 - u_0^2)] = 2 u_0 / (u_e + u_0) \quad (9)$$

Since $u_e > u_0$ in any real flight situation, this kinetic propulsive efficiency will be < 1 in any real situation and will approach 1 as u_e decreases toward u_0 . Of course, as u_e approaches u_0 , thrust will approach 0 unless \dot{m}_e increases. It is this basic relationship governing propulsive efficiency and thrust, that has driven the development of ever larger turboprop and fan/bypass engines which move larger masses of air at lower speeds, achieving significant thrust with higher propulsive efficiency. As an example, a typical exhaust speed for a turbojet engine would be $u_e \sim 500 \text{ m s}^{-1}$, at a cruise airspeed $u_0 \sim 175 \text{ m s}^{-1}$. This yields $\eta_{KE} \sim 52\%$. A fan/bypass engine that moved 2.6 times as much air at the lower speed of 300 m s^{-1} to produce the same thrust would yield $\eta_{KE} \sim 74\%$.

The efficiency with which combustion energy is converted to exhaust kinetic energy is

$$\eta_{CBKE} = P_{KE}/P_c = 1/2 \dot{m}_T (u_e^2 - u_0^2) / \dot{m}_f Q \quad (10)$$

This conversion efficiency must be < 1 , since $P_{KE} < P_T = P_c$, even in the ideal case where all combustion energy appears in the exhaust as heat and directed kinetic energy. The portion that

is present is heat represents energy that does not do propulsive work. Typical combustion-energy-conversion-to-kinetic-energy efficiencies would be ~40% for the turbojet example above. In general, a fan/bypass engine can produce the same thrust using less fuel, but specific data to derive an example fan/bypass engine to compare to the turbojet are not available at the time of writing this report.

The efficiency with which combustion energy is converted to propulsive work is the product of these last two efficiencies

$$\eta_{CBW} = \eta_{CBKE} \eta_{KE} = m_T (u_e - u_o) u_o / f_t Q \quad (11)$$

Following our examples above, the overall conversion of combustion energy to propulsive work would be ~20% for the example turbojet. Higher efficiencies are possible with fan/bypass engines because the same thrust can be generated with less fuel consumption, but again, specific fan/bypass parameters are not available.

Finally, a Carnot efficiency can be defined as

$$\eta_{CAR} = (T_{SC} - T_{SO})/T_{SC} \quad (12)$$

where T_{SC} is the maximum temperature reached in the combustion process, and T_{SO} is exhaust static temperature. Different authors define this efficiency differently, with some substituting for T_{SO} the quantity T_{se} , the environmental temperature. However, any thermal energy still in the exhaust at the exit plane can do no propulsive work as it mixes with the environment and cools. The maximum possible conversion of combustion energy to propulsive work would be achieved if the exiting airstream expanded to environmental temperature as it left the engine, i.e., all of the combustion energy was converted to kinetic energy. Fan/bypass engines have lower average exhaust gas temperatures for the same thrust and would have higher limiting thermodynamic efficiencies. The definition given here seems to be the most practical to use in the context of aircraft gas turbine engines.

The higher the combustion temperature, the higher the Carnot efficiency. Maximum possible temperature achieved during hydrocarbon combustion is ~2500°K. For a combustion temperature

of 2200°K and an exit temperature of 600°K, a limiting thermodynamic efficiency of 73% is derived. The higher the combustion temperature, and the lower the exhaust temperature, the higher is the limiting efficiency. If the combustion temperature was 2200°K and exit temperature was 400°K, then the efficiency would be increased to 82%. This efficiency relationship between combustion temperature and exit temperature, along with the desire to generate as much power in as small a volume as possible, has driven the development of materials and surface-cooling techniques to use to build engine components that can run at higher and higher temperatures, and to produce thrust with the lowest possible exhaust. Nevertheless, $\eta_{CBW} \ll \eta_{CAR}$.

Having defined these efficiencies it is now possible to present the arguments of Knollenberg, Schumann, and others, concerning the loss of energy used for propulsion from the exhaust plume. Steady constant-speed, constant-altitude flight by a single-engine aircraft will be assumed for simplicity. In this case, the propulsive power being produced by the engine, P_w , is just equal to the dissipation of energy produced as the aircraft moves through the air. This dissipated energy appears as wingtip vortices and wake turbulence initially far-removed from the engine exhaust plume. Then near the aircraft all of the water generated by combustion is in the exhaust plume, while some of the energy generated is not in the exhaust plume but is dispersed in the wider wake of the aircraft. At some great distance aft, the engine plume and aircraft wake become completely mixed, and all of the heat and water are mixed back together as the wake dilutes by mixing into the atmosphere.

Contrails, if they do form, may form near the aircraft as little as 10's of meters behind. Thus they often form in portion of the exhaust plume from which energy has been removed and before the aircraft wake energy mixes back in, again. The exhaust plume at this point would be characterized by a contrail factor higher than that calculated from the hydrogen content of the fuel and the fuel's heat of combustion.

Turbojets accelerate relatively smaller airstreams to relatively higher velocities and have relatively lower propulsion efficiencies, on the order of 10% to 20%. According to Schumann, the portion of the combustion-generated energy that does propulsive work should be subtracted from the plume, raising the contrail factor. Yet Appleman (1957) and Saatzer (1995b) were able to get reasonable agreement between theory and observations of turbojets without correcting the contrail factor for loss of energy used in propulsion. There are two possible resolutions for this quandary

In the case of Appleman's studies, he had estimated a contrail factor too high for the fuels then in use. A subtraction of 10% of the energy from the exhaust to drive the airplane would result in an increase in the contrail factor of ~10%. A 10% increase in contrail factor over the actual fuel-derived value of 0.0295 (g/kg) °C would bring the corrected contrail factor close to the value Appleman used in his analysis (0.0336 (g/kg) °C) and would help the agreement between observations he had available, and his theoretical analysis.

Saatzer's (1995b) work involved computation of contrail factor from engine parameters, assuming that 1.3 kg of water were generated for each kg of fuel consumed. This estimate is high compared to an estimate based on JP-4 specifications. These specifications suggest a proportion of 1.25, and actual fuel analyses of Jet-A (e.g. Busen and Schumann, 1995; Shumann et al, 1996) suggest a proportion closer to 1.22 may be common. It is possible that there was less water in the exhaust than Saatzer assumed, and that this compensated for the fact that there was actually less energy in the exhaust plume than he assumed due to removal of energy to do work. The propulsive efficiency of the turbojet engine in a T-33 is very low, ~10%. (Saatzer, personal communication, notes that a T-33 engine consumes as much fuel as a B-2 engine on a similar flight profile.) Thus the numerator and denominator terms in his contrail factor calculation may have been both overestimates, but the ratio, the contrail factor itself, not far off.

Another issue in the computation of contrail factor from engine parameters is the reference frame in which the computation is done. Saatzer (1995b, Ch 6) uses a theoretical framework that was developed by Osterle (in a sequel to Osterle (1956) which is no longer available). The control volume for plume energy analysis is a volume fixed to the exit plane of the engine, moving with the engine. Engine exhaust enters this volume with speed u_e , ambient air enters this volume with speed u_0 , and mixed air exits this volume at speed u_0 . According to the treatment presented in Saatzer, the stagnation enthalpy at the jet exit is $h_{e0} = h_e + (u_e^2 - u_0^2)/2$, where h_e is the static enthalpy. However, he uses measured exhaust gas temperature (EGT), determined by thermocouples inside the exhaust nozzle, as an estimate of T_{e0} , from which to estimate $h_{e0} = T_{e0}/c_p$, whereas a more correct equivalence in a frame of reference moving with the engine would be $h_{e0} = (EGT - u_0^2/2)/c_p$. This is a second possible source of error leading to an overestimate of heat in the exhaust plume using equation (3) to compute a contrail factor, compensating for an overestimate of water production by combustion.

Schumann et al (1996) estimate a combustion propulsion efficiency of ~20% for the 3:1 bypass ratio engines on the aircraft whose contrails they studied. Propulsion efficiencies η_{CBW} for modern high-bypass ratio engines may reach over 30% (e.g. Busen and Schumann, 1995), meaning up to ~1/3 of the energy generated by combustion is not in the exhaust plume near the exit plane where the contrail typically forms, according to this analysis. This would require an adjustment of the contrail factor computed from fuel properties upward by a factor ~4/3 and an increase in critical temperature of ~3°C.

The role of propulsion efficiency in accounting for heat lost from the engine plume is a difficult one to define. A jet propulsion system is an open one. Working fluid does not go through a complete cycle within a closed system, but is passed through the system and exits in a state different from that in which it entered. Closing the energy balance of this propulsion system can be difficult as it depends on the reference frame chosen.

The apparent success of the propulsive work correction in explaining the observations of Busen and Schumann (1995), Schumann et al (1996) and Schumann (1996), where contrail onset was at a higher temperature than predicted using a fuel-based contrail factor, is compromised by the fact that the engines involved were fan/bypass engines for which they assumed the fan and core streams were mixed by the time of contrail onset. According to Saatzer (1995a) an increase in contrail factor in these cases could also be explained by incomplete mixing of core and bypass streams. Schumann et al (1997), however, argue that incomplete mixing cannot account for the observed increase in contrail factor for fan/bypass jets.

An observation that contradicts the proposal of Schumann to subtract energy used to produce propulsive work from the energy involved in plume mixing and contrail formation is provided by Saatzer (personal communication). During a flight test, two T-33's were flying in formation, one being more loaded with pods under the wings and other protuberances around the airframe than the other. Assuming a steady-state, the more loaded aircraft would have to have been generating more thrust to maintain the same airspeed as the "clean" aircraft. According to equation (5) the engine on the more loaded aircraft would have been dissipating more power in work, P_w . Both were burning the same fuel and should have been generating the same ratio of water to heat, although air and fuel flow would have been higher on the more loaded T-33. Using equation (11) and assuming that the air-to-fuel flow ratio, m_T/f , is maintained constant on each aircraft, conversion of energy generated by combustion to propulsive work should be more efficient for the more loaded aircraft at a given airspeed u_0 . The more efficient system should have a higher

proportion of its energy converted to propulsive work and a higher contrail factor, if Schumann is correct. Yet the cleaner aircraft contrailed at a higher temperature, indicating that even though it was less efficient, it had the higher contrail factor.

4. Conclusions

Several engine-related causes of variation in the contrail factor, used in the mixing analysis to determine whether or not contrails will form in a given environment, have been identified. For a simple turbojet, non-steady-state engine operation can result in contrail factor variations of ~30% around the steady-state value. Variations in hydrogen content and heat of combustion can account for fluctuations of a few percent, as can variations in accessory bleed air extracted from the compressor section.

Fan/bypass and turboprop engines have contrail factors higher than simple turbojets. At a bypass ratio of ~5:1, contrail factors are typically 30% higher than for a simple turbojet burning the same fuel. Two possible reasons for this are (1) separation of heat from water in the engine core stream as energy is added to the fan/bypass/prop stream, and (2) a higher efficiency of conversion of fuel energy to work in these higher air-flow, lower exhaust speed engines. The available observations are not adequate to assess the relative importance of separation and efficiency in explaining the higher contrail factors.

The combination of all engine-related causes of variations in contrail factor can account for the possibility of <~50% variations in contrail factor about the value estimated from fuel properties. Changes in contrail factor can be roughly related to changes in contrail onset temperature by the relationship that a 10% increase in contrail factor results in a 1°C higher contrail onset temperature in a typical upper tropospheric environment for onset temperatures near -50°C.

5. References

- Appleman, H. S., 1953: The formation of exhaust condensation trails by jet aircraft. *Bull. Amer. Meteorol. Soc.*, **37**, 47-54.
- Appleman, H. S., 1957. *Derivation of Jet-Aircraft Contrail-Formation Curves*. AWS TR 105-145. Available from Air Force Combat Climatology Center/DOL (Air Weather Service), Scott Air Force Base, Illinois 62225-5206. 46 pp. [Replaces AWS TR 105-103 and AWS TR 105-112]
- Busen, R., and U. Schumann, 1995: Visible contrail formation from fuels with different sulfur contents. *Geophys. Res. Lett.*, **22**, 1357-1360.

Geddes, A. E. M., 1921. *Meteorology: An Introductory Treatise*. Blackie & Son, Ltd., London. 390 pp.

Haltiner, G. J., and F. L. Martin, 1957. *Dynamical and Physical Meteorology*. McGraw-Hill, New York. 470 pp.

Iribarne, J. V., and W. L. Godson, 1981. *Atmospheric Thermodynamics*. D. Reidel, Boston. 259 pp.

Knollenberg, R. G., 1972: Measurements of the growth of the ice budget in a persisting contrail. *J. Atmos. Sci.*, **29**, 1367-1374.

Konrad, T. G., and John C. Howard, 1974: Multiple contrail streamers observed by radar. *J. Appl. Meteor.*, **13**, 563-572.

Mattingly, J. D., 1990. On-Design and Off-Design Aircraft Engine Cycle Analysis Computer Programs. American Institute of Aeronautics and Astronautics, Inc., 370 L'Enfant Promenade, S. W., Washington, DC.

Osterle, F., 1956. *Condensation trail prediction*. AFCRC-TR-56-459. 25 pp.

Peters, J. L., 1993. *New Techniques for Contrail Forecasting*. AWS/TR--93/001. Available from Air Force Combat Climatology Center/DOL (Air Weather Service), Scott Air Force Base, Illinois 62225-5206. 31 pp.

Petterssen, S., 1956. *Weather Analysis and Forecasting, Vol II: Weather and Weather Systems*. McGraw-Hill, New York. 266 pp.

Pilie, R. J., and J. E. Jiusto, 1958: A laboratory study of contrails. *J. Appl. Meteor.*, **15**, 149-154.

Saatzer, P., 1995a. Presentation to 2nd Meeting of Contrail Technology IPT. Offutt AFB, NE. (variously paged)

Saatzer, P. 1995b. *Final Report: Pilot Alert System Flight Test*. Northrup Grumman Corporation, B-2 Division, 8900 East Washington Boulevard, Pico Rivera, CA 90660-3783. (variously paged)

Schumann, U., 1996: On conditions for contrail formation from aircraft exhausts. (*Meteorol. Z.*, **5**, 4-23.

Schumann, U., J. Strom, R. Busen, R. Baumann, K. Gierens, M. Krautstrunk, F. P. Schroder and J. Stingl, 1996: In situ observations of particles in jet aircraft exhausts and contrails for different sulfur-containing fuels. *J. Geophys. Res.*, **101**, 6853-6869.

Schumann, U., A. Doernbrack, T. Duerbeck, and T. Gerz, 1997: Large-eddy simulation of turbulence in the free atmosphere and behind aircraft. *Fluid Dyn. Res.* (in-press)

STUDIES OF ION-MOLECULE REACTION RATES
AT VERY HIGH TEMPERATURES

Itzhak Dotan
Associate Professor
The Open University of Israel
16 Klausner St.
Ramat-Aviv, Tel-Aviv
Israel

Final Report for:
Summer Faculty Research Program
Phillips Laboratory, Geophysics Directorate

Sponsored by:
Air Force Office of Scientific Research
Bolling Air Force Base, Washington, DC

September 1996

STUDIES OF ION-MOLECULE REACTION RATES AT VERY HIGH TEMPERATURES

Itzhak Dotan
Associate Professor
The Open University of Israel
16 Klausner St.
Ramat-Aviv, Tel-Aviv
Israel

Abstract

Rate coefficients for a few ion-molecule reactions have been measured in the range 300-1800K. The measurements were carried out in a flowing afterglow apparatus designed for the measurement of ion-molecule reaction rate coefficients at temperatures higher than any previous measurement. Reactions measured were $N_2^+ + O_2$, $O^+ + O_2$, $O^+ + N_2$. The results are compared with previous studies of temperature and transitional energy dependencies of ion-molecule reaction rate coefficients. Preliminary results were obtained for the reaction $O^+ + NO$. Experimental problems relating to operation of a flowing afterglow apparatus at high temperatures were solved and discussed.

STUDIES OF ION-MOLECULE REACTION RATES AT VERY HIGH TEMPERATURES

Itzhak Dotan
Associate Professor

Introduction

It has long been recognized that information on energy and temperature dependences of rate coefficients of ion-molecule reactions is desirable both for scientific and practical reasons {1}.

The immediate motivation for measuring rate coefficients at very high temperatures is to provide data and guidance for modeling high-temperature plasmas which occur naturally (e.g. auroras and the ionosphere) or man-made (e.g. around vehicles in hypersonic flight, re-entry vehicles, or engine exhausts). However, it is clear that many interesting questions arise at high temperatures: new reaction channels may become activated and esoterica such as "entropy-driven" reactions {2} become more accessible for study.

A typical variable-temperature flowing afterglow or selected ion-flow tube (SIFT) apparatus can operate at temperatures as high as 500-600K. In the early 1970s', Lindinger et al. {3} modified a flowing afterglow apparatus at the National Oceanic and Atmospheric Administration (NOAA) laboratories, to permit operation as high as 900K. At about the same time the same group built the flow-drift tube {4} which could measure rate coefficients between room temperature and 3eV center of mass translational energy.

The NOAA group reported temperature dependence of nine positive-ion reactions {3}. Reactions which were fast (collisional) at 300K were found to be temperature independent within experimental uncertainty. Reactions which were slow at 300K were seen to decrease with increasing temperature, but in two cases a shallow minimum was observed - for $O^+ + N_2$ at 850K and for $CO_2^+ + O_2$ at about 700K. For

most of the reactions studied by the NOAA group data also existed from flow-drift tube experiments. Generally speaking, the temperature variation of the reaction rate coefficients mimicked results from flow-drift tube data on the kinetic energy dependence of reaction rates.

A variable temperature static drift tube was built at the University of Pittsburgh (5). Measurements were carried out up to 930K for two reactions that had been previously studied by the NOAA group.

The measurements reported here were carried out in a recently developed High Temperature Flowing Afterglow (HTFA) machine (6). This summer for the first time we operated the machine to its maximum designed temperature of 1800K.

The data reported herein show a very good agreement with previous data for temperature and low-energy dependencies of rate coefficients. At higher temperatures there are distinct differences between temperature and kinetic energy dependence. The role of internal (vibrational and rotational) energy in ion-molecule reactions may be deduced from this comparison. It is known that many reactions are strongly dependent upon internal excitation {5}.

Experimental Details

In most aspects the High Temperature Flowing Afterglow (HTFA) is a standard flowing afterglow instrument {6}, consisting of an electron-impact ion-source, flow-tube, gas inlets and a detection system. Special properties to operate at high temperature include:

- ceramic (alumina) flow-tube.
- silicon carbide heaters in a 3-zone commercial furnace.
- upstream end of flow tube is out of the furnace; all electrical and gas connections are made through a cap that clamps to this end. The cap is water-cooled.

The downstream end of the furnace simply abuts the cooled metal mating piece.

This necessitates enclosing the whole apparatus in a vacuum box to prevent leaks into the flow-tube.

- The downstream end of the flow simply terminates $\sim 1R$ from sampling tube.
- All inlet tubes are ceramic.
- Sampling plate is molybdenum and sealed by a ceramic "O-ring".
- 100 amp 220 volts to run the furnace at full power.

A detailed description of the apparatus is given in Fig. 1.

Working at high temperatures causes experimental problems that we had to overcome.

The main problems are:

- Decrease in the signal due to diffusion. Diffusion rate is proportional to $T^{3/2}$.
Thermionic emission of (mainly) Na^+ ($M=23$) and K^+ ($M=39$) from the molybdenum sampling aperture plate. This causes a major problem in measuring Ar^+ ($M=40$) reactions.
- Positive and negative surface ionization on flow-tube walls.
- Possible decomposition of reactant gas on surfaces.

Technical Changes

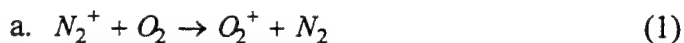
A flowing afterglow machine is very sensitive to the experimental conditions. I spent the first part of my stay trying to improve the performance of the system. The following changes were introduced. (See for comparison Ref. 6 and Fig 1).

1. All thermocouples were taken out of the flow tube in order not to disturb the flow conditions.
2. Reactant gas inlet was secured at the center of the flow tube.
3. The pumping of the vacuum box was separated from the pumping of the flow tube.
4. We introduced a turbo pump instead of the 4" diffusion pump, pumping the lens area.

The last two changes improved the vacuum and the flow conditions. The sensitivity of the system improved enabling us to measure rate constants as low as $5 \times 10^{-13} \text{ cm}^3 \text{ S}^{-1}$.

Results

Three positive ion-molecule reactions were studied as a function of temperature between 300 to 1800K. Preliminary results exist for one more reaction.



The results of reaction 1 are shown in Fig. 2. There is a very good agreement between our data and previously measured NOAA's temperature (3) and flow-drift tube (8) data. At the high temperature range (above 1000K) the HFTA data are higher than the FDT data by about a factor of 2.5 at 1800K.



Results for reaction (2) are shown in Fig. 3. Here again there is a good agreement at the low temperature between our data and NOAA's temperature (3) and FDT (9) data. At the high temperature range our data are higher than the FDT data. This difference is due to the role of vibrationally excited O_2 in driving the reaction. In the same figure we show the derived rate constants for vibrationally excited O_2 .



The rate constants of reaction (3) show basically the same behavior, i.e. agreement with NOAA's data at the low temperature (3) and energy (9) range and faster rates at the high temperature range (Fig. 4). This reaction has been measured by the NOAA group as a function of N_2 vibrational temperature (10). Combining these data and the FDT data enabled us to calculate the rate constants as a function of temperature, and as can be seen in Fig. 4 there is a very good agreement between the calculated and the measured rates.



Only preliminary data exist for reaction (4). The data seem to agree with previous measurements (9). We plan to measure this reaction at low temperature in the SIFT as well as high temperature in the HTFA.

Discussion

The results reported here and previously measured reactions establish the importance of measuring ion-molecule reaction rates at very high temperature by the HTFA machine. Low temperature rate constants show a very good agreement with previous data measured as a function of temperature or translational energy. In the high temperature range there are deviations between the HTFA and FDT data. The deviations are due to the role of internal energy in driving ion-molecule reactions.

All three reactions reported here are important atmospheric reactions. Existing models based on FDT data will have to be modified using the new data. In parts of the atmosphere where ion temperature is different from the neutral, both sets of data will be used.

References

1. See, for example, "Gas Phase Ion Chemistry", Vol. 2, Ed. M.T. Bowers (Academic Press, New York, 1979).
2. M. Meot-Ner (Mautner), J. Phys. Chem., **95** 6580 (1991).
3. W. Lindinger, F.C. Fehsenfeld, A.L. Schmeltekopf and E.E. Ferguson, J.G.R., **79** 4753 (1974).
4. McFarland, D.L. Albritton, F.C. Fehsenfeld, E.E. Ferguson and A.L. Schmeltekopf, J. Chem. Phys., **59** 6610 (1973).
5. A. Chem, R. Johnsen and M.A. Biondi, J. Chem. Phys. **69**, 2688 (1978).
6. P.M. Hierl, J.F. Friedman, T.M. Miller, I. Dotan, M. Menendez-Barreto, J.V. Seeley, J.S. Williamson, F. Dale, P.L. Mundis, R.A. Morris, J.F. Paulson and A.A. Viggiano Rev. Sci. Instrum **67** 2142 (1996).
7. A.A. Viggiano et al., J. Chem. Phys., **93** 1149 (1992).
8. M. McFarland, D.L. Albritton, F.C. Fehsenfeld, E.E. Ferguson, and A.L. Schmeltekopf, J. Chem Phys. **59** 6620 (1973).
9. D.L. Albritton, I. Dotan, W. Lindinger, M. McFarland, J. Tellinghuisen and F.C. Fehsenfeld, J. Chem Phys. **66**, 410 (1977).
10. A.L. Schmeltekopf, E.E. Ferguson, and F.C. Fehsenfeld, J. Chem Phys. **48** 2966 (1968).

Figure Captions

Fig. 1 - High Temperature Flowing Afterglow Apparatus.

Fig. 2 - Data for the reaction of N_2^+ ions with O_2 from 300 to 1800K. NOAA's temperature data is taken from Lindinger et al (3) and FDT data from Albritten et al (9).

Fig. 3 - Data for the reaction of O^+ ions with O_2 from 300 to 1800K. NOAA's temperature data is taken from Lindinger et al (3) and FDT data from Albritten et al (9).

Fig. 4 - Data for the reaction of O^+ ions with N_2 from 300 to 1800K. NOAA's temperature data is taken from Lindinger et al (3), FDT data from Albritten et al (9) and vibration data from Schmeltekopf et al (10).

HIGH TEMPERATURE FLOWING AFTERGLOW

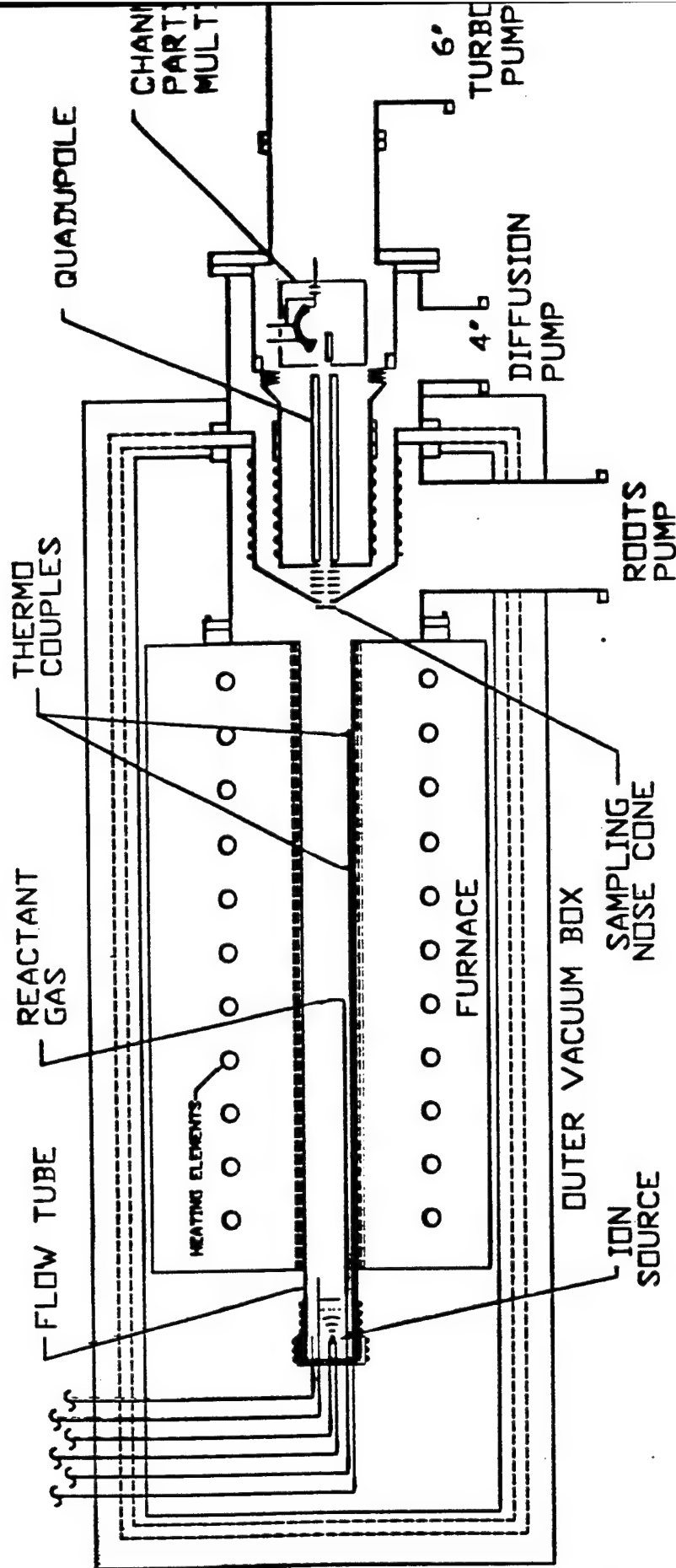


Fig 1

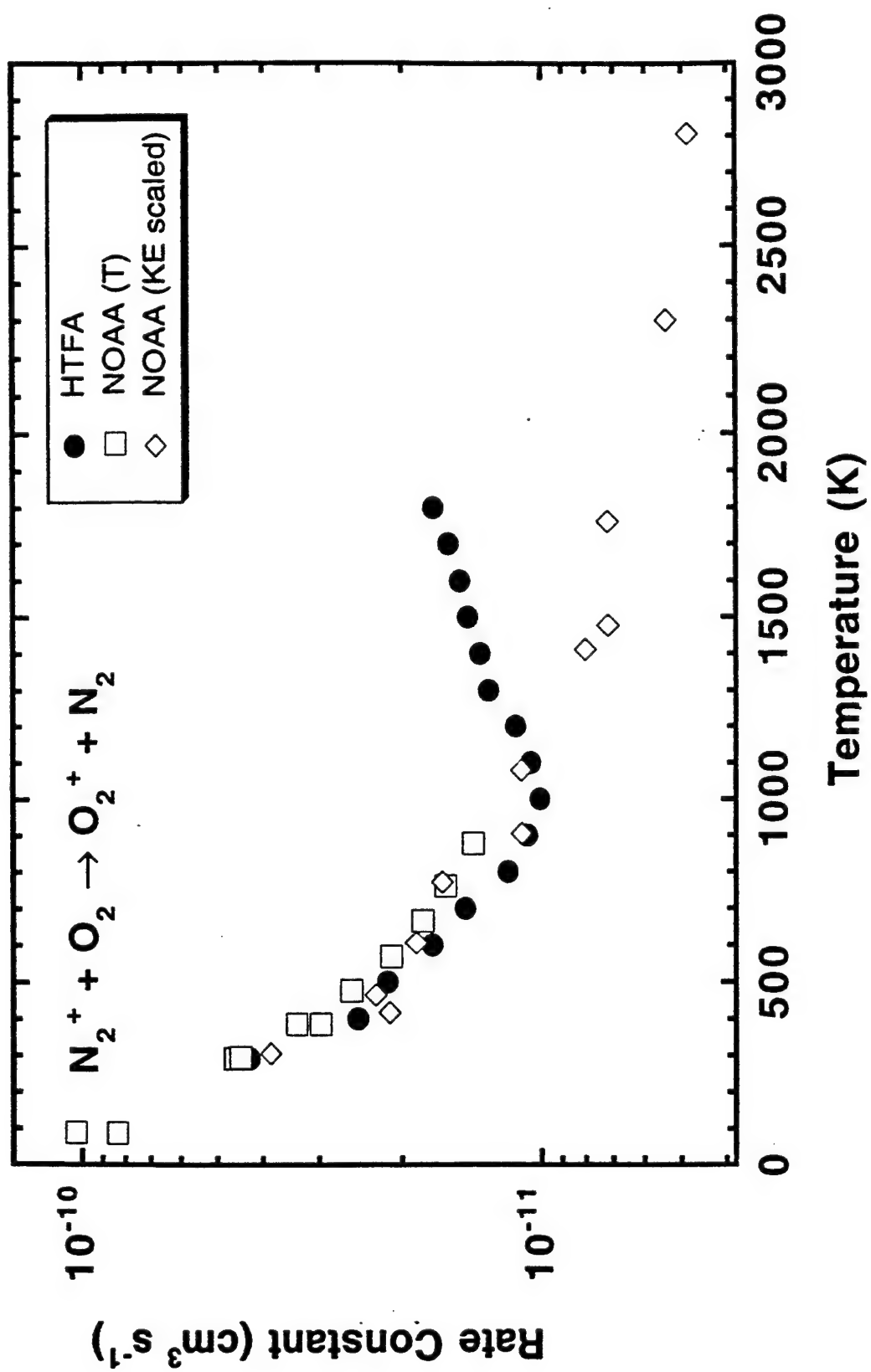


Fig 2

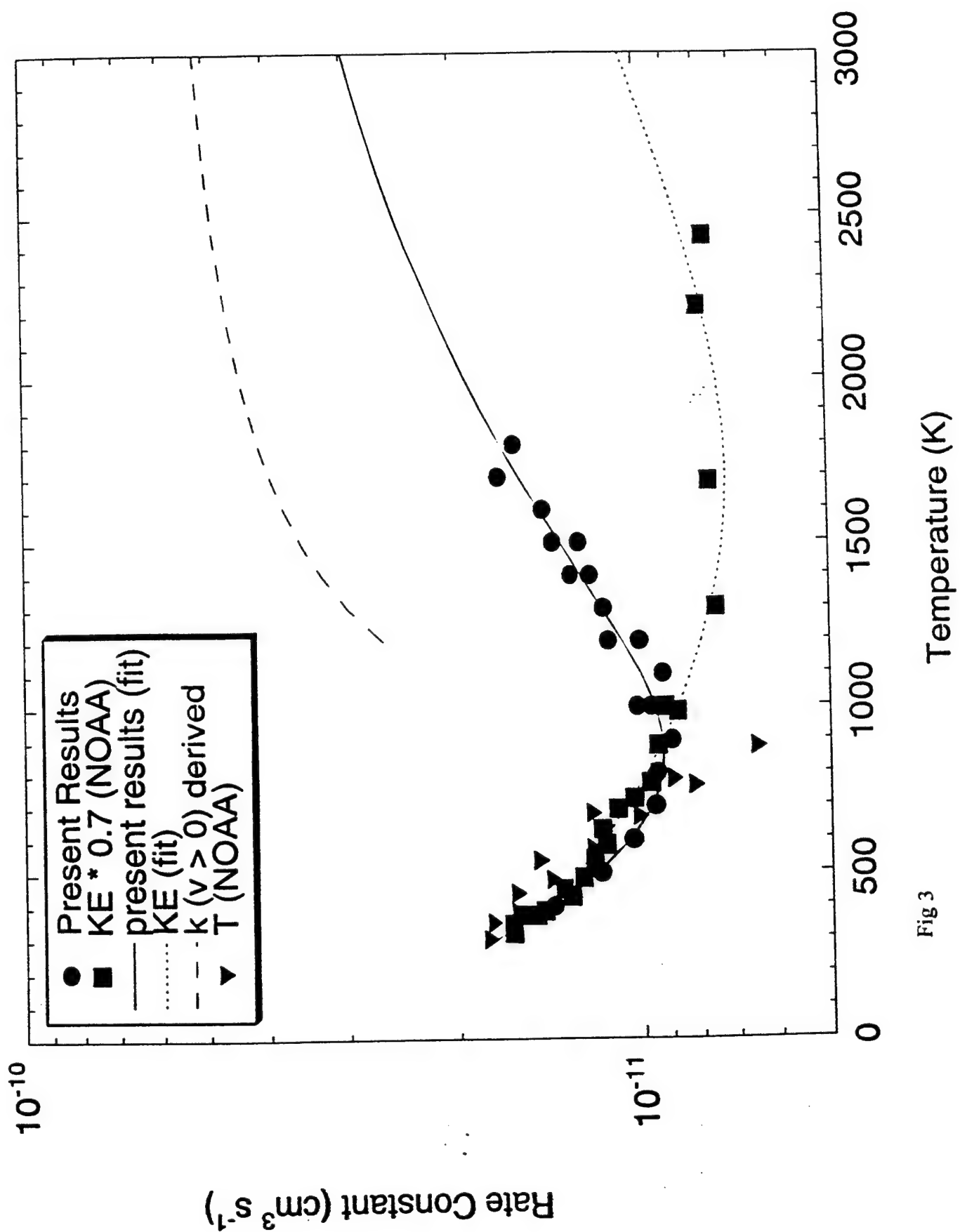


Fig 3

Main Reaction Controlling Ionospheric Electron Concentration

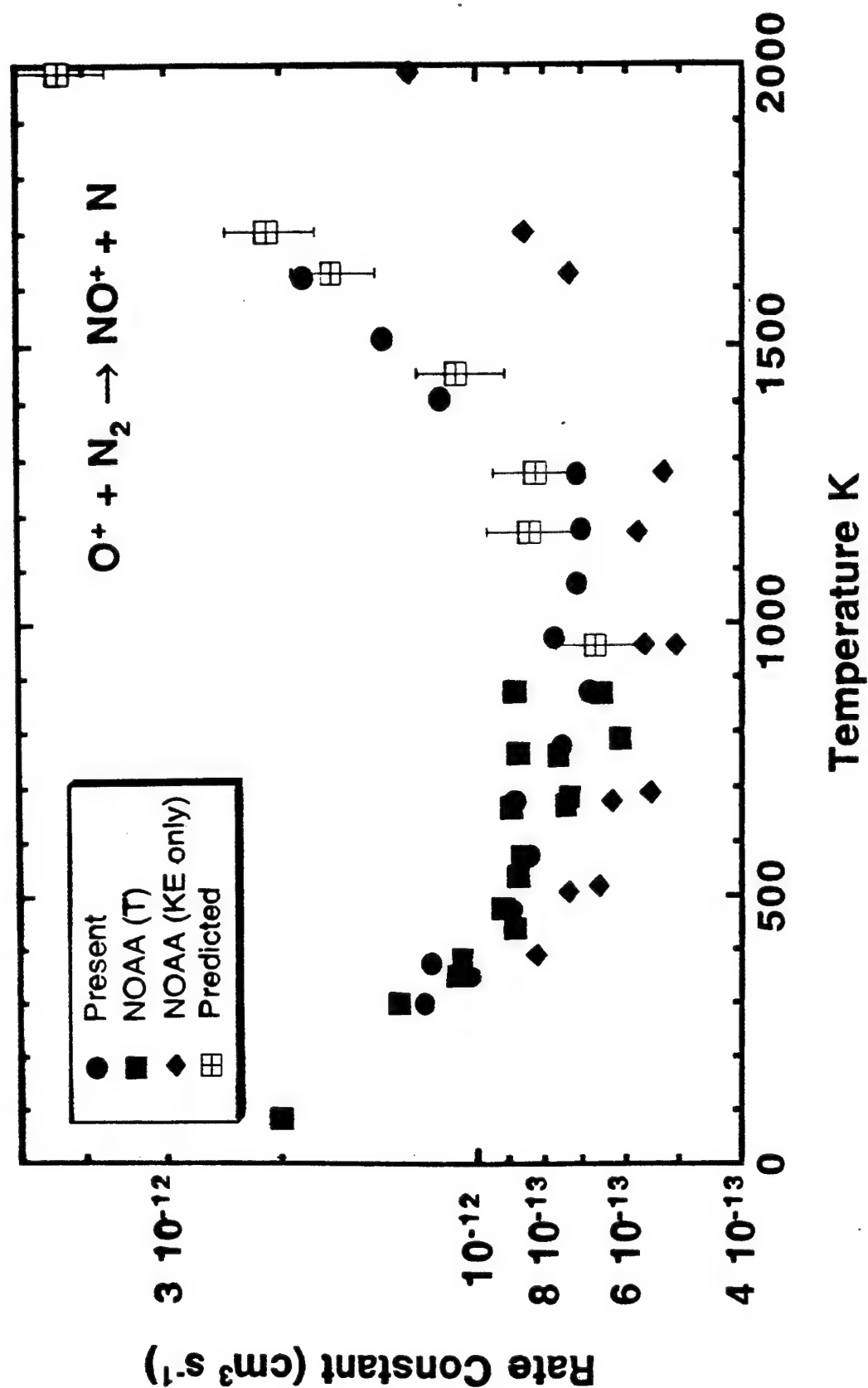


Fig 4

ON THE MATERIALS SELECTION OF DURABLE
COATINGS FOR CRYOGENIC ENGINE TECHNOLOGY

Omar S. Es-Said
Associate Professor
Mechanical Engineering Department

Loyola Marymount University
7900 Loyola Blvd.
Los Angeles, Ca 90045-8145

Final Report for:
Summer Faculty Research Program
Phillips Laboratory

Sponsored by:
Air Force Office of Scientific Research
Bolling Air Force Base, DC
and
Phillips Laboratory

September 1996

ON THE MATERIALS SELECTION OF DURABLE COATINGS FOR CRYOGENIC ENGINE TECHNOLOGY

Omar S. Es-Said
Associate Professor
Mechanical Engineering Department
Loyola Marymount University

Abstract

Many benefits can be realized by incorporating hydrostatic bearings into liquid hydrogen turbopumps, however, suitable material coatings must be used to avoid excessive wear during multiple starts and stops. A short list of eight coating materials is suggested. Nine manufacturers out of fifty contacted are identified as capable of depositing durable coatings on Inconel 718. A cost effective low temperature tribometer based on the hydrostatic bearing application should be designed and built prior to performing full scale tests in area I-14.

ON THE MATERIALS SELECTION OF DURABLE COATINGS FOR CRYOGENIC ENGINE TECHNOLOGY

Omar S. Es-Said
Associate Professor
Mechanical Engineering Department
Loyola Marymount University

Introduction

Turbopumps are pumps that supply the oxidizer and the fuel to a liquid rocket engine. At present, roller bearings around their rotating shafts are used. The aim of Phillips Laboratory is to replace these rolling elements with hydrostatic bearings, which have no inherent speed limitations because they are essentially non-contact devices. Pressurized hydrogen is then injected to keep the rotating shaft from touching the bearing during operation.

Discussion of Problem

The Rocket Propulsion Directorate of the U.S. Air Force, Phillips Laboratory is exploring rocket propulsion systems that use hydrostatic turbomachinery bearings in rocket engine turbopumps {1}. Current technology, which uses roller bearings around their rotating shafts requires that the turbopumps be rebuilt frequently and at great expense. These systems need materials that are capable of surviving high rates of rotation, are wear and abrasion resistant, and can undergo multiple starts and stops while operating in a liquid hydrogen environment {1}.

The bearing walls may be worn during start up and shutdown while the rotor shaft is in contact. This is due to the lack of pressure governing their placement in the center of the bearing. Moreover, debris (silicate minerals) passing through the clearance between the shaft and bearing may cause abrasive wear. This debris is present in the cryogenic fluid and the filtration systems are not able to keep small particles (about 30 micrometers) from entering the turbopump {2}.

The existing material, Inconel 718, of which the shaft and bearing are made, should not be changed or else design layout drawings, modified shop drawings, and casting

tooling would require major modification. Maintaining this material would constrain the deposition method to be carried out under 600 degrees Celsius, which is the maximum allowable temperature before softening occurs in Inconel 718. The aim of this work is to identify potential candidate material coatings and manufacturers who can deposit them on Inconel 718 substrates.

Methodology

Choosing the best material for this application requires experimentation. The wearing of a coated material depends on the processing method, processing conditions, surface preparations, and coating thickness. The suggested method for choosing the material involves four steps:

- 1) Identifying a short list of materials
- 2) Identifying a short list of manufacturers who can deposit and optimize these coatings.
- 3) Design and fabricate a small-scale tribological testing equipment (tribometer) to scale down the number of competing material coatings. This should be a simulation of the hydrostatic bearing application.
- 4) Perform full scale tests using an actual turbopump in area I-14

I. Short List of Materials

There are two categories of dry lubricant coatings to be considered for low temperature (liquid hydrogen) hydrostatic bearing. One is a *very low friction* coating that also reduces wear and the other is a harder *low wear* coating that provides some reduction in friction.

a. Low Friction Coatings

In the first category, very low friction candidates, soft, slippery coatings are considered, examples are Ag, and MoS₂. MoS₂ coatings have been used by the military as a dry lubricant for a harmonic drive assembly of gears and ball bearings, used to point an antenna on a classified satellite {3}. These coatings were tested successfully over lifetimes lasting hundreds of millions of revolutions on heavily loaded bearings, and are now standard coatings in the U.S. and European space programs. Moreover, MoS₂ is compatible with Inconel 718, the traditional material of the bearing and shaft {3}.

In a private communication with Mr. Ron Christy, owner of TRIBO COATING {4}, he suggested that MoS₂-Ni coating performed very well in tests ran at TRW in Redondo Beach, California at liquid helium temperature as a spacecraft bearing and gear

lubricant, and recently as a coating applied to cutting tools for machining aluminum. MoS₂ is researched in detail, and is presented in appendix 1.8 and MoS₂-Ni is a low friction potential candidate for the hydrostatic bearing application. The potential manufacturer is TRIBO COATING, 26615 Ocean Dr., Malibu, Ca 90265, Tel. No. 800-789-9974, Fax: (310) 457-2261.

b. Low Wear Coatings

Hard, wear resistant coatings are the primary candidates for hydrostatic bearing application. The wear mechanisms that are likely to predominate in the hydrostatic bearing application are adhesive wear (between the bearing and shaft), abrasive wear (due to the debris), and brittle fracture wear (for ceramic coating materials having low tensile strengths compared to their compressive strengths). Ceramics are especially well suited for this application {5,6}. Their low values of surface energy and high values of hardness lead to lower friction, low adhesive wear, low abrasive wear, and minimal loose debris particle size {6}. The material properties which are relevant to the selection of ceramic coatings for low temperature hydrostatic bearings are thermal expansion coefficient, Young's modulus, thermal expansion compatibility with the substrate, hardness, density (% theoretical), surface energy, and fracture toughness.

High hardness results in low wear and a low ratio of surface energy to hardness lowers the wear rate. Microcracking from contact stresses at asperities or wear debris requires a material with a high fracture toughness. A high H/E (hardness/Young's modulus) will provide better elastic compliance and decohesion on unloading and accordingly low wear {6}.

Fifteen materials were identified as potential candidates for coatings of hydrostatic bearings {5}. These are tabulated in table I, together with the relevant physical and mechanical properties to be used in ranking their suitability. It should be noted, however, that the data for some materials is unavailable in current literature.

An overall ranking process was then conducted based on the highest thermal conductivity, lowest difference in thermal expansion coefficient with Inconel 718 substrate, highest fracture toughness, highest ratio of hardness/Young's modulus, and highest ratio of tensile/compressive strength. This exercise resulted in identifying seven potential candidates for coating of the hydrostatic bearing application. The final ranking was arrived at on the basis of the total number of appearances of each material within the ranking table criteria (table II).

The seven most suitable candidates are from best to worst: Silicon carbide, Diamond, Silicon nitride, Boron carbide, Alumina, Tantalum carbide and Zirconia. Except for Diamond and Diamond Like Carbon (DLC), which were thoroughly researched by Dr. A. Phelps {1}, and Dr. A Gonzalez {2}, these materials are studied in detail and included in appendix 1, as a materials data base. Silicon carbide is included in appendix 1.1 (13 references), Boron carbide in appendix 1.3 (20 references), Silicon nitride in appendix 1.4 (16 references), Aluminum oxide in appendix 1.5 (4 references), and Zirconia in appendix 1.6 (6 references). Other materials in appendix 1 include Boron nitride in appendix 1.2 (10 references), Titanium nitride in appendix 1.7 (19 references), Molybdenum Disulfide in appendix 1.8 (14 references), and tungsten carbide in appendix 1.9 (5 references).

TABLE 1

Physical and Mechanical Properties of candidate coatings, data obtained from CMS 2.1, Cambridge Materials Selector, Cambridge U.K., Cambridge University, 1993.

	Density Mg/m ³	Thermal Conductivity W/m.K	Thermal Expansion Coefficient 10 ⁻⁶ /K
Alumina*	3.75 - 3.93	24 - 35	8 - 8.9
Boron carbide*	2.45 - 2.52	27 - 36	3.5 - 5.6
Boron nitride*	3.45 - 3.49	2 - 13	
Chromium carbide			9.8 **
Diamond	3.51 - 3.52	600 - 2.20E+3	0.8 - 1.2
Silicon carbide*	3 - 3.22	90 - 200	4.3 - 4.6
Silicon nitride*	2.8 - 3.44	15 - 43	2.6 - 3.3
Tantalum carbide	13.4 - 13.9	20 - 22.2	6.6 - 7.4 (8.0**)
Titanium boride			8.1 **
Titanium carbide	4.9 - 4.93	18 - 25	6.6 - 7.4 (8.0**)
Titanium nitride*	5.5		
Titanium oxide	4.25	8.37	8.9
Tungsten carbide*	15.5 - 15.63	28 - 88	4.5 - 7.1
Tungsten carbide/cobalt			
Zirconia*	5.7 - 6.1	2 - 12	7 - 9

* Researched in detail in appendices 1.1 - 1.9

** As reported from Ultramet, Pacoima, Ca 91331

TABLE I (cont.)

	Electrical Resistivity 10 ⁻⁸ ohm.m	Erosion GPa ⁻³ .m ^{-1/2}	Fracture Toughness MPa.m ^{1/2}
Alumina	3.16E+19 - 3.16E+20		3.5 - 4.5
Boron carbide	1.00E+5 - 1.00E+8		3.6 - 3.7
Boron nitride	10 - 10E+5		
Chromium carbide			
Diamond	1.00E+10 - 1.00E+20		2.3 - 3.4
Silicon carbide	1.00E+3 - 1.00E+5		3 - 5.1
Silicon nitride	1.00E+12 - 1.00E+15		4 - 5.4
Tantalum carbide	25.12 - 31.62		2-3.0
Titanium boride			
Titanium carbide	177.8 - 251.2		2-3.0
Titanium nitride			
Titanium oxide		0.65**	2.5
Tungsten carbide	63.1 - 100		2 - 3.8
Tungsten carbide/cobalt		0.1**	15
Zirconia	1.00E+17 - 1.00E+18		2 - 6.9

TABLE I (cont.)

	Shear Modulus GPa	Surface Energy kJ/m ²	Hardness MPa
Alumina	100 - 152		1.50E+4 - 1.65E+4
Boron carbide	186 - 190		3.10E+4 - 3.30E+4
Boron Nitride			
Chromium carbide			
Diamond	440 - 470		5.50E+4 - 1.12E+5
Silicon carbide	175 - 192	0.05**	2.50E+4 - 3.30E+4
Silicon nitride	112 - 122	0.1**	1.70E+4 - 2.3E+4
Tantalum carbide	145 - 151		1.30E+4 - 2.40E+4
Titanium boride			
Titanium carbide	165 - 187		2.50E+4 - 3.20E+4
Titanium nitride			2.45E+04
Titanium oxide			1.10E+04
Tungsten carbide	243 - 271		3.10E+4 - 3.60E+4
Tungsten carbide/cobalt			1.20E+04
Zirconia	60 - 80		1.20E+4 - 1.40E+4

TABLE I (cont.)

	Surface Energy/Hardness KJ/M ² MPa	Rank	Young's Modulus GPa
Alumina	1.21E-6 - 1.33E-6	1	330 - 400
Boron carbide			440 - 472
Boron Nitride			
Chromium carbide			
Diamond			1.00E+3 - 1.05E+3
Silicon carbide	1.52E-6 - 2.00E-6	2	390 - 440
Silicon nitride	4.35E-6 - 5.88E-6	3	280 - 310
Tantalum carbide			360 - 375
Titanium boride			
Titanium carbide			420 - 450
Titanium nitride			
Titanium oxide			283
Tungsten carbide			600 - 670
Tungsten carbide/cobalt			
Zirconia			180 - 240

TABLE I (cont.)

	Hardness/Young's Modulus *10-3	Rank	Tensile Strength MPa
Alumina	41.250 - 45.455	9	220 - 340
Boron carbide	69.915 - 70.455	5	330 - 380
Boron Nitride			
Chromium carbide			
Diamond	55.000 - 106.66	1	4.00E+3 - 6.00E+3
Silicon carbide	64.103 - 75.000	2	310 - 400
Silicon nitride	60.714 - 74.194	3	400 - 580
Tantalum carbide	36.111 - 64.000	7	260 - 280
Titanium boride			
Titanium carbide	59.523 - 71.111	4	260 - 330
Titanium nitride			
Titanium oxide	38.869	10	
Tungsten carbide	51.667 - 53.731	8	373 - 530
Tungsten carbide/cobalt			
Zirconia	58.333 - 66.667	6	110 - 240

TABLE I (cont.)

	Compressive Strength MPa	Tensile/ Compressive Strength	Rank
Alumina	1.75E+3 - 3.00E+3	0.113 - 0.126	4
Boron carbide	1.40E+3 - 3.40E+3	0.112 - 0.236	1
Boron Nitride			
Chromium carbide			
Diamond	3.00E+4 - 6.50E+4	0.092 - 0.133	3
Silicon carbide	2.00E+3 - 3.50E+3	0.114 - 0.155	2
Silicon nitride	1.10E+4 - 2.50E+4	0.023 - 0.036	9
Tantalum carbide	3.00E+3 - 3.90E+3	0.0718 - 0.0867	5
Titanium boride			
Titanium carbide	3.57E+3 - 5.85E+3	0.0564 - 0.0728	6
Titanium nitride			
Titanium oxide			
Tungsten carbide	6.60E+3 - 1.00E+4	0.053 - 0.057	8
Tungsten carbide/cobalt			
Zirconia	1.65E+3 - 3.60E+3	0.067	7

**TABLE II:
RANKING OF MATERIALS**

Thermal Conductivity	Difference in CTE*	Fracture Toughness K_{IC}	H/ E	Tensile/ Compression
Diamond	Zirconia	WC-Co	Diamond	Boron carbide
Chromium carbide	Silicon carbide	Chromium carbide	Zirconia	Silicon carbide
Alumina, Titanium oxide	Tungstent carbide	Alumina, Titanium oxide	Silicon nitride	Silicon nitride
Titanium boride	Silicon nitride	Titanium boride	Silicon carbide	Titanium carbide
Tantalum carbide	Boron carbide	Tantalum carbide	Tantalum carbide	Boron carbide

Final Ranking By Total Number Of Appearances:

- 1) Silicon Carbide
- 2) Diamond, Silicon nitride, Boron carbide, Alumina
- 3) Tantalum carbide, Zirconia

* Change in co-efficient of thermal expansion as compared to that of Inconel 718 (11.5 ppm/degrees Kelvins)

2. Short List of Manufacturers of Low Wear Coatings

Since the film coatings must be applied on Inconel 718 at deposition temperatures which do not exceed 600 degrees Celsius to avoid material softening, a list of 49 companies specializing in low wear coatings was compiled (ceramic source 1996, also included in appendix 2). All were contacted, but only eight companies advised us that they have the capacity to undertake the project within the temperature restriction. Below is a list of the 49 companies contacted in alphabetical order. The eight companies are highlighted using bold face print.

Once these eight companies confirmed their capability of depositing low temperature thin film coatings, further inquiries were made concerning their coating methods and film thickness. The responses were as follows:

According to Jerry Latin from Advanced Refractory Technologies, Inc., the coating method used is trademarked Dylyn, which is a PVD method. The deposition temperatures vary from room temperature to 250 degrees Celsius. The thickness of the coatings can vary from 1 to 10 μm . Although Inconel 718 has not been used as a substrate, a variety of metals, semiconductors, quartz, ceramics, polycrystalline diamond based materials, cements, polymers, composites, and other materials have. Out of seven materials selected for the bearings, only silicon carbide is available for coatings.

According to Dr. William Sproul, BIRL's Industrial Group Program Manager, (Basic Industry Research Lab), ex-General Chairman of the International Conference on Metallurgical Coatings, and 1996 President of the vacuum society, BIRL deposits films by unbalanced magnetron (UBM) sputter deposition by PVD. This method ensures high ion bombardment of the growing coating for high-quality coatings at low deposition temperatures (100-500 degrees Celsius). BIRL has six active applications, and can consult on equipment and methods to adopt PVD technologies. Coatings can be accomplished from 1 to 10 μm . BIRL can deposit all seven materials, but diamond can only be deposited at high temperatures.

As stated by Arnold H. Dutchman from Beam Alloy Corp., the coating method used is trademarked by Chromion, which is an advanced ion beam enhanced deposition which takes place in a clean, high vacuum chamber without the use of chemical plating solutions. The deposition temperatures occur at a maximum temperature of 100 degrees Celsius, with a deposition thickness of 1 to 10 μm . The coatings have not been used on Inconel 718, but they have been used on steel, nickel, and copper, and no adhesion problems have occurred. Beam Alloy Corp. has alumina, which is one of the seven materials ready for coating.

According to C.T. Chu, from Chemat Technology, Inc., the coating method used is sol-gel, which is a solution technique. The maximum temperature of the substrate is 450 degrees Celsius, and the typical thickness is 1 μm . Coatings on Inconel 706 have been applied for coatings: alumina, Zirconia, and silicon carbide. Alumina is available at any time, but Zirconia and silicon nitride can be made.

According to Mike Powers, from Commonwealth Scientific Corp., the coating method is ion beam sputtering with a deposition at room temperature. The typical thickness of the coating is 1 μm , which takes two hours. All seven materials can be applied as coatings.

As stated by Dr. Rick J. Yoon, President of I.J. Research, Inc, and Materials Scientist with 27 years experience in ceramics and metallurgical engineering, the coating methods used are DC magnetron sputtering, RF sputtering, and ion beam sputtering. Alumina and Zirconia are two of the seven materials used for coatings.

According to Conrad Lundgren, from System Images, the coating methods used are e-beam and thermo-evaporation, with a maximum temperature of 240 degrees Celsius. The typical thickness the company achieves is 10 to 1000 Å, although they can apply thicker coats. They have used Inconel 718 as a substrate and no adhesion problems have occurred.

According to Dr. Weinman, from Thin Films Concepts, Inc., the coating methods used are magnetron sputtering and their deposition temperatures do not exceed 250 degrees Celsius. The typical thickness is 1 to 5 μm , but they can apply thicker coats. Silicon nitride and alumina are two of the seven materials which they have used as a thin film.

The potential manufacturers of low wear coatings are BIRL's Industrial Group (Basic Industry Research Lab), and Commonwealth Scientific Corp., since they are capable of depositing all seven films.

In appendix 2, a listing of companies dealing with wear resistant coatings is included and in appendix 3, samples of companies responses to our investigation.

•ABB AIR
PREHEATER
Raymond Products
650 Warrenville Rd.
Lisle, IL 60532
(708) 971-2500
FAX: (708) 971-1076

•ABRESIST CORP.
Box 38
5541 North State Rd. 13
Urbana, IN 46990
(219) 774-3327
FAX: (219) 774-8188

•ADVANCED
CERAMICS CORP.
Box 94924
Cleveland, OH 44101-
4924
(800) 822-4322
FAX: (216) 529-3975

•ADVANCED
REFACTORY
TECHNOLOGIES,
INC.
699 Hertel Ave.
Buffalo, NY 14207
(716) 875-4091
FAX: (716) 875-0106
Employee: Jerry Latin
Deposition
processPVD

*AJA
INTERNATIONAL
2719 Cory Ave.
Box 246
N. Scituate, MA 02060
(617) 545-7365
FAX: (617) 545-4105

•AMERICAN ROLLER
CO. R&D
1400 13th Ave.
Union Grove, WI 53182
(414) 878-3751
FAX: (414) 878-3893

•ARCHER
TECHNICOAT INC.
430 10th St. NW, Suite
N-102
Atlanta, GA 30318
(404) 874-7240
FAX: (404) 874-8187

•AREMCO
PRODUCTS, INC.
23 Snowden Ave.
Box 429, Ossining, NY
10562
(914) 762-0685
FAX: (914) 762-1663

*BALZERS HIGH
VACUUM PRODUCTS
8 Sagamore Park Rd.
Hudson, NH 03051-
4914
(603) 889-: 6388
FAX: (603) 889-8573

•*BALZERS TOOL
COATING, INC.
661 Erie Ave.
North Tonawanda, NY
14120-0688
(716) 693-8557
FAX: (716) 695-1995

•BASIC INDUSTRY
RESEARCH LAB.
1801 Maple Ave.
Evaston, IL 60201-
3135
(847) 491-4108
FAX: (847) 467-1022
Employee: Bill Sproul
Deposition process:
sputtering

•BAY
STATE/STERLING
INC.
12 Union St.
Westboro, MA 01581
(800) 366-4431
FAX: (800) 366-4311

•*BEAM ALLOY
CORP.
Dublin Research Park
6360 Dublin Industrial
Estate
Dublin, OH 43017-
1277
(614) 766-3300
FAX: (614) 766-3306
Employee: Arnold
Dutchman
Deposition process: ion
beam enhanced
deposition

•BENCHMARK
STRUCTURAL
CERAMICS CORP.
350 Nagel DriveAve
Buffalo, NY 14225
(716) 685-4850
FAX: (716) 685-4859

•CARBONE OF
AMERICA CORP.
Ultra Carbon Div.
900 Harrison St.
Bay City, MI 48708-
8224
(517) 894-2911
FAX: (517) 895-7740

• *CHEMAT
TECHNOLOGY, INC.
19365 Business Center
Dr.
Suite 8 & 9,
Northridge, CA 91324
(818) 727-9786
FAX: (818) 727-9477
Employee: C.T. Chu
Deposition process:
Sol-Gel

*COMMONWEALTH
SCIENTIFIC CORP.
500 Pendleton St.
Alexandria, VA 22314
(730) 548-0800
FAX: (703) 548-7405
Employee: Mike
Powers
Deposition process: ion
beam sputtering

•DELKIC & ASSOC.
Int'l Technical Ceramics
Inc.
Box 1726
Ponte Vedra Beach, FL
32004
(904) 285-0200
FAX: (904) 273-1616

•DIAMONTE
PRODUCTS
453 W. McConkey St.
Shreve, OH 44676
(216) 567-2145
FAX: (216) 567-2260

•DIDIER WEARTECH
AG
Div. Of Moh g (Pty) Ltd.
Box 16992
N. Pretoria 0116,
SouthAfrica
(26) 11-880-2300
FAX: 011-880-3260

*DOW CORNING
CORP.
Box 994
Midland, MI 48686-
0994
(517) 496-4000
FAX: (517) 496-4586

•DYNAMIC-CERAMIC,
LTD.
Bournes Bank, Burslem
Stoke-on-trent
ST6 3DW, United
Kingdom
(78) 2-575537
FAX: (78) 2-575537

*ENGELHARD CORP.
101 Wood Ave.
Iselin, NJ 08830
(908) 205-5000
FAX: (908) 632-9253

•EPH ENGINEERING
ASSOCIATES, INC.
21 E. 400 South
Orem, UT 84058
(801) 226-1383
FAX: (801) 226-1437

•GREENLEAF CORP.
One Greenleaf Dr.
Saegerton, PA 16433
(814) 763-2915
FAX: (814) 763-4137

*GWENT
ELECTTRONIC
MATERIALS, LTD.
Monmouth House
Mamhilad Park
Pontypool
Gwent NP4 OHZ,
UNITED KINGDOM
(44) 495-750505
FAX: (44) 495-752121

• *IJ RESEARCH,
INC.
Glass & Ceramics
Division
1965 Blair Ave.
Santa Ana, CA 92705
(714) 253-8522
FAX: (714) 250-6338
Employee: Rick YOUNG
Deposition process:
sputtering

***INTERNATIONAL
APPLIED CONCEPTS**
Box 1435
S. Miami, FL 33243-
1435
(305) 534-3452
FAX: (305) 534-3462

•**KALENBORN
KALPROTECT**
*Dr. Mauritz GmbH &
Co. KG*
Vettelschoss 2 D-53558,
Germany
(26) 45-18-0
FAX: (26) 45-18-12

•**LANXIDE COATED
PRODUCTS**
Box 6077
1300 Marrows Rd.
Newmark, DE 19714-
6077
(302) 456-6200
FAX: (302) 454-1712

•**LWK
PLASMAKERAMIK
GMBH**
Box 31 02 85
D-51617 Gummersbach
31, Germany
(49) 2261-7092-0
FAX: (49) 2261-70924-0

•**MAN TECHNOLOGI
AG CMC-T**
LEIBIGSTR. 5a
d-85757 Karlsfeld,
Germany
(89) 15807389
FAX: (89) 15807722

***NATIONAL
MAGNETICS GROUP,
INC.**
1210 Win Dr.
Bethlehem, PA 18017-
7061
(610) 867-7600
FAX: (610) 867-0200

•**NIPPON STEEL
CORP.**
New Materials Div.
6-3, Otemachi, 2-chome
Chiyoda-ku
Tokyo, Japan
(03) 3242-4111
FAX: (03) 3211-2731

•**PEMCO PRODUCTS**
Enamels and Ceramics
Group
Bayer Corp.
5601 Eastern Ave.
Baltimore, MD 21224-
2791
(410) 633-9550
FAX: (410) 631-4354

•**PRAXAIR SURFACE
TECHNOLOGIES,
INC.**
1500 Polco St.
Indianapolis, IN 466224
(317) 240-2500
FAX: (317) 240-2426

•**RENITE CORP.**
Box 278
Bleachery Pl.
Chadwicks, NY 13319
(315) 737-7381
FAX: (315) 737-5709

•**SAUEREISEN**
160 Gamma Dr.
Pittsburgh, PA 15238-
2989
(412) 963-0303
FAX: (412) 963-7620

•**SCHUNK GRAPHITE
TECHNOLOGY**
W146 N9300 Held Dr.
Menomonee Falls, WI
53051
(414) 253-8720
FAX: (414) 255-1391

•**A.O. SMITH CORP.**
Protective Coatings Div.
8160 Holton Dr.
Florence, KY 41042
(606) 727-3500
FAX: (606) 727-6776

***SOLERAS, LTD**
Box BCBiddeford, ME
04005
(207) 282-5699
FAX: (207) 284-6118

•**STORK CELLRAMIC,
INC.**
8399 N. 87th St.
Box 24180
Milwaukee, WI 53224-
0180
(414) 357-0260
FAX: (414) 357-0267

***SUPERCONDUCTIVE COMPONENTS, INC.**

Targets Materials, Inc.
1145 Chesapeake Ave.
Columbus, OH 43212
(614) 486-0912
FAX: (614) 486-0912

***SWAIN TECH COATINGS**

35 Main St.
Scottsville, NY 14546
(716) 889-2786
FAX: (716) 889-52

SYSTEM IMAGES

(Referred to by J.R.
**Gain Super
Conductive
Components)**
823 Route 15
Dover Foxcroft, Maine
04426
(207) 564-2149
**Employee: Conrad
Lundgren**
**Deposition process:
E-Beam and Thermo-
Evaporation**

***THIN FILMS**

CONCEPTS, INC.
One Westchester Plaza
Elmsford, NY 10523
(914) 592-4700
FAX: (914) 592-0067
Employee: Dr.
Weinman
Deposition Process:
sputtering
Deposition Process:
sputtering

***THIN-FILMS**

RESEARCH
270 Littleton Rd.
Westford, MA 01866
(508) 692-9530
FAX: (508) 692-9531
***UNIVERSITY OF
WISCONSIN AT
MILWAUKEE**
Materials Dept.
3200 N. Cramer St.
Milwaukee, WI 53211
(414) 229-5161
FAX: (414) 229-6958

•WZM ENTERPRISES, INC.

101 South 5th St.
Harrison, NJ 07029
(201) 485-6035
FAX: (201) 485-6035

Foreign companies are in *italics*.

* refers to the companies that were found under wear resistant coatings.

• refers to the companies that were found under thin films.

Note: Some companies were found under both subheadings.

3. Design and Fabrication of a Tribometer

4. Full Scale Testing

These steps have not been addressed in the current report since they represent the second phase of this project.

Conclusions

Eight candidate materials are identified as potential coatings for hydrostatic bearings. MoS₂-Ni for low friction and Silicon carbide, Diamond, Silicon nitride, Boron carbide, Alumina, Tantalum carbide, and Zirconia for low wear in order of preference.

Nine manufacturers indicated that they could deposit these coatings on Inconel 718 below 600 degrees Celsius. Two are more likely capable of depositing the low wear coatings: BIRL (Basic Industry Research Lab) and Commonwealth Scientific.

References

1. A.W. Phelps, "Durable Coatings Synthesis for Cryogenic Engine Technology," Final Report AFSC Contract No. F04611-88-C-0020, 1993.
2. A.C. Gonzalez, "Mechanical Assessment of Diamond Films for Hydrostatic Bearing Surfaces," Final Report No. PL-TR-93-3085, 1996.
3. R. Christy, "Cutting Tool Engineering," Vol. 46, No. 1, Feb. 1994.
4. Private Communication with Mr. Ron Christy, President of Tribo Coating, Sept. 15, 1996.
5. Ernest Rabinowicz, Friction and Wear of Materials, John Wiley&Sons Inc., 1995.
6. F.J. Carigran and A.I. West, "Hard-on-Hard (Ceramic) Long Life Seals and Riders for Cryogenic Coolers," Final Report, Contract No. F33615-79-C-5029, 1981.

TESTING THE FROZEN SCREEN MODEL OF ATMOSPHERIC TURBULENCE
AND
AN INTERFEROMETER DESIGN
FOR MEASURING ATMOSPHERIC
TURBULENCE NEAR GROUND LEVELS

Jeffrey Foster Friedman
Assistant Professor
Department of Physics

University of Puerto Rico
Mayaguez campus

Final report for:
Summer Faculty Research Program
Phillips Laboratory

Sponsored by:
Air Force Office of Scientific Research
Bolling Air Force Base, DC

and

Phillips Laboratory

July 1996

TESTING THE FROZEN SCREEN MODEL OF ATMOSPHERIC TURBULENCE
AND
AN INTERFEROMETER DESIGN FOR MEASURING ATMOSPHERIC
TURBULENCE NEAR GROUND LEVELS

Jeffrey Foster Friedman
Assistant Professor
Department of Physics
University of Puerto Rico - Mayaguez campus

Abstract

Atmospheric turbulence is responsible for scattering of the light that makes its way through the atmosphere and therefore deteriorates the observations being made by any astronomical instrument. This study designs a triple coincidence experiment to test the frozen screen model of atmospheric turbulence and determine if we can put in place an interferometer or equivalent system that will measure the atmospheric turbulence in the near field. Various types of interferometers have been considered including the Fabry - Perot and the Mach - Zehnder arrangements. Other design considerations include the path lengths necessary for detection of small changes in the index of refraction of air, light sources and positioning of the interferometer.

The "frozen" screen model is to be tested to determine if it can be used as a predictive tool. If the turbulent disturbances travel as a frozen screen it should be possible to sample them upstream of a telescope and apply corrections in real time; or if this is not possible then downstream of the telescope for post detection corrections. We propose to build an 'Amato' (one arm in vacuum) Mach-Zehnder type interferometer with physically coupled arms that expand and contract together to null any pathlength changes in the system due to changes in the apparatus. This is to insure that all phase shifts in the fringe pattern are due to changes in the index of refraction of the air in the open arm, see section *. We propose to use two identical setups in an upwind/downwind configuration and check for time delayed coincidences in the fringe patterns. In parallel we propose to run a very high resolution Fabry-Perot Interferometer and very sensitive Microbarograph and do similar coincidence studies to see if any or all methods are useful in detecting and predicting atmospheric fluctuations.

TESTING THE FROZEN SCREEN MODEL OF ATMOSPHERIC TURBULENCE AND AN INTERFEROMETER DESIGN FOR MEASURING ATMOSPHERIC TURBULENCE NEAR GROUND LEVELS

Jeffrey Foster Friedman

A. Introduction. It is common knowledge that most, if not all, astronomical observations done on earth are affected by turbulence present in the earth's atmosphere. In fluid mechanics the motion of a liquid or gas is considered to be turbulent when it's velocity at any point is fluctuating in magnitude and direction in a chaotic and random manner. Furthermore what distinguishes turbulence from wave action is the fact that turbulence leads to increased rates of transport of heat, momentum and other properties like salt or water vapor [ref. 1]. The stability of density gradients can greatly modify turbulence and the transport that it produces and so can compressibility and electrical conductivity.

Atmospheric turbulence, which is the main concern of this study, is considered by meteorology as small scale motion. It's two major causes are: 1) mechanical turbulence due to the rapid change of large scale wind, and 2) heat convection, caused by heating from below or cooling from above, [ref. 1]. There are three regions in which turbulence is most important, these are: 1) near the ground, 2) in convective air flow, and 3) turbulence occurring in clear air between 25,000-40,000 feet, known as clear air turbulence (CAT). It is also important to notice that atmospheric turbulence is affected by natural factors. For example on a windy day turbulence is stronger near the ground and will therefore be dependent on wind velocity, this type of turbulence is stronger over rough terrain. Convection will increase the turbulence in the daytime and will suppress it at night.

The effects of turbulence are many, first it affects the distribution of the meteorological variables by its ability to produce vertical mixing which is weakest near the ground: therefore we encounter the strongest turbulence gradients immediately above the surface. It also has a marked effect on light that makes it way through the atmosphere, since the index of refraction of the atmosphere, even at a given wavelength, is not constant because the atmosphere's density and temperature are not constant. Some of the reasons why

atmospheric density is not constant are its decrease with altitude, heating by the sun, and turbulent wind flow. This creates localized changes in the index of refraction for different layers in the atmosphere which causes rays of light to be refracted.. Turbulence also creates irregular patches of temperature and moisture which in turn produce scattering of the electromagnetic and sound waves that go through it. For optical observations this effect creates a lot of trouble. When a telescope looks through an isoplanatic patch (a patch of the atmosphere where the angular size of a single atmospheric coherence cell is determined by the physical size of the cell and its elevation [ref. 2]) within a turbulent region the light is affected more or less uniformly. But if the telescope looks through patches sweeping by the effects of the different patches are combined and the visual image is deteriorated. Although this effect diminishes with increasing wavelength it still affects observations made in the visible and near to mid infrared range of the electromagnetic spectrum.

All of the above effects combine to degrade the image being observed by producing scintillation, "quivering", image motion and scattering. Several modern adaptive optics systems have been created to solve or at least diminish this problem, for example by using a laser beam to create an artificial beacon in the sky that serves as a guide star and measuring the effect of the atmosphere on the light from the guide star to adjust a deformable mirror to conjugate this effects [ref. 3]. The high cost and lack of availability of this system is one of it's biggest constraints. Other systems are available or under development [ref.13] but all suffer from similar drawbacks.

The issue we would like to address is the problem of light starvation. Since our method of correction does not use any light gathered by the telescope or have any elements in common with the telescope it does not use any of the photons available to the system and then lower it's sensitivity.

There have been many studies that have measured atmospheric turbulence at different locations and their findings are reasons to fuel the purpose of this project. For example, one of those used an acoustic echo sounder to measure the turbulence above Air Force Maui Optical Station (AMOS) and found that most of the optical turbulence above this site is in the first 7.5 to 100m above the ground [ref 5]. Another study performed at the Infrared Spatial Interferometer (ISI) located on Mt. Wilson, California

found that 20% of the fluctuation power observed from a star is caused by close ground turbulence. Furthermore, for $t=100$ seconds in the observations in that study 12% of the fringe fluctuation (temporal changes in the interference pattern of the light combined from the two telescopes of the interferometer) occurs close to the ground, specifically a few tens of meters from the ground [ref 8]. These among others are all facts that point towards the development of an instrument that can measure the atmospheric turbulence concentrated near the ground, and can do so without damaging the medium being measured or creating more turbulence.

B. Purpose

The purpose of this study is two fold: to determine if the frozen screen model of atmospheric turbulence is valid and, if it is, to design an interferometer, or equivalent system, that will be able to measure the atmospheric turbulence that is present near a telescope and which degrades the irradiance that is being observed. Then the interferometer can relay this information to the telescope so it can correct for the (image) degradation produced by the turbulence. Since 50 to 70 percent of the atmospheric turbulence that affects astronomical observations is located in the first 50 to 100 meters above the ground, a regime known as the surface layer of the atmosphere, the interferometer will be designed with the objective of measuring this part of the atmosphere as it will prove to give the best results for imaging correction. As an adjunct to our consideration of a vertically sampling interferometer we propose to test two other methods that will be simpler to implement. The first is telescope level sampling with a Fabry-Perot interferometer of fluctuations in the index of refraction of the air traveling over the telescope and the second is to use a microbarograph that will sample total column variations of pressure over the telescope which we hope to be able to translate into a correction. We will test these methods using coincidence techniques with the dual interferometers; and wind speed and direction monitors.

The most important characteristic that the system should possess is the ability to relay its information in real (or near real) time so the telescope may benefit from the information nearly instantaneously. This is something that couldn't be achieved by many of the atmospheric turbulence measuring devices seen

before because they needed to gather the information and then analyze it [ref 4,5]: a process which takes too much time for our purpose. However this may prove to be unreasonable and post observation corrections may still be necessary.

C. Considerations for Experimental Design

The atmosphere is a random medium whose behavior is hard to predict but has been studied quite extensively. The Kolmogorov model provides a means of understanding turbulent behavior and tells us that the small scale structure of motion has the property of being locally homogeneous and isotropic [ref6]. Although the details of this hypothesis are not important to us at this time Taylor's "frozen screen" model is. Taylor's hypothesis tells us that for a stationary and homogeneous random field $f(\mathbf{r}, t)$ where \mathbf{r} is a point in space and t is time, whose time changes are associated with a translation of the spatial field distribution with a constant velocity \mathbf{v} , and that this translation does not include any mixing (therefore a "frozen" field), then

$$f(\mathbf{r}, t + t') = f(\mathbf{r} - \mathbf{v}t', t)$$

where \mathbf{v} can be taken to be the mean wind velocity with which the field $f(\mathbf{r})$ is being transported [ref 6]. Therefore if we were measuring the atmospheric turbulence in two different points, point A and point B, where B sits downstream from A in terms of wind direction, we would expect to find the same atmospheric turbulence at point A as at point B if the Taylor's hypothesis holds.

The first part of this project will consist of the testing of the "frozen" screen model. This is crucial at this point because if we find out that the "frozen" screen model is not valid, like in other experiments (for example ref. 8), then there is no purpose in building this interferometer because then the turbulence the interferometer measures will not be the same one that is going over the telescope and the corrections that the telescope makes will not be valid. In order to test the "frozen" screen we intend to use two interferometers which will most likely resemble the final design except may be on a smaller scale, and place these interferometers in a similar positions as points A and B in the above example. This will confirm if the atmospheric turbulence we measure with the first one will be the same that we measure

with the second. We will put a Fabry-Perot and a microbaograph at one of these positions to test alternate approaches to the same correction. An important remark is that this experiment will eventually have to be done at the site of the telescope since turbulence varies with surrounding terrain and while on some locations or systems the Taylor model is not valid on others it often is, as seen in ref. 12. This is one reason we have designed a triple coincidence experiment to check the frozen screen model; the Fabry-Perot and microbarographs will be much simpler and more transportable and if we can show that they produce similar results to the larger interferometer testing at observing sites will be much simplified.

The "Amato" Interferometer will initially be built as a bench model to test the null hypothesis of equal arm length changes. Referring to figures 1 and 2; the optics of the open arm of the interferometer will be rigidly coupled to the evacuated light pipe under the assumption that expansion and contraction of both arms will be the same thereby nulling any phase change due to physical dimensional changes in the system. If this proves possible the field model will be constructed with most of the vacuum system, light source and detection system below ground surface level to reduce perturbing the air flow through the second (down wind) interferometer.

A few designs have been theorized and the first of these is shown in fig. 1. [Another can be seen in fig. 2 On page 10] It is a division-of-amplitude interferometer with a very simple design that consists of the light, after passing through the beam splitter, being divided into two rays by the wedge in the middle of the interferometer and then being reflected by the respective mirrors in lines *a* and *b*. The interference pattern being recorded by the detector. The most important part of this design is that line *a* is exposed to the atmospheric turbulence and line *b* is protected by being in a evacuated light pipe. What we hope to accomplish with this design is to have line *b* so well protected that any shift we see in the fringe pattern must be caused by the change in index of refraction of the medium through which line *a* was traveling.

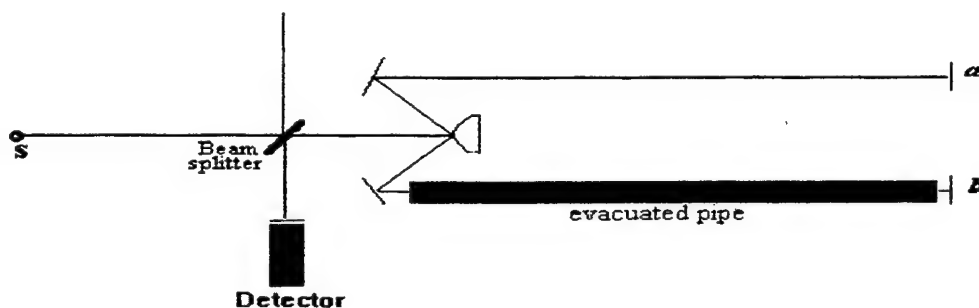


Fig. 1 - General interferometer design for testing "frozen screen" model, where *a* is the arm that is exposed to turbulence and *b* is the reference line.

We will need to insure that physical pathlength changes are identical in both arms. We plan to do this, as mentioned above, by making the evacuated pipe the mounting structure for the optics in arm *a*. Subsequently if we measure the fringe shift we can determine the amount of atmospheric turbulence, as represented by the change in the index of refraction of the air, by calculating the change in the light's optical path as a result of the light in line *a* passing through the turbulence. In order to maintain line *b* as controlled as possible a vacuum system will be desirable for thermal and pressure isolation; although a vacuum system introduces many variables of its own. It may even be buried so it is not affected by the wind and temperature variations can be better controlled. If burying the line proves to be successful a vacuum system may not be needed and a sealed (to isolate pressure changes) light pipe may suffice. As we said before since this design is to test the "frozen" screen it will require another interferometer just like this one but further down the wind direction, to make the same measurements and then use a correlation function for the data taken by both. The Fabry-Perot and differential pressure transducer will be run in parallel and similar cross correlations will be done. We will look for similar disturbance patters in each data set with time delays relating to the distance between the instruments and the wind speed.

Calculations have been made to have an idea of what physical path length the interferometer arms should have in order to see a half or quarter of wavelength change in the fringe pattern. These calculations have been done for different laser sources which include a He-Ne laser at .6328 microns, a CO₂ laser at 11.1 microns and a blue laser at 442 and 488 nm. The index of refraction for a temperature of 15°C and pressure of 760 mm Hg was calculated using the formula [ref 9]

$$(n_{15,760} - 1) 10^7 = 2726.43 + 12.288/(\lambda^2 \times 10^{-8}) + 0.355/(\lambda^4 \times 10^{-16})$$

where λ is the wavelength, and the Barrell and Sears equation was used for the change of the index of refraction with temperature and pressure [ref 10]

$$n_{tp} - 1 = (n_{15,760} - 1) [p(1 + \beta_{Tp})(1 + 15\alpha)] / 760 (1 + 760 \beta_{15})(1 + \alpha T)$$

where T = temperature

p = pressure

$\alpha = 0.00366$

$\beta_T = (1.049 - 0.015 T) 10^{-6}$

$\beta_{15} = 0.813 \times 10^{-6}$

The physical path length needed according to the wavelength and change in index of refraction is given by the formula $X = 0.5 \lambda / \Delta n$ where a variation of 0.01°C was used. These calculations resulted in the value of approximately 584 meters for the CO₂ laser, 33 m for the He-Ne laser, 0.624 m for the 442 nm blue laser and 1 m for the 488 nm blue laser. What these results mean is that, for example, if we used a CO₂ laser to see a half wavelength change in the fringe pattern the interferometer arm will have to be 584 meters long. Although this is not impossible it will not be convenient either; a He-Ne laser will be more convenient and then you can make the interferometer arm 5m and have the light bounce back and forth between the mirrors six times. In any case it would be most appropriate in the test phase to have the actual length (as opposed to the folded length) of the exposed arm approximately equal to the isoplanatic patch size at the appropriate wavelength.

This type of arrangement is shown in figure 2 which also demonstrates the other type of interferometer in consideration which is a Mach-Zehnder type of interferometer. As you can see in the figure the beam goes through a beam splitter and is divided into the two arms of the interferometer, one which is shielded

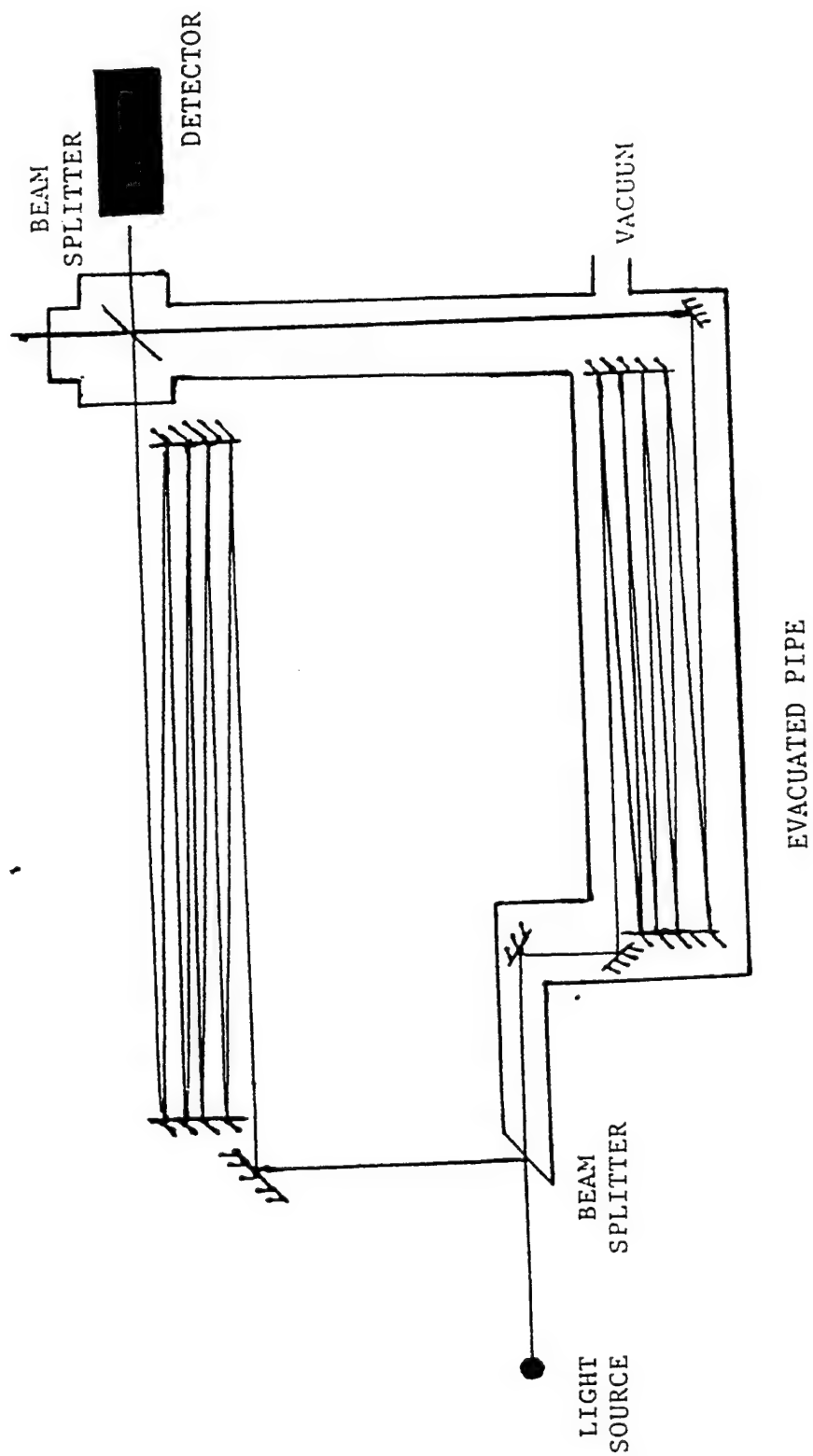


FIG. 2 - Prototype for Mach-Zender type interferometer.

by an evacuated light pipe and the other arm that will pass through the turbulence. In both arms you can see the multiple reflections of the light as described above and then the beams recombine at the second beam splitter and the interference pattern is captured at the detector. The arms need be equal only within the coherence length of the light source. With a laser source this is easily accomplished.

Additional experimental considerations address the time scale of the fluctuations which are of order 1 ms. Optical detectors routinely operate at much shorter time scales and consequently will present little problem for either the "Amato" Interferometer or the Fabry-Perot. We have found differential pressure transducers (off the shelf) with response times of 1-2 ms and accuracies of greater than one part in a million (up to 1 part in 10^8) and we feel these will be sufficient for our purposes.

Summary: We have designed an experimental procedure to test the "frozen screen" model of atmospheric turbulence. To do this we have also designed an (Amato) interferometer with one arm under vacuum rigidly coupled to a parallel arm that will sample the air. The interferometer design will be bench tested and then (hopefully) set up in the field as two instruments in an up wind / down wind configuration in conjunction with a microbarograph and Fabry-Perot Interferometer. The data will be cross correlated to see if there is a significant time delayed signal that relates to (distance of separation/wind speed) thus "proving" the frozen screen. If this is proven the experiment will be repeated with a vertical separation of the Amato Interferometers of order 50 meters; once again in coincidence with the microbarograph and Fabry-Perot. This will sample the near earth turbulent layer passing over a hypothetical observing instrument. It will require careful preparation to avoid adding turbulence to the field of view of a telescope, but if the frozen screen model proves correct the vertical sampling can be carried out downwind of the observing instrument. The principal reason for testing the microbarograph and Fabry-Perot is that they are less intrusive more mobile instruments and will cause less interference and prove more versatile in the observatory environment. In consideration of the geometry of observing off vertical one must envision an array of instruments that can sample the air path of the incident light.

References

- 1) *Encyclopedia of Atmospheric Sciences and Astrogeology*, edited by Fairbridge, R. W, Reinhold, publishing. New York, 1967.
- 2) *Encyclopedia of Lasers and Optical Technology*, edited by Meyers, R. A, Academic Press, California, 1991.
- 3) Collins, G.P., "Making Stars To See Stars: DOD Adaptive Optics Work is Declassified," *Physics Today*, pp 17-21, February 1992.
- 4) Hoover, C.R., *Investigation of a Single Point Temperature Probe for Measurement of Atmospheric Turbulence*, M.S. Thesis, Naval Postgraduate School , Monterey, California, December 1991.
- 5) Mattingly, T.S., *Measurement of Surface Layer Optical Turbulence Above AMOS*, M.S. Thesis, Naval Postgraduate School, Monterey, California, December 1991.
- 6) Tatarskii, V.I., *The Effects of the Turbulent Atmosphere on Wave Propagation*, National Science Foundation, Washington D.C. 1971.
- 7) Steel , W.H., *Interferometry* , 2nd edition Cambridge University Press 1983.
- 8) Bester, M., Danchi, W.C., Degiacomi, C.G., Greenhill, L.J. and Townes, C.H. *Atmospheric Fluctuations - Empirical Structure Functions and Projected Performance of Future Instruments*, Space Sciences Laboratory, University of California at Berkeley, 1991.
- 9) *CRC Handbook of Chemistry and Physics*, R.C. Weast editor in chief, CRC press, Florida, 1989.
- 10) *American Institute of Physics Handbook*, 3rd ed., edited by D.E. Gray, McGraw Hill, New York, 1972.
- 11) Tolansky, S., *An Introduction to Interferometry*, Longmans, Green and co., London, 1955.
- 12) Colavita , MM, Shao, M., Staelin, D.H., *Applied Optics*, Vol. 26 No. 19, 01 Oct 87, pg. 4106.
- 13) see for example: Ealey and Merkle, *Adaptive Optics in Astronomy*; 1994 Kona, SPIE vol. 2201.

ULTRA-WIDE-BAND MICROWAVE EFFECTS TESTING
ON AN ELECTRONIC SYSTEM

John A. Guthrie
Assistant Professor
Department of Physics

University of Central Oklahoma
100 N. University Drive
Edmond, OK 73034

Final Report for
Summer Faculty Research Program
Phillips Laboratory

Sponsored by
Air Force Office of Scientific Research
Bolling Air Force Base, DC

and

Phillips Laboratory

August 1996

ULTRA-WIDE-BAND MICROWAVE EFFECTS TESTING ON AN ELECTRONIC SYSTEM

John A. Guthrie
Assistant Professor
Department of Physics
University of Central Oklahoma

Abstract

Two ultrawide-band, high power microwave sources have been used to study the susceptibility of a particular electronic system to functional upset during irradiation. Both sources provided pulses with sub-nanosecond widths. Three distinct values of the peak electric field were achieved using the two sources; the peak field amplitudes at the test object scaled in the ratios 100:71:17. Pulse repetition frequencies were varied from 100 Hz to 60 kHz. The system under test demonstrated susceptibilities within this range of field amplitudes and pulse repetition frequencies, but reproducibility was poor. It appears that the poor reproducibility can be ascribed to differing conditions within the system under test at different points in time. In spite of the scatter in the test data, the general trend of the results will provide important insight into the response of the test system under ultrawide band microwave irradiation.

ULTRA-WIDE-BAND MICROWAVE EFFECTS TESTING ON AN ELECTRONIC SYSTEM

John A. Guthrie

1. Introduction

The Air Force is presently interested in the effects of high power microwaves on particular electronic systems, both foreign and domestic. Intensive efforts have been mounted in the design and construction of microwave sources and in quantifying microwave effects. In particular, work in this field has been ongoing at the Air Force Phillips Lab for over a decade, with the resulting production of several generations of sources and the testing of effects on numerous electronic systems of interest. This report describes procedures and general results of effects testing on a particular electronic system using two ultrawide-band (UWB) microwave sources. An ultrawide-band source is one for which the emitted radiation has, in the frequency domain, a bandwidth which is greater than 25% of the center frequency of the band.¹

In UWB microwave effects testing on electronic systems there are several parameters of the incident microwave field which can normally be varied and which are often important in producing an effect on the system. Some of these parameters, such as the center frequency, bandwidth, and pulse duration, are characteristic of the UWB source employed in the testing, and are typically not easily varied. Other parameters, such as the microwave electric field amplitude, the pulse repetition frequency, the field polarization, and the angle of incidence of the radiation with respect to some axis of the test system, are more easily varied. Most UWB sources do not allow simple variation of the output pulse peak amplitude, but some control over the field amplitude at the target may be exercised by changing the antenna-target distance. In this work the configuration of the test facilities, the design of the UWB sources, and the nature of the system under test made variation of the field polarization and radiation angle of incidence either difficult or superfluous. Therefore, in this work the only parameters which were varied were the microwave pulse repetition frequency (PRF) and the amplitude of the electric field at the system under test. In this work the electric field amplitude for one of the UWB sources was allowed to assume two unique values by changing the antenna-to-test-object distance. The peak amplitude of the electric field at the test

object was measured to be about 100 (arbitrary units, A.U.) and about 71 A.U., respectively, at the two distances. The antenna-to-object distance for the second source was not varied; the field amplitude at the test object was measured to be about 17 A.U. for this source.

Variation of the PRF can, in general, cause a functional effect in an electronic system in one of two ways. First, a functional effect may be generated in a particular system due simply to the increased power absorbed by the system with increasing PRF. In this case, the effect will occur at some threshold value of PRF and will persist for higher PRF's. A second type of effect may occur only when noise pulses generated by the radiation within the system occur at some characteristic frequency of the system itself. In this case the testing will indicate a "resonance" in the response of the system with changing PRF. In other words, an effect will be observed over some range of frequencies, but will not be observed at PRF's outside this range. Detailed knowledge of the functionality of the system under test can often be used to predict these "resonances".^{1,2,3} In this work the PRF's for both UWB sources were varied over their operational range, encompassing values from 100 Hz to 60 kHz.

The system under test demonstrated susceptibilities to UWB microwave radiation at field amplitudes within the range from 17 A.U. to 100 A.U., and over the PRF range from 100 Hz to 60 kHz. As is often the case in effects testing, reproducibility during this series of tests was poor. In the testing reported here, it is most likely that conditions within the system under test at the time of irradiation determined whether a functional upset occurred. In spite of the problems encountered with reproducibility, the general trend of the test results provide useful information regarding microwave effects on this particular electronic system. Section 2 of this report will describe the facilities, equipment, and procedures used during the testing. Section 3 will discuss results, and Section 4 will provide a summary.

2. Test Facilities, Equipment, and Procedures

The system under test was irradiated in an anechoic chamber with dimensions 6.1 m \times 6.1 m \times 12.2 m. Foam cones impregnated with carbon were mounted on the chamber walls, floor, and ceiling to provide microwave absorption. The purpose of the anechoic chamber is to provide an environment for

which the system under test is irradiated by a plane wave, with negligible irradiation by reflections from the room's surfaces.

The two microwave sources used for this series of tests were designed and built by personnel at the US Army Missile Command (MICOM) and its contractors, primarily BDM Technology. The sources are called by the names SLS-2B and IG-1C; the former is a high peak power source while the latter is a high average power source. The SLS-2B source uses a bank of lead acid batteries, providing 600 V, as the primary power supply. This voltage is switched into a pulse commutator assembly using a silicon-controlled rectifier. The commutator assembly consists of saturable core reactors (magnetic switches) and capacitors, and it serves to shorten the voltage pulse from the SCR. The voltage pulse encounters a voltage step-up transformer at the end of the commutator assembly. The pulse is then further shortened in the compression head of the source, also consisting of magnetic switches, capacitors, and a step-up transformer. After the pulse leaves the compression head it is sharpened and amplified by a coaxial line in which the inner conductor is uniformly tapered toward its end. The pulse rise time is shortened in a ferrite shock line. The shock line is a flowing-oil cooled coaxial assembly in which the inner conductor is encased in ferrite tubes. At the exit from the shock line the pulse has a width of less than a nanosecond, and a rise time of about 200 ps.

The pulse from the shock line is fed to a TEM horn using an impedance-matching coaxial assembly, which is insulated and cooled with flowing oil. The antenna plates diverge at an angle of 14° , and the plates are separated by about 80 cm at the horn exit aperture. The space between the plates is filled with a closed-cell foam to provide mechanical stability. The antenna has a numeric gain of about 2.5. The emitted wave is linearly polarized with the electric field oriented vertically. The SLS can operate for many minutes at a pulse-repetition frequency (PRF) of 100 Hz. It can provide a five-second burst at a PRF of 1 kHz, and a two-second burst at its maximum PRF of 7 kHz.

The IG-1C source was designed by MICOM to provide high average power by increasing the pulse repetition frequency. Its design is similar in many respects to the SLS. The primary power for the IG is derived from a commercial high voltage DC supply which provides 600 V. This voltage is switched in the pulse commutator assembly by a commercial insulated-gate bipolar junction transistor (IGBT),

capable of switching 1200 V at 600 A. The pulse commutator assembly for the IG performs the same function as for the SLS, shortening and amplifying the pulse using magnetic switches and capacitors. The pulse passes through a step-up transformer and is further sharpened in a pulse compression head, also using magnetic switches and capacitors. The pulse amplitude is increased by a stacked coaxial line transformer, consisting of five lengths of coax. The pulse proceeds through a ferrite shock line in order to reduce the rise time, and then passes to the same TEM horn described above; the emitted wave is vertically polarized. The voltage pulse at the antenna input has a rise time of about 200 ps, and a width of less than a nanosecond. Many of the components of the IG are cooled by rapidly flowing oil; the oil is cooled in turn by an air heat exchanger. Careful thermal engineering allows the IG to operate at PRF's as high as 60 kHz for two seconds and at 18 kHz for many minutes.

A critical parameter in UWB microwave effects testing is the peak magnitude of the electric field at the position of the system under test. It is common practice to measure the field at several points in space in the absence of the test object before testing begins; this process is termed field mapping. In this work testing occurred, and the field was mapped, under three different conditions, (1) using the SLS source with the test object located 5.7 m from the antenna, (2) using the SLS source with the test object located 7.7 m from the antenna, and (3) using the IG source with the test object located 5.7 m from the antenna. In each case the electric field waveform was measured at the positions indicated above, plus eight other positions in a horizontal plane; the results of these measurements will be discussed in Section 3.

The electric field probes used in this work measure the time derivative of the free-field electric displacement; they are commonly called D-dot probes. One probe, with 1 cm² cross section, was physically mounted to the antenna, and a second probe, an ACD-11 (3 cm² cross section), was mounted on the stand used to support the test object. The probe mounted on the test stand was used to map the field, and it remained in place during testing as the primary field diagnostic. The positive and negative outputs from the primary D-dot were both attenuated by 6 dB and connected to a Prodyne 100G 10 GHz balun. The probe signals were carried from the balun, through the wall of the anechoic chamber, and to an EMI-shielded screen room using half-inch foam flex cable. The D-dot mounted on the antenna served as the primary trigger for data acquisition during field mapping and during testing. All cables, baluns, and

attenuators had been previously calibrated using a network analyzer so that their frequency-dependent attenuation of the recorded signal could be corrected by the data acquisition software. In order to carry out these corrections the temporal signals from the D-dots were Fourier-transformed, the corrections were applied to the transforms, and the inverse transforms of the results were taken.

For field mapping purposes, the signal from the ACD-11 was recorded using a Tek SCD5000 digitizer; the SCD5000 has a maximum digitization rate of 4.5 GHz. The signal from the antenna D-dot was recorded by a second SCD5000. In order to ensure that both digitizers were triggered on the same UWB pulse, a pulse from the antenna probe was conditioned using a Tek 7104 oscilloscope. The trigger output from the 7104 was directed to an SRC 535 delay/pulse generator, whose output in turn was used to arm both SCD5000's after a preset delay; the pulse immediately following the delay was recorded by both digitizers. The delay could be tailored so that the digitizers recorded pulses at some frequency on the order of a few hertz, with the UWB sources running at several hundred or several thousand hertz. The recorded signal was transferred to the data acquisition computer, a Gateway Pentium 100, using the Hewlett-Packard General Purpose Interface Bus (GPIB) protocol. The data acquisition software, written by Voss Scientific, provided archive capabilities, correction for the attenuation by elements in the signal path, and a Fourier transform function in order to examine the frequency content of recorded signals. All electric field values reported here correspond to the value of the negative peak of the pulse.

During UWB effects testing on the system of interest, the signals from both D-dot probes were recorded in a similar manner. For this series of tests the test object was subjected to three-second bursts of radiation at the desired pulse repetition frequency (PRF), with roughly thirty seconds separating each burst. For each burst, three samples of the free-field and antenna waveforms were recorded by the data acquisition system. The free-field D-dot was mounted about 40 cm below the test object during testing. The conditioned trigger signal from the Tek 7104 was also used to clock a Hewlett-Packard 5245 pulse counter so that the total number of "good" pulses within a burst was recorded; this procedure helped to identify dropped pulses or misfires from the sources.

The test object was instrumented with a telemetry package for transmission of several critical signals using a fiber optic cable. The analog signals were digitized within the test object itself, the

digitized data were transmitted over the fiber, and the signals were converted back to analog form inside the shielded screen room. The signals were monitored using Tek 2440 100 MHz oscilloscopes and a Graphtec DMS1000 data management system, which provided a stripchart output. A functional upset within the test object under UWB microwave irradiation was clearly indicated by the monitored signals. The test object also required significant support equipment, both inside and outside the anechoic chamber, in order to function as designed. Test conditions were intended to produce as closely as possible a "normal" environment for the system under test.

Microwave pulse repetition frequencies were varied from 100 Hz to 7 kHz using the SLS-2B source, and from 100 Hz to 60 kHz using the IG-1C source. Repetition frequencies in general were increased in increments of 100 Hz from 100 Hz to 2 kHz, in increments of 1 kHz from 2 kHz to 10 kHz, and in increments of 5 kHz from 10 kHz to 60 kHz. There was reason to suspect that the system under test would be especially susceptible at a particular characteristic frequency and its harmonics, so these frequencies were explored thoroughly during the testing period.

3. Test Results

The field maps for the three different UWB irradiation conditions employed in this work are shown in Tables 1, 2 and 3. The nine positions in space for which the field was measured were laid out on a horizontal grid with 0.5 m between adjacent points. The tables report the peak magnitude of the electric field in the arbitrary units introduced in Section 2. During testing the system under test is centered within the area of the map. The field map values of the electric field recorded for the SLS source at close range (Table 1) are lower than the values measured during testing by about 30%; it appears that the batteries supplying power to the source may have been weak during the field mapping process. During testing the peak electric field at the test object consistently achieved values near 100 A.U.. The relative values of the fields reported in Table 1 are nevertheless believed to be reliable.

61	65	60
67	71	66
73	78 (toward the antenna)	72

Table 1. Field map for the SLS-2B source, close range. Field amplitudes are expressed in arbitrary units. The points are located on a horizontal plane, and adjacent points are separated by a distance of 0.5 m. The central point was located ~6.2 m from the antenna. During testing field amplitudes were consistently near 100 A.U. using the SLS-2B source at this range.

62	65	63
65	68	66
68	74 (toward the antenna)	70

Table 2. Field map for the SLS-2B source, long range. Field amplitudes are expressed in arbitrary units. The central point was located ~8.2 m from the antenna.

16	17	15
17	19	17
19	20 (toward the antenna)	19

Table 3. Field map for the IG-1C source. Field amplitudes are expressed in arbitrary units. The central point was located ~6.2 m from the antenna.

Figures 1 and 2 show the electric field waveform and the amplitude spectrum, respectively, for a representative pulse from the SLS-2B UWB source. The amplitude in Figure 2 is expressed in arbitrary units, but they are proportional to V/m-Hz. Figure 2 is derived from the Fourier transform of the voltage waveform, Figure 1. Figures 3 and 4 show the same data for a representative pulse from the IG-1C source.

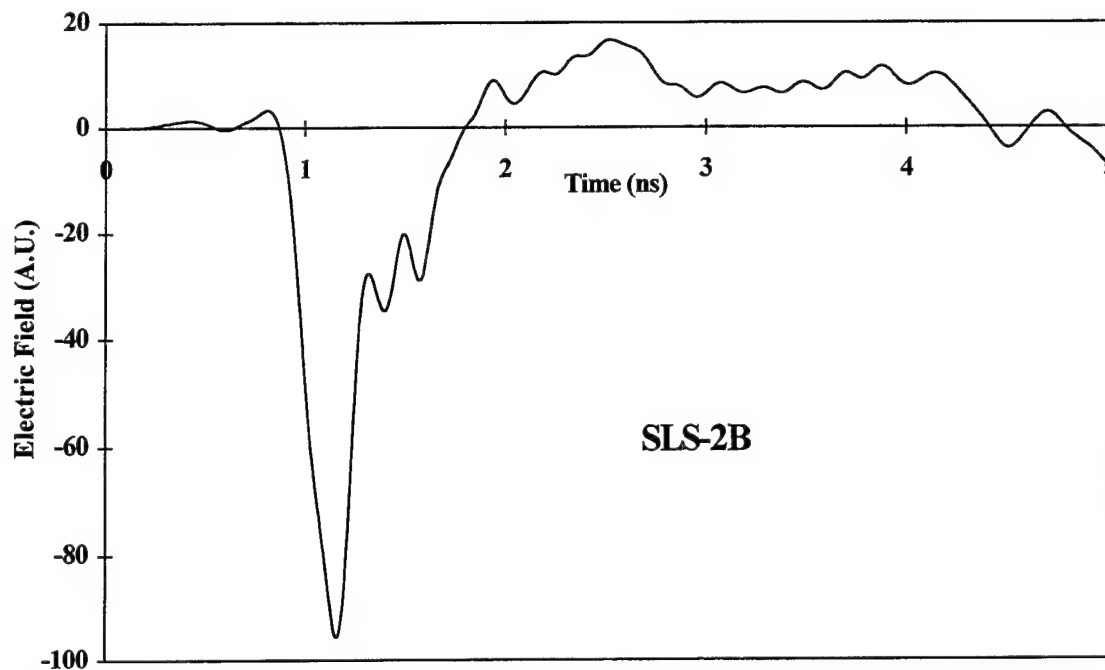


Figure 1. Representative pulse from the SLS-2B source. This plot represents the free-field waveform recorded by the D-dot. The digitized waveform was Fourier transformed, and the transform was corrected for attenuation by all components in the signal path. The plot is the inverse transform of the corrected data.

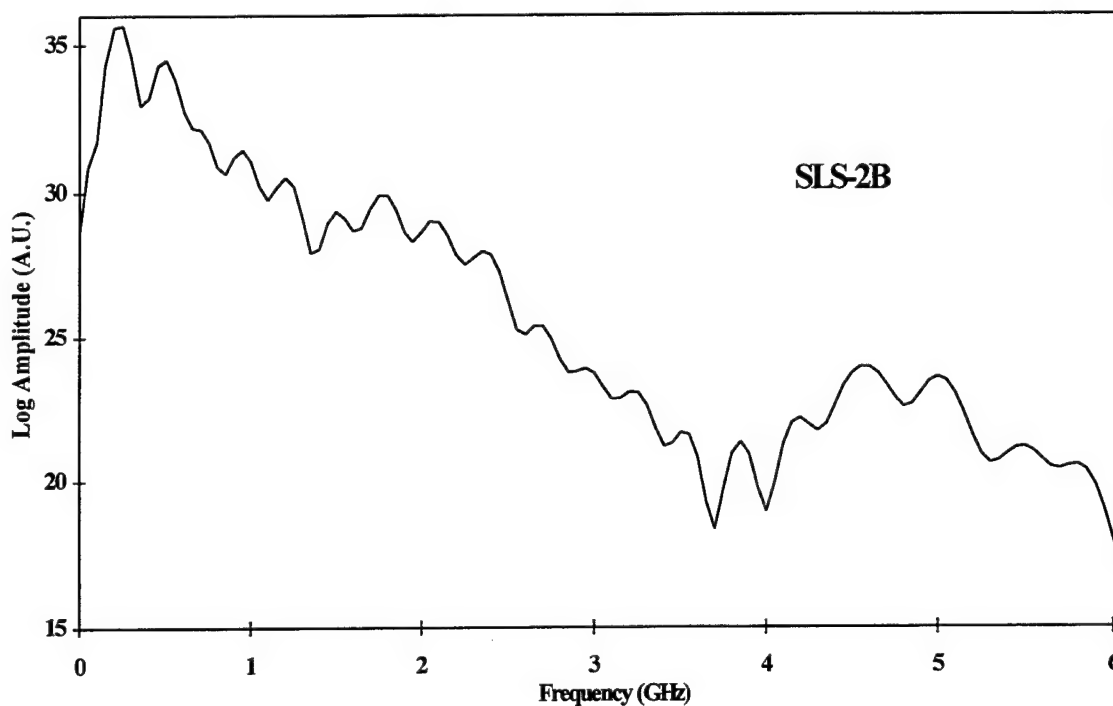


Figure 2. Amplitude spectrum of a representative pulse from the SLS-2B source. This plot is derived from the Fourier transform of Figure 1. The ordinate has arbitrary units, but they are proportional to $V/m \cdot Hz$; the ordinate has a logarithmic scale.

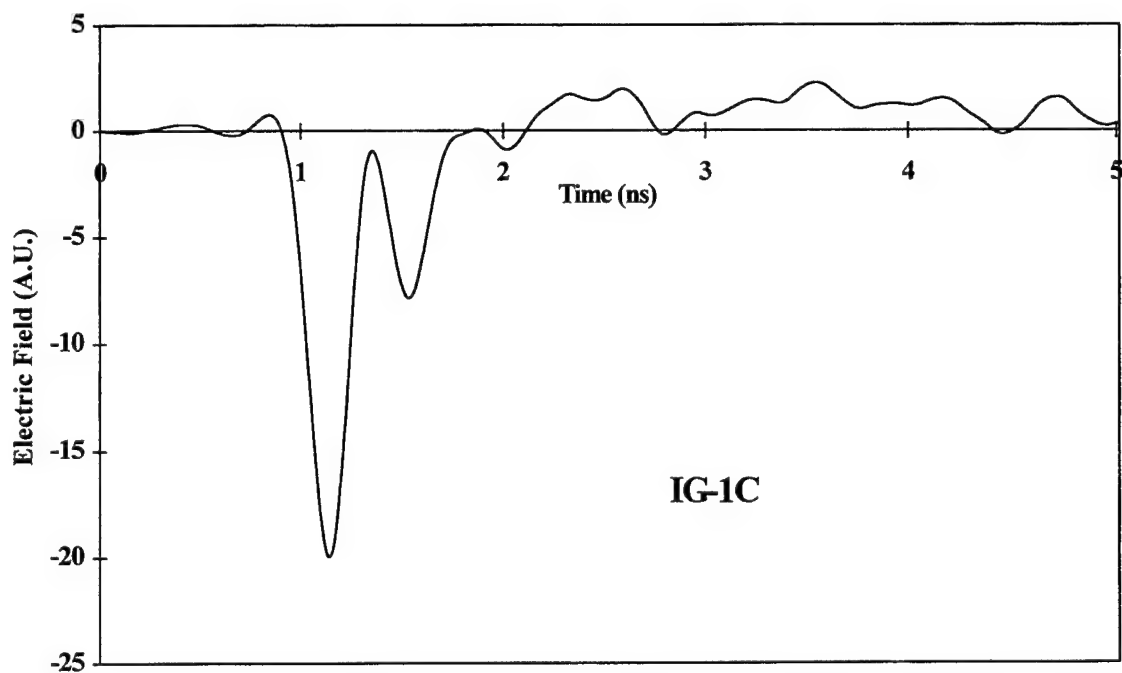


Figure 3. Representative pulse from the IG-1C source. This plot represents the free-field waveform recorded by the D-dot. The digitized waveform was Fourier transformed, and the transform was corrected for attenuation by all components in the signal path. The plot is the inverse transform of the corrected data.

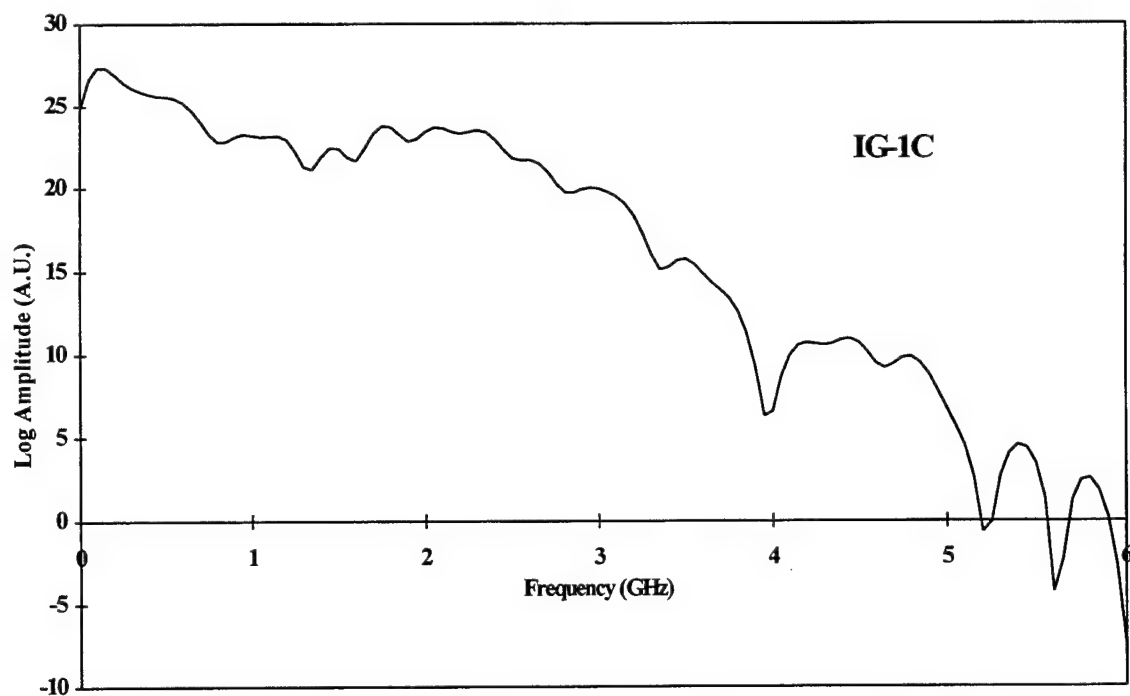


Figure 4. Amplitude spectrum of a representative pulse from the IG-1C source. This plot is derived from the Fourier transform of Figure 3. The ordinate has arbitrary units, but they are proportional to V/m-Hz; the ordinate has a logarithmic scale.

As discussed in Section 2, the system under test was exposed to bursts of UWB radiation at selected pulse repetition frequencies for three-second intervals of time, with roughly thirty seconds between bursts. The telemetered signals from the system under test were monitored for evidence of a functional upset during and following the UWB burst. Three different test conditions were employed, as discussed earlier: (1) using the SLS source with the test object located 5.7 m from the antenna, giving a peak field amplitude of $\sim 99.7 \pm 3.1$ A.U. (2) using the SLS source with the test object located 7.7 m from the antenna (field amplitude $\sim 71.1 \pm 2.4$ A.U.), and (3) using the IG source with the test object located 5.7 m from the antenna (field amplitude $\sim 16.5 \pm 0.39$ A.U.). As noted in Section 2, the pulse repetition frequency was varied from 100 Hz to 7 kHz for the SLS source, and from 100 Hz to 60 kHz for the IG source.

Over the range of electric field amplitudes from 17 A.U. to 100 A.U. and the PRF range from 100 Hz to 60 kHz the system under test demonstrated susceptibilities to functional upset. Unfortunately, reproducibility for this series of tests was poor. The most likely explanation for poor reproducibility is that conditions within the system under test were not identical for each burst at a particular PRF and field amplitude, in spite of attempts to exactly reproduce all experimental conditions. Furthermore, it appears that, depending upon the state of the test object at the time of irradiation, the field amplitudes used in this series of tests were only marginally sufficient to produce a functional upset. Nevertheless, the results of the testing show some general trends which will be of use to both experimentalists and analysts.

4. Summary and Conclusions

An electronic system of interest to the Air Force has been tested for susceptibility to functional upset under UWB microwave irradiation from two sources. One of the sources provided a maximum peak field amplitude at the target position of about 100 A.U. at a maximum PRF of 7 kHz, and the other provided a maximum amplitude of about 17 A.U. at a maximum PRF of 60 kHz. Telemetered electronic signals from the system under test were monitored for evidence of functional upset. Electric field waveforms were measured using D-dot probes.

Under the parameter range of electric field amplitudes and pulse repetition frequencies used in this series of tests, the electronic system under study demonstrated functional upset. However, reproducibility

of the upset under "identical" conditions was poor. The most likely explanation for this observation appears to be differing conditions within the system under test even when external conditions were carefully reproduced. In spite of the scatter in the data, the testing produced important results in terms of general trends for susceptibility of the test object to functional upset. These trends will be of use to experimentalists in the design of future tests and to analysts engaged in modeling efforts.

Acknowledgments. The financial support of the Air Force Office of Scientific Research is sincerely appreciated. The support and assistance of Dr. Tracey Bowen, the author's laboratory focal point, is gratefully acknowledged. The following individuals were involved in the testing reported here: Mr. Pat Hart (Phillips Lab), Mr. Darrell Holder (MICOM), Lt. Scott Johnson (Phillips Lab), Mr. Norman Keator (Voss Scientific), Dr. Gregory Nelson (Phillips Lab), Mr. Steve Syster (BDM Technology), and Lt. Wesley Turner (Phillips Lab). Each of these individuals' technical expertise and dedication to this series of tests is acknowledged.

References

1. Nancy J. Chesser, Editor, "Proceedings of the High Power RF Effects Assessment Methodology Short Course (U)", DoD No. DDV-92-0015, 1992.
2. Nancy J. Chesser, Editor, "Department of Defense Methodology Guidelines for High Power Microwave (HPM) Susceptibility Assessments (U)", DoD No. DDV-90-0017, January, 1990.
3. Phillips Laboratory Advanced Weapons and Survivability Directorate, "Tools and Techniques for Performing High-Power Ultra Wide-Band (UWB) Susceptibility Assessments (U)", DoD No. DDV-92-0004, February, 1992.

A VOLUMETRIC EIGENMODE EXPANSION METHOD
FOR DIELECTRIC BODIES

George W. Hanson
Assistant Professor
Department of Electrical Engineering and Computer Science

University of Wisconsin-Milwaukee
3200 North Cramer Street
Milwaukee, Wisconsin 53211

Final Report for:
Summer Faculty Research Program
Phillips Laboratory
Kirtland Air Force Base

Sponsored by:
Air Force Office of Scientific Research
Bolling Air Force Base, DC

and

Phillips Laboratory
Kirtland Air Force Base

August 1996

A VOLUMETRIC EIGENMODE EXPANSION METHOD FOR DIELECTRIC BODIES

George W. Hanson

Assistant Professor

Department of Electrical Engineering and Computer Science
University of Wisconsin-Milwaukee

Abstract

The work reported here relates to the electromagnetic characterization of a general dielectric target. The motivation for the problem is the detection and identification of a buried dielectric mine. An eigenmode expansion method (EEM) is developed for dielectric bodies residing completely within a homogeneous region of a generally inhomogeneous medium. The representation follows naturally from the EEM method previously developed for perfectly conducting bodies, including those with impedance loading. For the latter class of objects, the presence of loading shifts the eigenvalues from those of the unloaded case, but leaves the eigenmodes unchanged. It is observed from the governing integral equations that the dielectric body can be considered as a loading of the background space. As such, eigenmodes of homogeneous isotropic bodies are found to be independent of the material comprising the body, with eigenvalues dependent upon the material's characteristics in a simple fashion. Formulation of the eigenvalue problem is described for general dielectric bodies, and the EEM is applied to an infinite slab problem to demonstrate the method.

The EEM provides information concerning the effect of the external environment on the electromagnetic behavior of a dielectric target, and characterizes a target by a means which is independent of the material comprising the target. This may facilitate the development of detection technologies based on an object's singularity characteristics. Another, related project concerning the resonances of dielectric targets was also completed during the AFOSR Summer Faculty Research Program period. Due to space limitations, the results of that project are not included here, but may be found in Interaction Note 520¹.

¹G.W. Hanson and C.E. Baum, "Perturbation Formula for the Internal Resonances of a Dielectric Object Embedded in a Low-Impedance Medium," Interaction Note 520 (Phillips Laboratory Note Series, Kirtland AFB), Aug. 1996.

A VOLUMETRIC EIGENMODE EXPANSION METHOD FOR DIELECTRIC BODIES

George W. Hanson

Contents

<u>Section</u>	<u>Page</u>
I. Introduction.....	4
II. Formulation of Volume Integral Equations and Corresponding Eigenvalue Problem.....	4
III. Eigenmode Expansion Properties.....	11
IV. Conclusion.....	14
Appendix A. Eigenmode Expansion Applied to Infinite Slab.....	15
References.....	19

I. Introduction

In this report, the eigenmode expansion method (EEM) previously described [1]-[3] is developed explicitly for dielectric bodies residing within a single homogeneous region of a generally inhomogeneous medium. The motivation for the problem considered here is the study of dielectric targets buried in the ground, such as a dielectric mine.

The EEM developed previously, and principally applied to perfectly conducting objects, has been found to be useful for a variety of problems related to object characterization, and has a strong connection with the singularity expansion method (SEM) [3],[4]. Synthesis of desirable object response characteristics through control of eigenimpedance values is also possible through proper impedance loading, and is simply described via the EEM.

It should be noted that the EEM is similar to the method of characteristic modes, which has been described for conducting and dielectric objects [5],[6]. The characteristic modes are determined through a weighted eigenvalue equation, and for a unity weight become the same as the eigenmodes described here. As opposed to the treatment in [6], this report focuses attention on the fact that eigenmodes can be found which are independent of the medium interior to the target. The separation of the relevant integral operator into target medium dependent and independent parts was noted in [6]. In [6], though, separation of the operator in the eigenvalue problem, which leads to target medium independent modes, was not carried out. Explicit separation of the operator into target medium dependent and independent parts allows classification of target modes which are only dependent upon the shape of the target and on the medium surrounding the target, and constitutes the principle contribution of this report.

II. Formulation of Volume Integral Equation and Corresponding Eigenvalue Problem

In the following development, all electromagnetic quantities will be assumed to obey Maxwell's equations in the two-sided Laplace transform domain, governed by the transform pair

$$\begin{aligned}
 F(s) &= \int_{-\infty}^{\infty} F(t) e^{-st} dt \\
 F(t) &= \frac{1}{2\pi j} \int_{\Omega_0 - j\infty}^{\Omega_0 + j\infty} F(s) e^{st} ds
 \end{aligned}
 \tag{1}$$

where $s = \Omega + j\omega$, and Ω, ω are real quantities.

Consider the geometry shown in Fig.1, which depicts a closed surface S bounding volume V containing a generally inhomogeneous and anisotropic medium characterized by $\tilde{\epsilon}(\vec{r}), \mu_0$. The medium external to S is assumed for simplicity to be isotropic but generally inhomogeneous. In Fig. 1 multiple planar homogeneous layers are shown, but the formulation presented here applies to a generally inhomogeneous medium. The layered exterior medium case corresponds to the buried dielectric body problem as long as the ground can be approximated as consisting of planar layers. In each layer, as well as internal to S , material loss can be accommodated by defining the permittivity to be complex as $\epsilon \rightarrow \epsilon + \sigma/s$ for real conductivity σ .

A wave impedance and propagation constant can be defined for the j -th exterior region,

$$\begin{aligned}
 \gamma_j &= s[\mu_0 \epsilon_j]^{1/2} \\
 Z_j &= [\mu_0 \epsilon_j^{-1}]^{1/2}
 \end{aligned}
 \tag{2}$$

and formally extended to the interior region

$$\begin{aligned}
 \tilde{\gamma}(\vec{r}) &= s[\mu_0 \tilde{\epsilon}(\vec{r})]^{1/2} \\
 \tilde{Z}(\vec{r}) &= [\mu_0 \tilde{\epsilon}^{-1}(\vec{r})]^{1/2}
 \end{aligned}
 \tag{3}$$

noting the following combinations

$$\begin{aligned}
 \gamma_j Z_j &= s \mu_0, \quad \tilde{\gamma} \cdot \tilde{Z} = \tilde{I} s \mu_0, \\
 \gamma_i Z_j^{-1} &= s \epsilon_j, \quad \tilde{\gamma} \cdot \tilde{Z}^{-1} = s \tilde{\epsilon}
 \end{aligned}
 \tag{4}$$

The relationship between the electric field and an electric current source can be written

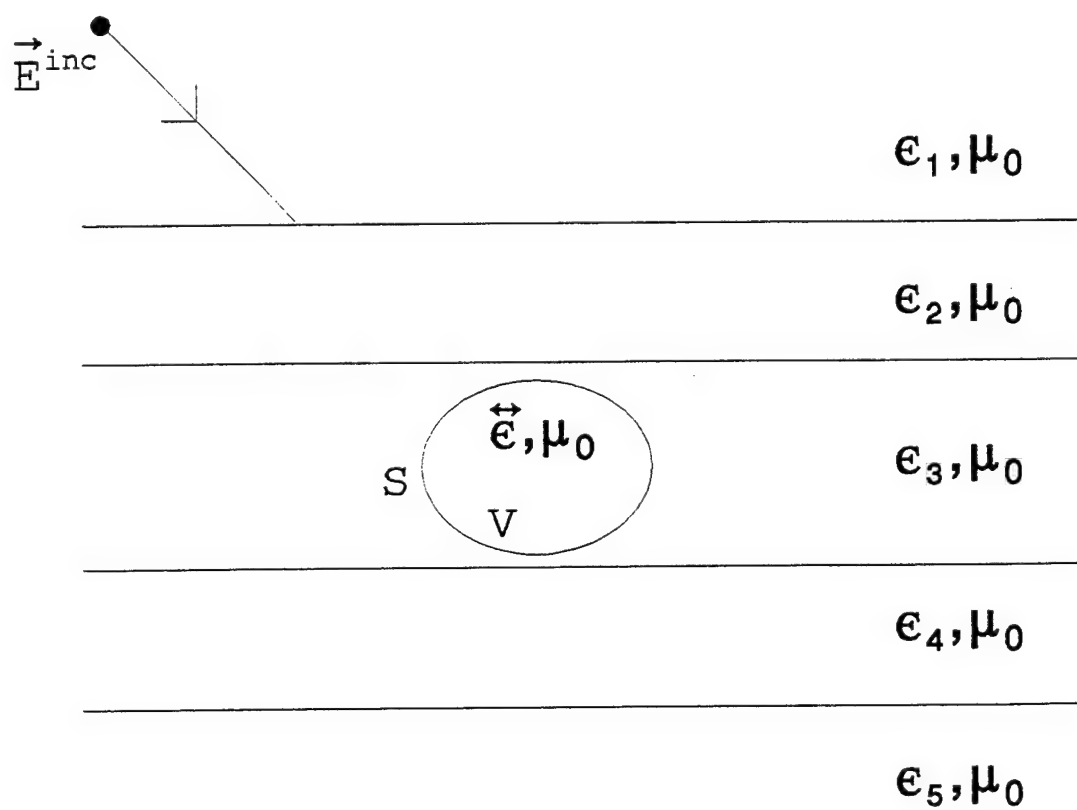


Fig. 1. Dielectric body in layered media.

as

$$\vec{E}(\vec{r}, \gamma_o) = - \langle \vec{Z}^e(\vec{r}|\vec{r}', \gamma_o) ; \vec{J}(\vec{r}') \rangle \quad (5)$$

where \langle , \rangle denotes integration of the two terms separated by the comma over common spatial coordinates, and the symbol above the comma indicates the real scalar product. The propagation constant γ_o is merely symbolic, and represents dependence on all of the exterior region layers, i.e., $\gamma_o \equiv \{\gamma_1, \gamma_2, \gamma_3, \dots\}$. The electric dyadic Green's function, $-\vec{Z}_{\alpha\beta}^e(\vec{r}|\vec{r}', \gamma_o)$, provides the α -th component of field at \vec{r} due to the β -th component of a Hertzian current element at \vec{r}' . In general, the Green's dyadic can be written as

$$\vec{Z}^e(\vec{r}|\vec{r}', \gamma_o) = s\mu_o \{ \vec{g}(\vec{r}|\vec{r}', \gamma_o) + \vec{L}_o \gamma^{-2} \delta(\vec{r} - \vec{r}') \} \quad (6)$$

where the first term is evaluated in a principle value sense for a specified exclusion volume [7]. The second term is the depolarizing dyad contribution, which depends on the shape of the exclusion volume as well as the material properties of the region which includes the source current (with the appropriate value of propagation constant assigned to γ). Details concerning (6), as well as general forms of the principal value term for homogeneous and layered media surround regions are provided in Appendix B of [8].

Next, a volume integral equation for scattering from a dielectric body completely contained within one layer of the surround region can be formulated [9]. Let the region containing the body be region i characterized by ϵ_i , and the region interior to S be characterized by unsubscripted symbols ($\vec{e}, \vec{\gamma}$). One can replace the medium internal to S with a homogeneous isotropic medium characterized by ϵ_i and containing unknown volume polarization currents

$$\begin{aligned} \vec{J}(\vec{r}, \gamma_o, \vec{\gamma}) &= \{ \vec{\gamma} \cdot \vec{Z}^{-1} - \gamma_i Z_i^{-1} \vec{I} \} \cdot \vec{E}(\vec{r}, \gamma_o, \vec{\gamma}) \\ &= \vec{Z}_d^{-1}(\gamma_i, \vec{\gamma}) \cdot \vec{E}(\vec{r}, \gamma_o, \vec{\gamma}) \quad \dots \quad \forall \vec{r} \in V \end{aligned} \quad (7)$$

where

$$\vec{E}(\vec{r}, \gamma_o, \vec{\gamma}) = \vec{E}^{inc}(\vec{r}, \gamma_o) + \vec{E}^s(\vec{r}, \gamma_o, \vec{\gamma}) \quad (8)$$

with \vec{E}^{inc} being the incident field (with the dielectric object removed) and \vec{E}^s is the scattered field due to currents excited by the material contrast.

Since

$$\vec{Z}_d(\gamma, \tilde{\gamma}) \cdot \vec{J}(\vec{r}, \gamma_o, \tilde{\gamma}) = \vec{E}^{inc}(\vec{r}, \gamma_o) + \vec{E}^s(\vec{r}, \gamma_o, \tilde{\gamma}) \quad (9)$$

with \vec{E}^s given by (5), an IE is obtained as

$$\langle \vec{Z}^e(\vec{r}|\vec{r}', \gamma_o) + \vec{Z}_d(\gamma_i, \tilde{\gamma}) \delta(\vec{r} - \vec{r}') ; \vec{J}(\vec{r}', \gamma_o, \tilde{\gamma}) \rangle = \vec{E}^{inc}(\vec{r}, \gamma_o) . \quad (10)$$

By suitable manipulation of (7), another form can be found as

$$\langle \vec{Z}^e(\vec{r}|\vec{r}', \gamma_o) \cdot \vec{Z}_d^{-1}(\gamma_i, \tilde{\gamma}) + \vec{I} \delta(\vec{r} - \vec{r}') ; \vec{E}(\vec{r}', \gamma_o, \tilde{\gamma}) \rangle = \vec{E}^{inc}(\vec{r}, \gamma_o) . \quad (11)$$

In (10) and (11), as well as in the development to follow, the IE will be enforced over a range equal to its domain, e.g., $\vec{r} \in V$ for the general three-dimensional case. The forms (10) and (11) are equivalent, and both forms have been used for computational work in scattering theory. The volume IE was originally proposed by Richmond [10], with subsequent work performed by many investigators.

It should be noted that in the absence of material contrast, i.e., $\vec{\epsilon} = \epsilon_i \vec{I}$, the IE reduces to $\vec{E} = \vec{E}^{inc}$. It will be implicitly assumed in the following that material contrast exists to maintain the polarization current (7).

If the exterior region is comprised of reciprocal media as assumed here, the Green's function involved in the above IE obeys the symmetry property

$$\vec{Z}^e(\vec{r}|\vec{r}', \gamma_o) = \vec{Z}^{eT}(\vec{r}'|\vec{r}, \gamma_o) \quad (12)$$

where the superscript T denotes the transpose operation. Thus, the Green's function is complex symmetric, but not Hermitian, for general complex frequencies. For the most general form of the impedance dyadic \vec{Z}_d , a set of eigenvalue equations for (10) can be defined as

$$\begin{aligned}
\langle \tilde{Z}^e(\bar{r}|\bar{r}', \gamma_o) + \tilde{Z}_d(\gamma_i, \tilde{\gamma}) \delta(\bar{r} - \bar{r}') ; \tilde{j}_\beta^r(\bar{r}', \gamma_o, \tilde{\gamma}) \rangle &= \lambda_\beta^{j,r}(\gamma_o, \tilde{\gamma}) \tilde{j}_\beta^r(\bar{r}, \gamma_o, \tilde{\gamma}) \\
\langle \tilde{j}_\beta^l(\bar{r}', \gamma_o, \tilde{\gamma}) ; \tilde{Z}^e(\bar{r}|\bar{r}', \gamma_o) + \tilde{Z}_d(\gamma_i, \tilde{\gamma}) \delta(\bar{r} - \bar{r}') \rangle &= \lambda_\beta^{j,l}(\gamma_o, \tilde{\gamma}) \tilde{j}_\beta^l(\bar{r}, \gamma_o, \tilde{\gamma})
\end{aligned} \tag{13}$$

and for (11) as

$$\begin{aligned}
\langle \tilde{Z}^e(\bar{r}|\bar{r}', \gamma_o) \cdot \tilde{Z}_d^{-1}(\gamma_i, \tilde{\gamma}) + \tilde{I} \delta(\bar{r} - \bar{r}') ; \tilde{e}_\beta^r(\bar{r}', \gamma_o, \tilde{\gamma}) \rangle &= \lambda_\beta^{e,r}(\gamma_o, \tilde{\gamma}) \tilde{e}_\beta^r(\bar{r}, \gamma_o, \tilde{\gamma}) \\
\langle \tilde{e}_\beta^l(\bar{r}', \gamma_o, \tilde{\gamma}) ; \tilde{Z}^e(\bar{r}|\bar{r}', \gamma_o) + \tilde{Z}_d(\gamma_i, \tilde{\gamma}) \delta(\bar{r} - \bar{r}') \rangle &= \lambda_\beta^{e,l}(\gamma_o, \tilde{\gamma}) \tilde{e}_\beta^l(\bar{r}, \gamma_o, \tilde{\gamma})
\end{aligned} \tag{14}$$

The left and right eigenmodes in (13) share the same eigenvalues, i.e., $\lambda_\beta^{j,l} = \lambda_\beta^{j,r} = \lambda_\beta^j$, and form a biorthogonal set,

$$\begin{aligned}
\langle \tilde{j}_\beta^r ; \tilde{j}_{\beta'}^l \rangle &= 0 \quad \lambda_\beta^j \neq \lambda_{\beta'}^j \\
\langle \tilde{j}_\beta^r ; \tilde{j}_\beta^l \rangle &\neq 0
\end{aligned} \tag{15}$$

and similarly for the modes in (14). Since the above implies a real inner product, and the eigenmodes may in general be complex, the second inner product in (15) is not guaranteed to be nonvanishing. This is discussed in [1], where a convincing argument is made for the second of (15).

Note that generally the eigenvalues and eigenmodes are functions of $\gamma_o, \tilde{\gamma}$. The eigenvalue problem for an inhomogeneous, anisotropic body is considered in more detail in Appendix A of [8]. If we now consider the special case of a homogeneous, isotropic body, IE's (10) and (11) are modified by replacing $\tilde{Z}_d, \tilde{Z}_d^{-1}$ with $Z_d \tilde{I}, Z_d^{-1} \tilde{I}$, respectively. The resulting kernels are then complex symmetric, in which case the resulting eigenvalue problems become

$$\begin{aligned}
\langle \tilde{Z}^e(\bar{r}|\bar{r}', \gamma_o) + Z_d(\gamma_i, \gamma) \tilde{I} \delta(\bar{r} - \bar{r}') ; \tilde{j}_\beta^r(\bar{r}', \gamma_o) \rangle &= \lambda_\beta^j(\gamma_o, \gamma) \tilde{j}_\beta^r(\bar{r}, \gamma_o) \\
\langle \tilde{Z}^e(\bar{r}|\bar{r}', \gamma_o) Z_d^{-1}(\gamma_i, \gamma) + \tilde{I} \delta(\bar{r} - \bar{r}') ; \tilde{e}_\beta^r(\bar{r}', \gamma_o) \rangle &= \lambda_\beta^e(\gamma_o, \gamma) \tilde{e}_\beta^r(\bar{r}, \gamma_o)
\end{aligned} \tag{16}$$

since $\tilde{j}_\beta^l = \tilde{j}_\beta^r = \tilde{j}_\beta$ for the symmetric case, and similarly for the other mode set. The eigenvalues $\lambda_\beta^{j,e}$ depend upon γ_o, γ , but the eigenmodes $\tilde{j}_\beta, \tilde{e}_\beta$ only depend upon the exterior region through

$\gamma_o \equiv \{\gamma_1, \gamma_2, \gamma_3, \dots\}$, and the shape of the object. The last observation follows from the spectral mapping theorem.

It is easy to show that the mode sets are related by

$$\begin{aligned}\vec{j}_\beta &= \vec{e}_\beta \\ \lambda_\beta^j &= Z_d \lambda_\beta^e\end{aligned}\tag{17}$$

in that with those substitutions the first of (16) becomes equal to the second, and vice versa. This is also consistent with the fact that λ_β^j should have dimensions of ohms [1], since (10) maps currents to electric fields, whereas λ_β^e should be dimensionless since (11) maps electric fields to electric fields. For purposes here, attention will be primary directed at the first of (16), with results obtained being generally applicable to the second of (16) as well.

To be consistent with earlier notation [1], let $\lambda_\beta^j \equiv Z_\beta$ and note that rather than (16), we can solve

$$\langle \vec{Z}^e(\vec{r}|\vec{r}', \gamma_o) ; \vec{j}_\beta(\vec{r}', \gamma_o) \rangle = Z_\beta^u(\gamma_o) \vec{j}_\beta(\vec{r}, \gamma_o)\tag{18}$$

and obtain the eigenvalue as

$$Z_\beta(\gamma_o, \gamma) = Z_\beta^u(\gamma_o) + Z_d(\gamma_\beta, \gamma)\tag{19}$$

where $Z_d(\gamma_\beta, \gamma) = (\gamma Z^{-1} - \gamma_\beta Z_\beta^{-1}) = s(e - e_\beta)$ provides a simple shift factor for the eigenvalues.

The significance of (18) is that one can solve an eigenvalue problem which is only dependent on the exterior region medium and the shape of the body, independent of the type of medium internal to the body. Explicit dependance on the interior region medium only comes from the shift in the eigenvalue through the term $Z_d(\gamma_\beta, \gamma)$, which only depends on the object's permittivity and that of the layer containing the object.

A further observation can be made for specific types of depolarizing dyad terms. If $\vec{L}_\beta = b\vec{I}$, such as for spherical or cubical exclusion volumes where $b = 1/3$, the eigenvalue problem becomes

$$\langle \tilde{g}(\vec{r}|\vec{r}', \gamma_o) ; \vec{j}_\beta(\vec{r}', \gamma_o) \rangle = \hat{Z}_\beta^u(\gamma_o) \vec{j}_\beta(\vec{r}, \gamma_o) \quad (20)$$

which involves only the principle value part of the electric Green's dyadic, and the resulting eigenvalues are obtained as

$$Z_\beta(\gamma_o, \gamma) = s \mu_0 \hat{Z}_\beta^u(\gamma_o) + b \gamma_i^{-2} + Z_d(\gamma, \gamma) . \quad (21)$$

III. Eigenmode Expansion Properties

The following properties of (18), the volume eigenvalue equation, follow directly from the previous EEM development [1]. Consider the general eigenvalue problem

$$\langle \tilde{Z}(\vec{r}|\vec{r}', \gamma_o) ; \vec{j}_\beta(\vec{r}', \gamma_o) \rangle = Z_\beta(\gamma_o) \vec{j}_\beta(\vec{r}, \gamma_o) \quad (22)$$

where \tilde{Z} represents either \tilde{Z}^e or \tilde{g} , and Z_β is either Z_β^u or \hat{Z}_β^u . It is easy to show that

$$\langle \vec{j}_{\beta'}(\vec{r}, \gamma_o) ; \vec{j}_\beta(\vec{r}, \gamma_o) \rangle = 0 \quad Z_{\beta'} \neq Z_\beta . \quad (23)$$

Assuming that the eigenmodes form a complete set of modes which span the domain of the integral operator, along with the normalization

$$\langle \vec{j}_{\beta'}(\vec{r}, \gamma_o) ; \vec{j}_\beta(\vec{r}, \gamma_o) \rangle = \delta_{\beta', \beta} \quad (24)$$

then

$$\vec{F}(\vec{r}, \gamma_o) = \sum_\beta \langle \vec{j}_\beta(\vec{r}, \gamma_o) ; \vec{F}(\vec{r}, \gamma_o) \rangle \vec{j}_\beta(\vec{r}, \gamma_o) \quad (25)$$

where \vec{F} is an arbitrary vector function in the domain of the operator. Further properties follow immediately as

$$\tilde{I} \delta(\vec{r} - \vec{r}') = \sum_\beta \vec{j}_\beta(\vec{r}, \gamma_o) \vec{j}_\beta(\vec{r}', \gamma_o) \quad (26)$$

$$\tilde{Z}^v(\vec{r}|\vec{r}', \gamma_o) = \sum_{\beta} Z_{\beta}^v(\gamma_o) \tilde{J}_{\beta}(\vec{r}, \gamma_o) \tilde{J}_{\beta}(\vec{r}', \gamma_o) \quad (27)$$

$$Z_{\beta}(\gamma_o) = \langle \tilde{J}_{\beta}(\vec{r}, \gamma_o) ; \tilde{Z}(\vec{r}|\vec{r}', \gamma_o) ; \tilde{J}_{\beta}(\vec{r}', \gamma_o) \rangle \quad (28)$$

$$\frac{d}{d\gamma_j} Z_{\beta}(\gamma_o) = \left\langle \tilde{J}_{\beta}(\vec{r}, \gamma_o) ; \frac{d}{d\gamma_j} \tilde{Z}(\vec{r}|\vec{r}', \gamma_o) ; \tilde{J}_{\beta}(\vec{r}', \gamma_o) \right\rangle \quad (29)$$

$$\left\langle \tilde{J}_{\beta}(\vec{r}, \gamma_o) ; \frac{d}{d\gamma_j} \tilde{J}_{\beta}(\vec{r}', \gamma_o) \right\rangle = 0 \quad (30)$$

where $\frac{\partial}{\partial \gamma_j}$ indicates differentiation with respect to the j-th region propagation constant.

The solution of IE (10) is

$$\tilde{J}(\vec{r}, \gamma_o, \gamma) = \sum_{\beta} \frac{1}{Z_{\beta}(\gamma_o, \gamma)} \langle \tilde{J}_{\beta}(\vec{r}', \gamma_o) ; \tilde{E}^{inc}(\vec{r}', \gamma_o) \rangle \tilde{J}_{\beta}(\vec{r}, \gamma_o) \quad (31)$$

where Z_{β} comes from (19) with $Z_{\beta}^u, \tilde{J}_{\beta}$ the solutions of (18). The field scattered by the object is

$$\begin{aligned} \tilde{E}^s(\vec{r}, \gamma_o, \gamma) &= -\langle \tilde{Z}^e(\vec{r}|\vec{r}', \gamma_o) ; \tilde{J}(\vec{r}) \rangle \\ &= -\sum_{\beta} \frac{1}{Z_{\beta}(\gamma_o, \gamma)} \langle \tilde{J}_{\beta}(\vec{r}, \gamma_o) ; \tilde{E}^{inc}(\vec{r}, \gamma_o) \rangle \langle \tilde{Z}^e(\vec{r}|\vec{r}', \gamma_o) ; \tilde{J}_{\beta}(\vec{r}', \gamma_o) \rangle \\ &= -\sum_{\beta} \frac{s\mu_0}{Z_{\beta}(\gamma_o, \gamma)} \langle \tilde{J}_{\beta}(\vec{r}, \gamma_o) ; \tilde{E}^{inc}(\vec{r}, \gamma_o) \rangle \langle \tilde{g}(\vec{r}|\vec{r}', \gamma_o) ; \tilde{J}_{\beta}(\vec{r}', \gamma_o) \rangle \end{aligned} \quad (32)$$

where the last relation is valid for fields outside of the object since $\vec{r} \neq \vec{r}'$.

It should be noted that in formulating the eigenvalue problem (16), and in subsequent expansions, e.g., (25), it is assumed that eigenmodes exist, and that they form a complete set of modes which span the domain of the integral operator. Since the kernel (and associated operator) are complex symmetric but not Hermitian, this is not guaranteed to always be correct.

For additional insight, it is helpful to consider the matrix form of the integral equation, such as would be obtained by employing a method of moments (MoM) solution. This reduces the IE to an $N \times N$ matrix equation. A matrix is said to be of simple structure if it is similar to a diagonal matrix, i.e., if it is diagonalizable. If the MoM matrix has N distinct eigenvalues, then the matrix is of simple structure and the eigenmode expansion is valid. This follows from the fact that eigenmodes corresponding to distinct eigenvalues are linearly independent, and so the N linearly independent eigenmodes would form a complete set. Even if the eigenvalues are not all distinct, an N -element linearly independent set may exist, although it is not guaranteed for a matrix lacking sufficient special properties. An important case of degenerate eigenvalues would occur at a branch point in the complex plane, where two or more eigenvalues coalesce. It has been conjectured that branch points may always be present when sufficient object symmetry is lacking [11]. The occurrence of branch points may invalidate the eigenmode expansion at certain points in the complex plane, although at other complex frequencies the expansion would remain complete. The eigenmode expansion would remain valid even at points of eigenvalue degeneracy if the geometric multiplicity of the eigenvalue is equal to its algebraic multiplicity, resulting in N linearly independent eigenmodes. It is assumed here that the matrix representation of the IE is of simple structure, such that the eigenmode expansion is valid, as was assumed in [1]. If this is not true, a generalized expansion may still be obtained involving root vectors [12], although this would considerably complicate the analysis. Some of these issues are summarized in [13], and further discussion can be found in [1], [14]. Lastly, it should be noted that for one of the examples used in [11] to illustrate the occurrence of eigenvalue branch points, the non-uniform transmission line, the geometric multiplicity was equal to the algebraic multiplicity for the cases checked, validating the EEM for that example. Perhaps this will be the case for most physically realistic problems of interest, although it would be premature to make that conjecture at this point.

IV. Conclusion

In this report the EEM previously developed is applied to dielectric bodies immersed in inhomogeneous media. It is found that for the case of a homogeneous, isotropic object, eigenmodes can be found which only depend upon the space external to the body, and the shape of the body. Eigenvalues for a specific interior medium are related to the set of interior-independent eigenvalues by a simple shift factor. This allows the general study of objects which may be considered as belonging to a certain class, which is defined by object shape and background environment, independent of the specific medium comprising the object.

Appendix A. Eigenmode Expansion Applied to Infinite Slab

As an example of the EEM method described here, consider the problem of an infinite dielectric slab immersed in homogeneous space, as depicted in Fig. A1. The appropriate IE is

$$\langle \tilde{Z}^e(z|z', \gamma_1) + Z_d(\gamma_1, \gamma_2) \tilde{I} \delta(z-z') ; \tilde{J}(z', \gamma_1, \gamma_2) \rangle = \tilde{E}^{inc}(z, \gamma_1) \quad (\text{A1})$$

with

$$\tilde{Z}^e(z|z') = s\mu_0 \left\{ \left(1 - \frac{\nabla_z \nabla_z \cdot}{\gamma^2} \right) \frac{[\tilde{I} e^{-p|z-z'|}]}{2p} + \frac{\hat{z}\hat{z} \delta(z-z')}{\gamma^2} \right\} \quad (\text{A2})$$

since $R_t^s = R_n^s = R_c^s = 0$ for the homogeneous background environment. If the incident field is

$$\tilde{E}^{inc}(\vec{r}) = \hat{y} e^{-j(k_x x + k_z z)} \quad (\text{A3})$$

with $jk_x = \gamma_1 \sin \theta_i$, $jk_z = \gamma_1 \cos \theta_i$, the correct transform domain field for the rhs of (A1) is $\hat{y} e^{-p_1 z}$

with $p_1 = \sqrt{k_x^2 + k_y^2 + \gamma_1^2} = \gamma_1 \cos \theta_i$. Integral equation (A1) becomes

$$\langle Z_{yy}(z|z', \gamma_1) + Z_d(\gamma_1, \gamma_2) \delta(z-z') ; J_y(z', \gamma_1, \gamma_2) \rangle = e^{-p_1 z} \quad (\text{A4})$$

with

$$Z_{yy}(z|z', \gamma_1) = s\mu_0 \frac{e^{-p_1|z-z'|}}{2p_1} \quad (\text{A5})$$

The relevant eigenvalue problem is

$$\left\langle \frac{e^{-p_1|z-z'|}}{2p_1} ; j_\beta(z', \gamma_1) \right\rangle = Z_\beta^u(\gamma_1) j_\beta(z, \gamma_1) \quad (\text{A6})$$

with actual eigenvalues for the object given by

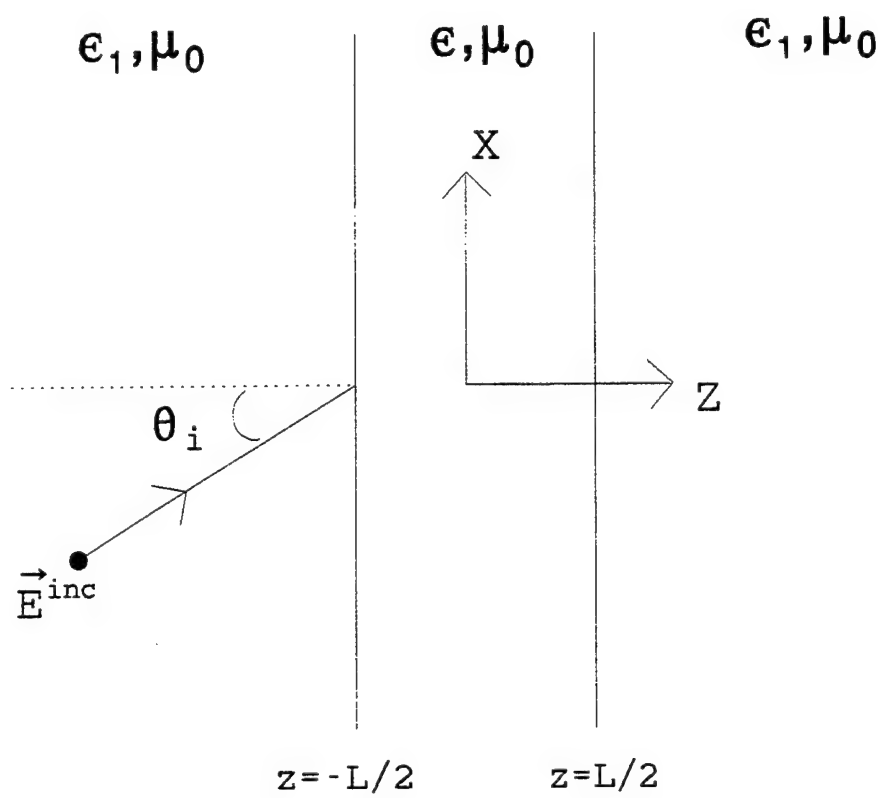


Fig. A1. Plane wave incident on infinite dielectric slab.

$$\begin{aligned}
Z_{\beta}(\gamma_1, \gamma_2) &= s\mu_0 Z_{\beta}''(\gamma_1) + Z_d(\gamma_1, \gamma_2) \\
&= s\mu_0 Z_{\beta}''(\gamma_1) + \left(\frac{\gamma_2}{Z_2} - \frac{\gamma_1}{Z_1} \right)^{-1}
\end{aligned} \tag{A7}$$

The kernel of (A6) is the traditional transmission line kernel, which can be derived from transmission line theory. The IE (A6) can be solved analytically by the method described in [15],[16]. Taking two derivatives of (A6), with regard to the fact that the integration implicitly omits the singular point $z=z'$, we obtain

$$\left(\frac{d^2}{dz^2} - \gamma_{\beta}^2 \right) j_{\beta}(z) = 0 \tag{A8}$$

where $\gamma_{\beta}^2 = p_1^2 - \frac{1}{z_{\beta}''}$. Boundary conditions for (A8) can be obtained by applying one derivative

to (A6), leading to

$$\begin{aligned}
j_{\beta}'(z) - p_1 j_{\beta}(z) \Big|_{z=-\frac{L}{2}} &= 0 \\
j_{\beta}'(z) + p_1 j_{\beta}(z) \Big|_{z=\frac{L}{2}} &= 0
\end{aligned} \tag{A9}$$

The solution is

$$j_{\beta}(z) = e^{\gamma_{\beta} z} - e^{-j\pi\pi} e^{-\gamma_{\beta} z} \tag{A10}$$

where γ_{β} satisfies

$$\gamma_{\beta} = \frac{j\beta\pi}{L} + \frac{1}{L} \ln \left(\frac{p_1 - \gamma_{\beta}}{p_1 + \gamma_{\beta}} \right). \tag{A11}$$

In [15], various properties of the modes were determined, such as symmetry of the eigenvalues, orthogonality of the eigenmodes, and completeness of the modes, thereby justifying the eigenmode expansion which follows. It was also shown that the nullspace of the integral

operator in (A6) is empty, which must be true based upon physical reasons.

Based upon an eigenmode expansion, the induced current in the slab is, from (31),

$$J_y(z) = \sum_{\beta} \frac{1}{N_{\beta}} \frac{1}{Z_{\beta}} \langle j_{\beta}(z); e^{-p_1 z} \rangle j_{\beta}(z) \quad (\text{A12})$$

where

$$N_{\beta} = \langle j_{\beta}(z); j_{\beta}(z) \rangle \quad (\text{A13})$$

and

$$Z_{\beta} = s\mu_0 \frac{1}{p_1^2 - \gamma_{\beta}^2} + Z_d(\gamma_1, \gamma_2) . \quad (\text{A14})$$

The backscattered field ($z < -L/2$) is, from (32),

$$\begin{aligned} E_y^s(z) &= -\langle Z_{yy}(z|z'); J_y(z') \rangle \\ &= -\sum_{\beta} \frac{1}{N_{\beta}} \frac{1}{Z_{\beta}} \frac{s\mu_0}{2p_1} \langle j_{\beta}(z); e^{-p_1 z} \rangle^2 e^{p_1 z} \end{aligned} \quad (\text{A15})$$

As a check, the reflection coefficient at the slab interface is

$$\Gamma = \frac{E_y^s}{E_y^{inc}} \bigg|_{z=-L/2} = -\sum_{\beta} \frac{1}{N_{\beta}} \frac{1}{Z_{\beta}} \frac{s\mu_0}{2p_1} \langle j_{\beta}(z); e^{-p_1 z} \rangle^2 e^{-p_1 L} \quad (\text{A16})$$

Numerical results based upon (A16) were compared to standard reflection coefficient formulas to verify the formulation presented here.

References

1. C. E. Baum, "On the Eigenmode Expansion Method for Electromagnetic Scattering and Antenna Problems, Part I: Some Basic Relations for Eigenmode Expansions, and Their Relation to the Singularity Expansion," *Interaction Note* 229, Jan. 1975.
2. C. E. Baum, "On the Eigenmode Expansion Method for Electromagnetic Scattering and Antenna Problems, Part II: Asymptotic Expansion of Eigenmode-Expansion Parameters in the Complex-Frequency Plane," *Interaction Note* 472, Nov. 1988.
3. C. E. Baum, "Emerging Technology for Transient and Broad-Band Analysis and Synthesis of Antennas and Scatterers," *Proceedings IEEE*, v. 64, pp. 1598-1616, Nov. 1976.
4. C. E. Baum, "On the Singularity Expansion Method for the Solution of Electromagnetic Interaction Problems," *Interaction Note* 88, Dec. 1971.
5. R. F. Harrington and J. R. Mautz, "Theory and Computation of Characteristic Modes for Conducting Bodies," *Interaction Note* 195, Dec. 1970.
6. R. F. Harrington and J. R. Mautz, "Characteristic Modes for Dielectric and Magnetic Bodies," *IEEE Trans. Antennas Propagat.*, v. AP-20, pp. 194-198, March 1972.
7. A. D. Yaghjian, "Electric Dyadic Green's Functions in the Source Region," *Proc. IEEE*, v. 68, pp. 248-263, Feb. 1980.
8. G.W. Hanson and C.E. Baum, "A Volumetric Eigenmode Expansion Method for Dielectric Bodies," *Interaction Note* 517 (Phillips Laboratory Note Series, Kirtland AFB), Aug. 1996.

9. R. F. Harrington, Time-Harmonic Electromagnetic Fields, McGraw-Hill, 1961.
10. J. H. Richmond, "Scattering by a Dielectric Cylinder of Arbitrary Cross Section Shape," *IEEE Trans. Antennas Propagat.*, v. AP-13, pp. 334-341, March 1965.
11. D. R. Wilton, K. A. Michalski, and L. W. Pearson, "On the Existence of Branch Points in the Eigenvalues of the Electric Field Integral Equation Operator in the Complex Frequency Plane," *IEEE Trans. Antennas Propagat.*, v. AP-31, pp. 86-91, Jan. 1983.
12. A. G. Ramm, "Theoretical and Practical Aspects of Singularity and Eigenmode Expansion Methods," *IEEE Trans. Antennas Propagat.*, v. AP-28, pp. 897-901, Nov. 1980.
13. L. W. Pearson, "Present Thinking on the Use of the Singularity Expansion In Electromagnetic Scattering Computation," *Wave Motion*, v. 5, pp. 355-368, 1983.
14. C. E. Baum, "Properties of Eigenterms of the Impedance Integral Equation," Interaction Note 487, April 1992.
15. T. M. Habashy, E. Y. Chow, and D. G. Dudley, "Profile Inversion Using the Renormalized Source-Type Integral Equation Approach," *IEEE Trans. Antennas Propagat.*, v. 38, pp. 668-682, May 1990.
16. I. Stakgold, Green's Functions and Boundary Value Problems, John Wiley and Sons, 1979.

Acknowledgment

I would like to thank AFOSR for their sponsorship of this project, and Dr. Carl E. Baum for his guidance and help during my stay at Phillips Laboratory.

Wavelets and Their Applications to the Analysis of Meteorological Data

MAYER HUMI

Professor

Department of Mathematical Sciences

Worcester, MA 01609-2280

Final report for: Summer Faculty Research Program

Phillips Laboratory

Sponsored by

Air Force Office of Scientific Research

Bolling AFB, DC

and

Phillips Laboratory

Hanscom AFB, MA

September 24, 1996

Wavelets and Their Applications to the Analysis of Meteorological Data

Mayer Humi

Professor

Department of Mathematical Sciences

Worcester Polytechnic Institute

ABSTRACT

The objective of this project was to apply wavelets and multiresolution analysis to stratospheric data in order to infer and extract the local turbulent structures. Local values for the Reynolds number and the spectrum of various meteorological variables has been obtained. Furthermore we devise an algorithm to construct and apply "data fitted wavelets" to detrend meteorological data.

1 Introduction

In the period between December, 1988 to February, 1989, NASA sponsored several missions to the stratosphere using ER2 planes [1]. The main objective of these flights was to measure the concentrations of ozone and other trace gases. However readings of other variables such as velocity temperature and pressure were also recorded along the flight path. (These readings do not constitute a time series per se as they were not taken at one space location. We shall refer therefore to this data as a "space-time series"). These measurements provide us with a glimpse about the state of the stratosphere and its structure constants. Furthermore they enable us to examine critically some of the fundamental assumptions about turbulence modeling.

In previous research conducted by the PI and O. Coté of Phillips Lab, spectral analysis and turbulence modeling have been used to extract [10] averaged values for the Richardson number Ri , C_n^2 (index of refraction structure constant), C_T^2 and others. However clear air turbulence is thought to be concentrated in thin layers. Accordingly the computation of local values for these structure constants is highly desirable in many practical applications (e.g. Air Borne Laser).

Wavelets which came on the scientific scene in the last decade consists of functions with compact support (in contrast to Fourier series). Multiresolution analysis with appropriate wavelets can resolve in principle the 'locality problem' mentioned above and add a new dimension to our understanding of the stratosphere. One of the major thrusts of this project concentrated on the development and application of these tools to the data collected by the ER2 mission.

However I participated also in the cloud modeling and simulation initiative at Phillips Lab and the modeling and analysis of meteorological data from the Antarctic British station.

2 Turbulence and the continuous wavelet transform.

Fourier series expansions and Fourier transform in $L^2(R)$ use $\{e^{ikt}\}$ as basis functions. These have a unique wave number but their support is R . Accordingly all local information about

a function f is lost when we apply the Fourier transform

$$\hat{f}(k) = \frac{1}{2\pi} \int_{-\infty}^{\infty} f(x) e^{ikx} dx.$$

Let ψ be a wavelet with compact support. The L^1 -wavelet transform of f is defined as

$$\tilde{f}(x, r) = \frac{1}{r} \int_{-\infty}^{\infty} f(x') \psi \left(\frac{x' - x}{r} \right) dx'.$$

Thus the wavelet transform yield a 2-D function which depend on the position x and the scale r .

Due to its (mathematical) properties the "Mexican Hat wavelet"

$$\psi = -\frac{d^2}{dx^2}(e^{-x^2/2}), \quad \hat{\psi} = k^2 e^{-k^2/2}$$

is a popular choice in the literature. We used it exclusively in our analysis. Mallot and Hwang [6] showed that singularities in $f(x)$ produce maximums in $|\tilde{f}(x, r)|$ and by following these maximums as $r \rightarrow 0$ one can obtain the position of the singularity. Using this multiresolution analysis one can hope to identify (at least some) turbulent structures in a data set.

Fourier spectrum density of a function $f(x)$ is defined as

$$E(k) = \frac{1}{2\pi} |\hat{f}(k)|^2, \quad k > 0$$

Using the L^2 wavelet transform

$$\tilde{f}(x, r) = \frac{1}{r^{1/2}} \int_{-\infty}^{\infty} f(x') \psi \left(\frac{x' - x}{r} \right) dx'$$

we now define the local energy spectrum of f as

$$\tilde{E}(x, k) = \frac{1}{2c_1 k_0} \left| \tilde{f} \left(x, \frac{k_0}{k} \right) \right|^2$$

where

k_0 = is the peak wave number of ψ

and

$$c_1 = \int_0^{\infty} \frac{\hat{\psi}(k)}{k} dk.$$

Similarly the local Reynold's number is defined as

$$\tilde{Re}(\mathbf{x}, r) = \tilde{u}(\mathbf{x}, r) \frac{r}{\nu}$$

where ν is the fluid viscosity and

$$\tilde{u}(\mathbf{x}, r) = \left(\frac{1}{3C_2} \sum_i |\tilde{u}_i(\mathbf{x}, r)| \right)^{1/2}$$

$$C_2 = \int_0^\infty (\hat{\psi})^2 / k^2 dk.$$

In this analysis the expectation is that as r approach the integral scale of the flow, the average of $\tilde{Re} \rightarrow Re$. Moreover the average of the local spectrum over all the data should approach the usual Fourier spectrum of the data.

3 Turbulence and the discrete wavelet transform

The discrete wavelet transform utilizes a discrete set of wavelet functions ψ_{ij} , $i, j = 1, \dots, \infty$. In this set the translation and dilation parameters are discrete. Deubechies et al [3] showed how to construct the functions ψ_{ij} so that they form a complete orthogonal set for $L^2(R)$. Thus for an appropriate wavelet basis we can define the wavelet coefficients

$$\tilde{f}_{ij} = \int_{-\infty}^{\infty} f(x) \psi_{ij}(x) dx$$

and

$$f(x) = \sum \tilde{f}_{ij} \psi_{ij}(x).$$

However Mallot et al [6] showed that one can compute the coefficients \tilde{f}_{ij} by multiplication with the coefficients of an appropriate filter of finite length.

When this filter is applied to a data vector of length 2^n it decomposes it into a smooth part and a detail. We can retain only the smooth part of the (transformed) data and iterate the process to obtain the smooth-smooth part of the data and so on.

Thus from this point of view wavelets form a natural methodology to detrend meteorological data by retaining only the smooth part that is left after m iterations of the filter. In fact after each iteration of the wavelet filter the smooth part represents the data at a larger (coarser) scale.

By applying the inverse wavelet transform m times on the smooth part of the data we obtain x_{smooth} . Taking the difference $x - x_{\text{smooth}}$ we obtain the turbulent residuals of the flow.

The fundamental question one has to answer before implementing the algorithm outlined above is how to choose "the optimal wavelet" and the number of iterations to use. To this end Coifman et al [4] developed the following filter bank methodology;

1. Create a library of wavelet basis
2. Let $\tilde{d} = W_F(d)$ be the transformed data under the action of the filter W_f
3. Compute the standardized entropy of \tilde{d} which is defined as

$$E(\tilde{d} | W_f) = H(\tilde{d}^2) / H\left(\frac{1}{h} \dots \frac{1}{h}\right)$$

where H is the Shannon entropy

$$H(\mathbf{p}) = - \sum_n p_n \ln(p_n).$$

4. Choose the wavelet from the library that minimizes E .

This procedure when coupled with a plot of the variance for the smoothed data vs. the number of iterations enables us to answer the questions raised above about the implementation of this algorithm.

Another approach to this problem is to design an appropriate basis of "data fitted wavelets". We developed as part of this project an algorithm for this purpose which we describe in the following sections.

4 Construction of Discrete Wavelets

To construct an orthogonal wavelet basis one has to find a function $\phi(x)$ - which is called the scaling function - which satisfies the dilation-difference equation

$$\phi(x) = \sum_n c_n \phi(2x - n) \tag{1}$$

subject to the following requirements;

1. $\int \phi(x) dx = 1.$

2. Using suitable coefficients $\{a_n\}$ one can approximate smooth function in $L^2(R)$ so that for some fixed p

$$\| f - \sum_n a_n \phi(2^m x - n) \| \leq C 2^{-mp} \| f^{(p)} \| \quad (2)$$

where $f^{(p)}$ is the p -th derivative of f .

3. Orthogonality

We require that

$$\phi_j(x) = \sum c_n \phi(2^j x - n) \quad (3)$$

and its translates $\phi_j(x - m)$ are orthogonal. That is

$$\int \phi_j(x - k) \phi_j(x - m) = \delta_{km}. \quad (4)$$

Together these conditions imply the following:

1. $\sum c_k = 2$
2. $\sum (-1)^k k_{c_k}^m = 0, \quad m = 0, 1, \dots, p-1$
3. $\sum c_k c_{k-2m} = 2\delta_{0m}.$

As an example we point out that the Haar function

$$\phi_0(x) = \begin{cases} 1, & 0 \leq x \leq 1 \\ 0, & \text{otherwise} \end{cases} \quad (5)$$

satisfies these conditions with $p = 1$ and $c_0 = c_1 = 1$.

Another family of scaling functions is due to Daubechies. One of the functions in this family, $D_4(x)$, satisfies eq. (1) with

$$c_0 = \frac{1}{4}(1 + \sqrt{3}), \quad c_1 = \frac{1}{4}(3 + \sqrt{3}), \quad c_2 = \frac{1}{4}(3 - \sqrt{3}), \quad c_3 = \frac{1}{4}(1 - \sqrt{3}). \quad (6)$$

Once a solution of the scaling equation is known a wavelet mother function can be defined as

$$\psi(x) = \sum (-1)^k c_{1-k} \phi(2x - k) \quad (7)$$

and a wavelet basis of $L^2(R)$ is defined by $\{\psi_{jk}\}$ where

$$\psi_{jk}(x) = 2^{j/2} \psi(2^j x - k) \quad (8)$$

Using such an orthogonal wavelet basis we can expand a function $f(x)$ in $L^2(R)$ as

$$f(x) = \sum_{j=-\infty}^{\infty} \sum_{k=-\infty}^{\infty} a_{jk} \psi_{jk}(x) \quad (9)$$

with

$$a_{jk} = \int_{-\infty}^{\infty} f(x) \psi(x - 2^{-j}k) dx. \quad (10)$$

In practice, when the wavelet transform is applied to a discrete time series, the application requires only the coefficients $\{c_i\}$ which are referred to as the wavelet filter coefficients. As a first step in this analysis one generates the transform matrix

$$C = \begin{bmatrix} c_0, & c_1, & c_n \dots, \\ c_n, & -c_{n-1} \dots & -c_0 \\ & c_0, & c_1 \dots c_n \\ & c_n, & -c_{n-1} \dots -c_0 \\ & \dots & \\ c_2, \dots, & c_n & c_0, c_1 \\ c_{n+2}, \dots, & -c_0 & c_n, -c_{n-1} \end{bmatrix} \quad (11)$$

(Here the number of coefficients is assumed to be even).

In this context $\{c_0, \dots, c_n\}$ is a smoothing filter while the mirror filter $\{c_n, -c_{n-1}, \dots, -c_0\}$ is the "detail" filter. Together these filters are referred to as "quadrature mirror filters".

When the filter matrix C is applied to a data vector of length 2^n

$$x = \begin{bmatrix} x_1 \\ \vdots \\ \vdots \\ x_{2^n} \end{bmatrix}$$

it decomposes it into a smooth part and a detail

$$Cx = \begin{bmatrix} s_1 \\ d_1 \\ \vdots \\ s_m \\ d_m \end{bmatrix}, m = 2^{n-1} \quad (12)$$

5 Data Fitted Wavelets

In the literature of the last few years several authors constructed a large number of wavelet bases. Each of these was found by imposing additional constraints on the properties of the desired basis beside those enumerated in section 4. As explained above these can be used as filters to detrend time series of meteorological observations. The fact remains however that each of these filters bears no intrinsic relationship to the data and its properties. In particular since meteorological data is assumed to be "scale invariant" (at least for some range of wave numbers) it is appropriate to try to use wavelet filters that are "data fitted". By this we mean that in constructing these wavelets the actual gross features of the data are taken into account. With these built in properties these filters should be better suited to identify any spectral-spikes which are due to turbulence effects.

To accomplish this objective we observe that from an algorithmic point of view the construction of a wavelet filter with n coefficients c_1, \dots, c_n requires n independent equations (for reasons that will become clear later we let $n = 2^k$). The constraints given by eqs. (5)-(7) with (let's say) $p = 1$ yield only $\frac{n}{2} + 2$ (nonlinear) equations. The remaining $\frac{n}{2} - 2$ equations should come from the imposition of additional "mathematical properties" or from the data.

To construct these additional equations from the data we first create a sample of n representative points $x_j = x(t_j)$, $i = 1, \dots, n$. The application of the yet to be found smoothing filter S (without the mirror filter) on $x = (x_1, \dots, x_n)$ yields a vector s of length

$n/2$ which is representative of the smooth data.

$$Sx = sS = \begin{bmatrix} c_1, \dots, & c_n \\ c_{n-1}, & c_n c_1 \dots c_{n-2} \\ c_3, \dots, c_n, c_1, c_2 \end{bmatrix}, s = \begin{bmatrix} x_1 \\ \vdots \\ s_{n/2} \end{bmatrix}$$

Some "generic" strategies can be used to obtain a representation of s .

1. We can compute s_i by some data-smearing-smoothing algorithm. E.G. we can let

$$s_i = \frac{x_{2i-1} + x_{2i}}{2}$$

2. Compute the least squares curve $f(t)$ (of appropriate order) to the vector x and let

$$s_i = \frac{f(t_{2i-1}) + f(t_{2i})}{2}$$

3. Apply a known wavelet filter to the whole data several times until the number of components in the smooth representation of this data is $\frac{n}{2}$ and use these values as a representation of s .

Remark: All these strategies yield $\frac{n}{2}$ equations for the filter coefficients. However we can reduce these to $\frac{n}{2} - 2$ by leaving out the two end point equations.

Of the strategies mentioned above the second and the third seems to be more robust and successful. However, even for these implementations one has to be careful about the choice of n . Small n leads to "small data input". That is the number of equations that are data dependent is small e.g. for $n = 8$ only 2 equations originate from the data. On the other hand when n is large (e.g. $n = 128$) the influence of the data on the filter coefficients is strong but we have to solve a large number of nonlinear equations.; Furthermore the set of equations becomes ill posed (due to the nature of eq. (7)) especially if the data contains large errors. Nevertheless in "mid-range" we were able to solve the resulting set of equations to obtain appropriate filter coefficients.

6 Implementation and results

As part of this project we write a Fortran package to implement the algorithms described in Sections 2, 3. The source code for this package is about 200k. In this implementation

the IMSL subroutine library was used and PVWAVE-ADV. was used to obtain graphs and visualizations of the results.

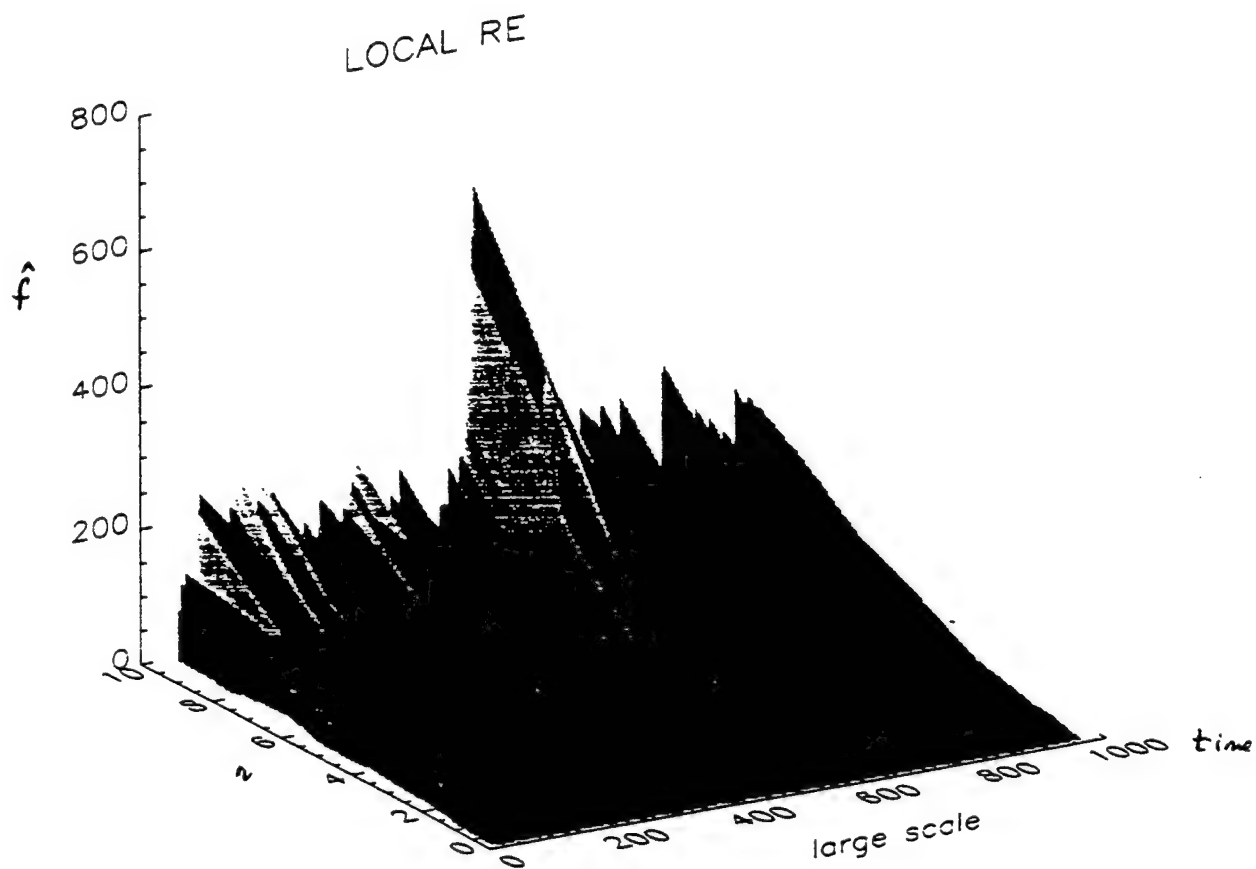
Of special interest to the meteorological community is the new possibility to plot $E(x, k)$ (for a fixed wave number) of a certain variable as a function of the location. This information can be used to isolate turbulent structures and make inferences about intermittency in the flow. Such information can not be obtained from the usual Fourier spectrum of the data.

Samples of graphs obtained from this package are given in Figures. 1-5.

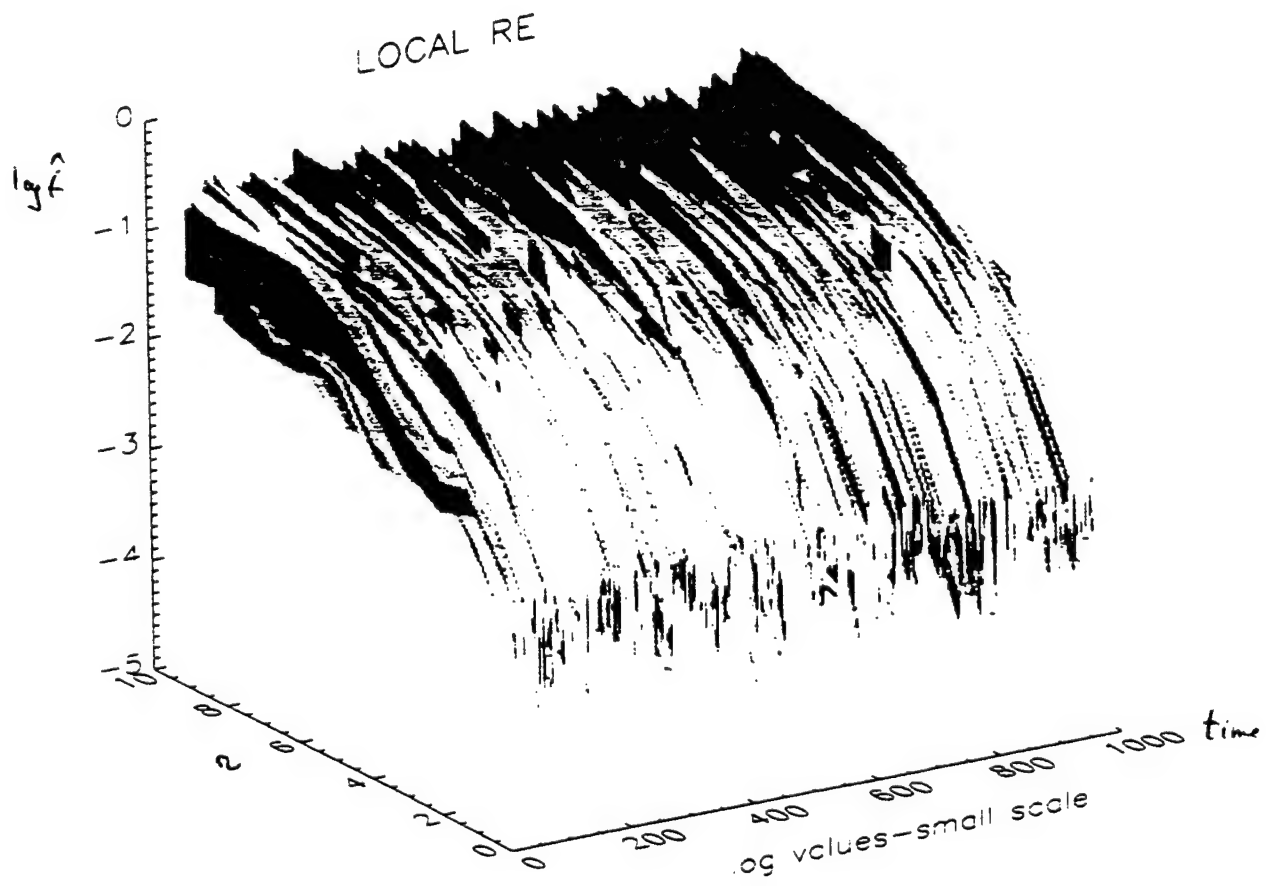
We plan to publish these results in a forthcoming paper.

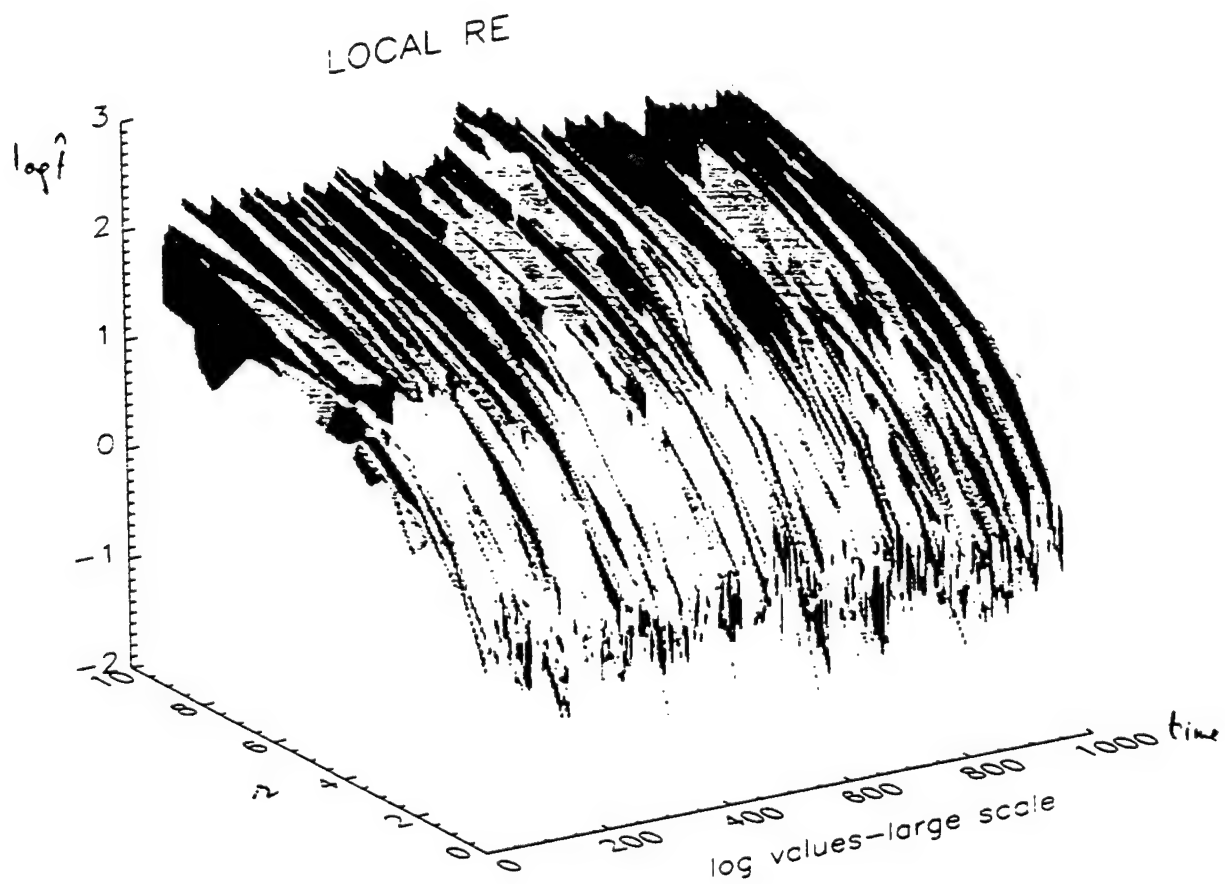
References

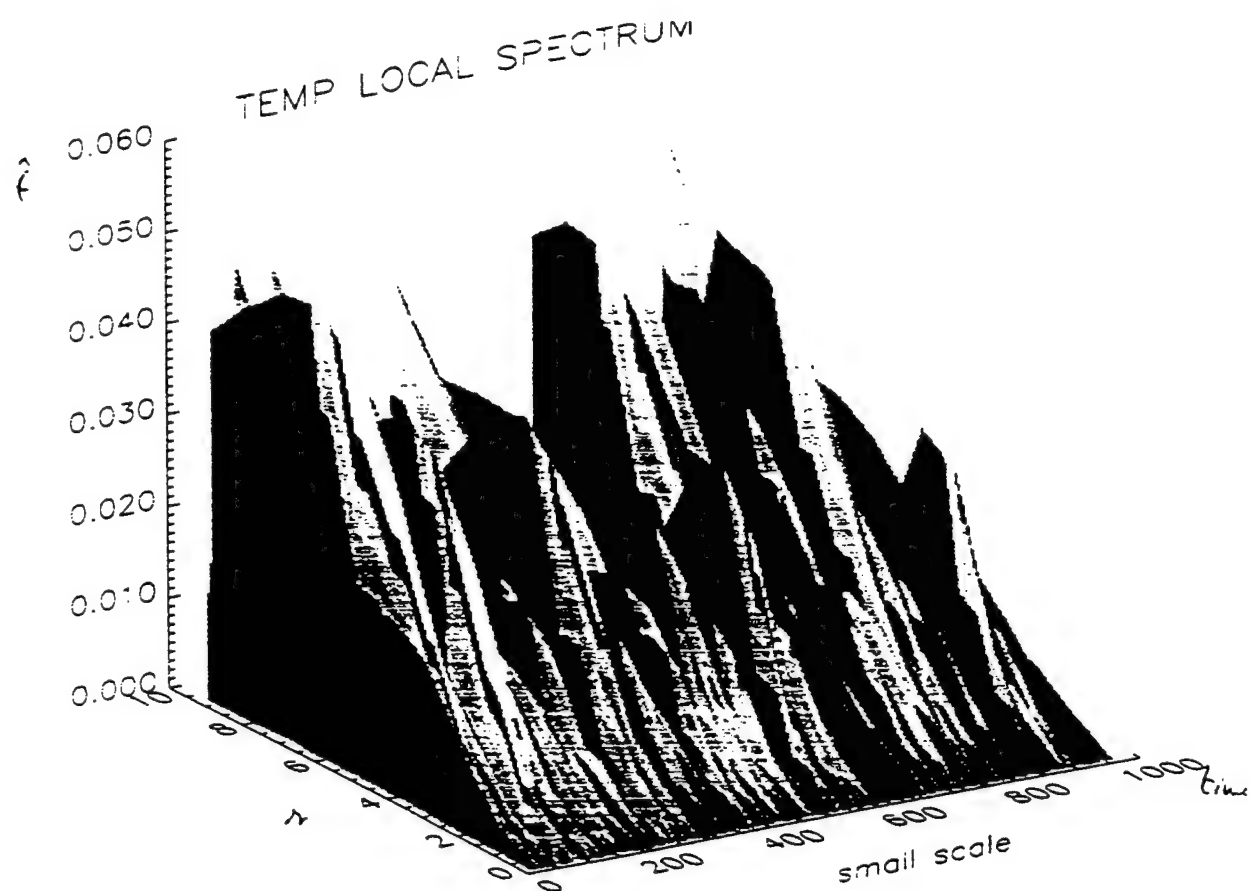
1. G. Box and G.M. Jenkins - Time series analysis, Holden Day 1976.
2. J. Morlet, et al. - Wave propagation and sampling theory, Geophysics **47** p. 202 (1982).
3. I. Deubechies. Ten lectures on wavelets, SIAM, Philadelphia, PA 1992.
4. R. Coifman, et al. - Wavelet analysis and signal analyst, IEEE Trans. Infor. Th. **36** p. 513-718 (1990).
5. M. Farge - Wavelet transforms and their applications to turbulence - Ann. Rev. Fluid Mech. p. 395-457 (1992).
6. S. Mallot and W. H. Hwang - Singularity detection, IEEE Trans. Infor. Th. **38** p. 617 (1992).
7. G. Katul, et al. - The partitioning of attached and detected eddy motion (preprint).
8. Coifman, et al. - Entropy based algorithm. IEEE Tras. Infor. Th. **38** P. 713 (1992).
9. M. Humi - Data fitted wavelets for meteorological analysis (in preparation).
10. M. Humi and O. Cote - Stratospheric structure constants and the Boussinesq-Kolmogorov hypothesis (submitted).
11. M. Farge, et al. - Wavelets and turbulence, Proc. IEEE, **84** p. 639 (1996).











SHAPE CONTROL OF AN
INFLATED THIN CIRCULAR DISK:
Preliminary Investigation

C. H. M. Jenkins, Ph.D., P.E.
Associate Professor
Mechanical Engineering Department

South Dakota School of Mines and Technology
Rapid City, SD 57701

Final Report for:
Summer Faculty Research Program
Phillips Laboratory

Sponsored by:
Air Force Office of Scientific Research
Bolling Air Force Base, DC

and

Phillips Laboratory

August 1996

SHAPE CONTROL OF AN INFLATED THIN CIRCULAR DISK:
Preliminary Investigation

C. H. M. Jenkins, Ph.D., P.E.
Associate Professor
Mechanical Engineering Department
South Dakota School of Mines and Technology

Abstract

Space-based inflatable technology is of current interest to NASA and DOD, and in particular to the Air Force and Phillips Laboratory. Potentially large gains in lowering launch costs, through reductions in structure mass and volume, are driving this activity. Diverse groups are researching and developing this technology for radio and radar antennae, optical telescopes, and solar power and propulsion applications. Regardless of the use, one common requirement for successful application is the accuracy of the inflated surface shape. The work reported here concerns a preliminary nonlinear finite element analysis of shape control of an inflated thin circular disk. Shape modification was achieved through enforced boundary displacements, which resulted in moving the inflated shape towards a desired parabolic profile. Conclusions and future work activities are provided.

SHAPE CONTROL OF AN INFLATED THIN CIRCULAR DISK: Preliminary Investigation

Christopher H. M. Jenkins

INTRODUCTION

There currently exists renewed interest in applications of inflatable structures in space. With increased pressure to reduce costs associated with design, fabrication, and launch of space structures, DOD and NASA are taking a new look at space-based inflatable structures. Applications for inflatable structures in space include lunar and planetary habitat, RF reflectors and waveguides, optical and IR imaging, solar concentrators for solar power and propulsion, sun shades, and solar sails [see, e.g., Grossman and Williams, 1990; Cassapakis and Thomas, 1995].

For many of these applications, particularly those involved with communications, imaging, power, and propulsion, accurate maintenance of the inflatable surface shape is critical. Surface accuracy ranges from a few percent of wavelength for low frequency applications, to a fraction of a percent of wavelength for visual wavelengths [see Hedgepeth, 1982]. The likelihood of achieving such tolerances by purely passive means is unlikely.

In what follows, background information on highly compliant structures and their analysis is first given. Then methods and results of an investigation into the shape control of a thin circular disk are discussed. Finally, conclusions and directions for future work are provided.

BACKGROUND

Structures formed from thin-walled material can be found in a diverse array of applications, from biological organisms to architectural structures to aerospace craft. Depending on the degree of bending resistance inherent in such structures, as well as the degree of participation of in-plane and bending reactions to loads, for certain analytical purposes they may be modeled successfully as membranes, whose unique feature is the absence of any resistance to bending.

For structures whose bending resistance is very small indeed (and we take here as fundamental that all real structures have some finite bending resistance, no matter how small),

compressive stresses result in a localized buckling or wrinkling. Hence, a further modeling restriction can be made that limits the membrane to allowable stresses greater than zero only, i.e., a no-compression membrane. The structure is then modeled as carrying loads only in tension or in tension fields [see Jenkins and Leonard, 1991; Jenkins, 1996b].

Finite element methods have made significant contributions to the analysis of large deformation, nonlinear structural problems. Yet the analysis of membrane structures that undergo large displacements during loading remains a difficult problem for which current finite element methods are unsuitable. The primary difficulties lie in the fact that the structural system is underconstrained, and stable equilibrium conditions only exist for loading fields that are orthogonal to the set of unconstrained degrees of freedom (see Kuznetsov, 1991). Furthermore, configurations exist that are not in the vicinity of such an equilibrium state. Consequently, large rigid body motions with concomitant, large configuration changes, must take place before elastic response is obtained.

A class of pneumatic envelopes provides dramatic examples of underconstrained systems: the stowed versus deployed configurations in air bags, balloons, or parachutes. There are several difficult aspects of the analysis of pneumatic envelopes. First of all, while structural stiffness is provided by structural components such as the skin, and any reinforcing elements such as cables or tapes, this stiffness can only be engaged in specific loaded configurations, and the stability of the structural system only exists under such loading. The structural system is thus said to be underconstrained.

Furthermore, the unloaded configuration may be far from any static equilibrium condition in solution space. Constraints are usually unilateral so that a structurally impossible state is obtained under a reversal of the load from an equilibrium state.

Even in a loaded configuration, the structural function of the skin may degenerate from a state of bi-axial tension, for which the membrane model is appropriate, to a state of uni-axial tension (since compression cannot be accommodated by thin films or cables). Under this latter condition the skin will wrinkle. This condition may be appropriately modeled by a tension field model which ignores the detail of the wrinkling but properly models the structural performance of the skin [Jenkins and Leonard, 1993]. Experimental verification is a challenge under such

conditions, since any contact with the structure readily disturbs that which was to be measured [Jenkins, 1995; Jenkins, et al., 1995; Jenkins, 1996a].

Balloons and parachutes are other important examples of pneumatic envelopes that are underconstrained. The service load environment for a balloon in ascent varies over a wide range of temperatures, configuration changes, and load path changes. During the ascent, when the balloon is not fully inflated, the envelope is underconstrained, and this provides for considerable computational challenge. [See, e.g., Schur, 1992; Schur, 1994; Schur and Jenkins, 1996.]

The three events that occur during a parachute mission are the deployment, inflation, and terminal descent phases. The deployment phase is a highly nonlinear, possibly non-unique and isometric process in which the parachute and suspension lines unfold from the deployment bag. The inflation phase is a highly transient and nonlinear phase in which the air flow about, and captured in, the canopy grossly distorts the shape to prestress and decelerate the parachute. The terminal descent phase is primarily a steady-state process in which the parachute and payload undergoes slower dynamic motion [Stein and Benney, 1994; Benny and Leonard, 1995].

SHAPE CONTROL OF AN INFLATED PLANE CIRCULAR DISK

It has been observed in inflatable reflectors, that their service shape deviates from the desired parabolic shape as a function of position on the reflector. This leads to the so-called "W-curve" discussed in more detail below. Hence, one fundamental motivation for shape control of a circular disk is to minimize the surface deviation from the desired target parabola.

Three processes that affect the service shape of an initially plane circular disk were investigated by use of a finite element model: inflation pressure, prestress, and boundary constraints. Although finite elements are used for the bulk of the study herein, a brief discussion of the theoretical foundations of the inflation problem is appropriate. This is required for validation of the FEM model, as well as for gaining useful insight into the disk response. Comparisons are made to large deflection theory of thin plates. Results are presented and conclusions are drawn.

Theoretical Foundation

We take here an initially plane circular disk of radius a and thickness h , with $h \ll a$. The boundary (circumference) of the disk is considered to be pinned. For a very thin disk, the

inflation process will result in transverse displacements w that are large relative to the disk thickness. We limit considerations here to displacements that are associated with “small” strain but “moderately” large rotations.

The governing field equations are the von Kármán plate equations [Timoshenko and Woinowsky-Krieger, 1959]:

$$D\nabla_r^4 w - Eh \frac{1}{r} \frac{d}{dr} \left(\frac{d\Phi}{dr} \frac{dw}{dr} \right) = p \quad (1)$$

$$\nabla_r^4 \Phi + \frac{1}{2r} \frac{d}{dr} \left(\frac{dw}{dr} \right)^2 = 0 \quad (2)$$

where p is the pressure, D is the bending rigidity given by

$$D = \frac{Eh^3}{12(1-\nu^2)} \quad (3)$$

and Φ is a stress function defined such that the radial and tangential stress resultants (force/length) are given respectively by:

$$N_r = \sigma_r h = \frac{Eh}{r} \frac{d\Phi}{dr} \quad (4)$$

$$N_t = \sigma_t h = Eh \frac{d^2 \Phi}{dr^2} \quad (5)$$

Finite Element Model

A quarter-symmetry model is used that consists of 42 second-order shell elements and 177 nodes, using the ABAQUS fem code. FEMAP is used for pre- and post-processing. For the values of the parameters chosen here, viz., radius $a = 21$ in (53.3 cm), $h = 0.005$ in (0.13 mm), $E = 500,000$ psi (3.45 Mpa), and $\nu = 0.4$, the bending rigidity D is extremely small (0.0062 lb-in), and the disk is essentially a membrane.

Inflation Analysis and Results

We take as the solution to (1) and (2) the three-term polynomial

$$w = w_0 \left(1 + \alpha_2 \frac{r^2}{a^2} + \alpha_4 \frac{r^4}{a^4} \right) \quad (6)$$

where w_0 is the deflection at $r = 0$, and α_2 and α_4 are constants which satisfy the boundary conditions. Using the membrane assumption, the central deflection w_0 can be shown to be:

$$w_0 = 0.665a \left(\frac{pa}{Eh} \right)^{1/3} \quad (7)$$

In the present case, the boundary conditions (at $r = a$) are given by the displacement $w = 0$, and a zero moment condition:

$$M_r = D \left(\frac{d^2 w}{dr^2} + \frac{\nu}{r} \frac{dw}{dr} \right) = 0 \quad (8)$$

Taking the assumed deflected shape (6) and substituting into the above boundary conditions leads to the following expressions for the α 's:

$$\alpha_2 = -\frac{6 + 2\nu}{5 + \nu} \quad (9)$$

$$\alpha_4 = \frac{1 + \nu}{5 + \nu} \quad (10)$$

For the Poisson's ratio of 0.4, the deflected shape becomes

$$w = w_0 \left(1 - 1.26 \frac{r^2}{a^2} + 0.259 \frac{r^4}{a^4} \right) \quad (11)$$

A better fit for the larger deflection results generated here is given by [Young, 1989]:

$$w = w_0 \left(1 - 0.9 \frac{r^2}{a^2} - 0.1 \frac{r^5}{a^5} \right) \quad (12)$$

Note that the equivalent parabola would be given by:

$$w = w_0 \left(1 - \frac{r^2}{a^2} \right) \quad (13)$$

Figure 1 compares the fem results with the parabolic curve, and the difference is apparent.

Figure 2 shows the deviation of fem results, as well as (11) and (12), from the equivalent parabola (13). The "W-curve" shape (one-half of the "W"), indicating deviation from a parabola, is evident in Figure 2. This will be discussed further below

It would be a common situation to find some prestress in the disk prior to inflation. The prestress could be thought of in the sense of the tightening of a drumhead. One would expect that the central deflection would be reduced as prestress increased. Fem results of center deflection for a variety of initial stress values confirmed this intuition.

Rim Control

It was seen above that the initially plane disk does not have an inflated shape that is parabolic. Questions naturally arise then about how could one move the shape to be more parabolic. More generally, the following question might be posed: Given "N" actuators equally spaced around the rim of an inflated disk (or disk pair), what combination of actuations would result in optimizing a desired effect at some location on the disk? Below we provide some results from an initial investigation of that question.

Radial displacements are imposed on the fem model after inflation. These displacements occur in various combinations at the 0, 45, and/or 90 degree positions around the model boundary (rim). Figure 3 shows the fem model with equal 0.1 in (2.54 mm) outward radial displacements at all positions. The center deflection has decreased, and the radial stress has generally increased everywhere (disregarding the local stress concentrations at the displacement points) relative to the inflated only case. The other case considered was where 0.1 in radial outward displacements are imposed at the 0 and 90 positions only.

We look at the results in graphical form, always looking along the 45 degree meridian. Figure 4 shows the percent variation in the model from the parabolic shape (at the 45 degree meridian) for each of the three cases: (1) inflation only without boundary displacements, (2) boundary displacements at the 0, 45, and 90 positions, and (3) boundary displacements at the 0 and 90 degree positions. The maximum variation goes from about 12.5% for the inflated only case, to a little over 7% for 3 boundary displacements. However, even when a displacement is not applied at the 45 degree meridian line, significant reduction in the variation from parabolic shape is observed.

Returning now to the "W" problem discussed above, Figure 5 shows the effect of boundary displacement on reducing the W-curve. The 3 boundary displacements case shows the maximum reduction in the W-curve, but even with 2 displacements, the W-error is reduced at positions distant from the application of the displacements.

CONCLUSIONS AND FUTURE WORK

Inflatable structures have been used for many years in terrestrial applications, from sports stadium roofs to automotive airbags. Inflatable will achieve their greatest potential, however, in space-based applications. Along with their high strength to weight ratio, the capability of reduced launch mass and volume make inflatables highly desirable candidates for space-based structures.

This preliminary investigation has focused on initial inquiries into the shape control of inflatable structures, specifically a thin inflated disk. Results have been compared to theory where possible. It has been shown that the shape of an initially plane circular disk is not inherently parabolic. Radial displacements at the boundary can, however, move the surface toward a parabolic shape. Moreover, this effect is pronounced at locations distant from the locations where the discrete boundary displacements are applied. The basis for the so-called "W-curve" has been demonstrated, and shown to be reduced by shape control actions.

Future work to be carried out from this point includes the following:

- * *Fully investigate the "N-actuator" problem.* Current inflatable reflector technology uses discrete points of connection between the reflector and the reaction ring (torus). It needs to be determined whether these attachment points could be used to advantage as shape control actuators. If the answer turns out to be in the affirmative, this would provide fairly rapid technology improvements over the current state of the art. The structure/control/optimization problem needs to be investigated, including the spatial rate of decay of rim force/displacement effects.
- * *Investigate the adequacy of PVDF (piezo-polymer) as a sensor/actuator for disk and torus applications.* Recently, polymer films have been developed with piezoelectric properties, i.e., strains that result in voltage production, and applied voltages that produce strain. This material is suitably matched to the space-based inflatable concept, due to its light weight and high compliance.
- * *Investigate the effects of variable disk thickness and fiber reinforcing on inflated shape.* Simple passive techniques for generating the desired inflated shape could be achieved through the tailoring of material parameters. Disk thickness may be made variable to control stress/strain

in specific locations, thus influencing the deflected shape. Fiber reinforcing would allow for modifying material stiffness in specific locations, again affecting the inflated shape.

* *Develop a more realistic numerical model.* The current fem model uses idealized boundary conditions. More realistic "elastic" boundary conditions should be applied to simulate the torus. This could be followed by modeling the torus itself. Prestress effects on deflected shape need to be verified. Piezo and thermal effects could be included in the model.

* *Assist in the design of effective ground demonstrations.* The model developed and the knowledge gained from it can be applied to the design of effective laboratory scale projects. An understanding is needed of how best to design laboratory fixtures to provide for the most optimum shape possible at the lowest cost.

ACKNOWLEDGMENTS

The author gratefully acknowledges the AFOSR Summer Faculty Research Program for their support of this investigation. The author is especially grateful to Lt. Jonathan Bishop, PL/VTS, for his help and support during this work, and to Mr. Dan Marker, PL/LI, for the many helpful discussions regarding space-based inflatable applications.

REFERENCES

- Benney, R., and Leonard, J.W. (1995). A 3-D finite element structural parachute model, Proc 13th AIAA Aerodynamic Decelerator Conf, Clearwater Beach, FL.
- Cassapakis, C., and Thomas, M. (1995). "Inflatable structures technology development overview," AIAA 95-3738.
- Grossman, G., and Williams, G. (1990). "Inflatable concentrators for solar propulsion and dynamic space power," J Solar Energy Engineering **112**, 229-236.
- Hedgepeth, J.M. (1982). "Accuracy potentials for large space antenna reflectors with passive structures," J Spacecraft **19**(3), 211-217.
- Jenkins, C.H., and Leonard, J.W. (1991). Nonlinear dynamic response of membranes: State of the art, Appl Mech Rev **44**, 319-328
- Jenkins, C.H., and Leonard, J.W. (1993). Dynamic wrinkling of viscoelastic membranes, J Appl Mech **60**, 575-582.

- Jenkins, C.H., Spicher, W., and Vedoy, A. (1995). Evaluation of membrane wrinkling by noncontact measurement," Proc 24th Midwestern Mechanics Conf, Ames, IA.
- Jenkins, C.H. (1995). "Membrane Wrinkling: Theoretical Predictions and Experimental Verifications," (invited), Symposium on Advances in Mechanics of Elastic and Bioelastic Membranes at the Int Mech Engr Conf Expo, ASME, San Francisco, CA.
- Jenkins, C.H. (1996a). "Experimental Measurement of Wrinkling in Plane Elastic Sheets," 1996 Spring Conference, Society of Experimental Mechanics, Nashville, TN.
- Jenkins, C.H. (1996b). "Nonlinear Dynamic Response of Membranes: State of the Art -- Update," Appl Mech Rev, (to appear).
- Kuznetsov, E.M. (1991). Underconstrained structural systems, Springer-Verlag, New York.
- Schur, W.W. (1992). Recent advances in the structural analysis of scientific balloons, 24th COSPAR - The World Space Cong, Washington, DC.
- Schur, W.W. (1994). Development of a practical tension field material model for thin films, 32nd Aerospace Sciences Meeting & Exhibit - AIAA, Reno, NV.
- Schur, W.W., and Jenkins, C.H. (1996). Large deflection analysis of pneumatic envelopes using a penalty parameter modified material model, Computers Structures (in review).
- Stein, K.R., and Benney, R.J. (1994). Parachute inflation: a problem in aeroelasticity, US Army Tech Report: Natick/TR-94/015.
- Timoshenko, S., and Woinowsky-Krieger, S. (1959). Theory of plates and shells. McGraw-Hill.
- Young, W.C. (1989). Roark's formulas for stress & strain, 6th ed. McGraw-Hill.

COMPARISON OF INFLATED SHAPE vs EQUIVALENT PARABOLA

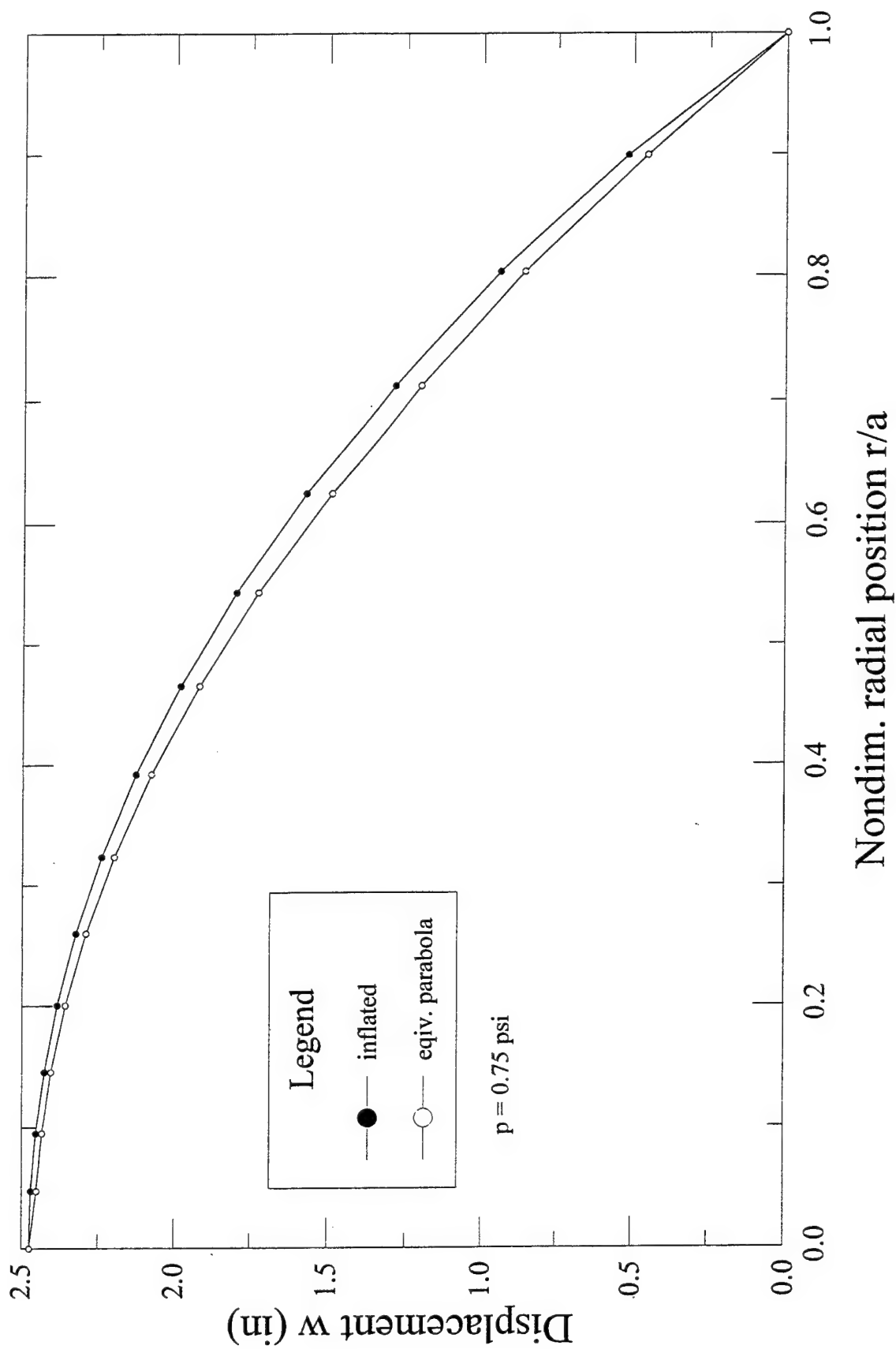


Figure 1

COMPARISON OF VARIOUS DEVIATION MEASURES

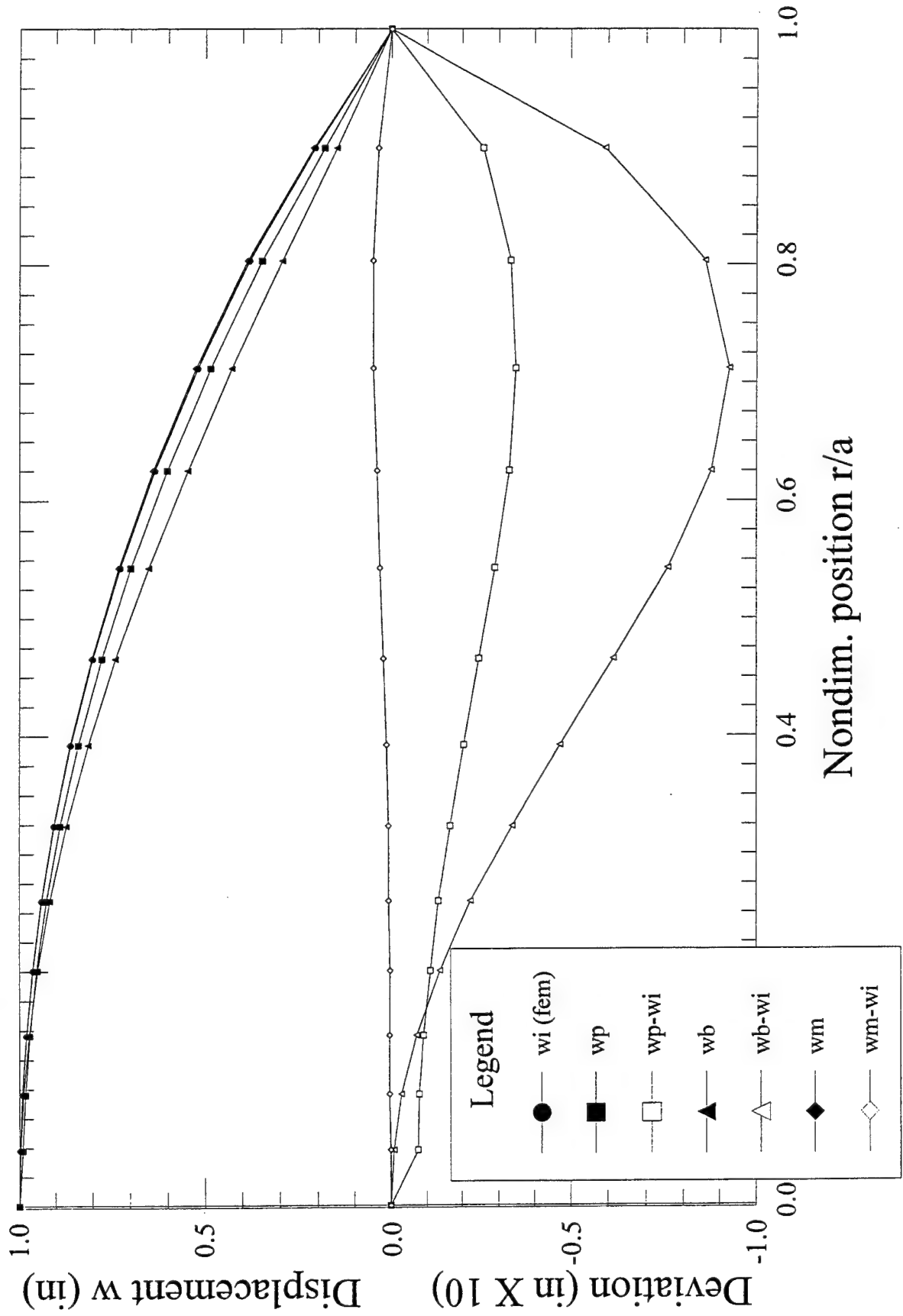
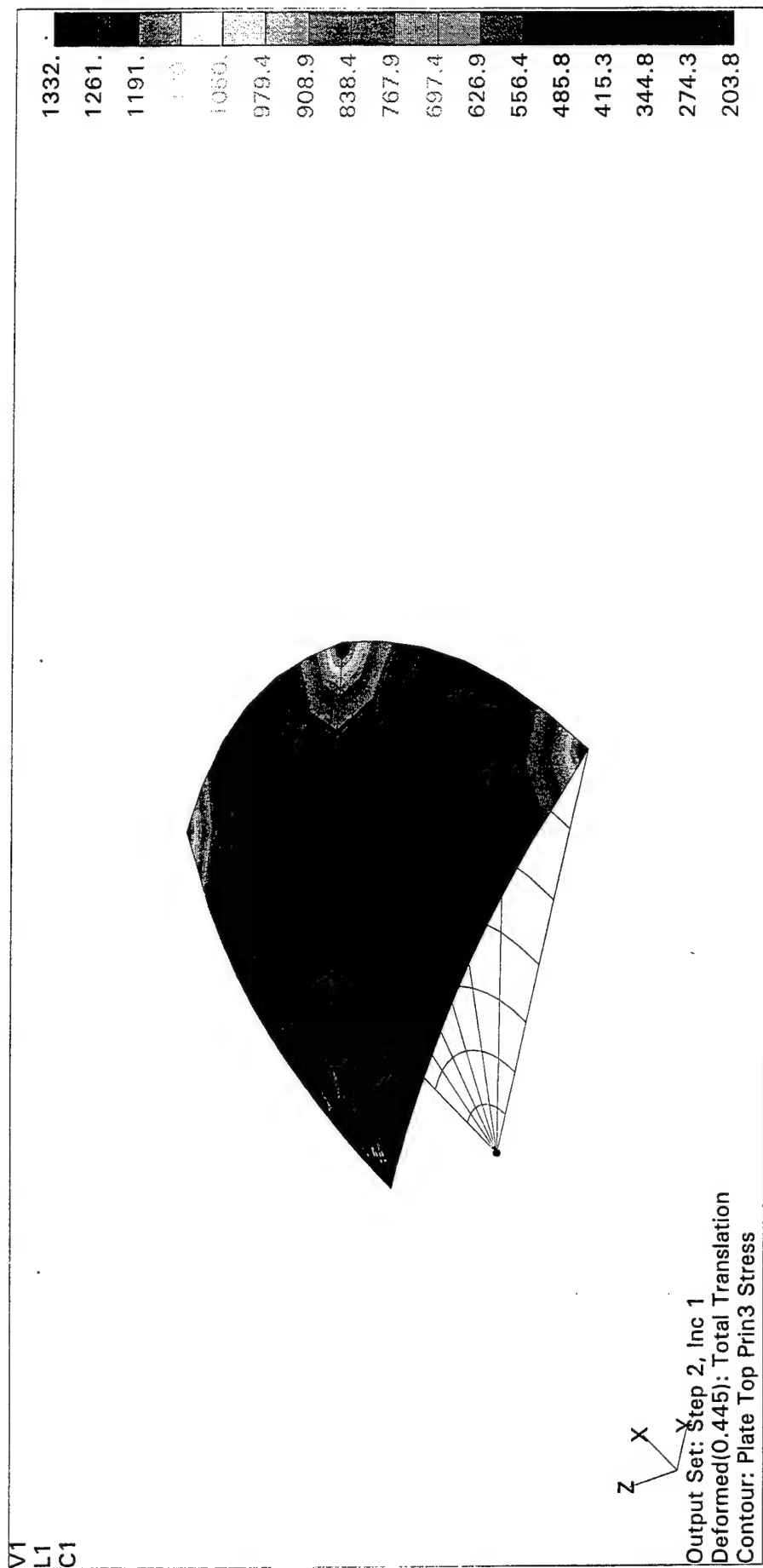


Figure 2

INFLATED DISK



Inflation & 3 Boundary Displacements

Figure 3

VARIATION IN MODEL SHAPE vs EQUIVALENT PARABOLA

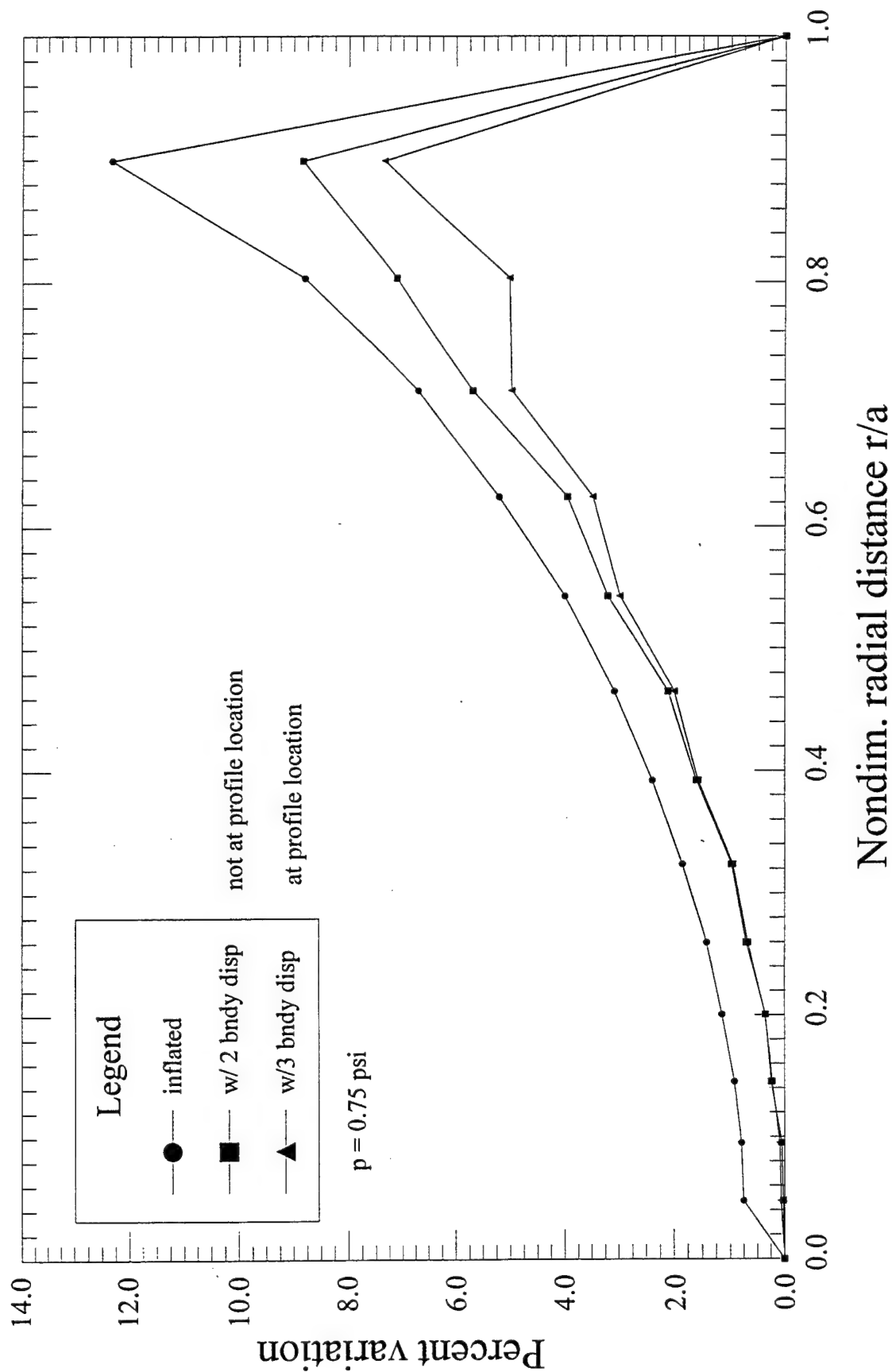


Figure 4

DEVIATION FROM EQUIVALENT PARABOLA

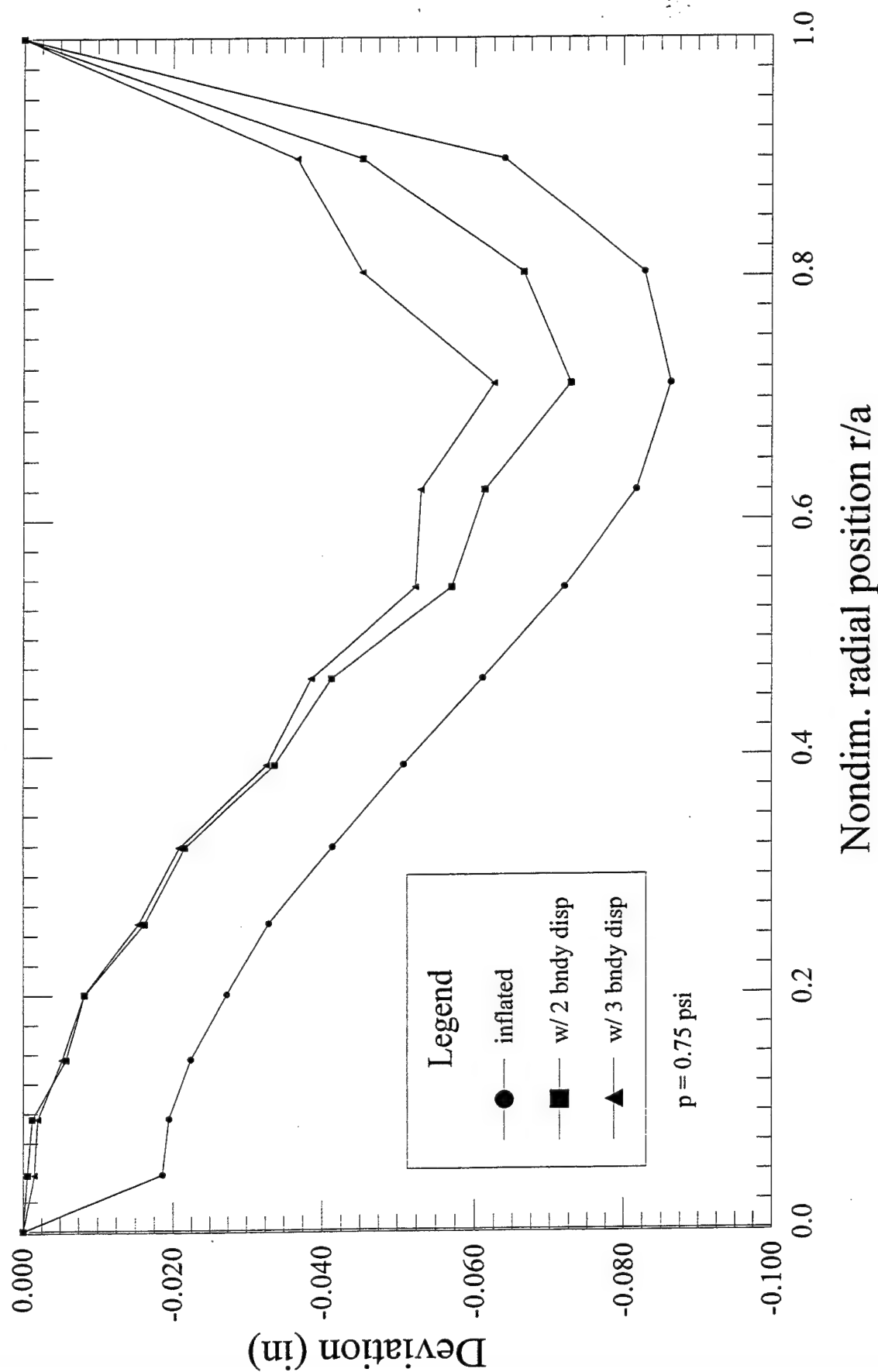


Figure 5

ELECTROMAGNETIC WAVE TRANSFORMATION IN A TWO - DIMENSIONAL -
SPACE - VARYING AND TIME - VARYING MAGNETOPLASMA MEDIUM

Dikshitulu K. Kalluri
Professor
Department of Electrical Engineering

University of Massachusetts Lowell
1 University Avenue
Lowell, MA 01854

Final Report for:
Summer Faculty Research Program
Phillips Laboratory / Geophysics Directorate

Sponsored by:
Air Force Office of Scientific Research
Bolling Air Force Base, DC

and

Phillips Laboratory / Geophysics Directorate

September 1996

ELECTROMAGNETIC WAVE TRANSFORMATION IN A TWO - DIMENSIONAL - SPACE - VARYING AND TIME - VARYING MAGNETOPLASMA MEDIUM

Dikshitulu K. Kalluri
Professor
Department of Electrical Engineering
University of Massachusetts Lowell
Lowell, MA 01854

Abstract

A magnetoplasma goes through a transient state due to various disturbances or stimulations that cause a temporal change in its parameters. Lightning induced effects in the ionosphere or the disturbances caused by the heating experiments are examples of such transient magnetoplasmas.

An electromagnetic wave is transformed in a remarkable way by a transient magnetoplasma. A new perspective on adiabatic analysis based on a slow change of the parameters is discussed.

The relevant field equations for the general case where the parameters of the magnetoplasma vary both in space and time are investigated. Yee's computational algorithm based on 'Finite Difference Time Domain method' is adapted to obtain numerical solution of these equations. Such a solution is useful in exploring new effects. It is also useful in validating the approximate analytical solutions of simpler physical models.

As a next step, the author of this report would like to (1) investigate the numerical stability, numerical dispersion and other numerical analysis aspects of the algorithm. (2) develop a code and investigate the effect of a transient magnetoplasma including the lightning induced effects in the ionosphere and the transformation of an electromagnetic wave during the ionospheric heating experiment.

ELECTROMAGNETIC WAVE TRANSFORMATION IN A TWO - DIMENSIONAL - SPACE - VARYING AND TIME - VARYING MAGNETOPLASMA MEDIUM

Dikshitulu K. Kalluri

I. Introduction

A magnetoplasma goes through a transient state due to various disturbances or stimulations that cause a temporal change in its parameters. Lightning induced effects in the ionosphere or the disturbances caused by the heating experiments are examples of such transient magnetoplasmas. An electromagnetic wave is transformed in a remarkable way by a transient magnetoplasma. The work done by the author last summer [1], [2] under this program showed two such remarkable effects:

1. Frequency Upshifting and Power Intensification of a Whistler Wave by a Collapsing Plasma Medium [1]
2. Conversion of a Whistler Wave into a Controllable Wiggler Magnetic Field by a Collapsing Magnetic Field [2].

An unbounded and homogeneous magnetoplasma with time - varying electron density profile in the presence of a constant static B field was the model used in [1]. An unbounded, homogeneous, and time - invariant plasma medium with a time - varying gyrofrequency was the model used in [2].

In the two cases mentioned above, it was possible to obtain analytical solutions because the differential equation (4.1) for the wave magnetic field , for longitudinal propagation, is relatively simple. It was possible to solve this differential equation for two cases of extreme approximations (i) Step change of the parameter (ii) Adiabatic analysis based on a slow change of the parameter. In this respect a new presentation of the associated adiabatic analysis is given in Section 4.

In the more general case, where the parameters of the magnetoplasma vary both in space and time, the equations are more complicated. It is not possible to obtain analytical solutions.

Numerical method based on Finite Difference Time Domain method using Yee's algorithm is quite suitable to generate computer solution to the general problem. Such a solution is useful in exploring new effects. It is also useful in validating the approximate analytical solutions of simpler physical models.

2. Basic Field Equations for a Cold Time - varying and Space - varying Magnetoplasma Medium

In the presence of a static magnetic field \mathbf{B}_0 , the force equation is given by (2.1)

$$m \frac{d\mathbf{v}_p}{dt} = -q [\mathbf{e}_p + \mathbf{v}_p \times \mathbf{B}_0] \quad (2.1)$$

In the above m is the mass and q is the absolute value of the charge and \mathbf{v}_p is the velocity of an electron. Using the current density \mathbf{j}_p instead of \mathbf{v}_p as the state variable [3], (2.1) may be converted to (2.2)

$$\frac{d\mathbf{j}_p}{dt} = \epsilon_0 \omega_p^2(\mathbf{r}, t) \mathbf{e}_p - \mathbf{j}_p \times \omega_b(\mathbf{r}, t) \quad (2.2)$$

where

$$\omega_b(\mathbf{r}, t) = \frac{q \mathbf{B}_0(\mathbf{r}, t)}{m} \hat{\mathbf{B}}_0 = \omega_b(\mathbf{r}, t) \hat{\mathbf{B}}_0 \quad (2.3)$$

In the above $\hat{\mathbf{B}}_0$ is a unit vector in the direction of \mathbf{B}_0 and $\omega_b(\mathbf{r}, t)$ is the absolute value of the electron gyrofrequency.

The Maxwell's Equations

$$\nabla \times \mathbf{e}_p = -\mu_0 \frac{\partial \mathbf{h}_p}{\partial t} \quad (2.4)$$

$$\nabla \times \mathbf{h}_p = \epsilon_0 \frac{\partial \mathbf{e}_p}{\partial t} + \mathbf{j}_p \quad (2.5)$$

and (2.2) are the basic equations that will be used in discussing the electromagnetic wave transformation by a magnetized cold plasma:

Taking the curl of (2.4) and eliminating \mathbf{h}_p the wave equation for \mathbf{e}_p may be derived:

$$\nabla^2 \mathbf{e}_p - \nabla (\nabla \cdot \mathbf{e}_p) - \frac{1}{c^2} \frac{\partial^2 \mathbf{e}_p}{\partial t^2} - \frac{1}{c^2} \omega_p^2(\mathbf{r}, t) \mathbf{e}_p + \mu_0 \mathbf{j}_p \times \omega_b(\mathbf{r}, t) = 0 \quad (2.6)$$

Similar efforts will lead to a wave equation for the magnetic field:

$$\nabla^2 \dot{\mathbf{h}}_p - \frac{1}{c^2} \frac{\partial^2 \dot{\mathbf{h}}_p}{\partial t^2} - \frac{1}{c^2} \left[\omega_p^2(\mathbf{r}, t) \right] \dot{\mathbf{h}}_p + \epsilon_0 \nabla \omega_p^2(\mathbf{r}, t) \times \mathbf{e}_p + \nabla \times (\mathbf{j}_p \times \mathbf{e}_p) = 0 \quad (2.7a)$$

where

$$\dot{\mathbf{h}}_p = \frac{\partial \mathbf{h}_p}{\partial t} \quad (2.7b)$$

If ω_p^2 and ω_b vary only with t , (2.7) becomes

$$\nabla^2 \dot{\mathbf{h}}_p - \frac{1}{c^2} \frac{\partial^2 \dot{\mathbf{h}}_p}{\partial t^2} - \frac{1}{c^2} \omega_p^2(t) \dot{\mathbf{h}}_p + \epsilon_0 \omega_b(t) (\nabla \cdot \dot{\mathbf{e}}_p) = 0 \quad (2.8)$$

Equations (2.6) and (2.7) involve more than one field variable. It is possible to convert them into higher order equations in one variable. In any case it is difficult to obtain meaningful analytical solutions to these higher order vector partial differential equations.

3. One Dimensional Equations: Longitudinal Propagation, L and R waves

Let us consider the particular case where (1) the variables are functions of one spatial coordinate only, say the z coordinate, (2) the electric field is circularly polarized, (3) the static magnetic field is z directed, and (4) the variables are denoted by

$$\mathbf{e}_p = (\hat{x} \mp j\hat{y}) \mathbf{e}(z, t) \quad (3.1a)$$

$$\mathbf{h}_p = (\pm j\hat{x} + \hat{y}) \mathbf{h}(z, t) \quad (3.1b)$$

$$\mathbf{j}_p = (\hat{x} \mp j\hat{y}) \mathbf{j}(z, t) \quad (3.1c)$$

$$\omega_p^2 = \omega_p^2(z, t) \quad (3.1d)$$

$$\omega_b = \hat{z} \omega_b(z, t) \quad (3.1e)$$

The basic equations for e , h and j take the following simple form:

$$\frac{\partial e}{\partial z} = -\mu_0 \frac{\partial h}{\partial t} \quad (3.2a)$$

$$-\frac{\partial h}{\partial z} = \epsilon_0 \frac{\partial e}{\partial t} + j \quad (3.2b)$$

$$\frac{dj}{dt} = \epsilon_0 \omega_p^2(z, t) e \pm j \omega_b(z, t) j \quad (3.2c)$$

$$\frac{\partial^2 e}{\partial z^2} - \frac{1}{c^2} \frac{\partial^2 e}{\partial t^2} - \frac{1}{c^2} \omega_p^2(z, t) e \mp \frac{j}{c^2} \omega_b(z, t) \frac{\partial e}{\partial t} \mp j \mu_0 \omega_b(z, t) \frac{\partial h}{\partial z} = 0 \quad (3.3a)$$

$$\begin{aligned} & \frac{\partial^2 h}{\partial z^2} - \frac{1}{c^2} \frac{\partial^2 h}{\partial t^2} - \frac{1}{c^2} \omega_p^2(z, t) h + \epsilon_0 \frac{\partial}{\partial z} \omega_p^2(z, t) e \mp j \omega_b(z, t) \frac{\partial^2 h}{\partial z^2} \\ & \pm \frac{1}{c^2} j \omega_b(z, t) \frac{\partial^2 h}{\partial t^2} \mp j \frac{\partial \omega_b(z, t)}{\partial z} \frac{\partial h}{\partial z} \mp j \epsilon_0 \frac{\partial \omega_b(z, t)}{\partial z} \frac{\partial e}{\partial t} = 0 \end{aligned} \quad (3.3b)$$

Even though we assumed only one dimensional space variation, yet we have complicated equations for e and h which are coupled. Equation for h is uncoupled if ω_p and ω_b are functions of time only; in that case (3.3b) reduces to

$$\begin{aligned} & \frac{\partial^2 h}{\partial z^2} - \frac{1}{c^2} \frac{\partial^2 h}{\partial t^2} - \frac{1}{c^2} \omega_p^2(t) h \mp j \omega_b(t) \frac{\partial^2 h}{\partial z^2} \\ & \pm \frac{1}{c^2} j \omega_b(t) \frac{\partial^2 h}{\partial t^2} = 0 \end{aligned} \quad (3.4)$$

4. Adiabatic Analysis for R wave in a time – varying space invariant magnetoplasma medium

The starting point for the adiabatic analysis of the R wave in a time-varying space-invariant magnetoplasma medium is obtained by substituting $\partial/\partial z = -j k$ in (3.4):

$$\frac{d^3 h}{dt^3} - j \omega_b(t) \frac{d^2 h}{dt^2} + [k^2 c^2 + \omega_p^2(t)] \frac{dh}{dt} - j \omega_b(t) k^2 c^2 h = 0 \quad (4.1)$$

Note that this equation for h does not involve the time derivatives of $\omega_b(t)$ or $\omega_p^2(t)$. The technique [3], [4], of obtaining an adiabatic solution of this equation is as follows. A complex instantaneous frequency function is defined such that

$$\frac{dh}{dt} = p(t) h(t) = [\alpha(t) + j \omega(t)] h(t) \quad (4.2)$$

Here $\omega(t)$ is the instantaneous frequency. Substituting (4.2) in (4.1) and neglecting α and all derivatives, a zero order solution may be obtained. The solution gives a cubic in ω giving the instantaneous frequencies of three waves created by the switching action,

$$\omega^3 - \omega_b(t) \omega^2 - (k^2 c^2 + \omega_p^2(t)) \omega + k^2 c^2 \omega_b(t) = 0 \quad (4.3)$$

The cubic has two positive real roots and one negative real root. At $t = 0$, one of the positive roots, say ω_m has a value ω_0 :

$$\omega_m(0) = \omega_0 \quad (4.4)$$

The m th wave is the modified source wave. An equation for α may now be obtained by substituting (4.2) into (4.1) and equating the real part to zero. In the adiabatic analysis we neglect the derivatives and powers of α .

$$\alpha = \dot{\omega} \frac{3\omega - \omega_b(t)}{k^2 c^2 + \omega_p^2(t) - 3\omega^2 + 2\omega \omega_b(t)} \quad (4.5)$$

The approximate solution to (4.1) may now be written as

$$h(t) \approx h_m(t) = H_m(t) \exp \left[j \int_0^t [\omega_m(\tau)] d\tau \right] \quad (4.6)$$

where

$$H_m(t) = H_0 \exp \left[\int_0^t \alpha_m(\tau) d\tau \right] \quad (4.7)$$

The amplitude of the other two modes (waves other than the m th mode) are of the order of the slopes at the origin of $\omega_b(t)$ and $\omega_p^2(t)$ and hence neglected in the adiabatic analysis.

The integral in (4.7) may be evaluated numerically but in the case of only one of the parameters varying with time, it may be evaluated analytically.

In the case of ω_b constant and ω_p^2 varying with time, we can eliminate $\omega_p^2(t)$ from (4.5), by using (4.3) and simplifying:

$$\omega_p^2(t) = \frac{(\omega^2 - k^2 c^2)(\omega - \omega_b)}{\omega} \quad (4.8a)$$

$$\alpha = -\omega \left(\frac{3\omega^2 - \omega\omega_b}{2\omega^3 - \omega^2\omega_b - k^2 c^2 \omega_b} \right), \quad \omega_b \text{ constant} \quad (4.8b)$$

Since the numerator in the bracketed fraction is one half of the derivative of the denominator with respect to ω in (4.8b), it may be written as

$$\alpha dt = -\frac{1}{2} \frac{dr}{r} \quad (4.9)$$

where

$$r = 2\omega^3 - \omega^2\omega_b - k^2 c^2 \omega_b, \quad \omega_b \text{ constant} \quad (4.10)$$

Equation (4.7) reduces to

$$\frac{H_m(t)}{H_0} = \left[\frac{2\omega_0^3 - \omega_b\omega_0^2 - k^2 c^2 \omega_b}{2\omega_m^3 - \omega_b\omega_m^2 - k^2 c^2 \omega_b} \right]^{1/2}, \quad \omega_b \text{ constant} \quad (4.11)$$

In the case of ω_p^2 constant and ω_b varying with time, we can eliminate $\omega_b(t)$ from (4.5) by using (4.3) and simplifying:

$$\omega_b(t) = \omega \left(1 - \frac{\omega_p^2}{\omega^2 - k^2 c^2} \right) \quad (4.12a)$$

$$\alpha = - \frac{\omega (2\omega^2 - 2k^2 c^2 + \omega_p^2)}{(\omega^2 - k^2 c^2)^2 + \omega_p^2 \omega^2 + k^2 c^2 \omega_p^2} \quad (4.12b)$$

As in the previous case we can integrate analytically and write

$$\int_0^t \alpha(\tau) d\tau = \ln \left(\frac{r[\omega(0)]}{r[\omega(t)]} \right)^{1/2} \quad (4.13)$$

where $r(\omega)$ is the denominator in the fraction on the right side of (4.12b). From (4.7)

$$\frac{H_m(t)}{H_0} = \left(\frac{(\omega_0^2 - k^2 c^2)^2 + \omega_p^2 \omega_0^2 + k^2 c^2 \omega_p^2}{(\omega_m^2(t) - k^2 c^2)^2 + \omega_p^2 \omega_m^2(t) + k^2 c^2 \omega_p^2} \right)^{1/2} \quad (4.14)$$

The electric field $E_m(t)$ is easily obtained from $H_m(t)$ by using the wave impedance concept:

$$E_m(t) = \eta_{pm} H_m(t) \quad (4.15a)$$

$$\eta_{pm} = \frac{\eta_0}{n_m} = \frac{\eta_0 \omega_m}{k c} \quad (4.15b)$$

In the above n_m is the refractive index of the medium when the frequency of the signal in the plasma is ω_m .

4A. Modification of the Source R Wave by a Slowly Created Plasma

Let us assume that a R wave of frequency ω_0 is propagating in free space. At $t = 0$ an unbounded homogeneous slowly varying transient plasma is created:

The fields are given by (4.11) with $k c = \omega_0$. A detailed derivation of the equations based on a different formulation is given in [4].

4 B. Modification of the Whistler Wave by a Collapsing Plasma Medium

The mode of propagation of the R wave in the frequency band $0 < \omega < \omega_b$ is called the whistler wave. In this band the refractive index is greater than one. In this section we look at the adiabatic transformation of the whistler wave by a collapsing plasma medium. If n_0 is the refractive index and ω_0 is the frequency of the whistler wave before the collapse begins, the wave magnetic field $H_m(t)$ during the collapse is given by (4.11) where $k^2 c^2 = \omega_0^2 n_0^2$ and the electric field is obtained from (4.15). Denoting the first wave as the modified source wave, i.e., $m=1$ and $\omega_m(0) = \omega_1(0) = \omega_0$

$$\frac{H_1(t)}{H_0} = \left[\frac{2\omega_0^3 - \omega_b \omega_0^2 - n_0^2 \omega_0^2 \omega_b}{2\omega_1^3 - \omega_b \omega_1^2 - n_0^2 \omega_0^2 \omega_b} \right]^{1/2}, \quad \omega_b \text{ constant} \quad (4B.1)$$

$$\frac{E_1(t)}{E_0} = \frac{\omega_1(t)}{\omega_0} \frac{H_1(t)}{H_0}, \quad \omega_b \text{ constant} \quad (4B.2)$$

The refractive index could be quite large when $\omega_0 \ll \omega_b$. In such a case

$$n_0 \approx n_w = \omega_{p0} / (\omega_0 \omega_b)^{1/2}, \quad \omega_0 \ll \omega_b \sim \omega_{p0} \quad (4B.3)$$

$$\omega_1(t \rightarrow \infty) \approx n_w \omega_0 \quad (4B.4)$$

$$\frac{E_1(t \rightarrow \infty)}{E_0} \approx \frac{n_w}{\sqrt{2}} \quad (4B.5)$$

$$\frac{H_1(t \rightarrow \infty)}{H_0} \approx \frac{1}{\sqrt{2}} \quad (4B.6)$$

$$\frac{S_1(t \rightarrow \infty)}{S_0} \approx \frac{n_w}{2} \quad (4B.7)$$

The above equations show that the whistler wave can have a substantial frequency upshift with power intensification of the signal. This aspect is thoroughly examined in [1] for a sudden collapse as well as a slow decay of the electron density of the plasma medium.

Before leaving this topic a comment is in order to explain the extra factor

$$\text{Factor} = \frac{\omega_b - \omega_1(t)}{\omega_b - \omega_0} \quad (4B.8)$$

in (14a) of [1] for $E_1(t)/E_0$ as compared to (4B.2) of this section. In [1], an alternative physical model for the collapsing plasma is assumed. However the final result for the whistler mode is still given by (4B.3) to (4B.7).

4C. Alternative Model for a Collapsing Plasma.

Equation (4.1) is obtained from a formulation where e, h, j are chosen as the state variables. The third state variable is chosen as the current density field j rather than the velocity field v for the following reason. In the process of creating the plasma, the electron density $N(t)$ increases because of the new electrons born at different times. The newly born electrons start with zero velocity and are subsequently accelerated by the fields. Thus all the electrons do not have the same velocity at a given time during the creation of the plasma. Therefore

$$j(t) \neq -q N(t) v(t) \quad (4C.1a)$$

but

$$\Delta j(t) = -q \Delta N_i v_i(t) \quad (4C.1b)$$

In the above ΔN_i is the electron density added at t_i and $v_i(t)$ is the velocity at t of the electrons ΔN_i born at t_i . $j(t)$ is given by the integral of (4C.1b) and not by (4C.1a). j obtained from (4C.1b) is a smooth function of time and has no discontinuities. It fits the requirements of a state variable. The initial conditions, in this formulation, are the continuity of e, h, j at $t = 0$. This is a good model for a building-up plasma. We may ask

the following questions regarding the modeling of a transient plasma. Is this the only model or are there other models? Is this a good model for a collapsing plasma? A lot depends on the physical processes responsible for the temporal change in the electron density [5].

Let us consider the following model for the collapse of the plasma. The decrease in electron density takes place by a process of sudden removal of $\Delta N(t)$ electrons; the velocities of all of the remaining electrons are unaffected by this capture and have the same instantaneous value $v(t)$. The initial conditions in this model are the continuity of e , h and v ; we can use these field variables as the state variables. The state variable equations are

$$\mu_0 \frac{dh}{dt} = j k e \quad (4C.2a)$$

$$\epsilon_0 \frac{de}{dt} = j k h + \epsilon_0 \omega_p^2(t) u \quad (4C.2b)$$

$$\frac{du}{dt} = -e + j \omega_b(t) u \quad (4C.2c)$$

where

$$u = q v / m \quad (4C.2d)$$

and the simplest higher order differential equation, when ω_b is a constant, is in the variable u and is given by

$$\begin{aligned} \frac{d^3 u}{dt^3} - j \omega_b \frac{d^2 u}{dt^2} + [k^2 c^2 + \omega_p^2(t)] \frac{du}{dt} \\ + [g(t) - j \omega_b k^2 c^2] u = 0, \omega_b \text{ constant} \end{aligned} \quad (4C.3a)$$

where

$$g(t) = \frac{d}{dt} [\omega_p^2(t)] \quad (4C.3b)$$

Equation (4C.3a) is slightly different from (4.1). The last term on the left side of (4.3a) has an extra parameter $g(t)$. Consequently, while the equation for ω remains the same as (4.3), the equation for α is a modified version of (4.5) and is given by (4C.4):

$$\alpha = \frac{-g(t) + \dot{\omega} [3\omega - \omega_b]}{[k^2 c^2 + \omega_p^2(t) - 3\omega^2 + 2\omega\omega_b]}, \omega_b \text{ constant} \quad (4C.4)$$

Substituting (4.8a) for $\omega_p^2(t)$ in (4C.4)

$$\alpha = \frac{g(t) - \dot{\omega} [3\omega^2 - \omega_b\omega]}{[2\omega^3 - \omega^2\omega_b - k^2 c^2 \omega_b]}, \omega_b \text{ constant} \quad (4C.5)$$

An expression for $g(t)$ may be obtained by differentiating (4.8a):

$$g(t) = \frac{d}{dt} [\omega_p^2(t)] = \frac{\dot{\omega}}{\omega} [2\omega^3 - \omega^2\omega_b - k^2 c^2 \omega_b], \omega_b \text{ constant} \quad (4C.6)$$

Substituting (4C.6) in (4C.5)

$$\alpha = \frac{\dot{\omega}}{\omega} - \dot{\omega} \frac{3\omega^2 - \omega_b\omega}{[2\omega^3 - \omega^2\omega_b - k^2 c^2 \omega_b]}, \omega_b \text{ constant} \quad (4C.7)$$

The velocity field of the modified source wave is obtained, by analytical integration, as before:

$$\frac{U_1(t)}{U_0} = \exp \left[\int_0^t \alpha_1(\tau) d\tau \right] = \frac{\omega_1(t)}{\omega_0} \left[\frac{2\omega_0^3 - \omega_b\omega_0^2 - n_0^2\omega_0^2\omega_b}{2\omega_1^3 - \omega_b\omega_1^2 - n_0^2\omega_0^2\omega_b} \right]^{1/2}, \omega_b \text{ constant} \quad (4C.8)$$

The electric field (4C.10) is now obtained by noting from (4C.2c)

$$E_1 = j[\omega_b - \omega_1(t)] U_1 \quad (4C.9a)$$

$$E_0 = j[\omega_b - \omega_0] U_0 \quad (4C.9b)$$

$$\frac{E_1(t)}{E_0} = \left[\frac{\omega_b - \omega_1(t)}{\omega_b - \omega_0} \right] \left[\frac{\omega_1(t)}{\omega_0} \right] \left[\frac{2\omega_0^3 - \omega_b \omega_0^2 - n_0^2 \omega_0^2 \omega_b}{2\omega_1^3(t) - \omega_b \omega_1^2(t) - n_0^2 \omega_0^2 \omega_b} \right]^{1/2}$$

, ω_b constant (4C.10)

When $\omega_0 \ll \omega_b \sim \omega_p$, $n_0 \approx n_w$ is large and the first bracketed term on the right side of (4C.10) may be approximated by

$$\frac{\omega_b - \omega_1(t)}{\omega_b - \omega_0} \approx \left[1 + \frac{\omega_0}{\omega_b} - \frac{\omega_p^2}{\omega_b} \sqrt{\frac{\omega_0}{\omega_b}} \right] \approx 1 \quad (4C.11)$$

4D. Modification of the Whistler Wave by a Collapsing Magnetic Field

Equation (4.14) can be directly applied to this case. Let us denote the third mode as the modified source wave, i.e., $\omega_3(0) = \omega_0$ and $kc = n_0 \omega_0$:

$$\frac{H_3(t)}{H_0} = \left(\frac{(\omega_0^2 - n_0^2 \omega_0^2)^2 + \omega_p^2 \omega_0^2 + n_0^2 \omega_0^2 \omega_p^2}{(\omega_3^2(t) - n_0^2 \omega_0^2)^2 + \omega_p^2 \omega_3^2(t) + n_0^2 \omega_0^2 \omega_p^2} \right)^{1/2} \quad (4D.1)$$

In this case it is immaterial whether we choose j or v as the state variable since the continuity of v ensures the continuity of j , the electron density N being a constant.

For the case when $\omega_0 \ll \omega_b \sim \omega_p$, $n_0 \approx n_w$ is large and it can be shown

$$H_3(\infty) \approx H_0 \quad (4D.2a)$$

$$E_3(\infty) \approx 0 \quad (4D.2b)$$

$$\omega_3(\infty) \approx 0 \quad (4D.2c)$$

5 FD - TD Method

In section 4 we chose suitable models and made approximations that permitted us to obtain an approximate analytical solution. These solutions are useful in giving us a qualitative picture of the effects of each type of complexity in the properties of the medium. In this section we shall consider numerical methods to handle the simultaneous presence of several complexities. The finite difference time domain technique [6] - [8] seems to be well suited for handling the problem of transformation of an electromagnetic wave by a time-varying and space-varying magnetoplasma medium.

The starting point is the discretization of the equations for the fields in the magnetoplasma repeated here as (5.1) – (5.3) for convenience:

$$\nabla \times \mathbf{e}_p = -\mu_0 \frac{\partial \mathbf{h}_p}{\partial t} \quad (5.1)$$

$$\nabla \times \mathbf{h}_p = \epsilon_0 \frac{\partial \mathbf{e}_p}{\partial t} + \mathbf{j}_p \quad (5.2)$$

$$\frac{d\mathbf{j}_p}{dt} + \nu \mathbf{j}_p = \epsilon_0 \omega_p^2(\mathbf{r},t) \mathbf{e}_p - \mathbf{j}_p \times \omega_b(\mathbf{r},t) \quad (5.3)$$

where ν is the collision frequency. It is convenient to combine the first two equations above into a second order equation before discretization:

$$\frac{1}{c^2} \frac{\partial^2 \mathbf{e}_p}{\partial t^2} = \nabla^2 \mathbf{e}_p - \nabla (\nabla \cdot \mathbf{e}_p) - \mu_0 \frac{\partial \mathbf{j}_p}{\partial t} \quad (5.4)$$

Let

$$\mathbf{j}_p = (j_x, j_y, j_z) \quad (5.5)$$

$$\mathbf{e}_p = (e_x, e_y, e_z) \quad (5.6)$$

$$\omega_b = \omega_b(l_x, l_y, l_z) \quad (5.7a)$$

$$l_x = \sin \theta \cos \phi \quad (5.7b)$$

$$l_y = \sin \theta \sin \phi \quad (5.7c)$$

$$l_z = \cos \theta \quad (5.7d)$$

Let us further assume that the spatial variations are restricted to the two independent variables x and z only:

$$\omega_b = b(x, z, t) \quad (5.8a)$$

$$\epsilon_0 \omega_p^2 = a(x, z, t) \quad (5.8b)$$

Extension to the three dimensional case is straightforward.

Vector equation (5.3) may be separated into three scalar equations for the Cartesian components of the field variables.

$$\frac{dj_x}{dt} + vj_x = a e_x + b(l_z j_y - l_y j_z) \quad (5.9)$$

$$\frac{dj_y}{dt} + vj_y = a e_y + b(l_x j_z - l_z j_x) \quad (5.10)$$

$$\frac{dj_z}{dt} + vj_z = a e_z + b(l_y j_x - l_x j_y) \quad (5.11)$$

Since

$$\nabla(\nabla \cdot \mathbf{e}_p) = \hat{x} \left(\frac{\partial^2 e_x}{\partial x^2} + \frac{\partial^2 e_z}{\partial x \partial z} \right) + \hat{z} \left(\frac{\partial^2 e_z}{\partial z^2} + \frac{\partial^2 e_x}{\partial x \partial z} \right) \quad (5.12)$$

Equation (5.4) may be written as three scalar equations given below:

$$\frac{1}{c^2} \frac{\partial^2 e_x}{\partial t^2} = \frac{\partial^2 e_x}{\partial z^2} - \frac{\partial^2 e_z}{\partial x \partial z} - \mu_0 \frac{\partial j_x}{\partial t} \quad (5.13)$$

$$\frac{1}{c^2} \frac{\partial^2 e_y}{\partial t^2} = \frac{\partial^2 e_y}{\partial x^2} + \frac{\partial^2 e_y}{\partial z^2} - \mu_0 \frac{\partial j_y}{\partial t} \quad (5.14)$$

$$\frac{1}{c^2} \frac{\partial^2 e_z}{\partial t^2} = \frac{\partial^2 e_z}{\partial x^2} - \frac{\partial^2 e_x}{\partial x \partial z} - \mu_0 \frac{\partial j_z}{\partial t} \quad (5.15)$$

The continuous (x, z) domain is discretized by a set of points which are the intersection points of the lines $i \Delta x$ and $k \Delta z$ and the time domain is discretized by $n \Delta t$: the continuous function $f(x, z, t)$ is represented by the value $f^n(i, k)$:

$$f(x, z, t) = f(i \Delta x, k \Delta z, n \Delta t) = f^n(i, k) \quad (5.16)$$

Using central difference approximations, the various partial derivatives of f at a given point are expressed in terms of the values of the function at the point and at the neighboring points:

$$\frac{\partial f}{\partial t}(i, k, n-1) = \frac{f^n(i, k) - f^{n-2}(i, k)}{2 \Delta t} \quad (5.17)$$

$$\frac{\partial^2 f}{\partial t^2}(i, k, n-1) = \frac{f^n(i, k) - 2f^{n-1}(i, k) + f^{n-2}(i, k)}{(\Delta t)^2} \quad (5.18)$$

$$\frac{\partial f}{\partial x}(i, k, n-1) = \frac{f^{n-1}(i+1, k) - f^{n-1}(i-1, k)}{2 \Delta x} \quad (5.19)$$

$$\frac{\partial f}{\partial z}(i, k, n-1) = \frac{f^{n-1}(i, k+1) - f^{n-1}(i, k-1)}{2 \Delta z} \quad (5.20)$$

$$\frac{\partial^2 f}{\partial x^2}(i, k, n-1) = \frac{f^{n-1}(i+1, k) - 2f^{n-1}(i, k) + f^{n-1}(i-1, k)}{(\Delta x)^2} \quad (5.21)$$

$$\frac{\partial^2 f}{\partial z^2}(i, k, n-1) = \frac{f^{n-1}(i, k+1) - 2f^{n-1}(i, k) + f^{n-1}(i, k-1)}{(\Delta z)^2} \quad (5.22)$$

$$\begin{aligned} \frac{\partial^2 f}{\partial x \partial z}(i, k, n-1) = \\ \frac{f^{n-1}(i+1, k+1) - f^{n-1}(i-1, k+1) - f^{n-1}(i+1, k-1) + f^{n-1}(i-1, k-1)}{4 \Delta x \Delta z} \end{aligned} \quad (5.23)$$

Applying the above finite difference approximations to (5.9) – (5.11) we can get the current density at the n th step in terms of the values of the current density and the electric field at the previous time steps.

$$j_x^n(i, k) = j_x^{n-2}(i, k) + 2 \Delta t \left\{ b^{n-1}(i, k) [l_z j_y^{n-1}(i, k) - l_y j_z^{n-1}(i, k)] + a^{n-1}(i, k) e_x^{n-1}(i, k) - v j_x^{n-1}(i, k) \right\} \quad (5.24)$$

$$j_y^n(i, k) = j_y^{n-2}(i, k) + 2 \Delta t \left\{ b^{n-1}(i, k) [l_x j_z^{n-1}(i, k) - l_z j_x^{n-1}(i, k)] + a^{n-1}(i, k) e_y^{n-1}(i, k) - v j_y^{n-1}(i, k) \right\} \quad (5.25)$$

$$j_z^n(i, k) = j_z^{n-2}(i, k) + 2 \Delta t \left\{ b^{n-1}(i, k) [l_y j_x^{n-1}(i, k) - l_x j_y^{n-1}(i, k)] + a^{n-1}(i, k) e_z^{n-1}(i, k) - v j_z^{n-1}(i, k) \right\} \quad (5.26)$$

Applying central difference formulas (5.17) - (5.23) to (5.13) - (5.15), we get the computational algorithm to update the electric field values at the n th step:

$$\begin{aligned} e_x^n(i, k) = & 2 e_x^{n-1}(i, k) - e_x^{n-2}(i, k) \\ & + \frac{c^2 (\Delta t)^2}{(\Delta z)^2} \left[e_x^{n-1}(i, k+1) - 2e_x^{n-1}(i, k) + e_x^{n-1}(i, k-1) \right] \\ & - \frac{c^2 (\Delta t)^2}{4 \Delta x \Delta z} \left[\begin{aligned} & e_z^{n-1}(i+1, k+1) - e_z^{n-1}(i-1, k+1) \\ & - e_z^{n-1}(i+1, k-1) + e_z^{n-1}(i-1, k-1) \end{aligned} \right] \\ & - \frac{\mu_0 c^2}{2} (\Delta t) \left[j_x^n(i, k) - j_x^{n-2}(i, k) \right] \quad (5.27) \end{aligned}$$

$$\begin{aligned}
e_y^n(i, k) &= 2e_y^{n-1}(i, k) - e_y^{n-2}(i, k) \\
&+ \frac{c^2(\Delta t)^2}{(\Delta x)^2} \left[e_y^{n-1}(i+1, k) - 2e_y^{n-1}(i, k) + e_y^{n-1}(i-1, k) \right] \\
&+ \frac{c^2(\Delta t)^2}{(\Delta z)^2} \left[e_y^{n-1}(i, k+1) - 2e_y^{n-1}(i, k) + e_y^{n-1}(i, k-1) \right] \\
&- \frac{\mu_0 c^2}{2}(\Delta t) \left[j_y^n(i, k) - j_y^{n-2}(i, k) \right] \quad (5.28)
\end{aligned}$$

$$\begin{aligned}
e_z^n(i, k) &= 2e_z^{n-1}(i, k) - e_z^{n-2}(i, k) \\
&+ \frac{c^2(\Delta t)^2}{(\Delta x)^2} \left[e_z^{n-1}(i+1, k) - 2e_z^{n-1}(i, k) + e_z^{n-1}(i-1, k) \right] \\
&- \frac{c^2(\Delta t)^2}{4\Delta x \Delta z} \left[\begin{aligned} &e_x^{n-1}(i+1, k+1) - e_x^{n-1}(i-1, k+1) \\ &- e_x^{n-1}(i+1, k-1) + e_x^{n-1}(i-1, k-1) \end{aligned} \right] \\
&- \frac{\mu_0 c^2}{2}(\Delta t) \left[j_z^n(i, k) - j_z^{n-2}(i, k) \right] \quad (5.29)
\end{aligned}$$

6. Conclusions

An electromagnetic wave is transformed in a remarkable way by a time - varying magnetoplasma medium. The field equation for the general case where the parameters of the magnetoplasma medium vary both in space and time are complicated. FD - TD method of numerical solution is used to generate the computer algorithm to solve the problem. Such a solution is useful in exploring new effects. It is also useful in validating the approximate analytical solutions of simpler physical models.

A code will be developed after investigating the numerical stability, numerical dispersion and other aspects of the algorithm. The code will be used to investigate the effect of a transient magnetoplasma including the lightning induced effects in the ionosphere and the transformation of an electromagnetic wave during the ionospheric heating experiments.

7. REFERENCES

- [1] D. K. Kalluri (1996), " Frequency Upshifting with Power Intensification of a Whistler Wave by a Collapsing Plasma Medium, " *Journal of Applied Physics*, Vol. 79, No. 8, pp. 3895 - 3899.
- [2] D. K. Kalluri (1996), " Conversion of a Whistler Wave into a Controllable Wiggler Magnetic Field," *Journal of Applied Physics*, Vol. 79, No. 9, pp. 6770 - 6774.
- [3] D. K. Kalluri, *Frequency Shifting by a Transient Magnetoplasma Medium*, to be published
- [4] D. K. Kalluri, V. R. Goteti and Andrew Sessler (1993), " WKB Solution for Wave Propagation in a Time - varying Magnetoplasma Medium: Longitudinal Propagation," *IEEE Transactions on Plasma Science*, Vol. 21, No. 1, pp. 70-76.
- [5] N. S. Stepanov (1976), " Dielectric Constant of Unsteady Plasma, " *Sov. Radiophys. and Quant. Electr.*, Vol. 19, No. 7, pp. 683 - 689.
- [6] K. S. Yee (1966), " Numerical Solution of Initial Boundary Value Problems Involving Maxwell's Equations in Isotropic Media, " *IEEE Trans. Antennas and Propagation*, Vol. 14, pp. 302 - 307.
- [7] Allen Taflove, *Computational Electrodynamics*, Boston: Artech. House, 1995.
- [8] L. J. Nickisch and P. M. Franke (1992), " Finite - Difference Time - Domain Solution of Maxwell's Equation for the Dispersive Ionosphere, " *IEEE Antennas and Propagation Magazine*, Vol. 34, No. 5, pp. 34 - 39.

**THICK SECTION CUTTING WITH CHEMICAL OXYGEN-IODINE LASER AND
SCALING LAWS**

**Aravinda Kar
Assistant Professor
Department of Mechanical and Aerospace Engineering
Center for Research and Education in Optics and Lasers**

**University of Central Florida
P. O. Box 162700
Orlando, FL 32816-2700**

**Final Report for:
Summer Faculty Research Program
Phillips Laboratory, Applied Laser Technology Branch (PL/LIDB)**

**Sponsored by:
Air Force Office of Scientific Research
Bolling Air Force Base, DC**

and

Phillips Laboratory, Applied Laser Technology Branch (PL/LIDB)

July 1995

THICK SECTION CUTTING WITH CHEMICAL OXYGEN-IODINE LASER AND SCALING LAWS

Aravinda Kar
Assistant Professor
Department of Mechanical and Aerospace Engineering
Center for Research and Education in Optics and Lasers
University of Central Florida

Abstract

Almost all laser-assisted materials processing involve melting, vaporization and plasma formation. These phenomena affect the utilization of laser energy for materials processing. To account for the effect of these phases, an effective absorptivity is defined, and a simple mathematical model is developed for thick-section stainless cutting with a high power Chemical Oxygen-Iodine Laser (COIL). The model is based on overall energy balance, and it relates the cutting depth with various process parameters that can be used to predict scaled laser materials processing performance to very thick sections. The effects of various process parameters such as laser power, spot size, cutting speed and cutting gas velocity on the cutting depth are discussed. The results of the mathematical model are compared with experimental data. Such comparison provides a means of determining the effective absorptivity during laser materials processing.

THICK SECTION CUTTING WITH CHEMICAL OXYGEN-IODINE LASER AND SCALING LAWS

Aravinda Kar

1. Introduction

Cutting is one of the earliest applications of laser technology. Currently, laser cutting machines are commercially available that are based on CO₂ and Nd:YAG lasers. The Chemical Oxygen-Iodine Laser (COIL) is a high power laser at wavelength 1.315 μm that can be used for various types of materials processing. The basic principle of COIL has been discussed briefly by Kar et al.¹ Atsuta, et al.² investigated the material processing capability of COIL by cutting stainless steel up to 5 mm thick, and demonstrated that the cutting capability of a 1 kW COIL is equivalent to a 1 kW Nd:YAG laser and about 2.5 times better than a 1 kW CO₂ laser. They presented a simple two-parameter model and empirically determined these two parameters by fitting the model to their experimental data in order to predict the scaled cutting capability of COIL².

Earlier studies on laser cutting of materials have been presented by Tikhomirov³, Schuocker⁴, and Powell⁵. The effects of cutting gas jet on laser cutting have been examined by Chryssolouris and Choi⁶, Biermann et al.⁷, and Molian and Baldwin⁸. Ohlsson et al.⁹ carried out a comparative study to examine the effectiveness of the laser and abrasive water jet cutting processes. Thompson¹⁰ presented experimental data for the laser cutting of highly reflective materials such as copper and aluminum. Hack et al.¹¹ used a Nd:YAG laser in a power range up to 2.3 kW to cut materials by using glass fibers to deliver the beam to the workpiece.

Besides experimental studies, mathematical models have also been developed to understand the effects of various process parameters on the cut quality. Schuocker and Abel¹² developed a mathematical model to analyze the material removal process during the laser cutting. Schuocker¹³ discussed the physical mechanism and theory of laser cutting to provide a better understanding of the process. Li and Mazumder¹⁴ presented a model for the laser cutting of wood. Mathematical models for evaporative cutting were developed by Modest and Abakians¹⁵, Bang and Modest¹⁶, and Roy and Modest¹⁷. Belic and Stanic¹⁸, and Belic¹⁹ presented a simple model involving empirical parameters for laser cutting.

This report presents a simple model to examine the effects of absorptivity and the velocity of the cutting gas jet on the kerf depth and width. The results of the model are compared with experimental data to verify the scaling law. In this study, the laser spot is considered to be rectangular because the laser beam that comes out of the resonator of a typical COIL device has rectangular cross section.

2. Mathematical Model

In Ref. [1], a simple scaling law was derived based on a mathematical model that was developed by using a lumped parameter technique in which the overall energy balance was considered without accounting for the pointwise distribution of temperature in the solid and liquid phases of the substrate. That scaling law has the following form.

$$\frac{d}{P} = \frac{A_0}{vw_k + A_3\sqrt{vw_k}} \quad (1)$$

where the coefficients are defined as

$$A_0 = \frac{A}{a_0} \quad (2)$$

$$A_3 = \frac{1}{a_0} \frac{w_k + 2l}{\sqrt{lw_k}} \frac{k(T_m - T_0)}{2\sqrt{\alpha}}, \text{ and} \quad (3)$$

$$a_0 = \rho[c_p(T_m - T_0) + L_m + \beta L_b] \quad (4)$$

Here all variables are in SI units. In Eq. (1), the term A_0 is related to the absorptivity of the workpiece at the laser-material interaction zone, and the term containing A_3 is due to the loss of energy by heat conduction in the solid region of the workpiece. In this study, a COIL beam of rectangular spot is used for which $l = 1.7 \times 10^{-3}$ m and $w = 1.2 \times 10^{-3}$ m. Using the thermophysical data for steel given in Table 1 with the assumptions that $T_0 = 293$ K and $\beta = 0.1$, we find: $A_0 = 8.1 \times 10^{-11}$ A [m³/J] and $A_3 = 3.31 \times 10^{-3}$ [m²/s]^{1/2}. It should be noted that w_k is taken to be equal to w only in Eq. (3) to estimate A_3 , and that its value for all other terms is obtained from an expression as discussed below. First, the effect of plasma on the absorptivity is discussed and then the effect of the cutting gas velocity on the kerf width is presented.

Table 1. Thermophysical properties of iron unless stated otherwise. Due to the lack of high temperature data, these values were used in this study to obtain various results although the substrate was 400 series stainless steel.

Thermophysical properties	Values of thermophysical properties
Density, ρ	7870 kg m ⁻³
Melting point, T_m	1809 K
Boiling point, T_b	3133 K
Specific heat, c_p	456 J kg ⁻¹ K ⁻¹
Thermal conductivity, k	78.2 W m ⁻¹ K ⁻¹
Thermal diffusivity, $\alpha = k/(\rho c_p)$	2.18×10^{-5} m ² s ⁻¹
Latent heat of melting, L_m	2.72×10^5 J kg ⁻¹
Latent heat of boiling, L_b	6.10×10^6 J kg ⁻¹
Density of Nitrogen*, ρ_g	2.786 kg m ⁻³
Viscosity of Nitrogen*, η_g	3.176×10^{-5} Pa s
Molecular diameter of Nitrogen, σ	3.75 Å

*Values calculated at the temperature 1000 K and pressure 827.37 kPa.

2.1. Absorptivity and the plasma effect

During laser cutting, the workpiece is melted and the molten material is removed by using a gas jet which is referred to as the cutting gas. Depending on the laser intensity, relative speed between the laser beam and workpiece, and the cutting gas velocity, the molten material can vaporize to form a plume consisting of the cutting gas molecules, metal vapor, liquid metal droplets, ejecta from the laser-material interaction zone, electrons and ions. This plume will be referred to as the vapor plume in this study. Such a plume is more likely to form in thick-section

laser cutting because it involves more melting and vaporization of materials than in thin-section laser cutting. The vapor plume absorbs laser energy as the beam passes through it, and therefore, it reduces the power of the laser beam that reaches the substrate surface. Considering only absorption in the vapor plume and neglecting the refraction and scattering effects of the plume, the power of the laser beam at the substrate surface can be written as follows by using the Beer-Lambert law.

$$P_s = P e^{-\mu h} \quad (5)$$

However, a fraction of P_s is utilized to cut the workpiece depending on the absorptivity (A_s) of the material at the laser-matter interaction zone. A_s depends on the temperature of the material. The absorbed power that is actually utilized to cut the workpiece is given by

$$P_u = A_s P_s = A_s P e^{-\mu h} = AP \quad (6)$$

where $A = A_s e^{-\mu h}$, which can be referred to as the effective absorptivity.

It should be noted that A_s , μ and h depend on the temperature at the laser-matter interaction zone. Since this temperature depends on the process parameters, A also depends on the process parameters. Using the Hagen-Rubien relation, the absorptivity (A_s) of liquid stainless steel at the melting temperature can be calculated as 39.7% for COIL. Typical values of μ have been reported²⁰ to be 0.5 and 0.1 mm⁻¹ for temperatures 15000 and 18000 K respectively for laser power density of 10⁵ W/cm². Through linear extrapolation of these values, μ is calculated to be 1.97 mm⁻¹ for a plume of temperature 4000 K.

The plume height, h can be estimated by noting that more vapor will be generated as the laser intensity and laser-material interaction time increase, and more vapor will be removed from the interaction zone as the pressure of the cutting gas jet increases. The first two process parameters and the last one will tend to increase and decrease h respectively. Therefore, by taking the laser intensity to be $P/(wl)$, h can be estimated from the following expression.

$$h = K_p \frac{I\tau}{P_g} = K_p \frac{P}{vwP_g} \quad (7)$$

Here K_p is the proportionality constant which will be referred to as the "plume coefficient." It should be noted that as the temperature of the vapor plume increases, the electron density in the plume will increase. If the electron density is sufficiently high such that the plasma frequency is equal to or higher than the frequency of the incident laser radiation, the laser beam will be

completely reflected by the plume. Under this condition, the beam will not be absorbed by the plume and will not reach the substrate surface. Consequently, the vaporization of the workpiece will cease, and the plume will collapse, that is, h will be zero. Since Eq. (7) is derived without considering this phenomenon, it is applicable when the plasma frequency is less than the frequency of the incident laser radiation which is usually the case in laser cutting.

2.2. Effect of cutting gas jet velocity

Cutting gas plays an important role in laser cutting. For certain materials, the presence of oxygen in the cutting gas enhances the cutting capability because of (i) the formation of oxides that increase the absorptivity at the laser-material interaction zone, and (ii) the heat of oxidation that supplies additional energy to the workpiece. The cutting gas also blows away the molten material to produce a definite kerf width. To investigate the material removal capability of the cutting gas, the geometry of the laser-material interaction zone is modeled as shown in Fig. 1 where Fig. 1a shows a three-dimensional view of the workpiece, the kerf width, depth, recast layer and cutting direction. Fig. 1b is a cross sectional view showing the molten layer, vapor plume and the direction in which the melt is removed by the cutting gas. Fig. 1c is a top view of the melt pool whose shape is considered to be a semicircular ring of width δ such that $\delta = (w_i - w_k)/2$. The geometry of the laser-material interaction zone is simplified in this manner in order to derive a scaling law for the kerf width.

A scaling law for the kerf depth is given by Eq. (1) which is based on average energy balance. Now a scaling law for the kerf width is obtained by considering the mass and momentum balances for the melt pool. Under quasi-steady state condition, the amount of solid melted, that is, the amount of melt entering into the melt pool must be equal to the amount of melt leaving the melt pool. This is equivalent to saying that the volume of the melt leaving the pool must be equal to the volume of the kerf, if the density of the workpiece is considered constant which is the case in this study. The mass balance leads to the following relationship between the melt pool width and kerf depth under the approximation that $w_i \approx w_k + \delta$.

$$\frac{\delta}{d} = \frac{2}{\pi} \frac{v}{\bar{v}} \quad (8)$$

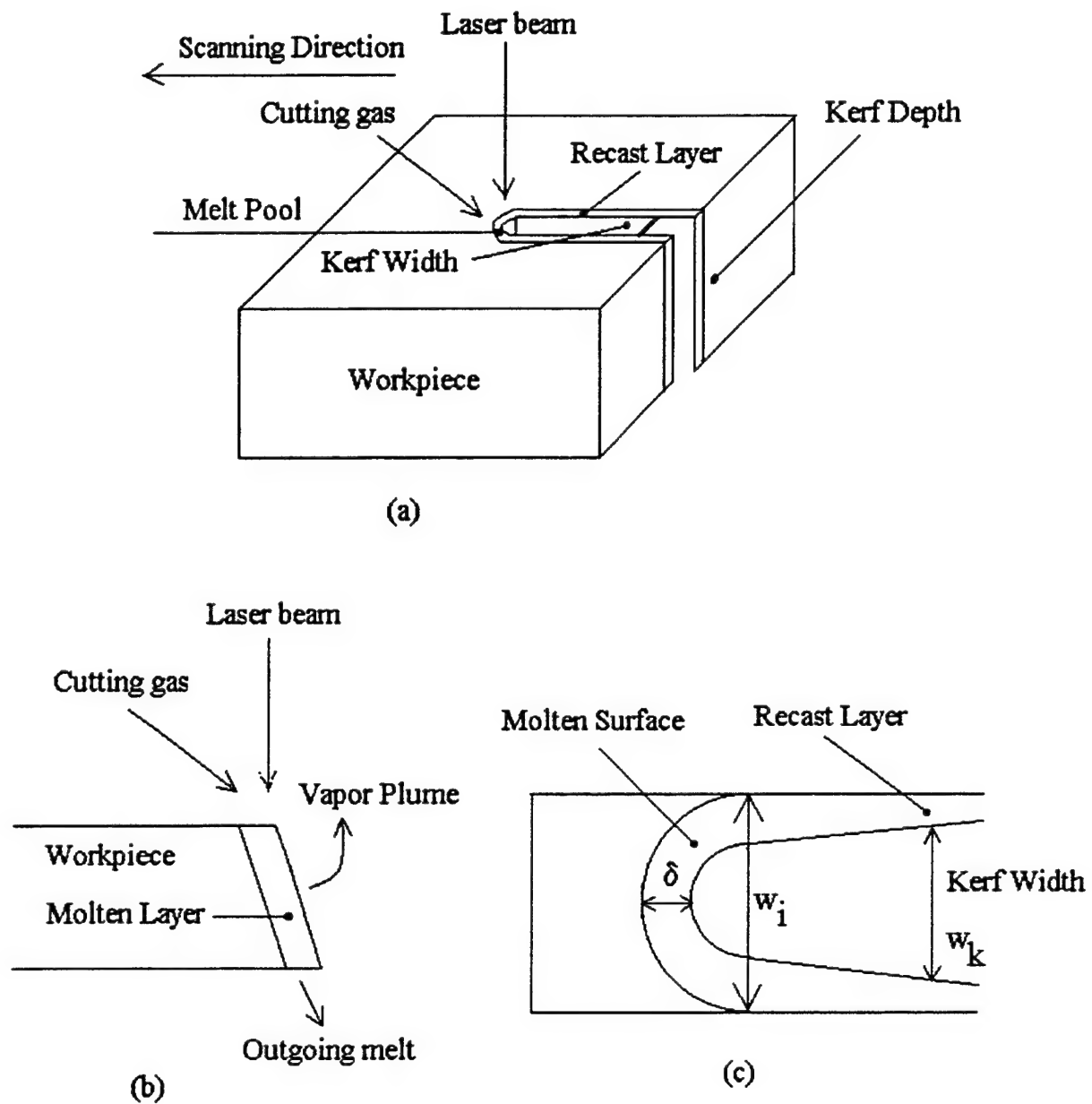


Figure 1. Geometric model for the laser-material interaction zone in laser cutting: (a) Three-dimensional view, (b) Cross sectional view and (c) Top view.

To determine the average velocity, \bar{v} , at which the melt is blown away by the cutting gas, the momentum balance is considered. The drag force generated by the cutting gas at the interface of the melt and cutting gas must be equal to the rate of change of momentum of the melt. This leads to the following expression for the average velocity of the melt under the approximation that

$$w_i - \delta = w_k - \delta \approx w_k.$$

$$\bar{v} = \left[\frac{2 \eta_g v_g d}{\pi \rho w_k \delta} \right]^{1/2} \quad (9)$$

Combining Eqs. (8) and (9), and noting that $\delta = (w_i - w_k)/2$, the following expression is obtained.

$$w_k = \frac{w_i}{1 + \frac{4 \rho v^2 d}{\pi \eta_g v_g}} \quad (10)$$

Eq. (10) involves the velocity and viscosity of the cutting gas. v_g is determined by using the following expression,

$$v_g = \sqrt{2\Delta P_g / \rho_g} = \sqrt{2fP_g / \rho_g} \quad (11)$$

where ΔP_g is the magnitude of the pressure drop across the kerf depth which depends on the kerf geometry and the frictions at the two side walls of the kerf and at the interface of the melt and the cutting gas. In this study, ΔP_g is taken to be a fraction of P_g , that is, $\Delta P_g = fP_g$, where f is a fraction ($0 \leq f \leq 1$). The density of the cutting gas, ρ_g , is determined by using the ideal gas law.

The viscosity of the cutting gas, η_g , is obtained by using the following expression²¹ which is also based on the ideal gas law approximation,

$$\eta_g = 2.927 \times 10^{-8} \frac{M}{\sigma^2} \sqrt{\frac{P_g}{\rho_g}} \quad (12)$$

where M and σ are in units of [gm/mol] and [\AA] respectively, and η_g , P_g and ρ_g are in SI units, that is, in units of [Pa s], [Pa] and [kg/m^3] respectively.

To estimate w_i in Eq. (10), the balance of heat flux at the maximum width of the liquid-solid interface ($y = w/2$) is used, which leads to the following expression under finite difference approximation.

$$w_i = 4\sqrt{\alpha l / v} \frac{T_s - T_m}{T_m - T_0} \quad (13)$$

Here T_s is the temperature at the surface of the melt pool along the center line ($y=0$). Eq. (13) is obtained for a melt pool having a semicircular surface. In this study, T_s is estimated by using the temperature distribution that was derived in Ref. [22] for a rectangular multimode beam. Applying that expression to a TEM_{00} mode beam and a substrate of initial temperature T_m , defining a scaling length $\bar{l} = (l + w)/2 \approx l \approx w$, and setting $v = 0$, the temperature at the center of the beam is found to be

$$T_s - T_m = \sqrt{\frac{\pi}{8}} \frac{A\eta_u P(l + w)}{lwk} \quad (14)$$

Here T_s is approximated as the temperature at the beam center, and $T_s - T_m$ represents the superheating temperature of the melt pool. It should be noted that the temperature distribution in Ref. [22] is based on three-dimensional heat conduction analysis in a semi-infinite medium. However, in laser cutting applications, the workpiece needs to be treated as finite dimensional at least in one direction. Most of the absorbed laser energy goes into heating up the workpiece and supplying the latent heats of melting and boiling, and is lost to the surrounding due to radiation and convection. Especially, the cutting gas can enhance the loss of energy by convection. Only a very small fraction (η_u) of the absorbed energy is utilized to superheat the melt pool, that is, to raise the temperature of the melt pool from T_m to T_s . To account for these phenomena, an energy utilization factor, η_u , which will be referred to as the "melt pool superheating factor," is introduced in Eq. (14).

Combining Eqs. (13) and (14), w_i is found to be

$$w_i = \sqrt{\frac{2\pi\alpha}{l}} \frac{A\eta_u(l + w)}{k(T_m - T_0)w} \frac{P}{\sqrt{v}} \quad (15)$$

Combining Eqs. (1), (10) and (15), the following expression is obtained.

$$vw_k = \frac{\sqrt{\frac{2\pi\alpha}{l}} \frac{A\eta_u(l + w)}{k(T_m - T_0)w} P\sqrt{v}}{1 + \frac{4 A_0 \rho v^2}{\pi \eta_g v_g} \frac{P}{vw_k + A_3 \sqrt{vw_k}}} \quad (16)$$

Eq. (16) is a transcendental equation for w_k that needs to be solved numerically. However, to obtain a simple scaling law, the heat loss term, $A_3\sqrt{vw_k}$ is retained, and w_k in the term $\sqrt{vw_k}$ is replaced with w since the kerf width is usually equal to the laser beam width, that is, $vw_k + A_3\sqrt{vw_k} \approx A_3\sqrt{vw_k} \approx A_3\sqrt{vw}$. Also, v^2 in the denominator is approximated as $v^2 \approx v\alpha / l$. With these simplifications, Eqs. (11), (12) and (16) leads to the following expression.

$$vw_k = \frac{2.51 \sqrt{\frac{\alpha}{l}} \frac{A\eta_u(l+w)}{k(T_m - T_0)w} P\sqrt{v}}{1 + 3.08 \times 10^7 \frac{A_0}{A_3\sqrt{f}} \frac{\rho\rho_g\sigma^2\alpha}{MP_g l\sqrt{w}} P\sqrt{v}} \quad (17)$$

Here all variables are in SI units except M and σ that are in units of [gm/mol] and [\AA] respectively as mentioned earlier. Eq. (17) is the scaling law that is used in this study to investigate the effects of various process parameters on w_k .

Eq. (17) is substituted in Eq. (1) to obtain

$$d = \frac{A_0(1 + B_1 P\sqrt{v})}{B_0\sqrt{v} + A_3\sqrt{\frac{B_0\sqrt{v}}{P}(1 + B_1 P\sqrt{v})}}, \text{ where} \quad (18)$$

$$B_0 = 2.51 \sqrt{\frac{\alpha}{l}} \frac{A\eta_u(l+w)}{k(T_m - T_0)w}, \text{ and} \quad (19)$$

$$B_1 = 3.08 \times 10^7 \frac{A_0}{A_3\sqrt{f}} \frac{\rho\rho_g\sigma^2\alpha}{MP_g l\sqrt{w}} \quad (20)$$

Eq. (18) shows how the kerf depth, d , varies as a function of P and v , while Eq. (1) represents a scaling law for d/P .

3. Results and Discussion

The above mathematical model is used to analyze the effects of various process parameters on the kerf depth and width. The predictions of this model are compared with the experimental data of Ref. [1] where the experimental set up and procedure have been discussed. Numerical values are obtained from this model by using the values of thermophysical properties as listed in

Table 1 where the data for nitrogen and steel are obtained from Refs. [21] and [23] respectively. The cutting gas is taken to be nitrogen at a pressure of 827.37 kPa (120 psi) which was used in Ref. [1]. Since the temperature of the cutting gas at the laser-material interaction zone is unknown, it is taken to be 1000 K to determine the density and viscosity of nitrogen. At this pressure and temperature, the density and viscosity of nitrogen are calculated by using the ideal gas law and Eq. (12) respectively (see Table 1). The molecular diameter of nitrogen is obtained from Ref. [24], and f is taken to be 0.5 in this study.

Figures 2 and 3 show comparisons between the scaling laws derived in this paper and experimental data. The experimental procedures and conditions to collect the data have been discussed in Ref. [1]. The scaling law in Fig. 2 involves only one dependent parameter, kerf

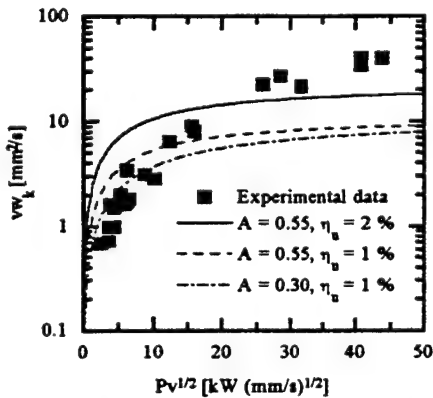


Figure 2. Comparison between experimental data and a scaling law involving the kerf width.

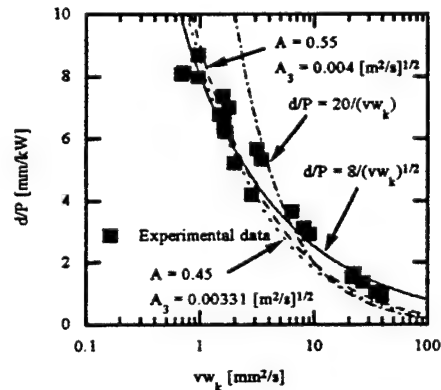


Figure 3. Comparison between experimental data and a scaling law involving the kerf depth and width.

width, and several independent parameters such as laser power, beam scanning speed and cutting gas pressure. On the other hand, the scaling law in Fig. 3 involves two dependent parameters, kerf depth and width, and several independent parameters. Since the effective absorptivity is an unknown parameter, it is varied around the theoretically calculated value of A_e , that is, $A_e = 39.7\%$ (see section 2.1) in order to obtain a good agreement between the model predictions and experimental data. Fig. 2 shows that the product vw_k becomes zero as $P\sqrt{v}$ tends to zero, and it reaches a constant value as $P\sqrt{v}$ increases. However, Fig. 3 shows that the kerf depth per unit laser power (d/P) increases as the product vw_k decreases. In Fig. 3, the curves corresponding to

$d/P = 8/\sqrt{vw_k}$ and $d/P = 20/(vw_k)$, which represent the effects of the heat loss and melt pool energy (energy used to produce the melt pool) respectively in Eq. (1), show that the former curve compares with the experimental data better than the latter curve. This means that the heat loss plays an important role in thick section cutting and that it has to be reduced to increase the depth of cut per unit laser power. It should be noted that the numbers 8 and 20 used for these two curves are selected arbitrarily to obtain good fits between the experimental data and each of these curves.

Figure 4 shows the effect of process parameters on the plume height for various values of the plume coefficient, K_p , and Fig. 5 represents the variation of the effective absorptivity as a function of the plume height for different values of the plume absorption coefficient. The plume

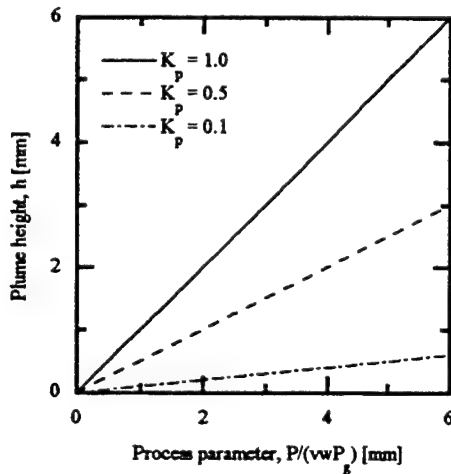


Figure 4. Effect of process parameters on the plume height.

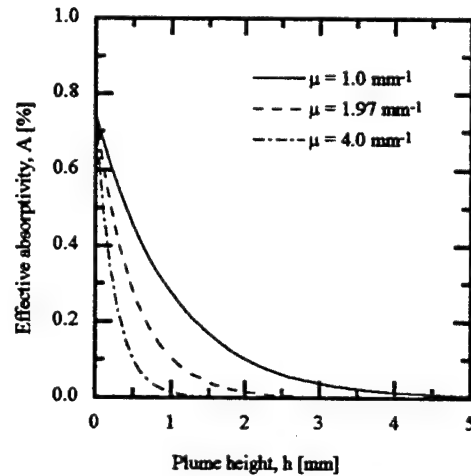


Figure 5. Effect of the plume height on the effective absorptivity.

height varies linearly with the ratio $P/(vwP_g)$ as shown in Fig. 4. Figure 5 shows that the effective absorptivity decreases as the plume height increases, which will reduce the heat input to the substrate. This will eventually produce less amount of vapor and ejecta that enters into the plume. Consequently, the plume volume will not be sustained and its height will decrease. The height of the plume will decrease to a certain value at which the effective absorptivity will be sufficiently

high to cause the formation of enough vapor and ejecta that can sustain the plume volume. This will cause fluctuation in the plume height before the quasi-steady state is reached. It should be noted that Fig. 5 provides a means of determining the plume absorption coefficient by measuring the absorptivity of the melt surface and plume height.

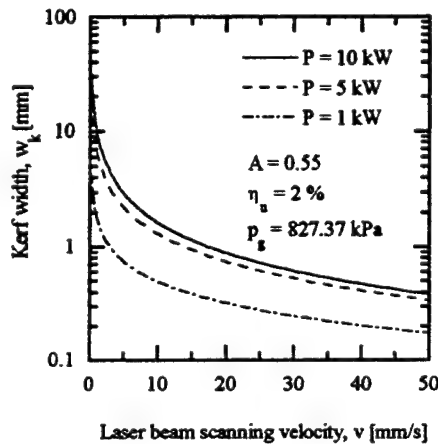


Figure 6. Variation of the kerf width with the laser beam scanning speed for various values of the incident laser power.

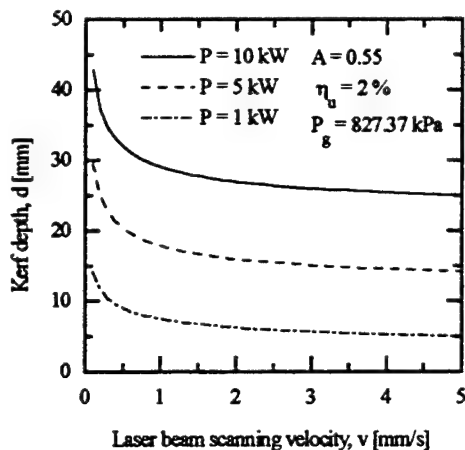


Figure 7. Variation of the kerf depth with the laser beam scanning speed for various values of the incident laser power.

Figures 6 and 7 show the effects of the laser beam scanning velocity on the kerf width and depth respectively for various laser powers. As the scanning velocity increases, the laser-substrate interaction time decreases which reduces the energy input to the workpiece resulting in smaller kerf width and depth. On the other hand, as the laser power increases, the energy input to the workpiece increases resulting in wider and deeper kerf as shown in Figs. 6 and 7 respectively.

Figures 8 and 9 show the effects of the cutting gas pressure on the kerf width and depth respectively for various laser powers. When the laser power increases, the energy input to the workpiece increases which produces wider and deeper kerf as shown in these figures. Figure 8 shows that the kerf width increases with the cutting gas pressure because more molten material is removed at high gas pressures. Since the melt is removed quickly at high gas pressures,

less energy is transferred from the melt to the solid region of the workpiece. This can reduce the

kerf depth as shown in Fig. 9. There is a maximum pressure of the cutting gas at which the maximum amount of the melt can be removed from the laser-material interaction zone. Above

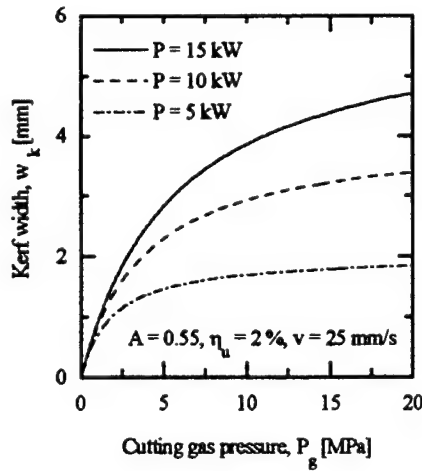


Figure 8. Variation of the kerf width with the cutting gas pressure for various values of the incident laser power.

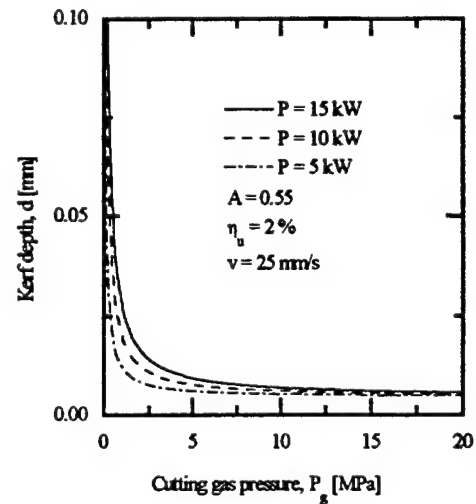


Figure 9. Variation of the kerf depth with the cutting gas pressure for various values of the incident laser power.

this maximum pressure, the cutting gas will have little effect on the kerf width and depth as demonstrated in Figs. 8 and 9 respectively. It should be noted that the cutting gas enhances the cutting performance by removing molten material from the melt zone, and reduces the cutting rate by inducing energy loss due to heat convection. Since the maximum melt removal is achieved at the above-mentioned maximum pressure, the cutting gas pressures exceeding this maximum pressure can be detrimental to the cutting rate because such higher pressures will cause more energy loss by convection than any increase in the melt removal. However, the energy loss by convection at high pressures can be beneficial because it can prevent metallurgical transformations at the kerf walls by cooling them rapidly.

4. Conclusions

Two scaling laws relating the kerf width and depth to various process parameters are presented. This study indicates that thick metal cutting performance may be improved by using a

laser beam of small width. The laser-plume interaction and effective absorptivity play an important role in the cutting performance of a laser beam. The kerf width and depth are affected significantly as the cutting gas pressure increases. However, they reach a constant value after a certain pressure of the cutting gas which means that there is a maximum pressure of the cutting gas that can be used for a given set of cutting parameters.

Nomenclature

A	Effective absorptivity of the substrate due to the plume
A_s	Absorptivity of the substrate in the absence of the plume
c_p	Specific heat of the substrate at constant pressure
d	Kerf depth
h	Height of the vapor plume
k	Thermal conductivity
K_p	Plume coefficient (Proportionality constant)
l	Length of the rectangular COIL beam spot
L_b	Latent heat of boiling
L_m	Latent heat of melting
P	Laser power of the incident beam at the top of the vapor plume
P_a	Laser power absorbed by the workpiece
P_g	Pressure of the cutting gas at the substrate surface
P_s	Laser power at the substrate surface
T_m	Melting temperature of the substrate
T_s	Temperature at the surface of the melt pool along $y=0$
T_0	Initial temperature of the substrate
v	Velocity of the scanning laser beam
\bar{v}	Average velocity of the outgoing melt
v_g	Average velocity of the cutting gas in the kerf
w	Width of the rectangular focal spot
w_i	Maximum width of the liquid-solid interface
w_k	Kerf width

Greek Symbols

α	Thermal diffusivity of the substrate
β	"Boiling coefficient", the fraction of the kerf width above the boiling temperature
δ	Width of the semicircular ring-shaped melt pool
ΔP_g	Magnitude of the pressure drop of the cutting gas across the kerf depth
ΔT	Excess surface temperature ($\Delta T = T_s - T_m$)
η_g	Viscosity of the cutting gas
η_u	Energy utilization factor (Melt pool superheating factor)
μ	Absorption coefficient of the vapor plume
ρ	Density of the substrate
ρ_g	Density of the cutting gas at the pressure P_g
τ	Laser-substrate interaction time

References

1. A. Kar, J. E. Scott and W. P. Latham, "Theoretical and Experimental Studies of Thick-Section Cutting with a Chemical Oxygen-Iodine Laser (COIL)," J. Laser Applications, Vol. 8, No. 3, June 1996, in Press.
2. T. Atsuta, K. Yasuda, T. Matsumoto, T. Sakurai and H. Okado, "COIL and the Material Processing," in Conference on Lasers and Electro-Optics (CLEO)'94, Vol. 8, 1994, OSA Technical Digest Series (Optical Society of America, Washington D. C.), P. 351, 1994.
3. A. V. Tikhomirov, "State of Laser Cutting Technology and Prospects for its Development," Bull. Academy of Sciences of the USSR, Vol. 47, 1983, pp. 23-28.
4. D. Schuocker, "Laser Cutting," in The Industrial Laser Annual Handbook, D. Belforte and M. Levitt, Editors, (PennWell Books, Tulsa, Oklahoma), 1986, pp. 87-107.
5. J. Powell, "Guidelines and Data for Laser Cutting," in The Industrial Laser Annual Handbook, D. Belforte and M. Levitt, Editors, (PennWell Books, Tulsa, Oklahoma), 1990, pp. 56-67.

6. G. Chryssoulouris and W. C. Choi, "Gas Jet Effects on Laser Cutting," in SPIE Proc. CO₂ Lasers and Applications, Vol. 1042, J. D. Evans and E. V. Locke, Editors, (Society of Photo-Optical Instrumentation Engineers - The International Society for Optical Engineering, Bellingham, Washington), 1989, pp. 86-96.
7. B. Biermann, S. Biermann and H. W. Bergmann, "Cutting of Al Alloys using High-Pressure Coaxial Nozzle," J. Laser Applications, Vol. 3, 1991, pp. 13-20.
8. P. A. Molian and M. Baldwin, "Combustion-Assisted Laser Cutting of a Difficult-to-Machine Superalloy," J. Laser Applications, Vol. 4, 1992, pp. 9-14.
9. L. Ohlsson, A. Powell, A. Ivanson and C. Magnusson, "Comparison between Abrasive Water Jet Cutting and Laser Cutting," J. Laser Applications, Vol. 3, 1991, pp. 46-50.
10. A. Thompson, "CO₂ Laser Cutting of Highly Reflective Materials," in The Industrial Laser Annual Handbook, D. Belforte and M. Levitt, Editors, (PennWell Books, Tulsa, Oklahoma), 1989, pp. 149-153.
11. R. Hack, F. Dausinger and H. Hugel, "Cutting and Welding Applications of High Power Nd:YAG Lasers with High Beam Quality," in Laser Materials Processing, Proc. ICALEO'94, Vol. 2500, T. D. McCay, A. Matsunawa and H. Hugel, Editors, (Laser Institute of America and The Society of Photo-Optical Instrumentation Engineers - The International Society for Optical Engineering, Orlando, Florida), 1994, pp. 210-219.
12. D. Schuocker and W. Abel, "Material Removal Mechanism of laser cutting," in SPIE Proc. Industrial Applications of High Power Lasers, Vol. 455, (Society of Photo-Optical Instrumentation Engineers - The International Society for Optical Engineering, Bellingham, Washington), 1984, pp. 88-95.
13. D. Schuocker, "The Physical Mechanism and Theory of Laser Cutting," in The Industrial Laser Annual Handbook, D. Belforte and M. Levitt, Editors, (PennWell Books, Tulsa, Oklahoma), 1987, pp. 65-79.
14. L. Li and J. Mazumder, "A Study of the Mechanism of Laser Cutting of Wood," Forest Products Journal, Vol. 41, 1991, pp. 53-59.
15. M. F. Modest and H. Abakians, "Evaporative Cutting of a Semi-Infinite Body with a Moving CW Laser," J. Heat Transfer, Vol. 108, 1986, pp. 602-607.

16. S. Y. Bang and M. F. Modest "Multiple Reflection Effects on Evaporative Cutting with a Moving CW Laser," J. Heat Transfer, Vol. 113, 1991, pp. 663-669.
17. S. Roy and M. F. Modest "Evaporative Cutting with a Moving CW Laser - Part I: Effects of Three-Dimensional Conduction and Variable Properties," Int. J. Heat Mass Transfer, Vol. 36, 1993, pp. 3515-3528.
18. I. Belic and J. Stanic, "A Method to Determine the Parameters of Laser Iron and Steel Cutting," Optics and Laser Technology, Vol. 19, 1987, pp. 309-311.
19. I. Belic, "A Method to Determine the Parameters of Laser Cutting," Optics and Laser Technology, Vol. 21, 1989, pp. 277-278.
20. A. G. Grigoryants, Basics of Laser Material Processing, (CRC Press, Boca Raton, Florida, U. S. A., 1994), pp. 74, 104.
21. J. O. Hirschfelder, C. F. Curtiss and R. B. Bird, Molecular Theory of Gases and Liquids, (John Wiley & Sons, New York, 1954), p. 14.
22. A. Kar, J. E. Scott and W. P. Latham, "Effects of Mode Structure on Three-Dimensional Laser Heating due to Single or Multiple Rectangular Laser Beams," J. Appl. Phys., Vol. 80, No. 2, July 1996 (in press).
23. E. A. Brandes, editor, Smithells Metals Reference Book, Sixth edition, (Butterworths, London, 1983), pp. 8-2 and 14-1.
24. E. H. Kennard, Kinetic Theory of Gases, (McGraw-Hill, New York, 1938), p. 149.

Associate did not participate in program.

Theory of Electron Acceleration by HF-Excited Langmuir Waves

S. P. Kuo
Professor
Department of Electrical Engineering

Polytechnic University
Route 110
Farmingdale, NY 11735

Final Report for:
Summer Research Projects
Geophysics Directorate of the Phillips Laboratory

Sponsored by:
Air Force Office of Scientific Research
Boiling Air Force Base, Washington, D. C.

August, 1996

Theory of Electron Acceleration by HF-Excited Langmuir Waves

Spencer Kuo
Professor
Department of Electrical Engineering
Polytechnic University

Abstract

A generalized Fokker-Planck equation is derived to describe the diffusion effect of the HF heater-excited Langmuir waves on the background electron distribution. It is shown that the quasi-linear diffusion process alone can not produce very energetic electron flux in 20 eV energy range due to the friction force of the bulk plasma. On the other hand, the diffusion coefficient contributed by nonlinear wave-particle interactions has a nonzero value in that energy range and the friction is not able to balance it. Such a nonlinear diffusion process is driven by the beat product at the frequency sum of two oppositely propagating Langmuir waves. The wide energy range continuously covered by this nonzero nonlinear diffusion coefficient enables some of the electrons to be accelerated continuously from its low energy end to the high energy level. The numerical results show that the energetic electron flux (>20 eV) thus produced is large enough to account for those detected in the in-situ particle measurement using a rocket fly at Tromsø and by the incoherent Backscatter Radar at Arecibo during the HF heating experiments.

Theory of Electron Acceleration by HF-Excited Langmuir Waves

Spencer Kuo

INTRODUCTION

The modification of the ionosphere by the ground-transmitted powerful hf heater waves has been extensively investigated during the past two decades. Among many fascinating phenomena observed in the experiments, the one studied in the present work is the appearance of very large energetic electron fluxes over a very large range during the heating experiments.

When enhanced plasma lines and ion lines were first detected by the backscatter radar in the ionospheric heating experiments at Arecibo, Puerto Rico [Carlson et al., 1972], it gave evidence to support the theoretical prediction [Perkins and Kaw, 1971] that the swelling effect of the ionospheric inhomogeneity should be able to enhance the field amplitude of the O-mode hf heater wave near its reflection height to exceed the threshold level for the excitation of parametric decay instability. However, in the later heating experiments at Arecibo, backscatter radar showed that some of the enhanced plasma lines could, in fact, be detected over a broad height range, even outside the heating region [Carlson et al., 1982], and there was no corresponding ion line enhancement. These enhanced plasma lines then become the indication of the generation of energetic electron fluxes with energies exceeding 10 eV [Carlson et al., 1982]. The radar observations were also confirmed by the in-situ particle measurement during the Tromso heating experiment, via a rocket fly conducted by the Scandinavian group [Grandel et al., 1983; Rose et al., 1985]. Electron fluxes with energy exceeding 25 eV were detected.

The existing theories ascribe the electron acceleration that produces superthermal electrons of the order of a few eV for airglow enhancement to a trapping process [Fejer and Graham, 1974] or a diffusion process [Weinstock, 1974; Nicholson, 1977] in the saturation spectrum of Langmuir waves produced by the parametric instability. Only linear and quasi-linear interactions between electrons and wave fields have been included in these theories. Therefore, a new theory is called for explaining the generation of tens eV electron fluxes observed in the heating experiments.

In the present work, we further elaborate the diffusion effect of Langmuir waves on the background electron distribution. Both quasi-linear and nonlinear process of wave-particle interactions are included in the formulation of the velocity diffusion equation (a generalized Fokker Planck diffusion equation (describing electron acceleration)). Our analysis shows that the cyclotron effect-broadened quasi-linear diffusion may be effective enough to produce up to 10 eV electron fluxes. However, the very energetic ones can only be generated by the diffusion process through nonlinear Landau damping of the beat wave of two oppositely propagating Langmuir waves.

DERIVATION OF ELECTRON DIFFUSION EQUATION

In the following analysis, Langmuir wave excited parametrically in the ionosphere by O-mode hf heater waves are considered to be the source of generating energetic electrons (> 10 eV), whose existence was first deduced from the backscatter radar measurements of enhanced plasma lines [Carlson and Ducan, 1977; Carlson et al., 1982] and confirmed later by the in-situ particle measurements [Grandal et al., 1983]. It is assumed that electron acceleration is via a continuous diffusion process driven by the Langmuir wave fields. A velocity diffusion equation for an electron plasma that is embedded in a uniform magnetic field in the presence of a broad spectrum of Langmuir waves is thus derived to describe the diffusion process.

Our analysis begins with the collisionless kinetic equation

$$\left\{ \frac{\partial}{\partial t} + \mathbf{v} \cdot \frac{\partial}{\partial \mathbf{r}} - \frac{e}{m} [\mathbf{E}(\mathbf{r}, t) + \frac{1}{c} \mathbf{v} \times \hat{\mathbf{z}} B_0] \cdot \frac{\partial}{\partial \mathbf{v}} \right\} f(\mathbf{v}, \mathbf{r}, t) = 0 \quad (1)$$

where $f(\mathbf{v}, \mathbf{r}, t)$ is the electron distribution function as a function of velocity (\mathbf{v}), position (\mathbf{r}), and time (t); the Earth's magnetic field (B_0) is taken to be the z axis of a rectangular coordinate system;

$$\mathbf{E}(\mathbf{r}, t) = -i \sum_k \mathbf{k} \phi_k \exp[i(\mathbf{k} \cdot \mathbf{r} - \omega_k t)] + c.c.$$

is the total electric field of the excited Langmuir waves, where ω_k and \mathbf{k} are the Langmuir wave frequency and wave vector, respectively. The distribution function, f , can be generally expressed as the sum of four parts [Dupree, 1966; Kuo and Cheo, 1981]:

$$f = \langle f \rangle + f^{(e)} + \tilde{f} + f_m = \langle f \rangle + f_1 + f_m \quad (2)$$

where $\langle f \rangle$ is the average distribution function; $f^{(e)}$ is the phase coherent response to the electric field, $\mathbf{E}(\mathbf{r}, t)$; \tilde{f} corresponds to the phase incoherent portion due to the nonlinear wave-wave interaction; f_m represents all other effects that are neglected here; the fluctuating portion of the distribution function, $f_1 = f^{(e)} + \tilde{f}$, can be Fourier-expanded as $\sum_k f_k \exp[i(\mathbf{k} \cdot \mathbf{r} - \omega_k t)]$.

Along the trajectory defined by

$$\frac{d}{dt} \mathbf{r} = \mathbf{v} \quad \text{and} \quad \frac{d}{dt} \mathbf{v} = -\left(\frac{eB_0}{mc}\right) \mathbf{v} \times \hat{z} \quad (3)$$

the equations for the average part ($\langle f \rangle$) and the fluctuating part (f_1) of the distribution function after substituting (2) into (1) are obtained as follows:

$$\frac{d}{dt} \langle f \rangle = i \frac{e}{m} \frac{\partial}{\partial \mathbf{v}} \cdot \sum_k \mathbf{k} \phi_k^* f_k + c.c. \quad (4)$$

$$\frac{d}{dt} f_k \exp[i(\mathbf{k} \cdot \mathbf{r} - \omega_k t)] = -i \frac{e}{m} \exp[i(\mathbf{k} \cdot \mathbf{r} - \omega_k t)]$$

$$\left\{ \phi_k \mathbf{k} \cdot \frac{\partial}{\partial \mathbf{v}} \langle f \rangle + \sum_{k' \neq k} [\phi_k \mathbf{k}' \cdot \frac{\partial}{\partial \mathbf{v}} f_{k-k'} - \phi_k^* \mathbf{k}' \cdot \frac{\partial}{\partial \mathbf{v}} f_{k+k'}] \right. \\ \left. + \sum_{k' \neq k} [\phi_{k-k'} (\mathbf{k} - \mathbf{k}') \cdot \frac{\partial}{\partial \mathbf{v}} f_{k'} + \phi_{k+k'} (\mathbf{k} + \mathbf{k}') \cdot \frac{\partial}{\partial \mathbf{v}} f_{k'}^*] \right\} \quad (5)$$

where $f_{k-k'}$ ($\phi_{k-k'}$) and $f_{k+k'}$ ($\phi_{k+k'}$) represent the amplitudes of the fluctuating distribution functions (electrical potential) bearing the phase functions varying in space and time in the forms of $\exp\{i[(\mathbf{k} - \mathbf{k}') \cdot \mathbf{r} - (\omega_k - \omega_{k'})t]\}$ and $\exp\{i[(\mathbf{k} + \mathbf{k}') \cdot \mathbf{r} - (\omega_k + \omega_{k'})t]\}$, respectively. On the RHS of (5), while the first and the second terms in the braces stem from the phase coherent responses to the electric field ($\mathbf{E}(\mathbf{r}, t)$), the third term is contributed from the nonlinear wave-wave interactions. Since in the diffusion process

under consideration, only wave-particle interaction is relevant, the wave-wave interaction term will be dropped in the following analysis of electron acceleration. Integrating (5) along the unperturbed trajectory defined by (3) and substituting the resultant form of f_k into (4), we can readily obtain the diffusion equation in a rather complicated form. The detail of integration is presented in the Appendix. This equation can be much simplified by the following approximations which can be reasonably made for the ionospheric heating experiments. The theoretical work [e.g., Fejer and Kuo, 1973; Perkins et al., 1974] shows that the saturation spectrum of Langmuir waves excited by the parametric decay instability is distributed in a narrow cone with an azimuthal symmetry with respect to the Earth's magnetic field. It is thus reasonable to assume that $\langle f \rangle$ is also azimuthally symmetric in the velocity space around the geomagnetic field. Further, the Langmuir wave spectrum is noted to peak along the magnetic field. We may expect the background electron distribution to be modified primarily in the direction of Earth's magnetic field. Thus in the present study, only electron acceleration along the magnetic field is considered to be significant, and the transverse component of the distribution function is assumed to maintain Maxwellian [i.e., $\langle f \rangle = h(v_\perp)g(v_z, t)$, where $h(v_\perp) = (m/2\pi T_e) \exp(-mv_\perp^2/2T_e)$].

With these assumptions in hand, the diffusion equation (A11) presented in the Appendix, after the integration over the transverse velocity coordinates (i.e., $\int v_\perp dv_\perp d\theta$), is reduced to a modified Fokker-Planck equation for $g(v_z, t)$ as

$$\frac{\partial}{\partial t} g = \frac{\partial}{\partial v_z} \left(D \frac{\partial}{\partial v_z} - A \right) g - \frac{\partial^2}{\partial v_z^2} \left(D_1 \frac{\partial}{\partial v_z} - A_1 \right) g \quad (6)$$

The diffusion coefficient (D), the friction coefficients (D_1 and A_1) associated with the higher order terms are defined, respectively, to be

$$\begin{aligned} D &= D^L + D_+^{NL} + D_-^{NL}, & A &= A^L + A_+^{NL} + A_-^{NL} \\ D_1 &= D_{1+} + D_{1-} & A_1 &= A_{1+} + A_{1-} \end{aligned}$$

$$\text{where } \begin{pmatrix} D^L \\ A^L \end{pmatrix} = 2\pi \left(\frac{e}{m} \right)^2 \sum_{k, \ell} \left(\frac{1}{\frac{m}{T_e} \frac{\ell \Omega}{k_z}} \right) k_z^2 |\phi_k|^2 \Lambda_\ell(\alpha) \delta(\omega - k_z v_z - \ell \Omega) \quad (7)$$

$$\begin{pmatrix} D_{\pm}^{NL} \\ A_{\pm}^{NL} \\ D_{1\pm} \\ A_{1\pm} \end{pmatrix} = 2\pi \left(\frac{e}{m}\right)^4 \sum_k |\phi_k|^2 |\phi_{k'}|^2 \sum_{\ell, q} \frac{k_z (k_z \pm k'_z)}{(\omega - k_z v_z - \ell \Omega)^2} \begin{pmatrix} a_{\ell, q}^{\pm} \\ \frac{m}{T_e} \frac{(\ell \pm q) \Omega}{k_z \pm k'_z} a_{\ell, q}^{\pm} \\ b_{\ell, q}^{\pm} \\ \frac{m}{T_e} \frac{(\ell \pm q) \Omega}{k_z \pm k'_z} b_{\ell, q}^{\pm} \end{pmatrix} \\
\times \delta[\omega \pm \omega' - (k_z \pm k'_z) v_z - (\ell \pm q) \Omega] \quad (8)$$

$$\text{and } a_{\ell, q}^{\pm} = 2\pi \int_0^{\infty} dv_{\perp} v_{\perp} h(v_{\perp}) \left\{ k_z k'_z \frac{J_{\ell}(\beta) J_q(\beta')}{\omega - k_z v_z - \ell \Omega} \right. \\
\left. + \frac{k_{\perp} k'_{\perp}}{2} \left[\frac{J_{\ell-1}(\beta) J_{q\pm 1}(\beta')}{\omega - k_z v_z - (\ell-1) \Omega} + \frac{J_{\ell+1}(\beta) J_{q\mp 1}(\beta')}{\omega - k_z v_z - (\ell+1) \Omega} \right] \right\}^2 \quad (9)$$

$$b_{\ell, q}^{\pm} = 2\pi \int_0^{\infty} dv_{\perp} v_{\perp} h(v_{\perp}) k'_z J_{\ell}(\beta) J_q(\beta') \left\{ k_z k'_z \frac{J_{\ell}(\beta) J_q(\beta')}{\omega - k_z v_z - \ell \Omega} \right. \\
\left. + \frac{k_{\perp} k'_{\perp}}{2} \left[\frac{J_{\ell-1}(\beta) J_{q\pm 1}(\beta')}{\omega - k_z v_z - (\ell-1) \Omega} + \frac{J_{\ell+1}(\beta) J_{q\mp 1}(\beta')}{\omega - k_z v_z - (\ell+1) \Omega} \right] \right\} \quad (10)$$

and the relationship

$$\frac{1}{\omega - k_z v_z - \ell \Omega} = P \frac{1}{\omega - k_z v_z - \ell \Omega} - i\pi \delta(\omega - k_z v_z - \ell \Omega)$$

is employed; the subscript "k" of ω in the above equations has been dropped for simplicity.

In (7), $\alpha = k_{\perp}^2 T_e / m \Omega^2$, and $\Lambda_n(\alpha) = I_n(\alpha) \exp(-\alpha)$, where I_n is the modified Bessel function of order n . The modified Fokker-Planck equation, (6), contains all the information about the quasi-linear and the lowest order nonlinear diffusion processes of Langmuir waves on electrons in a magnetized plasma. The quasi-linear and the nonlinear

diffusion processes are evidenced by the Deltafunction in (7) and the two Deltafunctions in (8), respectively. It is shown in (8) that the coefficients with the subscript "+" (i.e., D_+^{NL} , A_+^{NL} , D_{1+} , and A_{1+}) and with the subscript "-" (i.e., D_-^{NL} , A_-^{NL} , D_{1-} , and A_{1-}) represent the nonlinear interaction processes between electrons and the beat products, $\exp[-i(\omega \pm \omega')t]$ of the two Langmuir waves $\exp(-i\omega t)$ and $\exp(-i\omega' t)$.

ELECTRON ACCELERATION BY LANGMUIR WAVE TURBULENCE

For the evaluation of the coefficients given in (7) and (8), the idealized model used in Nicholson [1977] for the Langmuir wave spectrum is adopted here:

$$\begin{aligned}
 |\phi_k|^2 &= \frac{3.4(\nu_e / \omega_0) P^2 n_0 T_e}{(1 - P^{-1/2}) k_m^4} && \text{for both } 0 < \theta < \theta_0 \\
 & && \text{and } \pi - \theta_0 < \theta < \pi \\
 &= 0 && \text{for } \theta_0 < \theta < \pi - \theta_0
 \end{aligned} \tag{11}$$

where θ is the angle between the Langmuir wave vector (\mathbf{k}) and the Earth's magnetic field (\mathbf{B}_0); k_m corresponds to the Langmuir waves with peak intensities; θ_0 defined by $\cos^{-1}(P^{-1/2})$ is the maximum θ of the Langmuir waves; P is the squared ratio of the local electromagnetic pump field to the threshold field for the parametric decay instability. The other parameters in (11), n_0 , T_e , ν_e , ω_0 , have their conventional meanings as the local electron density, the electron temperature measured in the unit of electron volts, the electron-ion collision frequency, and the incident electromagnetic pump wave frequency, respectively.

For achieving the electron acceleration from the bulk region to the tail region, the diffusion coefficients must remain non-vanishing values through a wide range in the velocity space. The conditions can be derived from the Deltafunctions in (7), (8), and (11), which are rewritten as follows:

$$\delta(k - k_m) \delta(\omega - k_z v_z - \ell \Omega) = |k_m v_z|^{-1} \delta(k - k_m) \delta(\cos \theta - \cos \theta_1) \tag{12}$$

$$\begin{aligned} & \delta(k - k_m) \delta[\omega - \omega' - (k_z - k'_z) v_z - (\ell - q) \Omega] \\ & = |k_m v_z|^{-1} \delta(k - k_m) \delta[\cos \theta - (\cos \theta_2 + \cos \theta')] \end{aligned} \quad (13)$$

$$\begin{aligned} & \delta(k - k_m) \delta[\omega + \omega' - (k_z + k'_z) v_z - (\ell + q) \Omega] \\ & = |k_m v_z|^{-1} \delta(k - k_m) \delta[\cos \theta - (\cos \theta_3 - \cos \theta')] \end{aligned} \quad (14)$$

where

$$\begin{aligned} \cos \theta &= k_z / k_m, \cos \theta' = k'_z / k_m, \cos \theta_1 = (\omega_m - \ell \Omega) / k_m v_z, \\ \cos \theta_2 &= -(\ell - q) \Omega / k_m v_z, \text{ and } \cos \theta_3 = [2 \omega_m - (\ell + q) \Omega] / k_m v_z. \end{aligned} \quad (15)$$

The dispersion relation of Langmuir waves is approximately represented by $\omega \sim \omega' \sim \omega_m = \omega_{pe} (1 + 3k_m^2 / 2k_d^2)$ for propagation in a weakly ionized plasma at small angles with respect to the Earth's magnetic field, i.e., $(\Omega_e^2 / \omega_{pe}^2) \sin^2 \theta \ll 1$, where k_m , k_d , and ω_{pe} , are respectively, the wave number of Langmuir waves with peak intensity, the Debye wave number, and the local electron plasma frequency.

Since θ_0 is the maximum propagation angle of Langmuir waves, $\cos \theta_0 < \cos \theta$. We deduce that

$$\cos \theta_0 \leq |\cos \theta_1|, |\cos \theta_2 + \cos \theta'|, |\cos \theta_3 - \cos \theta'| \leq 1 \quad (16)$$

from the zero of the arguments of the Deltafunctions on the RHS's of (12) - (14). With the aid of (15), the inequalities in (16) yield the following three ranges of v_z

$$(1) \quad |\omega_m - \ell \Omega| / k_m \leq |v_z| \leq |\omega_m - \ell \Omega| / k_m \cos \theta_0 \quad (17a)$$

$$\begin{aligned} (2)-(A) \quad & \Omega / 2k_m \leq |v_z| \leq |\ell - q| \Omega / 2k_m \cos \theta_0 \\ -(B) \quad & |v_z| \geq |\ell - q| \Omega / 2k_m (1 - \cos \theta_0) \end{aligned} \quad (17b)$$

$$\begin{aligned} (3)-(A) \quad & |2\omega_m - (\ell + q) \Omega| / 2k_m \leq |v_z| \leq |2\omega_m - (\ell + q) \Omega| / 2k_m \cos \theta_0 \\ -(B) \quad & |v_z| \geq |2\omega_m - (\ell + q) \Omega| / k_m (1 - \cos \theta_0) \end{aligned} \quad (17c)$$

that assure the non-zeros of (1) D^L and A^L , (2) D_-^{NL} , A_-^{NL} , D_{1-} , and A_{1-} and (3) D_+^{NL} , A_+^{NL} , D_{1+} , and A_{1+} , respectively. The two sub-ranges, (2)-(A) and (2)-(B), overlap as $\cos\theta_0 \leq 1/3$, namely, $P \geq 9$ because θ_0 is defined by $\cos^{-1}(P^{-1/2})$, where P is the squared ratio of the local electromagnetic pump field to the threshold field for the parametric decay instability. The other two subranges, (3)-(A) and (3)-(B), also overlap as $\cos\theta_0 \leq 1/3$. While (2)-(A) and (3)-(B) are determined for Langmuir wave pairs propagating in opposite directions along the geomagnetic field, (2)-(B) and (3)-(A) are found for those propagating in the same direction along the geomagnetic field. Substituting (11) and (12) into (7) and integrating it over k yield

$$\left(\frac{D^L}{A^L} \right) = 4\pi^2 \left(\frac{e}{m} \right)^2 \frac{3.4(v_e/\omega_0)P^2 n_0 T_e}{(1-P^{-1/2})} \sum_{\ell=-\infty}^{\infty} \left(\frac{1}{\frac{m}{T_e} \frac{\ell\Omega}{k_m \cos\theta_1}} \right) \frac{\cos^2\theta_1 \Lambda_{\ell}(\alpha_m)}{k_m v_z} \\ \times [H(|v_z| - |\omega_m - \ell\Omega|/k_m) - H(|v_z| - |\omega_m - \ell\Omega|/k_m \cos\theta_0)]$$

where $\alpha_m = (k_m^2 T_e / m\Omega^2) \sin^2\theta_1$ and $H(x)$ is the Heaviside step function. The sufficient condition for the continuous acceleration of electrons requires that the ranges of v_z be overlapped for either large negative $\ell < (\omega_m/\Omega) - (1 - \cos\theta_0)^{-1}$ or large positive $\ell > (\omega_m/\Omega) + (1 - \cos\theta_0)^{-1}$ as found from (17a). In other words, overlap of quasi-linear diffusion regions can occur in a wide range of v_z with the aid of cyclotron harmonic shift.

However, it is noted from (18) that $A^L/D^L \sim -v_z(m/T_e)|\ell|\Omega/(\omega_m + |\ell|\Omega)$ for a large value of $k_m v_z$ (i.e., a large positive or negative value of ℓ). If only the quasi-linear diffusion effect is considered, namely, if we only retain the terms associated with D^L and A^L in (8):

$$\frac{\partial}{\partial t} g = \frac{\partial}{\partial v_z} (D^L \frac{\partial}{\partial v_z} - A^L) g \quad (19)$$

the steady state solution of (19) obtained by taking $(\partial/\partial t)g = 0$ has the Maxwellian form of

$$g(v_z, t \rightarrow \infty) \propto \exp\{-(m/2T_e)[|\ell|\Omega/(\omega_m + |\ell|\Omega)]v_z^2\}$$

in each cyclotron shifted region. The effective temperature of this modified distribution function is $(\omega_m + |\ell|\Omega)T_e/|\ell|\Omega$ that approximately equals the unperturbed electron temperature, T_e for a large $|\ell|$ (i.e., a large $k_m v_z$). This result shows that quasi-linear diffusion itself cannot produce very energetic electron fluxes (with $(1/2)mv_z^2 \geq (1/2)m(\ell\Omega/k_m)^2 \sim 10$ eV) because it is impeded by the friction force. This force, represented by A^L , is related to a finite Larmor radius (FLR) effect resulting from the coupling of electron parallel motion with transverse motion in the presence of Langmuir wave fields.

We next examine for other possible electron acceleration mechanisms the nonlinear wave-particle interaction terms neglected in (19), namely, $(D_-^{NL}, A_-^{NL}, D_{1-}, A_{1-})$ and $(D_+^{NL}, A_+^{NL}, D_{1+}, A_{1+})$, that correspond to the cases of Langmuir wave pairs propagating along the same and the opposite directions, respectively. Since $A_-^{NL}/D_-^{NL} \sim (m/T_e)v_z \sim A_{1-}/D_{1-}$ in the large parallel velocity (v_z) region, the diffusion of electrons is also impeded by frictions and no energetic electron flux can be produced by the process of nonlinear wave-particle interactions when the two Langmuir waves propagate in the same direction along the geomagnetic field. By contrast, it is found from (8) that in the region: $v_z > 2\omega_m/(1 - \cos\theta_0)k_m$,

$$D_+^{NL} \sim (2\pi)^3 \left(\frac{e}{m}\right)^4 \left[\frac{3.4(v_e/\omega_0)P^2 n_0 T_e}{(1 - P^{-1/2})} \right]^2 \left(\frac{4\omega_m}{k_m^4 v_z^6} \right) (1 - \cos\theta_0 - 2\frac{\omega_m}{k_m v_z})$$

$$D_{1+} \sim -v_z D_+^{NL} \quad (20)$$

and

$$A_+^{NL} \sim A_{1+} \sim 0 \quad (\text{negligibly small}).$$

The frictions are not able to prevent electrons from being accelerated in this case when electrons interact with the beat product (at the frequency sum) of two Langmuir waves that propagate in the opposite directions.

We note that the diffusion coefficients in this case have the largest values in comparison with those in the other two cases. Hence, in the calculation of the steady state

distribution function (i.e., $g(v_z, t \rightarrow \infty)$) for $v_z > 2\omega_m / (1 - \cos\theta_0)k_m$, only the coefficients given in (20) need to be retained in (6), i.e.,

$$\frac{\partial}{\partial v_z}(D_+^{NL} - \frac{\partial}{\partial v_z}D_{1+})\frac{\partial}{\partial v_z}g(v_z, t \rightarrow \infty) = 0 \quad (21)$$

The result is

$$g(v_z, t \rightarrow \infty) = g(v_{z1})[1 - \frac{F(\bar{v}_z, \bar{v}_{z1})}{F(\bar{v}_{z2}, \bar{v}_{z1})}] + g(v_{z2})\frac{F(\bar{v}_z, \bar{v}_{z1})}{F(\bar{v}_{z2}, \bar{v}_{z1})} \quad (22)$$

where $\bar{v}_z = v_z - v_c$, $\bar{v}_{z1,2} = v_{z1,2} - v_c$, and $v_c = 2\omega_m / (1 - \cos\theta_0)k_m$;

$$F(x, \bar{v}_{z1}) = \frac{1}{5}(x^5 - \bar{v}_{z1}^5) + \frac{5}{4}v_c(x^4 - \bar{v}_{z1}^4) + \frac{10}{3}v_c^2(x^3 - \bar{v}_{z1}^3) + 5v_c^3(x^2 - \bar{v}_{z1}^2) \\ + 5v_c^4(x - \bar{v}_{z1}) + v_c^5 \ln x / \bar{v}_{z1} \quad \text{for } v_c < v_{z1} < v_z < v_{z2}.$$

(22) holds for any $v_{z2} > v_z$ and $g(v_{z2}) \rightarrow 0$ as $v_{z2} \rightarrow \infty$. One can show that in a wide range of $v_z > v_c$, $g(v_z) \sim g(v_{z1}) \sim g(v_c)$, predicting the formation of a flat electron distribution (i.e., a plateau) in the tail region. This prediction agrees qualitatively with the observations reported in Carlson et al. [1982].

COMPARISON WITH EXPERIMENTAL OBSERVATIONS

The level of the plateau depends upon the value of $g(v_c)$. It is seen in (17c) that regions (3)-(A) and (3)-(B) become to overlap when $P \geq 9$ and that region (3)-(A) coincides with the quasi-linear diffusion region defined by (17a) for the case of $\ell = q = 0$. In fact, the plateau starts to be formed by the quasi-linear diffusion process in the superthermal region defined by (17a) for $\ell = 0$. This superthermal plateau can be further extended to the very energetic region defined by (3)-(B) in (17c) through the nonlinear diffusion process of electrons that interact with the beat waves having the sum frequencies of Langmuir wave pairs propagating in the opposite directions along the geomagnetic field. Therefore, $g(v_c)$ has the value of the distribution function in the superthermal plateau, that is $g(v_c) \leq g(5v_{th}) \sim n_0 \exp(-12.5)/(2\pi)^{1/2} v_{th}$, where $v_{th} (= (T_e/m)^{1/2})$ is the

electron thermal velocity. The energetic electron flux between the velocity interval (v_{z1} , v_{z2}), is then given by

$$\Phi \leq n_0 \exp(-12.5)(v_{z2}^2 - v_{z1}^2) / (2\pi)^{1/2} 2v_{th} \quad (23)$$

Under the typical ionospheric F region condition: $n_0 = 3 \times 10^5 \text{ cm}^{-3}$, $v_{th} \sim 1.8 \times 10^7 \text{ cm/sec}$, the calculated Φ from (23) is $2 \times 10^8 \text{ cm}^{-2} \text{ sec}^{-1}$ for $v_{z1} = 1.3 \times 10^8 \text{ cm/sec}$ $v_{z2} = 1.8 \times 10^8 \text{ cm/sec}$ corresponding to electron energies of 10 eV and 20 eV respectively. This theoretical energetic electron flux is greater than the experimentally deduced result, $(2 - 4) \times 10^7 \text{ cm}^{-2} \text{ sec}^{-1}$ [Carlson et al., 1982], by one order of magnitude. This difference is large enough to offset the simplifications used in the theoretical calculation.

The diffusion process discussed here will continue to proceed into the energy region exceeding 20 eV. Though there is no friction force to stop the diffusion, the maximum energy of the electron flux is limited by the finite size of the interaction region and the magnitude of the diffusion coefficients, which all depend on the pump power. Therefore, the proposed acceleration mechanism can also explain the generation of very energetic ($> 25 \text{ eV}$) electron flux measured in situ by Grandal et al. [1983] during Tromso's heating experiment. It should be noted that the energy of the electron flux in the radar measurements is inferred by the phase velocity ω/k of the enhanced plasma line, which is assumed to be excited by the electron flux through resonant wave-particle interaction. Since k is fixed by the radar frequency, i.e., $k = 2 k_{\text{radar}}$, and $\omega \cong \omega_{pe}$ for an eigen mode, the maximum energy of the detectable electron flux in the radar measurement is limited by the F peak density of the ionosphere, which corresponds to about 20 eV at Arecibo with 430 MHz radar.

CONCLUSION

The diffusion effect of Langmuir wave fields on the background electron distribution is evaluated as the process of generating energetic electrons deduced in the measurements of enhanced plasma lines at Arecibo [Carlson et al., 1982] and detected in the in-situ particle measurements at Tromso [Grandal et al., 1983]. Both quasi-linear and nonlinear processes of wave-particle interactions are analyzed in a generalized Fokker-Planck equation. Our analysis shows that the quasi-linear diffusion may be effective

enough to produce energetic electron flux with energies up to about 10 eV. However, the very energetic electron flux in the energy range from 10 to 20 eV reported in Carlson et al. [1982] and in the region exceeding 25 eV measured by Grandal et al. [1983] can only be generated by the nonlinear diffusion process of electrons that interact with the Langmuir wave pairs propagating in directions opposite to each other along the magnetic field. The proposed mechanism can indeed produce the energetic electron flux observed in HF ionospheric heating experiments.

ACKNOWLEDGMENT:

The author gratefully acknowledges useful discussions with Keith Groves, Santimay Basu, Ed Weber, Paul Kossey, and John Heckscher. This work was completed at the Air Force Phillips Laboratory, Hanscom AFB, MA, whose hospitality is appreciated.

REFERENCES

- Carlson, H. C., W. E. Gordon, and R. L. Showen, High frequency induced enhancements of the incoherent scatter spectrum at Arecibo, *J. Geophys. Res.*, 77, 1242, 1992.
- Carlson, H. C., V. B. Wickwar, and G. P. Mantas, Observation of fluxes of superthermal electron accelerated by HF excited instabilities, *J. Atmos. Terr. Phys.*, 44, 1089, 1992.
- Fejer, J. A., and K. N. Graham, Electron acceleration by parametrically excited Langmuir waves, *Radio Sci.*, 9, 1081, 1996.
- Grandal et al., Preliminary results from the HERO project, in-situ measurements of ionospheric modifications, using sounding rockets, *Proc. Int'l Symp Active Experiments in Space*, EAS, SP-195, 75, 1983.
- Kuo, K. P., and B. R. Cheo, Turbulent heating of parametric instabilities in unmagnetized plasmas, *Phys. Fluids*, 24, 1104, 1981.
- Kuo, S. P., and J. Huang, Nonlinear wave phenomena in ionospheric modification by powerful radio waves, *Current Topics in the Physics of Fluids*, 1, 357, 1994.
- Nichelson, D. R. Magnetic field effects on electrons during ionospheric modifications, *J. Geophys. Res.*, 82, 1839, 1977.
- Weinstock, J., Enhanced airglow, electron acceleration and parametric instabilities, *Radio Sci.*, 9, 1085, 1974.

APPENDIX

To solve (5), we decompose f_k into a sum of its linear parts f_k^L and nonlinear part, f_k^{NL} i.e., $f_k = f_k^L + f_k^{NL}$, where

$$\frac{d}{dt} f_k^L \exp[i(\mathbf{k} \cdot \mathbf{r} - \omega_k t)] = -i \frac{e}{m} \exp[i(\mathbf{k} \cdot \mathbf{r} - \omega_k t)] \phi_k \mathbf{k} \cdot \frac{\partial}{\partial \mathbf{v}} < f > \quad (\text{A1})$$

and

$$\begin{aligned} \frac{d}{dt} f_k^{NL} \exp[i(\mathbf{k} \cdot \mathbf{r} - \omega_k t)] = & -i \frac{e}{m} \exp[i(\mathbf{k} \cdot \mathbf{r} - \omega_k t)] \\ & \sum_{k' \neq k} [\phi_k \mathbf{k}' \cdot \frac{\partial}{\partial \mathbf{v}} f_{k-k'} - \phi_k^* \mathbf{k}' \cdot \frac{\partial}{\partial \mathbf{v}} f_{k+k'}] \end{aligned} \quad (\text{A2})$$

Using the cylindrical coordinate systems: $\bar{\mathbf{v}} = v_\perp (\hat{x} \cos \theta + \hat{y} \sin \theta) + \hat{z} v_z$, $\bar{\mathbf{k}} = k_\perp (\hat{x} \cos \varphi + \hat{y} \sin \varphi) + \hat{z} k_z$, $\bar{\mathbf{k}}' = k'_\perp (\hat{x} \cos \varphi' + \hat{y} \sin \varphi') + \hat{z} k'_z$, and the notations $\theta_1 = \theta - \varphi$, $\theta'_1 = \theta - \varphi'$, $\eta = k_\perp v_\perp / \Omega$, and $\eta' = k'_\perp v_\perp / \Omega$, where $\Omega = eB_0/mc$ is the electron cyclotron frequency, the right hand side (RHS) terms of (A1) and (A2) become

$$\mathbf{k} \cdot \frac{\partial}{\partial \mathbf{v}} < f > = [k_\perp \cos \theta_1 \frac{\partial}{\partial v_\perp} + k_z \frac{\partial}{\partial v_z}] < f >$$

and

$$\mathbf{k}' \cdot \frac{\partial}{\partial \mathbf{v}} f_{k \mp k'} = \{k'_\perp [\cos \theta'_1 \frac{\partial}{\partial v_\perp} - \sin \theta'_1 \frac{1}{v_\perp} \frac{\partial}{\partial \theta}] + k'_z \frac{\partial}{\partial v_z}\} f_{k \mp k'},$$

where $< f >$ is assumed to be an azimuthally symmetric function, and (A1) and (A2) are integrated along the unperturbed trajectory to be

$$f_k^L = \frac{e}{m} \phi_k e^{-i\eta \sin \theta_1} \sum_{\ell} \frac{e^{i\ell \theta_1}}{\omega_k - k_z v_z - \ell \Omega} Q^L < f > \quad (A3)$$

and

$$f_k^{NL} = -i \frac{e}{m} e^{-i\eta \sin \theta_1} \int_0^\infty d\tau e^{i(\omega_k - k_z v_z) \tau} e^{i\eta \sin(\theta_1 - \Omega \tau)} \\ \sum_{k' \neq k} (\phi_{k'} \{k'_\perp [\cos(\theta'_1 - \Omega \tau) \frac{\partial}{\partial v_\perp} - \sin(\theta'_1 - \Omega \tau) \frac{1}{v_\perp} \frac{\partial}{\partial \theta}] + k'_z \frac{\partial}{\partial v_z}\} f_{k-k'}(v_\perp, \theta - \Omega \tau, v_z) \\ - \phi_{k'}^* \{k'_\perp [\cos(\theta'_1 - \Omega \tau) \frac{\partial}{\partial v_\perp} - \sin(\theta'_1 - \Omega \tau) \frac{1}{v_\perp} \frac{\partial}{\partial \theta}] + k'_z \frac{\partial}{\partial v_z}\} f_{k+k'}(v_\perp, \theta - \Omega \tau, v_z)) \quad (A4)$$

where the operator

$$Q^L = J_\ell(\eta) [(\ell \Omega / v_\perp) \partial / \partial v_\perp + k_z \partial / \partial v_z] \quad (A5)$$

$f_{k \mp k'}$ are defined approximately by the following equations

$$\frac{d}{dt} f_{k \mp k'} \exp \{i[\mathbf{k} \mp \mathbf{k}'] \cdot \mathbf{r} - (\omega_k \mp \omega_{k'}) t\} = \\ -i \frac{e}{m} \exp \{i[\mathbf{k} \mp \mathbf{k}'] \cdot \mathbf{r} - (\omega_k \mp \omega_{k'}) t\} [\phi_k \mathbf{k} \cdot \frac{\partial}{\partial \mathbf{v}} f_{k'}^\mp - \phi_{k'}^\mp \mathbf{k}' \cdot \frac{\partial}{\partial \mathbf{v}} f_k^L] \quad (A6)$$

and the notations $f_{k'}^+ = f_{k'}^L$, $f_{k'}^- = f_{k'}^{L*}$, $\phi_{k'}^+ = \phi_{k'}$, and $\phi_{k'}^- = \phi_{k'}^*$, are employed.

Using the same procedure, (A6) are integrated to be

$$\begin{aligned}
 f_{k\mp k'} = & \left(\frac{e}{m}\right)^2 \phi_k \phi_{k'}^{\mp} \sum_{\ell, n} \frac{e^{-i\eta \sin \theta_1} e^{\pm i\eta' \sin \theta_1'} e^{i\ell \theta_1} e^{\mp i n \theta_1'}}{\omega_k \mp \omega_{k'} - (k_z \mp k'_z) v_z - (\ell \mp n) \Omega} \\
 & \left\{ \pm i \frac{k_{\perp} k'_{\perp}}{\Omega} \sin(\varphi - \varphi') J_n(\eta') J_{\ell}(\eta) \right. \\
 & \left[\frac{1}{\omega_k' - k_z' v_z - n\Omega} \left(\frac{n\Omega}{v_{\perp}} \frac{\partial}{\partial v_{\perp}} + k_z' \frac{\partial}{\partial v_z} \right) - \frac{1}{\omega_k - k_z v_z - \ell\Omega} \left(\frac{\ell\Omega}{v_{\perp}} \frac{\partial}{\partial v_{\perp}} + k_z \frac{\partial}{\partial v_z} \right) \right] \langle f \rangle \\
 & + [J_{\ell}(\eta) \left(\frac{\ell\Omega}{v_{\perp}} \frac{\partial}{\partial v_{\perp}} + k_z \frac{\partial}{\partial v_z} \right) \pm J_{\ell}'(\eta) \left(\frac{nk_{\perp}}{v_{\perp}} \right)] \frac{J_n(\eta')}{\omega_k' - k_z' v_z - n\Omega} \left(\frac{n\Omega}{v_{\perp}} \frac{\partial}{\partial v_{\perp}} + k_z' \frac{\partial}{\partial v_z} \right) \langle f \rangle \\
 & \mp [J_n(\eta') \left(\frac{n\Omega}{v_{\perp}} \frac{\partial}{\partial v_{\perp}} + k_z' \frac{\partial}{\partial v_z} \right) \pm J_n'(\eta') \left(\frac{\ell k_{\perp}'}{v_{\perp}} \right)] \frac{J_{\ell}(\eta)}{\omega_k - k_z v_z - \ell\Omega} \left(\frac{\ell\Omega}{v_{\perp}} \frac{\partial}{\partial v_{\perp}} + k_z \frac{\partial}{\partial v_z} \right) \langle f \rangle \}
 \end{aligned} \tag{A7}$$

Substituting (A7) into (A4), the integration can be carried out to be

$$f_k^{NL} = f_{k-}^{NL} + f_{k+}^{NL} \tag{A8}$$

where
$$f_{k\mp}^{NL} = \left(\frac{e}{m}\right) \phi_k e^{-i\eta \sin \theta_1} \sum_{\ell} \frac{e^{i\ell \theta_1}}{\omega_k - k_z v_z - \ell\Omega} Q_{\mp}^{NL} \langle f \rangle \tag{A9}$$

and the operators Q_{\mp}^{NL} are defined to be

$$\begin{aligned}
Q_{\mp}^{NL} = & \pm \left(\frac{e}{m}\right)^2 \sum_{k'} |\phi_{k'}|^2 \sum_{n,q} \frac{e^{\mp i(n-q)\theta_1}}{\omega_k - k_z v_z - [\ell \mp (n-q)]\Omega} \{J_q(\eta') [i(\frac{k_{\perp} k'_{\perp}}{\Omega}) \sin(\varphi - \varphi')] \\
& + (\frac{q\Omega}{v_{\perp}}) \frac{\partial}{\partial v_{\perp}} + k'_z \frac{\partial}{\partial v_z} + \frac{k'_z k_z}{\omega_k - k_z v_z - \ell\Omega}] \mp (\ell \mp n) (\frac{k_{\perp}}{v_{\perp}}) J'_q(\eta') \} \\
& \frac{1}{(\omega_k \mp \omega'_k) - (k_z \mp k'_z) v_z - (\ell \mp n)\Omega} \{ (\frac{k_{\perp} k'_{\perp}}{2\Omega}) [J_{\ell-1}(\eta) J_{n\mp 1}(\eta') - J_{\ell+1}(\eta) J_{n\pm 1}(\eta')] \\
& + i 2 J_{\ell}(\eta) J_n(\eta') \sin(\varphi - \varphi')] + k_z k'_z \frac{J_{\ell}(\eta) J_n(\eta')}{\omega_k - k_z v_z - \ell\Omega} \} [(n \mp \ell) \frac{\Omega}{v_{\perp}} \frac{\partial}{\partial v_{\perp}} + (k'_z \mp k_z) \frac{\partial}{\partial v_z}]
\end{aligned}
\tag{A10}$$

With the aid of (A3) and (A9), a diffusion equation is derived from (4) to be

$$\begin{aligned}
\frac{d}{dt} \langle f \rangle = & i \left(\frac{e}{m}\right)^2 \frac{\partial}{\partial v} \cdot \sum_k \mathbf{k} |\phi_k|^2 e^{-i\eta \sin \theta_1} \sum_{\ell} \frac{e^{i\ell \theta_1}}{\omega_k - k_z v_z - \ell\Omega} (Q^L + Q_-^{NL} + Q_+^{NL}) \langle f \rangle \\
& + c. c.
\end{aligned}
\tag{A11}$$